PET Imaging of Histone Deacetylases in the Brain using Silicon-Fluoride Acceptors

En Zhao, Department of Chemistry

McGill University, Montréal, QC

October 2023

A thesis submitted to McGill University in partial fulfillment of the requirements of the degree of Master of Science.

Acknowledgements

Throughout my journey in graduate studies and the composition of this thesis, I have been fortunate to receive extensive support from various sources. Foremost, I extend my profound gratitude to my supervisors, Prof. Jean-Philip Lumb and Prof. Alexey Kostikov, for their unwavering guidance, encouragement, and inspiration throughout my pursuit of advanced education.

I would also like to express my appreciation for the engaging discussions on both chemistry and life that I have had with my colleagues. In particular, I wish to acknowledge Dr. Thomas Singleton, Mr. Hyunjune June, Dr. Burham Hussein, Mr. Wenyu Chen, Mr. Simon Edelmann, and Mr. Darcy Burley for their invaluable editorial contributions during the thesis-writing process. In particular, I would like to extend my thanks towards Dr. Thomas Singleton, Dr. Burham Hussein, and Mr. Wenyu Chen for their input and extensive help in the editing of this thesis.

I would also like to thank all members of my fellow Lumb group members for their input in chemistry discussions and advice during my studies. Thank you to Carlos Razziel Azpilcueta Nicolas, Dr. Haiyan Huang, Madison Carroll, Derek Meng, Jackie Wu, Xueqing Wang, Laura Jeliazkov, and Yiming Zhang. I would also like to acknowledge members of the Gleason research group Ryan Berett and Zhizhong Gao for their extensive help in developing and troubleshooting the bioassays, as well as members of the Auclair research group Chunling Lan and Sanjay Campbell for their help with the UV detector and microwave reactor. I would also like to thank Mr. Peter Kunach of Rosa-Neto research group for his extensive help and input in PET image reconstruction and analysis.

The completion of this thesis would not have been possible without the dedicated assistance of the department's supporting staff. Special thanks go to Dr. Robin Stein and Dr. Tara Sprules for their expertise in NMR, Nadim and Alex for their assistance with HRMS, Arturo Aliaga for assisting with all the animal work, and the entire McGill Neurological Institute PET unit for their help in radiosynthesis. I am equally grateful to all the diligent staff members in the departmental stores. I would like to extend special thanks our industry partners Fuzionaire Theranostics for funding the project as well as Paraza Pharmaceuticals for their help and input in this project. In particular I would like to thank Dr. Christopher Waldmann, Dr. Alexandre Larivée, Bren jordanatienza, Prashant deore, Patrick deroy, and Carl Estrada for their frequent and helpful input.

Finally, I would like to thank my family for their continuous and unconditional support and encouragement throughout my studies, without whom none of this would have been possible.

Abstract / Abstrait

Histone deacetylases (HDACs) is a family of epigenetic enzymes which control vital biological processes, most importantly gene activation. Dysregulation of HDACs in the brain is implicated in Alzheimer's and Parkinson's diseases, and neuropsychiatric disorders. Mapping of HDAC levels within the normal and pathological brain can be accomplished via positron emission tomography (PET) using recently developed tracers [^{11}C]Martinostat and [^{18}F]Bavarostat. Widespread use of these tracers is hampered by their challenging radiosynthesis and poor radiochemical yields. We developed new potential HDAC PET tracers while leveraging the superior radiochemistry of silicon-fluoride acceptors (SiFAs). When attached to silicon, non-radioactive ^{19}F can undergo isotopic exchange with PET radioisotope 18F under mild conditions with high RCY. The resulting tracer is chemically identical to the precursor, negating the need for HPLC purification. SiFA usefulness is usually limited by their poor pharmacokinetic properties due to the bulky lipophilic groups required to prevent hydrolysis of the Si-F bond in vivo. However, in this case lipophilicity of these groups is leveraged to confer blood-brain barrier permeability, similarly to the adamantyl group. Pharmacokinetic properties can be further tuned by using diverse heteroaromatic rings. Using presented scaffolds, we developed new potential tracers for neurological HDAC imaging while maintaining high radiochemical yields of SiFA technology

Les histones désacétylases (HDACs) forment une famille d'enzymes épigénétiques qui régulent des processus biologiques vitaux, notamment l'activation des gènes. La dysrégulation des HDACs dans le cerveau est impliquée dans les maladies d'Alzheimer et de Parkinson, ainsi que dans les troubles neuropsychiatriques. L'élucidation des niveaux de HDAC dans le cerveau normal et pathologique peut être réalisée grâce à la tomographie par émission de positons (TEP) à l'aide de traceurs récemment développés tels que le [^{11}C]Martinostat et le [^{18}F]Bavarostat. Cependant, l'utilisation de ces traceurs est entravée par leur radiosynthèse complexe et leurs faibles rendements radiochimiques. Nous avons développé de nouveaux traceurs potentiels de TEP pour les HDAC en exploitant la radiochimie supérieure des accepteurs de fluorure de silicium (SiFAs). Lorsqu'ils sont liés au silicium, les atomes de fluor non radioactifs ^{19}F peuvent subir un échange isotopique avec l'isotope radioactif de la TEP ^{18}F dans des conditions douces et avec un rendement élevé. Le traceur résultant est chimiquement identique au précurseur, éliminant ainsi la nécessité de la purification par HPLC. La valeur des SiFAs est généralement limitée par leurs médiocres propriétés pharmacocinétiques en raison des groupes lipophiles volumineux nécessaires pour prévenir l'hydrolyse de la liaison Si-F in vivo. Cependant, dans ce cas, la lipophilicité de ces groupes est exploitée pour conférer une perméabilité à la barrière hémato-encéphalique, de manière similaire au groupe adamantyle. Les propriétés pharmacocinétiques peuvent être ajustées davantage en utilisant diverses structures hétéroaromatiques. À l'aide des structures présentées, nous avons développé de nouveaux traceurs potentiels pour l'imagerie des HDAC neurologiques tout en maintenant des rendements radiochimiques élevés grâce à la technologie des SiFAs.

Contribution of Authors

Radiolabeling was performed with help from McGill Neurological Institute (The Neuro) PET unit who produced and dispensed ^{18}F, as well as Dr. Tom Singleton and Dr. Alexey Kostikov who helped with radiolabeling experiments. Autoradiography and PET imaging was performed with help from Arturo Aliaga from The Neuro PET unit who performed brain slice preparation and performed animal injection and handling. PET image processing and analysis was performed with help from Peter Kunach from Prof. Pedro Rosa-Neto's Laboratory who performed standard uptake over time analysis and MRI image stitching. Automatic synthesis was performed with help from Dr. Alexey Kostikov who performed automatic synthesis unit programming and manipulations during high-activity synthesis. All other work was performed by me unless otherwise stated in the text. All manuscripts are co-authored by Dr. Jean-Philip Lumb and Dr. Alexey Kostikov who both acted as research co-supervisors.

Table of Contents

Table of Tables

Chapter 1:

Chapter 2:

Chapter 3:

Table of Schemes

Chapter 1:

Chapter 2

Table of Figures

Chapter 1

Chapter 2

Chapter 3

List of Abbreviations

°C	degrees Celsium
Ac	acetyl
AcOH	acetic acid
A_m	molar activity
Bn	benzyl
Boc	*tert*-butyoxycarbonyl
Bq	bequerel(s)
br	broad
cat.	catalytic quantity
CDMT	2-chloro-4,6-dimethoxy-1,3,5-triazine
Ci	curie(s)
*c*logP	calculated partition coefficient
d	day(s)
DCM	dichloromethane
DIPEA	*N,N*-diisopropylethylamine
DMF	N,N-dimethylformamaide
DMSO	dimethyl sulfoxide
EDC	1-ethyl-3-(3-dimethylaminopropyl)carbodiimide
equiv	equivalent(s)
Et_2O	diethyl ether
Et3N	triethylamine
EtOAc	ethylacetate
g	gram(s)

h	hour(S)
HATU	1-[bis(dimethylamino)methylene]-1H-1,2,3-triazolo[4,5-b]pyridinium 3-oxid hexafluorophosphate,
HBTU	*N,N,N',N'*-tetramethyl-O-(1H-benzotriazol-1-yl)uronium hexafluorophosphate
HDAC	histone deacetylase
Het	heteroaromatic
HOBt	hydroxybenzotriazole
HRMS	high resolution mass spectroscopy
Hz	Hertz
IC50	half-maximal inhibitory concentration
iPrMgCl	isopropyl magnesium chloride
IR	infrared (spectroscopy)
J	coupling constant
K222	4,7,13,16,21,24-hexaoxa-1,10-diazabicyclo[8.8.8]hexacosane
Ki	dissociation constant
LAH	lithium alluminum hydride
LiHMDS	lithium bis(trimethylsilyl)amide
m	multiplet or milli
m/z	mass to charge ratio
mCPBA	*meta*-chloroperoxybenzoic acid
MeCN	acetonitrile
MeOH	methanol
min	minute(s)
MHz	megahertz
mol	mole(s)

MsCl	methanesulfonyl chloride
n-BuLi	*n*-butyl lithium
NMR	nuclear magnetic resonance
OTf	trifluoromethanesulfonate
PEG	Polyethylene glycol
PET	positron emission tomography
PPh3	triphenylphosphine
q	quartet
r.t.	room temperature
Rf	retention factor
s	singlet
SAHA	suberoylanilide hydroxamic acid
sec	second(s)
SiFA	silicon fluoride acceptor
TBAF	tetra-*n*-butyl ammonium fluoride
TBAI	tetra-*n*-butyl ammonium iodide
TBDMS	*tert*-butyldimethyl silyl
tBu	*tert*-butyl
t-BuLi	*tert*-butyl lithium
TFA	trifluoroacetic acid
THF	tetrahydrofuran
THP	tetrahydropyran
TLC	thin layer chromatography
TMS	trimethylsilyl

TMSOTf	trimethylsilyl trifluoromethanesulfonate
Yamaguchi's reagent	2,4,6-trichlorobenzoyl chloride

Chapter 1: Introduction

1.1 Origins of Positron Emission Tomography

In 1929, physicist Paul Dirac postulated the existence of anti-particles with the same mass as electrons but holding an opposite charge[1]. Their existence was confirmed in 1932 by Carl Anderson who coined the term "positron" (β^+) to describe these particles[2]. During the 1930s, several groups studied β^+, and determined that certain radioactive isotopes are capable of emitting them, and also determined that they will undergo annihilation when they collide with an electron, forming two beams of gamma radiation. This annihilation must satisfy the law of conservation of linear momentum and total energy, which means the pair of gamma photons are always emitted at 180^o from each other to produce no net momentum in the system, and the beams of gamma radiation are always 511 KeV in energy due to conversion of the mass of the particles into emitted energy described by the equation $E = mc^2$. This annihilation event forms the core principle of positron emission tomography (PET) as it is possible to simultaneously detect the two gamma rays and trace backwards to find the point of annihilation. By combining a β^+ emitting radioisotope with a chemical vector that is capable of binding to a biologically important endogenous target in vivo (also known as a biomarker), it's possible to create a non-invasive tool that can visualize *in vivo* distribution and concentrations of the probe target. PET imaging can visualize both typical and pathological activity in tissues, and is an indispensable tool today for disease diagnosis and treatment, as well as for biological studies and drug development[3].

PET radioisotopes are produced using compact circular particle accelerators called cyclotrons which produce energetic particle beams to generate different radioisotopes by bombarding various targets. The first cyclotron was created by Ernest Lawrence in 1930 at the University of California, Berkley and used the same concepts that modern accelerators still use[4]. An unwinding spiral path that passes multiple times through two D-shaped electromagnets (a so-called "dee") and a cleft between them. The particles move with a constant speed and radius within the magnetic field, but accelerates in the electric field with every pass through the cleft, while a deep vacuum is maintained within the path to prevent loss due to molecular collision with gas particles. As the particles accelerate, their path also increases by the increasing radius of the path, eventually producing a highly energetic beam by the time it reaches the target at the end[1,5]. Lawrence proceeded to build a larger version with Stanley Livingston and David Sloan using stronger electromagnets and incorporating a second dee opposite the first, managing to produce a 1.2 MeV proton beam in 1931[5]. Though rudimentary compared to modern cyclotrons which can produce beams up to 2600 MeV using as many as 8 electromagnets[6], these early cyclotrons were used to good effect to produce an abundance of new synthetic radioisotopes during the 1930s[7]. The first human PET imaging experiment was performed in 1945 by the Tobias group, who wanted to determine the fate of inhaled CO in humans. Several test subjects were made to inhale [^{11}C]CO followed by pure oxygen, and the radioactivity of the various organs were measured using a Geiger counter, along with the exhaled CO_2 collected in soda lime, and the group determined that inhaled CO can be excreted[8].

After an initial burst of interest for PET radioisotopes in the 1940s, their use declined due to prevailing skepticism that their short half-lives would not be useful for biological applications. At the same time, the discovery of the long-lived ^{14}C offered a more flexible label for biological studies. However, by the mid 1950s, better detector technology were developed that could take advantage of the simultaneous gamma

ray emissions of β^+ annihilation[7,9]. In 1951, both the Wrenn, Good, Handler and Sweet and Brownell groups reported that it was possible to find the source of the simultaneous gamma emission of β^+ annihilation by placing newly-designed scintillation detectors opposite to each other[10, 11]. In 1953, Sweet constructed a PET scanner that could be used to detect brain tumors using two scintillation detectors mounted in parallel, and rigged to move together in a linear fashion. Improvements on scanners continued throughout the 1960s and 1970s with Rankowitz and Robertson designs using a circular array of 32 scintillation detector that is capable of scanning an entire horizontal slice, Kuhl and Edwards's developing the concept of overlaying the radioactivity map with body structures scan[12], and Cormack, Hounsfield, and Ambrose's work on producing of image reconstruction algorithms[13, 14]. By the 1970s, short-lived PET radioisotopes like ^{15}O, ^{13}N, ^{11}C, and ^{18}F found significant renewed interest due to their ability of producing higher resolution images compared to techniques using single photon emitter isotopes. Ter-Pogossian, Phelps, and Hoffman in collaboration with Oak Ridge National Laboratory constructed the PET tomograph for human imaging with 96 detectors in 1973. The group injected [^{11}C]*D*-glucose into human subjects to produce the first human PET scans of glucose metabolism, as well as studies using $^{13}NH_3$ and ^{11}CO to image various organs[46]. Today, PET/CT scanners employ hundreds of thousands of scintillation detectors and can achieve spatial resolutions of 2 – 3 mm using a wide variety of PET tracers for numerous biological targets[9, 14, 15]. The nomenclature for cyclotron nuclear reactions is presented as "Target Material (Beam Type, Emission) Resulting isotope". For example, the irradiation of ^{18}O by a beam of deuterium to produce ^{18}F with an emission of an alpha particle wall be written as $^{20}Ne(d, \alpha)^{18}F$.

A radiopharmaceutical is a group of drug compounds that contain radioactive isotopes for therapeutic or diagnostic purposes. Radioactivity is measured in the SI unit Becquerel (Bq) or non-SI but still widely used unit Curie (Ci). One Becquerel is defined as the amount of activity that gives rise to one nuclear disintegration per second (s^{-1}), and can be directly interconverted with Curie where 1 Ci = 37 MBq. Another relevant property in medicinal applications is the intensity of ionizing radiation the product emits, or the radiation dose measured in Gray (Gy) or Sieverts (Sv) as this is the measure that determines the effectiveness of the therapeutic radiopharmaceutical and dictate the final dose administered to the patient. The yields of radiochemical reactions are described in terms of radiochemical yield (RCY), which is the radioactivity of the product divided by the input radioactivity corrected for the decay to the same time, rather than overall chemical yields of the reactions. RCY reporting can be given either as decay corrected where product radioactivity is back-corrected to omit decay loss due to reaction time to better represent the reaction efficiency, or non-decay corrected where the product activity is reported directly to give a better representation of final product properties. This difference in reporting can result in very significant differences depending on isotope half-life and reaction time. The consensus in recent nomenclature is that RCY should be reported after correction for decay[16].

1.2 PET Radioisotopes

A PET tracer is a type of radiopharmaceutical used for non-invasive *in vivo* imaging of important biological targets that employs a radioisotope that decays by positron emission. In order to produce a PET tracer, a PET radioisotope is combined with a chemical vehicle capable of binding to the biological target of interest. Generally, the synthesis process involves pre-fabricating a cold precursor ready to be loaded with the isotope, producing the isotope and immediately performing the radiolabeling reaction as quickly as

possible, isolating and purifying the tracer, then sterilization and formulation of the radiopharmaceutical into an injectable matrix before being quickly administered to a patient[48]. The choice of isotope (Table 1-1) is an important decision in tracer design, with the half-life, emission properties, and available labeling chemistries being the most important factors to consider.

Entry	Radioisotope	Half-Life	Positron Energy E_{max} (KeV)	Positron decay (%)
1	^{76}Br	16.2 h	1310	54
2	^{11}C	20.3 min	961	100
3	^{62}Cu	9.8min	2910	98
4	^{64}Cu	12.8 h	656	19
5	^{18}F	110 min	634	97
6	^{52}Fe	8.2 h	800	57
7	^{66}Ga	9.5 h	4153	56
8	^{68}Ga	67.6 min	1899	89
9	^{124}I	4.2 d	2100	23
10	^{52}Mn	134.2 h	0.58	29
11	^{13}N	10.0 min	1190	100
12	^{15}O	2.1 min	1732	100
13	^{82}Rb	76 s	3150	95
14	^{94m}Tc	52.5 min	2470	72
15	^{86}Y	14.7h	3150	34
16	^{89}Zr	78.4 h	897	23

Table 1-1: List of common PET radioisotopes and their emission properties[17]

All PET radioisotopes will decay to stable products, so the produced tracer will only have a limited lifespan before it no longer has sufficient activity to produce a good image. It is important that the half-life of the chosen radioisotope is long enough to complete the chemical incorporation with the precursor, and the final tracer needs to match the biological timescale to provide adequate sensitivity while minimizing unnecessary radiation burden to the patient. Certain antibody – receptor binding processes may require several hours after injection to reach equilibrium with their target[17] and so must be conjugated with longer lived isotopes like ^{64}Cu ($t_{1/2}$ = 12.8 h), ^{89}Zr ($t_{1/2}$ = 78.4 h), or ^{124}I ($t_{1/2}$ = 4.2 d). Short-lived isotopes such as ^{15}O (Entry 12) and ^{13}N (Entry 11) are limited to very fast processes, as their half-lives do not usually allow for complex chemical transformations. The transportation time to move PET tracers from the manufacturing sites to the imaging facility can also impose significant logistical challenges depending on the isotope used, and may limit the availability of tracers that make use of these isotopes to sites with production capabilities on the premises.

As time passes between isotope production and injection the A_m of the tracer will decrease, which may impact the quality of the resulting PET image. Generally, the nature of the biological target will influence the stringency of A_m requirements for the particular tracer. Higher A_m is needed to achieve good image quality without eliciting a physiological response for easily saturable targets. As a rule of thumb, only ~1% of targets should be bound by the imaging agent in order to prevent negative effects in the patient (i.e. the tracer principle)[18]. For example, a tracer based on highly bioactive scaffolds such as [^{11}C]carfentanil used to investigate μ-opioid receptors has an injection limit of ≤0.03 μg/kg resulting in an A_m requirement of >75 GBq/μmol at injection to use[19]. Even more extreme, the tracer (+)-[^{18}F]flubatine designed using a highly toxic epibatidine alkaloid scaffold requires an A_m >700 GBq/μmol[20]. On the other hand, tracers

based on scaffolds of endogenous molecules like amino acids, fatty acids, or sugars typically have much less strict A_m requirements as there is low chance of toxicity and may go as far as only having total activity injection requirements[21].

Emitted β^+ also have different starting kinetic energies as they leave the nucleus depending on the isotope source, which has an impact on image resolution. A higher kinetic energy means a longer average travel distance before annihilation, resulting in blurring of the PET image. Low energy emitters like ^{18}F and ^{64}Cu have average β^+ travel distances lower than 1 mm in tissue which will provide high-resolution images, while high energy emitters like ^{13}N, ^{15}O, ^{68}Ga, and ^{124}I will have some degree of blurring. Current full-body PET imaging devices typically only have resolution of ~4 mm meaning the blurring from β^+ travel range is minimal for use in full body scans, but the impact may be fairly significant for applications like brain imaging or small animal scans which require much higher resolutions[22].

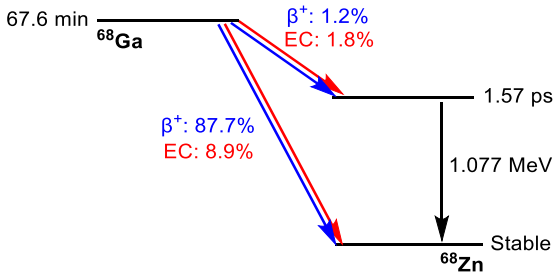

Figure 1-1: Different decay paths of ^{68}Ga[22]

PET radioisotopes can also undergo a mixture of different decay paths that produce non-β^+ emissions, reducing the detectable signal of the isotope. Additionally, the extraneous emissions can also contribute to signal contamination to reduce image quality. For example, ^{68}Ga decays to ^{68}Zn by β^+ emission (Figure 1-1) 89 % of the time and 11% by electron capture which is lost signal. Of the β^+ emission, 87.7 % decays directly to the ^{68}Zn ground state, while the remaining 1.2% decays to an excited state of ^{68}Zn which decays to the ground state through emission of an additional gamma photon at 1.077 MeV. Since PET detectors are tuned for the 511 KeV radiation emitted by β^+ annihilation, this emission does not directly interfere with scans, but it has been found to still contaminate the PET signal through a scattering interaction with tissue to generate lower energy gamma radiation within the detection range of most PET scanners. The same issue is present through the electron capture decay pathway, which does not contribute to a detectable PET signal but still results in signal contamination as 1.8 % of the decay path goes to this same excited state[22].

Isotopes also have different available chemistry to them for incorporation into tracers. Radiometals, such as ^{64}Cu and ^{68}Ga are currently limited to incorporation by chelation, which means a suitable chelator moiety must be designed into the probe rendering them unsuitable for applications in brain imaging due to their size. The available incorporation chemistry is also closely related to the half-life as the PET tracer needs to be synthesized, purified, sterilized, tested, and injected into the patient within the span of a few half-lives. This means most traditional synthetic reactions, particularly the ones requiring overnight stirring, are incompatible with very short-lived isotopes like ^{15}O and ^{13}N, and they cannot usually be incorporated into complex molecules fast enough to produce a tracer with high A_m. Besides time constraints, it is also preferable to complete radiolabeling reactions within as few steps as possible when

using isotopes with relative short half-lives such as ^{11}C, ^{18}F, or ^{124}I so ideally the reactions should be fast, simple, and highly tolerant to functional groups[17]. Commercial synthesis of PET tracers is usually performed using automated synthesis modules to allow safe handling of the high amounts of radioactivity. Depending on the labeling method, synthesis automation can often pose significant technical challenges as these systems are only capable of simple operations like fluid transfer, mixing, and heating. Small reaction volumes, sensitive manipulations, and unconventional reaction setups all introduce complications that can limit the widespread usability of a labeling strategy, even if manual synthesis produces good results[23]. Therefore, tracer design and labeling strategies also need to take into account the user friendliness of its steps in order to have a successful translation into the clinic.

Finally, PET tracers need to conform to all the biological targeting requirements that normally applies in drug development. The radioisotope needs to be incorporated into a drug platform that is capable of quickly delivering the isotope to its intended target with high selectivity and specificity in order to obtain a high-quality image. In order to achieve good image resolution while minimally impacting the biological function of the target, PET tracers are typically radiolabeled using the minimum quantity of starting material possible. This means that the resulting tracer typically need nanomolar binding affinity towards its target due to the relatively small quantity of injected drug material[24]. Off-target or non-specific binding would also negatively impact the PET image by creating background noise that interfere with target visualisation. The metabolic stability of the full drug construct also needs to be carefully evaluated. Radiopharmaceuticals are almost always administered intravenously, and degradation of the tracer by the kidneys and liver will usually begin to occur within minutes of injection. Biological half-lives of the tracer need to be adequately long to allow for the tracer to accumulate sufficiently at the target in order to obtain good signal to background ratios, but very few tracers can resist extensive metabolism *in vivo* over the full duration of a PET scan session irrespective of radionuclide used[25].

1.3 ^{18}F PET Tracers

With excellent decay properties of both low energy at 634 KeV and a high 97% decay by β^+ emission with only 3 % by EC with no interference, ^{18}F is capable of producing excellent resolution images. Additionally, with its superior half-life of 110 min, it's long-living enough to undergo complex synthesis and transport spanning up to several hours while still offering good A_m for injection, but is short-lived enough to limit the radiation dose to the patient[60]. With these properties, ^{18}F has become the most popular radioisotope used for PET tracers and makes up the majority of FDA approved commercial products[26, 27].

Entry	Target	Beam	Product	Approx. A_m (GBq/umol)
1	$[^{18}O]O_2$	H^+	$[^{18}F]F_2$	0.600
2	Ne	$^2H^+$	$[^{18}F]F_2$	0.100
3	$[^{18}O]H_2O$	H^+	$^{18}F^-_{(aq)}$	600
4	H_2O	$^3He^+$	$^{18}F^-_{(aq)}$	50

Table 1-2: Methods of ^{18}F Production by Cyclotron[17]

Several nuclear reactions are available to produce ^{18}F by cyclotron for either electrophilic or nucleophilic incorporation into PET tracers (Table 1-2), but the most widely used are proton beam bombardment of

water or of O_2 gas enriched with the stable isotope of oxygen ^{18}O. The nucleophilic form of fluoride forms in water as $^{18}F^-_{(aq)}$ and has a much higher A_m and is thus the preferred form for tracer production, requiring ~1 h bombardment of $[^{18}O]H_2O$ in a cyclotron (Entry 3). It is also possible to use naturally abundant $[^{16}O]H_2O$, but this method requires a costly ^3He source (Entry 4). The electrophilic form of ^{18}F is produced as $[^{18}F]F_2$ gas usually using deuteron bombardment of neon (Entry 2) or proton bombardment of $[^{18}O]O_2$ gas (Entry 1), depending on the target material and beam source availabilities. The drawback of resulting $[^{18}F]F_2$ gas is a tendency to be absorbed by transfer tubing requiring the addition of non-radioactive F_2 gas as a carrier to extract it out of the cyclotron's target. This results in cyclotron-produced electrophilic ^{18}F having a much lower A_m compared to its nucleophilic form, reducing its usefulness[17].

^{18}F has been used for radiolabeling of a wide variety of complex targeting moieties including small organic molecules, metabolic derivatives like carbohydrates, amino acids, and steroids, and higher molecular weight compounds like peptides, proteins, and oligonucleotides. The most common metabolic pathway of ^{18}F radiotracers is defluorination by cytochrome p450 oxidase, resulting in release of anionic $^{18}F^-$. The free $^{18}F^-$ is quickly taken up by the bone apatite[150] and thus the metabolic stability of ^{18}F radiotracers can be approximated by measurement of bone PET signal. The most widely used PET tracer today is the ^{18}F-based glucose derivative 2-deoxy-2-[^{18}F]fluoro-*D*-glucose ([^{18}F]FDG) originally reported in 1978 by Ido *et al*. mostly used for cancer imaging but has wide variety of applications[28].

To produce a novel ^{18}F PET tracer, late-stage incorporation into a complex scaffold must be undertaken in order to minimize loss due to decay. Numerous fluorination reactions are known, but many are not suitable for application in this context. In order for a fluorination method to be viable for ^{18}F, it should ideally have a fast reaction time of only a few minutes, as well as having very good orthogonality and functional group tolerance to minimize purification complexity of the molecule after radiosynthesis[25]. Methods to incorporate ^{18}F in aliphatic and aromatic scaffolds have been explored since the 1960s, and today a variety of methods exist in the radiofluorination toolbox to accommodate a wide variety of scaffolds and functional groups[30].

1.4 Electrophilic Radiofluorination

Due to the low A_m, use of electrophilic ^{18}F is typically limited to the substrates incompatible with nucleophilic fluorination methods[17]. Though available to be used as fluorine gas directly from the cyclotron, the highly reactive nature of $[^{18}F]F_2$ requires careful control of the reaction temperature or highly dilute solutions. Fluorine gas can be converted to less reactive fluorination reagents such as xenon difluoride, trifluoromethyl, perchloryl fluoride, or acetylhypofluorite before use to reduce reactivity[30, 31]. The most prominent example of electrophilic fluorination is with the original synthesis [^{18}F]FDG in 1978, which was fluorinated by both $[^{18}F]F_2$ (Scheme 1-1) and CF_3OF[32].

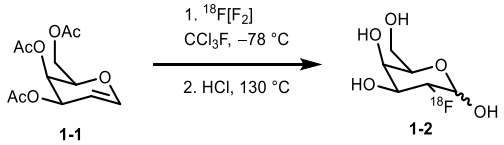

1-1 1-2

Scheme 1-1: Radiofluorination of [^{18}F]FDG

Highly reactive electrophilic fluorination agents can be used to directly fluorinate electron-rich arenes, but this often results in poor stereoselectivity which can significantly complicate purification due to undesired side reactions. For example, Murali *et al*. aimed to produce 6-[^{18}F]fluoro-*m*-tyrosine **1-4** using direct electrophilic fluorination for PET imaging aromatic L-amino acid decarboxylase enzymes [^{18}F]F_2 was converted to the less reactive [^{18}F]CH_3COOF by passing through a column of $NaOAc{\cdot}3H_2O$ and subjected precursor to direct fluorination hoping to use substituent effects to direct fluorination positions on the ring. However, though they did produce the desired regioisomer as the major product, they also produced significant quantities of both the 2-fluoro **1-5** and 2,6-difluoro **1-6** products resulting in a poor overall yield and requiring extensive purification (Scheme 1-2)[33].

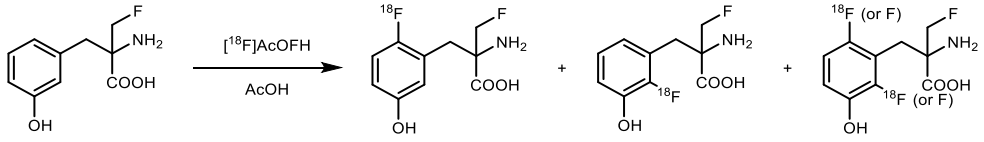

Scheme 1-2: Radiofluorination of [^{18}F]fluoromethyl-*m*-tyrosine

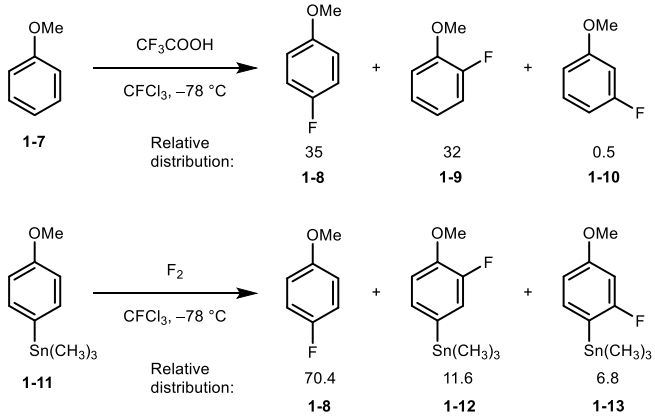

Scheme 1-3: Regioisomer distribution of direct fluorination and fluorodestannylation reactions

The poor selectivity of aromatic electrophilic substitution has since been addressed in several ways. Coenen and Moerlein found that demetallation strategy by employing trimethyltin, trimethylgermanium and trimethylsilicon derivatives of the aryl starting material **1-7** can significantly improve regioselectivity, with the tin derivative **1-11** being the most efficient substrates in this reaction (Scheme 1-3)[34, 35]. This method is well known for the applications in preparation of *L*-[^{18}F]-fluoro-DOPA **1-15**, a PET tracer used to image dopaminergic neurons for diagnosis of Parkinson's disease that has electron rich ring that is difficult to fluorinate by nucleophilic means. Namavari *et al*. used destannylation to achieve a decay corrected RCY of **1-15** of 25% (Scheme 1-4)[36].

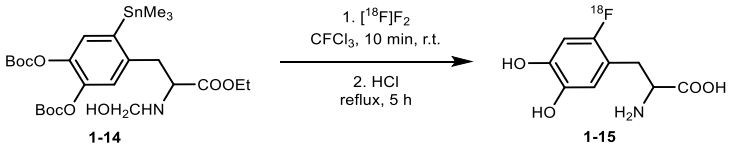

Scheme 1-4: Radiofluorination of *L*-[^{18}F]-fluoro-DOPA

Milder and more selective electrophilic N-^{18}F fluorination agents were also developed by several groups (Figure 1-2). [^{18}F]-*N*-fluoropyridinium triflate **1-16** and [^{18}F]-*N*-fluoro-2-pyridone **1-17** were both synthesized by Oberdorfer *et al*. through [^{18}F]F_2 fluorination of trimethylsilylpyridinium triflate[37] and 2-(trimethylsiloxy)-pyridine, respectively[38]. Satayamurthy *et al*. synthesized a series of [^{18}F]-*N*-fluoro-*N*-alkylsulfonamides and found [^{18}F]-*N*-fluoro-*endo*-norbornyl-*p*-tolylsulfonamide **1-18** to be the most reactive as a fluorination reagent. These [^{18}F]*N*-fluoro compounds are often used for radiolabeling Grignard and organolithium precursors (Scheme 1-5)[39].

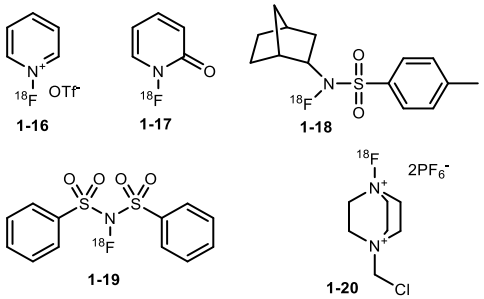

Figure 1-2: [^{18}F]*N*-fluoro compounds used for electrophilic radiofluorination

Teare *et al*. reported the synthesis and use of [^{18}F]*N*-fluorobenzenesulfonimide **1-19** which can be used for radiofluorination of allylsilanes and trimethylsilanol ethers[40].

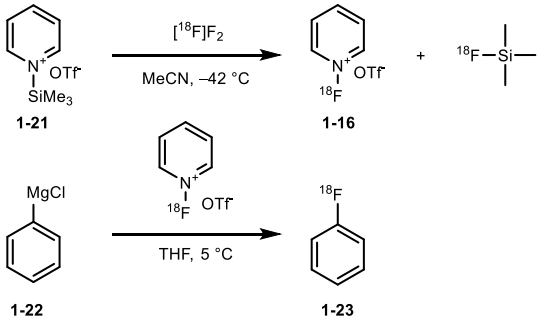

Scheme 1-5: Preparation of and radiofluorination using [^{18}F]*N*-fluoropyridinium triflate

The same group also managed to produce [^{18}F]Selectfluor **1-20**, the ^{18}F version of a commercial reagent commonly used for electrophilic fluorination, and successfully used it to radiofluorinate arylstannanes catalysed by AgOTf, achieving ~18 % decay corrected RCY (Scheme 1-6)[41].

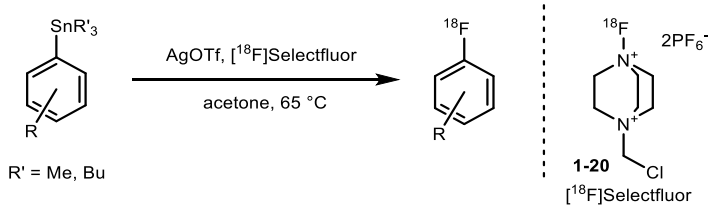

Scheme 1-6: Radiofluorination using [^{18}F]Selectfluor

Though useful in achieving milder labeling conditions with superior selectivity, these [^{18}F]*N*-fluoro compounds require high A_m in order to produce appreciable RCY in the final product. To improve A_m, Bergman and Solin introduced a strategy to produce [^{18}F]F_2 by using a high A_m nucleophilic fluoride.

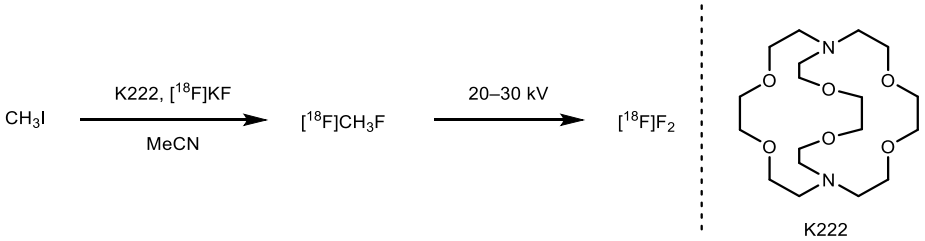

Scheme 1-7: Generation of high A_m [^{18}F]F_2 by electrical discharge chamber

^{18}F[KF] with Kryptofix$_{222}$ (K222) are standard nucleophilic radiofluorination conditions which will be discussed in Section 1.6. This complex is reacted with iodomethane through nucleophilic substitution to produce [^{18}F]CH_3F at 75 % RCY. The [^{18}F]CH_3F is then purified by gas chromatography and transferred to an electric discharge chamber preloaded with carrier fluorine gas. When subjected to electrical discharge, [^{18}F]CH_3F releases [^{18}F]F_2 at a higher A_m than the cyclotron-produced [^{18}F]F_2 (Scheme 1-7)[42] which Teare *et al*. used to produce the high A_m [^{18}F]Selectfluor **1-20** used in their methodology[73]. However, widespread use of this reagent has not been adopted despite its usefulness in radiosynthesis this method requires an electrical discharge chamber, significantly increasing process complexity for tracer synthesis[43].

Significant developments in synthetic strategy have made electrophilic ^{18}F useable in some situations, but the biggest hurdle yet to be overcome is low A_m. Though historically many PET tracers were originally synthesized by electrophilic means, its use has since been surpassed by nucleophilic methods to produce higher A_m tracers.

1.5 Preparation of [^{18}F]fluoride for Nucleophilic Radiofluorination

The most practical ^{18}F-fluorination method uses $^{18}F^-_{(aq)}$ produced by bombardment of [^{18}O]H_2O in the cyclotron, followed by delivery is from the target without the addition of a non-radioactive carrier. However, aqueous $^{18}F^-_{(aq)}$ must typically be dehydrated before it can undergo further reactions. Although fluoride is a good nucleophile, it has strong H-bonding interaction with water and become strongly hydrated (ΔH_{hydr} = 506 kJ/mol) [30] which deactivates it towards nucleophilic reactions. Typically, $^{18}F^-_{(aq)}$ from the cyclotron is trapped on a strong anion exchange (SAX) cartridge, which is packed with polymeric material functionalized with quaternary ammonium groups. The excess [^{18}O]H_2O is thus removed for

subsequent recovery and the cartridge can be rinsed with water to remove impurities. $^{18}F^-$ is then eluted by displacing it with a base, usually a poor nucleophile base such as carbonate or bicarbonate in a solution of acetonitrile (MeCN) with a low water content, typically 10-15 %

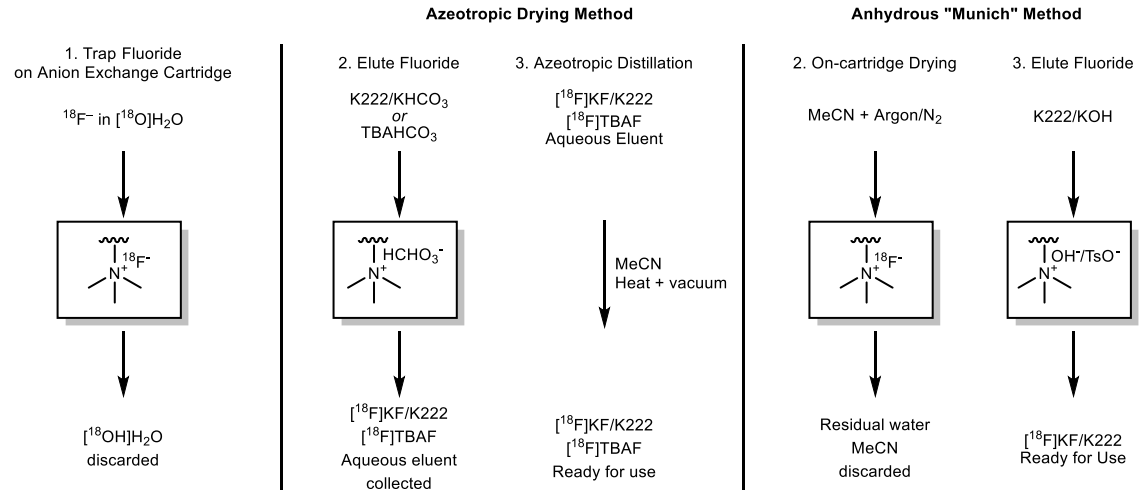

Figure 1-3: Methods for producing nucleophilic $^{18}F^-$ for radiofluorination

In order to improve the solubility and nucleophilicity of free fluoride in organic solvents, the counterion used for the fluoride is either bulky such as tetrabutylammonium (TBA), or an alkali metal like potassium enclosed within a crown ether 18-crown-6 or a kryptand kryptofix 2.2.2 (K222) which provide “naked” fluoride due to charge separation. This solution is used to elute the fluoride from the cartridge. The water in the eluate is then removed by azeotropic distillation with MeCN under vacuum for a few minutes to produce sufficiently anhydrous free fluoride in the form of $[^{18}F]KF/K222$ or $[^{18}F]TBAF$ for nucleophilic reactions. However, it is difficult to achieve completely anhydrous conditions with this method and trace quantities of water will usually be present despite best efforts. Under these basic conditions, trace water can produce free hydroxide which may contribute to competing hydrolysis or elimination reactions resulting in the formation of by-products[44]. Small variations in the azeotropic drying process are a common issue in RCY consistency from batch to batch, and some fluoride will always be lost during drying due to its volatility and absorption into the walls of drying vessels[45].

Azeotropic drying can be avoided entirely by eluting fluoride using anhydrous MeCN, but elution from SAX cartridge in this case requires strong base such as hydroxide in the eluent rather than weak carbonate bases. This approach is so-called “Munich method” of fluoride preparation, where fluoride is first captured on an anion exchange cartridge and washed with anhydrous MeCN and blown with dry argon to remove residual water. Next, a pre-complexed mixture of KOH/K222 is dissolved in anhydrous MeCN and used to elute the fluoride to produce an anhydrous solution of nucleophilic $[^{18}F]KF$. However, careful control of eluent quantity is required as this method results in large excess of hydroxide in the labeling solution. Therefore, careful neutralization and buffering with weak carboxylic acids, such as oxalic acid is needed to limit hydroxide competition while maintaining fluoride nucleophilicity (Figure 1-3)[46, 47].

1.6 Nucleophilic Aliphatic Radiofluorination

Direct nucleophilic radiofluorination of aliphatic substrates proceeds via an S_N2 mechanism, and reactions are typically performed at elevated temperatures up to ~100 °C in order to achieve suitably rapid reaction times. High temperatures in combination with the basic conditions means many substrates are susceptible to β-elimination to form the corresponding styrene, as well as competition by hydroxide to form alcohol side products. The presence of these side reactions also means products almost always require high performance liquid chromatography (HPLC) to purify the product after synthesis. Fluoride is easily protonated to form HF (E_B = 565 kJ/mol) which inactivates it towards nucleophilic reactions, so polar aprotic solvents such as dimethyl sulfoxide (DMSO), *N*,*N*-dimethylformamide (DMF), *N*,*N*-dimethylacetamide (DMA), and MeCN are the typical used[62]. There is also evidence that certain substrates benefit from the use of bulky protic solvents like *tert*-butanol and *tert*-amyl alcohol which prevent tight coordination, creating a reactive fluoride species with attenuated activity but adequate nucleophilicity to help prevent β-elimination[44].

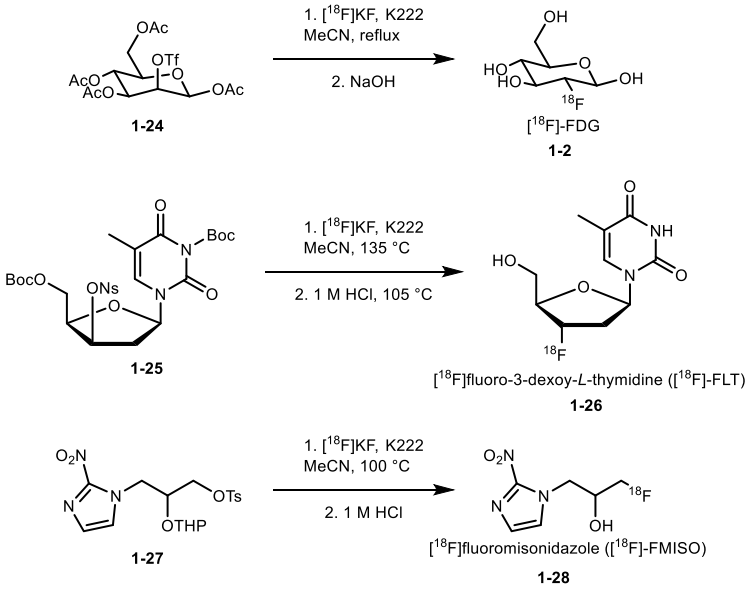

Scheme 1-8: Production of common PET tracers by direct nucleophilic aliphatic radiofluorination

The typical leaving groups employed are usually halogens or sulfonic acid esters. Sulfonic acid esters are better leaving groups than halogens for nucleophilic fluorination, with tosylate being the least and triflate being the most reactive. The overall order of reactivity of commonly used leaving groups is F < Cl < Br < I < 4-methylbenezenesulfonate (tosylate) ≈ methanesulfonate (mesylate) < 4-nitrobenzenesulfonate (nosylate) < trifluoromethanesulfonate (triflate)[54]. Using more reactive leaving groups is generally associated with higher RCY but also increases the potential for competing elimination reactions, especially at elevated temperatures[48]. Reaction conditions, including the fluoride preparation method, reaction temperature, solvent, and leaving group choice usually require extensive optimization to maximize RCY and minimize side products to facilitate purification. Sensitive functional groups on the precursor also often require protection, and a subsequent deprotection step is frequently employed after fluorination (Scheme 1-8)[26].

Despite these drawbacks, numerous commonly-used PET tracers are produced for clinical applications using this strategy, including [^{18}F]FDG **1-2**, nucleotide analogue [^{18}F]fluoro-3-deoxy-*L*-thymidine ([^{18}F]FLT) **1-26**, and [^{18}F]fluoromisonidazole ([^{18}F]FMISO) **1-28** just to name a few[16].

1.7 Nucleophilic Aromatic Radiofluorination

Nucleophilic radiofluorination of aromatic rings typically requires ring activation by electron-withdrawing groups (EWG) *ortho* or *para* to the leaving group, though certain substrates can also be fluorinated on weakly activated positions. Approximate ring activation ability of commonly used EWG are Ac < CHO < CN ≈ CF_3 < NO_2. Fluorination conditions are usually harsher than aliphatic nucleophilic conditions, with temperatures often exceeding 100 °C. Solvents compatible with this temperature are typically DMF or DMSO, while radiofluorination of substrates capable of reacting at lower temperatures can be performed in MeCN. Leaving groups are either halogens or electron-poor nitrogen groups, with the approximate order of reactivity being: I < Br < Cl < F < NO_2 ≈ NMe_3^+ (Table 1-3)[17].

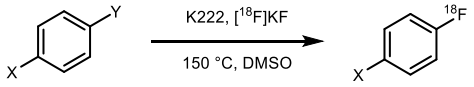

X substituent	Leaving group Y					
	HI	HBr	HCl	HF	NO_2	NMe_3^+
CN	-	33	24	70	73	68
NO_2	10	35	70	47	87	-

Table 1-3: Leaving group and EWG effect on RCY[60]

Fluorine can work as an adequate leaving group in certain substrates, allowing for isotopic exchange (IE) of ^{19}F by ^{18}F to produce a product that is chemically identical to the precursor. With this method, it's possible to simplify the purification process, as unreacted precursor does not need to be removed from the reaction mixture. However, the efficiency of IE is typically poor, and it usually results in tracers with low specific activity. Nevertheless, this strategy is sometimes useful for producing ^{18}F labelled versions of existing drugs containing aryl fluorine which can be used for pharmacokinetic studies[49] such is the case with the synthesis of [^{18}F]haloperidol **1-30**, the fluorinated version of a antipsychotic drug at 5% decay corrected RCY[50]. More commonly however, it is preferable to use a better leaving group such as NO_2 in order to achieve a higher A_m. For example, serotonin 2A receptor PET imaging agent [^{18}F]altanserin **1-32** is routinely produced by ^{18}F-fluorination of the nitro precursor in ~20 % decay corrected RCY with A_m above 1 Ci/µmol (Scheme 1-9)[49].

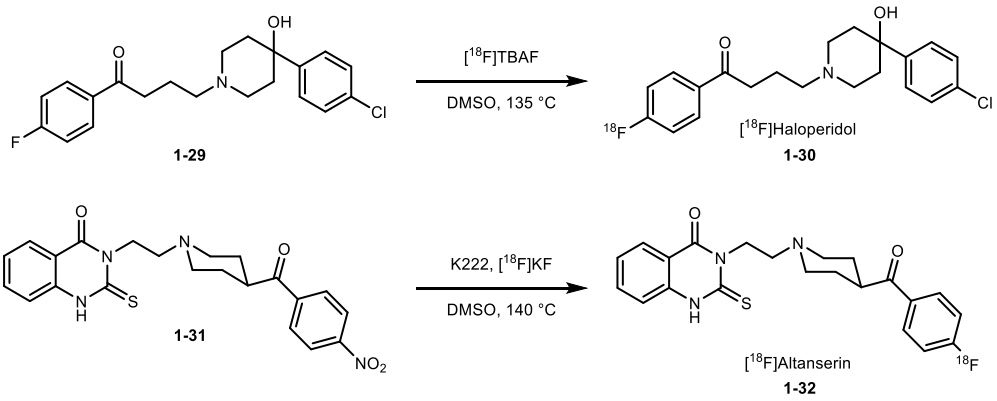

Scheme 1-9: Preparation of PET imaging agents by aromatic radiofluorination

Similar to aliphatic nucleophilic radiofluorination, the harsh conditions result in poor functional group tolerance, so radiosynthesis is often designed with protecting groups that are removed after radiosynthesis. In some cases, additional synthetic steps after radiolabeling are required, which significantly impact RCY. For example, Jacobson's protocol for synthesis of [^{18}F]hydroxyflutamide derivative **1-36**, (Scheme 1-10) results in 10% decay corrected RCY over 3 steps[51].

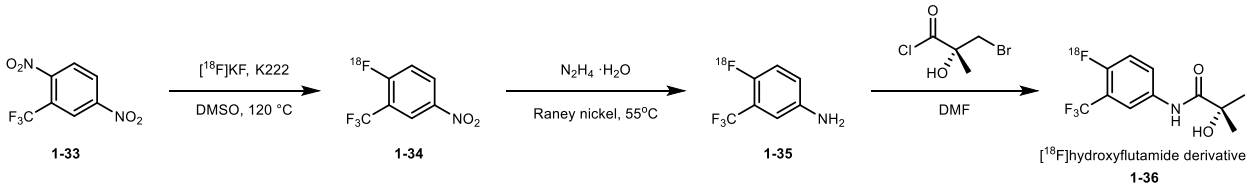

Scheme 1-10: Functional group manipulations after radiosynthesis of [^{18}F]hydroxyflutamide derivative

Heteroaromatic substrates containing nitrogen in the ring are generally more electron deficient than their non-heteroaromatic counterparts, and EWGs are not always required for ring activation. Substrates usually take advantage of the electronic structure of the heteroaromatic ring, with leaving groups at the most activated positions[48]. Radiolabeling conditions typically require high heat or microwave irradiation to keep reaction times low, for example serotonin 5-HT$_{1A}$ receptor imaging agent [^{18}F]WAY-100635 **1-38** was synthesised by conventional heating in 60–65 % RCY, while the use of the microwave reactor increased RCY to 93 %. However, though reaction times are low, total manipulation time to account for purification is 50–70 min, which results in a decay corrected RCY of 15–25 % (Scheme 1-11)[16].

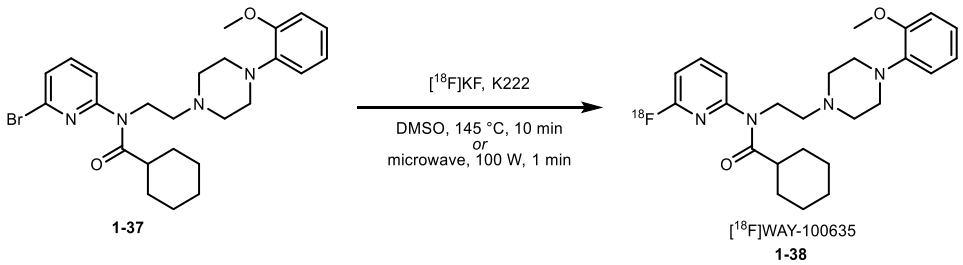

Scheme 1-11: Radiofluorination of 6-fluoropyridinyl analogue [^{18}F]WAY-100635

Attempts to improve functional group tolerance and yields of S_NAr led to the development of diaryliodonium salts precursors **1-39** as electrophiles. Introduced in 1995 by Pike and Aigbirhio, diaryliodonium reacts with nucleophilic fluoride to give the desired product **1-40** or **1-42** and an iodinated byproduct **1-41** or **1-43**[52]; regioselectivity can be guided by electronic or steric features as fluoride addition will occur on the more electron deficient ring. Regioselectivity is also guided by an "*ortho* effect" where addition is biased towards the aromatic ring that has a substituent *ortho* to the iodonium, and an *ortho* substituent can also generally improve the RCY of this class of reactions. The basis of the *ortho* effect is believed to be due to the formation of an iodine centered trigonal bipyramidal intermediate after fluoride addition. Due to the increased steric bulk of the ortho substituents, the bulkier ring will be positioned in the equatorial position, *syn* to the fluoride and thus promoting its introduction into the ring. For the selection of the ortho substituents, hydrophobic moieties such as alkyl can enhance the effect by producing a lipophilic microenvironment to support formation of the transition state on hypervalent iodine, while electron donating groups (EDG) such as an *ortho*-methoxy will direct fluorine away from the ring[52].

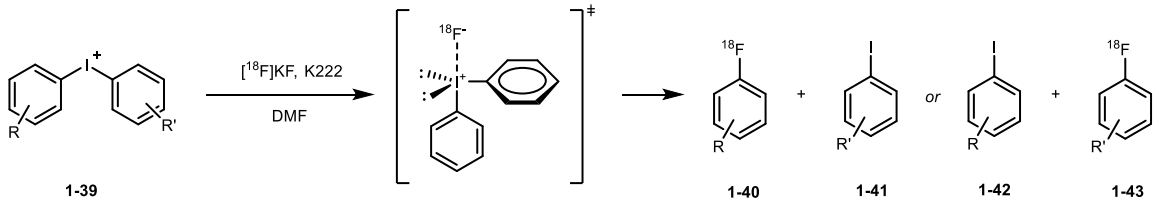

Scheme 1-12: Radiofluorination using diaryliodonium salts

The addition of a radical scavengers such as 2,2,6,6-tetramethylpiperidine 1-oxyl (TEMPO) can improve the yield, possibly by helping to stabilize the iodonium precursor during the relatively harsh radiolabeling conditions[53]. Pike *et al.*'s attempted to synthesize glutamate receptor mGluR5 PET imaging agent **1-45** using both bromo **1-44** and diaryliodonium tosylate salt **1-46** precursors. Using similar heating and microwave conditions, they achieved only 6 % decay corrected RCY on the bromo precursor with optimized conditions, but 28 % RCY using the diaryliodonium salt that had no *ortho* substituent, with only trace formation of [^{18}F]methoxyfluorobenzene side product **1-48** (Scheme 1-13)[52].

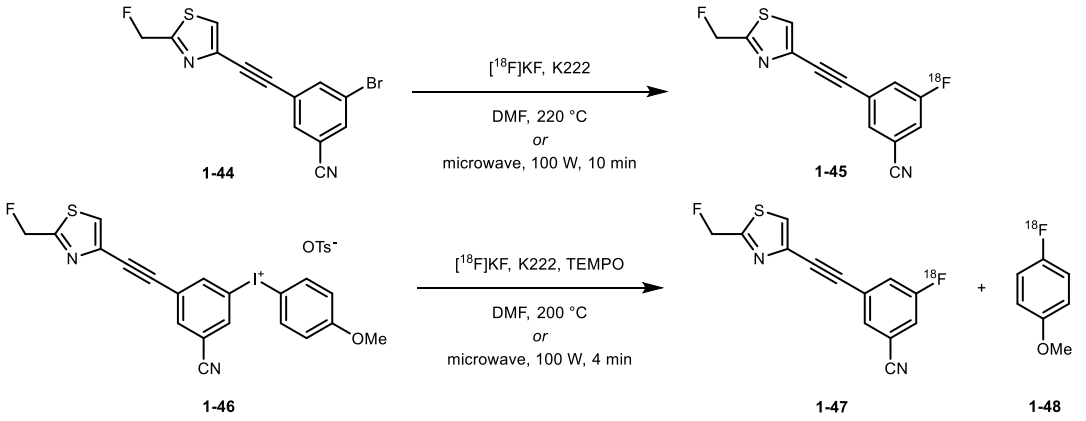

Scheme 1-13: Radiosynthesis of mGluR5 PET radioligands

The main limitation of using diaryliodonium salt precursors is their relative instability and difficulty in synthesis and purification. EWG substituents are still needed for ring activation and substituents must be capable of withstanding the oxidative conditions used to form the diaryliodonium salt. Using the method on complex substrate usually results in lower RCY as the precursor has a tendency to decompose under radiofluorination conditions[26].

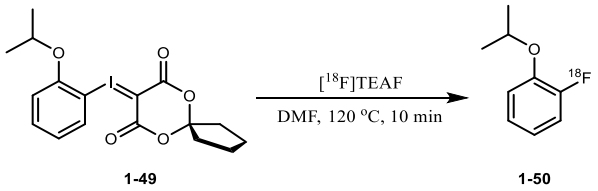

1-49 1-50

Scheme 1-14: Radiofluorination of non-activated arene using spirocyclic iodonium ylide

These issues were addressed by Rotstein *et al*., who advanced the strategy of using hypervalent iodonium precursors through introduction of spirocyclic iodonium ylides (SCIDY) for arene radiofluorination (Scheme 1-14). This neutral iodonium species has simplified precursor synthesis and purification compared to diaryliodonium salts and has the major advantage of being compatible in fluorinating hindered and electron-rich arenes. The superior RCY is achieved through using an optimized spirocyclic auxiliary which helps to stabilize the SCIDY precursor from decomposition and disproportionation issues seen in diaryliodonium precursors[54].

Spirocyclic iodonium ylides is a fairly recent radiofluorination method and one of the few that have successfully radiofluorinated non-activated and electron rich arenes like **1-49**. Though it is possible to fluorinate these substrates with the electrophilic methods discussed in Section 1.5, it would be preferential to have methods available to perform radiofluorination using high A_m nucleophilic fluoride instead. To this end, groups have developed and adapted transition metal mediated cross-coupling reactions for radiofluorination to address this gap in available methodologies.

1.8 Metal-Mediated Radiofluorination

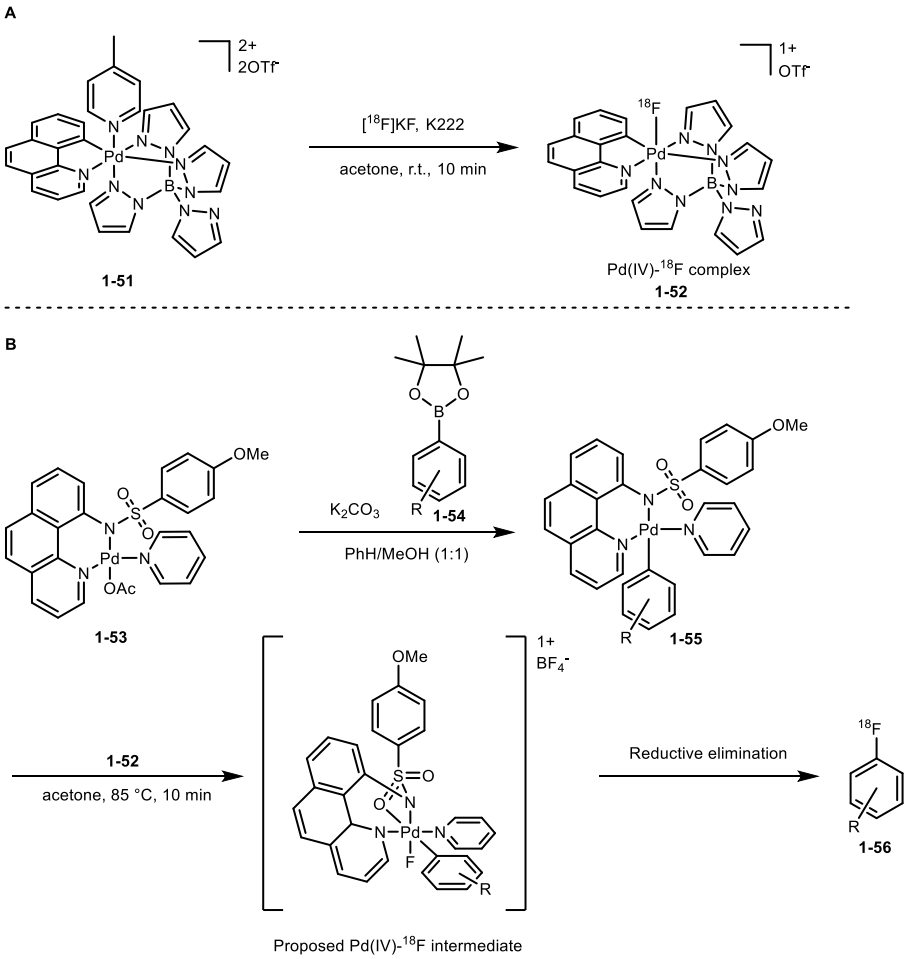

Scheme 1-15: Palladium-mediated radiofluorination

Methods of radiofluorination of arenes using transition metal-mediated cross-coupling reactions were developed in the early- to mid-2010's. Cross-coupling reactions to produce aryl fluoride were previously known, but usually required hour-long reaction times that are too slow for radiolabeling applications[55]. Ritter *et al*. first reported fast palladium-mediated cross-coupling conditions for radiofluorination. The method uses a two-step process with two different palladium complexes. First, standard nucleophilic fluorination conditions are used to coordinate fluoride to form a high oxidation state Pd(IV) species **1-52**, which functions as the oxidant (Scheme 1-15A). The substrate is prepared by installing a boronic ester at the site of desired fluorination to form **1-54** and is coupled to a second palladium complex **1-53** to form a Pd(II) complex **1-55** carrying the substrate. The two complexes are combined and fluoride-bearing palladium can then perform a ligand transfer *via* oxidative addition to the substrate palladium, forming a Pd(IV) complex with substrate and fluoride while reducing itself to Pd(II) in the process. Finally, reductive elimination of the fluoride and substrate produces the fluorinated final product **1-56** (Scheme 1-15B)[56].

The palladium strategy first produces an electrophilic fluorination reagent that can be subsequently used to fluorinate substrates intolerant to direct fluorination. Ritter *et al*. recognized the added reaction time and complexity of the two-step process and subsequently published an improved single step procedure by replacing palladium with a nickel complex (Scheme 1-16).

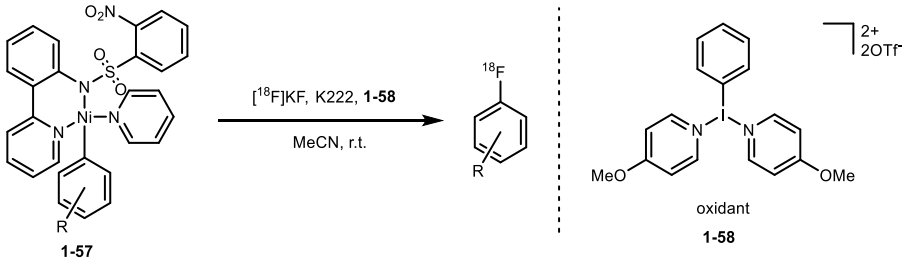

Scheme 1-16: Nickel-mediated radiofluorination

The reaction uses the same principle as the palladium method, and the substrate is borylated and coupled to nickel to form the initial complex **1-57**. However, the oxidant and fluoride source are separated, and a hypervalent iodine reagent **1-58** is used as an oxidant during the radiolabeling reaction such that there is no longer a need to prepare the fluoride as in the palladium reaction. The reaction also has the advantage of tolerance towards aqueous fluoride, so radiolabeling can be performed with aqueous ^{18}F directly from the cyclotron forgoing the usual ion exchange and azeotropic drying steps, which results in a faster synthesis[57]. Despite these advancements, this method exhibited complications during scaleup, as increases in cyclotron water in the reaction mixture caused significant degradation of both the oxidant and nickel complex. Basic reaction conditions resulting from anion exchange to dry the fluoride was also incompatible, and careful buffering was necessary to achieve any appreciable yield, adding further complexity and reproducibility issues to this method[58, 59].

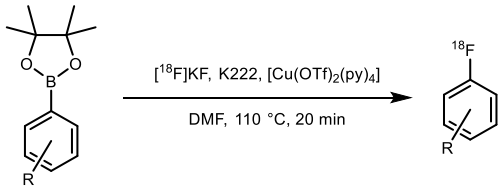

Scheme 1-17: Copper-mediated radiofluorination

Both the Gouverneur and Sanford groups reported radiofluorination of aryl and heteroaryl boronic esters and acids through adaptation of previously reported nonradioactive fluorination procedures using copper and KF. The main challenge was optimization of conditions for the arylboronate ester to be efficient with extremely low equivalents of fluoride typical for radiofluorination (Scheme 1-17)[60]. Sanford further developed copper-mediated fluorination by using arylstannane precursors rather than boronates as an alternative [61].

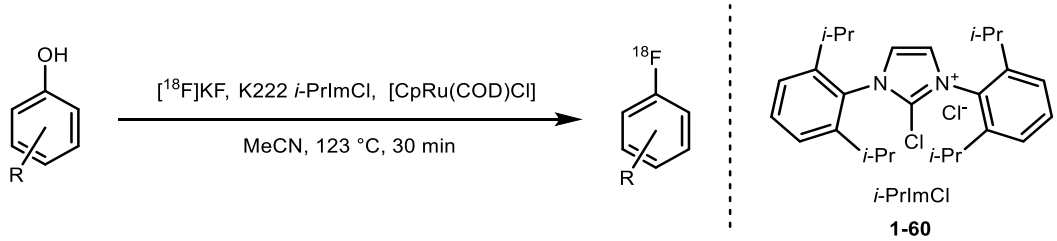

Scheme 1-18: Ruthenium-mediated radiofluorination

Finally, the Ritter group also developed ruthenium-mediated deoxyfluorination conditions using the chloroimidazolium salt fluorination reagent Phenofluor (*i*-PrImCl) **1-60** (Scheme 1-18). This reagent is known to be capable of activating electron-rich phenols for deoxyfluorination, but its use is usually limited to conditions where fluoride is in excess, since *i*-PrImCl forms a positively charged uronium intermediate after addition to the phenol which can sequester fluoride as the ion pair and decrease its nucleophilicity. The group devised a strategy to use ruthenium to coordinate to the ring and reduce the electron density to further activate the ring. Unlike the previously reviewed methods using Pd, Ni, and Cu, the ruthenium is used only for ring activation so the reactions are redox neutral and will be more tolerant towards redox-sensitive functional groups[62].

1.9 Non-Carbon Based Radiofluorination Strategies

Formation of C-^{18}F bond in complex substrates continue to have limitations irrespective of specific methodology. For most substrates and methods high temperatures are required to complete the reaction in a timeframe suitable for the half-life of ^{18}F. Furthermore, these methods often require lengthy and intensive purification procedures after radiosynthesis to remove side products and unreacted precursor, usually via HPLC which adds significant delays to total production time, despite the short reaction period. In order to circumvent these issues, strategies to introduce ^{18}F via non-carbon bonds have been developed to take advantage of strong and facile bond formation between fluorine and other atoms. These methods involve integrating certain functional groups into the probe to enable fast and mild radiolabeling, and currently, Si-^{8}F, B-^{18}F, Al-^{18}F, S-^{18}F, and P-^{18}F have been used for this purpose with varying degrees of success. Because these methods have clean reaction profiles purification of the final product can often be achieved via simple solid phase extraction method that uses small pre-packed disposable cartridges that do not require a pump to operate. These methods are highly reproducible, easily integrated into automated synthesis systems, and require only a fraction of the time that HPLC purification needs at a significantly reduced cost.

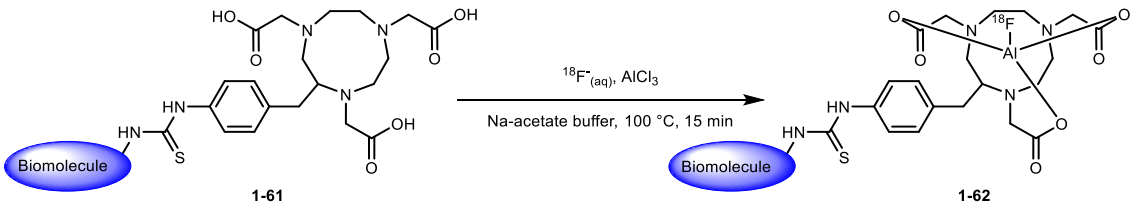

Scheme 1-19: Radiofluorination using aluminum

Anionic fluoride can coordinate strongly to Al(III) as a ligand (>670 kJ/mol), forming an Al-^{18}F complex even at low fluoride concentrations typical of radiofluorination. Introduced by McBride *et al*., this strategy involves integrating the Al-^{18}F metal complex to biomolecules through a chelator such as 1,4,7-triazacylononane-1,4,7-triacetic acid (NOTA; Scheme 1-19). After chelation, the construct could be subjected to simple cartridge purification before formulation for injection[63]. This method directly competes with PET radiometals such as ^{68}Ga with its comparable half-life, with ^{18}F having superior β^+ emission properties and lower production costs, but with the downside of a more complex radiosynthetic procedure. Similar to positron-emitting radiometals, this method is suitable for peptidyl and protein-based tracers but is usually incompatible with small molecule tracers due to the need for large chelator functionalities[64].

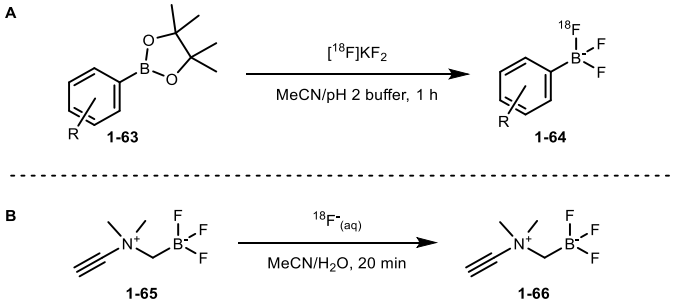

Scheme 1-20: Production of ^{18}F trifluoroborate salts

Ting *et al*. introduced the radiofluorination of boronic esters **1-63** to produce trifluoroborate salts **1-64**. This reaction can be performed in aqueous media and the resulting B–F bond is strong (~580 kJ/mol) and stable *in vivo*. The method requires mixing cyclotron fluoride with cold carrier fluoride source to ensure a minimum of 3 equivalents of fluoride to stoichiometrically occupy all boron valencies, but this does not always result in the low A_m. (Scheme 1-20A). However, reaction times are usually slow and low yielding unless it is performed in high concentrations at microliter volumes, and the need to concentrate eluted ^{18}F to this scale increase manufacturing challenges. Furthermore, this method often requires HPLC purification after radiosynthesis[63].

Gabbai *et al*. demonstrated the viability of ^{18}F-fluorination via isotope exchange (IE) on boron. IE is a method that uses a precursor that is chemically identical to the radiolabelled product, where the only transformation is exchange of pre-installed ^{19}F with ^{18}F (Scheme 1-20B). Since precursor **1-65** and product **1-66** are chemically identical, a time- and labor-consuming HPLC purification procedures can be circumvented using cartridge purification. This also simplifies automation as there is no requirements to integrate an HPLC system into the synthesis unit[65]. Perrin *et al*. further developed trifluoroborate IE and successfully labeled several synthons which were then appended to peptides such as a fluorescent dimeric RGD with high tumor uptake for oncological imaging [66].

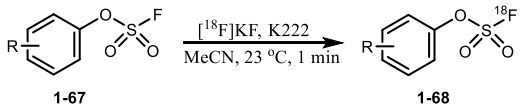

Scheme 1-21: Radiofluorination using arylfluorosulfate

Recently, the Sharpless group introduced sulfur radiofluorination through IE using arylfluorosulfate functionalities, dubbed SuFEx. Originally designed as a click chemistry functional handle to attach nucleophile targets, arylfluorosulfates **1-67** have also demonstrated its ability to capture ^{18}F for radiolabeling purposes (Scheme 1-21). The group demonstrated the efficiency and functional group tolerance of the method using 35 test substrates. SuFEx proceeds with >90 % RCY under mild conditions, and since radiolabeling is performed by IE the products could be purified by cartridge. Fluorosulfates have been previously used in the context of warheads for covalent protein modifications *in vivo,* but the group demonstrated that their reactivity in bulk water is low and it needs to be immobilized in the right orientation to its binding partner for activation. This means arylfluorosulfate-based radiotracers are typically stable *in vivo* avoiding covalent binding to nucleophilic amino acids. Sharpless *et al.* demonstrated the viability of this method by producing a [^{18}F]fluorosulfate-functionalized analog of Olaparib which targets tumor biomarker poly(ADP-ribose) polymerase 1. Though this method has only recently emerged, it holds great potential as a valuable addition to the radiofluorination toolkit[67].

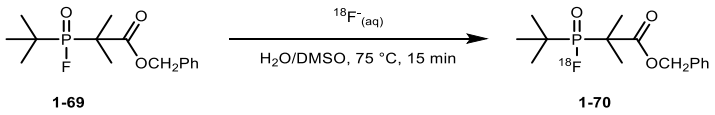

1-69 **1-70**

Scheme 1-22: Radiofluorination using fluorophosphine

Radiofluorination using fluorophosphines by IE was recently reported by Hong *et al.* The group studied radiolabeling efficiency and hydrolytic stability of differently substitueted phosphines and concluded that bulky substituents showed the best results as their lead compound contains two di-*tert* butyl groups on phosphine **1-69** (Scheme 1-22). This compound achieving RCY >97% with heating and 50% RCY at room temperature, and **1-70** maintained *in vivo* stability 120 minutes after injection in mice. Advantages of this method also include compatibility with aqueous solutions, which allows using fluoride directly from the cyclotron, and simple cartridge purification of the product. The group conjugated this fluorophosphine core onto human serum albumin and achieved direct radiofluorination of the protein conjugate at ~5% RCY[68].

1.10 Silicon-Fluoride Acceptors (SiFAs)

Similar to aluminum, boron, sulfur, and phosphorus, silicon can also form a strong bond with fluorine (565 kJ/mol for Si-F vs 485 kj/mol for C-F) and its use in ^{18}F radiochemistry dates back to the 1950s with synthesis of [^{18}F]SiF_4 using metal-fluoride complexes[50]. Early application in radiochemistry comes from the 1970s when hexamethyldisiloxane was used to capture [^{18}F]HF in order to facilitate ^{18}F transport in the form of fluorotrimethylsilane[69]. Though thermodynamically stable, the covalent radius of silicon is much larger compared to carbon and the Si-F bond is highly polarized, which contributes to poor kinetic stability and silicon's susceptibility towards nucleophilic attack. Additionally, silicon's low energy empty d-orbitals can allow a tetravalent silicon to act as a weak Lewis acid, further facilitating hydroxyl group attack in aqueous conditions. The hydrolysis of Si-F bond proceeds by S_N2-like mechanism, but contrary to carbon, a pentavalent intermediate is formed which assists in the substitution (Scheme 1-23)[25].

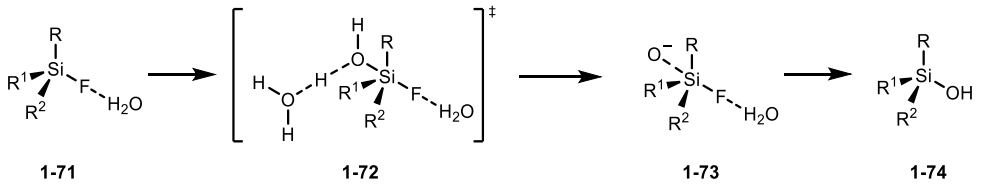

1-71 1-72 1-73 1-74

Scheme 1-23: Mechanism of hydrolysis of organofluorosilanes suggested by Hohne et al.[176]

The first *in vivo* evaluation of Si-^{18}F was performed in 1985 by Rosenthal et al. who synthesized [^{18}F]fluorotrimethylsilane from chlorotrimethylsilane and [^{18}F]tetraethylammonium fluoride with 80% RCY and administered it into mice. They observed immediate and extensive fluoride uptake into bone which indicated a lack of *in vivo* stability due to high defluorination[70]. These results highlight the major limitation of Si-F usage in biological settings, as the low kinetic stability of the bond means organofluorosilanes readily hydrolyze at biological pH. The group measured the half-life of [^{18}F]fluorotrimethylsilane and found it had <1.5 min lifetime at 20 °C in water, and speculated that the poor kinetic stability could be improved by using bulky groups on silicon to sterically shield the Si-F bond and prevent hydrolysis[70].

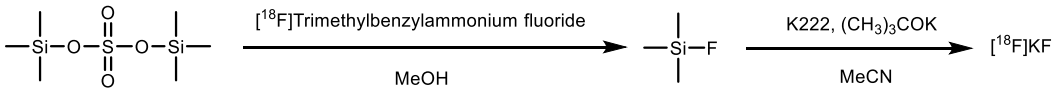

1-75 1-76 1-77

Scheme 1-24: Anhydrous fluoride production through [^{18}F]fluorotrimethylsilane

Early uses of Si-F by Gatley et al. exploited its ease of hydrolysis by using [^{18}F]fluorotrimethylsilane as a fluorination reagent. Aqueous ^{18}F from the cyclotron is captured on calcium phosphate and eluted using base into a solution of bistrimethylsilyl sulfate **1-75** to generate [^{18}F]fluorotrimethylsilane **1-76**. Afterwards, adding a base such as tetraethylammonium hydroxide or potassium *tert*-butoxide along with K222 can hydrolyze the Si-F bond in anhydrous MeCN to liberate nucleophilic fluoride for fluorination (Scheme 1-24). Using this method, azeotropic drying was not necessary to prepare nucleophilic fluoride and the group managed to produce [^{18}F]FDG achieving 30-60% RCY[71].

However, the incorporation of Si-F into PET tracers did not occur until validation of the claim by Rosenthal et al. using sterically hindered substituents to shield the Si-F bond, which was simultaneously performed by the Blower and Schirrmacher et al. in 2006. Both groups investigated a series of alkyl and aryl silylfluorides bearing different bulky substituents and concluded on the importance of *tert*-butyl groups on silicon to achieve sufficient hydrolytic stability for *in vivo* applications[72, 73] Silicon-fluoride acceptor (SiFA) is a term used to describe these molecules and Schirrmacher et al. established that di-*tert*-butyl phenyl SiFA **1-78** provided the best *in vivo* stability.

Schirrmacher et al. also established labeling procedures using IE with their test substrate di-*tert*-butyl phenyl SiFA, which proceeded at rt in 15 min using standard K222/[^{18}F]KF conditions in MeCN for nucleophilic radiofluorination, giving 80-95% RCY with A_m up to 194 – 230 GBq/μmol using 1 ug of precursor (Scheme 1-24). These conditions were also applied for direct one-step radiolabeling of complex substrates like a SiFA conjugated to a fully unprotected Tyr^3-octreotate (TATE) peptide which will be discussed in section 1.11. Similar to other previously described IE radiolabeling methods , HPLC purification was avoided and the compounds were successfully purified using C-18 cartridges[73].

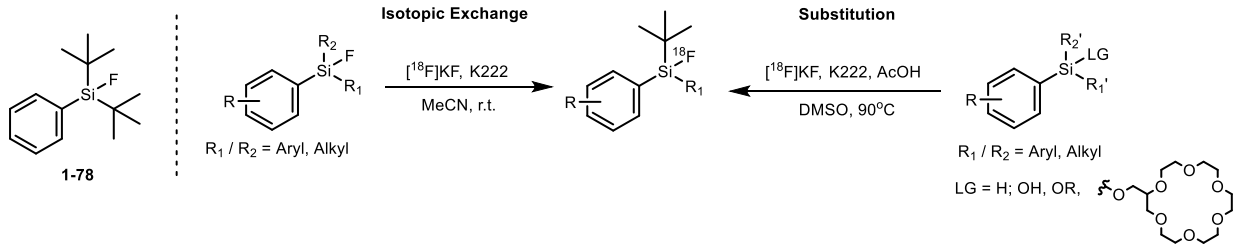

Scheme 1-25: Radiolabeling strategies for SiFA by isotopic exchange or leaving group strategies.

The Blower group employing a leaving group strategy for fluorination, employing silanes, silanols and silylethers as starting materials. The group converted *tert*-butyldiphenylmethoxysilane to [^{18}F]*tert*-butyldiphenylfluorosilane using aqueous $^{18}F^-$ without azeotropic drying in 5 minutes[72]. The leaving groups method was further developed by the Ametamey group and expanded to using hydride, hydroxy, and other alkoxy leaving groups to produce similar results as via IE. The method uses similar K222/[^{18}F]KF conditions with the addition of acetic acid to protonate hydroxy and alkoxy groups to improve their leaving ability, but unlike IE also required heating to 65 – 90 °C in order to achieve similar RCY[74]. Lu et al. also developed crown ether leaving groups capable of chelating potassium. This results in a conceptually elegant system that doesn't require K222 in the reaction cocktail, but the method is hampered by the poor solubility of [^{18}F]KF in organic solvents and only results in ~10% RCY (Scheme 1-25)[75]. DFT calculations in condensed phase (MeCN) show product formation by IE is isoenergetic, while using more stable silanol or silane precursors results in endergonic reactions. The anionic pentavalent hydrosilicate intermediates are also calculated to be higher in energy than fluorosilicate intermediate that for IE, resulting in higher energy requirements to employ LG strategy and the comparative efficiency of IE[65].

The requirement of bulky blocking groups for SiFA chemistry is an inherent limitation of this technology due to the high lipophilicity of these compounds. This lipophilicity issue has limited more widespread use of SiFA in radiotracers space despite its excellent radiolabeling properties. Compounds without *tert*-butyl groups rapidly hydrolyze even if aryl groups are used as steric blocking groups. Thus, [^{18}F]triphenylfluorosilane has a poor serum stability half-life of 5 min. Compounds bearing a single *tert*-butyl group, e.g. [^{18}F]*tert*-butyldiphenylfluorosilane, are stable to *in vitro* stability tests but had observable bone uptake after injection in rats[72] indicating hydrolysis of the Si-F bond in vivo. Only compounds bearing two *tert*-butyl groups such as [^{18}F]di-*tert*-butylphenylfluorosilane exhibited adequate stability for *in vivo* applications[71]. The steric blocking groups impact on biodistribution of tracers in vivo is generally characterized by high accumulation in the liver and non-specific uptake in organs resulting in poor pharmacokinetic properties and limited binding to the target. In brain imaging applications, some lipophilicity is necessary in order to cross the protective blood-brain barrier (BBB) membrane through passive diffusion, so attempts have been made to adapt SiFA for this application. However, if the compound is too lipophilic (logD > 4), it will instead tend to become trapped in the greasy portion of the bilayer and fail to penetrate[75]. The first small molecule SiFAs produced by the Blower and Schirrmacher groups exhibited the phenomenon.[3]

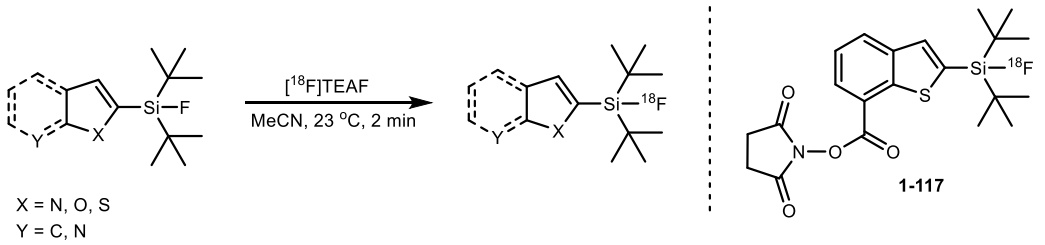

Scheme 1-26: Radiolabeling of heteroaromatic SiFAs

In an effort to reduce the inherent lipophilicity of SiFAs without modifying the di-*tert*-butyl groups, Murphy et al. developed a series of heteroaromatic SiFAs that replaces the phenyl ring with five-membered and fused heteroaromatic rings (Scheme 1-26). The group successfully used optimized radiolabeling conditions to successfully label all derivatives by IE with good RCCs from 81 to 91% after only 2 minutes using 150 nmol of precursor, and identified the benzothiophenes as their lead compound with >90% RCC for their derivatives. The group further demonstrated the applicability of hetSiFAs by synthesizing a *N*-hydroxy succinimide ester functionalized benzothiophene SiFA derivative **1-117** and conjugated it with a cholecystokinin tetrapeptide, and successfully fluorinated the peptide-hetSiFA conjugate with 58% decay corrected yield. The radiolabeled construct was injected into mice and was found to have good *in vivo* stability with minimal fluoride bone uptake[76].

1.11 SiFA Peptide Radiopharmaceuticals

Peptide biomolecules have seen widespread use in nuclear medicine, owing to their ability to interact with numerous pathologically significant targets expressed on cell surfaces. Work on the SiFA platform primarily involved trying to mitigate its lipophilicity through the introduction of hydrophilic auxiliaries and also using SiFA in conjunction with peptides which are more tolerant towards structural modifications as well as SiFA lipophilicity compared to small molecules[75]. Since peptides are not stable towards harsh C-^{18}F radiolabeling conditions, they are usually labeled indirectly through the conjugation of a ^{18}F bearing prosthetic group to the peptide by a functional handle. This synthetic method is multi-stepped and usually technically complex for automation, so the simplified labeling and purification of SiFA is well suited for this purpose. To this end, a series of SiFA building blocks were developed with functional handles that could be conjugated to a variety of peptides or linkers either before or after radiofluorination **1-80** to **1-92** (Figure 1-4)[65].

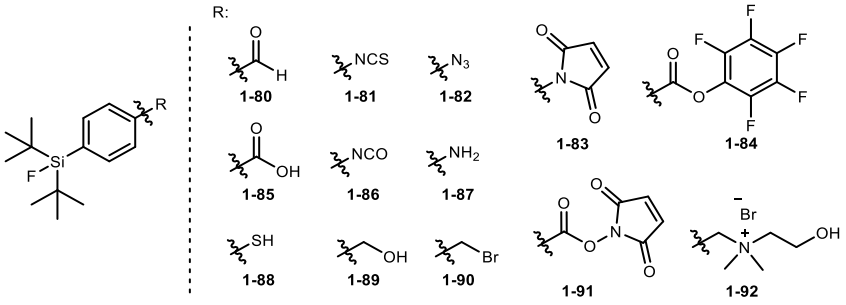

Figure 1-4: Functionalized phenyl SiFA for peptide conjugation

Derivatives of octapeptides octreotide or TATE with high affinity for somatostatin receptor subtype 2 (SSTR2), highly expressed in neuroendocrine tumors are used for clinical PET imaging of these tumors. The peptide construct is internalized into the cell after interacting with the receptor and accumulates in the cancerous cells, permitting PET imaging of the tumor[77]. Clinically used PET imaging agent [^{68}Ga]Ga-DOTA-TATE uses the PET radiometal ^{68}Ga attached to the targeting peptide through a metal chelator 1,4,7,10-tetraazacyclododecane-1,4,7,10-tetraacetic acid (DOTA). Early work by Schirrmacher et al. attempted to adapt this platform for SiFA use by directly removing the chelation moiety and replacing it with SiFA. They demonstrated that it's possible to label unprotected SiFA conjugated TATE directly, but the produced tracer suffered from low A_m and high lipophilicity, rendering it unsuitable for imaging[73]. This resulted in the subsequent development of 2-step procedures for peptide labeling, and Schirmaccher et al. first use an aldehyde functionalized SiFA core **1-80** which could be rapidly labeled with high A_m (>5000 Ci/mmol), quickly purified by C-18 cartridge, and subsequently conjugated at room temperature to a pre-installed *N*-terminal amino-oxy group on the TATE peptide[78]. The SiFA IE method was further improved via adoption of the previously mentioned "Munich method" for simplified fluoride preparation avoiding azeotropic drying. Furthermore, it has been shown that SiFA peptides can be successfully directly labeled in one step, without the need for a 2-step process[79, 80].

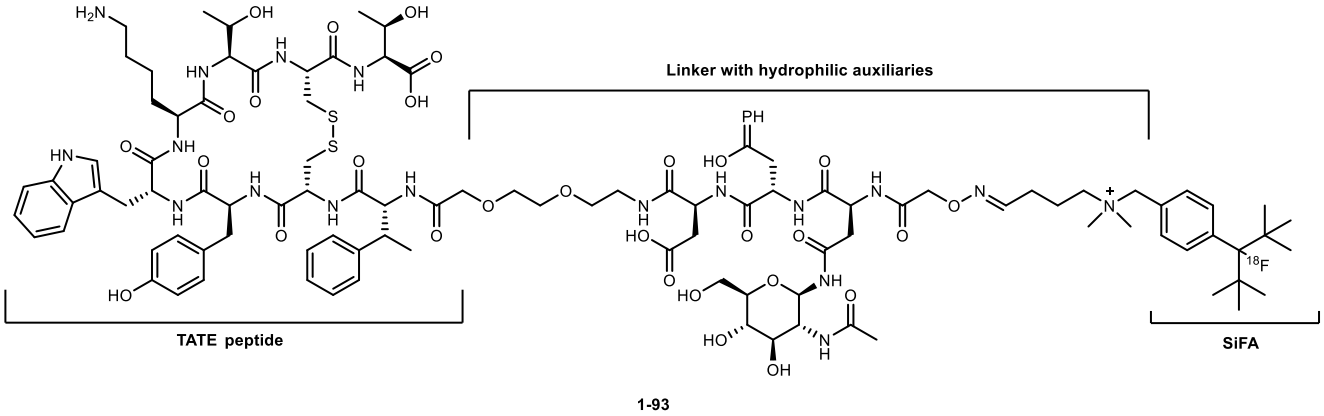

Figure 1-5: [^{18}F]SiFA*lin*-TATE use for SSTR2 imaging

The SiFA-TATE platform was progressed extensively and culminated with development of [^{18}F]SiFA*lin*-TATE **1-93**, which contains a variety of polar auxiliaries to mask the SiFA lipophilicity (Figure 1-5)[81]. [^{18}F]SiFA*lin*-TATE can be directly labeled using the Munich method, taking full advantage of SiFA radiochemistry. Studies that compare [^{68}Ga]Ga-DOTA-TATE to [^{18}F]SiFA*lin*-TATE in mice showed similar biodistribution profiles, with [^{18}F]SiFA*lin*-TATE showing superior tumor uptake (18.51% ± 4.89% vs. 14.10% ± 4.84% ID/g). These positive results of pre-clinical studies culminated in the first clinical study of [^{18}F]SiFA*lin*-TATE in 2019 in 13 patients which confirmed its usability as a PET imaging agent producing similar image quality as clinically validated [^{68}Ga]Ga-DOTA-TATE[79].

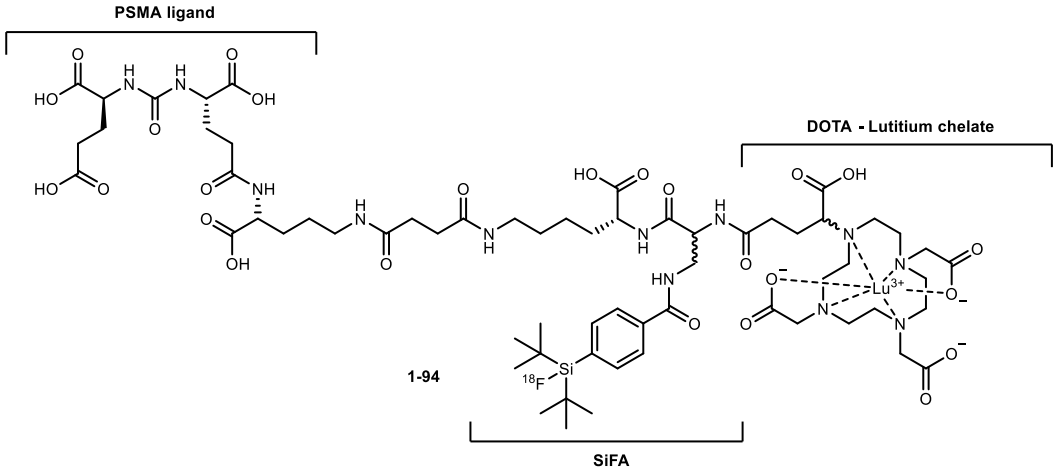

Figure 1-6: [^{18}F]Lu-rhPSMA-7 used for PSMA imaging and cancer treatment

The incorporation of SiFA into a variety of peptide-targeting moieties have been attempted by several groups, all following a similar strategy[18]. The typical construct consists of the peptide conjugated to a linker with built-in hydrophilic auxiliaries and a functional handle, which can be used to conjugate to the SiFA moiety before or after radiolabeling[82]. The Wester group conjugated SiFA onto prostate-specific membrane antigen inhibitor (PSMA) peptide used for targeting prostate cancer **1-94**. Their group introduced a DOTA which significantly decreases lipophilicity, and provides the option of chelating other radiometals such as ^{68}Ga, ^{111}In, and ^{177}Lu. ^{68}Ga provides another PET isotope option if ^{18}F is not available, ^{111}In can provide SPECT imaging modality, and ^{177}Lu is a beta radiation emitter that can kill cancer cells and is used for radioligand therapy (RLT) rather than imaging (Figure 1-6)[83]. The compound underwent clinical studies in 202 patients and showed excellent imaging resolution, tumor uptake, and biodistribution similar to ^{68}Ga based PMSA probes[84]. The capability of simultaneous imaging and treatment using SiFA and ^{177}Lu promises to improve dosimetry, as previously two chemically different compounds using ^{68}Ga for imaging and ^{177}Lu for treatment would have been necessary, affecting dosimetry precision[18].

Lindner et al. also conjugated phenyl SiFA to fluiclatide, a bicyclic peptide used for imaging integrin glycoproteins upregulated in many cancer types. Polar groups were used in the linker composition, and the group added several amino acids to improve pharmacokinetics resulting in a tracer that had good tumor uptake and biodistribution in mouse model[80].

Despite these successes, the difficulty in optimizing and refining pharmacokinetics of SiFA-peptide conjugates is not trivial. The Ametamay group conjugated SiFA to gastrin-releasing peptide receptor (GRPr) targeting peptides for use in several cancer types, utilizing the same strategy of adding polar groups to attenuate the SiFA lipophilicity, but was unable to produce a good candidate due to low tumor uptake and poor hepatobiliary clearance[85]. Lindner et al. also conjugated phenyl SiFA to GRPr targeting peptide bombesin, adding several polar groups such as PEG groups, carbohydrate, and amino acid residues. Despite these efforts, the conjugate still had high liver accumulation and could not be used to successfully image desired targets[80].

1.12 SiFA in Proteins

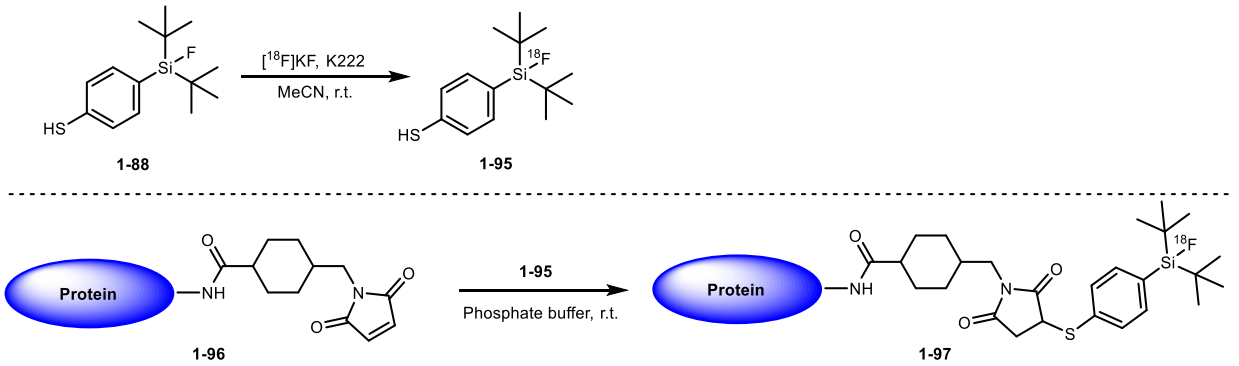

Scheme 1-27: Two-step SiFA radiolabeling of proteins

Radiofluorination of large biomolecules such as proteins and antibodies are typically performed using carbon based ^{18}F prosthetic groups which are labeled, HPLC purified, and finally conjugated. The reaction is technically difficult and can take upwards of several hours to deliver the final product[65]. With the success and ease of SiFA conjugation on peptides, similar strategies can be applied to proteins to simplify this process. A two-step procedure is usually used, first with SiFA radiolabeling of a prosthetic group, followed by the conjugation of the latter to the protein of interest (Scheme 1-27). These prosthetic groups include maleimide **1-83** or thiol **1-88** functionalized SiFA cores which were used to label rat serum albumin (RSA) with adequate RCY (~5%) for blood pooling imaging and had good *in vivo* stability[86]. Isocyanate functionalized SiFA **1-86** was later developped to enable direct conjugation to lysine sidechains, eliminating the need to pre-functionalize the protein for conjugation. This method was used to label RSA, apotransferrin, and bovine IgG with 30 – 80% RCY depending on SiFA/protein ratio and good A_m (2.7 – 4.5 Ci/μmol)[87]. Though SiFA IE remained efficient in the presence of most functional groups, base-sensitive active-esters, e.g. *N*-hydroxysuccinimide esters (NHS) hydrolyze under normal radiolabeling conditions. However, buffering the labeling cocktail with oxalic acid solved this issue, and active ester [^{18}F]SiFB was labeled using this cocktail in 56% RCY while avoiding hydrolysis. RSA was also labeled with [^{18}F]SiFB and showed similar biodistribution to established tracer [^{18}F]RSA, but with the advantage of a technically simplified radiosynthetic procedure[88].

Glaser et al. was also able to apply SiFA IE methodology to label human epidermal growth factor-targeted affibody $Z_{HER2:2891}$, used for imaging HER2-positive breast cancer. A C-terminus cysteine modification was used to conjugate the affibody to a maleimide functionalized SiFA. Remarkably, the construct was directly labelled in aqueous conditions with heating to 95 °C for 15 min in RCY of 38%. Unfortunately, the tracer had poor hydrolytic stability with high ^{18}F uptake in bones as well as poor tumor uptake, so it was not further evaluated[89]. Nevertheless, the ability to apply SiFA IE for direct one-step ^{18}F-labeling of a large biomolecule is noteworthy.

1.13 SiFA in Small Molecules

The use of SiFA in small molecules has been limited because SiFA motif significantly alters the physicochemical properties and pharmacokinetics of the small molecule targeting vector of similar size[18]. As a result, only a handful of small molecule PET tracers integrating SiFA have been reported, with only a single report of a relatively successful tracer.

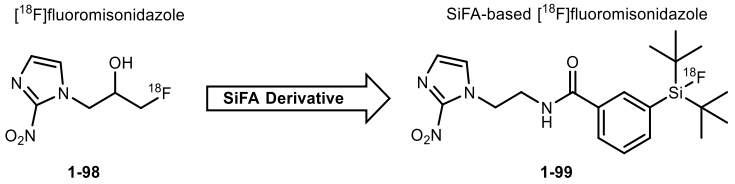

Scheme 1-28: SiFA based [^{18}F]fluoromisonidazole for hypoxia imaging

Bohn et al. reported SiFA labeled version of [^{18}F]fluoromisonidazole **1-98** which is used clinically to image hypoxia, and attempted to decrease the size of the bulky substituents on SiFA to limit lipophilicity despite consistent reports of steric requirements on silicon. Bohn et al. synthesized several alkyl and aryl derivatives of a SiFA based [^{18}F]fluoromisonidazole and found that only dinaphthyl and di-*tert*-butyl derivatives **1-99** were sufficiently stable in vivo(Scheme 1-28). These sterically hindered compounds were unsuccessful as PET tracers in preclinical studies due to high lipophilicity resulting in retention of those tracers in lung capillaries[90].

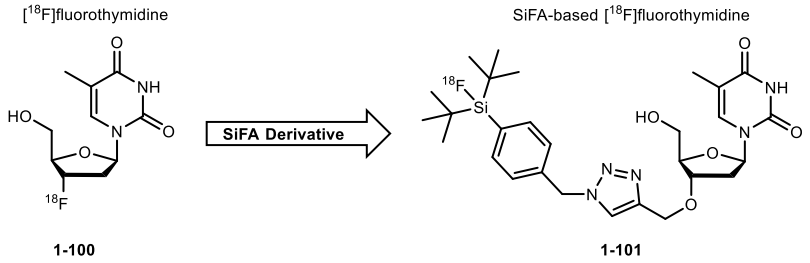

Scheme 1-29: SiFA based [^{18}F]fluorothymidine for cancer imaging

The Schulz group produced SiFA analogues of nucleosides and nucleotides with ~40% RCY and high A_m (10 Ciμmol) from the corresponding hydrosilane starting material as a potential replacement for [^{18}F]fluorothymidine **1-100** used in cancer imaging, but did not test them to generate *in vivo* data due to concerns about the compound's high lipophilicity (Scheme 1-29)[91].

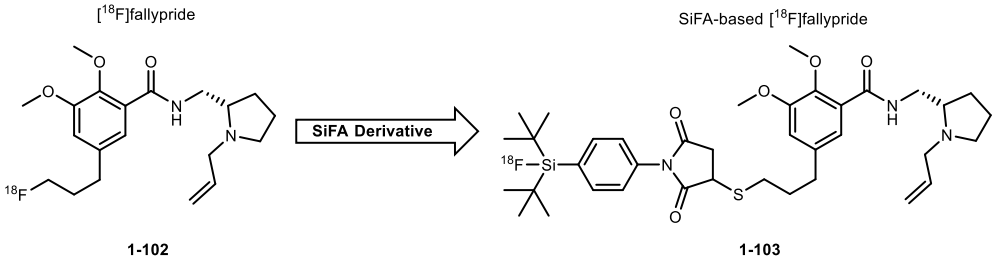

Scheme 1-30: SiFA based [^{18}F]fallypride for D_2-receptor imaging

Wängler et al. developed SiFA analogues (e.g. **1-103**) of the D_2-receptor imaging agents [^{18}F]fallypride **1-102** and [^{18}F]desmethoxyfallypride. However, these tracers had 44- to 650-fold lower affinity to D_2, though still in a usable nanomolar range. Some of these tracers were successfully labeled by IE in ~60% RCY, but the lead candidate **1-103** with the highest affinity towards D_2-receptor target was labeled in RCY of only 16.6% and could not be purified using simple cartridge purification (Scheme 1-30). The group did not report an *in vivo* evaluation of this tracer[92].

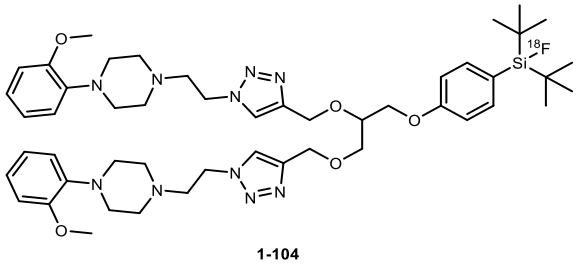

1-104

Scheme 1-31: SiFA based bivalent 5-HT_{1A} serotonin receptor ligands

Hazari et al. developed putative SiFA based bivalent 5-HT_{1A} serotonin receptor ligand **1-104**. The tracer uses two 5-HT_{1A} targeting domains based on evidence suggesting the target 5-HT receptors exist in dimeric and oligomeric forms. This multimeric approach also serves to help masking the lipophilicity of SiFA. The tracer was radiolabeled from the hydrosilane precursor resulting in ~50% RCY and high Am (13 Ci/μmol) (Scheme 1-31). The compound readily crossed the BBB, and exhibited high uptake 5-HT_{1A} rich regions in rat models as well as expected reduction of uptake in serotonin-depleted rat models. This is a rare example of a relatively successful *in vivo* imaging result using SiFA in small molecules and suggests it is possible to compensate for the lipophilicity of SiFA on small molecules with adequate masking[93]. However, no further evaluation of this tracer has been reported in almost a decade since the original publication.

Irrespective of imaging target, binding motif, and labeling methodology, the intrinsic lipophilicity of SiFA remains a major drawback of this method and limits its widespread use in small molecule space despite the benefits in purification and radiolabeling. Peptide and protein-based tracers address this problem through the introduction of adequate hydrophilicity to mask the SiFA and have found recent success in clinical trials with good imaging quality due to the advantage of much simpler radiosynthesis compared to carbon-based ^{18}F PET tracers. However, small molecules are usually unable to tolerate the extensive structural modifications necessary to employ this strategy while maintaining bioactivity and cannot typically employ SiFA as the imaging motif, and the issue of lipophilicity usually presents a major problem[65]. Strategy to derivatize existing small molecule PET tracers with SiFA technology has mostly failed due to the massive change in the pharmacokinetics of the targeting moiety that cannot be easily overcome. However, there has also been some success in employing SiFA in the context of brain imaging if adequate masking of its lipophilicity is present, and SiFA derivatives seems to retain their ability to cross the BBB. The greatest potential for successfully integrating SiFA in small molecules is to integrate it into a PET imaging probe scaffold that already have a significant hydrophilic binding region present to offset the lipophilicity of SiFA. In this manner, the high lipophilicity of SiFA will theoretically have minimal impact on binding, while conferring brain permeability and a highly simplified radiolabeling process. In this thesis I report a potential

scaffold that meets these requirements, which can be used to PET image histone deacetylases (HDACs) in the brain.

1.14 Histone Deacetylases

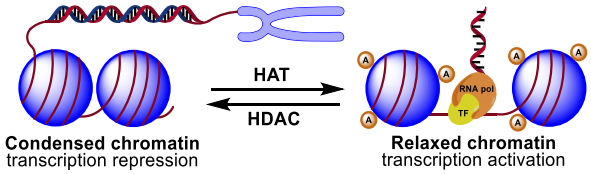

Figure 1-7: Histone acetylation control on gene expression

In the nucleus eukaryotic cells, DNA is wrapped tightly around histone proteins by ionic interaction of positively charged histones with the negatively charged DNA backbone. This restricts access of transcription machinery to DNA, preventing gene expression under normal circumstances. Epigenetic modifications to chromatin either in the form of DNA or histone modifications are necessary to allow gene transcription. One such epigenetic modification is histone acetylation, where the positively charged ε-amino group of lysine on the histone is neutralized by acetylation, decreasing ionic interactions and loosening the bound DNA to allow for transcription. This reversible acetylation process controls gene expression levels, with histone of lysine acetyltransferase enzymes (HATs) transferring acetyl groups from acetyl-CoA to lysine residues on histones to activate gene transcription and HDACs removing the acetyl groups to deactivate the transcription (Figure 1-7)[94].

Entry	Protein	Class	Cofactor	Subcellular localization
1	HDAC 1	I	Zn^{2+}	Nucleus
2	HDAC 2	I	Zn^{2+}	Nucleus
3	HDAC 3	I	Zn^{2+}	Nucleus/Cytoplasm
4	HDAC 8	I	Zn^{2+}	Nucleus
5	HDAC 4	IIa	Zn^{2+}	Nucleus/Cytoplasm
6	HDAC 5	IIa	Zn^{2+}	Nucleus/Cytoplasm
7	HDAC 7	IIa	Zn^{2+}	Nucleus/Cytoplasm
8	HDAC 9	IIa	Zn^{2+}	Nucleus/Cytoplasm
9	HDAC 6	IIb	Zn^{2+}	Cytoplasm
10	HDAC 10	IIb	Zn^{2+}	Cytoplasm
11	HDAC 11	IV	Zn^{2+}	Nucleus
12	Sirtuin 1	III	NAD^{+}	Nucleus
13	Sirtuin 2	III	NAD^{+}	Nucleus
14	Sirtuin 3	III	NAD^{+}	Nucleus/Cytoplasm
15	Sirtuin 4	III	NAD^{+}	Mitochondria
16	Sirtuin 5	III	NAD^{+}	Mitochondria
17	Sirtuin 6	III	NAD^{+}	Mitochondria
18	Sirtuin 7	III	NAD^{+}	Nucleus
19	Sirtuin 8	III	NAD^{+}	Nucleus

Table 1-4: Classes, types and localization of mammalian histone deacetylases

18 HDACs discovered in mammals can be divided into two groups depending on the cofactor: zinc-dependent “classic” HDACs and nicotinamide-adenine-dinucleotide (NAD)-dependent sirtuins which are also referred to as class III Sir2-like proteins. The zinc-dependent HDACs are numbered according to their chronological order of discovery and are divided into 4 classes based on DNA sequence similarity (Table 1-4)[94].

Class I (HDACs 1-3, 8) share sequence similar to the yeast transcription regulator reduced potassium dependency 3 (Rpd3) protein and share high homology within the class, with 45 – 95% amino acid sequence identity between the four individual HDACs. They are mainly located in the nucleus but can also be localized in the cytoplasm or other cell organelles which suggests they interact with other targets beyond histones. Classes IIa (HDACs 4, 5, 7, 9) and IIb (HDACs 6, 10) share some similarities in their catalytic domains as Class I, but also contain sequence domains that differ significantly and instead are similar to yeast histone deacetylase 1 protein (Hda1p). Also similar to Class I is the highly conserved catalytic domain within the members of Class II, and the 4 HDACs of Class IIa share 48 – 57% sequence identity. HDAC 10 and HDAC 6 share a sequence identity of 55% and differ from the other Class II members in that they share a unique feature of a duplicate independently functioning catalytic domain not seen in any other HDAC. . All members of Class II HDACs show some presence in cytoplasm which suggests their major roles in deacetylating non-histone targets. HDAC 11 is the only Class IV member which shares catalytic domain sequence homology with both Class I and II. It is known to regulate protein stability of DNA replication factor CDT1 and expression of anti-inflammatory cytokine interleukin 10[95].

All classic HDACs isoforms share a common catalytic deacetylation mechanism and a conserved active site amino acid sequence. The site consists off a tubular pocket, a zinc-binding site, and active residues of a tyrosine and two histidine that are H-bonded with two aspartic acids. Using HDAC8 as an example, once an acetylated ε-amino group of lysine enters the pocket, it coordinates to the zinc, and then histidine residue H143 acts as a base and facilitates nucleophilic attack of the carbonyl by activating a water molecule also coordinated to zinc. The other histidine H142 helps to stabilize the tetrahedral intermediate as an electrostatic catalyst along with a tyrosine residue is also positioned near zinc, opposite to the histidine residues[96]. The zinc and tyrosine residues also participate in activating the target carbonyl for nucleophilic attack (Scheme 1-32). These catalytic residues are conserved across all zinc-based HDAC isoforms except for Class IIa, where the tyrosine residue is replaced by histidine, thought to function in a similar capacity[95].

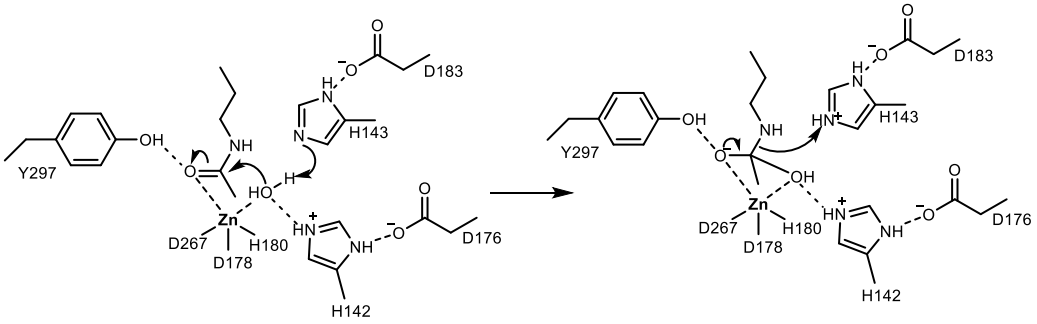

Scheme 1-32: Catalytic Mechanism of HDAC 8

HATs have high substrate specificity with each class having a particular histone that it acts upon, but this is not observed in HDACs which appear to have diverse targets and details of substrate specificity is still under investigation. Biological evaluation of HDACs is difficult, as most HDACs have significantly decreased activity when purified to homogeneity and tested *in vitro.* HDACs appear also to have an adequate level of redundancy as studies in knockout animal models show that different isoforms can compensate for the lack of activity of the knocked-out enzyme both within the same class and sometimes from another class. However, constitutive knockout of multiple HDACs is lethal either during embryonic or early postnatal development, highlighting their individual importance[97]. Beyond histones, a study identified over 1700 individual cytoplasmic, mitochondrial, and nuclear proteins involved in diverse cellular processes as targets for deacetylation[98]. Given the wide-ranging biological implication of HDACs, they likely play vital roles in regulating numerous protein activities through control of acetylation levels along with their obvious roles in opposing the function of HATs to control gene expression. Aberrant expression of HDAC has been shown to affect gene expression directly, and it is implicated in many human diseases including cancer, neurological disorders, inflammatory diseases, metabolic disorders, cardiac diseases, and pulmonary diseases[95].

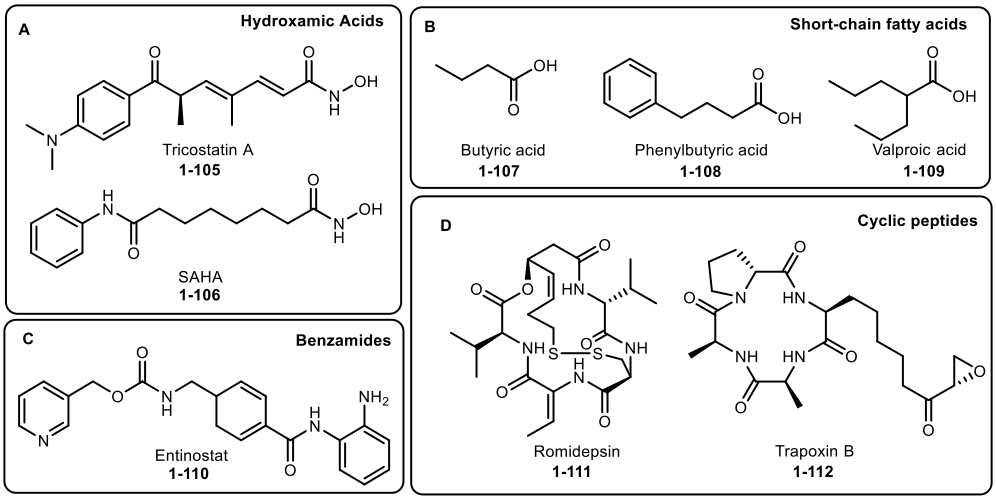

Figure 1-8: Classes of HDACi

Beside low *in vivo* activity, biological evaluation of the functions of individual HDAC isoform is also complicated by the lack of tools to selectively inhibit HDAC isoforms. This obstacle is due to highly homologous HDAC active sites, making selectivity an ongoing issue when designing HDAC inhibitors (HDACi). The first identified HDACi was the short-chain fatty acid *n*-butyrate **1-107** in 1977 in a report by Riggs et al. that showed millimolar concentrations of **1-107** was capable of inducing accumulation of acetylated histones (Figure 1-8B)[99]. Next, the natural product Trichostatin A **1-105**, isolated from a strain of *Streptomyces* in 1990 by Yoshida et al., was found to increase acetylation, and was the first member of the group of HDACi bearing a hydroxamic acid motif[171]. This class of HDACi bind by insertion of a long aliphatic chain into the binding pocket, allowing the hydroxamic acid to coordinate to the zinc center in a bidentate fashion through the carbonyl and the hydroxyl groups (Figure 1-8A)[95]. Trapoxin, the first in the group of cyclic peptide-based HDACis, was isolated in 1993 and was also the first HDACi found to irreversibly inhibit HDAC activity through an epoxyketone moiety (Figure 1-8D)[100]. Two important HDACi reported in 1998 greatly accelerated their clinical interest: suberoylanilide hydroxamic acid (SAHA) **1-106** a hydroxamic acid HDACi was reported by Richon et al[101]; and romidepson, a cyclic peptide was isolated from *Chromabaterium violaceum*. The latter coordinates the HDAC zinc center through a thiol chain that arises from *in vivo* reduction of an intramolecular disulfide bond[102]. Romidepson underwent phase I clinical trials and was found to be effective against T-cell lymphoma, which quickly spiked interest in HDACi as potential chemotherapy agents for cancer. SAHA was approved by FDA in 2006 for chemotherapy use, followed in 2009 by romidepsin **1-111**[95]. The final class of HDACi are benzamides, with the first report in 1999 of entinostat **1-110** (Figure 1-8C)[103]. This class of HDACi binds to the zinc center through the carbonyl and amino group to form a chelate complex and is characterized by slow binding resulting in time-dependent inhibition, as it converts from a transiently bound form to a strongly bound pseudo-irreversible form[104].

These early HDACi such as SAHA and Trichostatin A are “pan-HDAC inhibitors”, capable of binding to nearly all HDACs. Affinity to individual isoform may vary, with some isoform inhibition requiring concentrations higher than pharmacologically feasible levels, but these HDACi are generally considered non-selective[95]. Development of selective inhibitors is challenging due to binding site homology, but selective inhibition of some isoforms is easier to achieve than others. Both *n*-butyrate and trapoxin **1-112** could not inhibit HDAC

6, which suggested distinct differences in its binding pockets[105]. Benzamide class inhibitors also preferentially inhibit Class I HDACs, except for HDAC 8. These insights, along with high-throughput screening methods, have resulted in recent reports of a few isoform-specific HDACi[95], but the development of specific HDACi for every isoform is still an ongoing challenge. The limited selectivity of available HDACi is likely the source of opposing results in their biological evaluation, such as conflicting reports of pan-HDACi promoting both pro- and anti-inflammatory effects when administered to different cell lines contributing to inflammatory pathways[106]. Despite these challenges, HDACi has led to significant advances in furthering our understanding of the diverse roles of HDACs in pathology of different diseases including neurological disorders. Association between aberrant HDAC expression patterns and several neurological disorders has been well established, and the potential application of HDACi to treat these disorders was investigated in mouse and cell models[107].

1.15 Implication of HDACs in Neurological Disorders

Despite poor isoform selectivity, treatment of neurological conditions with HDACi has emerged as an attractive approach to treat both acute injury and a variety of chronic neurological issues. The HDACi valproic acid **1-109** is commonly used as an antiepileptic drug and mood stabilizer and has been tested in stroke models, suggesting it acts through CNS targets. Cerebral ischemia is a mechanism of acute brain injury resulting from impaired blood flow to the brain, which can cause ischemic stroke leading to permanent disability or death. Both *in vitro* and *in vivo* data has suggested that HDACi promotes neuroprotection following ischemia by reducing brain infarction and suppressing neuroinflammation[108]. Though evidence suggests global HDAC inhibition is sufficient to induce neuroprotective effects after ischemia, the explanation for these beneficial effects remains controversial due to the non-selective nature of the inhibition and the large array of targets implicated in the neuronal function and survival in response to injury. However, one established and important mode of neuroprotection is via decreasing inflammation to prevent secondary tissue damage after ischemia. Administering HDACi has been shown to decrease cerebral inflammation through up-regulation of numerous cell survival-promoting factors such as interleukin-10 which restricts inflammatory gene activation, erythroid 2-related factor Nrf2 which increases resistance to oxidative stress, heat-shock protein HSP70 a key anti-apoptotic which suppresses death-promoting factors, and anti-apoptotic Bcl2 protein which suppress microglia and monocyte activation[109].

HDACi has also been tested in animal models of various neurodegenerative diseases. Alzheimer's disease (AD) is the most common neurodegenerative disorder which affects ~1 in 9 people aged 65 and older. The disease involves progressively worsening cognitive impairment and memory loss leading to dementia and noncognitive symptoms such as delusions, agitation, personality changes, and mood swings[110]. The relationship between acetylation patterns and AD has been studied using *in vivo* and *in vitro* models and has shown the ability of HDACi to reduce the severity of AD symptoms and affect the buildup of intracellular neurofibrillary tangles of abnormally phosphorylated tau-proteins, a hallmark of AD pathology. Several studies in mouse model using a variety of different HDACi have shown improvements in memory function, synaptic plasticity, and ameliorated cognitive deficiencies. The positive effects on memory were achieved even when HDACi was administered at a late stage after the onset of neuronal cell death. Though the HDACi used in the studies were not isoform-specific, the most suitable isoform targets

for AD have been identified as HDAC2 and HDAC6[107]. Overexpression of HDAC2 has been shown to negatively impact memory and decrease synaptic plasticity[111], while post-mortem analysis of AD brain samples showed aberrant expression levels of HDAC6 in cortices and hippocampi[112]. HDAC6 is known to interact with non-histone targets α-tubulin and tau proteins, both of which are related to learning and memory. Acetylating α-tubulin improves axonal transport[113], and acetylating tau protein protects them from hyperphosphorylation which causes aggregation[114]. The link between decreasing HDAC6 expression in AD mouse model causing restored learning and memory is likely related to increased acetylation of these two non-histone targets.

Parkinson's disease (PD) is a common neurodegenerative disorder affecting ~2% of people above the age of 65. The disease is characterized by motor dysfunctions such as resting tremors, muscle rigidity, difficulty in starting a movement, and hypokinesia. The pathological feature of PD is the presence of neuronal misfolded α-synuclein protein deposits, as well as degeneration of dopaminergic neurons in the substantia nigra pars compacta region of the brain causing dopamine depletion[115]. Though the exact causes and molecular basis for PD are not yet fully understood, *in vitro* and *in vivo* models, as well as clinical data suggest a link between disease pathology and altered histone acetylation-mediated gene expression[107]. Data suggests α-synuclein binds to histones resulting in a reduction of acetylation and causing damage to dopaminergic neurons[116]. Due to this relationship between histone acetylation and PD, HDACi has been speculated as a promising treatment with several being tested in preclinical studies and clinical trials. Pan-HDACi valproic acid showed good promise in animal models through the activation of numerous neuroprotection targets as well as suppressing neuroinflammation which accompanies neurodegradation of PD, but the 2 clinical trials conducted in PD patients both failed to elicit any improvement of symptoms[117]. Other pan-HDACi sodium phenylbutyrate, vorinostat, and Trichostatin A have also been tested, and all exhibited beneficial neuroprotective activity through activation of neurotrophic factors which helps preserve dopaminergic neurons from neurotoxicity, as well as neuroinflammation suppression. However, reports also indicate adverse effects of HDACi, such as valproic acid inducing apoptosis in differentiating neurons in the hippocampus and Trichostatin A inducing cell death in dopaminergic neurons. These conflicting results is likely due to studies performed using homogeneous cell cultures with the function of the inhibitor differing depending on cell type[107]. The role of individual HDACs in PD pathology is not fully elucidated and it is likely that additional trials are warranted with isoform-specific inhibitors to elucidate the correct pharmacological use of HDACi in PD.

Huntington's disease (HD) is an inherited autosomal dominant genetic neurodegenerative disorder that affects ~2 in 100 000 people worldwide. The disease is characterized by progressive movement dysfunction, cognitive impairment, and behavioral disturbances. The disease currently has no treatment to halt or slow its progression, and it is eventually fatal ~20 years after symptom onset. The key feature of HD pathology is an abnormally high count of a CAG sequence at the 5' end of the huntingtin gene coding region, which results in a misfolded huntingtin with a polyglutamate region causing aggregation. This aggregation eventually cause HD symptoms through inducing cell apoptosis, mitochondrial dysfunction, transcriptional dysregulation, and eventually neurodegeneration[118]. Due to the connection between transcriptional dysregulation and disease pathology as well as studies in mouse models and human HD patients showing reduced histone acetylation, HDACi is currently undergoing trials as potential treatments. Several pan-HDACi were tested *in vitro* and *in vivo* with positive results, increasing lifespan in animal models of HD and improving their motor performance. The pan-HDACi phenylbutyrate was tested

in human trials with good results in patients exhibiting early HD symptoms, with blood samples showing marked decrease in transcriptional abnormalities[119]. Identifying the roles of different HDAC isoforms in HD is an ongoing process, but knockout studies have implicated HDAC1 as an important target as it led to acetylation and degradation of the huntingtin by increasing acetylation of a lysine residue on the protein[120]. Reports also implicate HDAC3 and HDAC6 as important in the pathophisiology of HD, though studies with these two isoforms had conflicting results. [107]. These issues are the result of the lack of isoform specific HDACi to fully elucidate the implication of different HDACs in HD.

Amyotrophic lateral sclerosis (ALS) is a fatal neurodegenerative disorder affecting ~5 in 100 000 people worldwide. The disease is characterized by damage to motor neurons leading to progressive muscle atrophy, paralysis, and death within 2 – 5 years after the onset of symptoms[121]. Studies in animal models and in human patients reveal a large variety of pathological issues such as cell apoptosis, defective axonal transport, oxidative stress, mitochondrial dysfunction, and sustained immunological response, but the primary trigger for motor neuron death is still a matter of debate. Postmortem study of human tissues shows some evidence that decreased histone acetylation may contribute to ALS pathogenesis which initiated several preclinical studies and clinical trials to investigate potential benefits of HDACi in ALS[107]. Valproic acid was studied in mouse models and demonstrated the ability to delay disease onset and improve survivability with chronic treatment before symptom onset[122], but human clinical trials did not show such benefits in slowing down disease progression or improving survivability when administered to patients[123]. Similarly, phenylbutyrate also showed promise in *in vivo* studies and was able to improve neuronal survival and survivability even when administered after disease onset. Clinical trials conducted using phenylbutyrate had positive results as it could slow down disease progression when administered after symptom onset[124]. Additionally, trials using it in combination with an antioxidant agent also being tested for ALS treatment showed more promising results, with higher survivability than each treatment achieved individually[125]. A major obstacle in developing HDACi for ALS treatment is the lack of understanding of the mechanism of neuroprotection that HDAC inhibition confers in this setting, which limits translation into the clinic. ALS pathology is also marked by dysregulation of many cellular processes, and HDACi's effects on non-epigenetic processes, such as microtubule dynamics and intracellular transport, are also likely a contributing factor. Mouse model experiments using Trichostatin A showed that inhibition of HDAC6 increased tubulin acetylation, which is associated with prolongation of survival in ALS[126], but the exact role of HDAC6 in this context beyond epigenetic mechanisms is yet to be fully elucidated[107]. Again, there is a lack of tools to help determine HDAC isoform activity in ALS to help develop more personalized treatment options.

Spinal muscular atrophy (SMA) is a childhood-onset neurodegenerative disease that affects ~1 in 10 000 people worldwide and is one of the leading genetic causes of childhood mortality which remains untreatable[126]. The disease pathology involves loss of α-motor neurons in the spinal cord which causes limb and trunk muscle atrophy The genetic cause of α-motor neuron loss is the deletion or mutation of the survival motor neuron gene SMN1 resulting in SMN protein deficiency. However, the redundant SMN2 is retained and capable of producing SMN proteins and the SMA symptom severity depends on the copy number of SMN2 and, consequently, the SMN levels [127]. This provides a basis for treating SMA by HDACi as increasing histone acetylation has been shown to induce SMN2 transcription to increase SMN protein levels. Several *in vivo* studies were conducted in mouse models, and HDACi sodium butyrate, valproic acid, Trichostatin A, and SAHA all showed increased SMN protein levels as well as improved motor function,

muscle mass, and survivability[107]. However, despite early results of motor function improvement, full-scale human clinical trials with phenylbutyric acid **1-108** failed to confer any improvement in the severity of SMA symptoms despite increasing survival rate by 250% in mouse models[128, 129]. The exact mechanism of HDACi's beneficial effects and isoform contribution is not yet elucidated, and drug development is complicated by inter-animal and inter-individual variability in responses[107].

1.20 PET Neuroimaging of HDACs

HDAC involvement in brain function is extensive but remains poorly characterised. Beyond neurodegenerative diseases, evidence also indicates a role for HDACs in autism spectrum disorders, addiction, stress, and depression through numerous studies, though the exact mechanisms are poorly defined. Most studies report increased or decreased expression of HDACs, but are unable to draw clear conclusions on whether their involvement is upstream or downstream from disease pathogenesis. Mechanistic studies of the exact role of HDACs in neurological diseases are slowly being elucidated, but the lack of availability of isoform-selective probes has hindered progress[130]. Translation of *in vivo* and *in vitro* results to a clinical setting has benefited from the availability of new non-invasive tools to directly visualize HDAC expression in the brain, more conclusively linking the expression levels to symptom progression. These tools helped elucidate of the roles of HDACs in these diseases as well as guided treatment options.

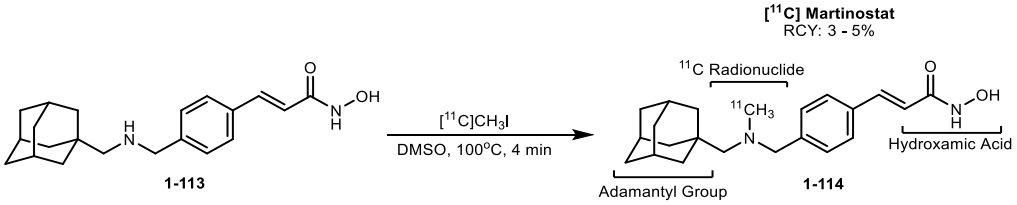

Scheme 1-33: Radiosynthesis of [^{11}C]Martinostat

The Hooker group addressed this urgent need for non-invasive tools for HDAC neuroimaging, by developing the HDAC PET imaging tracer [^{11}C]Martinostat **1-114** in 2014. Similar to other HDACi in its class, [^{11}C]Martinostat uses a hydroxamic acid as a chelator zinc-cofactor located at the binding site of classic HDACs. PET imaging modality is added via an ^{11}C PET radioisotope, and an adamantyl moiety is used as a capping group that increases the lipophilicity to allow the molecule to penetrate the BBB (Scheme 1-33). Isoform binding affinity assay showed that the tracer selectively binds to HDAC isoforms 1 – 3 with high affinity as well as to HDAC6 with somewhat lower affinity[131]. To date, [^{11}C]Martinostat has been used in several clinical studies on HDAC dysregulation in neurological diseases, including AD and schizophrenia[132, 133].

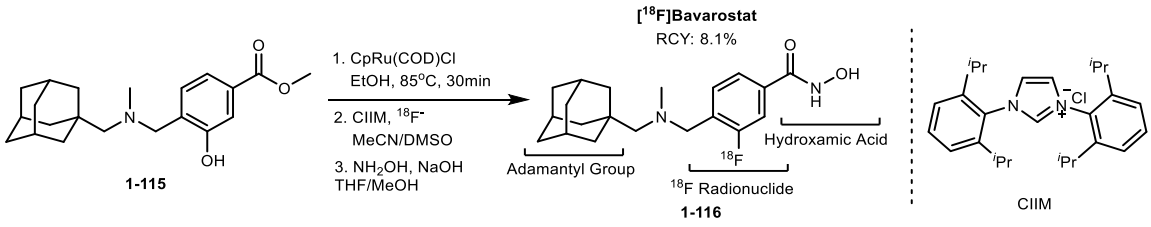

Scheme 1-34: Radiosynthesis of [^{18}F]Bavarostat

Despite its success, the Hooker group recognised the limited HDAC isoform selectivity of [^{11}C]Martinostat and developed the second generation HDAC PET tracer [^{18}F]Bavarostat (**1-116**) reported in 2017. They noted that the main issues of [^{11}C]Martinostat are its relatively poor isoform selectivity, the relatively short half-life of ^{11}C at just over 20 minutes making it difficult to handle and transport, and its poor RCY. They addressed these issues with the new tracer, which is selective for HDAC 6, while being labeled with the longer-lived ^{18}F using ruthenium catalyzed deoxyfluorination of the precursor **1-115**. However, the downside of [^{18}F]Bavarostat is a complex 3-steps radiosynthesis, using cumbersome ruthenium catalyst, resulting in a relatively low 8.1% non-decay corrected RCY after HPLC purification (Scheme 1-34)[134].

The difficult radiochemistry limits widespread use and availability of [^{18}F]Bavarostat due to the significant technical challenges in providing sufficiently large doses and continuous supply of this tracer. This issue presents an opportunity to employ a superior radiolabeling methodology to produce an HDAC PET tracer that retains the advantages of ^{18}F and isoform selectivity while drastically improving the convenience of the synthesis and the RCY of the tracer. Both [^{11}C]Martinostat and [^{18}F]Bavarostat employ an adamantyl group to increase lipophilicity, as the otherwise highly hydrophilic hydroxamic and amine-functionalized tracer would not be able to cross the blood-brain barrier[134]. The convenient presence of a highly lipophilic auxiliary on the core scaffold that does not directly interact with its target is an ideal situation to employ SiFA, which has already shown promise in brain imaging settings. We aimed to leverage SiFA lipophilicity to our advantage by directly replacing the adamantyl group as the lipophilic portion of the molecule. Using the [^{18}F]Bavarostat scaffold, we anticipated that replacement of the adamantly cap with SiFA or HetSiFA scaffold will maintain HDAC 6 isoform selectivity while significantly improving the ease of radiosynthesis and yield. Lipophilicity can be further tuned by using different heteroaromatic SiFA cores, and we expect that the resulting product could eventually be a more accessible alternative to these currently available tracers.

1.17 References

1. Dirac, M.; Adrien P. A Theory of Electrons and Protons. *Proceedings of the Royal Society of London. Series A, Containing Papers of a Mathematical and Physical Character* **1930**, *126* (801), 360–365.
2. Anderson, C. D. The Positive Electron. *Physical Review* **1933**, *43* (6), 491–494.
3. Vaquero, J. J.; Kinahan, P. Positron Emission Tomography: Current Challenges and Opportunities for Technological Advances in Clinical and Preclinical Imaging Systems. *Annual Review of Biomedical Engineering* **2015**, *17* (1), 385–414.
4. Lawrence, E. O.; Sloan, D. H. The Production of High Speed Canal Rays without the Use of High Voltages. *Proceedings of the National Academy of Sciences* **1931**, *17* (1), 64–70.
5. Livingston, M. S. Part I, History of the Cyclotron. *Physics Today* **1959**, *12* (10), 18–23.
6. Seidel M. Cyclotrons for high-intensity beams. CERN. arXiv preprint arXiv:1302.1001. **2013**.
7. Ter-Pogossian, M. M. The Origins of Positron Emission Tomography. *Seminars in Nuclear Medicine* **1992**, *22* (3), 140–149.
8. Tobias, C. A.; Lawrence, J. H.; Roughton, F. J.; Root, W. S.; Gregersen, M. I. The Elimination of Carbon Monoxide from the Human Body with Reference to the Possible Conversion of CO to Co2. *American Journal of Physiology-Legacy Content* **1945**, *145* (2), 253–263.
9. Wagner, H. N. A Brief History of Positron Emission Tomography (PET). *Seminars in Nuclear Medicine* **1998**, *28* (3), 213–220.
10. Wrenn, F. R.; Good, M. L.; Handler, P. The Use of Positron-Emitting Radioisotopes for the Localization of Brain Tumors. *Science* **1951**, *113* (2940), 525–527.
11. Sweet, W. H. The Uses of Nuclear Disintegration in the Diagnosis and Treatment of Brain Tumor. *New England Journal of Medicine* **1951**, *245* (23), 875–878.
12. Kuhl, D. E.; Edwards, R. Q. Image Separation Radioisotope Scanning. *Radiology* **1963**, *80* (4), 653–662.
13. Cormack, A. M. Representation of a Function by Its Line Integrals, with Some Radiological Applications. *Journal of Applied Physics* **1963**, *34* (9), 2722–2727.
14. Nutt, R. The History of Positron Emission Tomography. *Molecular Imaging & Biology* **2002**, *4* (1), 11–26.
15. Nadig, V.; Herrmann, K.; Mottaghy, F. M.; Schulz, V. Hybrid Total-Body Pet Scanners—Current Status and Future Perspectives. *European Journal of Nuclear Medicine and Molecular Imaging* **2021**, 49 (2), 445–459.
16. Dollé, F. [18F]Fluoropyridines: From Conventional Radiotracers to the Labeling of Macromolecules Such as Proteins and Oligonucleotides. *Ernst Schering Research Foundation Workshop* **2007**, 113–157.
17. Li, Z.; Conti, P. S. Radiopharmaceutical Chemistry for Positron Emission Tomography. *Advanced Drug Delivery Reviews* **2010**, *62* (11), 1031–1051.
18. Gower-Fry, L.; Kronemann, T.; Dorian, A.; Pu, Y.; Jaworski, C.; Wängler, C.; Bartenstein, P.; Beyer, L.; Lindner, S.; Jurkschat, K.; Wängler, B.; Bailey, J. J.; Schirrmacher, R. Recent Advances in the Clinical Translation of Silicon Fluoride Acceptor (SIFA) 18F-Radiopharmaceuticals. *Pharmaceuticals* **2021**, *14* (7), 701.
19. Perkins G, Sheth R, Greguric I, Pascali G. Optimisation of [11C]Raclopride production using a Synthra GPextent system. *Curr Radiopharm*. **2014**, 7(2):100–6.

20. Smits R, Fischer S, Hiller A, Deuther-Conrad W, Wenzel B, Patt M, et al. Synthesis and biological evaluation of both enantiomers of [18F]flubatine, promising radiotracers with fast kinetics for the imaging of α4β2-nicotinic acetylcholine receptors. *Bioorganic Med Chem.* **2014**, 22(2):804–12.
21. Luurtsema, G.; Pichler, V.; Bongarzone, S.; Seimbille, Y.; Elsinga, P.; Gee, A.; Vercouillie, J. EANM Guideline for Harmonisation on Molar Activity or Specific Activity of Radiopharmaceuticals: Impact on Safety and Imaging Quality. *EJNMMI Radiopharmacy and Chemistry* **2021**, *6* (1).
22. Conti, M.; Eriksson, L. Physics of Pure and Non-Pure Positron Emitters for PET: A Review and a Discussion. *EJNMMI Physics* **2016**, *3* (1).
23. Shao, X.; Hoareau, R.; Hockley, B. G.; Tluczek, L. J.; Henderson, B. D.; Padgett, H. C.; Scott, P. J. Highlighting the Versatility of the TRACERLAB Synthesis Modules. Part 1: Fully Automated Production of [18F]Labelled Radiopharmaceuticals Using a Tracerlab FXFN. *Journal of Labelled Compounds and Radiopharmaceuticals* **2011**, *54* (6), 292–307.
24. Zhang, L.; Villalobos, A. Strategies to Facilitate the Discovery of Novel CNS Pet Ligands. *EJNMMI Radiopharmacy and Chemistry* **2016**, *1* (1).
25. Kuchar, M.; Mamat, C. Methods to Increase the Metabolic Stability of 18F-Radiotracers. *Molecules* **2015**, *20* (9), 16186–16220.
26. Jacobson, O.; Kiesewetter, D. O.; Chen, X. Fluorine-18 Radiochemistry, Labeling Strategies and Synthetic Routes. *Bioconjugate Chemistry* **2014**, *26* (1), 1–18.
27. Cardinal Health. FDA-approved radiopharmaceuticals. https://www.cardinalhealth.com/content/dam/corp/web/documents/fact-sheet/cardinal-health-fda-approved-radiopharmaceuticals.pdf (accessed Jan 18, 2023). (accessed Jan 18, 2023).
28. Taïeb, D.; Timmers, H. J.; Shulkin, B. L.; Pacak, K. Renaissance of 18F-FDG Positron Emission Tomography in the Imaging of Pheochromocytoma/Paraganglioma. *The Journal of Clinical Endocrinology & Metabolism* **2014**, *99* (7), 2337–2339.
29. Shukla, A. K.; Kumar, U. Positron Emission Tomography: An Overview. *Journal of Medical Physics* **2006**, *31* (1), 13.
30. Coenen, H. H. Fluorine-18 Labeling Methods: Features and Possibilities of Basic Reactions. *Ernst Schering Research Foundation Workshop* **2017,** 64, 15–50.
31. Teare, H.; Robins, E. G.; Årstad, E.; Luthra, S. K.; Gouverneur, V. Synthesis and Reactivity of [18f]-n-Fluorobenzenesulfonimide. *Chem. Commun.* **2007**, No. 23, 2330–2332.
32. Ido T, Wan C-N, Casella V, Fowler JS, Wolf SP, Reivich M, Kuhl DE Labeled 2-deoxy-D-glucose analogs. 18F-labeled 2-deoxy-2-fluoro-D-glucose, 2-deoxy-2-fluro-D-mannose, and C-14–2-deoxy-2-fluoro-D-glucose. *J Label Compd Radiopharm* **1978**, 14:175–182.
33. Murali, D.; Flores, L. G.; Roberts, A. D.; Nickles, R. J.; DeJesus, O. T. Aromatic L-Amino Acid Decarboxylase (AAAD) Inhibitors as Carcinoid Tumor-Imaging Agents: Synthesis of 18F-Labeled α-Fluoromethyl-6-Fluoro-m-Tyrosine (FM-6-Fmt). *Applied Radiation and Isotopes* **2003**, *59* (4), 237–243.
34. Coenen, H. H.; Gee, A. D.; Adam, M.; Antoni, G.; Cutler, C. S.; Fujibayashi, Y.; Jeong, J. M.; Mach, R. H.; Mindt, T. L.; Pike, V. W.; Windhorst, A. D. Consensus Nomenclature Rules for Radiopharmaceutical Chemistry — Setting the Record Straight. *Nuclear Medicine and Biology* **2017**, *55*, v-xi.

35. Coenen, H. H.; Moerlein, S. M. Regiospecific Aromatic Fluorodemetallation of Group IVB Metalloarenes Using Elemental Fluorine or Acetyl Hypofluorite. *Journal of Fluorine Chemistry* **1987**, *36* (1), 63–75.
36. Namavari, M.; Bishop, A.; Satyamurthy, N.; Bida, G.; Barrio, J. R. Regioselective Radiofluorodestannylation with $[^{18}F]F_2$ and [18F]CH3COOF: A High Yield Synthesis of 6-[18F]Fluoro-L-DOPA. *International Journal of Radiation Applications and Instrumentation. Part A. Applied Radiation and Isotopes* **1992**, *43* (8), 989–996.
37. Teare, H.; Robins, E. G.; Årstad, E.; Luthra, S. K.; Gouverneur, V. Synthesis and Reactivity of [18f]-n-Fluorobenzenesulfonimide. *Chem. Commun.* **2007**, No. 23, 2330–2332.
38. Oberdorfer, F.; Hofmann, E.; Maier-Borst, W. Preparation of a New 18F-Labelled Precursor: 1-[18F]Fluoro-2-Pyridone. *International Journal of Radiation Applications and Instrumentation. Part A. Applied Radiation and Isotopes* **1988**, *39* (7), 685–688.
39. Satyamurthy, N.; Bida, G. T.; Phelps, M. E.; Barrio, J. R. [18F]-N-Fluoro-N-Alkylsuulfonamids: Novel Reagents for Mild and Regioselective Radiofluorination. *International Journal of Radiation Applications and Instrumentation. Part A. Applied Radiation and Isotopes* **1990**, *41* (8), 733–738.
40. Teare, H.; Robins, E. G.; Årstad, E.; Luthra, S. K.; Gouverneur, V. Synthesis and Reactivity of [18F]-n-Fluorobenzenesulfonimide. *Chem. Commun.* **2007**, No. 23, 2330–2332.
41. Teare, H.; Robins, E. G.; Kirjavainen, A.; Forsback, S.; Sandford, G.; Solin, O.; Luthra, S. K.; Gouverneur, V. Radiosynthesis and Evaluation of [18F]Selectfluor Bis(Triflate). *Angewandte Chemie International Edition* **2010**, *49* (38), 6821–6824.
42. Bergman, J.; Solin, O. Fluorine-18-Labeled Fluorine Gas for Synthesis of Tracer Molecules. *Nuclear Medicine and Biology* **1997**, *24* (7), 677–683.
43. Sinclair, W. K. Geiger-Mueller Counters and Proportional Counters. *Radiation Dosimetry* **1956**, 213–243.
44. Kim, D. W.; Jeong; Lim, S. T.; Sohn, M.-H.; Katzenellenbogen, J. A.; Chi, D. Y. Facile Nucleophilic Fluorination Reactions Using *Tert*-Alcohols as a Reaction Medium: Significantly Enhanced Reactivity of Alkali Metal Fluorides and Improved Selectivity. *The Journal of Organic Chemistry* **2008**, *73* (3), 957–962.
45. Inkster, J. A.; Akurathi, V.; Sromek, A. W.; Chen, Y.; Neumeyer, J. L.; Packard, A. B. A Non-Anhydrous, Minimally Basic Protocol for the Simplification of Nucleophilic 18F-Fluorination Chemistry. *Scientific Reports* **2020**, *10* (1).
46. Wessmann, S. H.; Henriksen, G.; Wester, H.-J. Cryptate Mediated Nucleophilic 18F-Fluorination without Azeotropic Drying. *Nuklearmedizin* **2011**, *50* (1), 1–8.
47. Höhne, A.; Yu, L.; Mu, L.; Reiher, M.; Voigtmann, U.; Klar, U.; Graham, K.; Schubiger, P. A.; Ametamey, S. M. Organofluorosilanes as Model Compounds for18F-Labeled Silicon-Based Pet Tracers and Their Hydrolytic Stability: Experimental Data and Theoretical Calculations (PET=positron Emission Tomography). *Chemistry - A European Journal* **2009**, *15* (15), 3736–3743.
48. Jacobson, O.; Chen, X. Pet Designated Flouride-18 Production and Chemistry. *Current Topics in Medicinal Chemistry* **2010**, *10* (11), 1048–1059.
49. Blom, E.; Karimi, F.; Långström, B. [18f]/19F Exchange in Fluorine Containing Compounds for Potential Use in18F-Labeling Strategies. *Journal of Labelled Compounds and Radiopharmaceuticals* **2009**, *52* (12), 504–511.

50. Kellogg, K. B.; Cady, G. H. Trifluoromethyl Hypofluorite. *Journal of the American Chemical Society* **1948**, *70* (12), 3986–3990.
51. Jacobson, O.; Bechor, Y.; Icar, A.; Novak, N.; Birman, A.; Marom, H.; Fadeeva, L.; Golan, E.; Leibovitch, I.; Gutman, M.; Even-Sapir, E.; Chisin, R.; Gozin, M.; Mishani, E. Prostate Cancer Pet Bioprobes: Synthesis of [18F]-Radiolabeled Hydroxyflutamide Derivatives. *Bioorganic & Medicinal Chemistry* **2005**, *13* (22), 6195–6205.
52. Pike, V. W.; Aigbirhio, F. I. Reactions of Cyclotron-Produced [18f]Fluoride with Diaryliodonium Salts—a Novel Single-Step Route to No-Carrier-Added [18F]Fluoroarenes. *J. Chem. Soc., Chem. Commun.* **1995**, No. 21, 2215–2216.
53. Telu, S.; Chun, J.-H.; Siméon, F. G.; Lu, S.; Pike, V. W. Syntheses of mglur5 Pet Radioligands through the Radiofluorination of Diaryliodonium Tosylates. *Organic & Biomolecular Chemistry* **2011**, *9* (19), 6629.
54. Rotstein, B. H.; Stephenson, N. A.; Vasdev, N.; Liang, S. H. Spirocyclic Hypervalent Iodine(Iii)-Mediated Radiofluorination of Non-Activated and Hindered Aromatics. *Nature Communications* **2014**, *5* (1).
55. Watson, D. A.; Su, M.; Teverovskiy, G.; Zhang, Y.; García-Fortanet, J.; Kinzel, T.; Buchwald, S. L. Formation of ARF from LPDAR(F): Catalytic Conversion of Aryl Triflates to Aryl Fluorides. *Science* **2009**, *325* (5948), 1661–1664.
56. Lee, E.; Kamlet, A. S.; Powers, D. C.; Neumann, C. N.; Boursalian, G. B.; Furuya, T.; Choi, D. C.; Hooker, J. M.; Ritter, T. A Fluoride-Derived Electrophilic Late-Stage Fluorination Reagent for PET Imaging. *Science* **2011**, *334* (6056), 639–642.
57. Lee, E.; Hooker, J. M.; Ritter, T. Nickel-Mediated Oxidative Fluorination for Pet with Aqueous [18F] Fluoride. *Journal of the American Chemical Society* **2012**, *134* (42), 17456–17458.
58. Ren, H.; Wey, H.-Y.; Strebl, M.; Neelamegam, R.; Ritter, T.; Hooker, J. M. Synthesis and Imaging Validation of [18F]MDL100907 Enabled by Ni-Mediated Fluorination. *ACS Chemical Neuroscience* **2014**, *5* (7), 611–615.
59. Zlatopolskiy, B. D.; Zischler, J.; Krapf, P.; Zarrad, F.; Urusova, E. A.; Kordys, E.; Endepols, H.; Neumaier, B. Copper-Mediated Aromatic Radiofluorination Revisited: Efficient Production of Pet Tracers on a Preparative Scale. *Chemistry - A European Journal* **2015**, *21* (15), 5972–5979.
60. Tredwell, M.; Preshlock, S. M.; Taylor, N. J.; Gruber, S.; Huiban, M.; Passchier, J.; Mercier, J.; Génicot, C.; Gouverneur, V. A General Copper-Mediated Nucleophilic 18F Fluorination of Arenes. *Angewandte Chemie International Edition* **2014**, *53* (30), 7751–7755.
61. Makaravage, K. J.; Brooks, A. F.; Mossine, A. V.; Sanford, M. S.; Scott, P. J. Copper-Mediated Radiofluorination of Arylstannanes with [18F]KF. *Organic Letters* **2016**, *18* (20), 5440–5443.
62. Beyzavi, H.; Mandal, D.; Strebl, M. G.; Neumann, C. N.; D'Amato, E. M.; Chen, J.; Hooker, J. M.; Ritter, T. 18F-Deoxyfluorination of Phenols via Ru π-Complexes. *ACS Central Science* **2017**, *3* (9), 944–948.
63. Smith, G. E.; Sladen, H. L.; Biagini, S. C.; Blower, P. J. Inorganic Approaches for Radiolabeling Biomolecules with Fluorine-18 for Imaging with Positron Emission Tomography. *Dalton Transactions* **2011**, *40* (23), 6196.
64. Archibald, S. J.; Allott, L. The Aluminium-[18f]Fluoride Revolution: Simple Radiochemistry with a Big Impact for Radiolabelled Biomolecules. *EJNMMI Radiopharmacy and Chemistry* **2021**, *6* (1).

65. Bernard-Gauthier, V.; Wängler, C.; Schirrmacher, E.; Kostikov, A.; Jurkschat, K.; Wängler, B.; Schirrmacher, R. 18F-Labeled Silicon-Based Fluoride Acceptors: Potential Opportunities for Novel Positron Emitting Radiopharmaceuticals. *BioMed Research International* **2014**, *2014*, 1–20.
66. Liu, Z.; Pourghiasian, M.; Radtke, M. A.; Lau, J.; Pan, J.; Dias, G. M.; Yapp, D.; Lin, K.-S.; Bénard, F.; Perrin, D. M. An Organotrifluoroborate for Broadly Applicable One-Step 18F-Labeling. *Angewandte Chemie* **2014**, *126* (44), 12070–12074.
67. Zheng, Q.; Xu, H.; Wang, H.; Du, W.-G. H.; Wang, N.; Xiong, H.; Gu, Y.; Noodleman, L.; Sharpless, K. B.; Yang, G.; Wu, P. Sulfur [18f]Fluoride Exchange Click Chemistry Enabled Ultrafast Late-Stage Radiosynthesis. *Journal of the American Chemical Society* **2021**, *143* (10), 3753–3763.
68. Hong, H.; Zhang, L.; Xie, F.; Zhuang, R.; Jiang, D.; Liu, H.; Li, J.; Yang, H.; Zhang, X.; Nie, L.; Li, Z. Rapid One-Step 18F-Radiolabeling of Biomolecules in Aqueous Media by Organophosphine Fluoride Acceptors. *Nature Communications* **2019**, *10* (1).
69. Gens, T. A.; Wethongton, J. A.; Brosi, A. R. The Exchange of F18between Metallic Fluorides and Silicon Tetrafluoride. *The Journal of Physical Chemistry* **1958**, *62* (12), 1593–1593.
70. Rosenthal, M. S.; Bosch, A. L.; Nickles, R. J.; Gatley, S. J. Synthesis and Some Characteristics of No-Carrier Added [18f]Fluorotrimethylsilane. *The International Journal of Applied Radiation and Isotopes* **1985**, *36* (4), 318–319.
71. Gatley, S. J. Rapid Production and Trapping of [18f]Fluorotrimethylsilane, and Its Use in Nucleophilic Fluorine-18 Labeling without an Aqueous Evaporation Step. *International Journal of Radiation Applications and Instrumentation. Part A. Applied Radiation and Isotopes* **1989**, *40* (6), 541–544.
72. Choudhry, U.; Martin, K. E.; Biagini, S.; Blower, P. J. A49 Alkoxysilane Groups for Instant Labeling of Biomolecules with 18F. *Nuclear Medicine Communications* **2006**, *27* (3), 293.
73. Schirrmacher, R.; Bradtmöller, G.; Schirrmacher, E.; Thews, O.; Tillmanns, J.; Siessmeier, T.; Buchholz, H. G.; Bartenstein, P.; Wängler, B.; Niemeyer, C. M.; Jurkschat, K. 18F-Labeling of Peptides by Means of an Organosilicon-Based Fluoride Acceptor. *Angewandte Chemie International Edition* **2006**, *45* (36), 6047–6050.
74. Mu, L.; Höhne, A.; Schubiger, P. A.; Ametamey, S. M.; Graham, K.; Cyr, J. E.; Dinkelborg, L.; Stellfeld, T.; Srinivasan, A.; Voigtmann, U.; Klar, U. Silicon-Based Building Blocks for One-STEP18F-Radiolabeling of Peptides for PET Imaging. *Angewandte Chemie International Edition* **2008**, *47* (26), 4922–4925.
75. Wängler, C.; Kostikov, A.; Zhu, J.; Chin, J.; Wängler, B.; Schirrmacher, R. Silicon-[18F]Fluorine Radiochemistry: Basics, Applications and Challenges. *Applied Sciences* **2012**, *2* (2), 277–302.
76. Narayanam, M. K.; Toutov, A. A.; Murphy, J. M. Rapid One-Step 18F-Labeling of Peptides via Heteroaromatic Silicon-Fluoride Acceptors. *Organic Letters* **2020**, *22* (3), 804–808. DOI:10.1021/acs.orglett.9b04160.
77. Tan, T. H.; Lee, B. N.; Hassan, S. Z. Diagnostic Value of 68ga-Dotatate PET/CT in Liver Metastases of Neuroendocrine Tumours of Unknown Origin. *Nuclear Medicine and Molecular Imaging* **2013**, *48* (3), 212–215.
78. Schirrmacher, E.; Wängler, B.; Cypryk, M.; Bradtmöller, G.; Schäfer, M.; Eisenhut, M.; Jurkschat, K.; Schirrmacher, R. Synthesis of P-(Di-Tert-Butyl[18F]Fluorosilyl)Benzaldehyde ([18F]SiFA-A) with High Specific Activity by Isotopic Exchange: A Convenient Labeling Synthon for the 18F-Labeling of N-Amino-Oxy Derivatized Peptides. *Bioconjugate Chemistry* **2007**, *18* (6), 2085–2089.
79. Ilhan, H.; Lindner, S.; Todica, A.; Cyran, C. C.; Tiling, R.; Auernhammer, C. J.; Spitzweg, C.; Boeck, S.; Unterrainer, M.; Gildehaus, F. J.; Böning, G.; Jurkschat, K.; Wängler, C.; Wängler, B.; Schirrmacher, R.; Bartenstein, P. Biodistribution and First Clinical Results of 18F-Sifalin-Tate Pet:

A Novel 18F-Labeled Somatostatin Analog for Imaging of Neuroendocrine Tumors. *European Journal of Nuclear Medicine and Molecular Imaging* **2019**, *47* (4), 870–880.

80. Lindner, S.; Michler, C.; Leidner, S.; Rensch, C.; Wängler, C.; Schirrmacher, R.; Bartenstein, P.; Wängler, B. Synthesis and in Vitro and in Vivo Evaluation of SIFA-Tagged Bombesin and RGD Peptides as Tumor Imaging Probes for Positron Emission Tomography. *Bioconjugate Chemistry* **2014**, *25* (4), 738–749.
81. Kostikov, A. P.; Iovkova, L.; Chin, J.; Schirrmacher, E.; Wängler, B.; Wängler, C.; Jurkschat, K.; Cosa, G.; Schirrmacher, R. N-(4-(Di-Tert-Butyl[18f]Fluorosilyl)Benzyl)-2-Hydroxy-N,N-Dimethylethylammonium Bromide ([18f]Sifan+Br−): A Novel Lead Compound for the Development of Hydrophilic SIFA-Based Prosthetic Groups for 18F-Labeling. *Journal of Fluorine Chemistry* **2011**, *132* (1), 27–34.
82. Tietze, L.; Schmuck, K. Sifa Azide: A New Building Block for PET Imaging Using Click Chemistry. *Synlett* **2011**, *2011* (12), 1697–1700.
83. Wurzer, A.; Di Carlo, D.; Herz, M.; Richter, A.; Robu, S.; Schirrmacher, R.; Mascarin, A.; Weber, W.; Eiber, M.; Schwaiger, M.; Wester, H.-J. Automated Synthesis of [18F]Ga-RHPSMA-7/ -7.3: Results, Quality Control and Experience from More than 200 Routine Productions. *EJNMMI Radiopharmacy and Chemistry* **2021**, *6* (1).
84. Oh, S. W.; Wurzer, A.; Teoh, E. J.; Oh, S.; Langbein, T.; Krönke, M.; Herz, M.; Kropf, S.; Wester, H.-J.; Weber, W. A.; Eiber, M. Quantitative and Qualitative Analyses of Biodistribution and Pet Image Quality of a Novel Radiohybrid PSMA, 18F-RHPSMA-7, in Patients with Prostate Cancer. *Journal of Nuclear Medicine* **2019**, *61* (5), 702–709.
85. Höhne, A.; Mu, L.; Honer, M.; Schubiger, P. A.; Ametamey, S. M.; Graham, K.; Stellfeld, T.; Borkowski, S.; Berndorff, D.; Klar, U.; Voigtmann, U.; Cyr, J. E.; Friebe, M.; Dinkelborg, L.; Srinivasan, A. Synthesis,18F-Labeling, and in Vitro and in Vivo Studies of Bombesin Peptides Modified with Silicon-Based Building Blocks. *Bioconjugate Chemistry* **2008**, *19* (9), 1871–1879.
86. Wängler, B.; Kostikov, A. P.; Niedermoser, S.; Chin, J.; Orchowski, K.; Schirrmacher, E.; Iovkova-Berends, L.; Jurkschat, K.; Wängler, C.; Schirrmacher, R. Protein Labeling with the Labeling Precursor [18F]SIFA-SH for Positron Emission Tomography. *Nature Protocols* **2012**, *7* (11), 1964–1969.
87. Rosa-Neto, P.; Wängler, B.; Iovkova, L.; Boening, G.; Reader, A.; Jurkschat, K.; Schirrmacher, E. [18F]SIFA-Isothiocyanate: A New Highly Effective Radioactive Labeling Agent for Lysine-Containing Proteins. *ChemBioChem* **2009**, *10* (8), 1321–1324.
88. Kostikov, A. P.; Chin, J.; Orchowski, K.; Niedermoser, S.; Kovacevic, M. M.; Aliaga, A.; Jurkschat, K.; Wängler, B.; Wängler, C.; Wester, H.-J.; Schirrmacher, R. Oxalic Acid Supported Si–18F-Radiofluorination: One-Step Radiosynthesis of N-Succinimidyl 3-(Di-Tert-Butyl[18F]Fluorosilyl)Benzoate ([18F]SiFB) for Protein Labeling. *Bioconjugate Chemistry* **2012**, *23* (1), 106–114.
89. Glaser, M.; Iveson, P.; Hoppmann, S.; Indrevoll, B.; Wilson, A.; Arukwe, J.; Danikas, A.; Bhalla, R.; Hiscock, D. Three Methods for 18F Labeling of the HER2-Binding Affibody Molecule Zher2:2891 Including Preclinical Assessment. *Journal of Nuclear Medicine* **2013**, *54* (11), 1981–1988.
90. Bohn, P.; Deyine, A.; Azzouz, R.; Bailly, L.; Fiol-Petit, C.; Bischoff, L.; Fruit, C.; Marsais, F.; Vera, P. Design of Silicon-Based Misonidazole Analogues and 18F-Radiolabeling. *Nuclear Medicine and Biology* **2009**, *36* (8), 895–905.
91. Schulz, J.; Vimont, D.; Bordenave, T.; James, D.; Escudier, J. M.; Allard, M.; Szlosek-Pinaud, M.; Fouquet, E. Silicon-Based Chemistry: An Original and Efficient One-Step Approach to [18 f]-Nucleosides and [18 f]-Oligonucleotides for PET Imaging. *Chemistry – A European Journal* **2011**, *17* (11), 3096–3100.

92. Iovkova-Berends, L.; Wängler, C.; Zöller, T.; Höfner, G.; Wanner, K. T.; Rensch, C.; Bartenstein, P.; Kostikov, A.; Schirrmacher, R.; Jurkschat, K.; Wängler, B. T-bu2sif-Derivatized D2-Receptor Ligands: The First SIFA-Containing Small Molecule Radiotracers for Target-Specific PET-Imaging. *Molecules* **2011**, *16* (9), 7458–7479.
93. Hazari, P. P.; Schulz, J.; Vimont, D.; Chadha, N.; Allard, M.; Szlosek-Pinaud, M.; Fouquet, E.; Mishra, A. K. A New Sif-Dipropargyl Glycerol Scaffold as a Versatile Prosthetic Group to Design Dimeric Radioligands: Synthesis of the [18f]Bmppsif Tracer to Image Serotonin Receptors. *ChemMedChem* **2013**, *9* (2), 337–349.
94. Li, G.; Tian, Y.; Zhu, W.-G. The Roles of Histone Deacetylases and Their Inhibitors in Cancer Therapy. *Frontiers in Cell and Developmental Biology* **2020**, *8*.
95. Seto, E.; Yoshida, M. Erasers of Histone Acetylation: The Histone Deacetylase Enzymes. *Cold Spring Harbor Perspectives in Biology* **2014**, *6* (4).
96. Gantt, S. L.; Joseph, C. G.; Fierke, C. A. Activation and Inhibition of Histone Deacetylase 8 by Monovalent Cations. *Journal of Biological Chemistry* **2010**, *285* (9), 6036–6043.
97. Jaworska, J.; Ziemka-Nalecz, M.; Zalewska, T. Histone Deacetylases 1 and 2 Are Required for Brain Development. *The International Journal of Developmental Biology* **2015**, *59* (4-5–6), 171–177.
98. Choudhary, C.; Kumar, C.; Gnad, F.; Nielsen, M. L.; Rehman, M.; Walther, T. C.; Olsen, J. V.; Mann, M. Lysine Acetylation Targets Protein Complexes and Co-Regulates Major Cellular Functions. *Science* **2009**, *325* (5942), 834–840.
99. RIGGS, M. G.; WHITTAKER, R. G.; NEUMANN, J. R.; INGRAM, V. M. N-Butyrate Causes Histone Modification in Hela and Friend Erythroleukaemia Cells. *Nature* **1977**, *268* (5619), 462–464.
100. Kijima, M.; Yoshida, M.; Sugita, K.; Horinouchi, S.; Beppu, T. Trapoxin, an Antitumor Cyclic Tetrapeptide, Is an Irreversible Inhibitor of Mammalian Histone Deacetylase. *Journal of Biological Chemistry* **1993**, *268* (30), 22429–22435.
101. Richon, V. M.; Emiliani, S.; Verdin, E.; Webb, Y.; Breslow, R.; Rifkind, R. A.; Marks, P. A. A Class of Hybrid Polar Inducers of Transformed Cell Differentiation Inhibits Histone Deacetylases. *Proceedings of the National Academy of Sciences* **1998**, *95* (6), 3003–3007.
102. Nakajima, H.; Kim, Y. B.; Terano, H.; Yoshida, M.; Horinouchi, S. FR901228, a Potent Antitumor Antibiotic, Is a Novel Histone Deacetylase Inhibitor. *Experimental Cell Research* **1998**, *241* (1), 126–133.
103. Saito, A.; Yamashita, T.; Mariko, Y.; Nosaka, Y.; Tsuchiya, K.; Ando, T.; Suzuki, T.; Tsuruo, T.; Nakanishi, O. A Synthetic Inhibitor of Histone Deacetylase, MS-27-275, with Marked *in Vivo* Antitumor Activity against Human Tumors. *Proceedings of the National Academy of Sciences* **1999**, *96* (8), 4592–4597.
104. Bressi, J. C.; Jong, R. de; Wu, Y.; Jennings, A. J.; Brown, J. W.; O'Connell, S.; Tari, L. W.; Skene, R. J.; Vu, P.; Navre, M.; Cao, X.; Gangloff, A. R. Benzimidazole and Imidazole Inhibitors of Histone Deacetylases: Synthesis and Biological Activity. *Bioorganic & Medicinal Chemistry Letters* **2010**, *20* (10), 3138–3141.
105. Matsuyama, A. In Vivo Destabilization of Dynamic Microtubules by HDAC6-Mediated Deacetylation. *The EMBO Journal* **2002**, *21* (24), 6820–6831.
106. Halili MA, Andrews MR, Sweet MJ, Fairlie DP Histone deacetylase inhibitors in inflammatory disease. *Curr Top Med Chem* **2009**, 9, 309–319.
107. Ziemka-Nalecz, M.; Jaworska, J.; Sypecka, J.; Zalewska, T. Histone Deacetylase Inhibitors: A Therapeutic Key in Neurological Disorders? *Journal of Neuropathology & Experimental Neurology* **2018**, *77* (10), 855–870.

108. Sinn DI, Kim S. J., Chu K, Jung K. H., Lee S.T., Song E. C., Kim J. M., Park D. K., Kun Lee S, Kim M, Roh J. K. Valproic acid-mediated neuroprotection in intracerebral hemorrhage via histone deacetylase inhibition and transcriptional activation. *Neurobiol Dis* **2007**, 26, 464–472
109. Ziemka-Nalecz M, Zalewska T. Neuroprotective effects of histone deacetylase inhibitors in brain ischemia. *Acta Neurobiologiae Experimentalis*. **2014,** 74(4), 383-395.
110. Hardy J, Selkoe DJ. The amyloid hypothesis of Alzheimer's disease: Progress and problems on the road to therapeutics. *Science* **2002,** 297, 353–356
111. Gräff, J.; Rei, D.; Guan, J.-S.; Wang, W.-Y.; Seo, J.; Hennig, K. M.; Nieland, T. J.; Fass, D. M.; Kao, P. F.; Kahn, M.; Su, S. C.; Samiei, A.; Joseph, N.; Haggarty, S. J.; Delalle, I.; Tsai, L.-H. An Epigenetic Blockade of Cognitive Functions in the Neurodegenerating Brain. *Nature* **2012**, *483* (7388), 222–226.
112. Ding, H.; Dolan, P. J.; Johnson, G. V. Histone Deacetylase 6 Interacts with the Microtubule-Associated Protein Tau. *Journal of Neurochemistry* **2008**, *106* (5), 2119–2130.
113. Govindarajan, N.; Rao, P.; Burkhardt, S.; Sananbenesi, F.; Schlüter, O. M.; Bradke, F.; Lu, J.; Fischer, A. Reducing HDAC6 Ameliorates Cognitive Deficits in a Mouse Model for Alzheimer's Disease. *EMBO Molecular Medicine* **2012**, *5* (1), 52–63.
114. Cook C.; Stankowski J. N.; Carlomagno Y. et al. Acetylation: A new key to unlock tau's role in neurodegeneration. *Alzheimers Res Ther.* **2014**; 6, 29
115. Benskey, M. J.; Perez, R. G.; Manfredsson, F. P. The Contribution of Alpha Synuclein to Neuronal Survival and Function – Implications for Parkinson's Disease. *Journal of Neurochemistry* **2016**, *137* (3), 331–359.
116. Goers J.; Manning-Bog A. B.; McCormack A. L.; et al. Nuclear localization of alpha-synuclein and its interaction with histones. *Biochemistry (Mosc)* **2003**, 42, 8465–8471
117. Price P. A.; Parkes J. D.; Marsden C. D.; Sodium valproate in the treatment of levodopa-induced dyskinesia. *J Neurol Neurosurg Psychiatry* **1978**, 41, 702–706
118. Flier, J. S.; Underhill, L. H.; Martin, J. B.; Gusella, J. F. Huntingtons Disease. *New England Journal of Medicine* **1986**, *315* (20), 1267–1276.
119. Ebbel, E. N.; Leymarie, N.; Schiavo, S.; Sharma, S.; Gevorkian, S.; Hersch, S.; Matson, W. R.; Costello, C. E. Identification of Phenylbutyrate-Generated Metabolites in Huntington Disease Patients Using Parallel Liquid Chromatography/Electrochemical Array/Mass Spectrometry and off-Line Tandem Mass Spectrometry. *Analytical Biochemistry* **2010**, *399* (2), 152–161.
120. Jeong, H.; Then, F.; Melia, T. J.; Mazzulli, J. R.; Cui, L.; Savas, J. N.; Voisine, C.; Paganetti, P.; Tanese, N.; Hart, A. C.; Yamamoto, A.; Krainc, D. Acetylation Targets Mutant Huntingtin to Autophagosomes for Degradation. *Cell* **2009**, *137* (1), 60–72.
121. Rowland, L. P.; Shneider, N. A. Amyotrophic Lateral Sclerosis. *New England Journal of Medicine* **2001**, *344* (22), 1688–1700.
122. Sugai, F.; Yamamoto, Y.; Miyaguchi, K.; Zhou, Z.; Sumi, H.; Hamasaki, T.; Goto, M.; Sakoda, S. Benefit of Valproic Acid in Suppressing Disease Progression of ALS Model Mice. *European Journal of Neuroscience* **2004**, *20* (11), 3179–3183.
123. Piepers, S.; Veldink, J. H.; De Jong, S. W.; Van Der Tweel, I.; Van Der Pol, W.-L.; Uijtendaal, E. V.; Schelhaas, H. J.; Scheffer, H.; De Visser, M.; De Jong, J. M.; Wokke, J. H.; Groeneveld, G. J.; Van Den Berg, L. H. Randomized Sequential Trial of Valproic Acid in Amyotrophic Lateral Sclerosis. *Annals of Neurology* **2009**, *66* (2), 227–234.
124. Paganoni, S.; Macklin, E. A.; Hendrix, S.; Berry, J. D.; Elliott, M. A.; Maiser, S.; Karam, C.; Caress, J. B.; Owegi, M. A.; Quick, A.; Wymer, J.; Goutman, S. A.; Heitzman, D.; Heiman-Patterson, T.;

Jackson, C. E.; Quinn, C.; Rothstein, J. D.; Kasarskis, E. J.; Katz, J.; Jenkins, L.; Ladha, S.; Miller, T. M.; Scelsa, S. N.; Vu, T. H.; Fournier, C. N.; Glass, J. D.; Johnson, K. M.; Swenson, A.; Goyal, N. A.; Pattee, G. L.; Andres, P. L.; Babu, S.; Chase, M.; Dagostino, D.; Dickson, S. P.; Ellison, N.; Hall, M.; Hendrix, K.; Kittle, G.; McGovern, M.; Ostrow, J.; Pothier, L.; Randall, R.; Shefner, J. M.; Sherman, A. V.; Tustison, E.; Vigneswaran, P.; Walker, J.; Yu, H.; Chan, J.; Wittes, J.; Cohen, J.; Klee, J.; Leslie, K.; Tanzi, R. E.; Gilbert, W.; Yeramian, P. D.; Schoenfeld, D.; Cudkowicz, M. E. Trial of Sodium Phenylbutyrate–Taurursodiol for Amyotrophic Lateral Sclerosis. *New England Journal of Medicine* **2020**, *383* (10), 919–930.

125. Ryu, H.; Smith, K.; Camelo, S. I.; Carreras, I.; Lee, J.; Iglesias, A. H.; Dangond, F.; Cormier, K. A.; Cudkowicz, M. E.; H. Brown, R.; Ferrante, R. J. Sodium Phenylbutyrate Prolongs Survival and Regulates Expression of Anti-Apoptotic Genes in Transgenic Amyotrophic Lateral Sclerosis Mice. *Journal of Neurochemistry* **2005**, *93* (5), 1087–1098.
126. Tisdale, S.; Pellizzoni, L. Disease Mechanisms and Therapeutic Approaches in Spinal Muscular Atrophy. *Journal of Neuroscience* **2015**, *35* (23), 8691–8700.
127. Lefebvre, S.; Burlet, P.; Liu, Q.; Bertrandy, S.; Clermont, O.; Munnich, A.; Dreyfuss, G.; Melki, J. Correlation between Severity and SMN Protein Level in Spinal Muscular Atrophy. *Nature Genetics* **1997**, *16* (3), 265–269.
128. Butchbach, M. E. R.; Lumpkin, C. J.; Harris, A. W.; Saieva, L.; Edwards, J. D.; Workman, E.; Simard, L. R.; Pellizzoni, L.; Burghes, A. H. M. Protective Effects of Butyrate-Based Compounds on a Mouse Model for Spinal Muscular Atrophy. *Experimental Neurology* **2016**, *279*, 13–26.
129. Mercuri, E.; Bertini, E.; Messina, S.; Solari, A.; D'Amico, A.; Angelozzi, C.; Battini, R.; Berardinelli, A.; Boffi, P.; Bruno, C.; Cini, C.; Colitto, F.; Kinali, M.; Minetti, C.; Mongini, T.; Morandi, L.; Neri, G.; Orcesi, S.; Pane, M.; Pelliccioni, M.; Pini, A.; Tiziano, F. D.; Villanova, M.; Vita, G.; Brahe, C. Randomized, Double-Blind, Placebo-Controlled Trial of Phenylbutyrate in Spinal Muscular Atrophy. *Neurology* **2006**, *68* (1), 51–55.
130. Volmar, C.-H.; Wahlestedt, C. Histone Deacetylases (HDACS) and Brain Function. *Neuroepigenetics* **2015**, *1*, 20–27.
131. Wang, C.; Schroeder, F. A.; Wey, H.-Y.; Borra, R.; Wagner, F. F.; Reis, S.; Kim, S. W.; Holson, E. B.; Haggarty, S. J.; Hooker, J. M. In Vivo Imaging of Histone Deacetylases (HDACS) in the Central Nervous System and Major Peripheral Organs. *Journal of Medicinal Chemistry* **2014**, *57* (19), 7999–8009.
132. Pascoal, T. A.; Chamoun, M.; Lax, E.; Wey, H.-Y.; Shin, M.; Ng, K. P.; Kang, M. S.; Mathotaarachchi, S.; Benedet, A. L.; Therriault, J.; Lussier, F. Z.; Schroeder, F. A.; DuBois, J. M.; Hightower, B. G.; Gilbert, T. M.; Zürcher, N. R.; Wang, C.; Hopewell, R.; Chakravarty, M.; Savard, M.; Thomas, E.; Mohaddes, S.; Farzin, S.; Salaciak, A.; Tullo, S.; Cuello, A. C.; Soucy, J.-P.; Massarweh, G.; Hwang, H.; Kobayashi, E.; Hyman, B. T.; Dickerson, B. C.; Guiot, M.-C.; Szyf, M.; Gauthier, S.; Hooker, J. M.; Rosa-Neto, P. [11c]Martinostat Pet Analysis Reveals Reduced HDAC I Availability in Alzheimer's Disease. *Nature Communications* **2022**, *13* (1).
133. Gilbert, T. M.; Zürcher, N. R.; Wu, C. J.; Bhanot, A.; Hightower, B. G.; Kim, M.; Albrecht, D. S.; Wey, H.-Y.; Schroeder, F. A.; Rodriguez-Thompson, A.; Morin, T. M.; Hart, K. L.; Pellegrini, A. M.; Riley, M. M.; Wang, C.; Stufflebeam, S. M.; Haggarty, S. J.; Holt, D. J.; Loggia, M. L.; Perlis, R. H.; Brown, H. E.; Roffman, J. L.; Hooker, J. M. PET Neuroimaging Reveals Histone Deacetylase Dysregulation in Schizophrenia. *Journal of Clinical Investigation* **2018**, *129* (1), 364–372.
134. Strebl, M. G.; Campbell, A. J.; Zhao, W.-N.; Schroeder, F. A.; Riley, M. M.; Chindavong, P. S.; Morin, T. M.; Haggarty, S. J.; Wagner, F. F.; Ritter, T.; Hooker, J. M. HDAC6 Brain Mapping with [18f]Bavarostat Enabled by a RU-Mediated Deoxyfluorination. *ACS Central Science* **2017**, *3* (9), 1006–1014.

Chapter 2: Synthesis and evaluation of HDAC PET tracer candidates

2.1: Introduction

To accomplish the plan outlined in section **1-20** we aimed to develop a SiFA-based HDAC-targeting PET tracer that greatly outperforms [^{18}F]Bavarostat in radiolabeling efficiency, while maintaining similar biodistribution properties and imaging quality. To achieve this goal, we planned to synthesize a series of potential tracers that incorporate both phenyl and heteroaromatic SiFA cores into the Bavarostat scaffold, as well as develop a pipeline to evaluate the binding efficiency and pharmacokinetics of our products. Radiolabeling of compounds containing hydroxamic acid is also known to be difficult,[1] so we decided to first synthesize a substrate using the well-established phenyl SiFA core to verify the efficiency of SiFA radiochemistry in presence of a free hydroxamic acids. Once we demonstrated the ability to label hydroxamic acids using phenyl SiFA, we would proceed with the synthesis of additional compounds using other HetSiFA cores developed by our group, as well as evaluating biological behavior of these compounds with *in vitro* and *in vivo* assays.

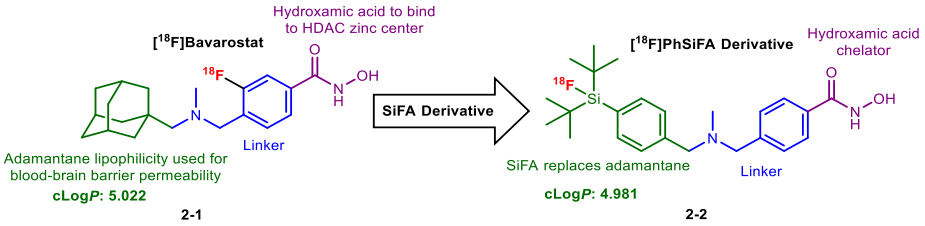

Scheme 2-1: Proposed phenyl SiFA-Bavarostat derivative

This first substrate **2-2** involves direct replacement of the adamantane moiety in [^{18}F]Bavarostat **2-1** with phenyl SiFA (Scheme 2-1). The rough estimation of lipophilicity of adamantane using ChemDraw's calculated octanol/water partition coefficient c*Log*P revealed that it is fairly similar to that of phenyl SiFA value at 5.022 compared to 4.981 of phenyl SiFA, and we predicted that this change would have minimal impact to the molecule's pharmacokinetic properties. Adamantane has been demonstrated to be an effective auxiliary that can be used to help compounds cross the blood-brain barrier,[1] which prompted its use in the design of the brain HDAC PET tracers [^{18}F]Bavarostat and [^{11}C]Martinostat.[2] Other studies studies have shown that silicon compounds have similar effect on blood-brain barrier permeability[3] so we expected that **2-2** would have a capacity of penetrating the blood-brain barrier.

2.2: Synthesis of PhSiFA-based [^{18}F]Bavarostat derivative

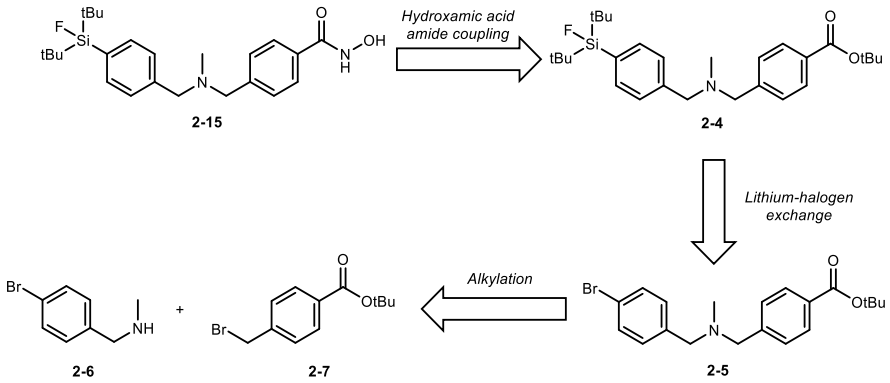

Scheme 2-2: Retrosynthetic plan of phSiFA derivative **2-15**

Our initial plan was to first form the core structure of the molecule **2-5** through alkylation of the benzyl bromide **2-7** with the secondary amine fragment **2-6**. As discussed previously in section **1-10**, the synthesis of functionalized phenyl SiFA cores is well established, and our initial plan hinged on using lithium-halogen exchange to install the SiFA on **2-5**. Hydroxamic acid functionalities are commonly installed by reacting a methyl or ethyl ester in the presence of hydroxyl amine and a base (KOH or NaOH), which is the method used in the synthesis of [^{18}F]Bavarostat and [^{11}C]Martinostat. However, an alternative method must be used for our substrates to avoid hydrolysis of the Si-F bond in the presence of hydroxide. Therefore, we opted to use amide coupling of the carboxylic acid with hydroxylamine to form the desired product **2-15**.

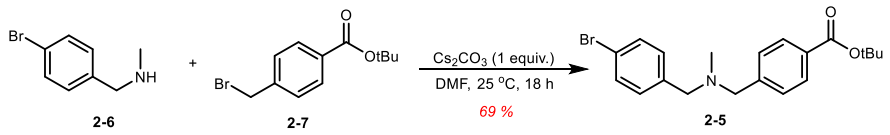

Scheme 2-3: Synthesis of **2-5**

Compound **2-5** was successfully synthesized by alkylation of (4-bromophenyl)methylamine **2-6** with *tert*-butyl 4-(bromomethyl)benzoate **2-7** using cesium carbonate in 69% yield (Scheme 2-3), but subsequent lithiation attempts to install the SiFA using this substrate were unsuccessful.

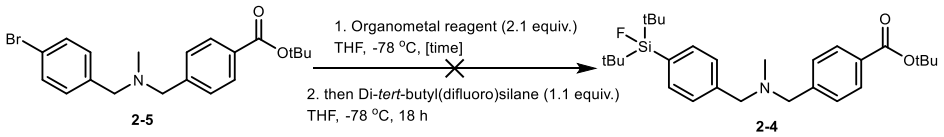

Entry	Organometal reagent	Time before quench	Result
1	*tert*-butyl lithium	30 min	Complex mixture
2	*tert*-butyl lithium	10 min	Complex mixture
3	*tert*-butyl lithium	3 min	**2-5** recovered
4	*tert*-butyl lithium	1 min	**2-5** recovered
5	*i*PrMgCl	1.5 h	**2-5** recovered

Table 2-1: Conditions for SiFA installation using organometal reagents

We initially attempted to use previously established protocols for SiFA installation through lithium-halogen exchange (Table 2-1), letting the starting material react with *tert*-butyl lithium for 30 minutes at -78 °C before quenching with di-*tert*-butyl(difluoro)silane (Entry 1). This was unsuccessful and resulted in a complex mixture, and no desired products could be isolated. We suspected that the issue might be decomposition of the lithiated intermediate so we decided to decrease the reaction time before adding di-*tert*-butyl(difluoro)silane. Decreasing the reaction time to 10 minutes produced the same result (Entry 2), so we decided to attempt the reaction at 3 minutes (Entry 3) and 1 minute (Entry 4) before quenching. However with this reaction time, only starting material **2-5** was recovered. We also attempted to switch to a Grignard reagent using *i*PrMgCl instead of lithium-halogen exchange, but this attempt was also unsuccessful with mostly starting material **2-5** recovered (Entry 5).

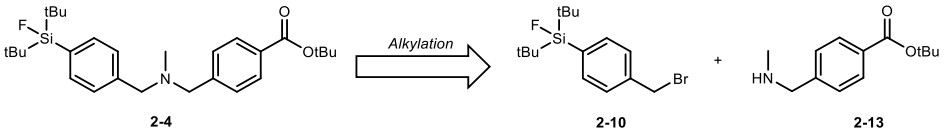

Scheme 2-4: Alternative route for synthesis of phenyl SiFA derivative **2-4**

Due to the challenges faced in the lithiation of **2-5**, we decided to pursue an alternative strategy (Scheme 2-4). SiFA installation could be performed in the early stage, and we planned to employ a benzyl bromide functionalized SiFA **2-10** which has been previously been synthesized by Kostikov *et al*.[6] The fragment **2-10** would be used to alkylate the secondary amine **2-13**, after which the hydroxamic acid could be installed.

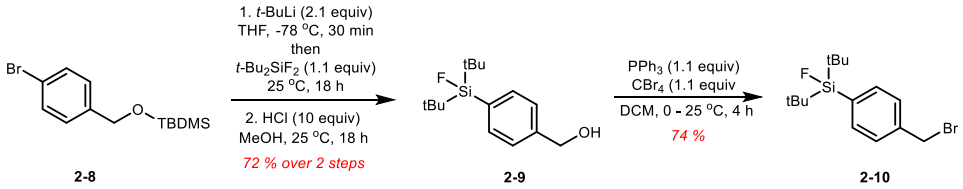

Scheme 2-5: Synthesis of phenyl SiFA benzyl-bromide **2-10**

The benzyl bromide phenyl SiFA core **2-10** was synthesized (Scheme 2-5) from commercially available TBDMS protected 4-bromobenzyl alcohol **2-8** via lithium halogen exchange using *tert*-butyl lithium and di-*tert*-butyldifluorosilane, followed by removal of the TBDMS protection group with HCl to form the free alcohol **2-9** and subsequent conversion to the benzyl bromide through Appel reaction.

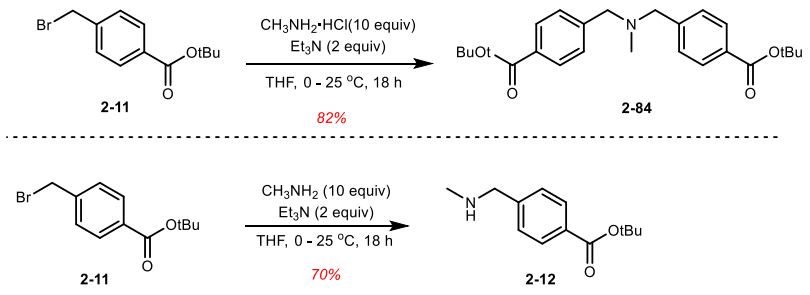

Scheme 2-6: Synthesis of *tert*-butyl 4-((methylamino)methyl)benzoate **2-10**

The second fragment **2-12** was synthesized from commercially available *tert*-butyl 4-(bromomethyl)benzoate **2-11** via alkylation with methylamine using a published procedure by Hjelmgaard *et al*. (Scheme 2-6)[25] An initial attempt to use more readily available methylamine HCl salt resulted in over alkylation, producing the *bis*-alkylated tertiary amine product **2-84** rather than the desired product. However, switching reagents to free methylamine solution in THF was successful in producing the desired product **2-12** in 70% yield. We presume that this difference in reactivity was possibly due to the lack of available free methylamine when using the HCl salt, which results in overalkylation. Another potential solution to this issue would be the addition of a stronger base or pre-mixing the methylamine salt with the base to produce more available free amine for the alkylation.

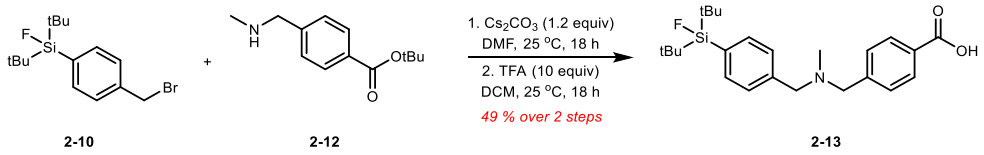

Scheme 2-7: Synthesis of **2-13** through alkylation using phenyl SiFA benzyl bromide

With the key fragments **2-10** and **2-12** in hand, we proceeded with alkylation using cesium carbonate as the base and were able to produce the desired compound **2-4** in 54% yield. After alkylation, the *tert*-butyl ester was hydrolyzed using trifluoroacetic acid to give the free carboxylic acid **2-13** (Scheme 2-7) as a precursor for hydroxamic acid installation.

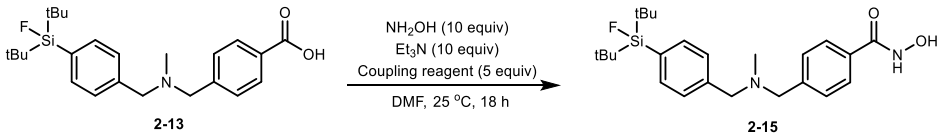

Entry	Coupling reagent	Hydroxylamine	Yield (%)
1	EDC	NH_2OH	23
2	HBTU	NH_2OH	52
3	Yamaguchi's reagent	NH_2OH	61

Table 2-2: Optimization for installation of hydroxamic acid

We first used EDC as the amide coupling reagent with hydroxylamine as it was commonly used for hydroxamic acid formation in literature[4] but had a poor result with only 23% yield from the coupling (Entry 1), so we also tried reagents we had on hand including HBTU (Entry 2) and 2,4,6-trichlorobenzoyl chloride

(Yamaguchi's reagent) (Entry 3), with both affording **2-15** in moderate yields. As Yamaguchi's reagent provided the marginally better result at 61% yield, we decided to use it as the standard coupling reagent for hydroxamic acid installation on subsequent derivatives.

We found that it was impractical to purify **2-15** by normal phase column chromatography due to a strong tailing effect in a normal phase. It was feasible to use reverse phase HPLC for purification. However we lacked the capacity for preparative scale separation and it significantly limited our throughput. A common strategy to simplify the purification process of hydroxamic acids is to synthesize the *O*-protected hydroxamic acids,[4] which can be readily deprotected to generate the desired hydroxamic acids usually with minimal purification.

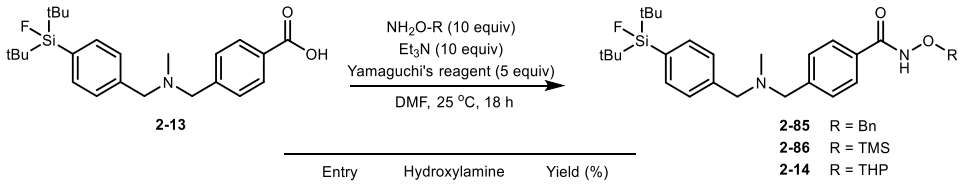

Entry	Hydroxylamine	Yield (%)
1	NH_2-OBn	54
2	NH_2-OTMS	0
3	NH_2-OTHP	62

Table 2-3: Optimization for installation of hydroxamic acid

We decided to try commercially available benzyl, trimethylsilyl, and tetrahydropyran protected hydroxylamine as the coupling partner to produce the corresponding protected hydroxamic acids (Table 2-3). The benzyl protected derivative **2-85** was successfully synthesized in 54% yield (Entry 1) and we were pleased to find that it can be easily purified on normal phase silica. However, when subjected to hydrogenation conditions using H_2 and palladium on carbon for deprotection, we observed formation of significant quantities of side products, making this protecting group unsuitable for our purposes. We found trimethylsilyl protecting group to be too labile as **2-86** underwent significant deprotection during normal phase column purification on silica gel (Entry 2). Finally, we found that THP protected derivative **2-14** worked well for our purposes, allowing it to be purified using silica gel column chromatography and deprotected by hydrolysis in HCl without necessitating additional column purification (Entry 3).

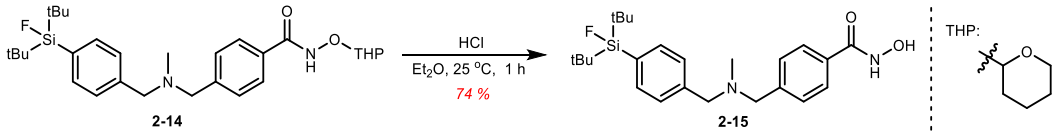

Scheme 2-8: Deprotection of THP protected hydroxamic acid **2-14**

Treating the THP protected derivative **2-14** with ethereal HCl produces the free hydroxamic acid **2-15** (Scheme 2-8) which can be purified through trituration with additional ether to afford the product. We also found that deprotection could be achieved within 15 minutes using 5 M aqueous HCl, then purified by cartridge purification using C-18 cartridges, which is a part of a standard SiFA radiosynthesis protocol. This means that it is feasible to ^{18}F-label the THP-protected compound **2-14**, remove THP group, and then purify a free hydroxamic acid by cartridge, similarly to a SiFA radiosynthesis process.

2.3 Synthesis of methoxy pyridine HetSiFA-based [^{18}F]Bavarostat derivatives

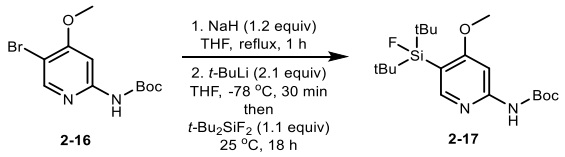

Scheme 2-9: Synthesis of methoxy aminopyridine SiFA core

In a separate project, our group has been developing less lipophilic heteroaromatic HetSiFA cores, including a methoxy pyridine SiFA functionalized with an amino group **2-17** (Scheme 2-9) that serves as a functional handle and point of attachment to peptides. To expand the scope of HDACi candidates in hand we decided to incorporate this HetSiFA core with the Bavarostat scaffold to produce a less lipophilic candidate.

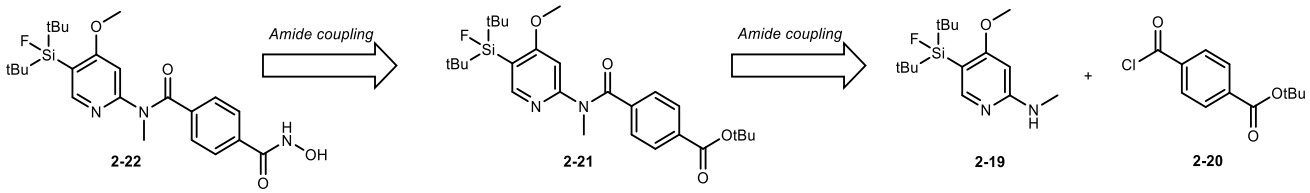

Scheme 2-10: Strategy for synthesis of HetSiFA amide derivative

The first derivative we aimed to make was **2-22** which attaches the pyridine hetSiFA core **2-19** to the aryl hydroxamic acid via an amide functionality. With Boc-protected amino-pyridine SiFA core **2-17** already in hand from other projects, we decided to first synthesize **2-19** which can be amide-coupled with the acyl chloride **2-20** to produce **2-21**, followed by installation of the hydroxamic acid using the same strategy as for the phenyl SiFA derivative **2-14** (Scheme 2-10).

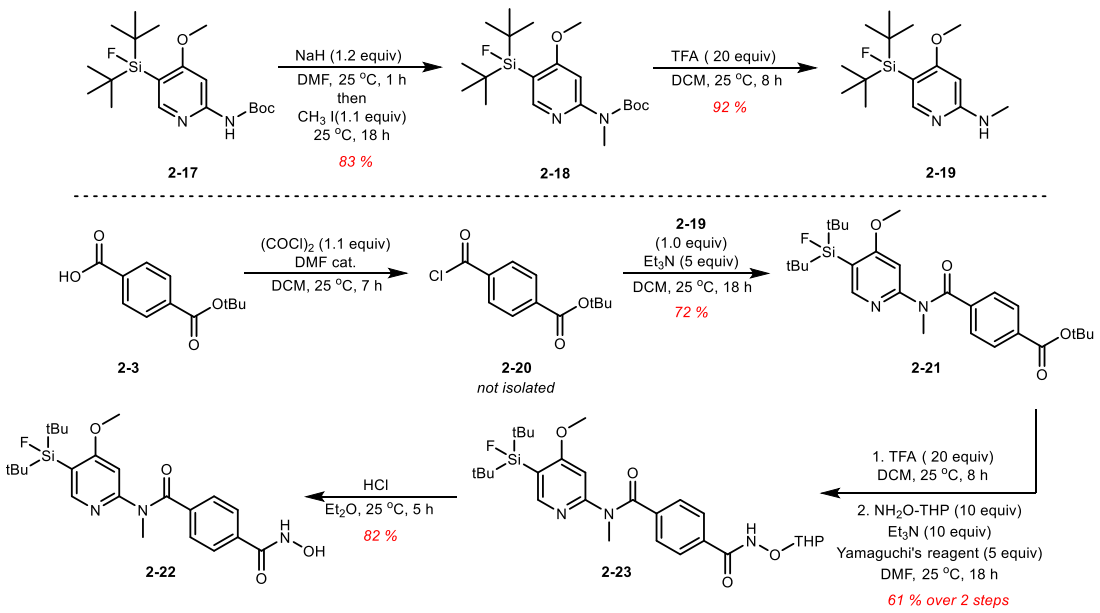

Scheme 2-11: Synthesis of methoxy aminopyridine SiFA core

To avoid over-alkylation, we attempted to directly install the methyl group on the Boc-protected SiFA core **2-17** synthesized by other group members for different projects. We were pleased to find that **2-17** could be methylated using sodium hydride base and iodomethane, producing the desired product **2-18** at 83% yield which was then subjected to TFA deprotection to form the desired hetSiFA core **2-19** ready for amide coupling.

Tert-butyl 4-(chlorocarbonyl)benzoate **2-20** was prepared using commercially available 4-(*tert*-butoxycarbonyl)benzoic acid **2-3** by a known procedure, [5] and used immediately without purification to amide couple with **2-19** to produce **2-21**. Subsequent *tert*-butyl ester deprotection and installation of the THP-protected hydroxamic acid functionality to produce **2-23** uses the same amide coupling procedure developed for the phenyl SiFA derivative **2-14** described above. The THP group was removed using ethereal HCl to produce the free hydroxamic acid **2-22** which was purified by trituration as described above (Scheme 2-11).

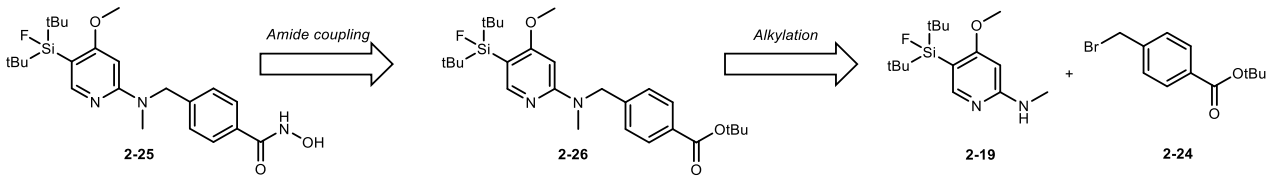

Scheme 2-12: Strategy for synthesis of HetSiFA amine derivative **2-25**

A second methoxy pyridine derivative we aimed to synthesize was **2-25** which has the amine functionality in the linker between the benzohydroxamic acid and HetSiFA core as opposed to the amide linker of **2-21**. We aimed to use the same SiFA core **2-19** and commercially available 4-(bromomethyl)benzoic acid *tert*-

butyl ester **2-24** and assembe the two fragments by alkylation followed by deprotection and amide coupling to install the hydroxamic acid in **2-25** (Scheme 2-12).

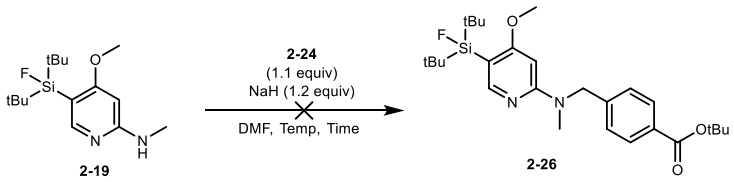

Entry	Temperature (°C)	Time (min)	Base	Result
1	25 °C	18 h	Cs_2CO_3	No conversion
2	60 °C	18 h	Cs_2CO_3	No conversion
3	25 °C	18 h	LiHMDS	No conversion
4	60 °C	18 h	LiHMDS	Complex Mixture
5	25 °C	18 h	NaH	No conversion
6	90 °C	24 h	NaH	Complex Mixture

Table 2-4: Attempts of synthesis of **2-26** by direct alkylation of **2-19**

We experienced considerable difficulty performing the key alkylation step (Table 2-4), likely due to poor nucleophilicity of the secondary amine of **2-19** conjugated to the pyridine ring. First, alkylation attempts were made using cesium carbonate as the base (Entry 1), but even upon heating to 60 °C (Entry 2) there was no conversion. Lithium bis(trimethylsilyl)amide (Entry 3, 4) and sodium hydride (Entry 5, 6) both resulted in no conversion at room temperature, while elevating the temperature resulted in complex mixtures with no desired product.

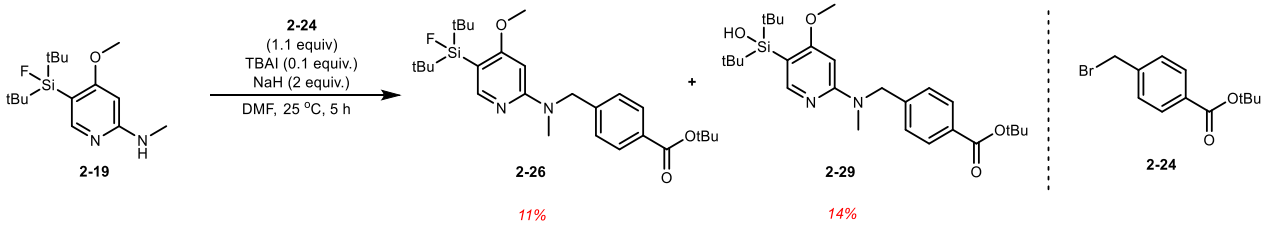

Scheme 2-13: Attempted alkylation of **2-19** using **2-24** with TBAI

We decided to attempt activation of benzyl bromide **2-24** prior to alkylation by addition of 10 mol% tetrabutylammonium iodide (TBAI) to effect *in-situ* generation of a more electrophilic benzyl iodide through Finkelstein reaction. We were pleased that under these conditions, alkylation proceeded to form **2-26**, although only in 11% yield due to the concurrent hydrolysis of the silicon-fluoride bond to form the silanol side product **2-29** (Scheme 2-13). While we were unable to confirm the source of OH^-, we suspect that the hydrolysis occurred either during aqueous work-up or due to the traces of water in the reagents as the silanol side product was observed even after drying tetrabutylammonium iodide on vacuum for 24 h along with using freshly distilled DMF.

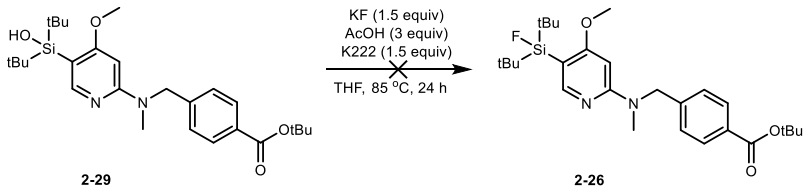

Scheme 2-14: Attempted re-fluorination of silanol **2-29**

We attempted to re-fluorinate the silanol byproduct **2-29** to recover the desired product (Scheme 2-14), but were unable to detect formation of **2-26** after heating at 85 °C for 24 h. This prompted us to consider a different strategy for preparation of the SiFA core **2-19** via LAH reduction of the corresponding Boc-protected amine.

Reduction of the Boc-protecting group on **2-17** to the methyl using lithium aluminum hydride to produce **2-19** in one step had high conversion, but generated mixture of the desired product **2-19** and the over-reduced silane **2-30**. This mixture was carried forward as is, as the silane could be re-fluorinated after the alkylation step. It was possible to fully convert **2-17** into the silane **2-30** if the reaction was allowed to proceed for 24 h, but we found significant decrease in yield of this reaction due to decomposition which would have decreased the utility of this reaction sequence to maximize the yield of **2-26**.

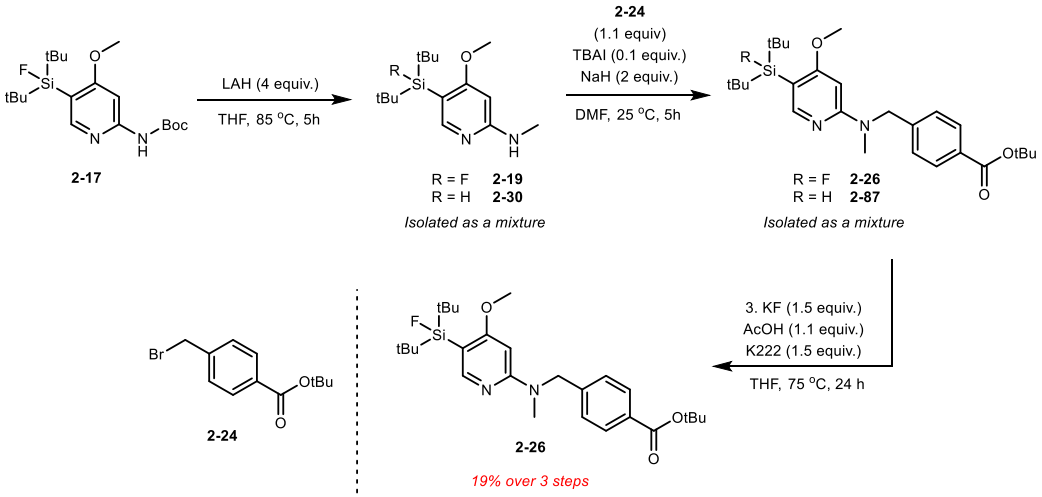

Scheme 2-15: Synthesis of **2-26** by reduction of **2-17**, alkylation, then re-fluorination

The mixture of **2-19** and **2-30** was used to alkylate **2-24** in presence of sodium hydride and tetrabutylammonium iodide and the resulting mixture of **2-26** and **2-87** was subjected to fluorination conditions using Kryptofix 2.2.2., KF, and acetic acid to successfully produce **2-26** in an overall 19% yield over 3 steps (Scheme 2-15).

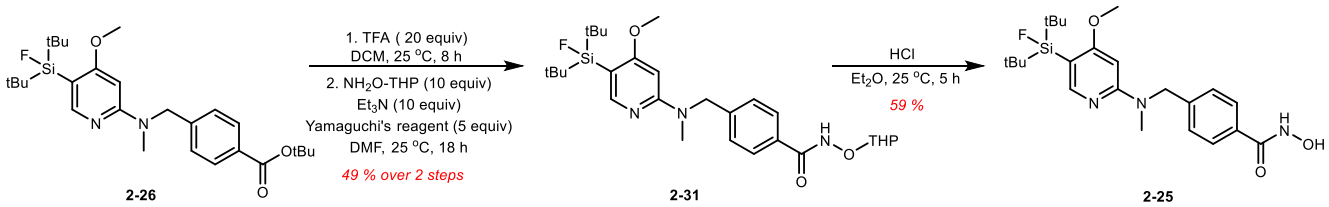

Scheme 2-16: Synthesis of final product **2-25** from **2-26**

With **2-26** in hand, we deprotected the carboxylic acid followed by amide coupling to install the THP protected hydroxamic acid **2-31**. The latter was deprotected with ethereal HCl to form free hydroxamic acid final product **2-25** (Scheme 2-16) as described above.

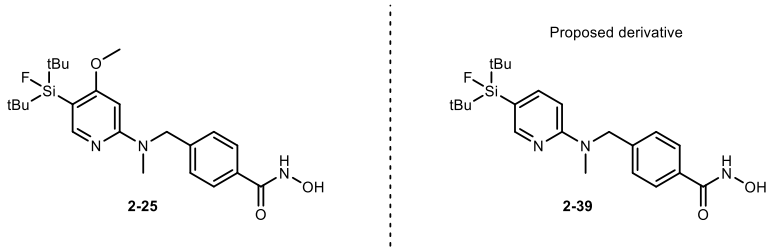

Scheme 2-17: Proposed derivative **2-39** compared to **2-25**

During the development of pyridine SiFA cores, we found that the presence of the methoxy group helped improve the hydrolytic stability of the Si-F bond, but at the cost of decreased radiolabeling efficiency. On the other hand, the desmethoxy pyridine SiFAs were adequately stable for PET applications and showed excellent efficiency in ^{18}F-labeling via SiFEx. As such, we next designed desmethoxy pyridine SiFA hydroxamic acid **2-39** expecting better radiolabeling efficiency while maintaining adequate hydrolytic stability (Scheme 2-17).

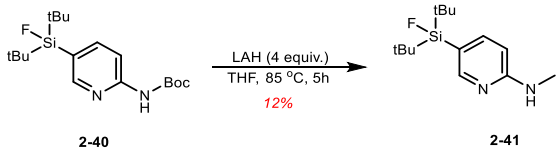

Scheme 2-18: Synthesis of **2-41** from **2-40** by reduction of Boc protecting group

The pyridine SiFA core was provided by other members of the group as the Boc-protected starting material **2-40**. We decided first to employ the previously successful Boc-reduction using LAH, to produce **2-41**, but the reaction resulted in only 12% yield with significant loss of product by decomposition through protodesilylation (Scheme 2-18).

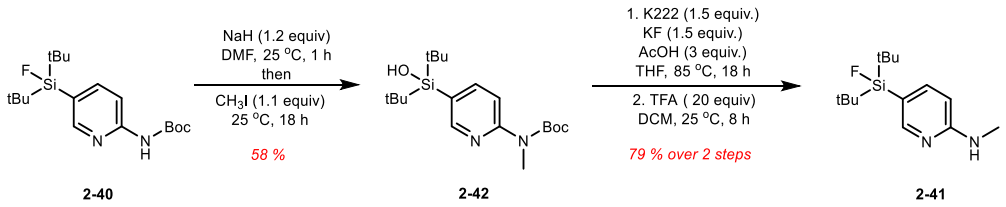

Scheme 2-19: Synthesis of **2-41** from **2-40** by alkylation with iodomethane

Next, we tried alkylation of **2-40** with iodomethane, and found that while the reaction had good conversion it resulted in the hydrolysis of the Si-F bond to give the silanol **2-42**, even when performing the reaction using freshly distilled DMF. However, we were pleased to discover that the silanol could be re-fluorinated, and after Boc-deprotection we obtained our desired methylated fragment **2-41** (Scheme 2-19).

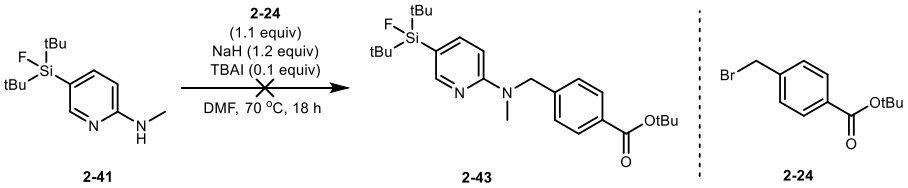

Scheme 2-20: Attempted synthesis of **2-43** from **2-41** by alkylation with **2-24**

To install **2-24** on **2-41**, we first tried to use the same activation strategy through using 10 mol % tetrabutyl ammonium iodide, but this failed to produce any desired product (Scheme 2-20).

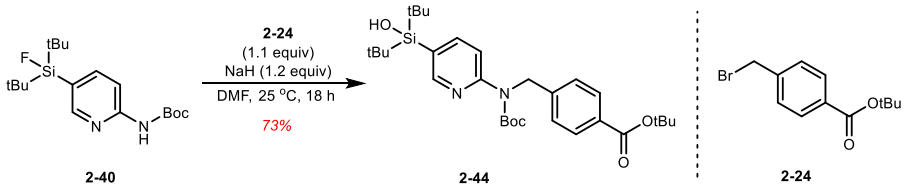

Scheme 2-21: Attempted synthesis of **2-43** from **2-41** by alkylation with **2-24**

We then tried to reverse the order of alkylation, and successfully alkylated **2-24** on the Boc-protected starting material **2-40** with good conversion, but again only managed to isolate the corresponding silanol **2-44** (Scheme 2-21).

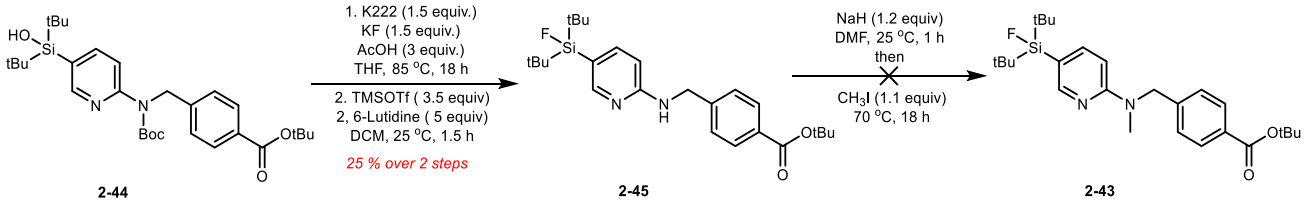

Scheme 2-22: Attempted synthesis of **2-43** from **2-44** by alkylation using iodomethane

We used the same fluorination conditions and managed to successfully fluorinate **2-44** to produce the corresponding silyl fluoride, which we attempted to selectively deprotect the Boc group using TMSOTf and 2,6-lutidine. We found the selectivity for Boc deprotection was fairly poor and significant product loss due to global deprotection was observed, though the desired product **2-45** was still isolated at 25% yield over 2 steps. However, attempts to alkylate **2-45** with iodomethane were unsuccessful with poor conversion (Scheme 2-22).

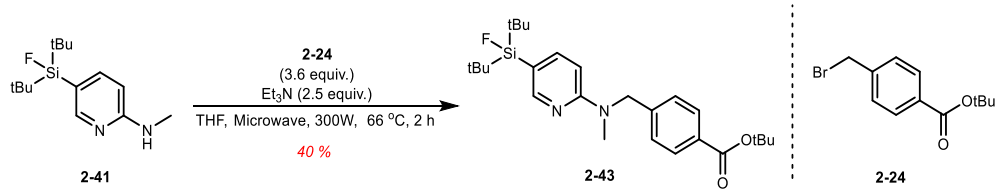

Scheme 2-23: Synthesis of **2-43** from **2-41** by microwave-assisted alkylation with **2-24**

For the next attempt, we decided to use the previously synthesized substrate **2-41** and attempt alkylation of **2-24** through activation by microwave irradiation. Using a published protocol[10] we successfully performed the alkylation to produce **2-43** at 40% yield (Scheme 2-23).

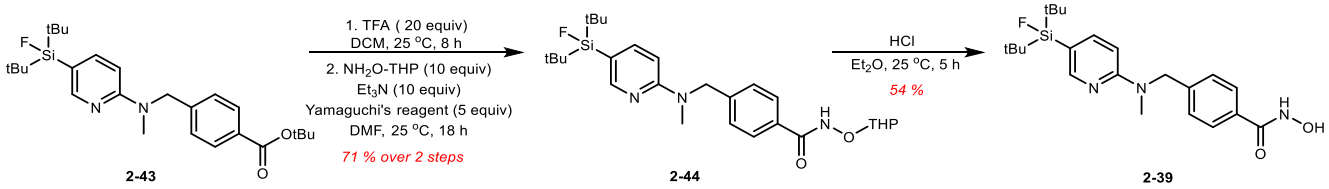

Scheme 2-24: Synthesis of **2-43** from **2-41** by microwave-assisted alkylation with **2-24**

With **2-43** in hand, we proceeded with *tert*-butyl ester deprotection then installation of THP protected hydroxamic acid using our previous conditions to produce **2-44**, which was then deprotected using ethereal HCl to provide the free hydroxamic acid **2-39** (Scheme 2-24).

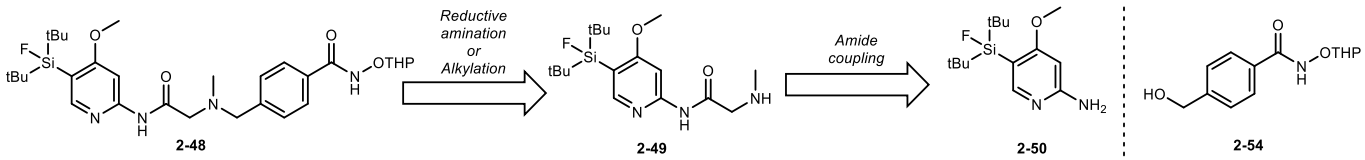

Scheme 2-25: Retrosynthetic plan of long amide derivative **2-48**

The binding pocket of HDACs are linear to accommodate lysine side chains as their main biological target. We decided to produce an elongated variant of our amide derivative **2-22** in hopes that the longer design might improve substrate binding. We designed **2-48** elongated by one glycine unit to maintain a similar structure in the binding portion compared to our other substrates, but spacing the SiFA further away from the hydroxamic acid. For the synthesis of the amide derivative **2-48**, we attempted a more convergent synthesis by pre-installing the THP protected aryl hydroxamic acid fragment **2-54** to reduce the number of

functional group manipulations at the end of the synthesis. Fragment **2-54** could be functionalized into an aldehyde and coupled to **2-29** to directly produce the desired product **2-48** (Scheme 2-25).

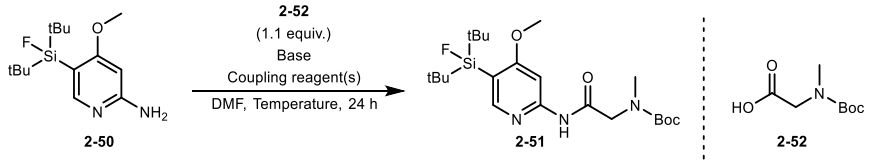

Entry	Coupling reagent 1	Coupling reagent 2	Base	Temp (°C)	Yield (%)
1	HATU (1.1 equiv.)	HOBt (1.1 equiv.)	DIPEA (5 equiv.)	25	35
2	HATU (1.1 equiv.)	HOBt (1.1 equiv.)	DIPEA (5 equiv.)	40	28
3	HATU (1.1 equiv.)	HOBt (3 equiv.)	DIPEA (5 equiv.)	60	42
4	HATU (1.1 equiv.)	HOBt (5 equiv.)	DIPEA (5 equiv.)	60	34
5	$POCl_3$ (3.5 equiv.)	-	Pyridine (10 equiv.)	25	22
6	HATU	-	DIPEA (5 equiv.)	25	69

Table 2-5: Optimization of amide coupling of **2-50** with **2-52** to produce **2-51**

Boc-deprotection of the methoxy pyridine SiFA core provided **2-50**, and we began by attempting to install the *N*-Boc sarcosine fragment **2-52** by amide coupling (Table 2-5). Our first attempt was successful in producing the desired product **2-51**, but only in 35% yield (Entry 1), due to poor conversion. We tried to address the low conversion by increasing both the equivalents of HOBt used and the reaction temperature (Entry 2 – 4), but eventually found that using only HATU as the coupling reagent and performing the reaction at room temperature provided the best result (Entry 6).

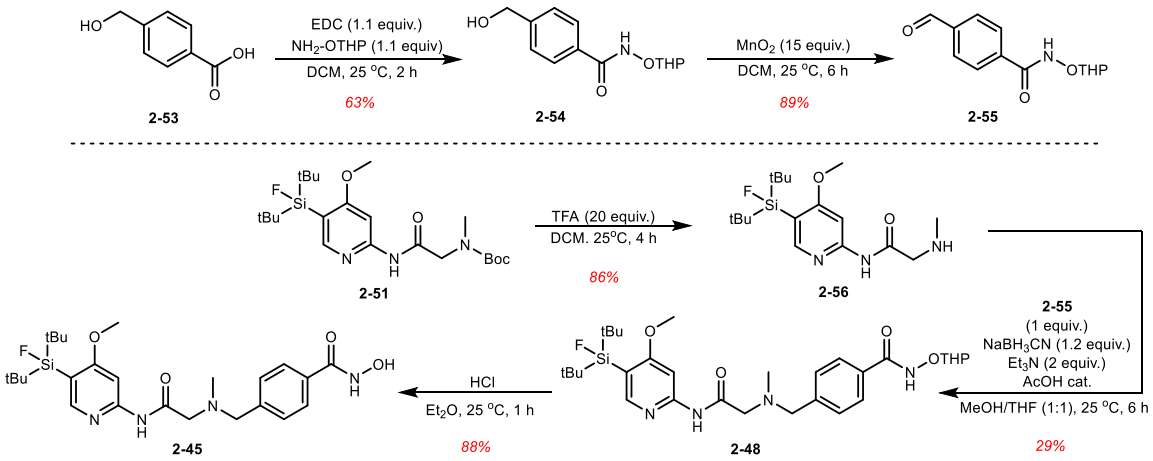

Scheme 2-26: Synthesis of **2-45** from **2-51** by reductive amination

The aldehyde functionalized hydroxamic acid fragment **2-55** was synthesized in 2 steps from the 4-(hydroxymethyl)benzoic acid **2-53** using a literature procedure[20]. We then successfully coupled it to **2-56** by reductive amination to produce **2-48** at 29% yield. We also attempted to convert **2-54** to the corresponding benzyl bromide and benzyl mesylate for alkylation as an alternative route, but both reactions failed to produce the desired product. THP protected **2-48** was then deprotected using ethereal HCl to produce the free hydroxamic acid **2-45** (Scheme 2-26).

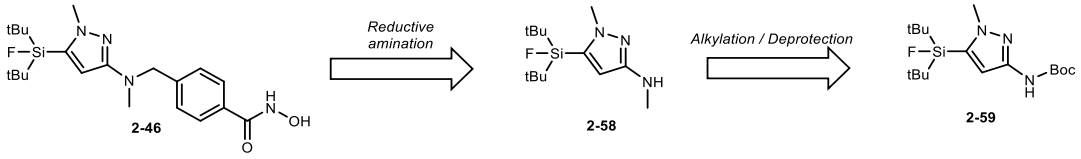

Scheme 2-27: Retrosynthetic plan for synthesis of pyrazole derivative **2-46**

The pyrazole derivative **2-46**, could be made by the same reductive amination strategy using the previously synthesized hydroxamic acid aldehyde fragment **2-55**. The main pyrazole core was synthesized by other members and provided as the Boc-protected fragment **2-59** (Scheme 2-27).

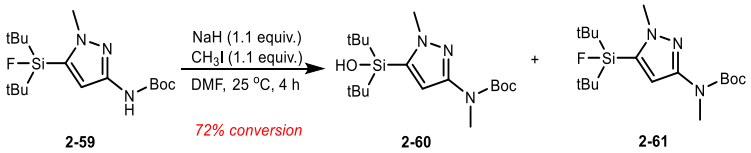

Scheme 2-28: Alkylation of pyrazole SiFA core **2-59**

The methylation of **2-59** progressed with good conversion, but produced a mixture of the desired product **2-61** and the corresponding silanol **2-60** (Scheme 2-28) despite the use of the freshly distilled solvents.

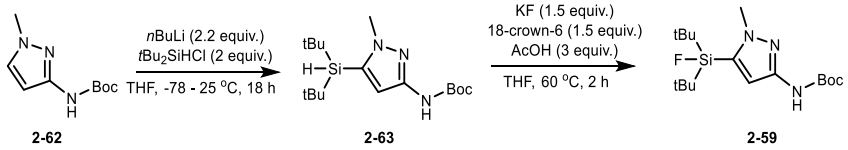

Scheme 2-29: Synthesis of pyrazole SiFA core **2-59**

The synthesis of the pyrazole SiFA core developed by our group is 2-steps from commercially available pyrazole starting material **2-62**. The reaction sequence passes through the silane precursor **2-63** before fluorination to form **2-59** (Scheme 2-29). We decided to address the hydrolysis issues we observed by switching the reaction sequences and performing the alkylation steps on the silane intermediate then performing fluorination afterwards.

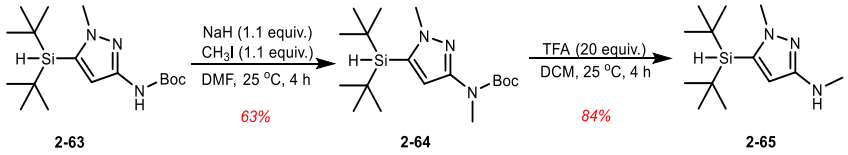

Scheme 2-30: Synthesis **2-65** from silane starting material **2-63**

Using the silane **2-63**, we successfully performed the alkylation using iodomethane to produce **2-64**, which was then deprotected to produce **2-65** (Scheme 2-30).

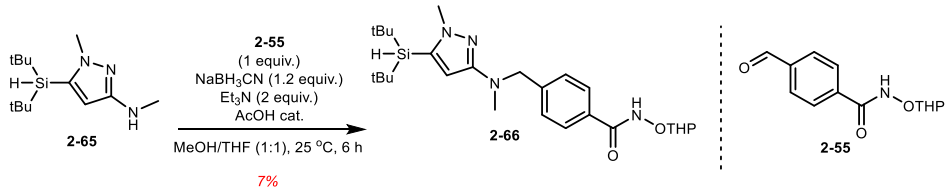

Scheme 2-31: Synthesis **2-66** from **2-65** by reductive amination

Reductive amination was performed using the previously synthesized hydroxamic acid fragment **2-55** to produce **2-66**. The reaction had high conversion, but only produced 7% isolated yield of **2-66** (Scheme 2-31). Due to the poor yield, we decided to try an alternative alkylation sequence to verify if we could obtain a better overall yield.

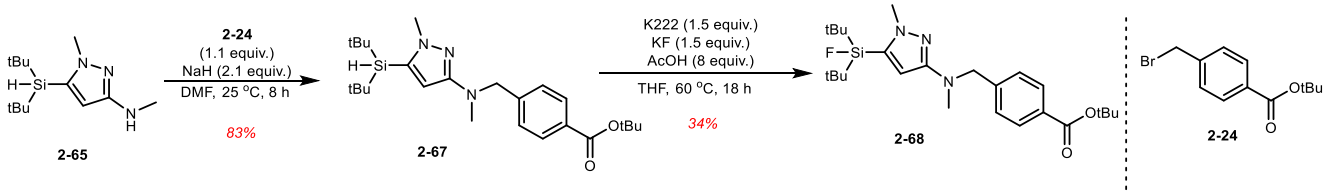

Scheme 2-32: Synthesis **2-67** from **2-65** by alkylation

We found the alkylation of the silane core **2-65** using the benzyl bromide **2-24** proceeded efficiently and produced **2-67** in 83% yield. We decided to fluorinate this substrate before proceeding with the hydroxamic acid installation, and found that the reaction was slow and required 8 equivalents of acetic acid to proceed, obtaining **2-68** in 34% yield (Scheme 2-32).

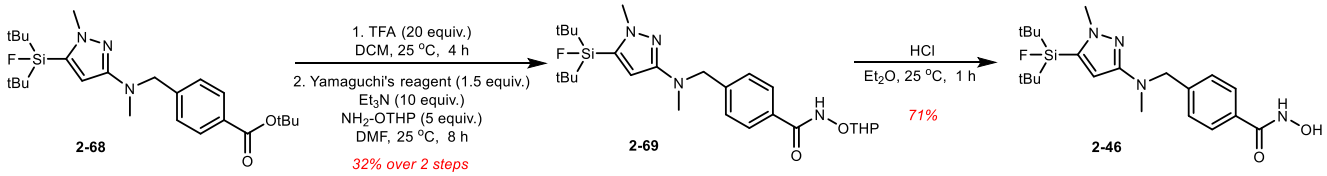

Scheme 2-33: Synthesis **2-67** from **2-65** by alkylation

With **2-68** in hand, we proceeded with *tert*-butyl ester deprotection and amide coupling to install the THP protected hydroxamic acid to form **2-69**, which was then deprotected using ethereal HCl to form the free hydroxamic acid **2-46** (Scheme 2-33).

2.4 Synthesis of SAHA – based SiFA tracers

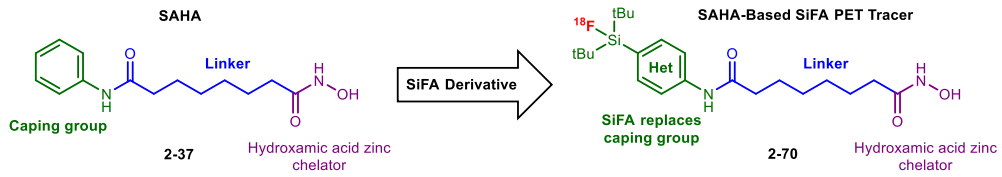

Scheme 2-34: Proposed SAHA based SiFA PET tracers

We designed the next generation of HetSiFA-hydroxamic acid PET tracer candidates based on the structure of the clinically validated HDACi Vorinostat (SAHA) **2-37**. Besdies its application as an anticancer drug, SAHA was tested in clinical trials for neurological applications, but failed due to its poor brain bioavailability. This is likely due to SAHA being a target for active efflux by Pgp and Bcrp1 efflux transporters[16]. A SiFA derivative using this scaffold would replace the capping benzene ring with either a phenyl or a heteroaromatic SiFA core (Scheme 2-34). The addition of silicon and *tert*-butyl groups was hypothesized to prevent these SiFA derivatives from being targeted by the same efflux transporters and allow for its use in neurological imaging. Even if this isn't the case, a SiFA PET tracer based on the SAHA scaffold could still be useful for non-neurological applications, similar to how [^{11}C]Martinostat which was originally developed for brain PET imaging had also been successfully used for other organs[17].

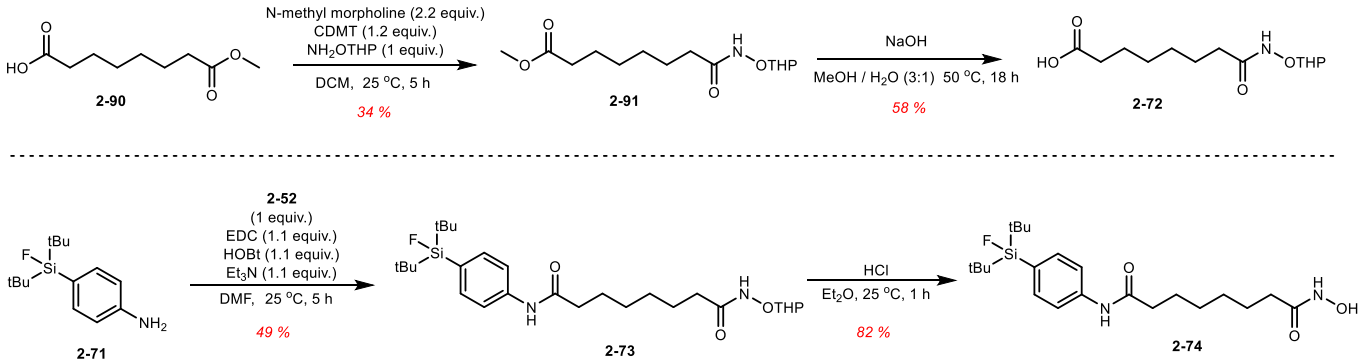

Scheme 2-35: Synthesis of phenylSiFA-SAHA derivative **2-74**

THP protected hydroxamic acid **2-72** was successfully synthesized from commercially available suberic acid monomethyl ester **2-90** using a literature procedure[21], and served as the coupling partner to several amine functionalized SiFA cores to produce the tracer candidates. For the phenylSiFA derivative, aniline SiFA **2-71** was prepared via published procedure[22], and was successfully coupled to the hydroxamic acid fragment **2-72** by amide coupling using EDC and HOBt to produce the THP protected derivative **2-73**, which was then deprotected using ethereal HCl to form the free hydroxamic acid **2-74** (Scheme 2-35).

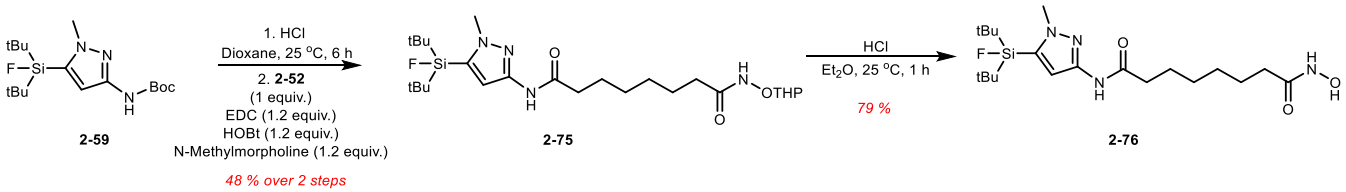

Scheme 2-36: Synthesis of pyrazoleSiFA-SAHA derivative **2-76**

For the HetSiFA derivatives, we employed the pyrazole SiFA core to synthesize the first tracer candidate. The previously synthesized Boc-amino pyrazole core **2-59** was deprotected then amide coupled to the hydroxamic acid fragment **2-52** with EDC and HOBt to form **2-75**, which was then deprotected to produce the final free hydroxamic acid **2-76** (Scheme 2-36).

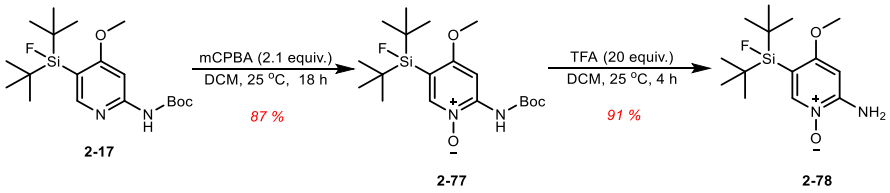

Scheme 2-37: Synthesis of pyridine N-oxide SiFA core **2-78**

We next synthesized pyridine *n*-oxide SiFA derivative. This core was chosen over the previously employed parent pyridine to both increase the hydrophilicity of the final compound as well as improving the substrate's radiolytic stability. The mechanism of radiolytic decomposition of these scaffolds is proposed to be mainly due to oxidation from reactive oxygen species formed by the radiolysis of water[11]. Previously synthesized pyridine SiFA core **2-17** was oxidized using mCPBA to successfully produce the pyridine *n*-oxide SiFA **2-77** which was Boc deprotected to give the free amine **2-78** (Scheme 2-37).

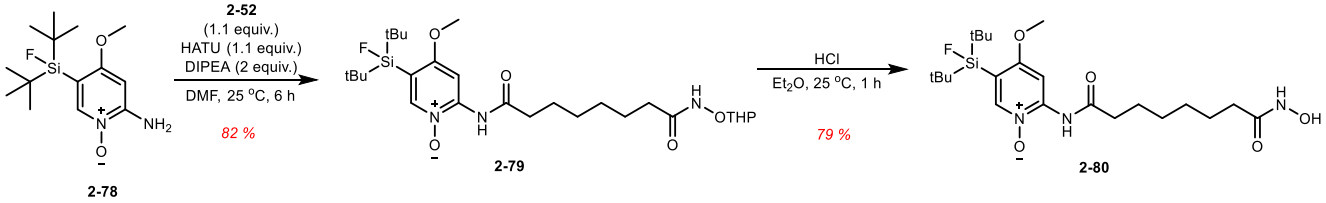

Scheme 2-38: Synthesis of pyridine N-oxide SiFA -SAHA derivative **2-80**

The SiFA core **2-78** was then successfully amide coupled to the hydroxamic acid fragment **2-52** using HATU to form **2-79**. After coupling, the free hydroxamic acid can be produced through deprotection using ethereal HCl (Scheme 2-38).

2.5 Radiolabeling

With the precursors in hand, we proceeded to attempt radiolabeling of the substrates. Free hydroxamic acids are known to be difficult to radiolabel[1], so our initial goal was to first verify if SiFA labeling was compatible with this functional group using our phenyl SiFA derivatives **2-14** and **2-15** which had good literature precedence on superior radiochemistry. PhenylSiFA is known to be capable of achieving >90% radiochemical conversion (RCC) within a few minutes at room temperature[6], so that would be a best-case scenario in our radiolabeling tests with free hydroxamic acids. However, even if the conversion is half of that value, it would still likely indicate a much higher performance than [^{18}F]Bavarostat's reported RCY of 8.1%[1].

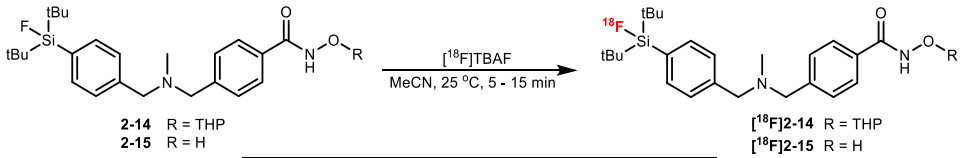

2-14 R = THP
2-15 R = H

[^{18}F]2-14 R = THP
[^{18}F]2-15 R = H

Entry	R	Reaction time (min)	Radiochemical conversion (%)
1	H	5	48
2	H	10	62
3	H	15	64
4	THP	5	88
5	THP	10	92
6	THP	15	99

Table 2-6: Radiolabeling results of Phenyl SiFA derivative

Since the THP group could be quickly removed as part of the SiFA labeling procedure, we decided to attempt to radiolabel both the THP protected and free hydroxamic acid derivatives **2-14** and **2-15** (Table 2-6). Aqueous ^{18}F from the cyclotron was captured on an anion exchange QMA cartridge and eluted with tetrabutylammonium tosylate to provide nucleophilic fluoride in the form of [^{18}F]TBAF, and then azeotropically distilled to dryness before reconstituted in anhydrous MeCN. Both free hydroxamic acid **2-15** (Entry 1-3) and THP protected **2-14** (Entry 4-6) precursors were radiolabeled, and RCC was measured by radioTLC at 5-minute intervals. As discussed in the introduction, reproducibility of radiolabeling reactions in these conditions is sometimes an issue due to inconsistent drying of the fluoride, so a phenyl SiFA standard is also used as a point of comparison for these compounds.

We were pleased to find that both THP-protected and free hydroxamic acids are capable of radiolabeling (Table 2-6), with the THP protected **2-14** having a comparable performance to the phenyl SiFA standard. While the free hydroxamic acid functionality of **2-15** negatively impacted the labeling efficiency, the reaction is still highly efficient especially when compared to ^{18}F-labeling of [^{18}F]Bavarostat. After radiolabeling, we confirmed that we could successfully deprotect the THP protected compound in aqueous HCl and purify it by SPE using C-18 cartridge.

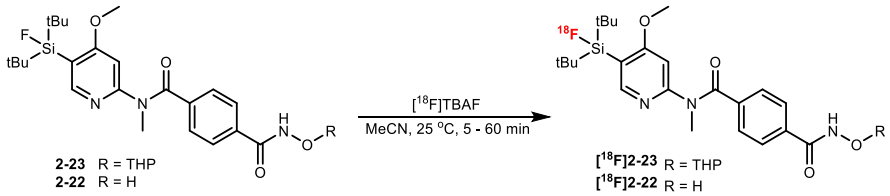

2-23 R = THP
2-22 R = H

[18F]2-23 R = THP
[18F]2-22 R = H

Entry	R	Reaction time (min)	Radiochemical conversion (%)
1	H	5	0
2	H	10	0
3	H	15	0
4	H	60	0
5	THP	5	41
6	THP	10	43
7	THP	15	48
8	THP	60	63

Table 2-7: Radiolabeling of **2-23** and **2-22** using [^{18}F]TBAF

We proceeded to radiolabel the THP protected and free hydroxamic acids of the derivatives bearing our hetSiFA cores. The amide derivatives **2-23** and **2-22** were subjected to [^{18}F]TBAF radiolabeling conditions. Unfortunately, the free hydroxamic acid derivative **2-22** failed to label even after 60 minutes (Entry 1-4), while THP protected **2-23** was successfully labeled at 48% RCC after 15 minutes (Entry 7) and 63% after 60 minutes (Entry 8).

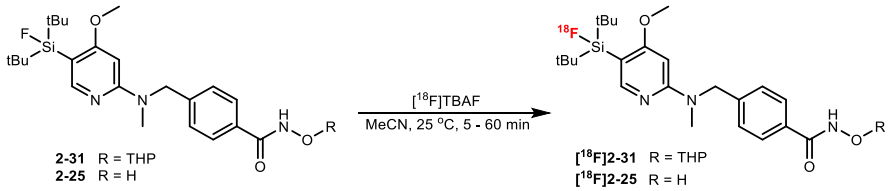

2-31 R = THP
2-25 R = H

[18F]2-31 R = THP
[18F]2-25 R = H

Entry	R	Reaction time (min)	Radiochemical conversion (%)
1	H	5	0
2	H	10	0
3	H	15	0
4	THP	5	22
5	THP	10	37
6	THP	15	43

Table 2-8: Radiolabeling of **2-31** and **2-25** using [^{18}F]TBAF

The amine derivatives **2-31** and **2-25** showed comparable behavior to the amide derivatives during radiolabeling (Table 2-8). The free hydroxamic acid **2-25** also failed to label (Entry 1-3) while the THP-protected derivative **2-31** achieved 43% conversion after 15 minutes (Entry 6). Since the success of radiolabeling free hydroxamic acids observed in the phenylSiFA derivative did not translate to the HetSiFA derivatives, a two-stepped approach would have been necessary for radiolabeling our HetSiFA candidates. However, we decided to work towards maintaining the advantage of the simple one-step radiolabeling process of SiFAs.

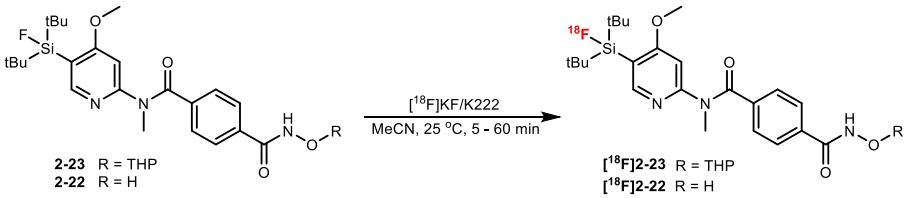

2-23 R = THP
2-22 R = H

[18F]2-23 R = THP
[18F]2-22 R = H

Entry	R	Reaction time (min)	Radiochemical conversion (%)
1	H	5	30
2	H	10	46
3	H	15	55
4	H	60	86
5	THP	5	73
6	THP	10	84
7	THP	15	87
8	THP	60	87

Table 2-9: Radiolabeling of **2-23** and **2-22** using "Munich" method

We re-attempted radiolabeling of our candidates using the "Munich" method described in section 1.5, following literature precedence of its successful implementation with SiFA with high RCY[14]. We were pleased to find both amideSiFA derivatives **2-23** and **2-22** had significantly improved results using these conditions (Table 2-9). The free hydroxamic acid **2-22** was successfully labeled to 55% RCC within 15 minutes (Entry 3) and the THP protected derivative **2-23** achieved 87% conversion within 15 minutes (Entry 7), comparable with the RCC of the phenylSiFA standard.

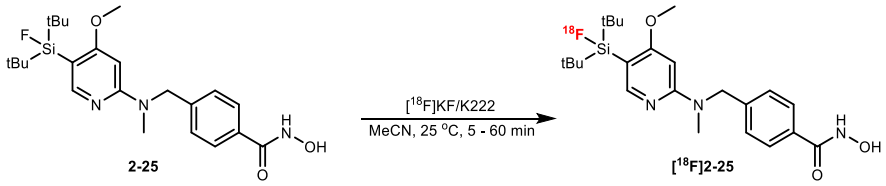

2-25

[18F]2-25

Entry	Reaction time (min)	Radiochemical conversion (%)
1	5	3
2	10	5
3	15	7
4	60	13

Table 2-10: Radiolabeling of **2-25** using "Munich" method

The free hydroxamic acid **2-25** was also labeled using the "Munich" method (Table 2-10), albeit only achieving a RCC of 7% after 15 minutes (Entry 3) and 13% after 60 minutes (Entry 4).

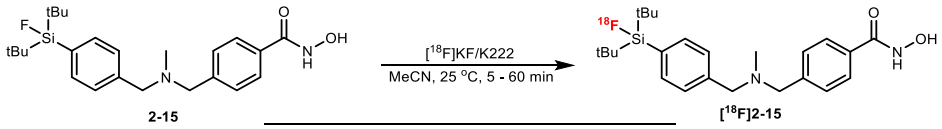

2-15

[18F]2-15

Entry	Reaction time (min)	Radiochemical conversion (%)
1	5	43
2	10	66
3	15	72
4	60	82

Table 2-11: Radiolabeling of **2-15** using the "Munich" method

PhenylSiFA derivative **2-15** was also relabeled using the Munich method (Table 2-11), providing an improvement to 72% after 15 minutes (Entry 3). Since all three substrates had better results using the Munich method, we decided to use this protocol for radiolabeling subsequent derivatives.

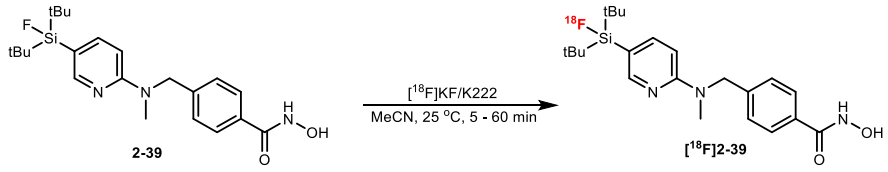

Entry	Reaction time (min)	Radiochemical conversion (%)
1	5	76
2	10	79
3	15	84
4	60	87

Table 2-12: Radiolabeling of **2-39** using "Munich" method

We decided to focus our efforts to radiolabel the free hydroxamic acid as the "Munich" method has demonstrated its tolerance towards this functional group. The DesmethoxySiFA derivative **2-39** was also successfully labeled (Table 2-12) with a RCC of 83% after 15 min at 25 °C (Entry 3), comparable to the phenylSiFA standard.

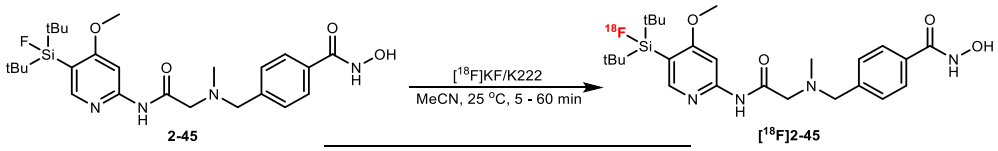

Entry	Reaction time (min)	Radiochemical conversion (%)
1	5	6
2	10	23
3	15	28
4	60	59

Table 2-13: Radiolabeling of **2-45** using "Munich" method

The elongated amide derivative **2-49** was also successfully radiolabeled (Table 2-13) with a RCC of 28% after 15 min (Entry 3). This RCC is lower than desired, but may still be adequate for radiotracer production.

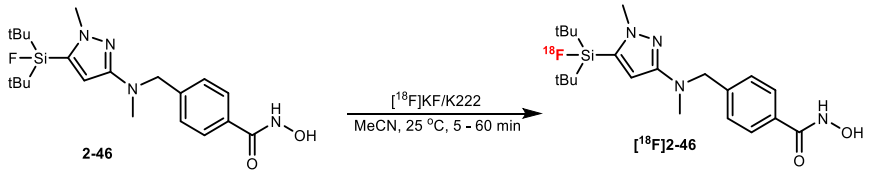

Entry	Reaction time (min)	Radiochemical conversion (%)
1	5	0
2	10	0
3	15	0
4	60	6

Table 2-14: Radiolabeling of **2-46** using “Munich” method

Unfortunately, the pyrazole derivative labeled poorly (Table 2-14), achieving 6% RCC after 60 min (Entry 4). Successful implementation of this compound would require a two-step process with labeling of the THP protected precursor then performing deprotection afterwards to achieve adequate A_m.

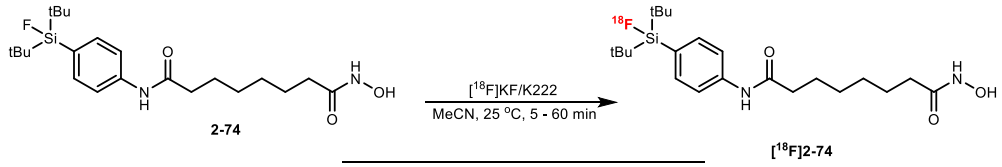

2-74 **[18F]2-74**

Entry	Reaction time (min)	Radiochemical conversion (%)
1	5	60
2	10	71
3	15	82
4	60	89

Table 2-15: Radiolabeling of **2-74** using “Munich” method

The phenylSiFA – SAHA derivative **2-74** was successfully labeled using “Munich” method (Table 2-15) reaching 82% conversion after 15 minutes (Entry 3), similar RCC to the phenylSiFA standard.

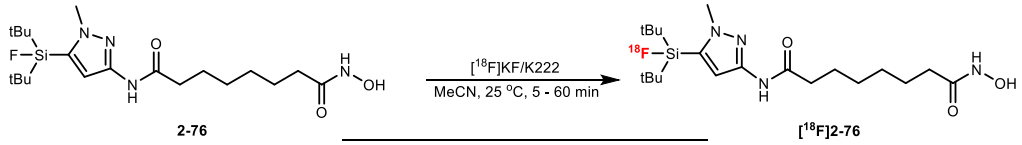

2-76 **[18F]2-76**

Entry	Reaction time (min)	Radiochemical conversion (%)
1	5	33
2	10	37
3	15	42
4	60	47

Table 2-16 Radiolabeling of **2-76** using “Munich” method

We were pleased to see that this pyrazole - SAHA derivative **2-76** provided better radiolabeling results (Table 2-16) compared to the Bavarostat pyrazole derivative, achieving 42% RCC after 15 minutes (Entry 3).

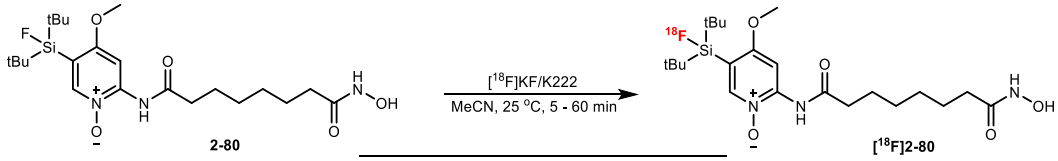

2-80 **[18F]2-80**

Entry	Reaction time (min)	Radiochemical conversion (%)
1	5	64
2	10	74
3	15	81
4	60	80

Table 2-17: Radiolabeling of **2-80** using “Munich” method

Finally, the pyridine *N*-Oxide – SAHA derivative **2-80** was also successfully labeled (Table 2-17), having a similar RCC to phenylSiFA standard with 81% conversion after 15 minutes (Entry 3). This RCC is similar to the phenyl SiFA – SAHA derivative **2-74**, and we were pleased to see one of our more hydrophilic heteroaromatic cores perform equally well as the phenyl SiFA version.

Entry	Precursor	Labeling Method	RCC at 15 min (%)	Structure
1	PhenylSiFA - THP	TBAOTs	99	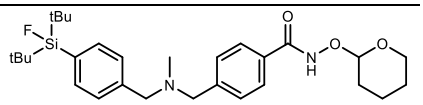 **2-14**
2	PhenylSiFA	TBAOTs	64	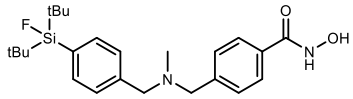 **2-15**
3	PhenylSiFA	Munich	72	
4	AmideSiFA - THP	TBAOTs	48	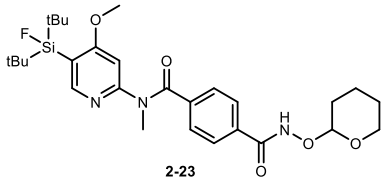 **2-23**
5	AmideSiFA - THP	Munich	87	
6	AmideSiFA	TBAOTs	0	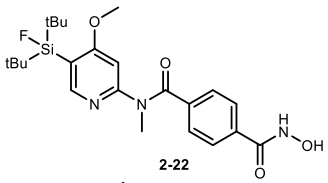 **2-22**
7	AmideSiFA	Munich	55	
8	AmineSiFA - THP	TBAOTs	43	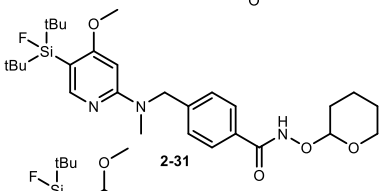 **2-31**
9	AmineSiFA	TBAOTs	0	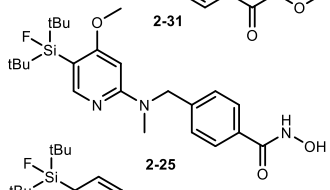 **2-25**
10	AmineSiFA	Munich	7	
11	DesmethoxySiFA	Munich	84	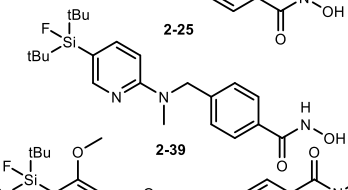 **2-39**
12	Long amideSiFA	Munich	28	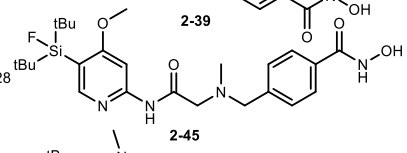 **2-45**
13	PyrazoleSiFA	Munich	0	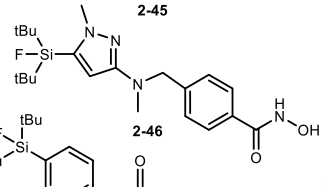 **2-46**
14	PhenylSiFA - SAHA	Munich	82	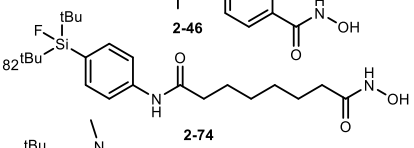 **2-74**
15	PyrazoleSiFA - SAHA	Munich	42	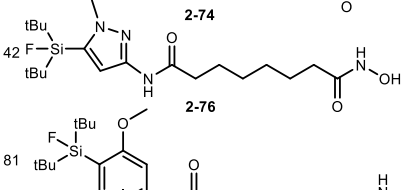 **2-76**
16	N-OxideSiFA - SAHA	Munich	81	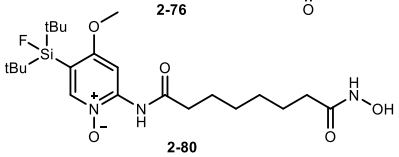 **2-80**

Table 2-18: Summary of radiolabeling results

2.6. Hydrolytic stability.

The hydrolytic stability of our SiFA compounds was evaluated to confirm that these compounds would be adequately stable towards hydrolysis in the timeframe of a PET scan (Table 2-19). The compounds were fully dissolved in a 1:1 mixture of MeCN and water then subjected to a pH 10 buffer as a stress-test as some half-lives in more biologically representative pH 7 buffer were too long to measure. Most of our compounds had excellent hydrolytic stability even in pH 10 with half-lives in the tens of hours. Only the PyrazoleSiFA – SAHA **2-76** (Entry 7) and N-OxideSiFA – SAHA **2-80** (Entry 8) derivatives had slightly decreased stability, but are still likely adequately stable for *in vivo* applications.

Entry	Compound	Half-Life at pH 10 (h)	Structure
1	PhenylSiFA	115	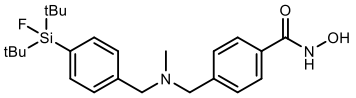 **2-15**
2	AmineSiFA	2135	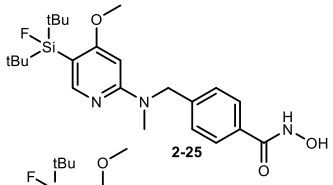 **2-25**
3	AmideSiFA	76	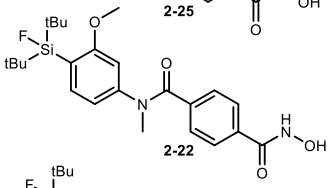 **2-22**
4	Desmethoxy	59	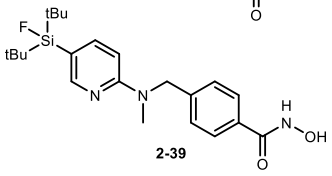 **2-39**
5	Long AmideSiFA	74	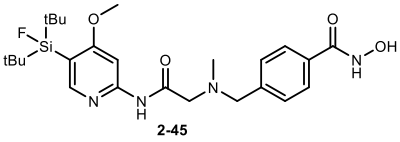 **2-45**
6	PhenylSiFA - SAHA	86	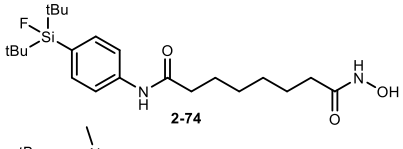 **2-74**
7	PyrazoleSiFA - SAHA	0.23	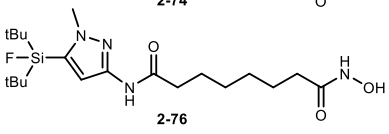 **2-76**
8	N-OxideSiFA - SAHA	2.7	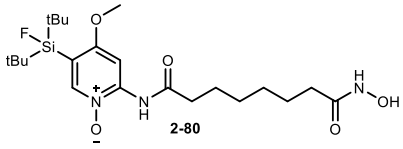 **2-80**

Table 2-19 – Hydrolytic stability assay of SiFA HDAC PET tracers

2.7 Evaluation of HDAC binding activity

We performed *in vitro* binding affinity assay of our compounds to HDAC6 enzyme to evaluate their efficacy. HDAC6 was chosen as this was the target isoform of Bavarostat[1].

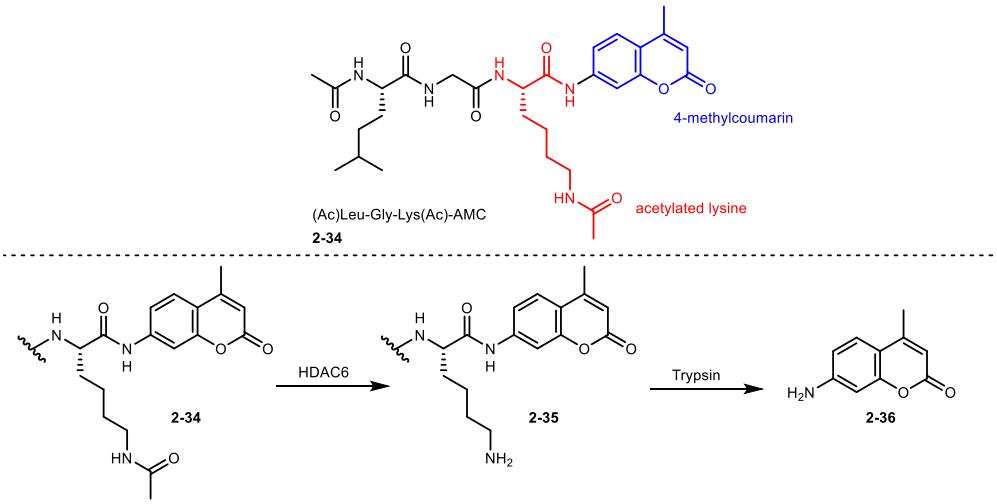

Scheme 2-39: *In vitro* HDAC inhibition assay

The assay uses a peptide substrate **2-34** with an acetylated lysine unit and a fluorescent 4-methylcoumarin moiety that is inactive while attached to the peptide. When treated with HDAC, the lysine will deacetylate to form **2-35**, making the substrate susceptible to digestion by the peptidase trypsin. Once digested, 4-methylcoumarin **2-36** will be released which is detected by a UV detector, and the corresponding signal will relate to HDAC activity (Scheme 2-39)[7]. A serial-dilution of our potential HDAC inhibitors is performed and the sulutions of different concentrations are incubated with this substrate **2-34** and HDAC6, then digested with trypsin and the fluorescence is measured to determine the half maximal inhibitory concentration (IC_{50}). This value describes the molar concentration of inhibitor that will decrease HDAC6 activity by 50%, so a lower value indicates a higher potency of the inhibitor.

As IC_{50} is a measurement of competitive displacement between **2-34** and the inhibitor, the resulting value will be dependent on the quantity of **2-34** used in the assay and its specific binding affinity. Due to this factor, direct comparison of literature IC_{50} is sometimes difficult since this value is only comparable if the same substrate and loading quantity was used. We thus convert IC_{50} to the inhibitory constant K_i, which describes the intrinsic binding affinity of the inhibitor to the enzyme, irrespective of the assay setup. This conversion was done using the Cheng-Prusoff equation $K_i = IC_{50}/(1 + [L]/ K_D)$), where [L] is the concentration of the ligand **2-34** used and K_D is the affinity constant which is the equilibrium concentration of **2-34** that occupies 50% of receptor sites in the HDAC in the absence of any competition[19].

Entry	Compound	Measured K_i n = 3 (nM)	pK_i (nM)	Structure
1	SAHA	21.3 ± 9.7	7.72 ± 0.21	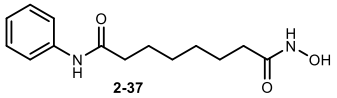 **2-37**
2	Martinostat	23.7 ± 9.2	7.66 ± 0.19	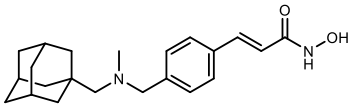 **2-38**
3	PhenylSiFA	575 ± 217	6.27 ± 0.17	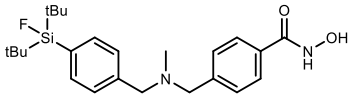 **2-15**
4	AmideSiFA	6127 ± 226	5.21 ± 0.02	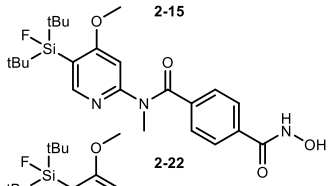 **2-22**
5	AmineSiFA	159 ± 38	6.81 ± 0.11	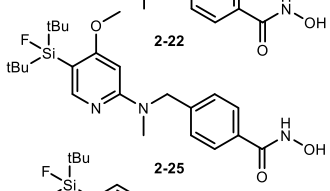 **2-25**
6	DesmethoxySiFA	983 ± 335	6.03 ± 0.15	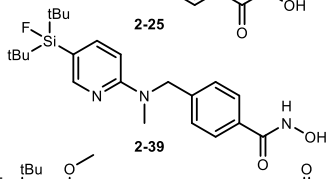 **2-39**
7	Long amideSiFA	650 ± 82	6.19 ± 0.06	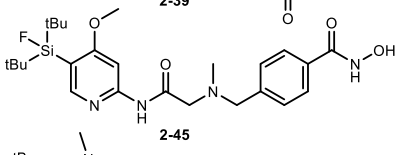 **2-45**
8	PyrazoleSiFA	1017 ± 240	6.01 ± 0.10	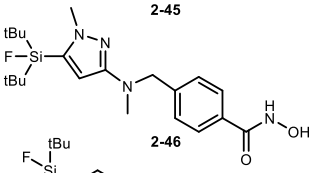 **2-46**
9	PhenylSiFA - SAHA	177 ± 31	6.76 ± 0.08	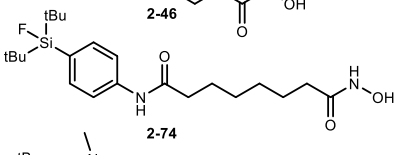 **2-74**
10	PyrazoleSiFA - SAHA	242 ± 13	6.62 ± 0.02	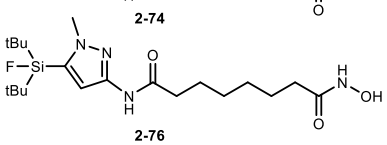 **2-76**
11	N-OxideSiFA - SAHA	210 ± 39	6.69 ± 0.08	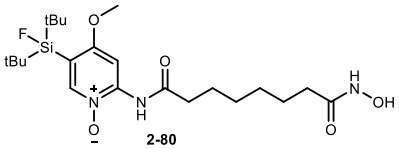 **2-80**

Table 2-20: Measured K_i of SiFA compounds and standards against HDAC6

The fluorogenic peptide substrate was synthesized using literature procedures[7] and HDAC6 binding affinity of all substrates were determined (Table 2-20). In order to validate the effectiveness of the binding assay, Martinostat **2-38** was synthesized according to literature procedure[9], and commercially available SAHA **2-**

37 was purchased to use as standards. The determined SAHA K_i of 21.3 ± 9.7 nM (Entry 1) is comparable to literature values of 22 ± 9 nM in the publication of assay methodology using this substrate[8].

The performance of Martinostat and SAHA were comparable in this assay, similar to the conclusion from the assay performed in the Martinostat publication, but our determined binding affinities do not match their reported values which determined binding affinities for both compounds to be one order of magnitude lower.[1, 2]. SAHA and Martinostat assays were repeated multiple times in an attempt to reproduce the values in the Martinostat publication, but measured K_i was consistent across all assays. SAHA measurement was also performed with every subsequent assay to validate the result for the SiFA candidates. We eventually concluded that this assay was performing as intended, and that the numerical differences are likely due to an inherent limitation of this particular methodology as the SAHA results reported in the original publication of this assay did match our results[8]. Since the relative performance of Martinostat and SAHA also matches literature, we felt that the assay should also be adequate at evaluating the relative performance of compounds against standards and help us determine a lead candidate.

The reported binding affinity of Bavarostat against HDAC6 is 60 nM[1], which is one order of magnitude worse than Martinostat's at 4.1 nM, but has the advantage of isoform selectivity towards HDAC6. As such, we foresaw a similar decrease in potency for our tracers in comparison to the standard. The overall best performing compound was the Pyridyl SiFA derivative **2-25** at 159 ± 38 nM (Entry 5), followed closely by the three SAHA derivatives **2-74**, **2-76**, and **2-80**. The Amide derivative **2-22** had the worst performance with a measured K_i greater than 50 uM (Entry 4). Elongating the amide linkage appears to improve the binding affinity, with the HetSiFA derivative **2-45** having a K_i of 650 nM (entry 7). Somewhat surprisingly, the DesmethoxySiFA derivative **2-39**, experienced a marked decrease in affinity compared to its methoxy counterpart with a K_i of 983 nM (Entry 6) despite having a structural modification far removed from the binding portion of the molecule. However, this was in agreement with our computational docking results which will be discussed in section 2.8. Generally, we were pleased that all substrates except **2-22** maintained activity towards HDAC6 with several substrates having relative K_i towards SiFA and Martinostat that suggest they would have similar activity as Bavarostat.

Since SAHA was a better HDAC6 binder than Bavarostat, we expected that the SiFA compounds based off its scaffold would have better binding affinities than the compounds based on Bavarostat. We were pleased to find that this is the case for all three hydroxamic acids as they had similar binding affinities that were better than all non-SAHA substrates except **2-25** (Entry 9 - 11). However, the di-*t*-butylfluorosilyl substituent incurred some penalty in bind affinity of these compounds, and they are all about one order of magnitude worse in measured K_i compared to SAHA.

2.8 Computational evaluation of substrates

After experimentally determining K_i values of several hydroxamic acid derivatives, we decided to evaluate the possibility of using a protein docking software FITTED to design future derivatives. By evaluating docking scores against our experimental values, we hope to validate the effectiveness of using software assistance in designing more potent future derivatives. The software has been specifically designed to use an optimized energy function designed for metalloenzyme coordination, and have shown good results with modeling the zinc coordination of HDACi[26]. Another reason this software was used is its usability as

a screening software that can quickly produce results without employing significant computational power. All docking studies were performed on a consumer computer using 10 binding iterations to minimize time, and binding predictions would likely increase significantly by increasing iterations.

Entry	Compound	Compound Code	K_i (nM)	FITTED Score	FITTED Energy	**FITTED MScore**	Hybrid Score
1	Bavarostat	**2-1**		-86.90	-65.63	**132.56**	-108.11
2	SAHA	**2-37**	21.3 ± 9.7	-85.69	-97.17	**77.88**	-98.15
3	Martinostat	**2-38**	23.7 ± 9.2	-34.79	-64.25	**109.54**	-52.31
4	PhenylSiFA	**2-15**	575 ± 217	-81.28	-17.71	**146.56**	-104.73
5	AmideSiFA	**2-22**	6127 ± 226	-85.97	-38.54	**102.45**	-104.33
6	AmineSiFA	**2-25**	159 ± 38	-84.64	-12.78	**136.11**	-106.42

Table 2-21: Docking scores of potential HDACi against HDAC6 – Bavarostat cocrystal using FITTED

We first performed self-docking of Bavarostat with the reported Bavarostat – HDAC6 crystal to verify if the docking software could successfully reproduce the crystal structure. This validation was successful and the resulting scores are used as a baseline to compare against our candidates (Table 2-21). We next docked our completed substrates with the Bavarostat – HDAC6 crystal structure to validate docking results against the measured K_i. FITTED generates five scores based on different factors, so experimental values were used to determine which score best represented our compounds. We found that the FITTED MScore (positive is better) best correlated to experimental results, with the AmideSiFA **2-22** (entry 5) scoring worse than the PhenylSiFA **2-15** (Entry 4) and the AmineSiFA **2-25** (Entry 6) derivatives. The FITTED score (negative is better) and hybrid score (negative is better) scored the three compounds similarly while the FITTED energy score (negative is better) was not representative of experimental results with AmideSiFA **2-22** scoring the best of the three compounds. We also tried docking SAHA **2-37** (Entry 2) and Martinostat **2-38** (Entry 3) to this model, but these two compounds were both better represented by FITTED Energy rather than the MScore.

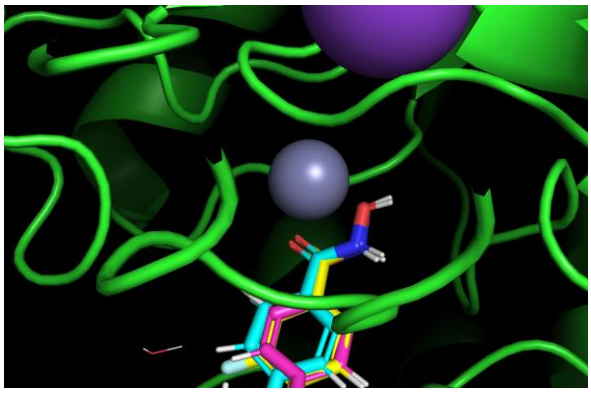

Figure 2-1: Overlap of candidates docking at zinc centre of Bavarostat – HDAC6 cocrystal

Fitted was able to successfully docking all compounds by bi-dentate chelation of the hydroxamic acid to the zinc centre (Figure 2-1) despite the low number of docking iterations, suggesting correct modeling of the binding portion of the molecule.

Entry	Compound	Compound Code	K_i (nM)	FITTED Score	FITTED Energy	**FITTED MScore**	Hybrid Score
1	Bavarostat	**2-1**	-	-81.19	-52.47	**91.22**	-95.79
2	Martinostat	**2-38**	23.7 ± 9.2	-32.99	-61.15	**61.22**	-42.79
3	PhenylSiFA	**2-15**	575 ± 217	-34.72	-7.41	**90.67**	-49.23
4	AmideSiFA	**2-22**	6127 ± 226	-77.06	-11.33	**88.79**	-91.27
5	AmineSiFA	**2-25**	159 ± 38	-77.23	-8.44	**93.45**	-92.18

Table 2-22: Docking scores of potential HDACi against HDAC6 – SAHA cocrystal using FITTED

We suspected that the poor docking result for SAHA and Martinostat might be due to poor compatibility to the Bavarostat cocrystal, so we re-performed the docking using HDAC6 – SAHA cocrystal to verify the validity of using the FITTED MScore for our compounds (Table 2-22). We found that the FITTED Mscore was still the most representative of the experimental results of the SiFA substrates (Entry 3 – 5) while none of the other scores were representative. Bavarostat and Martinostat were also evaluated using this model, and while Bavarostat scored within the same range as our SiFA compounds (Entry 1), Martinostat still scored poorly (Entry 2). With these results, we concluded that the computational estimation of binding efficiency of our SiFA compounds is best done using the FITTED MScore, but the scores are likely not representative of the actual magnitude of difference in K_i. The validity of the binding score is likely also tied to the mode of binding, and modifications of the aryl hydroxamic acid portion of the molecule would likely require re-evaluation of the different FITTED scores using experimental results.

Entry	Compound	Cocrystal Ligand	FITTED MScore	Structure
1	Long Amide	Bavarostat	112.72	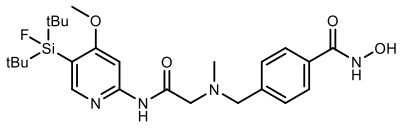 **2-45**
2	Long Amide	SAHA	87.49	
3	Pyrazole Amine	Bavarostat	133.08	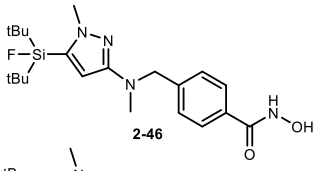 **2-46**
4	Pyrazole Amine	SAHA	88.07	
5	Pyrazole Amide	Bavarostat	107.70	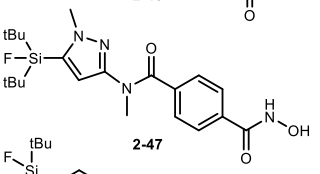 **2-47**
6	Pyrazole Amide	SAHA	74.00	
7	Des-methoxy	Bavarostat	118.51	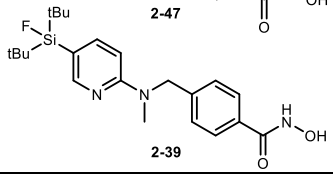 **2-39**
8	Des-methoxy	SAHA	89.66	

Table 2-23: Docking results of new set of proposed compounds

With validation completed, we proceeded to evaluate potential ideas for the next set of potential compounds using FITTED (Table 2-23). To address the poor binding result of the amideSiFA derivative **2-22**, we wanted to design an elongated derivative to produce a better fit in the linear binding channel of HDAC6. We designed derivative **2-45** with hybrid scores of 112.72 and 87.49 against the Bavarostat and SAHA cocrystals respectively (Entry 1 – 2), which is an improvement against the evaluation for **2-22** using the Bavarostat cocrystal where it scored 102.45.

The group had also produced a pyrazole SiFA core that we wanted to incorporate into this scaffold, and we decided to compare the Pyrazole amine **2-46** (Entry 3 – 4)and Pyrazole amide **2-47** (Entry 5 – 6)derivatives. This is because in addition to optimizing hydrolytic stability and radiolabeling efficiency in the development of PET tracers, radiolysis is also a potential issue that needs to be evaluated during radiosynthesis scale-up. The choice of the pyrazole core was due to concerns of radiolytic stability of pyridine SiFA compounds that occurred during scale-up validation of pyridine SiFA tracers. Using FITTED, we concluded that the Pyrazole amine **2-46** would be the superior choice with superior MScore results over the amide derivative **2-47** using both cocrystal models (Entry 2 – 5).

Finally, evaluation of the des-methoxy pyridine derivative **2-39** (Entry 7 – 8) resulted in lower scores compared to its methoxy counterpart AmineSiFA **2-25**, even though the structural changes are far-removed from the binding portion of the molecule. This result was then correlated with its measured K_i which was worse than the AmineSiFA, supporting the validity of this FITTED score at predicting binding.

2.9 Autoradiography

Next, we employed autoradiography to evaluate the affinity of our tracer candidates to HDACs in the brain tissues in competitive binding experiments with validated tracer [^{11}C]Martinostat.

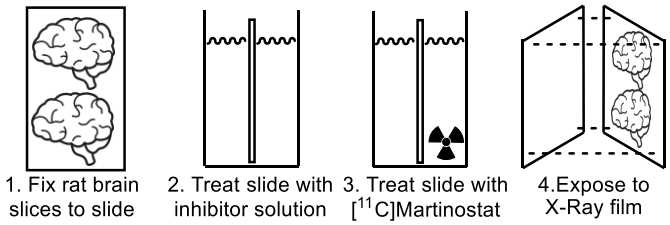

Figure 2-2: Evaluation of candidate tracers using autoradiography

Rat brain slices fixed to the glass slides were incubated with SiFA HDAC tracer candidates then incubated in [^{11}C]Martinostat which competitively binds to the same targets. The brain slides are then exposed to X-Ray film to measure radioactivity distribution (Figure 2-2). A superior HDAC inhibitor would result in more efficient displacement of [^{11}C]Martinostat, resulting in lower tissue radioactivity signal compared to the baseline experiment when the slides are incubated in a solution of [^{11}C]Martinostat alone. A negative control was performed using non-radioactive Martinostat in a self-blocking competition and a baseline was set by directly subjecting the brain slice to [^{11}C]Martinostat. Signal from tracer slides were compared against the baseline and negative control results to evaluate candidate performance, and the signal difference between grey and white matter regions were also evaluated as an indicator of binding specificity.

Greasy compounds can potentially bind non-specifically through hydrophobic interactions with the cell membranes. White matter rich regions are made up primarily of myelinated neuronal axons which are about 70% lipid. Unspecific binding in the brain is thus characterized by high compound accumulation in these regions. As gray matter is primarily made up of neuronal cell bodies where HDACs are located, we expect specific binding to targets to occur primarily in gray-matter rich regions[12]. In the context of autoradiography, if the cold tracer successfully binds to its target in the gray matter-rich regions,

[^{11}C]Martinostat would accumulate less in those regions resulting in a lower signal. Conversely, if our candidates have low non-specific binding, they would not accumulate in white matter-rich regions such as the corpus collosum and cerebellum arbor vitae which would allow excess [^{11}C]Martinostat to accumulate in those regions resulting in a higher signal.

Entry	Compound	Autoradiography	Structure
1	Baseline	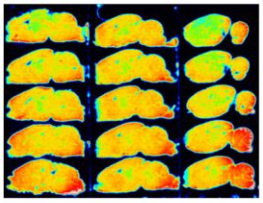	N/A
2	Martinostat	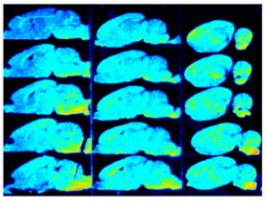	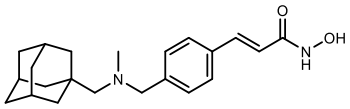 **2-38**
3	PhenylSiFA	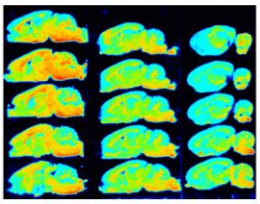	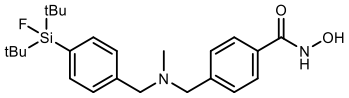 **2-15**
4	AmineSiFA	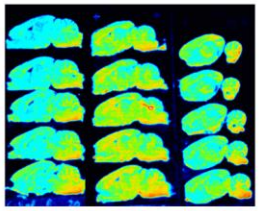	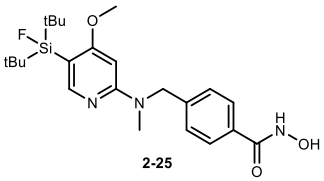 **2-25**
5	AmideSiFA	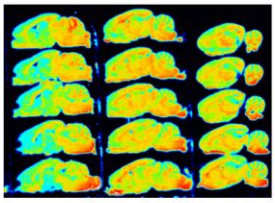	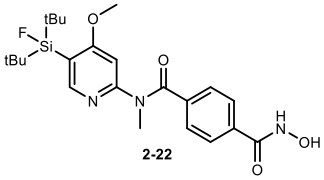 **2-22**
6	Long AmideSiFA	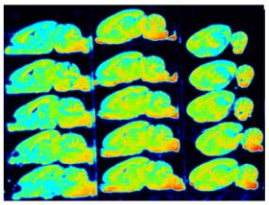	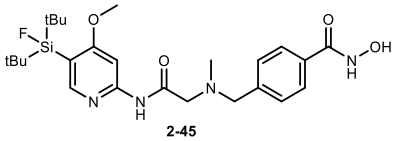 **2-45**
7	Pyrazole SiFA	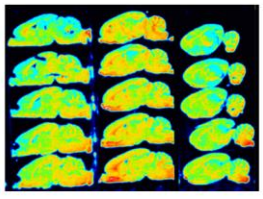	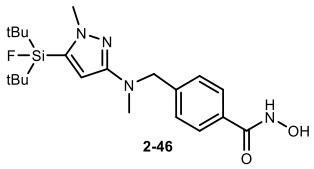 **2-46**

Table 2-24: Autoradiography result using [^{11}C]Martinostat

Slides of 5 brain slices were prepared, and each compound was tested in quadruplet using 3 slides to verify binding potency and distribution (Table 2-24). The slides were pre-incubated in a solution of 0.6 mM

solution of the our candidate tracer and cold Martinostat, washed, then treated to a solution containing 80 µCi of [^{11}C]Martinostat. As expected, the baseline control without tracer treatment showed strong signal in all areas, with no visible differentiation between gray and white-matter tissues (Entry 1). The lack of differentiation in the baseline test is due to excessive [^{11}C]Martinostat required to perform the incubation, which results in complete saturation of the brain slice.

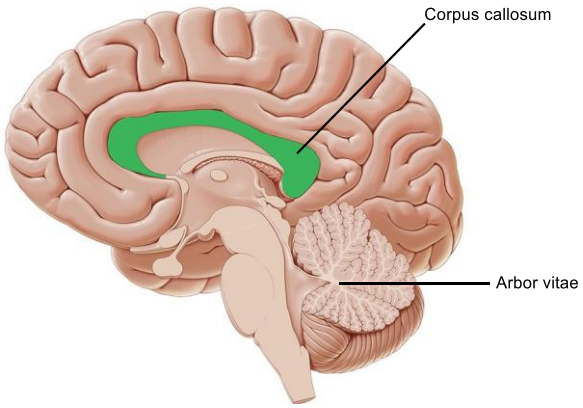

Figure 2-3: White matter-rich regions in the brain

We were pleased to see all SiFA-based HDAC tracer candidates showed clear signal differences between t he white-matter rich regions of the corpus callosum and arbor vitae in the cerebellum, indicating low non-specific binding (Entry 3 – 7). Self-blocking using cold Martinostat **2-38** (Entry 2) showed lower overall signal compared to the SiFA derivatives, which correlates to its superior performance in HDAC6 IC50 experiments. As expected, compounds with >1 uM binding affinities showed less signal reduction in comparison to those with nanomolar affinities, though interestingly, even the worse performing derivative in the *in vitro* assay AmideSiFA **2-22** (Entry 5) showed a similar distribution pattern as the other tracers. This distribution pattern suggests that **2-22** is binding to a target, though it is likely not HDAC6 as the K_i results suggests it is not selective for this isoform. The compound could be specific to another HDAC isoform, but there is also the possibility of off-target binding as HDACi are known to sometimes also target the hERG potassium ion channel protein both in humans and animal models, which is also prevalent in similar brain regions as HDACs[13].

Entry	Compound	Signal decrease (%)	K_i (nM)	Structure
1	Martinostat	53 ± 2	23.7 ± 9.2	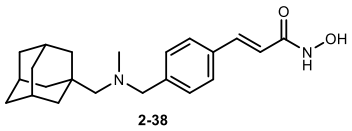 **2-38**
2	PhenylSiFA	38 ± 6	575 ± 217	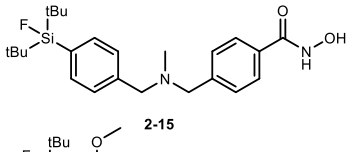 **2-15**
3	AmineSiFA	37 ± 9	159 ± 38	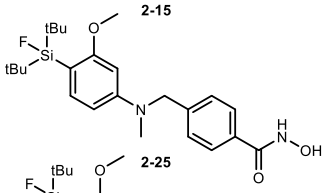 **2-25**
4	AmideSiFA	28 ± 13	6127 ± 226	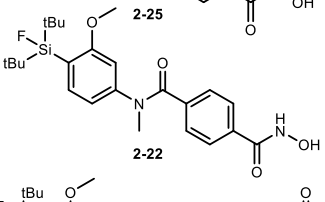 **2-22**
5	Long AmideSiFA	37 ± 8	650 ± 82	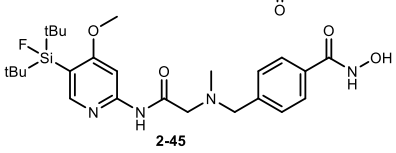 **2-45**
6	Pyrazole SiFA	29 ± 5	1017 ± 240	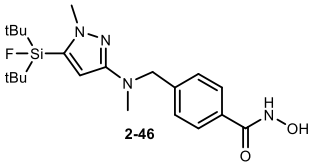 **2-46**

Table 2-25: Quantification of signal change in cerebellum of [^{11}C]Martinostat autoradiography

The autoradiography signal data is quantified, and signal change between baseline and SiFA inhibitors can be compared against Martinostat self-blocking results. Signal in the gray-matter rich region of the cerebellum is used to compare signal changes. Signal was taken from 3 different points in each brain slice and averaged, and the average signal is compared to the blank baseline, where the greater the percent decrease in signal indicate greater inhibition (Table 2-25). Self blocking with Martinostat **2-38** showed a signal decrease at 53%, consistent with both visual analysis of the slides and its performance in the *in vitro* HDAC6 assay (Entry 1). Of the SiFA derivatives, phenylSiFA **2-** (Entry 2), amineSiFA **2-25** (Entry 3) and long amideSiFA **2-45** (Entry 5) derivatives all had similar performances. The performance of **2-45** closely matches its HDAC6 assay result which was comparable to **2-15**, but it is somewhat surprising that that **2-25** did not perform measurably better than the other substrates despite having the best experimental K_i. This may suggest **2-25** having a superior isoform specificity towards HDAC6, resulting in similar overall binding profile as the rest in autoradiography, but cannot be concluded with only these results. Similarly, the pyrazole derivative **2-46** surprisingly performed worse than the AmideSiFA **2-22**, despite having *K*i values closer to that of the PhenylSiFA derivative **2-15**. This may again suggest unequal isoform selectivity across these compounds but again it is difficult to draw definitive conclusions with limited autoradiography results.

2.10 *In vivo* evalutation

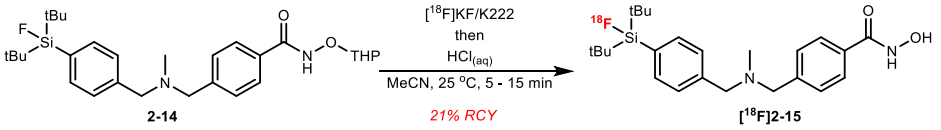

Entry	Viewing Plane	PET Image	PET/MRI Overlay
1	Horizontal	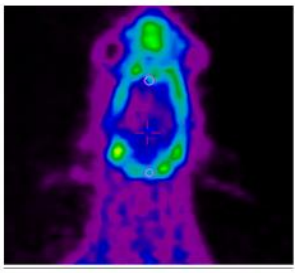	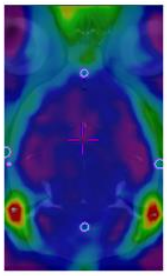
2	Sagittal	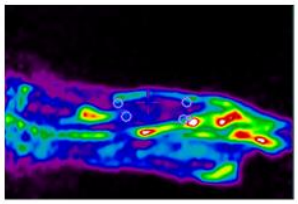	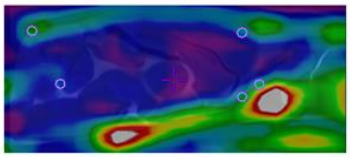
3	Coronal	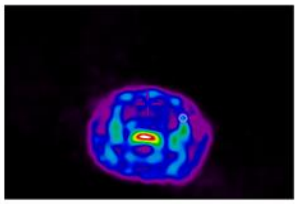	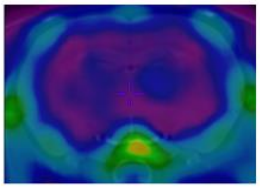

Table 2-26: *In vivo* PET imaging result using phenylSiFA derivative [^{18}F]**2-15**

We proceeded with *in vivo* evaluation of a candidate in rat model in order to validate the capability of SiFA hydroxamic acids to penetrate the blood-brain barrier and determine the cerebral distribution. High activity radiosynthesis was performed using modified automation setup developed Lindler *et al*.[14], and the THP protected phenylSiFA derivative **2-14** was chosen as the lead candidate due to its good performance in *in vitro* assays and excellent RCC in radiolabeling experiments. The THP protected precursor **2-14** was successfully radiolabeled with 830 mCi of [^{18}F]KF via SiFEx followed by deprotection by HCl to afford [^{18}F]**2-15** with a measured activity of 174 mCi at the end of synthesis, a non-decay-corrected RCY of 21%. The tracer was formulated in 15 mL phosphate buffered saline then neutralized with addition of 22 µL 5 M NaOH and a Sprague-Dawley rat was injected with 60 mCi of tracer and a brain PET scan was acquired immediately for 1 hour (Table 2-26). The PET scan was then overlayed with a generic rat brain MRI to identify signal distribution in different brain regions. Upon visual analysis, [^{18}F]**2-15** appeared to have poor blood-brain barrier permeability, with most of the PET signal distributed in the soft tissue outside the skull.

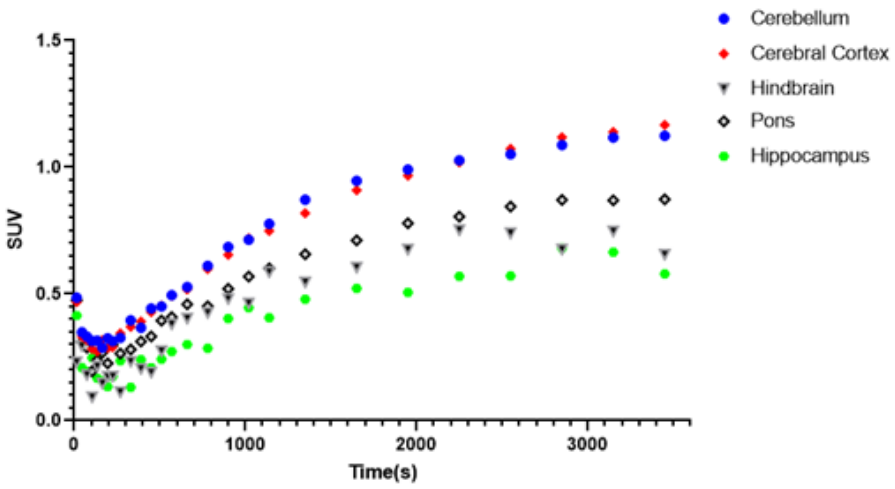

Figure 2-4: Brain region standard uptake over time of phenylSiFA derivative [^{18}F]**2-15**

However, when the time-activity curve (i.e. plots of standardized uptake values vs. time) was determined for cerebellum, cerebral cortex, hindbrain, pons, and hippocampus, we were pleased to see that there was a steady increase in uptake which suggests that the compound is successfully accumulating over time in the brain, though the kinetics of accumulation was slow (Figure 2-3). Over time, accumulation was highest in the cortex and cerebellum while hippocampus had the lowest accumulation. This biodistribution pattern is promising as it does correlate to literature data using rodent models, which saw the same pattern of nearly doubled cerebellum accumulation in relation to the hippocampus[15]. This data, in conjunction with HDAC6 binding assay and autoradiography all help support that [^{18}F]**2-15** might be binding to its intended target.

3. Summary and future direction

3.1 Summary

Histone deacetylases are important targets for PET imaging in the brain due to their involvement in numerous neurological conditions. Current PET tracers that address this need are [^{18}F]Bavarostat and [^{11}C]Martinostat, but both tracers suffer from difficult radiosynthesis, and poor RCY[2]. We attempted to address this issue through using SiFAs, which are capable of fast and high yielding radiolabeling reactions at room temperature through isotopic exchange, and do not require HPLC purification. The primary disadvantage of SiFAs is the requirement for lipophilic *tert* butyl groups on silicon for kinetic shielding to prevent hydrolysis of the Si-F bond, which has a significant impact on the pharmacokinetic properties of the tracers. Due to this limitation, successful applications of SiFAs are mostly limited to peptides where the lipophilicity can be masked using hydrophilic auxiliaries. There are very few literature examples of SiFAs successfully used to design small molecule PET tracers as these platforms cannot usually tolerate SiFA lipophilicity modification. We identified [^{18}F]Bavarostat as a potential small molecule scaffold that could be used with SiFA as this core could replace the lipophilic adamantane auxiliary used to cross the blood-brain barrier.

Entry	Compound	K_i HDAC 6 (nM)	RCC at 15 minutes (%)	Structure
1	PhenylSiFA	575 ± 217	72	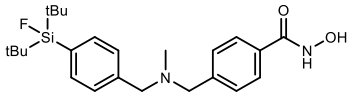 **2-15**
2	AmineSiFA	6127 ± 226	7	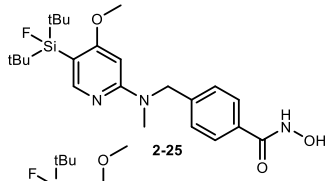 **2-25**
3	AmideSiFA	159 ± 38	55	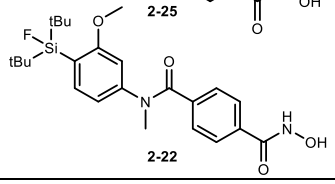 **2-22**

Table 3-1: HDAC6 binding affinity and radiolabeling result of first set of Bavarostat derivatives

We first incorporated phenyl and pyridine SiFA cores into the Bavarostat scaffold and synthesized three potential candidates and evaluated them using an *in vitro* HDAC6 binding assay and found that **2-15** and **2-25** had good target specificity. We also managed to successfully label the substrates using "Munich" method and demonstrate the applicability of SiFA radiochemistry in the presence of free hydroxamic acids, which typically inhibits ^{18}F-fluorination methods based on C-^{18}F bond formation (Table 3-1)[1].

Entry	Compound	K_i HDAC 6 (nM)	RCC at 15 minutes (%)	Structure
1	DesmethoxySiFA	983 ± 335	84	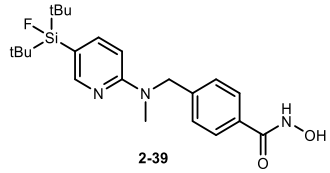 **2-39**
2	Long amideSiFA	650 ± 82	28	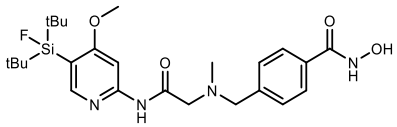 **2-45**
3	PyrazoleSiFA	1017 ± 240	0	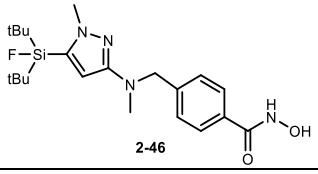 **2-46**

Table 3-2: HDAC6 binding affinity and radiolabeling result of the second set of Bavarostat derivatives

We successfully improved radiolabeling efficiency of AmineSiFA **2-25** with DesmethoxySiFA derivative **2-39** but this reduced binding affinity (Entry 1), and we improved the poor HDAC6 specificity of AmideSiFA derivative **2-22** with **2-45**, but the substrate had worse RCC (Entry 2). We also produced the PyrazoleSiFA derivative **2-47** to address potential issues of radiolysis with the pyridine SiFA cores, but this compound was labeled in poor RCC (Table 3-2). We then validated the docking software FITTED as a potential tool that could guide our design of future candidates.

We validated biodistribution of our compounds using autoradiography and found that all compounds had differentiated accumulation in gray and white-matter rich regions of the brain, indirectly indicative of specific binding. This result is particularly interesting for **2-22**, which had no HDAC6 specificity according to our binding assay, and suggests either affinity towards other HDAC isoforms or off-target binding. We continued with *in vivo* evaluation of phenylSiFA derivative **2-15**, successfully performing radiolabeling in high radioactivity using automated synthesis unit and confirming blood brain barrier penetration and *in vivo* stability. We found that though the kinetics of brain penetration was slow, the compound was able to cross the blood brain barrier, while the biodistribution of PET signal in the brain regions suggested selective binding to HDAC targets.

Entry	Compound	K_i HDAC 6 (nM)	RCC at 15 minutes (%)	Structure
1	PhenylSiFA - SAHA	177 ± 31	82	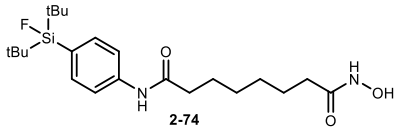 2-74
2	PyrazoleSiFA - SAHA	242 ± 13	42	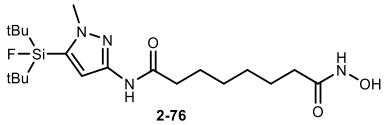 2-76
3	N-OxideSiFA - SAHA	210 ± 39	81	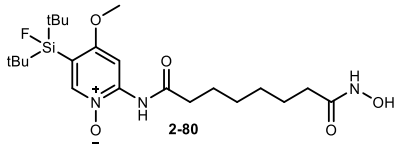 2-80

Table 3-3: HDAC6 binding affinity and radiolabeling result of SAHA derivatives

We also synthesized three SiFA derivatives of SAHA as the next generation of putative HFAC tracers for PET imaging. Though SAHA was not successfully used for treatment of neurological conditions, its poor bioavailability in the brain is likely due to active efflux. Therefore, its modification to reduce susceptibility to the same efflux transporters may provide higher brain bioavailability, thus adapting them for PET imaging . Even if these candidates are poor brain imaging tools, they could also be used for HDAC imaging in other organs. All three compounds exhibited good HDAC6 binding affinity and were successfully labeled with good RCC (Table 3-3). SAHA and Bavarostat derivatives were also evaluated in hydrolytic stability assay and were confirmed to all have adequate stability against hydrolysis for *in vivo* applications.

3.2 Future direction

With the autoradiography result, our next step is to increase the scope of the binding assay to include other HDAC isoforms. Though Bavarostat had the highest binding affinity towards HDAC6, it still showed moderate affinity towards HDACs 4, 5, 7, 8, 10, and 11[1]. Additionally, SAHA is considered a pan-HDACi capable of inhibiting class I, II, and IV HDACs[23], so a PET imaging agent based on this scaffold would likely also have poor isoform selectivity. As we only performed HDAC6 binding assay, our result is not representative of the full capabilities of these candidates, and expanding the *in vitro* binding assay to all twelve isoforms would be required to properly evaluate these compounds.

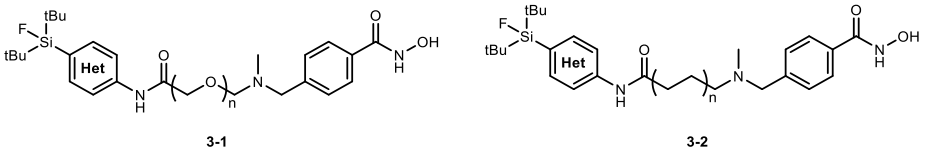

3-1 3-2

Figure 3-1: Potential candidates for new Bavarostat based SiFA PET tracers

We were pleased to find that our SiFA hydroxamic acids still retained some affinity towards HDAC6, but all derivatives also had higher K_i values compared to Martinostat and SAHA, and thus will not translate into good PET imaging agents. In our attempt to improve amideSiFA derivative **2-22**, we validated our idea that

a longer linker portion may improve target binding, and as such we believe that a way to improve the affinity of the Bavarostat derivatives to HDACs is to elongate the molecule through introduction of either an alkyl or polyethylene glycol (PEG) linker domain to increase the distance between the SiFA core from the hydroxamic acid (Figure 3-1). The length of this linker could also be adjusted to verify if it influences binding and to find the optimal linker length for optimal binding affinity.

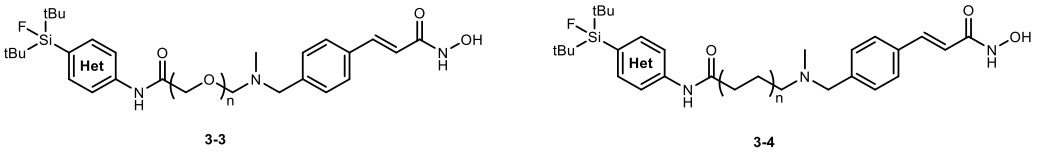

Figure 3-2: Potential candidates for Martinostat based SiFA PET tracers for HDAC imaging.

Additionally, we would also like to adapt the Martinostat scaffold to produce the corresponding SiFA PET tracers (Figure 3-2). Martinostat's higher binding affinity means a SiFA PET tracer based on its scaffold would likely also result in better binding, similar to the results we observed with the SiFA – SAHA compounds. While Martinostat is hindered by its poor isoform selectivity, it has already seen successful use in drug development[17], demonstrating the usefulness of a pan-HDAC PET tracer. Using SiFA could result in a tracer with improved RCY and a more user-friendly radiosynthesis which would result in a more widely available HDAC PET tracer for similar applications.

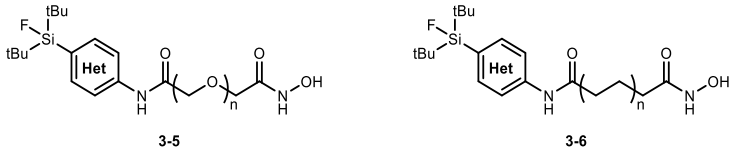

Figure 3-3: Potential candidates for new SAHA based SiFA PET tracers for HDAC imaging.

The SiFA PET tracers based on the SAHA scaffold showed promise in their binding affinity and radiolabeling results, but the addition of a SiFA to the already lipophilic SAHA chain might result in poor pharmacokinetics and higher non-differentiated binding. We did not have the opportunity to validate these compounds using autoradiography, but we believe that the lipophilicity could be improved if we replaced the SAHA alkyl chain with a PET linker. Oxygen-incorporated SAHA analogues have been shown to retain good HDAC inhibitory activity[24], and a SiFA analogue using this scaffold would result in a less lipophilic compound that would be less susceptible to non-specific binding. We also aim to vary the length of both of the alkyl chain on both our current SAHA derivatives and the proposed PEG chain derivatives to see if we could find an optimal distance between the SiFA and the hydroxamic acid to maximize binding affinity, and if it could have an effect on isoform selectivity (Figure 3-3).

We hope that these modifications would result in a lead candidate that could eventually be brought to human trial. To achieve this goal, we would need to perform more in-depth biological evaluation of the candidate beyond evaluating its binding affinity towards all HDAC isoforms. We would first need to perform *in vivo* evaluation of our compounds in primate models that more closely replicate human biology to evaluate both brain and organ biodistribution and verify that there is minimal bone uptake during the course of the scan, indicative of defluorination *in vivo*. Studies using knock-out animal models would

conclusively validate both successful target and potential off-target binding. Finally, toxicology studies would also need to be performed to evaluate safety and metabolic profile of the compound.

3.3 References

1. Strebl, M. G.; Campbell, A. J.; Zhao, W.-N.; Schroeder, F. A.; Riley, M. M.; Chindavong, P. S.; Morin, T. M.; Haggarty, S. J.; Wagner, F. F.; Ritter, T.; Hooker, J. M. HDAC6 Brain Mapping with [18f]Bavarostat Enabled by a RU-Mediated Deoxyfluorination. *ACS Central Science* **2017**, *3* (9), 1006–1014.
2. Wang, C.; Schroeder, F. A.; Wey, H.-Y.; Borra, R.; Wagner, F. F.; Reis, S.; Kim, S. W.; Holson, E. B.; Haggarty, S. J.; Hooker, J. M. In Vivo Imaging of Histone Deacetylases (HDACS) in the Central Nervous System and Major Peripheral Organs. *Journal of Medicinal Chemistry* **2014**, *57* (19), 7999–8009.
3. Wanka, L., Iqbal, K. & Schreiner, P. R. The lipophilic bullet hits the targets: Medicinal chemistry of adamantane derivatives. *Chem. Rev.* **113**, 3516–3604 (2013).
4. Alam, M. A. Methods for Hydroxamic Acid Synthesis. *Current Organic Chemistry* **2019**, *23* (9), 978–993.
5. Kumagai, N.; Shibasaki, M.; Adachi, S. Thieme Chemistry Journals Awardees – Where Are They Now? Bis(2-Pyridyl)Amides as Readily Cleavable Amides under Catalytic, Neutral, and Room-Temperature Conditions. *Synlett* **2017**, *29* (03), 301–305.
6. Kostikov, A. P.; Iovkova, L.; Chin, J.; Schirrmacher, E.; Wängler, B.; Wängler, C.; Jurkschat, K.; Cosa, G.; Schirrmacher, R. N-(4-(Di-Tert-Butyl[18f]Fluorosilyl)Benzyl)-2-Hydroxy-N,N-Dimethylethylammonium Bromide ([18f]Sifan+br−): A Novel Lead Compound for the Development of Hydrophilic SIFA-Based Prosthetic Groups for 18F-Labeling. *Journal of Fluorine Chemistry* **2011**, *132* (1), 27–34.
7. Madsen, A. S.; Olsen, C. A. Substrates for Efficient Fluorometric Screening Employing the NAD-Dependent Sirtuin 5 Lysine Deacylase (KDAC) Enzyme. *Journal of Medicinal Chemistry* **2012**, *55* (11), 5582–5590
8. Villadsen, J. S.; Stephansen, H. M.; Maolanon, A. R.; Harris, P.; Olsen, C. A. Total Synthesis and Full Histone Deacetylase Inhibitory Profiling of Azumamides A–E as Well as β2- *Epi*-Azumamide E and β3-*Epi*-Azumamide e. *Journal of Medicinal Chemistry* **2013**, *56* (16), 6512–6520.
9. Seetharamsingh, B.; Ramesh, R.; Dange, S. S.; Khairnar, P. V.; Singhal, S.; Upadhyay, D.; Veeraraghavan, S.; Viswanadha, S.; Vakkalanka, S.; Reddy, D. S. Design, Synthesis, and Identification of Silicon Incorporated Oxazolidinone Antibiotics with Improved Brain Exposure. *ACS Medicinal Chemistry Letters* **2015**, *6* (11), 1105–1110.
10. Chmielewski, M. K. Novel Thermolabile Protecting Groups with Higher Stability at Ambient Temperature. *Tetrahedron Letters* **2012**, *53* (6), 666–669.
11. Scott, P. J. H.; Hockley, B. G.; Kung, H. F.; Manchanda, R.; Zhang, W.; Kilbourn, M. R. Studies into Radiolytic Decomposition of Fluorine-18 Labeled Radiopharmaceuticals for Positron Emission Tomography. *Applied Radiation and Isotopes* **2009**, *67* (1), 88–94.
12. Bramlett, H.; Dietrich, D. Quantitative Structural Changes in White and Gray Matter 1 Year Following Traumatic Brain Injury in Rats. *Acta Neuropathologica* **2002**, *103* (6), 607–614.

13. Spence, S.; Deurinck, M.; Ju, H.; Traebert, M.; McLean, L.; Marlowe, J.; Emotte, C.; Tritto, E.; Tseng, M.; Shultz, M.; Friedrichs, G. S. Histone Deacetylase Inhibitors Prolong Cardiac Repolarization through Transcriptional Mechanisms. *Toxicological Sciences* **2016**, *153* (1), 39–54.
14. Lindner, S.; Simmet, M.; Gildehaus, F. J.; Jurkschat, K.; Wängler, C.; Wängler, B.; Bartenstein, P.; Schirrmacher, R.; Ilhan, H. Automated Production of [18f]Sitate on a Scintomics GRPTM Platform for Pet/Ct Imaging of Neuroendocrine Tumors. *Nuclear Medicine and Biology* **2020**, *88–89*, 86–95.
15. Bai, P.; Mondal, P.; Bagdasarian, F. A.; Rani, N.; Liu, Y.; Gomm, A.; Tocci, D. R.; Choi, S. H.; Wey, H.-Y.; Tanzi, R. E.; Zhang, C.; Wang, C. Development of a Potential Pet Probe for HDAC6 Imaging in Alzheimer's Disease. *Acta Pharmaceutica Sinica B* **2022**, *12* (10), 3891–3904.
16. Hanson, J. E.; La, H.; Plise, E.; Chen, Y.-H.; Ding, X.; Hanania, T.; Sabath, E. V.; Alexandrov, V.; Brunner, D.; Leahy, E.; Steiner, P.; Liu, L.; Scearce-Levie, K.; Zhou, Q. Saha Enhances Synaptic Function and Plasticity in Vitro but Has Limited Brain Availability in Vivo and Does Not Impact Cognition. *PLoS ONE* **2013**, *8* (7).
17. Chen, Z.; Wang, X.; Yang, X.; Xu, Y.; Yang, Y.; Wang, H.; Li, T.; Bai, P.; Yuan, G.; Chen, H.; Yang, J.; Fiedler, S. A.; Striar, R.; Bernales, D. R.; Koegel, R. E.; Cao, Q.; Ran, C.; Xiang, B.; Li, H.; Wang, C. Imaging Assisted Evaluation of Antitumor Efficacy of a New Histone Deacetylase Inhibitor in the Castration-Resistant Prostate Cancer. *European Journal of Nuclear Medicine and Molecular Imaging* **2020**, *48* (1), 53–66.
18. Londregan, A.; Piotrowski, D.; Xiao, J. Rapid and Selective in Situ Reduction of Pyridine-N-Oxides with Tetrahydroxydiboron. *Synlett* **2013**, *24* (20), 2695–2700.
19. Bradner, J. E.; West, N.; Grachan, M. L.; Greenberg, E. F.; Haggarty, S. J.; Warnow, T.; Mazitschek, R. Chemical Phylogenetics of Histone Deacetylases. *Nature Chemical Biology* **2010**, *6* (3), 238–243.
20. Yingjie, Z; Wenfang, X; Qianwen, Q; Chunlong, Z. Preparation of histone deacetylase 6 inhibitor amide-derivatives and used as preventing or treating diseases related to the abnormal activity or expression of HDAC6. Patent CN 111848454, October 30, 2020.
21. Whiting, A.; Ambler, C.; Chisholm, D. Fluorescent systems for biological imaging and uses thereof. U.S. Patent WO2021009506, January 1, 2021.
22. Iovkova, L.; Wängler, B.; Schirrmacher, E.; Schirrmacher, R.; Quandt, G.; Boening, G.; Schürmann, M.; Jurkschat, K. *Para*-Functionalized Aryl-Di-*Tert*-Butylfluorosilanes as Potential Labeling Synthons for18F Radiopharmaceuticals. *Chemistry - A European Journal* **2009**, *15* (9), 2140–2147.
23. Seto, E.; Yoshida, M. Erasers of Histone Acetylation: The Histone Deacetylase Enzymes. *Cold Spring Harbor Perspectives in Biology* **2014**, *6* (4).
24. Kim, S.-A.; Jin, Y. L.; Kim, H. S. Structure-Activity Relationship Studies of Novel Oxygen-Incorporated Saha Analogues. *Archives of Pharmacal Research* **2009**, *32* (1), 15–21.
25. Hjelmgaard, T.; Faure, S.; Staerk, D.; Taillefumier, C.; Nielsen, J. Expedient Solution-phase Synthesis and NMR Studies of Arylopeptoids. *European Journal of Organic Chemistry* **2011**, *2011* (22), 4121–4132.

26. Pottel, J.; Therrien, E.; Gleason, J. L.; Moitessier, N. Docking Ligands into Flexible and Solvated Macromolecules. 6. Development and Application to the Docking of Hdacs and Other Zinc Metalloenzymes Inhibitors. *Journal of Chemical Information and Modeling* **2014**, *54* (1), 254–265.

Materials and Methodologies:

Chemicals and solvents were purchased from Sigma Aldrich, Alfa Aesar, Strem Chemicals, TCI or Oakwood Chemicals. Chemicals were used as received without further purification. Solvents were dried and purified using a PureSolv MD 7 (from Innovative Technology) or MB SPS 800 (from MBraun). DMF was distilled over CaH2 under a positive pressure of N2. Unless otherwise noted, reactions were performed in flame-dried glassware under a positive pressure of N2 using standard synthetic organic, inert atmosphere techniques.

Proton nuclear magnetic resonance (^{1}H NMR) spectra were acquired using Varian Mercury 400 MHz, Bruker AVIIIHD 800 MHz, Varian Inova QANUC 500 MHz, Varian VNMRS 500 MHz, Bruker AVIIIHD 500 MHz, or Bruker AVIIIHD 400 MHz spectrometers. Chemical shifts (δ) are reported in parts per million (ppm) and are calibrated to the residual solvent peak. Coupling constants (*J*) are reported in Hz. Multiplicities are reported using the following abbreviations: *s* = singlet; *brs*=broad singlet; *d* = doublet; *t* = triplet; *q* = quartet; *m* = multiplet (range of multiplet is given). Carbon nuclear magnetic resonance (^{13}C NMR) spectra were acquired using Varian VNMRS 125 MHz, Bruker AVIIIHD 125 MHz, or Bruker AVIIIHD 101 MHz spectrometers. Chemical shifts (δ) are reported in parts per million (ppm) and are calibrated to the residual solvent peak. (^{19}F NMR) spectra were acquired using Varian VNMRS 470 MHz, Bruker AVIIIHD 470 MHz or Bruker AVIIIHD 376 MHz spectrometers. Chemical shifts (δ) are reported in parts per million (ppm) and are calibrated to the residual solvent peak.

High resolution mass spectra (HRMS) were recorded using a Bruker maXis Impact TOF mass spectrometer. Fourier-transform infrared (FT-IR) spectra were recorded on an alpha Bruker FT-IR spectrometer. Analytical thin-layer chromatography was performed on pre-coated 250 mm layer thickness silica gel 60 F254 plates (EMD Chemicals Inc.). Visualization was performed by ultraviolet light and/or by staining with potassium permanganate. Purifications by column chromatography were performed using Biotage IsoleraTM One, Santai SepaBeam, Agilent 1260 Infinity, or standard column chromatography using silica gel (40-63 μm, 230-400 mesh).

Compound 2-4:

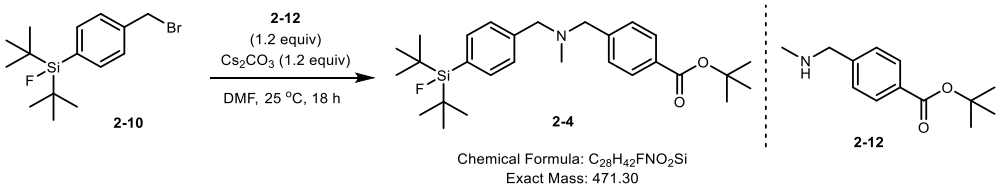

Procedure: A flame-dried 50 mL round bottom flask equipped with a Teflon-coated stir bar and a rubber septum was charged with 25 mL dry DMF. The reaction vessel was evacuated and backfilled with N_2, and **2-10** (422 mg, 1.28 mmol, 1 equiv.) was added followed by **2-12** (332 mg, 1.5 mmol, 1.2 equiv.) and cesium carbonate (489 mg, 1.5 mmol, 1.2 equiv.). The mixture was allowed to stir at ambient temperature for 18 h then quenched with 40 mL of cold distilled water. The resulting heterogeneous, biphasic reaction mixture was then extracted with EtOAc (25 mL x 3). The combined organic phases were washed with 25 mL of brine then dried over Na_2SO_4, filtered, and concentrated *in vacuo*. The resulting oil was purified by silica gel column chromatography (10% EtOAc in hexanes) to afford **2-4** as a clear oil (380 mg, 0.81 mmol) in 54% yield.

Characterization:

R_f = (EtOAc/hexane 20:80): 0.57; **IR** (neat) ν = 2955.92, 2927.72, 2857.28, 2360.55, 1700.73, 1588.39, 1538.61, 1507.00, 1473.29, 1396.72, 1245.18, 1227.29, 1201.13, 1133.87, 1085.46, 1028.63, 950.42, 825.33, 808.88, 766.08, 646.03, 478.96 cm^{-1}; **^{1}H NMR** (500 MHz, CDCl3) δ 8.00 – 7.94 (m, 2H), 7.60 – 7.55 (m, 2H), 7.49 – 7.43 (m, 2H), 7.41 – 7.35 (m, 2H), 3.60 (s, 2H), 3.54 (s, 2H), 2.22 (s, 3H), 1.62 (s, 9H), 1.07 (d, J = 1.2 Hz, 18H) **^{13}C NMR** (126 MHz, CDCl3) δ 165.79, 144.30, 140.58, 133.99, 133.96, 132.11, 130.80, 129.44, 128.60, 128.07, 80.84, 61.81, 61.75, 42.45, 28.23, 27.36, 20.32, 20.23; **^{19}F NMR** (471 MHz, CDCl3) δ -188.98; **HRMS:** Calcd. for $C_{28}H_{42}FNNaO_2Si$ $[M+Na]^+$ = 494.2861 m/z, found = 494.2851 m/z.

Compound 2-13:

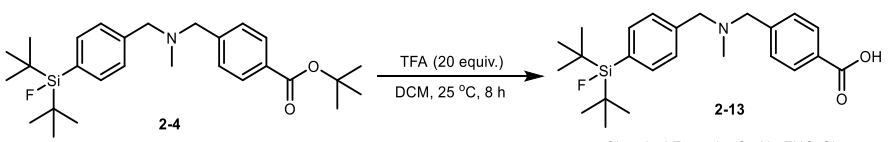

Chemical Formula: $C_{24}H_{34}FNO_2Si$
Exact Mass: 415.23

Procedure: A flame-dried 25 mL round bottom flask equipped with a Teflon-coated stir bar and a rubber septum was charged with 15 mL of DCM, **2-4** (380 mg, 0.81 mmol, 1 equiv.), and trifluoroacetic acid (1.24 mL, 16.2 mmol, 20 equiv.). The mixture was then stirred at ambient temperature for 8 h then concentrated *in vacuo*. To the resulting oil was added 1 mL toluene and the resulting mixture was concentrated *in vacuo*. The resulting residue was purified by silica gel column chromatography (5% MeOH in DCM) to afford the TFA salt of **2-13** as a white solid (189 mg, 0.337 mmol) in 85% yield.

Characterization:

R_f = (MeOH/DCM 10:90): 0.48; **IR** (neat) v = 2961.09, 2934.18, 2891.43, 2860.07, 1702.54, 1668.92, 1611.77, 1555.33, 1470.33, 1418.12, 1389.83, 1365.87, 1264.19, 1196.88, 1179.38, 1134.11, 1107.38, 1014.64, 935.93, 824.12, 812.66, 737.22, 702.98, 675.71, 587.27, 482.98 cm^{-1}; **^{1}H NMR** (500 MHz, CDCl3) δ 8.05 – 7.99 (m, 2H), 7.61 – 7.56 (m, 2H), 7.50 – 7.45 (m, 2H), 7.38 (d, J = 7.6 Hz, 2H), 3.93 (s, 3H), 3.61 (s, 2H), 3.55 (s, 2H), 2.22 (s, 3H), 1.07 (d, J = 1.2 Hz, 18H); **^{13}C NMR** (126 MHz, CDCl3) δ 170.20, 134.57, 134.54, 132.04, 130.48, 130.34, 129.52, 60.16, 59.80, 39.95, 27.30, 20.28, 20.18; **^{19}F NMR** (471 MHz, CDCl3) δ -188.97; **HRMS:** Calcd. for $C_{24}H_{35}FNO_2Si$ $[M+H]^+$ = 416.2416 m/z, found = 416.2422 m/z.

Compound 2-14:

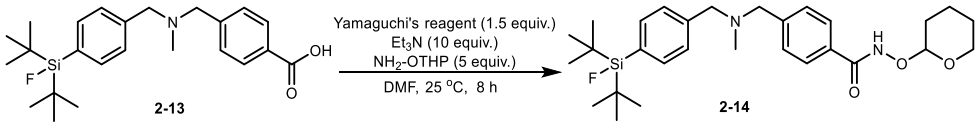

Chemical Formula: $C_{29}H_{43}FN_2O_3Si$
Exact Mass: 514.30

Procedure: A flame-dried 25 mL round bottom flask equipped with a Teflon-coated stir bar and a rubber septum flushed with nitrogen and charged with 10 mL of DMF and **2-13** (203 mg, 0.383 mmol 1 equiv.). While stirring, the mixture is cooled in an ice bath and triethylamine (528 uL, 3.83 mmol, 10 equiv.) is added, followed by Yamaguchi's reagent (89 uL, 0.575 mmol, 1.5 equiv.). The mixture is stirred at 0 °C for 15 min and NH_2OTHP (223 mg, 1.91 mmol, 5 equiv.) is added, and the solution is removed from the ice bath and stirred at ambient temperature for 8 h. The mixture is poured into 25 mL EtOAc and washed with 25 mL saturated aqueous $NaHCO_3$ followed by brine, and the retained organic phase then dried over Na_2SO_4, filtered, and concentrated *in vacuo*. The resulting oil is purified by silica gel column chromatography (1 – 5% MeOH in DCM) to afford **2-14** as a clear gel that solidified on standing (121 mg, 0.235 mmol) in 62% yield.

Characterization:

R_f = (MeOH/DCM 5:95): 0.78; **IR** (neat) ν = 3246.35, 2935.94, 2858.59, 2796.40, 1722.36, 1656.40, 1577.81, 1474.78, 1446.11, 1384.47, 1285.60, 1207.58, 1115.18, 1027.71, 946.52, 904.86, 825.57, 810.48, 730.06, 646.88, 470.82 cm^{-1}; **^{1}H NMR** (500 MHz, CDCl3) δ 8.85 – 8.75 (m, 1H), 7.77 – 7.72 (m, 2H), 7.61 – 7.55 (m, 2H), 7.48 (d, J = 8.0 Hz, 2H), 7.38 (d, J = 7.7 Hz, 2H), 5.10 (t, J = 3.2 Hz, 1H), 4.03 (ddd, J = 11.6, 9.4, 2.9 Hz, 1H), 3.72 – 3.64 (m, 1H), 3.59 (s, 2H), 3.54 (s, 2H), 2.21 (s, 3H), 1.97 – 1.90 (m, 1H), 1.93 – 1.84 (m, 2H), 1.67 (s, 1H), 1.72 – 1.59 (m, 1H), 1.07 (d, J = 1.2 Hz, 18H); **^{13}C NMR** (126 MHz, CDCl3) δ 144.09, 140.48, 134.01, 133.98, 130.69, 129.08, 128.05, 127.20, 102.75, 62.73, 61.83, 61.61, 42.43, 28.09, 27.36, 25.06, 20.32, 20.23, 18.69; **^{19}F NMR** (471 MHz, $CDCl_3$) δ -188.96; **HRMS:** Calcd. for $C_{29}H_{44}FN_2O_3Si$ $[M+H]^+$ = 515.3105 m/z, found = 515.3110 m/z.

Compound 2-15:

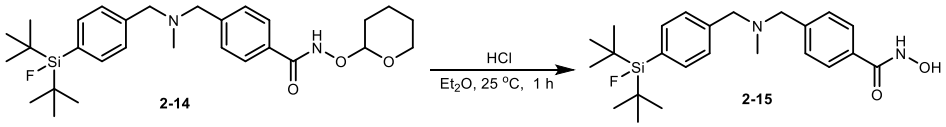

Chemical Formula: $C_{24}H_{35}FN_2O_2Si$
Exact Mass: 430.25

Procedure: A 5-dram glass vial equipped with a Teflon-coated stir bar and a rubber septum was charged with 3 mL diethyl ether and **2-14** (50 mg, 0.097 mmol, 1 equiv.). 3mL of 1 M ethereal HCl is added dropwise while stirring, and the resulting suspension was stirred at ambient temperature for 1 h. The vial is sealed and put into a -20 °C freezer for 1h and the supernatant is carefully removed and discarded. The white precipitate is triturated 3 times with cold diethyl ether, and then dried to provide the HCl salt of **2-15** as a white solid (31 mg, 0.072 mmol) in 74% yield.

Characterization: R_f = (MeOH/DCM 10:90): 0.44; **IR** (neat) v = 3168.47, 2960.88, 2933.89, 2891.76, 2860.03, 2712.19, 2632.90, 1644.55, 1469.37, 1366.07, 1314.37, 1217.09, 1156.01, 1107.26, 1014.09, 936.34, 896.72, 823.78, 813.43, 734.90, 676.08, 647.30, 586.20, 536.13, 483.80 cm^{-1}; **^{1}H NMR** (500 MHz, DMSO) δ 11.39 (d, J = 17.1 Hz, 2H), 9.13 (s, 1H), 7.83 (d, J = 8.0 Hz, 2H), 7.76 – 7.70 (m, 4H), 7.64 (d, J = 7.7 Hz, 2H), 4.43 (td, J = 10.7, 4.6 Hz, 2H), 4.35 – 4.21 (m, 2H), 2.52 (dd, J = 5.0, 3.1 Hz, 3H), 1.02 (d, J = 1.2 Hz, 18H); **^{13}C NMR** (126 MHz, DMSO) δ 163.89, 134.70, 134.59, 134.38, 134.34, 134.05, 133.44, 132.19, 131.92, 131.20, 127.65, 58.62, 58.36, 38.73, 27.48, 20.22, 20.12; **^{19}F NMR** (471 MHz, DMSO) δ -187.29; **HRMS:** Calcd. for $C_{24}H_{36}FN_2O_2Si$ $[M+H]^+$ = 431.2525 m/z, found = 431.2523 m/z.

Compound 2-18:

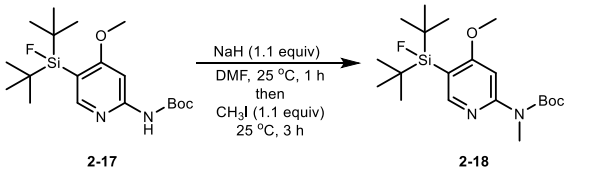

2-17 **2-18**

Chemical Formula: $C_{20}H_{35}FN_2O_3Si$
Molecular Weight: 398.59

Procedure: A flame-dried 25 mL round bottom flask equipped with a Teflon-coated stir bar and a rubber septum was charged with 10 mL dry DMF. The reaction vessel was evacuated and backfilled with N_2, and **2-17** (340 mg, 0.884 mmol, 1 equiv.) was added followed by sodium hydride (47 mg, 0.972 mmol, 1.1 equiv.). The mixture was then stirred at ambient temperature for 1 h and iodomethane (61 uL, 0.972 mmol, 1.1 equiv.) was added dropwise. The resulting mixture was stirred for 3 h at ambient temperature under N_2 then quenched with 25 mL of cold distilled water. The resulting heterogeneous, biphasic reaction mixture was then extracted with EtOAc (25 mL x 3). The combined organic phases were washed with 25 mL of brine then dried over Na_2SO_4, filtered, and concentrated *in vacuo*. The resulting residue was purified by silica gel column chromatography (5% EtOAc in hexanes) to afford **2-18** as a clear gel (292 mg, 0.884 mmol) in 83% yield.

Characterization:

R_f = (EtOAc/hexane 5:95): 0.78; **IR** (neat) ν = 2966.66, 2934.93, 2893.23, 2859.79, 1708.67, 1580.50, 1550.89, 1473.66, 1423.52, 1363.50, 1352.23, 1299.50, 1246.36, 1221.73, 1142.23, 1071.01, 1030.67, 894.90, 824.71, 809.79, 771.10, 644.38, 586.20, 494.71, 443.55 cm^{-1}; **^{1}H NMR** (500 MHz, $CDCl_3$) δ 8.32 (s, 1H), 7.45 (s, 1H), 3.87 (s, 3H), 3.46 (s, 3H), 1.57 (s, 9H), 1.05 (d, J = 1.4 Hz, 18H); **^{13}C NMR** (126 MHz, CDCl3) δ 169.76 (d, J = 4.2 Hz), 158.37, 154.42, 153.97, 153.91, 113.01, 112.89, 99.35, 81.29, 54.33, 34.15, 28.36, 27.24 (d, J = 1.5 Hz), 20.57, 20.48; **^{19}F NMR** (471 MHz, CDCl3) δ -187.15; **HRMS:** Calcd. for $C_{20}H_{36}FN_2O_3Si$ $[M+H]^+$ = 399.2479 m/z, found = 399.2476 m/z.

Compound 2-19:

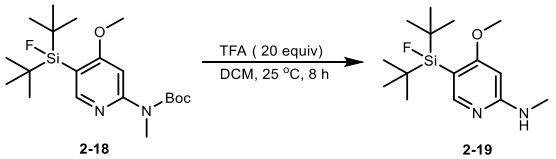

Chemical Formula: $C_{15}H_{27}FN_2OSi$
Molecular Weight: 298.48

Procedure: A flame-dried 25 mL round bottom flask equipped with a Teflon-coated stir bar and a rubber septum was charged with 10 mL of DCM, **2-18** (270 mg, 0.693 mmol, 1 equiv.), and trifluoroacetic acid (1.05 mL, 13.9 mmol, 20 equiv.). The mixture was then stirred at ambient temperature for 8 h then concentrated *in vacuo*. To the resulting clear liquid was added 1 mL toluene and the resulting mixture was concentrated *in vacuo*. The resulting residue was purified by silica gel column chromatography (1 - 5% MeOH in DCM) to afford the TFA salt of **2-19** as a white solid (262 mg, 0.627 mmol) in 92% yield.

Characterization:

R_f = (MeOH/DCM 10:90): 0.48; **IR** (neat) v = 3268.81, 2955.41, 2937.28, 2895.07, 2862.50, 1680.35, 1645.90, 1612.62, 1472.41, 1428.70, 1391.24, 1234.89, 1197.73, 1180.05, 1131.12, 1110.95, 1055.79, 1020.14, 932.77, 824.77, 720.18, 647.70, 586.49, 484.20, 461.62, 437.64 cm^{-1}; **^{1}H NMR** (500 MHz, CDCl3) δ 15.87 (s, 1H), 10.31 – 10.12 (m, 1H), 7.75 (s, 1H), 5.89 (s, 1H), 3.99 (s, 3H), 2.99 (d, J = 4.7 Hz, 3H), 1.04 (d, J = 1.3 Hz, 18H); **^{13}C NMR** (126 MHz, $CDCl_3$) δ 173.08, 164.45, 164.17, 157.38, 144.08, 144.02, 117.66, 115.34, 108.23, 108.10, 86.57, 55.62, 28.70, 27.07, 20.47, 20.38; **^{19}F NMR** (471 MHz, CDCl3) δ -76.06, -186.05; ; **HRMS:** Calcd. for $C_{15}H_{28}FN_2OSi$ $[M+H]^+$ = 299.1954 m/z, found = 299.1949 m/z.

Compound 2-21:

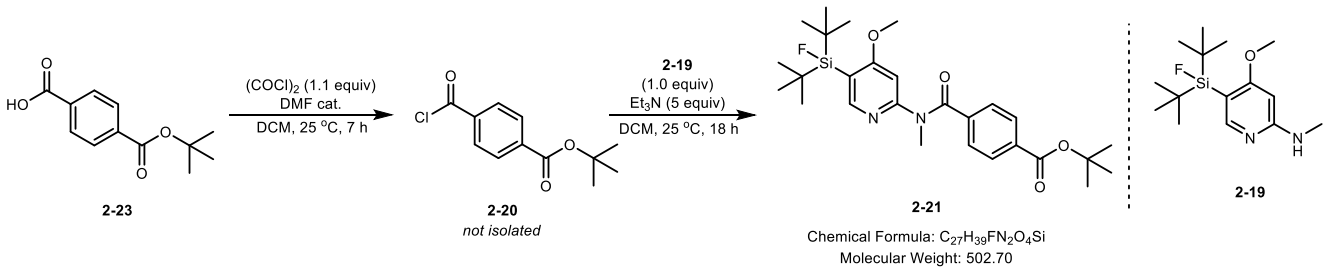

Procedure:

To a 5-dram vial equipped with Teflon-coated stir bar and a rubber septum was added TFA salt **2-19** (212 mg, 0.608 mmol, 0.8 equiv.) and 10 mL of 1M ethereal HCl. The suspension was stirred at ambient temperature for 15 min then concentrated *in vacuo* to afford a white residue. A flame-dried 25 mL round bottom flask equipped with a Teflon-coated stir bar and a rubber septum was charged with 10 mL dry DCM. The reaction vessel was evacuated and backfilled with N_2, and cooled in an ice bath to 0 °C, and **2-23** (135 mg, 0.609 mmol, 1.0 equiv.) was added. Next, oxalyl chloride (57 uL, 0.660 mmol, 1.1 equiv.) was added dropwise, followed by one drop of DMF. The mixture was stirred for 10 min at 0 °C then removed from the ice bath and allowed to come to ambient temperature and stirred for 2 h under N_2 before being concentrated *in vacuo*. The resulting residue was dissolved in 5 mL dry DCM, cooled in an ice bath to 0 °C, and to it was added the material from the 5-dram vial along with triethylamine (354 uL, 2.54 mmol, 5 equiv.). The mixture was stirred for 10 min at 0 °C then removed from the ice bath and allowed to come to ambient temperature. The mixture is stirred for 18 h at ambient temperature under N_2 then quenched with 25 mL of distilled water. The resulting heterogeneous, biphasic reaction mixture was then extracted with EtOAc (25 mL x 3). The combined organic phases were washed with 25 mL of brine then dried over Na_2SO_4, filtered, and concentrated *in vacuo*. The resulting residue was purified by silica gel column chromatography (25% EtOAc in hexanes) to afford **2-21** as a clear gel (220 mg, 0.437 mmol) in 72% yield.

Characterization:

R_f = (EtOAc/hexane 25:75): 0.32; **IR** (neat) v = 2967.88, 2935.02, 2893.87, 1714.47, 1658.50, 1574.79, 1552.26, 1473.74, 1447.02, 1363.93, 1287.40, 1222.70, 1163.21, 1116.28, 1072.70, 1014.84, 924.19, 824.98, 809.51, 732.99, 703.25, 645.96, 624.17, 583.30, 489.99, 444.37 cm^{-1}; **^{1}H NMR** (400 MHz, cdcl$_3$) δ 8.36 (s, 1H), 7.87 – 7.80 (m, 2H), 7.41 – 7.31 (m, 2H), 6.35 (s, 1H), 3.59 (s, 3H), 3.49 (s, 3H), 1.56 (s, 9H), 0.98 (d, *J* = 1.3 Hz, 18H); **^{13}C NMR** (126 MHz, $CDCl_3$) δ 170.39, 169.88, 169.84, 164.79, 159.34, 155.10, 155.04, 140.10, 133.24, 129.85, 129.33, 129.07, 127.97, 115.83 (d, *J* = 14.6 Hz), 103.25, 81.51, 54.49, 35.85, 28.12, 27.12, 20.47, 20.38; **^{19}F NMR** (376 MHz, cdcl$_3$) δ -186.62; **HRMS:** Calcd. for $C_{27}H_{40}FN_2O_4Si$ $[M+H]^+$ = 503.2736 m/z, found = 503.2747 m/z.

Compound 2-91:

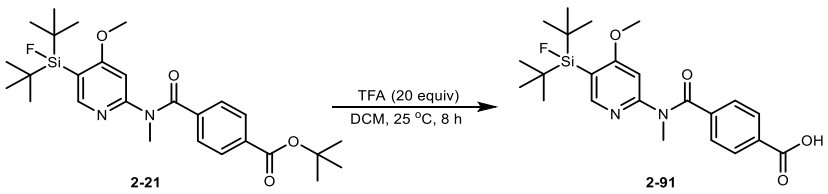

Chemical Formula: $C_{23}H_{31}FN_2O_4Si$
Exact Mass: 446.20

Procedure: A flame-dried 25 mL round bottom flask equipped with a Teflon-coated stir bar and a rubber septum was charged with 10 mL of DCM, **2-21** (200 mg, 0.397 mmol, 1 equiv.), and trifluoroacetic acid (610 uL, 7.94 mmol, 20 equiv.). The mixture was then stirred at ambient temperature for 8 h then concentrated *in vacuo*. To the resulting clear liquid was added 1 mL toluene and the resulting mixture was concentrated *in vacuo*. The resulting residue was purified by silica gel column chromatography (5% MeOH in DCM) to afford the TFA salt of **2-91** as a white solid (189 mg, 0.337 mmol) in 85% yield.

Characterization:

R_f = (MeOH/DCM 10:90): 0.64; **IR** (neat) v = 3225.84, 3118.24, 3061.72, 2935.03, 2860.40, 1657.38, 1568.77, 1503.16, 1470.34, 1425.91, 1286.41, 1204.66, 1114.39, 1089.65, 1037.50, 1021.10, 949.47, 896.64, 874.46, 837.31, 824.72, 734.60, 661.37, 602.50, 509.52, 439.79 cm^{-1}; **^{1}H NMR** (400 MHz, cdcl$_3$) δ 8.38 (s, 1H), 8.01 – 7.94 (m, 2H), 7.49 – 7.42 (m, 2H), 6.37 (s, 1H), 3.61 (s, 3H), 3.52 (s, 3H), 0.99 (d, *J* = 1.3 Hz, 17H); **^{13}C NMR** (126 MHz, cdcl$_3$) δ 170.13, 170.09, 170.03, 159.02, 154.92, 154.87, 141.07, 130.87, 129.84, 128.22, 116.32, 103.30, 54.58, 36.01, 27.08, 20.45, 20.36; **^{19}F NMR** (471 MHz, $CDCl_3$) δ -75.82, -186.40; **HRMS:** Calcd. for $C_{23}H_{31}FN_2NaO_4Si$ $[M+Na]^+$ = 469.1929 m/z, found = 469.1917 m/z.

Compound 2-23:

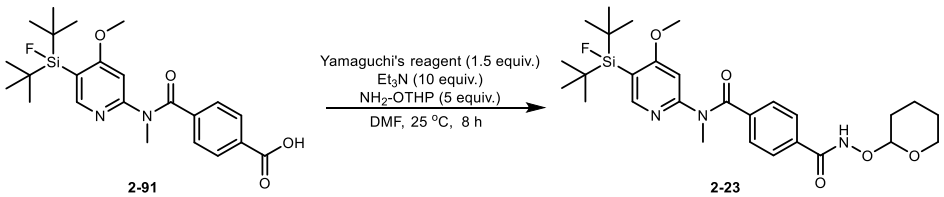

Procedure: A flame-dried 25 mL round bottom flask equipped with a Teflon-coated stir bar and a rubber septum flushed with nitrogen and charged with 10 mL of DMF and **2-91** (130 mg, 0.232 mmol 1 equiv.). While stirring, the mixture is cooled in an ice bath and triethylamine (323 uL, 2.32mmol, 10 equiv.) is added, followed by Yamaguchi's reagent (54 uL, 0.348 mmol, 1.5 equiv.). The mixture is stirred at 0 °C for 15 min and NH_2OTHP (136 mg, 1.16 mmol, 5 equiv.) is added, and the solution is removed from the ice bath and stirred at ambient temperature for 8 h. The mixture is poured into 25 mL EtOAc and washed with 25 mL saturated aqueous $NaHCO_3$ followed by brine, and the retained organic phase then dried over Na_2SO_4, filtered, and concentrated *in vacuo*. The resulting oil is purified by silica gel column chromatography (1 – 5% MeOH in DCM) to afford **2-23** as a clear gel that solidified on standing (62 mg, 0.114 mmol) in 49% yield.

Characterization:

R_f = (MeOH/DCM 10:90): 0.86; **IR** (neat) ν = 221.60, 2937.30, 2894.60, 2860.04, 1656.13, 1575.56, 1553.10, 1520.72, 1473.87, 1446.41, 1426.37, 1357.73, 1305.55, 1277.14, 1223.32, 1184.37, 1129.16, 1115.20, 1074.10, 1014.58, 949.82, 903.11, 825.81, 810.56, 736.15, 647.17 cm^{-1}; **^{1}H NMR** (500 MHz, cdcl3) δ 9.29 (s, 1H), 8.36 (s, 1H), 7.60 (d, J = 7.9 Hz, 2H), 7.42 – 7.28 (m, 2H), 6.32 (s, 1H), 5.07 (s, 1H), 4.01 (t, J = 10.1 Hz, 1H), 3.69 – 3.61 (m, 1H), 3.58 (s, 3H), 3.49 (s, 3H), 1.94 – 1.78 (m, 3H), 1.61 (q, J = 16.1 Hz, 3H), 1.02 – 0.94 (m, 18H); **^{13}C NMR** (126 MHz, $cdcl_3$) δ 170.09, 169.85, 159.18, 155.20, 155.14, 139.57, 133.54, 128.33, 126.99, 103.03, 102.66, 62.59, 54.51, 35.93, 28.05, 27.11, 25.01, 20.46, 20.36, 18.55; **^{19}F NMR** (376 MHz, cdcl3) δ -186.55; **HRMS:** Calcd. for $C_{28}H_{41}FN_3O_5Si$ $[M+H]^+$ = 546.2794 m/z, found = 546.2797 m/z.

Compound 2-22:

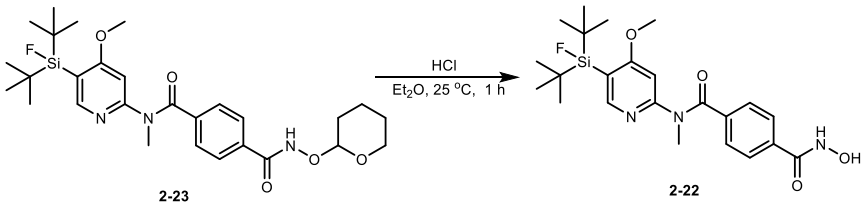

Chemical Formula: $C_{23}H_{32}FN_3O_4Si$
Exact Mass: 461.21

Procedure: A 5-dram glass vial equipped with a Teflon-coated stir bar and a rubber septum was charged with 3 mL diethyl ether and **2-23** (30 mg, 0.055 mmol, 1 equiv.). 3mL of 1 M ethereal HCl is added dropwise while stirring, and the resulting suspension was stirred at ambient temperature for 1 h. The vial is sealed and put into a -20 °C freezer for 1h and the supernatant is carefully removed and discarded. The white precipitate is triturated 3 times with cold diethyl ether, and then dried to provide the HCl salt of **2-22** as a white solid (22 mg, 0.045 mmol) in 82% yield.

Characterization: $\mathbf{R_f}$ = (MeOH/DCM 10:90): 0.62; **IR** (neat) v = 3217.74, 2955.77, 2935.57, 2893.67, 2860.47, 2361.57, 1645.21, 1575.65, 1553.82, 1473.68, 1446.61, 1357.35, 1306.83, 1223.59, 1074.94, 1026.70, 1014.11, 825.45, 810.32, 738.01, 703.58, 647.00 cm^{-1}; **^{1}H NMR** (500 MHz, DMSO) δ 10.28 (s, 0H), 8.08 (s, 1H), 7.66 – 7.61 (m, 2H), 7.36 – 7.30 (m, 2H), 6.91 (s, 1H), 3.63 (s, 3H), 3.49 (s, 3H), 0.95 (d, *J* = 1.3 Hz, 20H); **^{13}C NMR** (126 MHz, $CDCl_3$) δ 174.84, 168.19, 143.86, 139.00, 133.10, 131.58, 109.01, 60.59, 40.78, 32.08, 25.17 (d, *J* = 11.9 Hz); **^{19}F NMR** (376 MHz, cdcl$_3$) δ -186.54; **HRMS:** Calcd. for $C_{23}H_{33}FN_3O_4Si$ $[M+H]^+$ = 462.2219 m/z, found = 462.2218 m/z.

Compound 2-26:

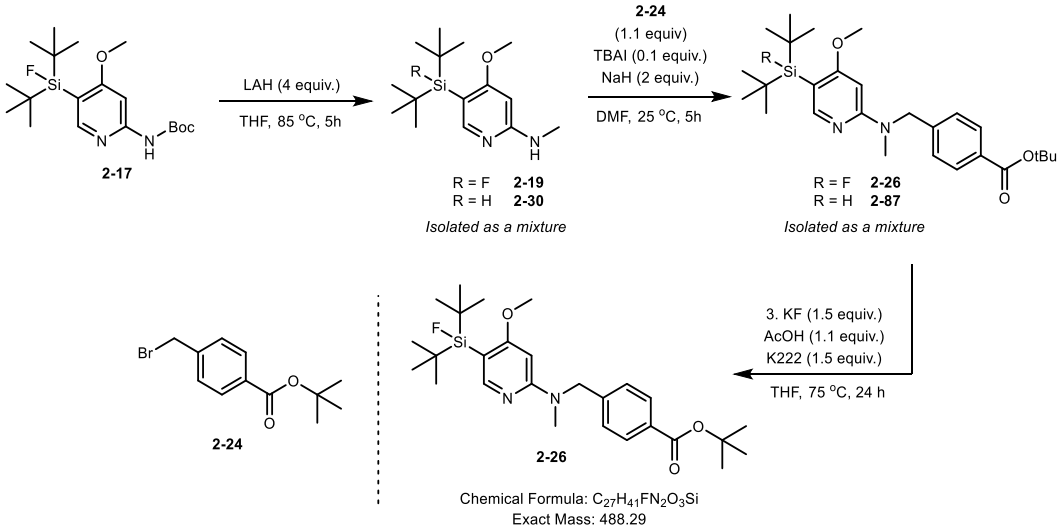

Procedure: A flame-dried 100 mL round bottom flask equipped with a Teflon-coated stir bar and a rubber septum was charged with 30 mL of dry THF, and **2-17** (250 mg, 0.65 mmol, 1 equiv.). The vial is cooled in an ice bath to 0 °C, and 1M solution of LAH in THF (2.6 mL, 2.6 mmol, 4 equiv.) was added dropwise to the solution while stirring. After addition, the solution is removed from the ice bath and allowed to warm to room temperature, and a reflux condenser is fitter to the flask. The vial is then placed in an oil bath and heated to 85 °C for 5 h, then removed from the oil bath and placed into an ice bath to cool to 0 °C. The reaction is then quenched with a solution of of 0.5 mL acetone in 5 mL of water, and the resulting mixture was filtered through a pad of celite, which is subsequently washed with EtOAc (3 x 25 mL) which is collected and combined with the filtrate. The combined filtrate is washed with 20 mL of brine then dried over Na_2SO_4, filtered, and concentrated *in vacuo*. The resulting oil is purified by silica gel column chromatography (5% EtOAc in hexane) to produce 178 mg white solid as a mixture of **2-19** and **2-30**.

The 178 mg of white solid mixture of **2-19** and **2-30** is added to a flame-dried 20 mL round bottom flask equipped with a Teflon-coated stir bar and a rubber septum was charged with 10 mL of dry DMF. While stirring at ambient temperature, NaH (61 mg, 1.26 mmol, 2 equiv.) is slowly added, and the dark heterogeneous mixture is allowed to stir at ambient temperature for 1 h, next 4-bromomethylbenzoic acid *tert*-butyl ester (189 mg, 0.70 mmol, 1.1 equiv.) is added, followed by TBAI (20 mg, 0.065 mmol, 0.1 equiv.) and the mixture is allowed to stir for an additional 4h at ambient temperature, then quenched with 20 mL of distilled water. The resulting heterogeneous, biphasic reaction mixture was then extracted with EtOAc (20 mL x 3). The combined organic phases were washed with 25 mL brine retaining the organic phase, which is dried over Na_2SO_4, filtered, and concentrated *in vacuo*. The resulting oil was purified by silica gel column chromatography (5% EtOAc in hexanes) to afford 70 mg of an off-white solid mixture of **2-26** and **2-87**.

The 70 mg of off white solid is added to a flame-dried 20 mL round bottom flask equipped with a Teflon-coated stir bar and a reflux condenser was charged with 10 mL dry THF, and Kryptofix

2.2.2. (85 mg, 0.22 mmol, 1.5 equiv.), KF (13 mg, 0.22 mmol, 1.5 equiv.), and AcOH glacial (9.3 uL, 0.16 mmol, 1.1 equiv.) was added. The mixture is heated in an oil bath to 85 °C and stirred for 48 h then quenched with 15 mL of water. The resulting heterogeneous, biphasic reaction mixture was then extracted with EtOAc (25 mL x 3). The combined organic phases were washed with 25 mL of brine then dried over Na_2SO_4, filtered, and concentrated *in vacuo*. The resulting residue was purified by silica gel column chromatography (5% EtOAc in hexanes) to afford **2-26** as an off-white solid (61 mg, 0.12 mmol) in 19% overall yield over 3 steps.

Characterization:

R_f = (EtOAc/Hexane 20:80): 0.58; **IR** (neat) v = 2955.92, 2927.72, 2857.28, 2360.55, 1700.73, 1588.39, 1538.61, 1507.00, 1473.29, 1396.72, 1245.18, 1227.29, 1201.13, 1133.87, 1085.46, 1028.63, 950.42, 825.33, 808.88, 766.08, 646.03, 478.96 cm^{-1}; **^{1}H NMR** (400 MHz, $cdcl_3$) δ 8.14 (s, 1H), 7.98 – 7.91 (m, 2H), 7.32 – 7.26 (m, 2H), 4.89 (s, 2H), 3.75 (s, 3H), 3.06 (s, 3H), 1.58 (s, 9H), 1.03 (d, *J* = 1.3 Hz, 18H); **^{13}C NMR** (126 MHz, $cdcl_3$) δ 170.64, 170.61, 165.65, 161.88, 155.39, 155.33, 143.60, 130.85, 129.74, 126.92, 105.23, 105.11, 86.16, 80.88, 53.77, 53.05, 36.14, 29.70, 28.20, 27.35, 20.65, 20.55; **^{19}F NMR** (376 MHz, $cdcl_3$) δ -187.46; **HRMS:** Calcd. for $C_{27}H_{42}FN_2O_3Si$ $[M+H]^+$ = 489.2943 m/z, found = 489.2952 m/z.

Compound 2-92:

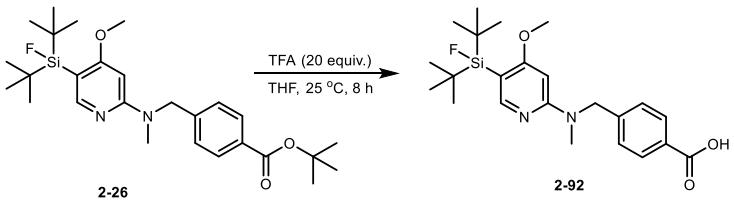

Procedure: A flame-dried 10 mL round bottom flask equipped with a Teflon-coated stir bar and a rubber septum was charged with 5 mL of DCM, **2-26** (61 mg, 0.12 mmol, 1 equiv.), and trifluoroacetic acid (184 uL, 2.4 mmol, 20 equiv.). The mixture was then stirred at ambient temperature for 8 h then concentrated *in vacuo*. To the resulting clear liquid was added 1 mL toluene and the resulting mixture was concentrated *in vacuo*. The resulting residue was purified by silica gel column chromatography (1 - 5% MeOH in DCM) to afford the TFA salt of **2-92** as an off-white solid (64 mg, 0.11 mmol) in 96% yield.

Characterization:

$\mathbf{R_f}$ = (EtOAc/hexane 70:30): 0.37; **IR** (neat) v = 2956.33, 2936.34, 2897.91, 2862.70, 1693.52, 1674.44, 1613.12, 1475.22, 1426.43, 1253.57, 1197.40, 1136.13, 1087.15, 1018.22, 825.72, 811.05, 718.71, 649.78 cm^{-1}; **^{1}H NMR** (500 MHz, $cdcl_3$) δ 9.08 (s, 1H), 8.16 (s, 1H), 8.04 (d, *J* = 7.9 Hz, 2H), 7.34 (d, *J* = 7.9 Hz, 2H), 5.90 (s, 1H), 4.94 (s, 2H), 3.78 (s, 3H), 3.14 (s, 3H), 1.03 (s, 18H); **^{13}C NMR** (126 MHz, cd_3od) δ 172.77, 172.74, 167.93, 155.79, 143.34, 143.28, 140.21, 130.52, 130.14, 126.49, 109.71, 89.92, 55.41, 54.35, 37.08, 26.17, 19.93, 19.84; **^{19}F NMR** (376 MHz, cd_3od) δ -76.88, -187.12; **HRMS:** Calcd. for $C_{23}H_{34}FN_2O_3Si$ $[M+H]^+$ = 433.2317 m/z, found = 433.2313 m/z.

Compound 2-31:

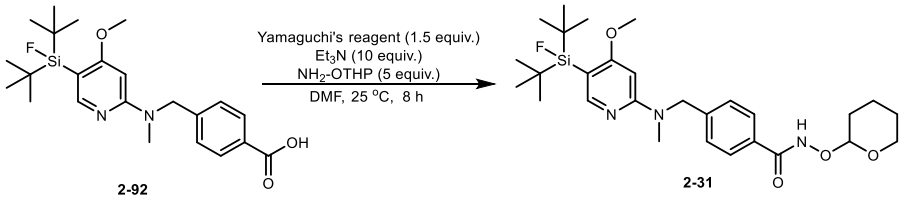

Procedure: A flame-dried 10 mL round bottom flask equipped with a Teflon-coated stir bar and a rubber septum flushed with nitrogen and charged with 5 mL of DMF and **2-92** (62 mg, 0.11 mmol 1 equiv.). While stirring, the mixture is cooled in an ice bath and triethylamine (267 uL, 1.1 mmol, 10 equiv.) is added, followed by Yamaguchi's reagent (26 uL, 0.17 mmol, 1.5 equiv.). The mixture is stirred at 0 °C for 15 min and NH_2OTHP (65 mg, 0.55 mmol, 5 equiv.) is added, and the solution is removed from the ice bath and stirred at ambient temperature for 8 h. The mixture is poured into 15 mL EtOAc and washed with 15 mL saturated aqueous $NaHCO_3$ followed by brine, and the retained organic phase then dried over Na_2SO_4, filtered, and concentrated *in vacuo*. The resulting oil is purified by silica gel column chromatography (35% EtOAc in hexane) to afford **2-31** as a clear oil that solidified on standing (30 mg, 0.056 mmol) in 51% yield.

Characterization:

R_f = (MeOH/DCM 10:90): 0.63; **IR** (neat) v = 3228.05, 2935.32, 2893.97, 2858.36, 1651.59, 1587.85, 1537.59, 1499.30, 1473.24, 1435.22, 1399.25, 1204.57, 1084.71, 1027.27, 807.99, 644.59, 477.97 cm^{-1}; **^{1}H NMR** (500 MHz, $cdcl_3$) δ 9.04 (s, 1H), 8.14 (s, 1H), 7.70 (d, *J* = 7.8 Hz, 2H), 7.29 (d, *J* = 7.9 Hz, 2H), 5.87 (s, 1H), 5.07 (s, 1H), 4.88 (s, 2H), 3.99 (td, *J* = 10.4, 2.8 Hz, 1H), 3.77 (s, 3H), 3.63 (dd, *J* = 10.4, 5.3 Hz, 1H), 3.05 (s, 3H), 1.89 (dt, *J* = 10.5, 5.3 Hz, 1H), 1.68 – 1.55 (m, 4H), 1.03 (s, 18H); **^{13}C NMR** (126 MHz, $cdcl_3$) δ 170.67, 170.64, 161.83, 155.34, 155.28, 143.29, 130.75, 127.51, 127.34, 105.35, 105.24, 102.68, 86.17, 62.65, 53.80, 52.94, 36.17, 28.07, 27.35, 25.02, 20.64, 20.54, 18.64; **^{19}F NMR** (376 MHz, $cdcl_3$) δ -187.39; **HRMS:** Calcd. for $C_{28}H_{43}FN_3O_4Si$ $[M+H]^+$ = 532.3007 m/z, found = 532.2999 m/z.

Compound 2-25:

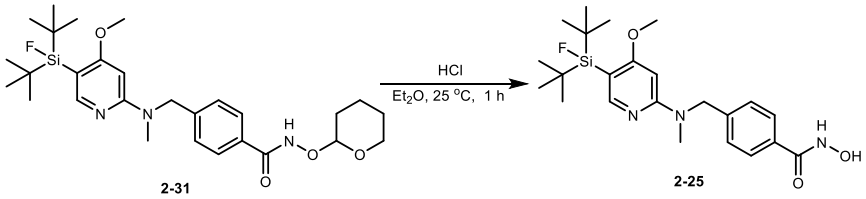

Chemical Formula: $C_{23}H_{34}FN_3O_3Si$
Exact Mass: 447.24

Procedure: A 5-dram glass vial equipped with a Teflon-coated stir bar and a rubber septum was charged with 3 mL diethyl ether and **2-31** (15 mg, 0.028 mmol, 1 equiv.). 3mL of 1 M ethereal HCl is added dropwise while stirring, and the resulting suspension was stirred at ambient temperature for 1 h. The vial is sealed and put into a -20 °C freezer for 1h and the supernatant is carefully removed and discarded. The white precipitate is triturated 3 times with cold diethyl ether, and then dried to provide the HCl salt of **2-25** as a white solid (8 mg, 0.027 mmol) in 59% yield.

Characterization:

R_f = (MeOH/DCM 10:90): 0.42; **IR** (neat) v = 3117.13, 2932.25, 2859.26, 1627.67, 1595.16, 1474.55, 1417.21, 1291.78, 1228.09, 1087.15, 1004.23, 823.48, 807.55, 739.61, 645.23, 577.01, 478.50, 437.04 cm^{-1}; **^{1}H NMR** (500 MHz, DMSO) δ 13.62 (s, 1H), 11.25 (s, 1H), 9.04 (s, 1H), 7.80 – 7.75 (m, 2H), 7.65 (s, 1H), 7.44 – 7.39 (m, 2H), 6.55 (s, 1H), 5.01 (d, *J* = 6.0 Hz, 2H), 3.96 (s, 3H), 3.25 (d, *J* = 3.4 Hz, 3H), 1.02 (d, *J* = 1.3 Hz, 18H); **^{13}C NMR** (126 MHz, MeOD) δ 172.73, 155.85, 138.99, 131.94, 127.55, 126.72, 109.67, 89.91, 55.41, 54.27, 37.10, 26.16, 19.94, 19.85; **^{19}F NMR** (376 MHz, $cdcl_3$) δ -185.34; **HRMS:** Calcd. for $C_{23}H_{35}FN_3O_3Si$ $[M+H]^+$ = 448.2426 m/z, found = 448.2424 m/z.

Compound 2-50:

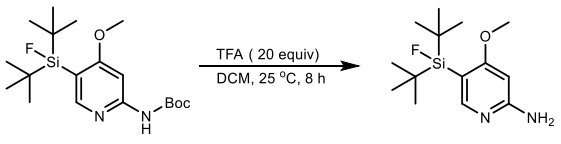

2-17 **2-50**

Chemical Formula: $C_{14}H_{25}FN_2OSi$
Exact Mass: 284.17

Procedure: A flame-dried 25 mL round bottom flask equipped with a Teflon-coated stir bar and a rubber septum was charged with 10 mL of DCM, **2-17** (570 mg, 1.48 mmol, 1 equiv.), and trifluoroacetic acid (2.3 mL, 29.7 mmol, 20 equiv.). The mixture was then stirred at ambient temperature for 8 h then concentrated *in vacuo*. To the resulting clear liquid was added 1 mL toluene and the resulting mixture was concentrated *in vacuo*. The resulting residue was purified by silica gel column chromatography (1 - 5% MeOH in DCM) to afford the TFA salt of **2-50** as a white solid (530 mg, 1.33 mmol) in 90% yield.

Characterization:

R_f = (MeOH/DCM 10:90): 0.61; **IR** (neat) ν = 3294.81, 3123.10, 2938.25, 2862.61, 1668.11, 1615.98, 1551.29, 1471.88, 1415.45, 1365.47, 1301.41, 1239.17, 1182.02, 1134.37, 1091.26, 1018.65, 826.30, 810.30, 765.03, 722.31, 648.44, 579.87, 529.96, 473.86 cm^{-1}; **^{1}H NMR** (500 MHz, CDCl3) δ 14.90 (s, 1H), 7.96 (s, 2H), 7.67 (s, 1H), 6.23 (s, 1H), 3.92 (s, 3H), 1.04 (d, J = 1.4 Hz, 18H); **^{13}C NMR** (126 MHz, CDCl3) δ 172.60, 172.56, 157.57, 142.65, 142.58, 109.95, 109.83, 91.08, 55.74, 27.05, 20.44, 20.34; **^{19}F NMR** (471 MHz, CDCl3) δ -75.90, -186.07; **HRMS:** Calcd. for $C_{14}H_{26}FN_2OSi$ $[M+H]^+$ = 285.1793 m/z, found = 285.1787 m/z.

Compound 2-51:

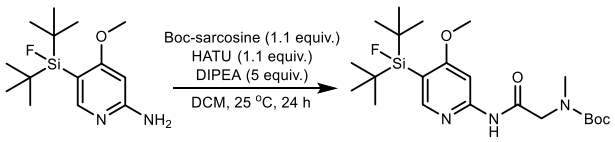

2-50 **2-51**

Chemical Formula: $C_{22}H_{38}FN_3O_4Si$
Exact Mass: 455.26

Procedure: A flame-dried 25 mL round bottom flask equipped with a Teflon-coated stir bar and a rubber septum was charged with 10 mL of THF, is cooled in an ice bath to 0 °C. Boc-sarcosine (260 mg ,1.37 mmol, 1.1 equiv.) and HATU (522 mg, 1.37 mmol, 1.1 equiv.) are added, followed by DIPEA (1.1 mL, 6.25 mmol, 5 equiv.). The solution is removed from the ice bath and allowed to warm to ambient temperature, and allowed to stir for 15 min. **2-50** (500 mg, 1.25 mmol, 1 equiv.) is added to the mixture and the mixture is stirred at ambient temperature for 24 h then quenched with 30 mL of distilled water. The resulting heterogeneous, biphasic reaction mixture was then extracted with EtOAc (25 mL x 3). The combined organic phases were washed with 25 mL saturated aqueous $NaHCO_3$ followed by brine retaining the organic phase, which is dried over Na_2SO_4, filtered, and concentrated *in vacuo*. The resulting oil was purified by silica gel column chromatography (15% EtOAc in hexanes) to afford **2-51** as a clear oil (391 mg, 0.86 mmol) in 69% yield.

Characterization:

R_f = (EtOAc/Hexane 20:80): 0.40; **IR** (neat) v = 2968.28, 2935.25, 2896.36, 2860.25, 2360.05, 1699.24, 1574.85, 1509.43, 1473.23, 1447.94, 1376.50, 1303.77, 1245.90, 1206.20, 1149.03, 1092.44, 1031.01, 825.82, 810.28, 769.64, 695.75, 646.37, 483.94 cm^{-1}; **^{1}H NMR (500 MHz, CDCl3)** δ 8.56 (s, 1H), 8.23 (s, 1H), 7.86 (s, 1H), 4.11 – 3.98 (m, 2H), 3.90 (s, 3H), 3.02 (s, 3H), 1.51 (s, 9H), 1.05 (d, J = 1.3 Hz, 18H); **^{13}C NMR** (126 MHz, CDCl3) δ 170.88, 154.57, 154.27, 95.49, 81.20, 54.63, 35.96, 28.31, 27.24, 27.23, 20.58, 20.48; **^{19}F NMR** (471 MHz, $CDCl_3$) δ -187.01; **HRMS:** Calcd. for $C_{22}H_{39}FN_3O_4Si$ $[M+H]^+$ = 456.2688 m/z, found = 456.2681 m/z.

Compound 2-56:

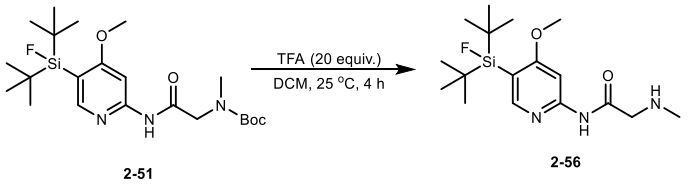

Procedure: A 10 mL round bottom flask equipped with a Teflon-coated stir bar and a rubber septum was charged with 5 mL of DCM, **2-51** (100 mg, 0.22 mmol, 1 equiv.), and trifluoroacetic acid (336 uL, 4.4 mmol, 20 equiv.). The mixture was then stirred at ambient temperature for 4 h then concentrated *in vacuo*. To the resulting clear liquid was added 1 mL toluene and the resulting mixture was concentrated *in vacuo*. The resulting residue was purified by silica gel column chromatography (1 - 5% MeOH in DCM) to afford the TFA salt of **2-56** as a white solid (90 mg, 0.19 mmol) in 86% yield.

Characterization:

R_f = (MeOH/DCM 10:90): 0.48; **IR** (neat) v = 3239.18, 3088.96, 3032.64, 2968.42, 2935.98, 2895.42, 2861.14, 1680.09, 1573.21, 1524.05, 1472.87, 1446.92, 1375.65, 1363.97, 1198.78, 1178.68, 1134.75, 1091.36, 1031.70, 969.50, 824.48, 807.57, 721.73, 676.28, 644.96, 579.92, 484.58, 441.85 cm^{-1}; **^{1}H NMR** (500 MHz, CDCl3) δ 8.21 (s, 1H), 7.68 (d, J = 8.1 Hz, 1H), 4.00 (s, 2H), 3.90 (s, 3H), 2.78 (s, 3H), 1.05 – 1.01 (m, 18H); **^{13}C NMR** (126 MHz, $CDCl_3$) δ 163.05, 162.77, 153.58, 117.69, 115.37, 55.14, 33.95, 27.11, 20.51, 20.42; **^{19}F NMR** (471 MHz, $CDCl_3$) δ -75.88, -186.57; **HRMS:** Calcd. for $C_{17}H_{31}FN_3O_2Si$ $[M+H]^+$ = 356.2164 m/z, found = 356.2163 m/z.

Compound 2-48:

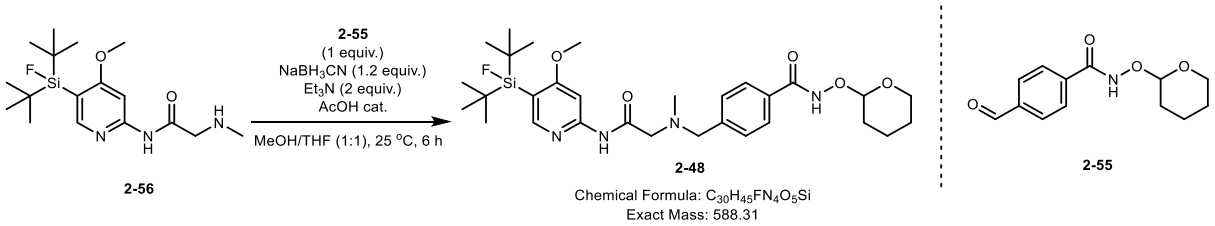

Procedure: A flame-dried 10 mL round bottom flask equipped with a Teflon-coated stir bar and a rubber septum was charged with 4 mL 1:1 mixture of THF and MeOH. **2-56** (90 mg, 0.19 mmol, 1 equiv.) along with **2-55** (47 mg, 0.19 mmol, 1 equiv.) are added, followed by Et_3N (53 uL, 0.38 mmol, 2 equiv.). The flask in heated in an oil bath to 40 °C and stirred for 1 h, and $NaBH_3CN$ (46 mg, 0.23 mmol, 1.2 equiv.) is added, followed by 1 drop of AcOH glacial. The mixture is removed from the oil bath and allowed to come to ambient temperature, and stirred for 6 h then concentrated *in vacuo*. The resulting residue is dissolved in 15 mL EtOAc and washed with 10 mL saturated aqueous $NaHCO_3$ followed by brine retaining the organic phase, which is dried over Na_2SO_4, filtered, and concentrated *in vacuo*. The resulting oil was purified by silica gel column chromatography (1 - 5% MeOH in DCM) to afford **2-48** as a clear liquid that solidified on standing (32 mg, 0.054 mmol) in 29% yield.

Characterization:

R_f = (MeOH/DCM 15:85): 0.84; **IR** (neat) v = 3246.35, 2935.94, 2858.59, 2796.40, 1722.36, 1656.40, 1577.81, 1474.78, 1446.11, 1384.47, 1285.60, 1207.58, 1115.18, 1027.71, 946.52, 904.86, 825.57, 810.48, 730.06, 646.88, 470.82 cm^{-1}; **^{1}H NMR** (400 MHz, CDCl3) δ 9.69 (s, 1H), 9.05 (s, 1H), 8.27 (s, 1H), 7.86 (s, 1H), 7.77 (d, J = 7.8 Hz, 2H), 7.47 (d, J = 7.9 Hz, 2H), 5.10 (t, J = 3.0 Hz, 1H), 4.02 (td, J = 10.4, 2.9 Hz, 1H), 3.89 (s, 3H), 3.71 (s, 2H), 3.67 (dd, J = 10.5, 5.4 Hz, 1H), 3.19 (s, 2H), 2.39 (s, 3H), 1.89 (q, J = 7.3 Hz, 3H), 1.65 (qd, J = 10.5, 6.8 Hz, 3H), 1.05 (d, J = 1.3 Hz, 18H); **^{13}C NMR** (126 MHz, $CDCl_3$) δ 171.76, 170.24, 154.20, 154.14, 153.14, 143.05, 132.04, 132.02, 127.93, 127.92, 127.18, 114.54, 114.42, 102.73, 96.69, 96.67, 82.64, 65.87, 62.71, 58.15, 54.60, 40.40, 40.37, 29.72, 28.04, 27.28, 27.16, 25.02, 20.62, 20.52, 20.49, 20.39, 18.64; **^{19}F NMR** (471 MHz, $CDCl_3$) δ -186.93; **HRMS:** Calcd. for $C_{30}H_{46}FN_4O_5Si$ $[M+H]^+$ = 589.3216 m/z, found = 589.3209 m/z.

Compound 2-45:

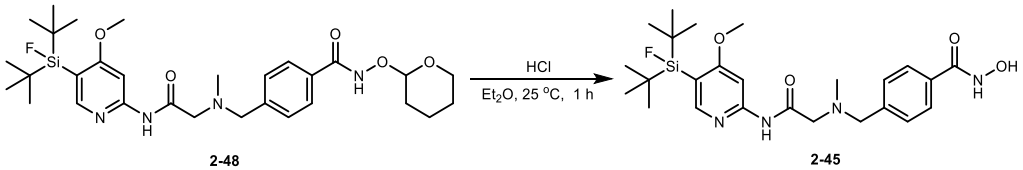

2-48 2-45

Chemical Formula: $C_{25}H_{37}FN_4O_4Si$
Exact Mass: 504.26

Procedure: A 5-dram glass vial equipped with a Teflon-coated stir bar and a rubber septum was charged with 3 mL diethyl ether and **2-48** (18 mg, 0.031 mmol, 1 equiv.). 3mL of 1 M ethereal HCl is added dropwise while stirring, and the resulting suspension was stirred at ambient temperature for 1 h. The vial is sealed and put into a -20 °C freezer for 1h and the supernatant is carefully removed and discarded. The white precipitate is triturated 3 times with cold diethyl ether, and then dried to provide the HCl salt of **2-45** as a white solid (14 mg, 0.027 mmol) in 88% yield.

Characterization: $\mathbf{R_f}$ = (MeOH/DCM 15:85): 0.48; **IR** (neat) v = 3238.37, 3119.83, 3061.67, 2966.36, 2935.03, 2898.50, 1726.78, 1574.95, 1472.14, 1427.93, 1391.27, 1366.65, 1243.53, 1166.09, 1153.56, 1096.93, 1003.14, 825.11, 660.94, 600.80, 517.13, 439.78 cm^{-1}; **^{1}H NMR** (500 MHz, MeOD) δ 8.57 (s, 2H), 8.17 (d, *J* = 2.5 Hz, 1H), 7.88 (d, *J* = 1.4 Hz, 1H), 7.84 – 7.79 (m, 1H), 7.76 (d, *J* = 8.0 Hz, 1H), 7.58 (d, *J* = 8.0 Hz, 1H), 7.49 (d, *J* = 8.3 Hz, 1H), 3.93 (d, *J* = 1.0 Hz, 3H), 3.77 (d, *J* = 14.0 Hz, 2H), 3.27 (d, *J* = 3.4 Hz, 2H), 2.41 (s, 3H), 1.07 (d, *J* = 1.3 Hz, 18H); **^{13}C NMR** (126 MHz, MeOD) δ 174.74, 167.08, 150.37, 144.61, 141.94, 126.69, 126.63, 117.60, 102.43, 96.03, 56.28, 50.07, 32.39, 26.08, 26.07, 20.00, 19.91; **^{19}F NMR** (376 MHz, cd_3od) δ -186.51; **HRMS:** Calcd. for $C_{25}H_{38}FN_4O_4Si$ $[M+H]^+$ = 505.2641 m/z, found = 505.2640 m/z.

Compound 2-42:

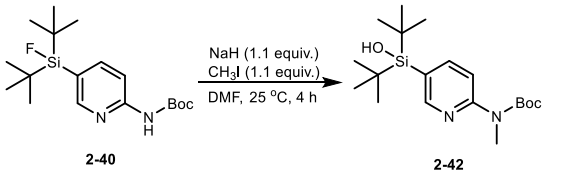

2-40 **2-42**

Chemical Formula: $C_{19}H_{34}N_2O_3Si$
Exact Mass: 366.23

Procedure: A flame-dried 50 mL round bottom flask equipped with a Teflon-coated stir bar and a rubber septum was charged with 20 mL dry DMF. The reaction vessel was evacuated and backfilled with N_2, and **2-40** (450 mg, 1.26 mmol, 1 equiv.) was added followed by sodium hydride (55 mg, 1.38 mmol, 1.1 equiv.). The mixture was then stirred at ambient temperature for 1 h and iodomethane (86 uL, 1.38 mmol, 1.1 equiv.) was added dropwise. The resulting mixture was stirred for 4 h at ambient temperature under N_2 then quenched with 30 mL of cold water. The resulting heterogeneous, biphasic reaction mixture was then extracted with EtOAc (25 mL x 3). The combined organic phases were washed with 25 mL of brine then dried over Na_2SO_4, filtered, and concentrated *in vacuo*. The resulting residue was purified by silica gel column chromatography (10% EtOAc in hexanes) to afford **2-42** as an oil (270 mg, 0.73 mmol) in 58% yield.

Characterization:

R_f = (EtOAc/Hexane 20:80): 0.52; **IR** (neat) v = 3501.04, 2965.07, 2932.14, 2889.30, 2857.42, 2359.15, 1712.83, 1687.75, 1579.52, 1548.06, 1473.36, 1427.45, 1365.11, 1310.67, 1282.16, 1255.65, 1235.60, 1152.19, 1100.64, 1019.34, 857.24, 822.44, 766.60, 638.69, 443.55 cm^{-1}; **^{1}H NMR** (500 MHz, $CDCl_3$) δ 8.61 (dd, *J* = 2.0, 0.9 Hz, 1H), 7.89 (dd, *J* = 8.3, 2.0 Hz, 1H), 7.75 (dd, *J* = 8.3, 1.0 Hz, 1H), 3.45 (s, 3H), 1.55 (s, 10H), 1.09 – 1.03 (m, 2H), 1.05 (s, 17H); **^{13}C NMR** (126 MHz, $CDCl_3$) δ 155.59, 154.42, 152.50, 143.05, 125.56, 117.89, 81.27, 77.23, 34.00, 28.32, 27.77, 20.32; **HRMS:** Calcd. for $C_{19}H_{35}N_2O_3Si$ $[M+H]^+$ = 367.2411 m/z, found = 367.2409 m/z.

Compound 2-93:

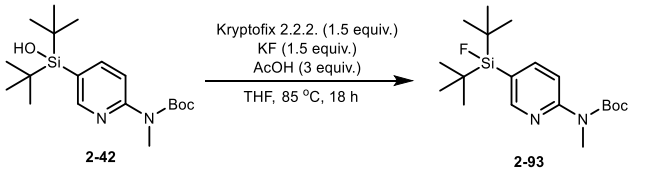

Chemical Formula: $C_{19}H_{33}FN_2O_2Si$
Exact Mass: 368.23

Procedure: A flame-dried 50 mL round bottom flask equipped with a Teflon-coated stir bar and a reflux condenser was charged with 20 mL dry THF and **2-42** (140 mg, 0.38 mmol, 1 equiv.), Kryptofix 2.2.2. (215 mg, 0.57 mmol, 1.5 equiv.), KF (32 mg, 0.57 mmol, 1.5 equiv.), and AcOH glacial (65 uL, 1.14 mmol, 3 equiv.) was added. The mixture is heated in an oil bath to 85 °C and stirred for 18 h then quenched with 30 mL of water. The resulting heterogeneous, biphasic reaction mixture was then extracted with EtOAc (25 mL x 3). The combined organic phases were washed with 25 mL of brine then dried over Na_2SO_4, filtered, and concentrated *in vacuo*. The resulting residue was purified by silica gel column chromatography (5% EtOAc in hexanes) to afford **2-93** as an oil (129 mg, 0.35 mmol) in 92% yield.

Characterization:

R_f = (EtOAc/Hexane 10:90): 0.87; **IR** (neat) ν = 2963.20, 2934.07, 2892.60, 2860.85, 2360.55, 1712.01, 1582.13, 1545.88, 1473.12, 1424.20, 1391.34, 1353.13, 1310.98, 1279.40, 1255.82, 1236.62, 1152.04, 1141.40, 1100.52, 1017.72, 858.18, 837.12, 823.57, 766.45, 649.51, 625.16, 584.28, 505.86, 442.67 cm^{-1}; **^{1}H NMR** (500 MHz, $CDCl_3$) δ 8.57 (dd, *J* = 1.8, 1.1 Hz, 1H), 7.86 – 7.78 (m, 2H), 3.45 (s, 3H), 1.56 (s, 9H), 1.08 (d, *J* = 1.2 Hz, 18H); **^{13}C NMR** (126 MHz, $CDCl_3$) δ 156.04, 154.36, 152.02, 151.98, 142.49, 142.46, 123.11, 123.00, 117.89, 81.41, 33.89, 28.31, 27.16, 20.32, 20.22; **^{19}F NMR** (471 MHz, $CDCl_3$) δ -189.22; **HRMS:** Calcd. for $C_{19}H_{33}FN_2O_2SiNa$ $[M+Na]^+$ = 391.2188 m/z, found = 391.2174 m/z.

Compound 2-41:

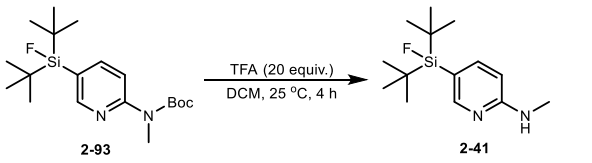

2-93 **2-41**

Chemical Formula: $C_{14}H_{25}FN_2Si$
Exact Mass: 268.18

Procedure: A 10 mL round bottom flask equipped with a Teflon-coated stir bar and a rubber septum was charged with 5 mL of DCM, **2-93** (129 mg, 0.35 mmol, 1 equiv.), and trifluoroacetic acid (535 uL, 7.1 mmol, 20 equiv.). The mixture was then stirred at ambient temperature for 4 h then concentrated *in vacuo*. To the resulting clear liquid was added 1 mL toluene and the resulting mixture was concentrated *in vacuo*. The resulting residue was purified by silica gel column chromatography (40% EtOAc in hexane) to afford the TFA salt of **2-41** as a white solid (115 mg, 0.30 mmol) in 86% yield.

Characterization:

R_f = (EtOAc/Hexane 60:40): 0.61; **IR** (neat) v = 3251.46, 3195.93, 3115.68, 2936.32, 2895.16, 2862.63, 1685.86, 1649.09, 1611.44, 1472.23, 1200.34, 1180.72, 1131.52, 1060.38, 1003.09, 824.30, 812.02, 799.73, 721.23, 652.69, 510.43, 454.63, 438.70 cm^{-1}; **^{1}H NMR** (500 MHz, $CDCl_3$) δ 10.31 (s, 1H), 7.93 (dd, *J* = 9.0, 1.7 Hz, 1H), 7.87 (d, *J* = 1.4 Hz, 1H), 6.79 (d, *J* = 9.0 Hz, 1H), 3.02 (d, *J* = 4.0 Hz, 3H), 1.07 (d, *J* = 1.2 Hz, 18H); **^{13}C NMR** (126 MHz, $CDCl_3$) δ 154.98, 147.71, 147.67, 141.56, 114.67, 108.74, 28.66, 26.96, 20.27, 20.18; **^{19}F NMR** (471 MHz, $CDCl_3$) δ -76.08, -188.04; **HRMS:** Calcd. for $C_{14}H_{26}FN_2Si$ $[M+H]^+$ = 269.1844 m/z, found = 269.1847 m/z.

Compound 2-43:

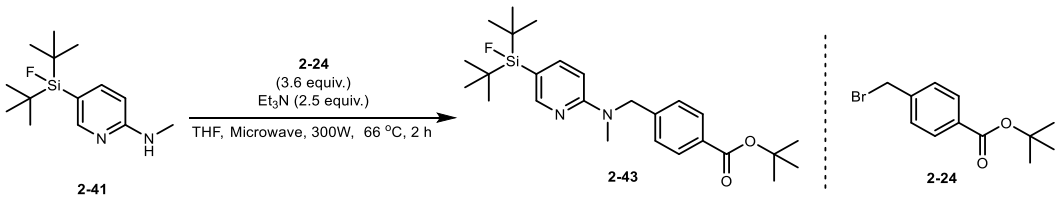

Chemical Formula: $C_{26}H_{39}FN_2O_2Si$
Exact Mass: 458.28

Procedure: A flame-dried 10 mL microwave reactor vial equipped with a Teflon-coated stir bar was charged with 3 mL dry THF and **2-41** (107 mg, 0.27 mmol, 1 equiv.), Et_3N (96 uL, 0.69 mmol, 2.5 equiv.), and 4-bromomethylbenzoic acid *tert*-butyl ester **2-24** (269 mg, 0.99 mmol, 3.6 equiv.) was added to the vial, which is then closed with a rubber cover and crimp seal. The microwave is set to heat to 66 °C for 2 h and the vial is placed into the reactor cavity and subjected to microwave irradiation. After reaction end, the vial is allowed to cool to ambient temperature. The crip and rubber cap are removed and the mixture was concentrated *in vacuo*. The resulting residue was purified by silica gel column chromatography (5% EtOAc in hexane) to afford **2-43** as a clear gel that solidified on standing (48 mg, 0.11 mmol) in 40% yield.

Characterization:

R_f = (EtOAc/Hexane 10:90): 0.52; **IR** (neat) v = 2962.55, 2932.66, 2893.04, 2859.25, 2361.39, 1712.00, 1538.69, 1502.32, 1472.31, 1391.92, 1366.61, 1291.31, 1255.34, 1163.62, 1107.79, 1012.49, 937.10, 813.11, 752.53, 648.16, 579.53, 485.42, 441.0 cm^{-1}; **^{1}H NMR** (500 MHz, $CDCl_3$) δ 8.39 (dd, *J* = 2.0, 0.9 Hz, 1H), 7.99 – 7.92 (m, 2H), 7.65 (dd, *J* = 8.6, 2.0 Hz, 1H), 7.33 – 7.28 (m, 2H), 6.55 (dd, *J* = 8.5, 0.9 Hz, 1H), 4.89 (s, 2H), 3.09 (s, 3H), 1.60 (s, 10H), 1.08 (d, *J* = 1.3 Hz, 18H); **^{13}C NMR** (126 MHz, $cdcl_3$) δ 165.63, 159.13, 153.12, 153.08, 143.44, 143.02, 142.98, 130.87, 129.77, 126.83, 113.97, 105.21, 80.87, 52.79, 35.95, 28.20, 27.28, 20.45, 20.35; **^{19}F NMR** (376 MHz, $cdcl_3$) δ -74.90, -189.50; **HRMS:** Calcd. for $C_{26}H_{40}FN_2O_2Si$ $[M+H]^+$ = 459.2838 m/z, found = 459.2819 m/z.

Compound 2-94:

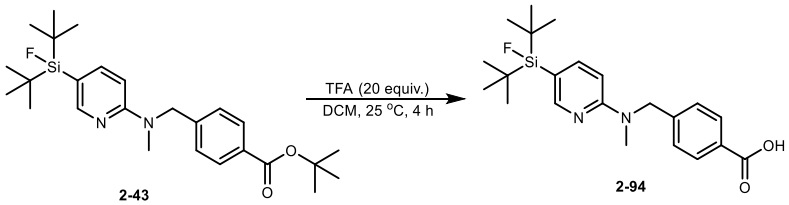

Procedure: A 10 mL round bottom flask equipped with a Teflon-coated stir bar and a rubber septum was charged with 3 mL of DCM, **2-43** (48 mg, 0.11 mmol, 1 equiv.), and trifluoroacetic acid (170 uL, 2.2 mmol, 20 equiv.). The mixture was then stirred at ambient temperature for 4 h then poured into 15 mL EtOAc and washed with saturated $NaHCO_3$ solution then concentrated *in vacuo*. The resulting residue was purified by silica gel column chromatography (60% EtOAc in hexane) to afford **2-94** as a white solid (37 mg, 0.092 mmol) in 84% yield.

Characterization:

R_f = (MeOH/DCM 10:90): 0.54; **IR** (neat) v = 2959.98, 2933.12, 2893.33, 2859.53, 2361.04, 1692.49, 1589.75, 1539.89, 1504.81, 1471.50, 1395.16, 1273.54, 1138.39, 1107.64, 1016.37, 937.12, 824.23, 813.13, 755.13, 649.48, 485.94 cm^{-1}; **^{1}H NMR** (500 MHz, $CDCl_3$) δ 8.40 (dd, *J* = 2.0, 0.9 Hz, 1H), 8.10 – 8.05 (m, 2H), 7.68 (dd, *J* = 8.5, 2.0 Hz, 1H), 7.37 (d, *J* = 8.1 Hz, 2H), 6.57 (dd, *J* = 8.6, 0.9 Hz, 1H), 4.93 (s, 2H), 3.12 (s, 3H), 1.08 (d, *J* = 1.2 Hz, 18H); **^{13}C NMR** (126 MHz, $CDCl_3$) δ 159.08, 153.03, 145.06, 143.13, 130.58, 127.07, 114.21, 105.29, 52.92, 36.10, 27.28, 20.46, 20.36; **^{19}F NMR** (471 MHz, $CDCl_3$) δ -189.45; **HRMS:** Calcd. for $C_{22}H_{32}FN_2O_2Si$ $[M+H]^+$ = 401.2212 m/z, found = 403.2214 m/z.

Compound 2-44:

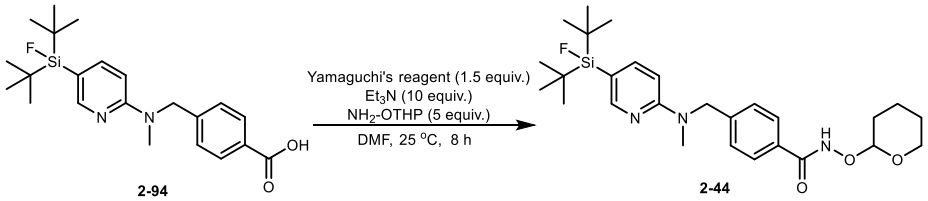

Procedure: A flame-dried 10 mL round bottom flask equipped with a Teflon-coated stir bar and a rubber septum flushed with nitrogen and charged with 5 mL of DMF and **2-94** (30 mg, 0.058 mmol 1 equiv.). While stirring, the mixture is cooled in an ice bath and triethylamine (81 uL, 0.58 mmol, 10 equiv.) is added, followed by Yamaguchi's reagent (14 uL, 0.087 mmol, 1.5 equiv.). The mixture is stirred at 0 °C for 15 min and NH_2OTHP (34 mg, 0.29 mmol, 5 equiv.) is added, and the solution is removed from the ice bath and stirred at ambient temperature for 8 h. The mixture is poured into 15 mL EtOAc and washed with 15 mL saturated aqueous $NaHCO_3$ followed by brine, and the retained organic phase then dried over Na_2SO_4, filtered, and concentrated *in vacuo*. The resulting oil is purified by silica gel column chromatography (35% EtOAc in hexane) to afford **2-44** as a clear oil that solidified on standing (24 mg, 0.049 mmol) in 84% yield.

Characterization:

R_f = (MeOH/DCM 10:90): 0.72; **IR** (neat) v = 3208.57, 2933.47, 2893.77, 2858.80, 1649.77, 1588.36, 1537.98, 1502.52, 1471.74, 1393.27, 1346.05, 1205.57, 1109.86, 1012.72, 935.96, 904.17, 814.07, 649.01, 579.59, 559.06, 537.93, 484.16 cm^{-1}; **^{1}H NMR** (500 MHz, $CDCl_3$) δ 8.80 (s, 1H), 8.38 (dd, *J* = 2.0, 0.9 Hz, 1H), 7.76 – 7.70 (m, 2H), 7.66 (dd, *J* = 8.5, 2.0 Hz, 1H), 7.36 – 7.30 (m, 2H), 6.55 (dd, *J* = 8.6, 1.0 Hz, 1H), 5.09 (t, *J* = 3.1 Hz, 1H), 4.89 (s, 2H), 4.02 (ddd, *J* = 11.9, 9.6, 3.0 Hz, 1H), 3.67 (dtd, *J* = 11.1, 4.2, 1.8 Hz, 1H), 3.09 (s, 3H), 1.97 – 1.83 (m, 3H), 1.73 – 1.59 (m, 3H), 1.08 (d, *J* = 1.2 Hz, 18H); **^{13}C NMR** (126 MHz, $CDCl_3$) δ 159.09, 153.12, 153.08, 143.26, 143.08, 143.05, 130.76, 127.53, 127.35, 114.25, 114.14, 105.22, 102.76, 62.73, 52.72, 36.01, 28.08, 27.28, 25.04, 20.46, 20.36, 18.6; **^{19}F NMR** (471 MHz, $CDCl_3$) δ -189.47; **HRMS:** Calcd. for $C_{27}H_{41}FN_3O_3Si$ $[M+H]^+$ = 502.2896 m/z, found = 502.2890 m/z.

Compound 2-39:

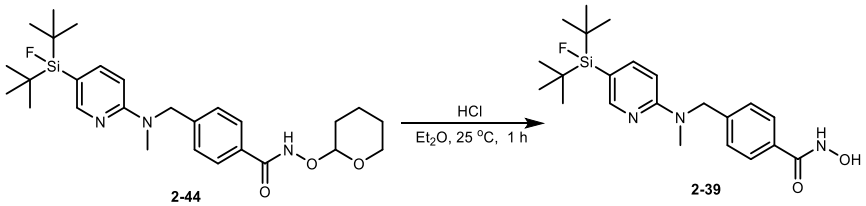

Procedure: A 5-dram glass vial equipped with a Teflon-coated stir bar and a rubber septum was charged with 3 mL diethyl ether and **2-44** (10 mg, 0.020 mmol, 1 equiv.). 3mL of 1 M ethereal HCl is added dropwise while stirring, and the resulting suspension was stirred at ambient temperature for 1 h then concentrated *in vacuo*. The resulting residue is purified by reverse phase HPLC (C-18 column, 5 – 95% MeCN in 0.1% aqueous formic acid) to afford the formate salt of **2-39** as a white solid (5 mg, 0.011 mmol) 54% yield.

Characterization: $\mathbf{R_f}$ = (MeOH/DCM 10:90): 0.62; **IR** (neat) v = 3212.43, 2959.98, 2933.12, 2893.33, 2859.53, 2361.04, 1692.49, 1589.75, 1539.89, 1504.81, 1471.50, 1395.16, 1273.54, 1138.39, 1107.64, 1016.37, 937.12, 824.23, 813.13, 755.13, 649.48, 485.94 cm^{-1}; **^{1}H NMR** (500 MHz, MeOD) δ 8.03 – 7.97 (m, 2H), 7.82 – 7.76 (m, 2H), 7.44 – 7.39 (m, 2H), 7.18 (d, *J* = 9.2 Hz, 1H), 4.98 (s, 2H), 3.32 (s, 3H), 1.11 (d, *J* = 1.2 Hz, 18H); **^{13}C NMR** (126 MHz, MeOD) δ 159.18, 152.37, 152.33, 142.92, 142.88, 126.84, 126.58, 113.60, 113.49, 105.76, 52.35, 35.32, 26.31, 19.85, 19.75; **^{19}F NMR** (376 MHz, cd_3od) δ -190.34; **HRMS:** Calcd. for $C_{22}H_{33}FN_3O_2Si$ $[M+H]^+$ = 418.2321 m/z, found = 418.2306 m/z.

Compound 2-44:

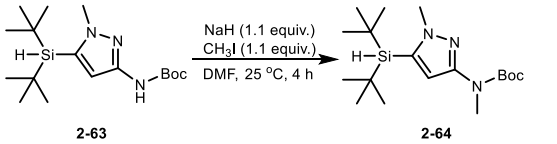

2-63 **2-64**

Chemical Formula: $C_{18}H_{35}N_3O_2Si$
Exact Mass: 353.25

Procedure: A flame-dried 50 mL round bottom flask equipped with a Teflon-coated stir bar and a rubber septum was charged with 20 mL dry DMF. The reaction vessel was evacuated and backfilled with N_2, and **2-43** (460 mg, 1.35 mmol, 1 equiv.) was added followed by sodium hydride (64 mg, 1.38 mmol, 1.1 equiv.). The mixture was then stirred at ambient temperature for 1 h and iodomethane (92 uL, 1.38 mmol, 1.1 equiv.) was added dropwise. The resulting mixture was stirred for 4 h at ambient temperature under N_2 then quenched with 30 mL of cold water. The resulting heterogeneous, biphasic reaction mixture was then extracted with EtOAc (25 mL x 3). The combined organic phases were washed with 25 mL of brine then dried over Na_2SO_4, filtered, and concentrated *in vacuo*. The resulting residue was purified by silica gel column chromatography (10% EtOAc in hexanes) to afford **2-44** as an oil (315 mg, 0.85 mmol) in 63% yield.

Characterization:

R_f = (EtOAc/Hexane 10:90): 0.58; **IR** (neat) v = 2964.74, 2930.69, 2890.53, 2857.47, 2113.74, 1702.53, 1516.82, 1469.14, 1453.41, 1425.03, 1404.76, 1391.35, 1365.34, 1323.57, 1254.42, 1222.94, 1145.53, 1081.55, 1012.54, 819.56, 799.80, 766.36, 625.41, 584.91 cm^{-1}; **^{1}H NMR** (500 MHz, $CDCl_3$) δ 6.52 (s, 1H), 4.06 (s, 1H), 3.92 (s, 3H), 3.37 (s, 3H), 1.53 (s, 9H), 1.08 (s, 18H); **^{13}C NMR** (126 MHz, $CDCl_3$) δ 153.70, 150.49, 138.26, 80.67, 39.48, 34.47, 28.53, 28.45, 19.06; **HRMS:** Calcd. for $C_{18}H_{35}N_3O_2SiNa$ $[M+Na]^+$ = 376.2391 m/z, found = 376.2397 m/z.

Compound 2-65:

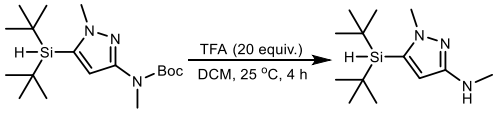

2-64 **2-65**

Chemical Formula: $C_{13}H_{27}N_3Si$
Exact Mass: 253.20

Procedure: A 10 mL round bottom flask equipped with a Teflon-coated stir bar and a rubber septum was charged with 5 mL of DCM, **2-64** (315 mg, 0.85 mmol, 1 equiv.), and trifluoroacetic acid (1.3 mL, 17 mmol, 20 equiv.). The mixture was then stirred at ambient temperature for 4 h then concentrated *in vacuo*. To the resulting clear liquid was added 1 mL toluene and the resulting mixture was concentrated *in vacuo*. The resulting residue was purified by silica gel column chromatography (40% EtOAc in hexane) to afford the TFA salt of **2-65** as a yellow gel that solidified on standing (262 mg, 0.71 mmol) in 84% yield.

Characterization:

$\mathbf{R_f}$ = (EtOAc/Hexane 50:50): 0.48; **IR** (neat) v = 3287.97, 2932.59, 2892.22, 2859.16, 2124.94, 1672.94, 1644.08, 1553.07, 1469.75, 1411.84, 1390.69, 1366.06, 1285.04, 1180.88, 1135.22, 1012.50, 820.20, 797.18, 719.16, 464.44, 443.23 cm^{-1}; **^{1}H NMR** (500 MHz, $CDCl_3$) δ 5.67 (s, 1H), 4.01 (s, 1H), 3.88 (s, 3H), 2.89 (s, 3H), 1.09 (s, 18H); **^{13}C NMR** (126 MHz, $CDCl_3$) δ 163.89, 155.16, 143.17, 96.86, 37.89, 31.02, 28.38, 19.00; **HRMS:** Calcd. for $C_{13}H_{38}N_3Si$ $[M+H]^+$ = 254.2047 m/z, found = 254.2056 m/z.

Compound 2-67:

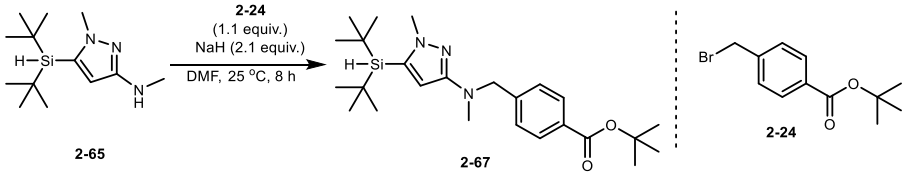

Chemical Formula: $C_{25}H_{41}N_3O_2Si$
Exact Mass: 443.30

Procedure: A flame-dried 25 mL round bottom flask equipped with a Teflon-coated stir bar and a rubber septum was charged with 10 mL dry DMF. The reaction vessel was evacuated and backfilled with N_2, and **2-65** (250 mg, 0.65 mmol, 1 equiv.) was added followed by sodium hydride (55 mg, 1.36 mmol, 2.1 equiv.). The mixture was then stirred at ambient temperature for 1 h and 4-bromomethylbenzoic acid *tert*-butyl ester (194 mg, 0.71 mmol, 1.1 equiv.). The resulting mixture was stirred for 8 h at ambient temperature under N_2 then quenched with 30 mL of cold water. The resulting heterogeneous, biphasic reaction mixture was then extracted with EtOAc (25 mL x 3). The combined organic phases were washed with 25 mL of brine then dried over Na_2SO_4, filtered, and concentrated *in vacuo*. The resulting residue was purified by silica gel column chromatography (10% EtOAc in hexanes) to afford **2-67** as an oil (210 mg, 0.54 mmol) in 83% yield.

Characterization:

R_f = (EtOAc/Hexane 20:80): 0.61; **IR** (neat) ν = 2962.29, 2929.60, 2889.00, 2855.86, 2361.26, 2112.85, 1711.72, 1610.88, 1538.11, 1468.94, 1432.19, 1413.07, 1365.88, 1289.43, 1254.46, 1163.40, 1113.99, 1017.90, 929.86, 849.61, 820.72, 804.29, 750.07, 707.72 cm^{-1}; **^{1}H NMR** (500 MHz, $CDCl_3$) δ 7.97 – 7.92 (m, 2H), 7.40 – 7.34 (m, 2H), 5.74 (s, 1H), 4.48 (s, 2H), 4.03 (s, 1H), 3.89 (s, 3H), 2.84 (s, 3H), 1.61 (s, 9H), 1.06 (s, 18H); **^{13}C NMR** (126 MHz, $CDCl_3$) δ 165.78, 158.85, 143.83, 139.29, 130.75, 129.51, 127.67, 98.95, 80.83, 56.45, 39.18, 37.43, 28.56, 28.22, 19.05; **HRMS:** Calcd. for $C_{25}H_{42}N_3O_2Si$ $[M+H]^+$ = 444.3041 m/z, found = 444.3047 m/z.

Compound 2-68:

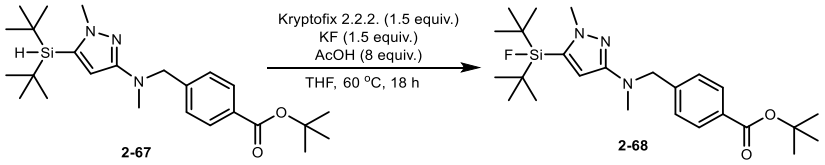

Chemical Formula: $C_{25}H_{40}FN_3O_2Si$
Exact Mass: 461.29

Procedure: A flame-dried 50 mL round bottom flask equipped with a Teflon-coated stir bar and a reflux condenser was charged with 20 mL dry THF and **2-67** (200 mg, 0.45 mmol, 1 equiv.), Kryptofix 2.2.2. (254 mg, 0.68 mmol, 1.5 equiv.), KF (39 mg, 0.68 mmol, 1.5 equiv.), and AcOH glacial (206 uL, 3.6 mmol, 8 equiv.) was added. The mixture is heated in an oil bath to 60 °C and stirred for 18 h then quenched with 30 mL of water. The resulting heterogeneous, biphasic reaction mixture was then extracted with EtOAc (25 mL x 3). The combined organic phases were washed with 25 mL of brine then dried over Na_2SO_4, filtered, and concentrated *in vacuo*. The resulting residue was purified by silica gel column chromatography (10% EtOAc in hexanes) to afford **2-68** as an oil (66 mg, 0.14 mmol) in 32% yield.

Characterization:

R_f = (EtOAc/Hexane 20:80): 0.60; **IR** (neat) v = 2964.22, 2934.17, 2892.48, 2860.16, 1711.78, 1611.04, 1540.83, 1471.45, 1434.12, 1412.43, 1391.56, 1366.39, 1289.48, 1254.20, 1163.27, 1114.09, 1018.04, 929.64, 837.23, 824.79, 814.23, 751.91, 658.03, 598.94, 504.13, 440.58 cm^{-1}; **^{1}H NMR** (400 MHz, $cdcl_3$) δ 7.92 (d, *J* = 8.0 Hz, 2H), 7.34 (d, *J* = 7.9 Hz, 2H), 5.70 (s, 1H), 4.44 (s, 2H), 3.88 (d, *J* = 1.4 Hz, 3H), 2.80 (s, 3H), 1.58 (s, 9H), 1.05 (s, 18H); **^{13}C NMR** (126 MHz, $CDCl_3$) δ 165.77, 159.12, 143.86, 130.75, 129.51, 127.67, 80.84, 56.42, 39.76, 37.44, 28.22, 26.94, 20.59, 20.49; **^{19}F NMR** (471 MHz, $CDCl_3$) δ -182.52; **HRMS:** Calcd. for $C_{25}H_{41}FN_3O_2Si$ $[M+H]^+$ = 462.2952 m/z, found = 462.2956 m/z.

Compound 2-95:

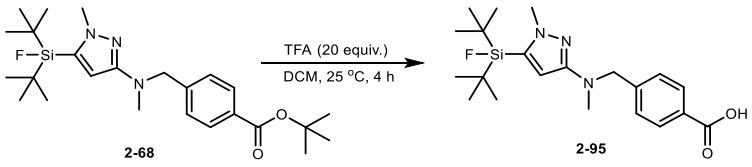

Chemical Formula: $C_{21}H_{32}FN_3O_2Si$
Exact Mass: 405.22

Procedure: A 10 mL round bottom flask equipped with a Teflon-coated stir bar and a rubber septum was charged with 3 mL of DCM, **2-68** (66 mg, 0.14 mmol, 1 equiv.), and trifluoroacetic acid (214 uL, 2.8 mmol, 20 equiv.). The mixture was then stirred at ambient temperature for 4 h then poured into 15 mL EtOAc and washed with saturated $NaHCO_3$ solution then concentrated *in vacuo*. The resulting residue was purified by silica gel column chromatography (40% EtOAc in hexane) to afford **2-95** as an off-white solid (45 mg, 0.11 mmol) in 79% yield.

Characterization:

R_f = (EtOAc/Hexane 50:50): 0.55; **IR** (neat) v = 2934.75, 2895.56, 2860.85, 2360.16, 1692.40, 1612.09, 1548.55, 1471.42, 1415.91, 1365.89, 1283.98, 1248.75, 1173.12, 1112.89, 1017.64, 930.83, 837.86, 824.85, 814.17, 752.96, 658.78, 597.61, 503.92, 439.74 cm^{-1}; **^{1}H NMR** (400 MHz, $cdcl_3$) δ 8.03 (d, *J* = 8.2 Hz, 2H), 7.40 (d, *J* = 8.0 Hz, 2H), 5.69 (s, 1H), 4.48 (s, 2H), 3.89 (d, *J* = 1.3 Hz, 3H), 2.85 (s, 3H), 1.05 (d, *J* = 1.0 Hz, 18H); **^{13}C NMR** (126 MHz, $cdcl_3$) δ 170.08, 159.08, 145.42, 130.29, 127.78, 99.14, 56.50, 37.66, 26.92, 20.58, 20.48; **^{19}F NMR** (471 MHz, $CDCl_3$) δ -182.52; **HRMS:** Calcd. for $C_{21}H_{33}FN_3O_2Si$ $[M+H]^+$ = 406.2321 m/z, found = 406.2320 m/z.

Compound 2-69:

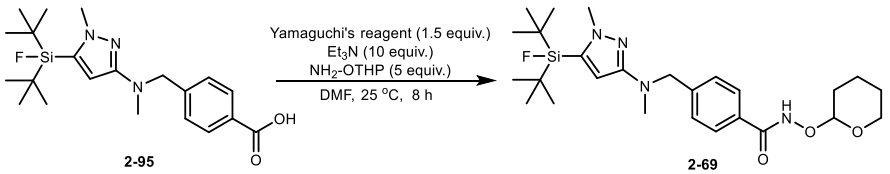

Chemical Formula: $C_{26}H_{41}FN_4O_3Si$
Exact Mass: 504.29

Procedure: A flame-dried 10 mL round bottom flask equipped with a Teflon-coated stir bar and a rubber septum flushed with nitrogen and charged with 5 mL of DMF and **2-95** (45 mg, 0.11 mmol 1 equiv.). While stirring, the mixture is cooled in an ice bath and triethylamine (155 uL, 1.1 mmol, 10 equiv.) is added, followed by Yamaguchi's reagent (25 uL, 0.16 mmol, 1.5 equiv.). The mixture is stirred at 0 °C for 15 min and NH_2OTHP (65 mg, 0.55 mmol, 5 equiv.) is added, and the solution is removed from the ice bath and stirred at ambient temperature for 8 h. The mixture is poured into 15 mL EtOAc and washed with 15 mL saturated aqueous $NaHCO_3$ followed by brine, and the retained organic phase then dried over Na_2SO_4, filtered, and concentrated *in vacuo*. The resulting oil is purified by silica gel column chromatography (3% MeOH in DCM) to afford **2-69** as a clear oil that solidified on standing (23 mg, 0.047 mmol) in 41% yield.

Characterization:

R_f = (MeOH/DCM 10:90): 0.71; **IR** (neat) v = 3214.84, 2936.06, 2894.95, 2860.35, 2359.35, 2323.52, 1652.83, 1612.03, 1542.05, 1491.33, 1471.44, 1437.04, 1411.88, 1365.14, 1284.15, 1204.53, 1113.36, 1038.89, 1012.53, 950.76, 903.78, 836.21, 824.35, 736.90, 657.82, 598.21, 502.67, 439.15 cm^{-1}; **^{1}H NMR** (400 MHz, cdcl$_3$) δ 8.78 (s, 1H), 7.73 – 7.66 (m, 2H), 7.37 (d, *J* = 8.0 Hz, 2H), 5.69 (s, 1H), 5.08 (t, *J* = 3.0 Hz, 1H), 4.44 (s, 2H), 4.00 (dd, *J* = 11.4, 8.9 Hz, 1H), 3.88 (d, *J* = 1.3 Hz, 3H), 3.69 – 3.59 (m, 1H), 2.80 (s, 3H), 1.88 (q, *J* = 11.9 Hz, 3H), 1.05 (d, *J* = 1.1 Hz, 18H); **^{13}C NMR** (126 MHz, $CDCl_3$) δ 159.04, 143.59, 130.64, 128.08, 127.29, 102.71, 99.18, 62.68, 56.31, 39.73, 39.67, 37.52, 28.10, 26.93, 25.05, 20.58, 20.48, 18.67; **^{19}F NMR** (376 MHz, cdcl$_3$) δ -182.54; **HRMS:** Calcd. for $C_{26}H_{42}FN_4O_3Si$ $[M+H]^+$ = 505.3005 m/z, found = 505.3005 m/z.

Compound 2-46:

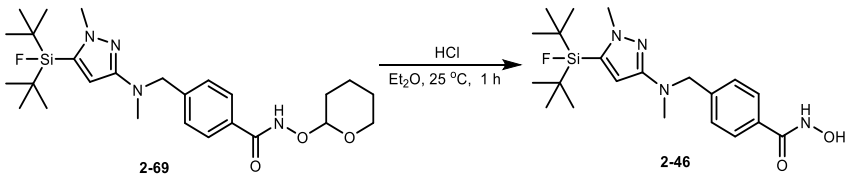

Chemical Formula: $C_{21}H_{33}FN_4O_2Si$
Exact Mass: 420.24

Procedure: A 5-dram glass vial equipped with a Teflon-coated stir bar and a rubber septum was charged with 3 mL diethyl ether and **2-69** (10 mg, 0.020 mmol, 1 equiv.). 3mL of 1 M ethereal HCl is added dropwise while stirring, and the resulting suspension was stirred at ambient temperature for 1 h then concentrated *in vacuo*. The resulting residue is purified by reverse phase HPLC (C-18 column, 5 – 95% MeCN in 0.1% aqueous formic acid) to afford the formate salt of **2-46** as a white solid (6 mg, 0.014 mmol) 71% yield.

Characterization:

R_f = (MeOH/DCM 10:90): 0.41; **IR** (neat) v = 2965.03, 2934.47, 2893.74, 2860.68, 1712.11, 1611.24, 1541.65, 1471.69, 1434.32, 1412.60, 1391.65, 1366.50, 1254.14, 1163.01, 1113.47, 1018.06, 929.57, 836.85, 824.26, 813.77, 751.49, 657.33, 597.95, 503.12, 439.86 cm^{-1}; **^{1}H NMR** (500 MHz, MeOD) δ 7.71 (d, *J* = 7.9 Hz, 2H), 7.38 (d, *J* = 7.9 Hz, 2H), 5.82 (s, 1H), 4.48 (s, 2H), 3.86 (d, *J* = 1.2 Hz, 3H), 2.87 (s, 2H), 1.07 (d, *J* = 1.2 Hz, 18H); **^{13}C NMR** (126 MHz, MeOD) δ 166.58, 159.04, 142.98, 130.82, 127.55, 126.80, 99.22, 55.80, 36.74, 25.91, 20.00, 19.90; **^{19}F NMR** (471 MHz, MeOD) δ -183.10; **HRMS:** Calcd. for $C_{21}H_{34}FN_4O_2Si$ $[M+H]^+$ = 421.2430 m/z, found = 421.2414 m/z.

2. Phenyl SiFAHA

Compound 2-73:

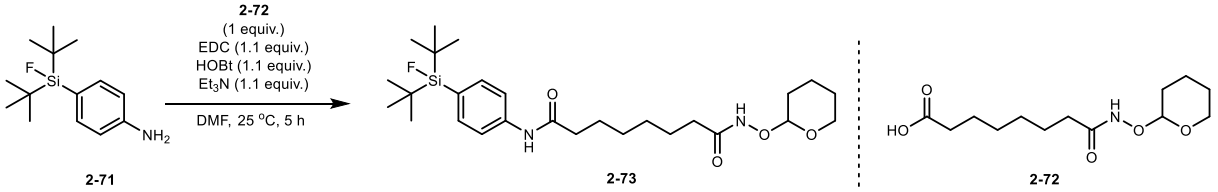

Procedure: A flame-dried 10 mL round bottom flask equipped with a Teflon-coated stir bar and a rubber septum flushed with nitrogen and charged with 5 mL of DMF and **2-72** (54 mg, 0.20 mmol 1 equiv.). While stirring, the mixture is cooled in an ice bath and EDC (34 mg, 0.22 mmol, 1.1 equiv.) is added, followed by **2-71** (50 mg, 0.22 mmol, 1 equiv.) along with Et_3N (30 uL, 0.22 mmol, 1.1 equiv.). The mixture is stirred at 0 °C for 15 min and HOBt (29 mg, 0.22 mmol, 1.1 equiv.) is added, and the solution is removed from the ice bath and stirred at ambient temperature for 5 h. The mixture is poured into 15 mL EtOAc and washed with 15 mL saturated aqueous $NaHCO_3$ followed by brine, and the retained organic phase then dried over Na_2SO_4, filtered, and concentrated *in vacuo*. The resulting oil is purified by silica gel column chromatography (3% MeOH in DCM) to afford **2-73** as a white solid (23 mg, 0.098 mmol) in 49% yield.

Characterization:

R_f = (MeOH/DCM 2:98): 0.22; **IR** (neat) ν = 2967.88, 2935.02, 2893.87, 1714.47, 1658.50, 1574.79, 1552.26, 1473.74, 1447.02, 1363.93, 1287.40, 1222.70, 1163.21, 1116.28, 1072.70, 1014.84, 924.19, 824.98, 809.51, 732.99, 703.25, 645.96, 624.17, 583.30, 489.99, 444.37 cm^{-1}; **^{1}H NMR** (500 MHz, $CDCl_3$) δ 8.37 (s, 1H), 7.58 (s, 4H), 7.41 (s, 1H), 4.98 (s, 1H), 3.97 (s, 1H), 3.66 (ddt, *J* = 9.5, 5.6, 2.8 Hz, 1H), 2.38 (t, *J* = 7.4 Hz, 2H), 2.16 (s, 2H), 1.87 – 1.65 (m, 5H), 1.61 (d, *J* = 4.4 Hz, 1H), 1.42 (dd, *J* = 7.2, 3.7 Hz, 5H), 1.28 (s, 2H), 1.07 (d, *J* = 1.1 Hz, 18H); **^{13}C NMR** (126 MHz, $CDCl_3$) δ 171.80, 170.68, 162.57, 139.52, 134.79, 134.76, 128.70, 128.59, 118.75, 102.44, 62.51, 37.35, 36.52, 33.05, 29.71, 28.42, 28.31, 27.99, 27.32, 25.23, 25.00, 20.33, 20.23, 18.53; **^{19}F NMR** (471 MHz, $CDCl_3$) δ -188.86; **HRMS:** Calcd. for $C_{21}H_{34}FN_4O_2Si$ $[M+H]^+$ = 421.2430 m/z, found = 421.2414 m/z.

Compound 2-74:

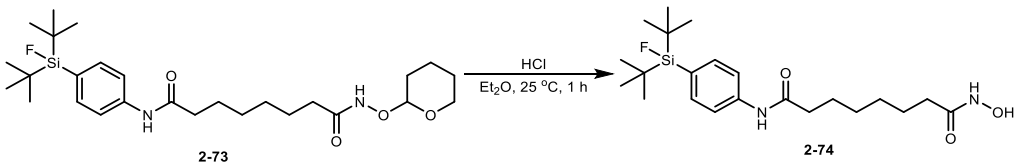

2-73

2-74

Chemical Formula: $C_{22}H_{37}FN_2O_3Si$
Exact Mass: 424.26

Procedure: A 5-dram glass vial equipped with a Teflon-coated stir bar and a rubber septum was charged with 3 mL diethyl ether and **2-73** (10 mg, 0.020 mmol, 1 equiv.). 3mL of 1 M ethereal HCl is added dropwise while stirring, and the resulting suspension was stirred at ambient temperature for 1 h then concentrated *in vacuo*. The resulting residue is purified by reverse phase flash chromatography (C-18 column, 5 – 95% MeCN in 0.1% aqueous formic acid) to afford the formate salt of **2-74** as a white solid (8 mg, 0.016 mmol) 82% yield.

Characterization:

R_f = (MeOH/DCM 10:90): 0.52; **IR** (neat) ν = 2934.42, 2850.93, 2050.85, 1660.77, 1574.71, 1471.00, 1429.80, 1391.74, 1365.95, 1090.18, 1012.88, 858.54, 825.32, 661.76, 602.77, 507.96 cm^{-1}; **^{1}H NMR** (400 MHz, cd_3od) δ 7.60 (d, *J* = 8.0 Hz, 2H), 7.54 (d, *J* = 8.0 Hz, 2H), 2.38 (t, *J* = 7.5 Hz, 2H), 2.09 (t, *J* = 7.4 Hz, 2H), 1.74 – 1.59 (m, 5H), 1.40 (s, 4H), 1.05 (s, 18H); **^{13}C NMR** (126 MHz, MeOD) δ 173.39, 171.57, 168.75, 140.02, 134.32, 134.28, 118.89, 78.14, 77.88, 77.62, 53.40, 36.51, 32.29, 28.50, 28.43, 26.41, 25.29, 25.18, 19.76, 19.66; **^{19}F NMR** (376 MHz, cd_3od) δ -189.82; **HRMS:** Calcd. for $C_{22}H_{37}FN_2O_3SiNa$ $[M+Na]^+$ = 447.2450 m/z, found = 447.2440 m/z.

Compound 2-59:

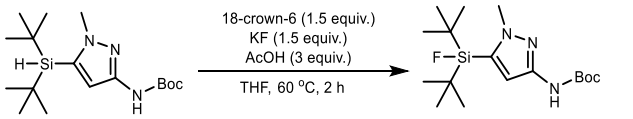

2-63 **2-59**

Chemical Formula: $C_{17}H_{32}FN_3O_2Si$
Exact Mass: 357.22

Procedure: A flame-dried 50 mL round bottom flask equipped with a Teflon-coated stir bar and a reflux condenser was charged with 20 mL dry THF and **2-63** (315 mg, 0.93 mmol, 1 equiv.), 18-crown-6 (367 mg, 1.4 mmol, 1.5 equiv.), KF (81 mg, 1.4 mmol, 1.5 equiv.), and AcOH glacial (159 uL, 2.8 mmol, 3 equiv.) was added. The mixture is heated in an oil bath to 60 °C and stirred for 2 h then quenched with 30 mL of water. The resulting heterogeneous, biphasic reaction mixture was then extracted with EtOAc (25 mL x 3). The combined organic phases were washed with 25 mL of brine then dried over Na_2SO_4, filtered, and concentrated *in vacuo*. The resulting residue was purified by silica gel column chromatography (25% EtOAc in hexanes) to afford **2-59** as a clear gel that solidified on standing (303 mg, 0.85 mmol) in 91% yield.

Characterization:

R_f = (MeOH/DCM 10:90): 0.52; **IR** (neat) v = 3238.37, 3119.83, 3061.67, 2966.36, 2935.03, 2898.50, 1726.78, 1574.95, 1472.14, 1427.93, 1391.27, 1366.65, 1243.53, 1166.09, 1153.56, 1096.93, 1003.14, 825.11, 660.94, 600.80, 517.13, 439.78 cm^{-1}; **^{1}H NMR** (500 MHz, $CDCl_3$) δ 6.66 (s, 1H), 3.93 (t, *J* = 1.4 Hz, 3H), 1.53 (s, 9H), 1.10 (d, *J* = 1.1 Hz, 18H); **^{13}C NMR** (126 MHz, $CDCl_3$) δ 152.56, 146.79, 103.86, 39.84, 39.77, 29.72, 28.39, 26.89, 20.60, 20.51; **^{19}F NMR** (471 MHz, $CDCl_3$) δ -182.35; **HRMS:** Calcd. for $C_{17}H_{33}FN_3O_2Si$ $[M+H]^+$ = 358.2321 m/z, found = 358.2316 m/z.

Compound 2-96:

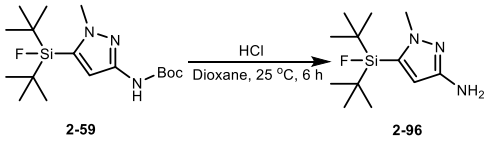

2-59 **2-96**

Chemical Formula: $C_{12}H_{24}FN_3Si$
Exact Mass: 257.17

Procedure: A 10 mL round bottom flask equipped with a Teflon-coated stir bar and a rubber septum was charged with **2-59** (85 mg, 0.24 mmol, 1 equiv.), and 5 mL of 4 M HCl solution in dioxane was added to flask. The mixture was then stirred at ambient temperature for 4 h then concentrated *in vacuo*. The resulting residue was purified by silica gel column chromatography (40% EtOAc in hexane) to afford **2-96** as an off-white solid (47 mg, 0.17 mmol) in 73% yield.

Characterization:

R_f = (EtOAc/Hexane 60:0): 0.70; **IR** (neat) v = 3429.37, 3328.57, 3212.27, 2959.33, 2933.84, 2896.38, 2860.48, 1696.53, 1614.68, 1535.93, 1470.82, 1434.60, 1413.64, 1283.05, 1092.70, 1010.31, 936.49, 837.23, 824.96, 814.37, 769.88, 658.26, 597.39, 509.72, 438.82 cm^{-1}; **^{1}H NMR** (500 MHz, $CDCl_3$) δ 5.78 (s, 1H), 3.85 (d, *J* = 1.4 Hz, 3H), 1.07 (d, *J* = 1.3 Hz, 18H); **^{13}C NMR** (126 MHz, $CDCl_3$) δ 153.57, 137.00 (d, *J* = 14.6 Hz), 101.55 (d, *J* = 4.9 Hz), 39.44 (d, *J* = 8.2 Hz), 26.86, 20.55, 20.45; **^{19}F NMR** (471 MHz, $CDCl_3$) δ -182.66; **HRMS:** Calcd. for $C_{12}H_{25}FN_3Si$ $[M+H]^+$ = 258.1796 m/z, found = 258.1786 m/z.

Compound 2-75:

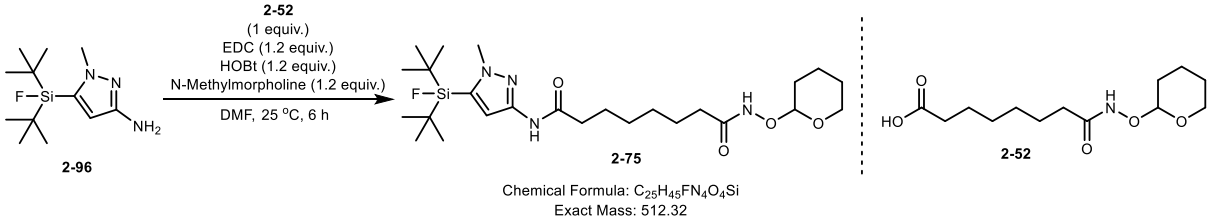

Procedure: A flame-dried 10 mL round bottom flask equipped with a Teflon-coated stir bar and a rubber septum flushed with nitrogen and charged with 5 mL of DMF and **2-52** (26 mg, 0.11 mmol 1 equiv.). While stirring, the mixture is cooled in an ice bath and EDC (18 mg, 0.12 mmol, 1.2 equiv.) is added, followed by **2-96** (32 mg, 0.11 mmol, 1 equiv.) along with *N*-methyl morpholine (13 uL, 0.12 mmol, 1.2 equiv.). The mixture is stirred at 0 °C for 15 min and HOBt (16 mg, 0.12 mmol, 1.2 equiv.) is added, and the solution is removed from the ice bath and stirred at ambient temperature for 5 h. The mixture is poured into 15 mL EtOAc and washed with 15 mL saturated aqueous $NaHCO_3$ followed by brine, and the retained organic phase then dried over Na_2SO_4, filtered, and concentrated *in vacuo*. The resulting oil is purified by silica gel column chromatography (3% MeOH in DCM) to afford **2-75** as a white solid (38 mg, 0.074 mmol) in 64% yield.

Characterization:

R_f = (MeOH/DCM 5:95): 0.42; **IR** (neat) ν = 3225.84, 3118.24, 3061.72, 2935.03, 2860.40, 1657.38, 1568.77, 1503.16, 1470.34, 1425.91, 1286.41, 1204.66, 1114.39, 1089.65, 1037.50, 1021.10, 949.47, 896.64, 874.46, 837.31, 824.72, 734.60, 661.37, 602.50, 509.52, 439.79 cm^{-1}; **^{1}H NMR** (400 MHz, $cdcl_3$) δ 8.79 (s, 1H), 8.08 (s, 1H), 6.89 (s, 1H), 4.98 (s, 1H), 3.91 (s, 3H), 3.61 (d, *J* = 11.2 Hz, 1H), 2.32 (t, *J* = 7.3 Hz, 2H), 2.08 (s, 2H), 1.79 (d, *J* = 10.0 Hz, 1H), 1.35 (s, 5H), 1.07 (s, 18H); **^{13}C NMR** (126 MHz, $CDCl_3$) δ 170.48, 146.47, 105.58, 102.31, 62.38, 39.89, 39.82, 36.62, 33.02, 29.71, 28.36, 27.96, 26.84, 25.11, 25.02, 20.60, 20.50, 18.44; **^{19}F NMR** (471 MHz, $CDCl_3$) δ -182.40; **HRMS:** Calcd. for $C_{25}H_{45}FN_4O_4SiNa$ $[M+Na]^+$ = 535.3086 m/z, found = 535.3093 m/z.

Compound 2-76:

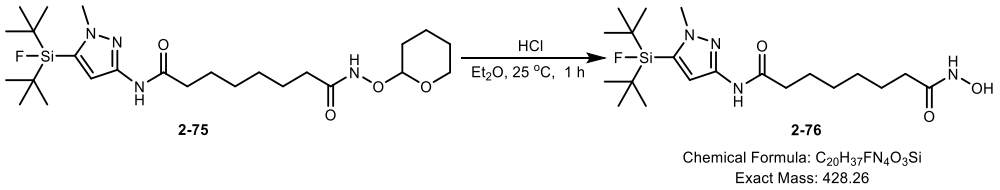

Procedure: A 5-dram glass vial equipped with a Teflon-coated stir bar and a rubber septum was charged with 3 mL diethyl ether and **2-75** (12 mg, 0.023 mmol, 1 equiv.). 3mL of 1 M ethereal HCl is added dropwise while stirring, and the resulting suspension was stirred at ambient temperature for 1 h then concentrated *in vacuo*. The resulting residue is purified by reverse phase flash chromatography (C-18 column, 5 – 95% MeCN in 0.1% aqueous formic acid) to afford the formate salt of **2-76** as a white solid (8 mg, 0.018 mmol) 79% yield.

Characterization:

R_f = (MeOH/DCM 10:90): 0.47; **IR** (neat) v = 3258.65, 2934.42, 2860.93, 2050.85, 1660.77, 1574.71, 1471.00, 1426.80, 1391.74, 1365.95, 1090.18, 1012.88, 838.57, 825.35, 661.76, 602.77, 507.91, 441.12 cm^{-1}; **^{1}H NMR** (400 MHz, cd_3od) δ 8.54 (s, 1H), 6.80 (s, 1H), 3.90 (s, 3H), 2.36 (t, *J* = 7.4 Hz, 2H), 2.09 (t, *J* = 7.3 Hz, 1H), 1.74 – 1.55 (m, 3H), 1.38 (s, 5H), 1.08 (s, 18H); **^{13}C NMR** (201 MHz, MeOD) δ 172.61 (d, *J* = 11.1 Hz), 146.54, 136.22, 105.74, 38.84, 35.77 (d, *J* = 18.2 Hz), 32.27, 28.47, 28.39, 25.86, 25.19 (d, *J* = 8.0 Hz), 20.00 (d, *J* = 11.9 Hz); **^{19}F NMR** (376 MHz, cd_3od) δ -183.27; **HRMS:** Calcd. for $C_{20}H_{38}FN_4O_3Si$ $[M+H]^+$ = 429.2692 m/z, found = 429.2686 m/z.

Compound 2-77:

Chemical Formula: $C_{19}H_{33}FN_2O_4Si$
Exact Mass: 400.22

Procedure: A flame-dried 10 mL round bottom flask equipped with a Teflon-coated stir bar and a rubber septum flushed with nitrogen and charged with 5 mL of DCM and **2-17** (200 mg, 0.52 mmol 1 equiv.) along with mCPBA (188 mg, 1.09 mmol, 2.1 equiv.). The solution is stirred at ambient temperature for 18 h then washed with 15 mL saturated aqueous $NaHCO_3$ followed by brine, and retaining the organic phase. The aqueous phases were each extracted 3 x with 10 mL DCM, which was retaining and combined with the other organic phases, then dried over Na_2SO_4, filtered, and concentrated *in vacuo*. The resulting oil is purified by silica gel column chromatography (40% EtOAc in hexane) to afford **2-77** as a clear gel (182 mg, 0.046 mmol) in 87% yield

Characterization:

R_f = (EtOAc/hex 60:40): 0.82; **IR** (neat) ν = 2977.69, 2954.91, 2932.70, 2859.13, 1726.35, 1608.01, 1564.82, 1516.36, 1458.58, 1394.26, 1366.47, 1266.54, 1174.77, 1146.52, 1048.19, 996.93, 901.57, 824.13, 804.88, 765.95, 655.95, 610.78, 582.50, 488.11, 462.60, 450.39 cm^{-1}; **^{1}H NMR** (500 MHz, $CDCl_3$) δ 9.49 (s, 1H), 8.22 (s, 1H), 7.76 (d, *J* = 1.0 Hz, 1H), 3.91 (s, 3H), 1.56 (s, 10H), 1.05 (d, *J* = 1.4 Hz, 18H); **^{13}C NMR** (126 MHz, $CDCl_3$) δ 161.96, 161.92, 151.63, 146.01, 142.51, 142.45, 112.68, 112.55, 94.61, 82.47, 55.61, 28.12, 27.13, 20.60, 20.50; **^{19}F NMR** (471 MHz, $CDCl_3$) δ -185.72; **HRMS:** Calcd. for $C_{19}H_{34}FN_2O_4Si$ $[M+H]^+$ = 401.2266 m/z, found = 401.2270 m/z.

Compound 2-78:

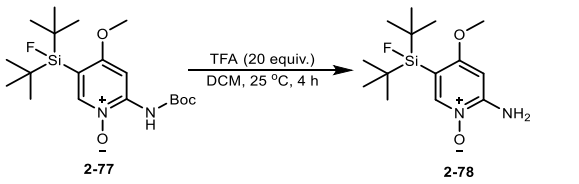

Procedure: A 10 mL round bottom flask equipped with a Teflon-coated stir bar and a rubber septum was charged with 3 mL of DCM, **2-77** (137 mg, 0.34 mmol, 1 equiv.), and trifluoroacetic acid (526 uL, 6.9 mmol, 20 equiv.). The mixture was then stirred at ambient temperature for 4 h then concentrated *in vacuo*. To the resulting clear liquid was added 1 mL toluene and the resulting mixture was concentrated *in vacuo*. The resulting residue was purified by silica gel column chromatography (10% MeOH in DCM) to afford the TFA salt of **2-78** as an off-white solid (128 mg, 0.31 mmol) in 91% yield.

Characterization:

R_f = (MeOH/DCM 15:85): 0.53; **IR** (neat) v = 3401.72, 3284.31, 2956.08, 2935.55, 2892.86, 2860.61, 1634.29, 1562.53, 1460.53, 1407.20, 1364.51, 1270.77, 1224.57, 1183.23, 1075.67, 998.47, 824.48, 808.55, 663.89, 644.82, 609.19, 474.18, 457.601 cm^{-1}; **^{1}H NMR** (500 MHz, $CDCl_3$) δ 8.00 (s, 1H), 6.66 (s, 2H), 6.36 – 6.33 (m, 1H), 3.80 (s, 3H), 1.01 (d, *J* = 1.4 Hz, 18H); **^{13}C NMR** (126 MHz, $CDCl_3$) δ 162.98, 162.95, 152.09, 143.14, 143.08, 108.06, 107.94, 90.58, 55.32, 27.16, 27.15, 20.55, 20.45; **^{19}F NMR** (471 MHz, $CDCl_3$) δ -75.15, -185.85; **HRMS:** Calcd. for $C_{14}H_{36}FN_2O_2Si$ $[M+H]^+$ = 301.1742 m/z, found = 301.1736 m/z.

Compound 2-79:

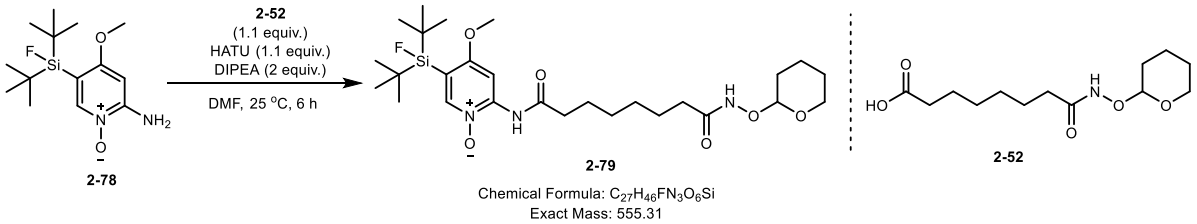

Chemical Formula: $C_{27}H_{46}FN_3O_6Si$
Exact Mass: 555.31

Procedure: A flame-dried 20 mL round bottom flask equipped with a Teflon-coated stir bar and a rubber septum flushed with nitrogen and charged with 15 mL of DMF and **2-52** (80 mg, 0.29 mmol 1.1 equiv.). While stirring, DIPEA (92 uL, 0.53 mmol, 2 equiv.) is added, followed by HATU (111 mg, 0.29 mmol, 1.1 equiv.). The mixture is stirred at ambient temperature 15 min then **2-78** (107 mg, 0.26 mmol, 1 equiv.). is added, stirred at ambient temperature for 6 h then poured into 20 mL of distilled water. The resulting heterogeneous, biphasic reaction mixture was then extracted with EtOAc (15 mL x 3) and the combined organic phase was washed with 15 mL saturated aqueous $NaHCO_3$ followed by 15 mL of brine brine, then dried over Na_2SO_4, filtered, and concentrated *in vacuo*. The resulting oil is purified by silica gel column chromatography (5% MeOH in DCM) to afford **2-79** as an oil that solidified on standing (132 mg, 0.024 mmol) in 82% yield.

Characterization:

R_f = (MeOH/DCM 15:85): 0.80; **IR** (neat) v = 3165.52, 3131.94, 2935.39, 2860.31, 1700.06, 1668.99, 1605.99, 1561.44, 1504.56, 1459.63, 1392.12, 1281.07, 1239.71, 1194.07, 1179.67, 1114.76, 992.92, 897.51, 825.05, 809.44, 731.52, 644.94, 600.34, 481.09 cm^{-1}; **^{1}H NMR** (500 MHz, $CDCl_3$) δ 10.23 (s, 1H), 9.01 – 8.98 (m, 1H), 8.25 (s, 1H), 8.07 (d, *J* = 1.0 Hz, 1H), 4.97 (s, 1H), 3.98 (s, 1H), 3.92 (s, 3H), 3.67 – 3.59 (m, 1H), 2.56 (t, *J* = 7.2 Hz, 2H), 2.14 (s, 2H), 1.87 – 1.67 (m, 4H), 1.44 (tt, *J* = 7.9, 3.7 Hz, 4H), 1.06 (d, *J* = 1.3 Hz, 18H); **^{13}C NMR** (126 MHz, $CDCl_3$) δ 172.42, 162.26, 145.22, 142.31, 142.25, 114.12, 102.41, 96.12, 62.47, 55.74, 37.75, 32.98, 28.43, 28.04, 27.12, 25.04, 24.77, 20.61, 20.52, 18.59; **^{19}F NMR** (471 MHz, $CDCl_3$) δ -185.60; **HRMS:** Calcd. for $C_{27}H_{47}FN_3O_6Si$ $[M+H]^+$ = 556.3213 m/z, found = 556.3208 m/z.

Compound 2-80:

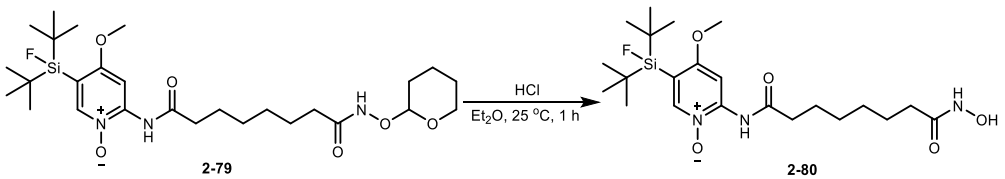

2-79

2-80

Chemical Formula: $C_{22}H_{38}FN_3O_5Si$
Exact Mass: 471.26

Procedure: A 5-dram glass vial equipped with a Teflon-coated stir bar and a rubber septum was charged with 3 mL diethyl ether and **2-79** (26 mg, 0.023 mmol, 1 equiv.). 3mL of 1 M ethereal HCl is added dropwise while stirring, and the resulting suspension was stirred at ambient temperature for 1 h then concentrated *in vacuo*. The resulting residue is purified by reverse phase flash chromatography (C-18 column, 5 – 95% MeCN in 0.1% aqueous formic acid) to afford the formate salt of **2-80** as a white solid (8 mg, 0.018 mmol) 79% yield.

Characterization:

R_f = (MeOH/DCM 15:85): 0.62; **IR** (neat) v = 3180.49, 2934.93, 2860.31, 2359.36, 2341.74, 2324.03, 1704.60, 1660.95, 1637.29, 1607.57, 1561.51, 1506.20, 1459.34, 1393.67, 1365.24, 1279.59, 1240.18, 1194.75, 1180.58, 1127.51, 993.81, 825.90, 810.44, 749.23, 667.29, 481.80 cm^{-1}; **^{1}H NMR** (500 MHz, MeOD) δ 8.57 (s, 0H), 8.21 (d, *J* = 1.0 Hz, 1H), 8.09 (s, 1H), 3.98 (s, 3H), 2.64 (t, *J* = 7.4 Hz, 2H), 2.12 (t, *J* = 7.4 Hz, 2H), 1.76 (p, *J* = 7.2 Hz, 2H), 1.66 (p, *J* = 7.4 Hz, 2H), 1.42 (dtd, *J* = 17.4, 8.1, 4.2 Hz, 3H), 1.09 (d, *J* = 1.3 Hz, 18H); **^{13}C NMR** (126 MHz, MeOD) δ 173.27, 171.50, 164.02, 145.79, 142.06, 141.99, 96.56, 55.18, 36.62, 32.25, 28.38, 28.29, 26.14, 25.14, 24.52, 20.01, 19.91; **^{19}F NMR** (471 MHz, MeOD) δ -186.69; **HRMS:** Calcd. for $C_{22}H_{39}FN_3O_5Si$ $[M+H]^+$ = 472.2637 m/z, found = 472.2634 m/z.

HDAC6 fluorogenic inhibition assay

The procedure for *in vitro* HDAC6 binding assay was adapted from previous reports[7, 8]. All assays were performed using black medium binding Fluorotrac 200 96-well plates from Greiner Bio-One. Fluorescence measurements were performed using Molecular Devices SpectraMax i3x plate reader set to 10 scans per well with excitation and emission wavelengths of 360 and 460 nm respectively and 15 nm bandwidth. Assay buffer was formulated using 50 mM Tris base, 137 mM NaCl, 2.7 mM KCl, 1 mM $MgCl_2$ in distilled water and adjusted to pH 8.0 using 1M HCl, then adding 0.5 mg/mL bovine serum albumin and 1.7 vol% DMSO. The buffer was passed through a 50 µM filter and used immediately. Human recombinant HDAC6 was purchased from the Cayman Chemical Company (>90% as determined by SDS-PAGE), was divided into 6.25 µg aliquots and stored at –80 °C. Aliquot were thawed on ice and diluted with buffer to provide a stock solution of 4 ng/µL the day of use. HDAC substrate Ac-Leu-Gly-Lys(Ac)-AMC synthesized through published procedure[7] was dissolved in DMSO to 8.0 mM then diluted to 8.0 µM with assay buffer. Trypsin from porcine pancreas (25 g/L in 0.9% NaCl from Sigma Aldrich) was thawed on ice then diluted to 0.4 mg/mL with assay buffer immediately before use. Dilution series of inhibitor candidates were prepared at 12 concentrations from 50 µM DMSO stock solutions with assay buffer. Due to poor substrate affinity of **2-22**, it was prepared at 12 concentrations from 500 µM DMSO stock solution.

Plates were set up with duplicate or triplicate measurements of HDAC inhibitors at 12 concentrations each, along with 6 wells of control. Negative controls received 25 µL of assay buffer, and 25 µL fluorogenic substrate solution, while positive controls received 10 µL of buffer, 15 µL of HDAC enzyme solution, and 25 µL of fluorogenic substrate solution. Other wells received 10 µL of inhibitor solution and 15 µL of HDAC enzyme solution. The assays were initiated by addition of 25 µL of substrate (final concentration of 3.75 µM) to all wells. The plate was gently tapped and incubated at 37 °C for 30 mins, then 50 µL of trypsin solution was added to all wells and incubation was continued for a further 30 mins at 25 °C. Endpoint fluorescence measurements were then recorded and IC_{50} values were calculated by nonlinear regression using a sigmoidal 4PL analysis with GraphPad Prism 8.2. The IC_{50} were converted to K_i using Cheng-Prusoff equation $K_i = IC_{50}/(1+ [S]/K_m)$ where [S] is the concentration of the substrate and K_m is the affinity constant of the substrate at 6 µM for HDAC6 according to literature[19].

Manual radiolabeling protocol #1

Irradiated cyclotron target carrying [^{18}F]fluoride in ^{18}O-enriched water was moved using negative pressure and passed through a pre-conditioned Sep-Pak Light QMA cartridge (Waters) as an aqueous solution, and the water was collected in a waste bottle. Trapped [^{18}F]fluoride (5 – 10 mCi (185 – 370 MBq) was eluted with 1.8 mg tetrabutylammonium tosylate (TBAOTs) dissolved in 2 mL EtOH and 20 µL H2O into a vial. [^{18}F]fluoride was azeotropically dried by evaporation at 90°C first under a flow of nitrogen for 10 minutes, then under vacuum for 15 minutes. Activity was then redissolved in 2 mL MeCN. Aliquots of activity were added to vials containing 50 nmol of precursor in MeCN (100 µL). The reactions were aged at the temperature and analyzed in triplicate by Raytest MiniGITA radioTLC at the indicated time points.

Manual radiolabeling protocol #2 "Munich" method

Irradiated cyclotron target carrying [^{18}F]fluoride in ^{18}O-enriched water was moved using negative pressure and passed through a pre-conditioned Sep-Pak Light QMA cartridge (Waters) as an aqueous solution, and the water was collected in a waste bottle. The cartridge is then rinsed with MeCN (10 mL) to remove the traces of water. K222/KOH eluent is prepared by dissolving 91 µmol Kryptofix-222 and 83 µmol KOH in water and lyophilised, then dissolving the lyophilized powder in 0.5mL MeCN. Trapped [^{18}F]fluoride (5 – 10 mCi (185 – 370 MBq)) is eluted using K222/KOH eluent, then diluted with 0.5mL MeCN and 20uL of 1 M oxalic acid was added. Aliquots of activity were added to vials containing the 50 nmol of precursor in MeCN (100 µL). The reactions were aged at the temperature and analyzed in triplicate by Raytest MiniGITA radioTLC at the indicated time points.

Autoradiography

Sodium HEPES buffer was formulated using 30 mM Na HEPES, 110 mM NaCl, 5 mM KCl, 2.5 mM $CaCl_2$, and 1.2 mM $MgCl_2$ in distilled water then adjusted to pH 7.4 using aqueous 5 M NaOH solution and passed through a 50 µM filter and stored in the refrigerator. Solutions of inhibitor candidates were prepared using 50 µM DMSO stock solutions diluted with HEPES buffer to 10 µM solutions. Frozen Sprague-Dawley rat brain tissue sections affixed to glass slides were thawed at room temperature and pre-incubated in Na HEPES buffer for 10 minutes. The sections were allowed to fully air dry and then incubated for 20 minutes with HDAC inhibitor solution, then washed for 1 minute with cold sodium HEPES buffer and allowed to fully air-dry. Negative control was incubated with sodium HEPES buffer for 20 minutes then air-dried. [^{11}C]Martinostat was synthesized by the Montreal Neurological Institute PET Chemistry Unit and 473 µCi [^{11}C]Martinostat was dissolved in 85 mL of sodium HEPES buffer. Brain slides were incubated with [^{11}C]Martinostat solution for 20 minutes then the slides were washed 3 times successively (1 minute/each) in ice-cold sodium HEPES buffer, then immersed in ice-cold distilled water for 30 seconds. Slides were air dried, and were then exposed on Fujifilm sensitive phosphor imaging plates (FUJIFILM BAS 500) for 4 hours. Imaging plates were imaged using an Amersham Typhoon biomolecular imager (50 mm spatial resolution).

Automated radiosynthesis of 2-2B

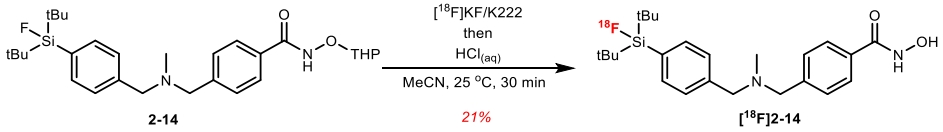

No-carrier-added aqueous [^{18}F]fluoride was produced by ^{18}O(p,n)^{18}F nuclear reaction using an enriched [^{18}O]H_2O target with the cyclotron (IBA Cyclone 18/9 MeV cyclotron) at the Montreal Neurological Institute-Hospital. Radiolabeling and purification were carried out using an automated radiosynthesis unit Scintomics GRP equipped with a previously described manifold setup[14]. 150 nmol of **2-14** (1 mM solution in MeCN) was loaded into the reaction vial along with 20 µL of 1 M oxalic acid solution.

Irradiated cyclotron target carrying [^{18}F]fluoride in ^{18}O-enriched water was moved using negative pressure and passed through a pre-conditioned Sep-Pak Light QMA cartridge (Waters) as an aqueous solution, and the water was collected in a waste bottle. The QMA cartridge captured [^{18}F]fluoride was measured using a dose calibrator (Capintec CRC) to be 830 mCi (30.7 GBq) then washed with 10 mL MeCN. K222/KOH eluent is prepared by dissolving 137 µmol Kryptofix-222 and 125 µmol KOH in in water and lyophilised, then dissolving the lyophilized powder in 0.5mL MeCN. Trapped [^{18}F]fluoride is eluted using K222/KOH eluent into the reaction vial pre-loaded with precursor and oxalic acid. Reaction vial was allowed to sit for 15 minutes at 25 °C, then 2 mL of 5 M HCl solution was added to the vial via syringe. The reaction vial was allowed to sit for another 15 minutes at 25 °C. The reaction mixture was diluted with 10 mL of phosphate-buffered saline, then removed from the reaction vial and passed through a Sep-Pak C-18 Plus Light cartridge (Waters), collecting into the waste bottle. The C-18 cartridge was washed with a further 10 mL of phosphate-buffered saline, collected into the waste bottle, then eluted using 3 mL of EtOH through a sterile filter into a sterile vial. The solution was diluted with 15 mL phosphate buffered saline then neutralized with addition of 22 µL 5 M NaOH. The desired product **[^{18}F]2-14** was obtained in non-decay-corrected RCY of 21% 174 mCi (6.44 GBq) with a total synthesis time of 39 minutes.

PET Acquisition and processing.

PET acquisition was performed using a CTI Concorde R4 microPET for small animals (Siemens Medical Solutions). A Sprague-Dawley rat was first anesthetized using 5% isoflurane in oxygen and then maintained throughout the procedure with 2% isoflurane. A transmission scan was first performed using a rotating ^{57}Co source for attenuation correction. Freshly produced radiotracer **[^{18}F]2-14** was injected of the in the tail vein (5.7 mCi (211 MBq) in 600 µL, with a molar activity of 1.14 Ci/ µmol (42.2 GBq/µmol)), concomitant with the beginning of the emission scan, which lasted for 60 min in list mode. Breathing rate was monitored throughout and temperature was monitored using a rectal thermometer and maintained at 37 ± 1°C using an electric blanket.

Images for both tracers were reconstructed using a maximum a posteriori (MAP) algorithm (voxel size: 0.6 × 0.6 × 1.2 mm) and corrected for scatter, dead time, and decay.

MINC tools (www.bic.mni.mcgill.ca/ServicesSoftware) was used for image processing and analysis. Dynamic tissue-activity images were averaged and co-registered with generic Sprague-Dawley rat brain sMRI using six degrees of freedom. For standard uptake value, co-registered dynamic tissue-activity images were reframed into 27 sequential time frames of increasing durations (8 × 30 s, 6 × 1 min, 5 × 2 min, and 8 × 5 min), and individual sub-structure activity levels were quantified.

Appendix

^{1}H, ^{13}C, and ^{19}F NMR Spectra Relevant to Chapter 2

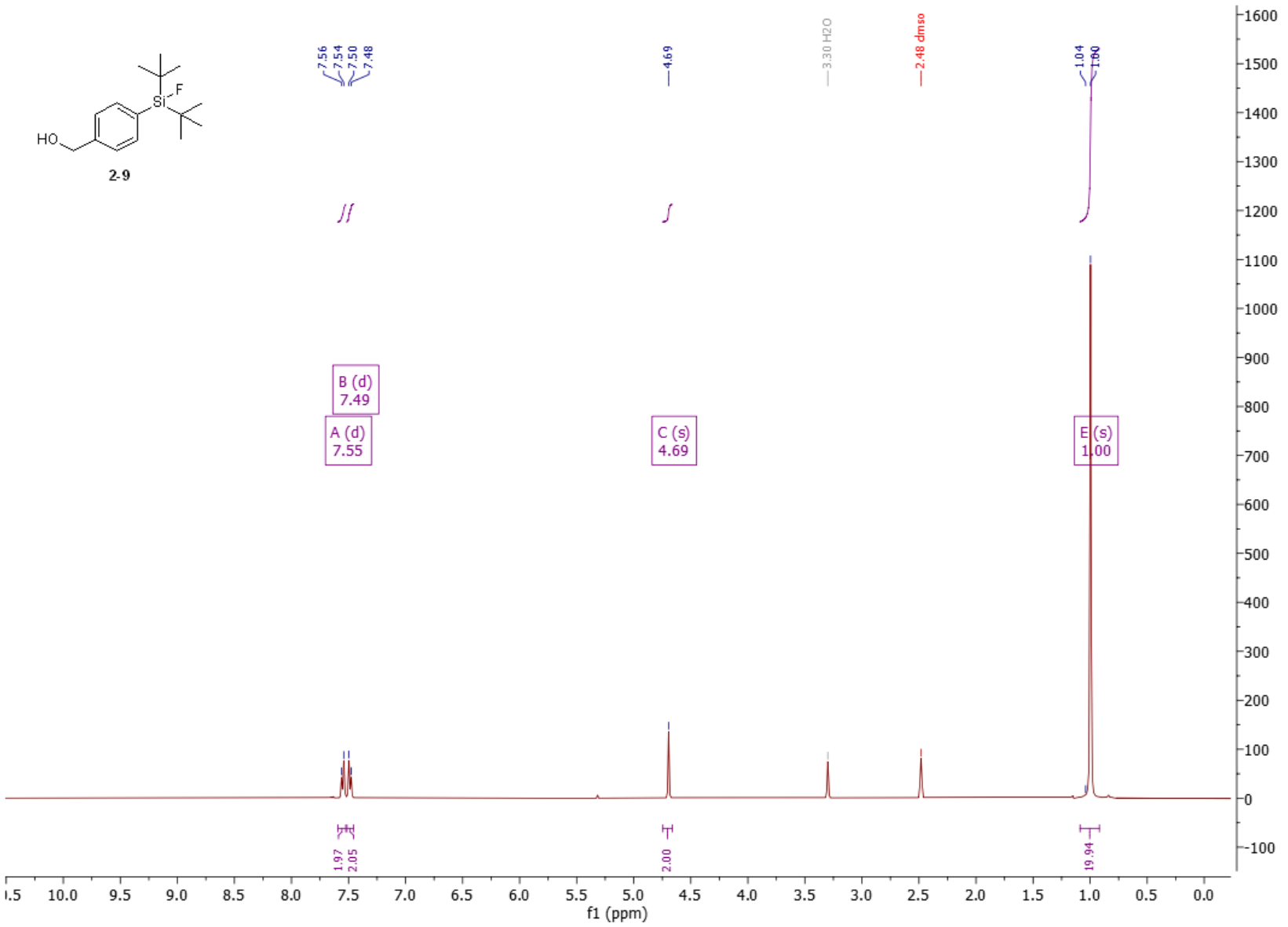
HO
Si
F
2-9
7.56
7.54
7.50
7.48
4.69
3.30 H2O
2.48 dmso
1.04
1.00
B (d)
7.49
A (d)
7.55
C (s)
4.69
E (s)
1.00
1.97
2.05
2.00
19.94
f1 (ppm)

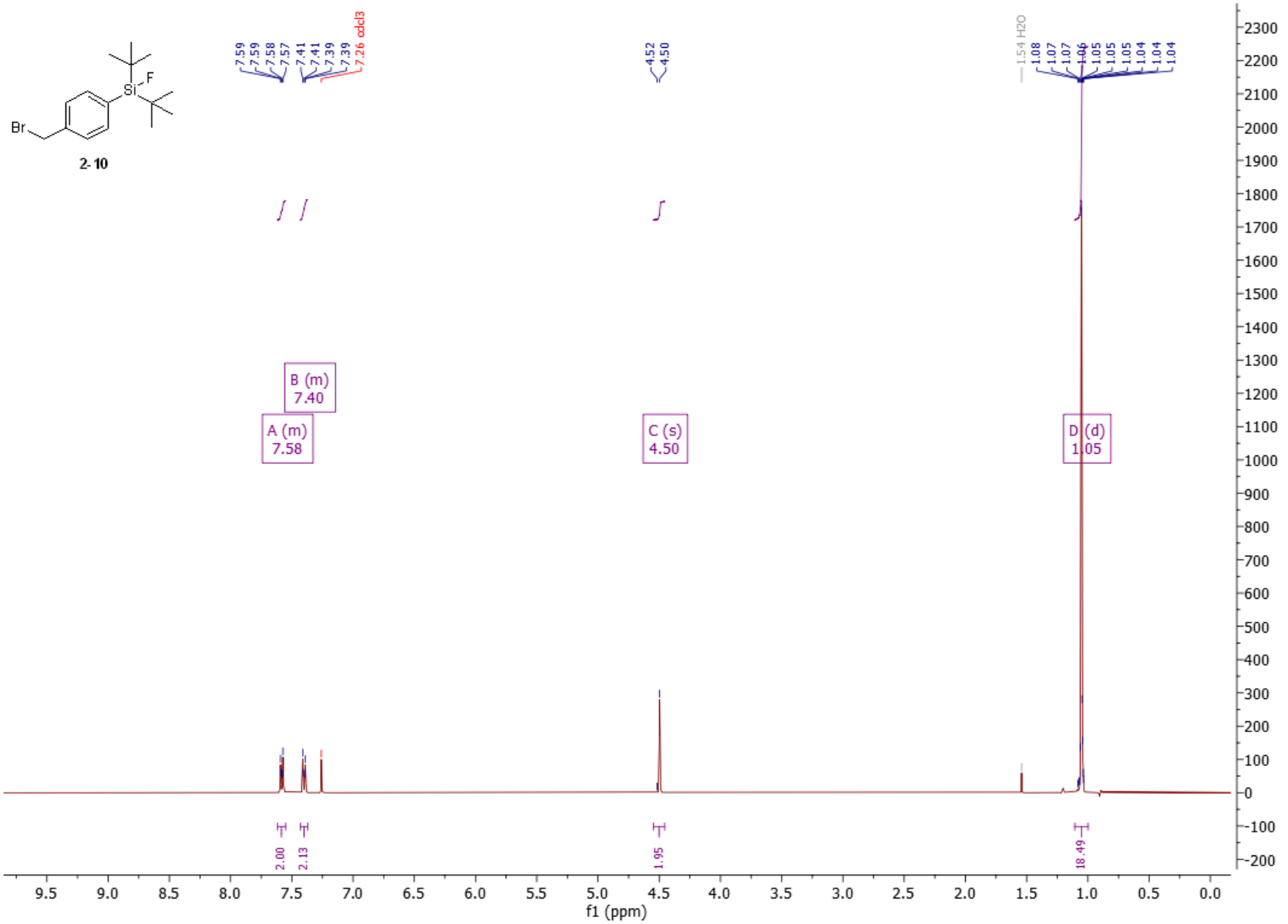
Br
Si
F
2-10
7.59
7.59
7.58
7.57
7.41
7.41
7.39
7.39
7.26 cdcl3
4.52
4.50
1.54 H2O
1.08
1.07
1.07
1.06
1.05
1.05
1.05
1.04
1.04
1.04
B (m)
7.40
A (m)
7.58
C (s)
4.50
D (d)
1.05
2.00
2.13
1.95
18.49
f1 (ppm)

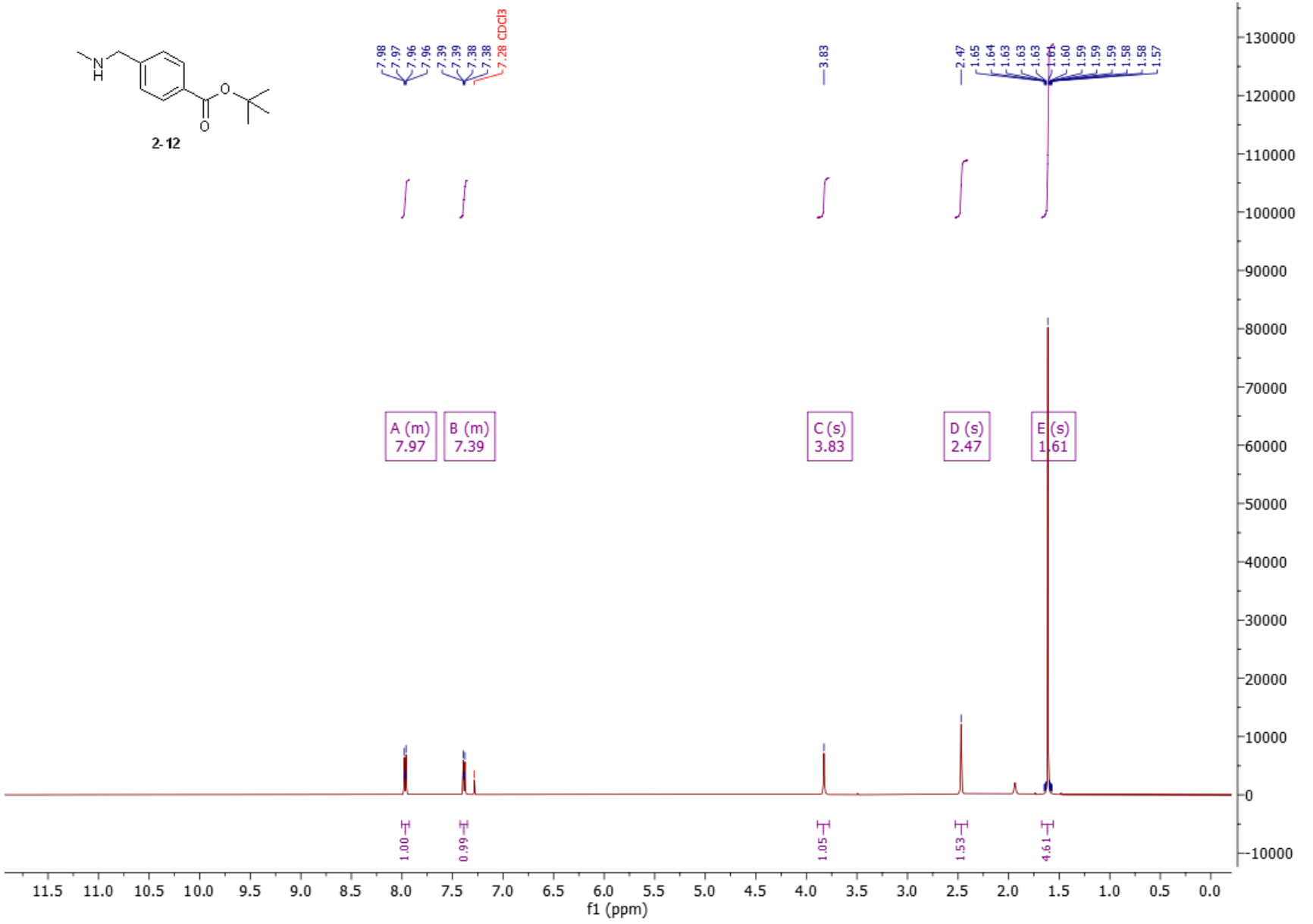
2-12
7.98
7.97
7.96
7.96
7.39
7.39
7.38
7.38
7.28 CDCl3
3.83
2.47
1.65
1.64
1.63
1.63
1.63
1.61
1.60
1.59
1.59
1.59
1.58
1.58
1.57
A (m) 7.97
B (m) 7.39
C (s) 3.83
D (s) 2.47
E (s) 1.61
1.00
0.99
1.05
1.53
4.61
f1 (ppm)


2-4
B (m) 7.58
A (m) 7.97
C (m) 7.45
D (m) 7.38
F (s) 3.54
E (s) 3.60
G (s) 2.22
H (s) 1.62
I (d) 1.07
f1 (ppm)

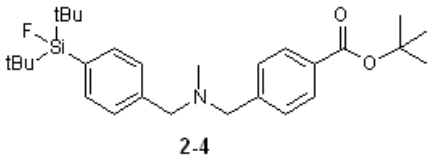
tBu
F
Si
tBu
N
O
O

2-4

-188.98
A (s)
-188.98
1.00
450
400
350
300
250
200
150
100
50
0
-50
10
0
-10
-20
-30
-40
-50
-60
-70
-80
-90
-100
-110
-120
-130
-140
-150
-160
-170
-180
-190
-200
-210
f1 (ppm)

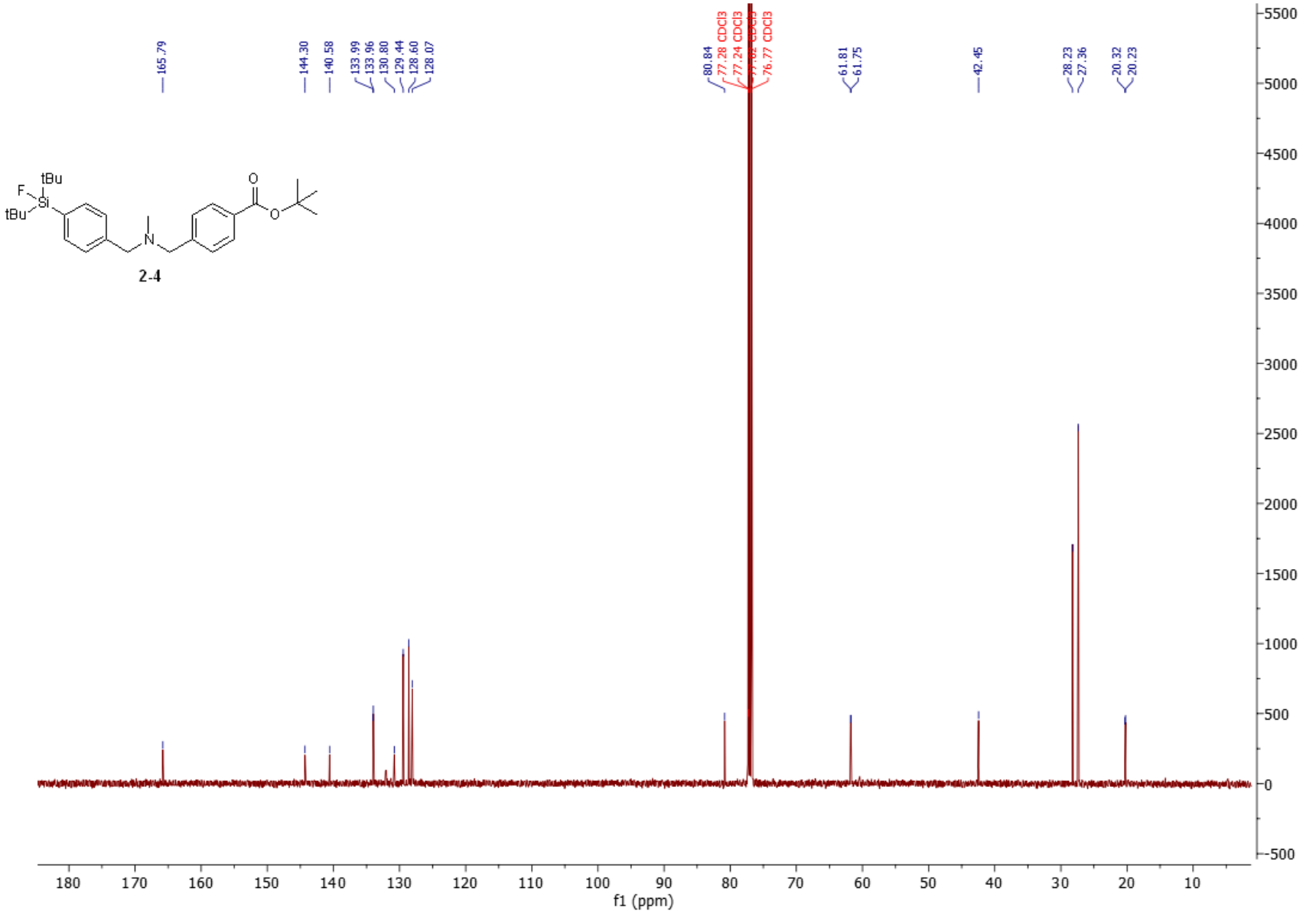
165.79
144.30
140.58
133.99
133.96
130.80
129.44
128.60
128.07
80.84
77.28 CDCl3
77.24 CDCl3
76.77 CDCl3
61.81
61.75
42.45
28.23
27.36
20.32
20.23
tBu
F
Si
tBu
O
O
N
2-4
f1 (ppm)

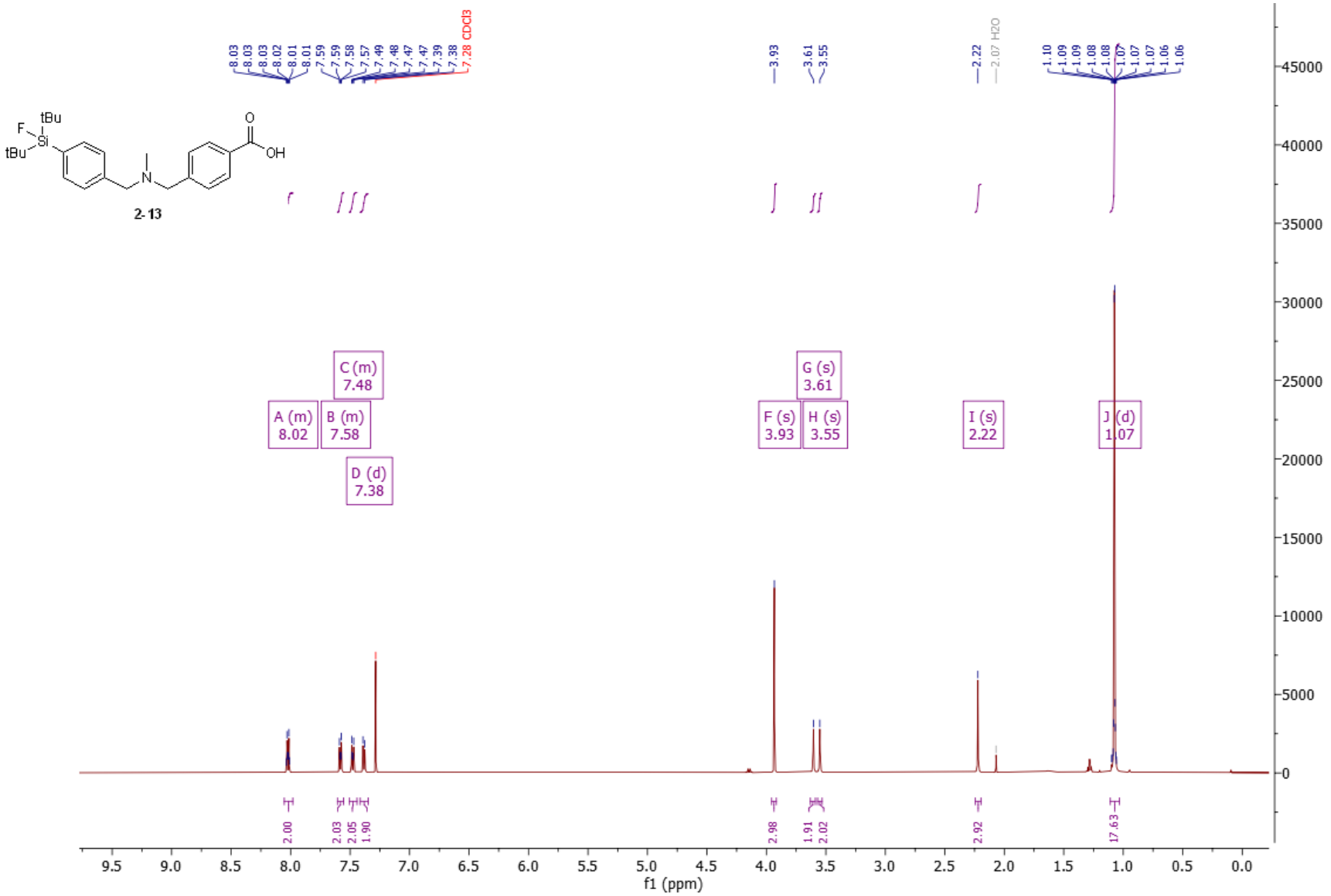
2-13
8.03 8.03 8.03 8.02 8.01 8.01 7.59 7.59 7.58 7.57 7.49 7.48 7.47 7.47 7.39 7.38 7.28 CDCl3
3.93 3.61 3.55 2.22 2.07 H2O 1.10 1.09 1.09 1.08 1.08 1.07 1.07 1.07 1.06 1.06
C (m) 7.48
A (m) 8.02
B (m) 7.58
D (d) 7.38
G (s) 3.61
F (s) 3.93
H (s) 3.55
I (s) 2.22
J (d) 1.07
2.00 2.03 2.05 1.90 2.98 1.91 2.02 2.92 17.63
f1 (ppm)

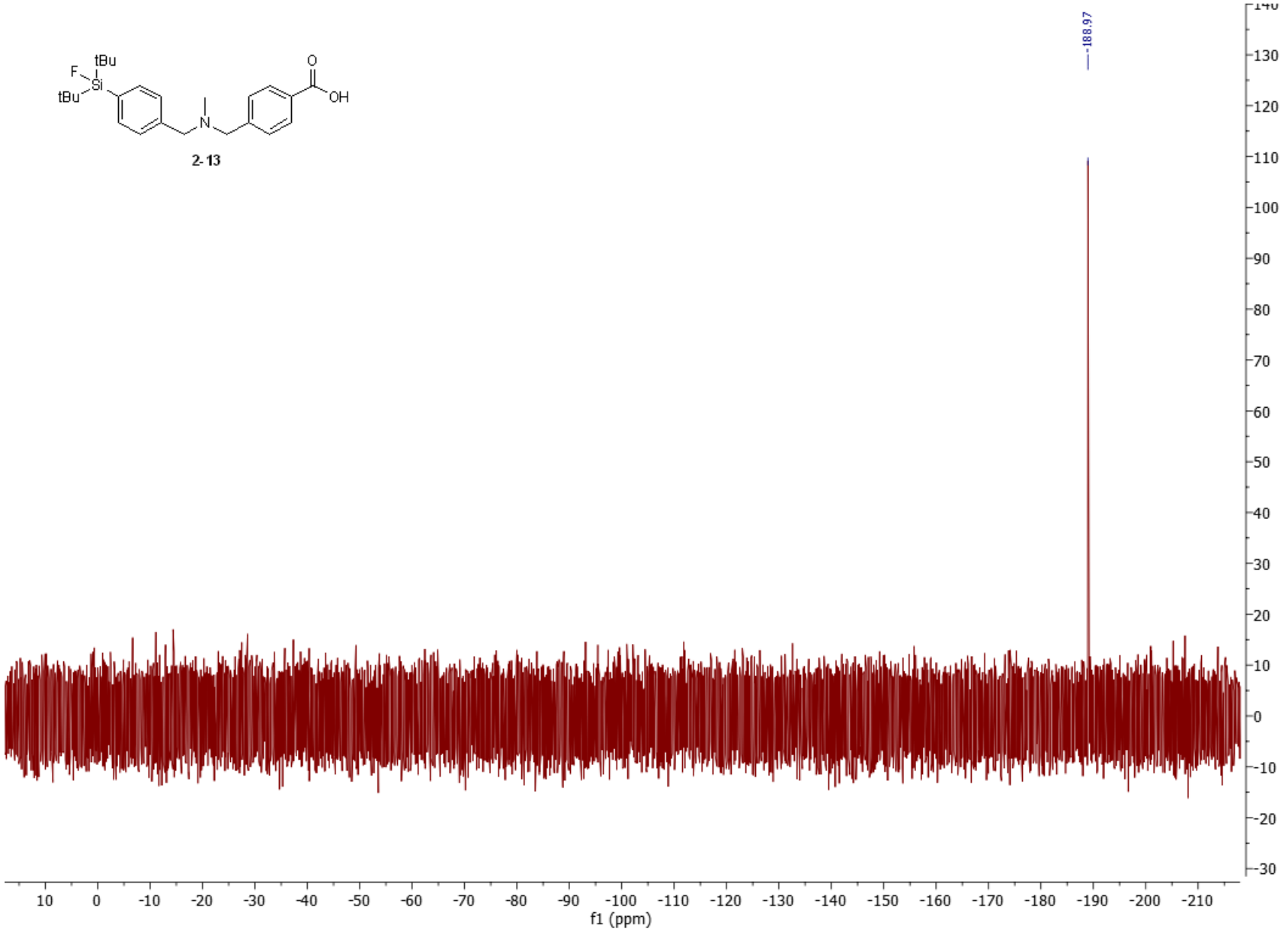
tBu
F
Si
tBu
O
OH
N
2-13
-188.97
f1 (ppm)

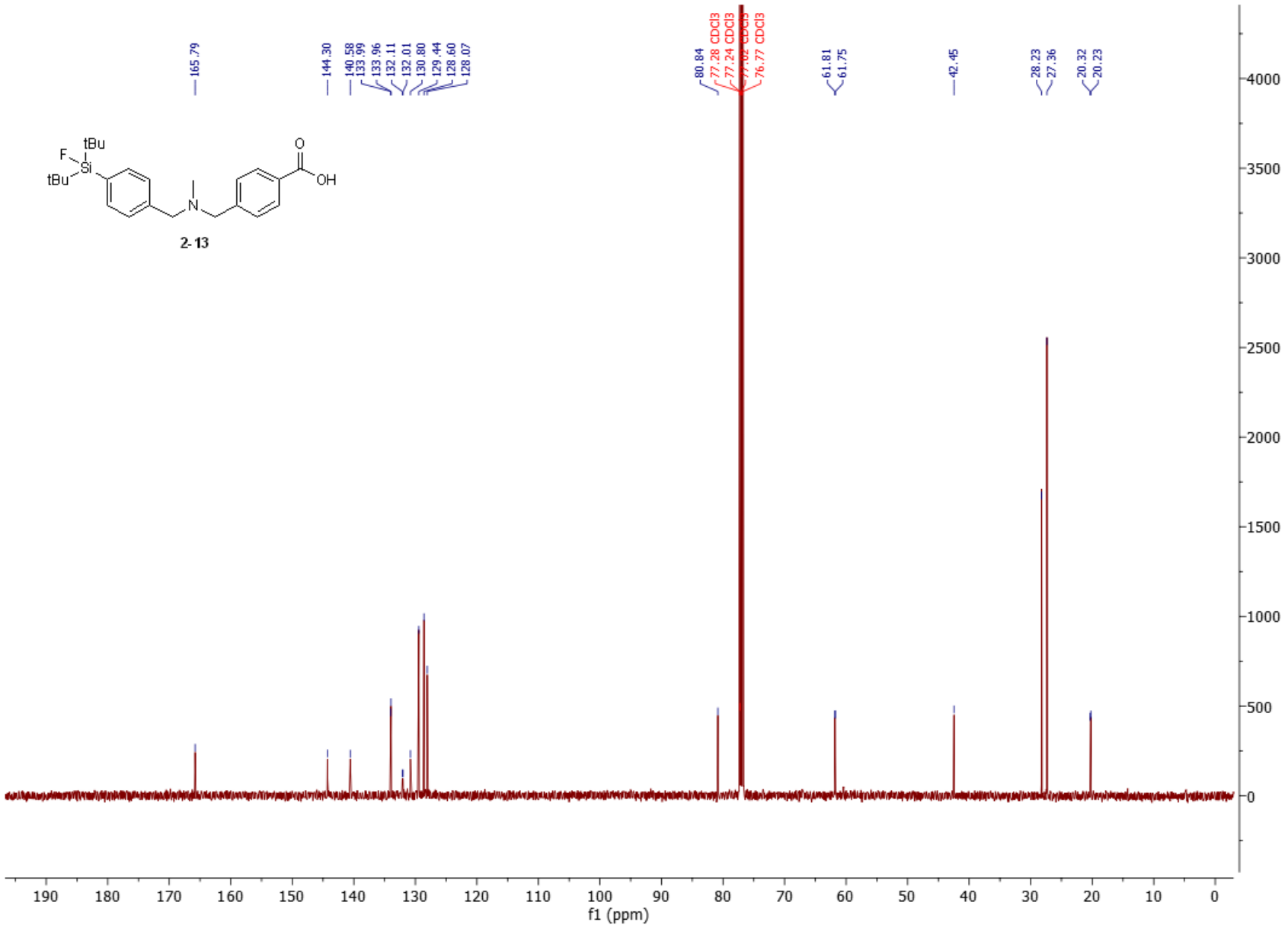
165.79
144.30
140.58
133.99
133.96
132.11
132.01
130.80
129.44
128.60
128.07
80.84
77.28 CDCl3
77.24 CDCl3
76.77 CDCl3
61.81
61.75
42.45
28.23
27.36
20.32
20.23
tBu
F
Si
tBu
N
O
OH
2-13
4000
3500
3000
2500
2000
1500
1000
500
0
190
180
170
160
150
140
130
120
110
100
90
80
70
60
50
40
30
20
10
0
f1 (ppm)

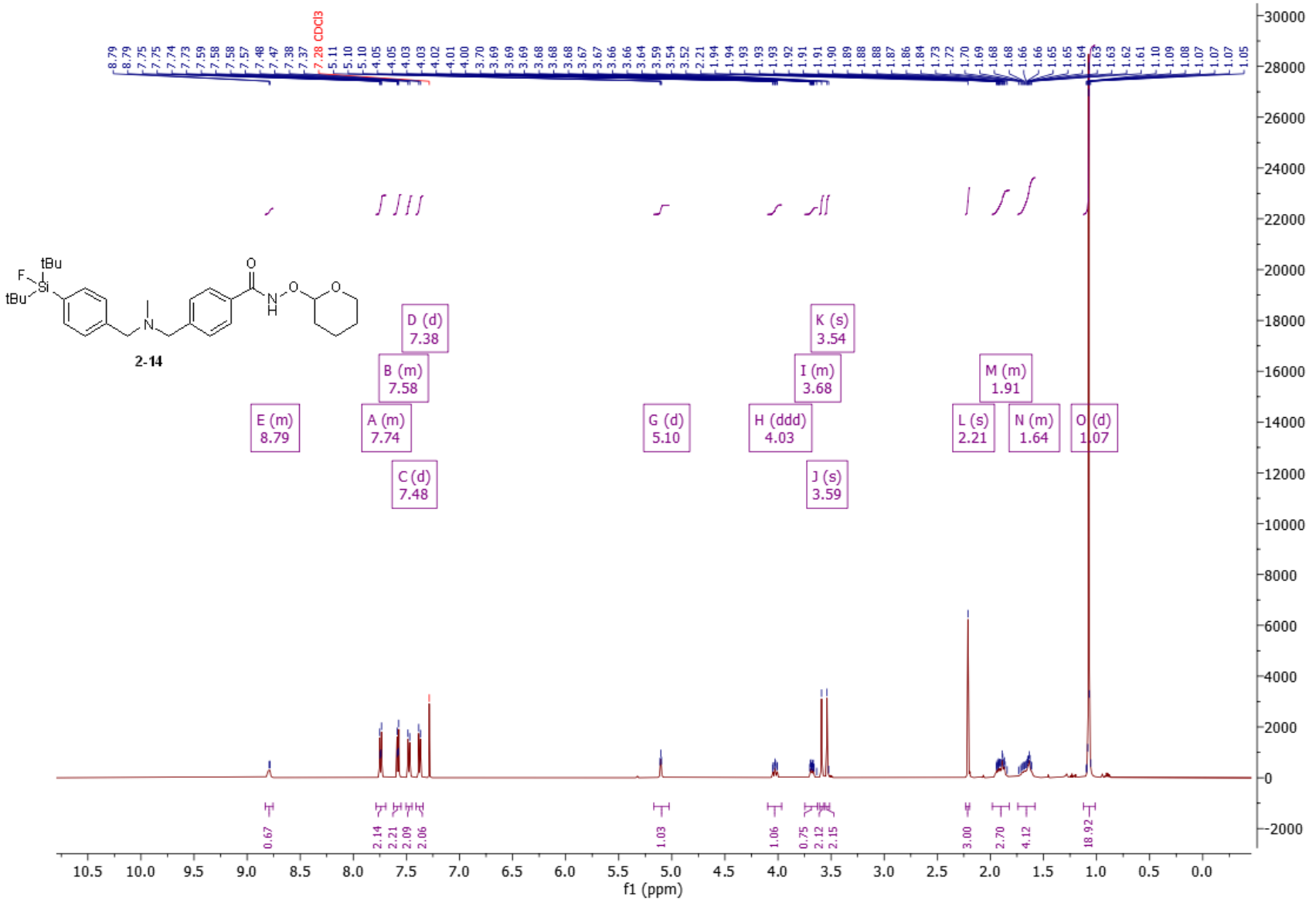
2-14
D (d) 7.38
B (m) 7.58
E (m) 8.79
A (m) 7.74
C (d) 7.48
G (d) 5.10
K (s) 3.54
I (m) 3.68
H (ddd) 4.03
J (s) 3.59
M (m) 1.91
L (s) 2.21
N (m) 1.64
O (d) 1.07
f1 (ppm)

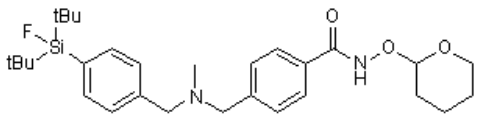
tBu
F
Si
tBu
O
N
H
O
O
N

2-14

188.96
1.00
190
180
170
160
150
140
130
120
110
100
90
80
70
60
50
40
30
20
10
0
-10
-20
-30
-40
-50
10
0
-10
-20
-30
-40
-50
-60
-70
-80
-90
-100
-110
-120
-130
-140
-150
-160
-170
-180
-190
-200
-210
f1 (ppm)

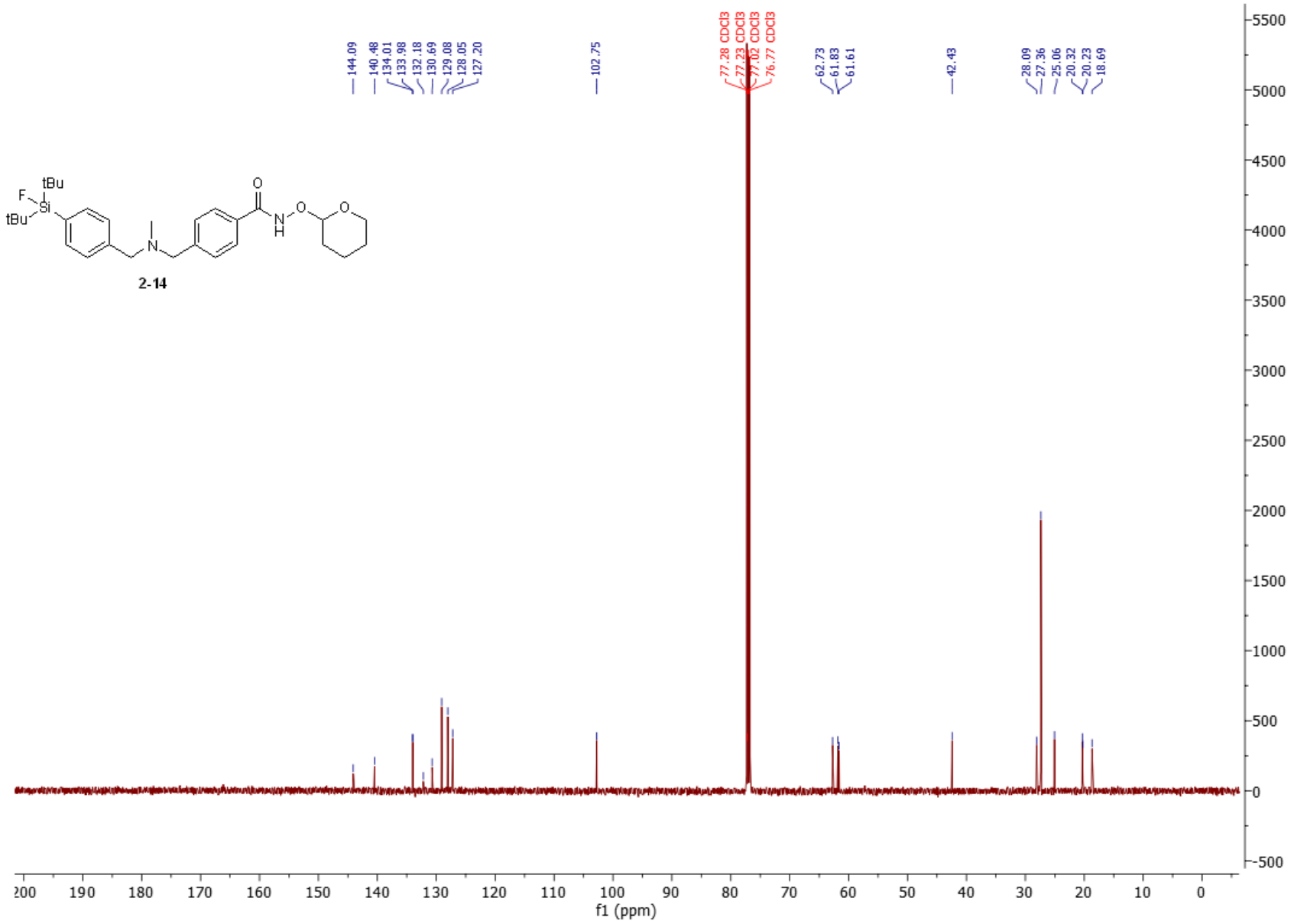
144.09
140.48
134.01
133.98
132.18
130.69
129.08
128.05
127.20
102.75
77.28 CDCl3
77.23 CDCl3
77.02 CDCl3
76.77 CDCl3
62.73
61.83
61.61
42.43
28.09
27.36
25.06
20.32
20.23
18.69
tBu
F
Si
tBu
N
O
N
H
O
O
2-14
f1 (ppm)

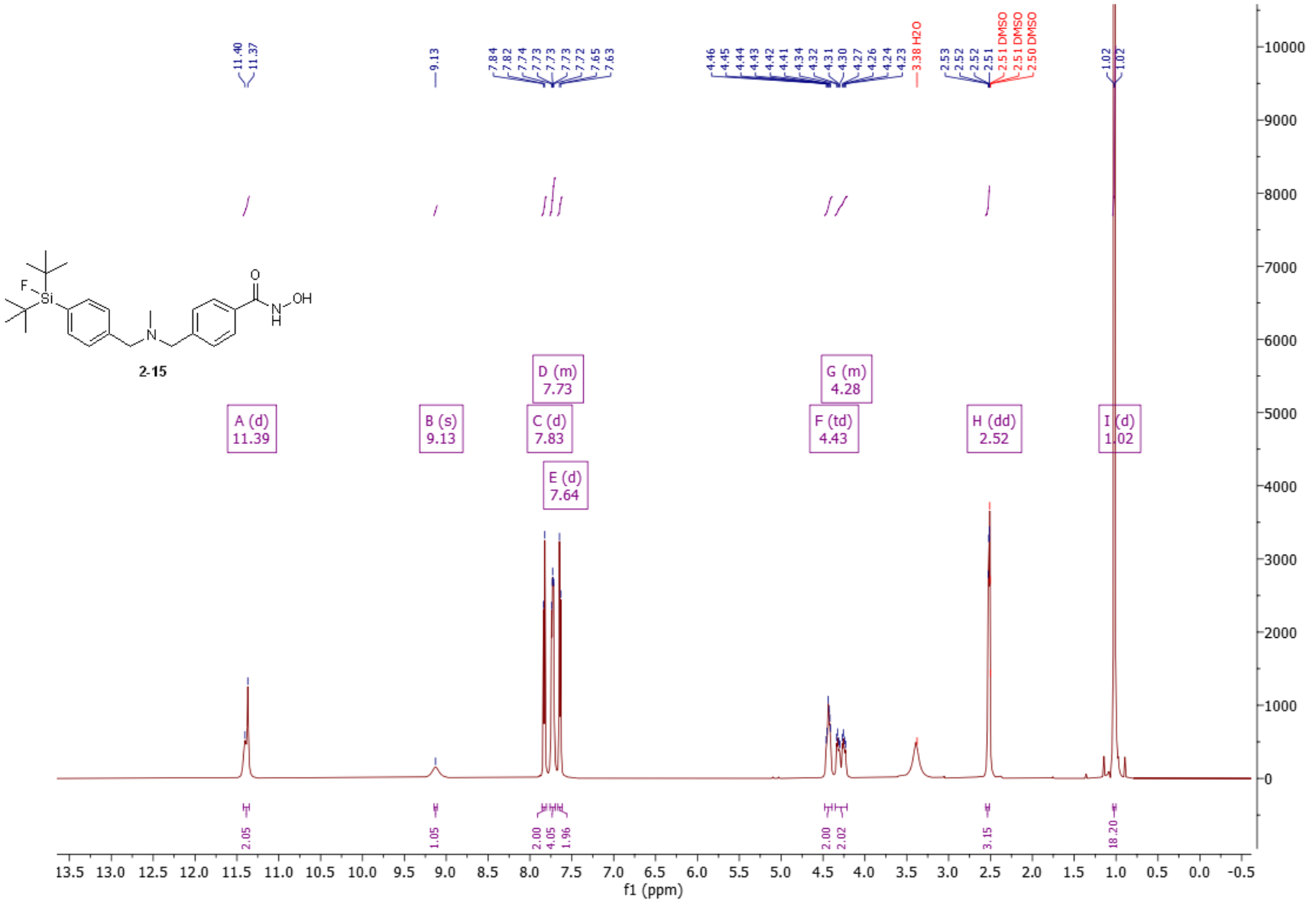
11.40
11.37
9.13
7.84
7.82
7.74
7.73
7.73
7.73
7.72
7.65
7.63
4.46
4.45
4.44
4.43
4.42
4.41
4.34
4.32
4.31
4.30
4.27
4.26
4.24
4.23
3.38 H2O
2.53
2.52
2.52
2.51
2.51 DMSO
2.51 DMSO
2.50 DMSO
1.02
1.02
F
Si
O
N
OH
H
2-15
A (d)
11.39
B (s)
9.13
C (d)
7.83
D (m)
7.73
E (d)
7.64
F (td)
4.43
G (m)
4.28
H (dd)
2.52
I (d)
1.02
2.05
1.05
2.00
4.05
1.96
2.00
2.02
3.15
18.20
f1 (ppm)

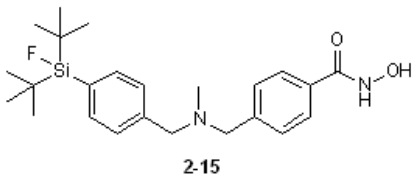
F
Si
O
N
OH
H

2-15

187.29
1.00
550
500
450
400
350
300
250
200
150
100
50
0
-50
10
0
-10
-20
-30
-40
-50
-60
-70
-80
-90
-100
-110
-120
-130
-140
-150
-160
-170
-180
-190
-200
-210
f1 (ppm)

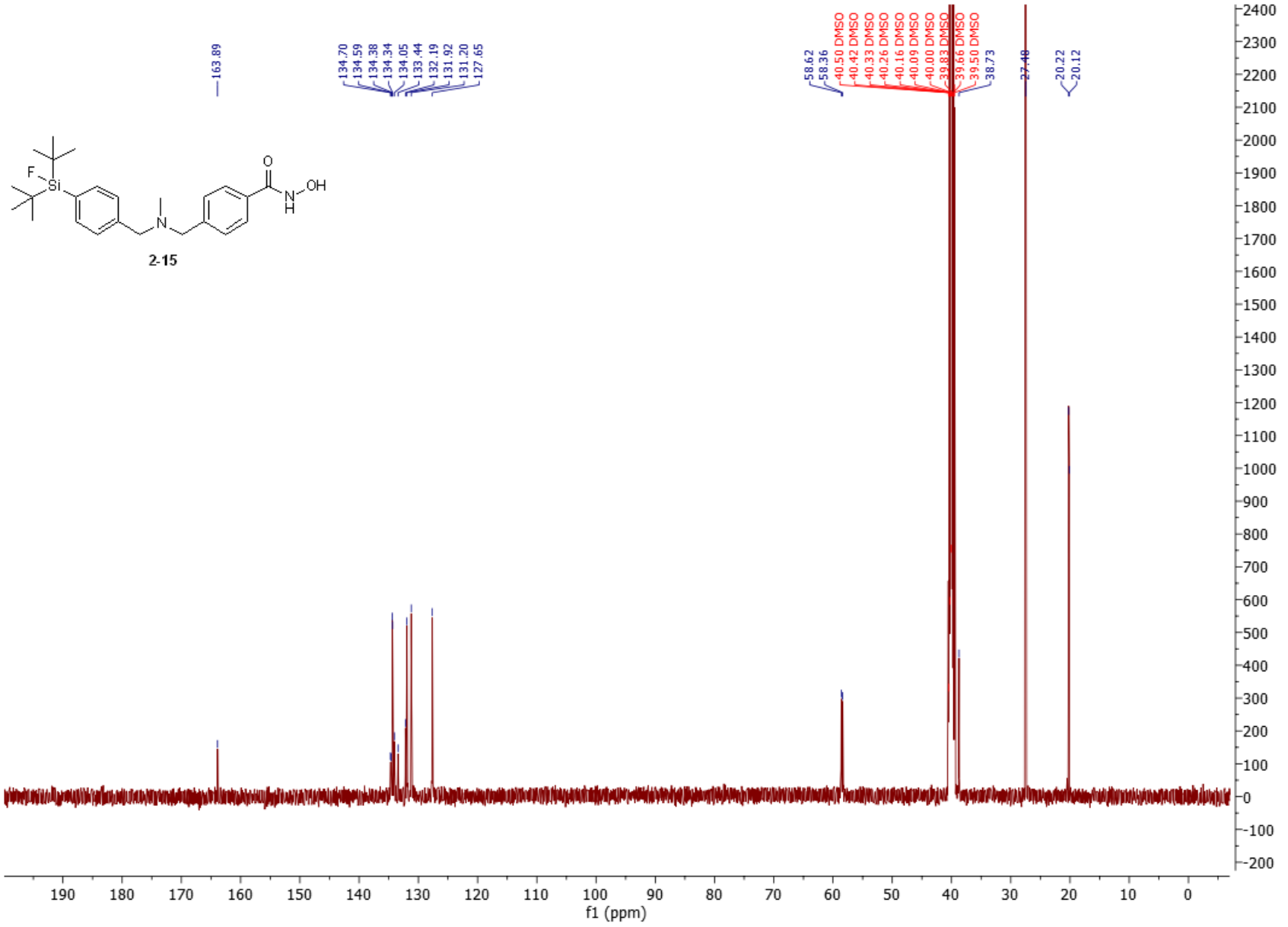
163.89
134.70
134.59
134.38
134.34
134.05
133.44
132.19
131.92
131.20
127.65
58.62
58.36
40.50 DMSO
40.42 DMSO
40.33 DMSO
40.26 DMSO
40.16 DMSO
40.09 DMSO
40.00 DMSO
39.83 DMSO
39.66 DMSO
39.50 DMSO
38.73
27.48
20.22
20.12
F
Si
N
O
N
H
OH
2-15
f1 (ppm)

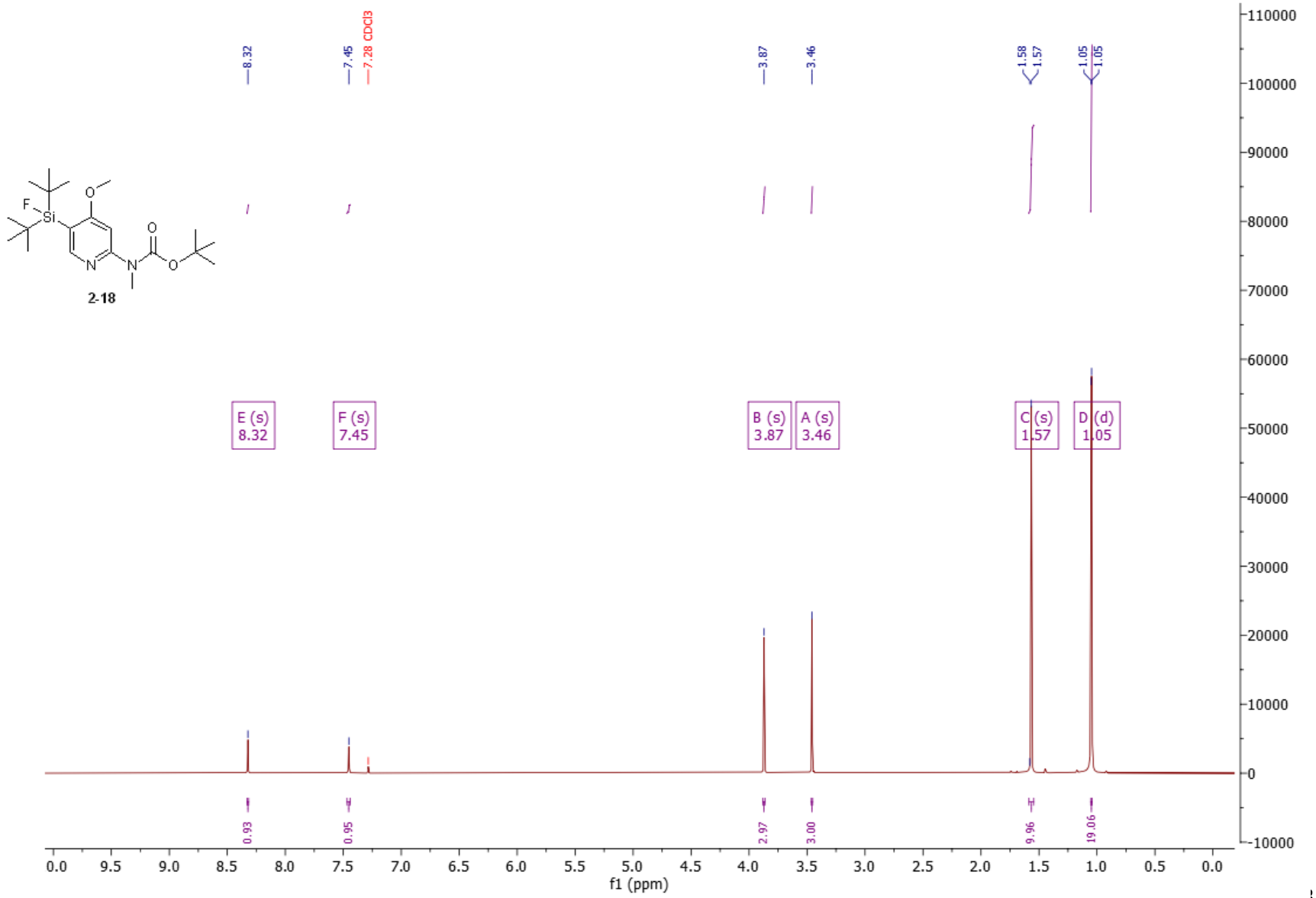
2-18
8.32
7.45
7.28 CDCl3
3.87
3.46
1.58
1.57
1.05
1.05
E (s) 8.32
F (s) 7.45
B (s) 3.87
A (s) 3.46
C (s) 1.57
D (d) 1.05
0.93
0.95
2.97
3.00
9.96
19.06
f1 (ppm)

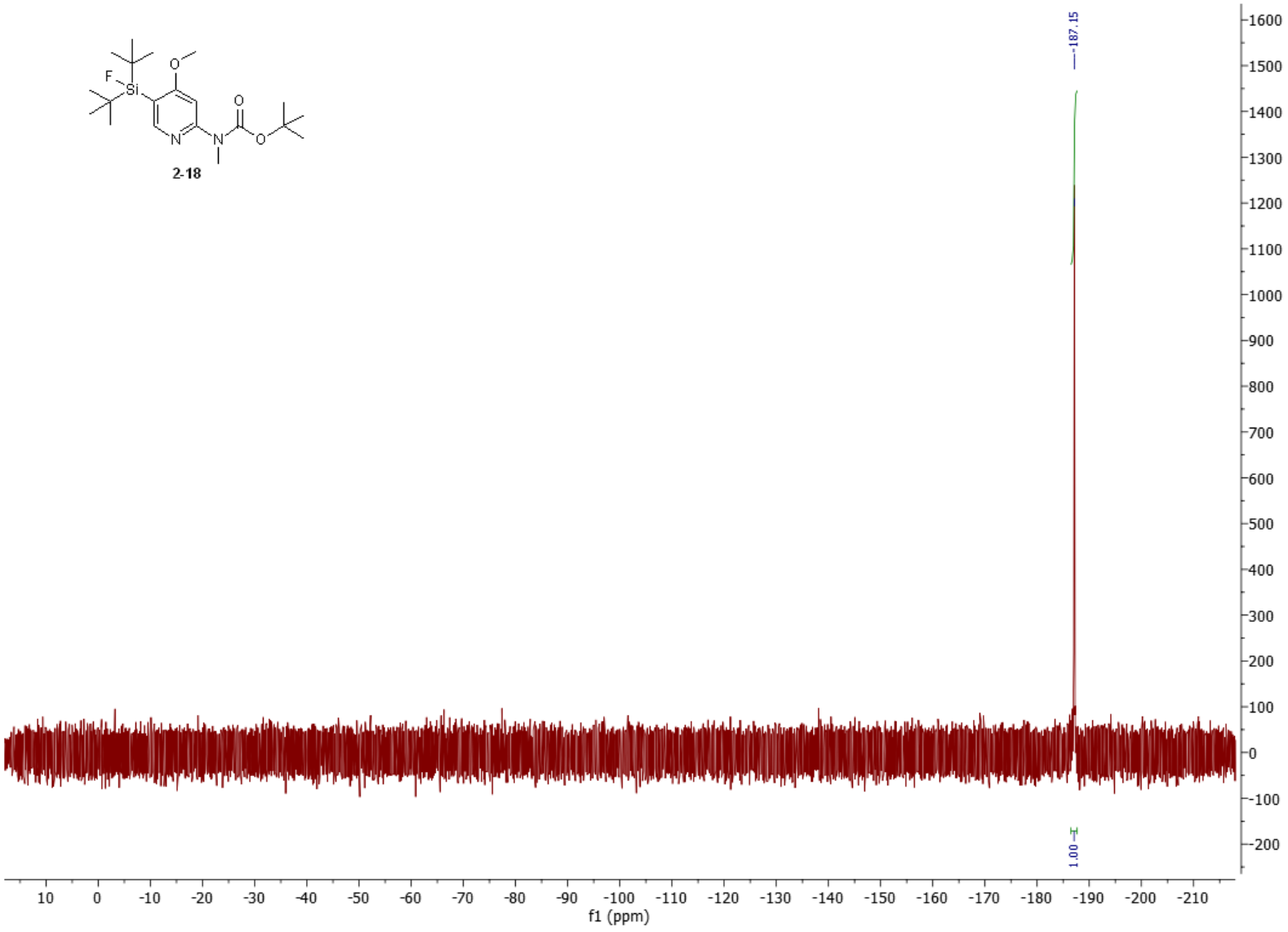
F
Si
O
O
N
N
O
2-18
-187.15
1.00
1600
1500
1400
1300
1200
1100
1000
900
800
700
600
500
400
300
200
100
0
-100
-200
10
0
-10
-20
-30
-40
-50
-60
-70
-80
-90
-100
-110
-120
-130
-140
-150
-160
-170
-180
-190
-200
-210
f1 (ppm)

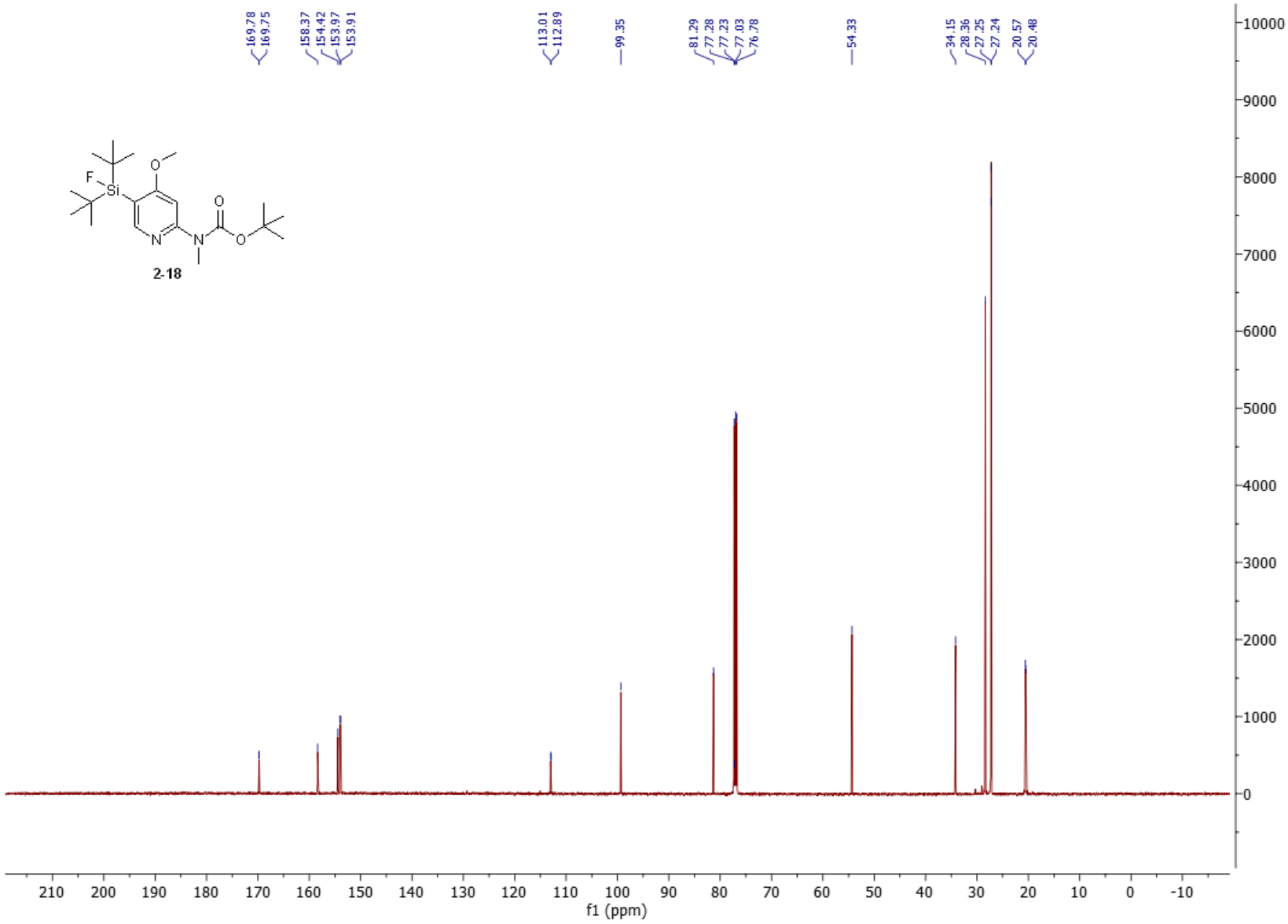
169.78
169.75
158.37
154.42
153.97
153.91
113.01
112.89
99.35
81.29
77.28
77.23
77.03
76.78
54.33
34.15
28.36
27.25
27.24
20.57
20.48
F
Si
O
N
N
O
O
2-18
f1 (ppm)

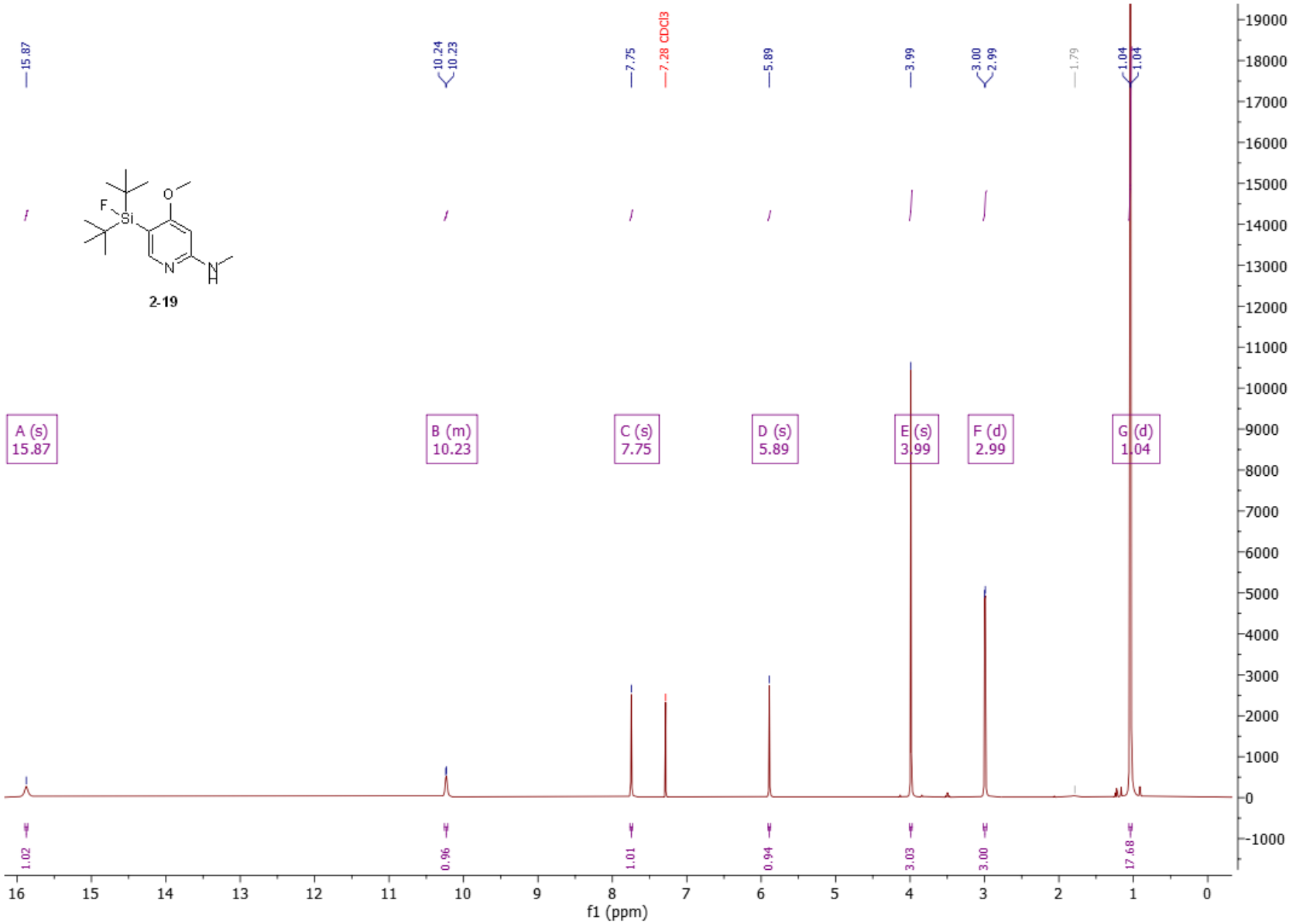
15.87
10.24
10.23
7.75
7.28 CDCl3
5.89
3.99
3.00
2.99
1.79
1.04
1.04
F
Si
O
N
H
N
2-19
A (s)
15.87
B (m)
10.23
C (s)
7.75
D (s)
5.89
E (s)
3.99
F (d)
2.99
G (d)
1.04
1.02
0.96
1.01
0.94
3.03
3.00
17.68
f1 (ppm)

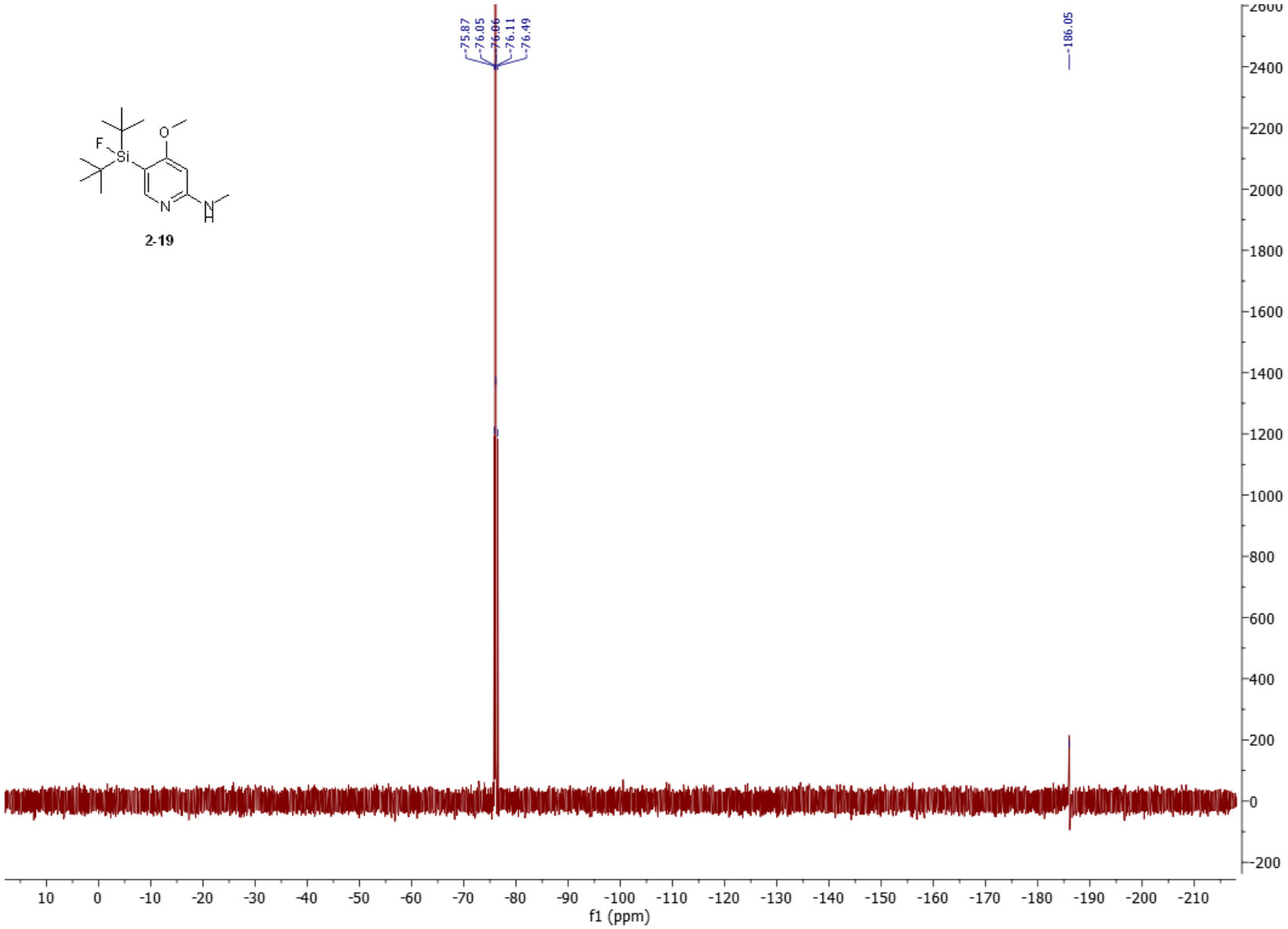
F
Si
O
N
H
2-19
-75.87
-76.05
-76.06
-76.11
-76.49
-186.05
2600
2400
2200
2000
1800
1600
1400
1200
1000
800
600
400
200
0
-200
10 0 -10 -20 -30 -40 -50 -60 -70 -80 -90 -100 -110 -120 -130 -140 -150 -160 -170 -180 -190 -200 -210
f1 (ppm)

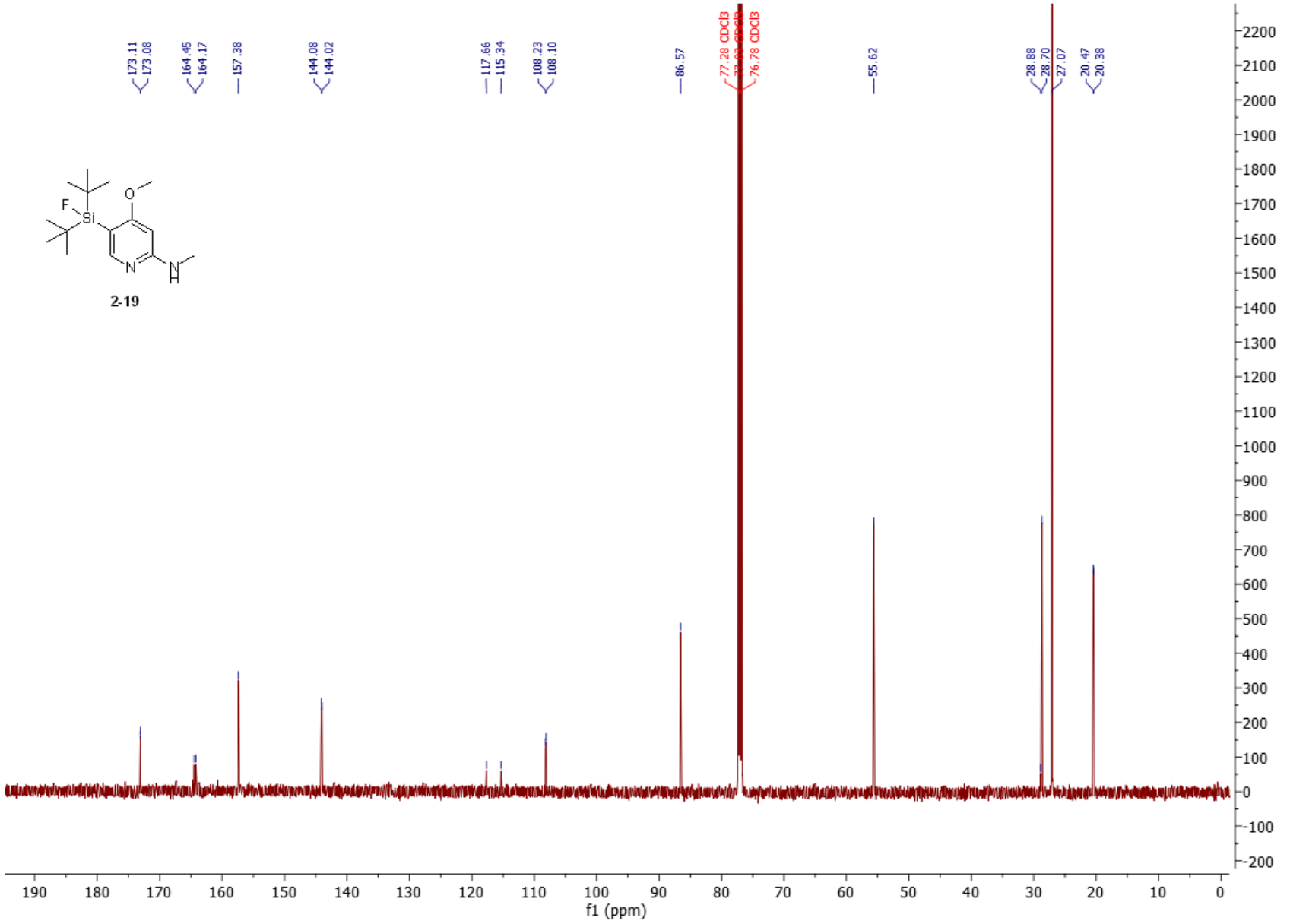
173.11
173.08
164.45
164.17
157.38
144.08
144.02
117.66
115.34
108.23
108.10
86.57
77.28 CDCl3
76.78 CDCl3
55.62
28.88
28.70
27.07
20.47
20.38
F
Si
O
N
N
H
2-19
f1 (ppm)

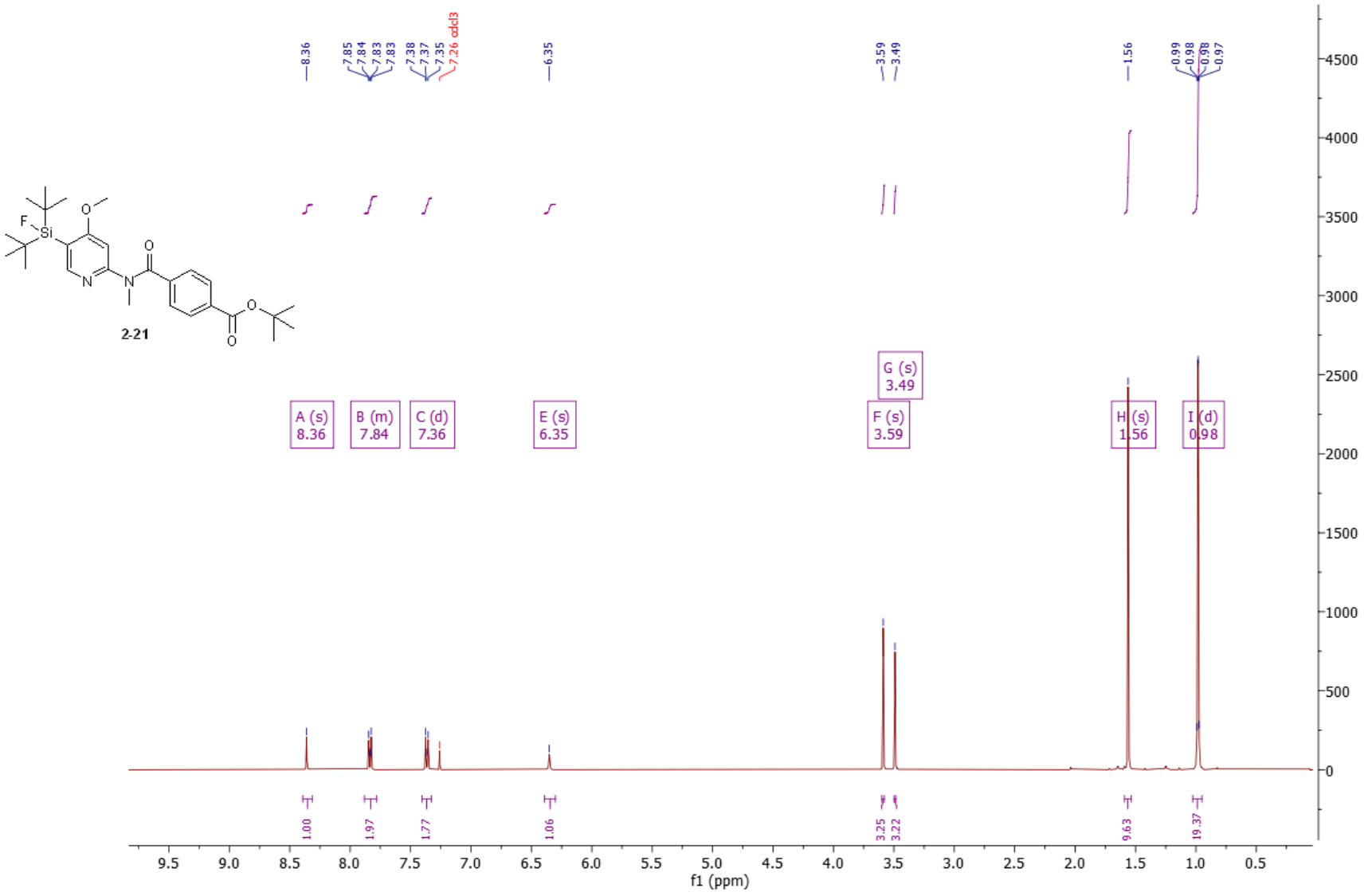
2-21
8.36
7.85
7.84
7.83
7.83
7.38
7.37
7.35
7.26 cdcl3
6.35
3.59
3.49
1.56
0.99
0.98
0.98
0.97
A (s) 8.36
B (m) 7.84
C (d) 7.36
E (s) 6.35
G (s) 3.49
F (s) 3.59
H (s) 1.56
I (d) 0.98
1.00
1.97
1.77
1.06
3.25
3.22
9.63
19.37
f1 (ppm)

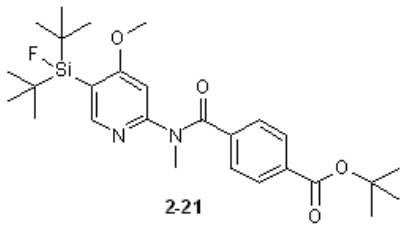
F
Si
O
N
N
O
O
O

2-21

-186.62
3800
3600
3400
3200
3000
2800
2600
2400
2200
2000
1800
1600
1400
1200
1000
800
600
400
200
0
-200
-400
10
0
-10
-20
-30
-40
-50
-60
-70
-80
-90
-100
-110
-120
-130
-140
-150
-160
-170
-180
-190
-200
f1 (ppm)

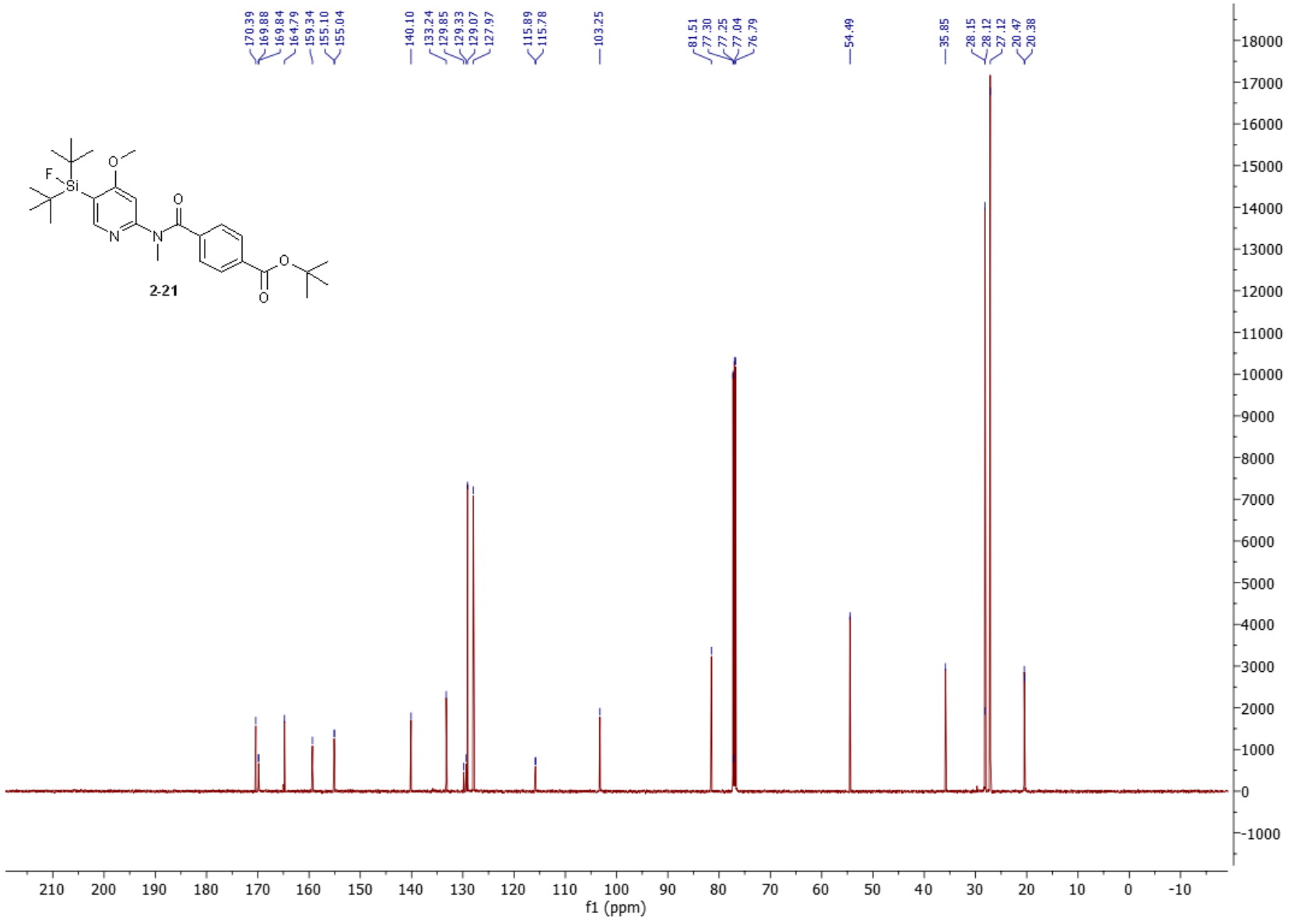
170.39
169.88
169.84
164.79
159.34
155.10
155.04
140.10
133.24
129.85
129.33
129.07
127.97
115.89
115.78
103.25
81.51
77.30
77.25
77.04
76.79
54.49
35.85
28.15
28.12
27.12
20.47
20.38
2-21
f1 (ppm)

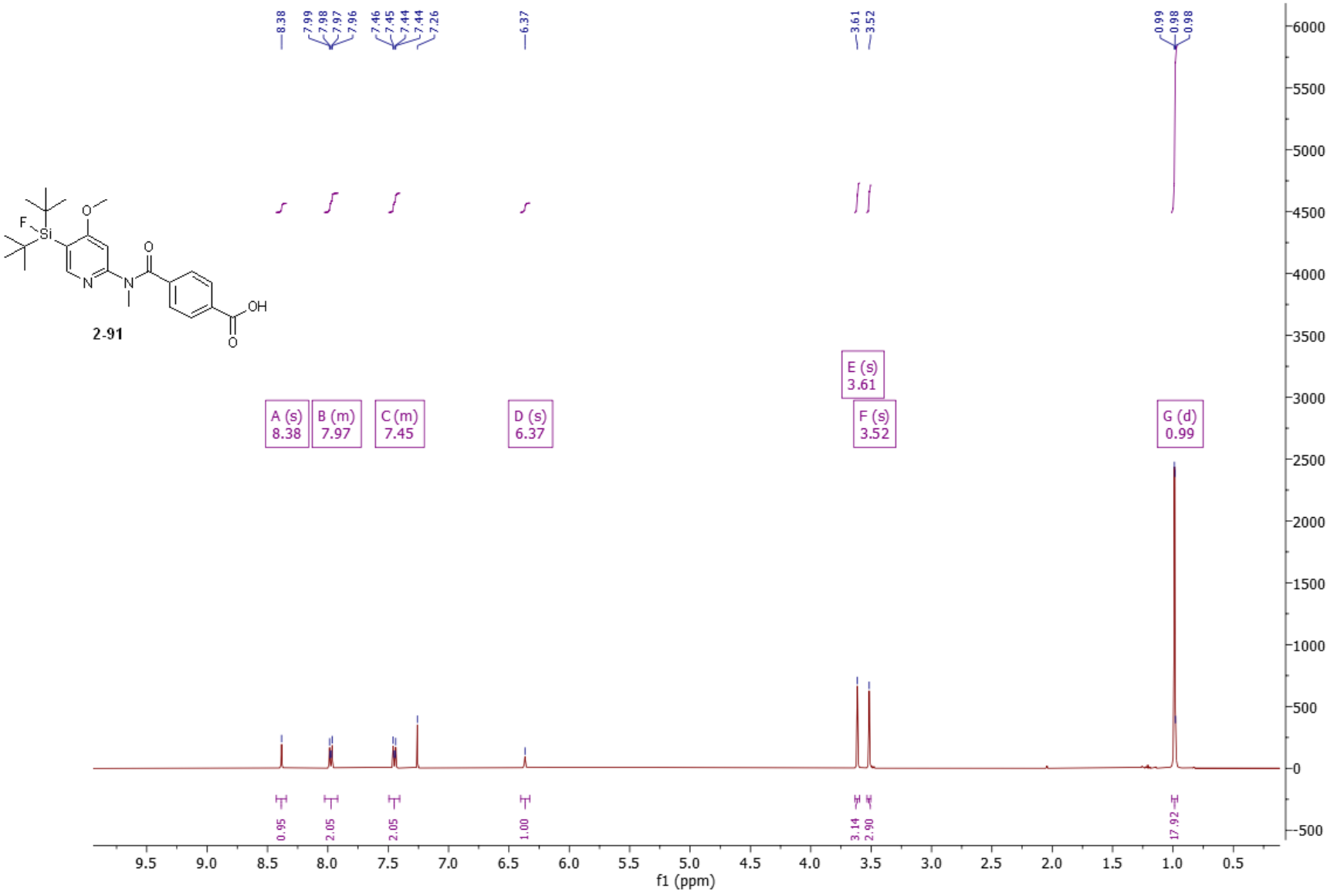
8.38
7.99
7.98
7.97
7.96
7.46
7.45
7.44
7.44
7.26
6.37
3.61
3.52
0.99
0.98
0.98
F
Si
O
N
N
O
OH
O
2-91
A (s) 8.38
B (m) 7.97
C (m) 7.45
D (s) 6.37
E (s) 3.61
F (s) 3.52
G (d) 0.99
0.95
2.05
2.05
1.00
3.14
2.90
17.92
f1 (ppm)

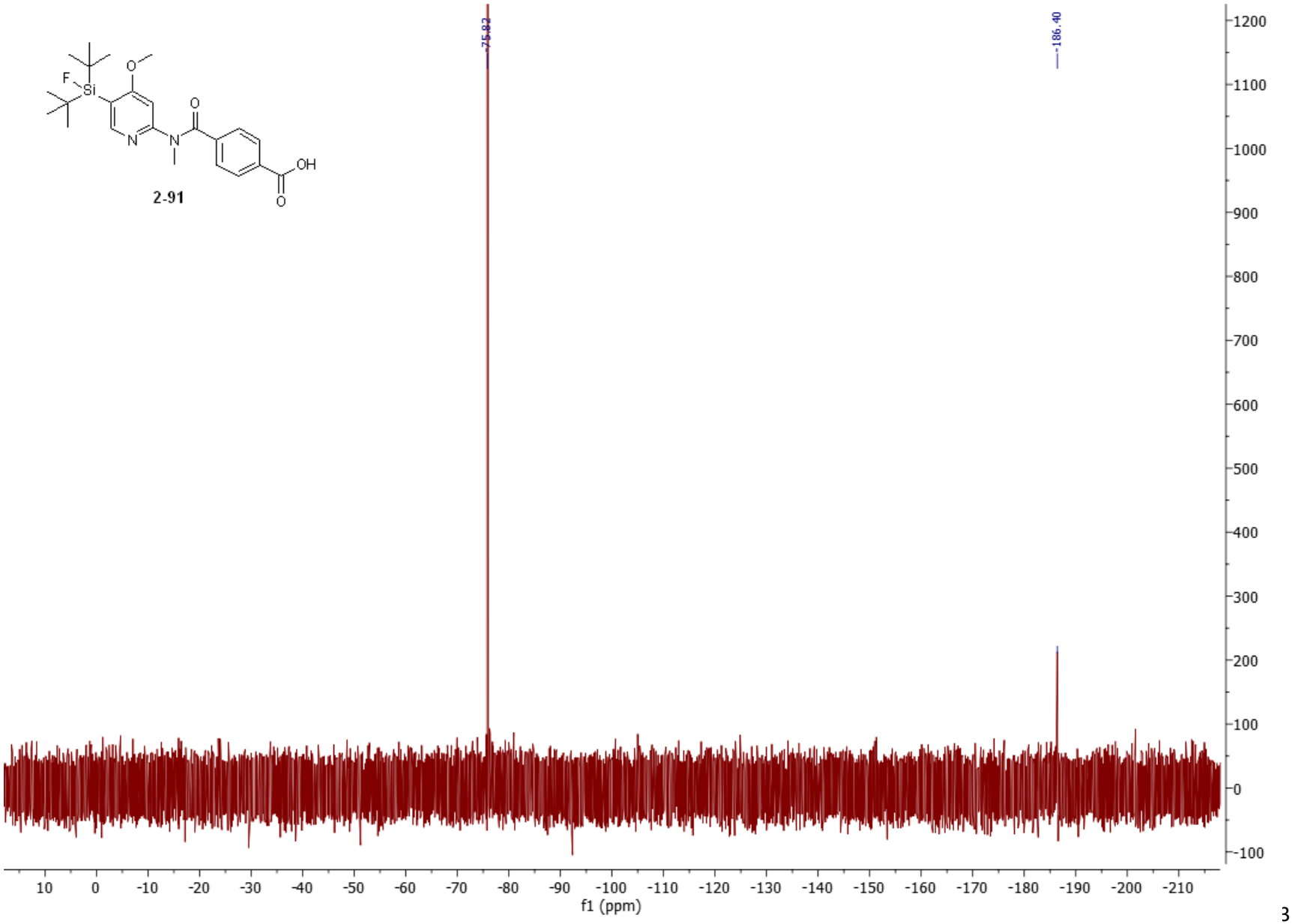
F
Si
O
O
N
N
O
OH
O
2-91
-75.82
-186.40
1200
1100
1000
900
800
700
600
500
400
300
200
100
0
-100
10
0
-10
-20
-30
-40
-50
-60
-70
-80
-90
-100
-110
-120
-130
-140
-150
-160
-170
-180
-190
-200
-210
f1 (ppm)

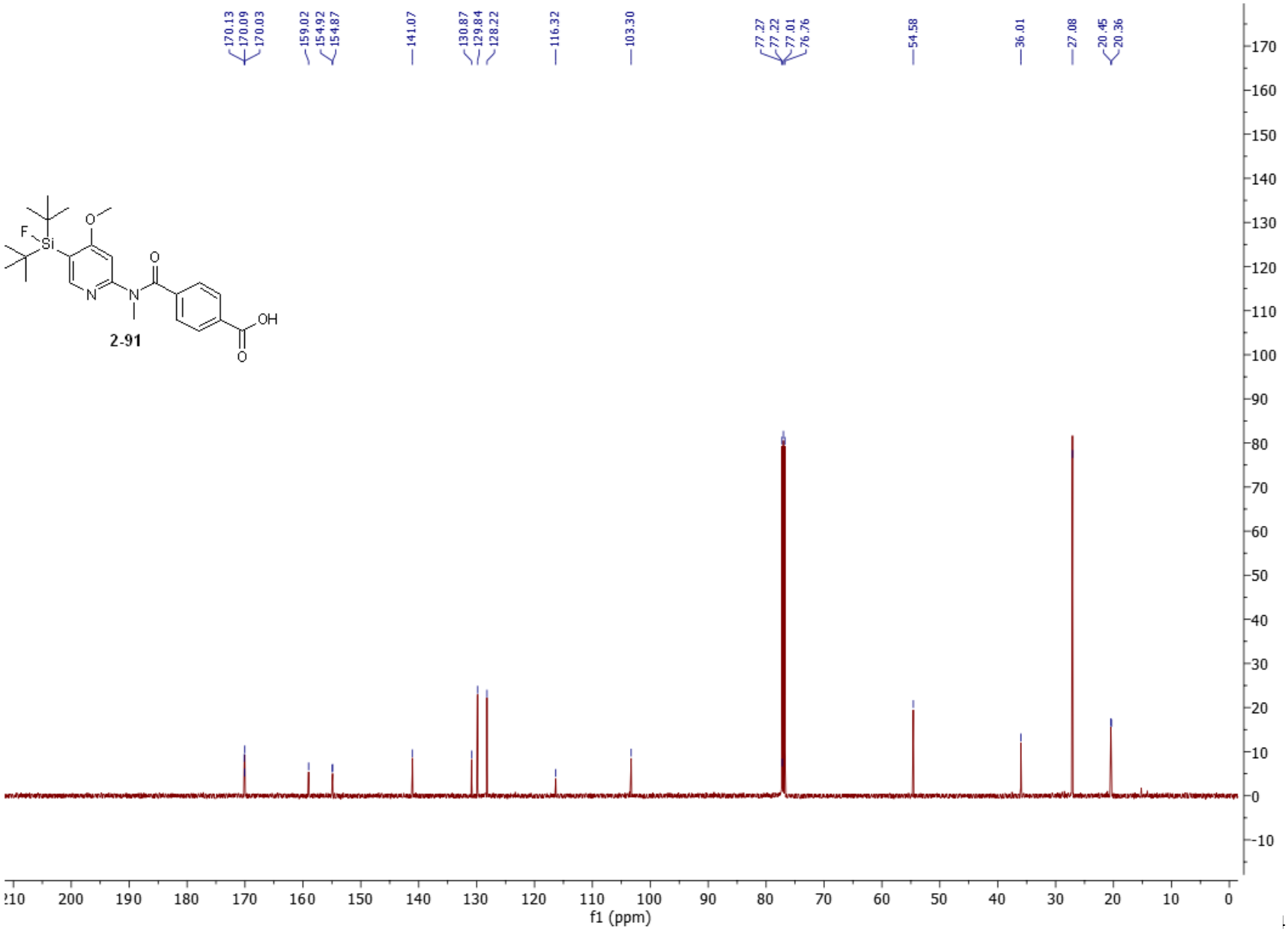
170.13
170.09
170.03
159.02
154.92
154.87
141.07
130.87
129.84
128.22
116.32
103.30
77.27
77.22
77.01
76.76
54.58
36.01
27.08
20.45
20.36
F
Si
O
N
O
N
OH
O
2-91
f1 (ppm)

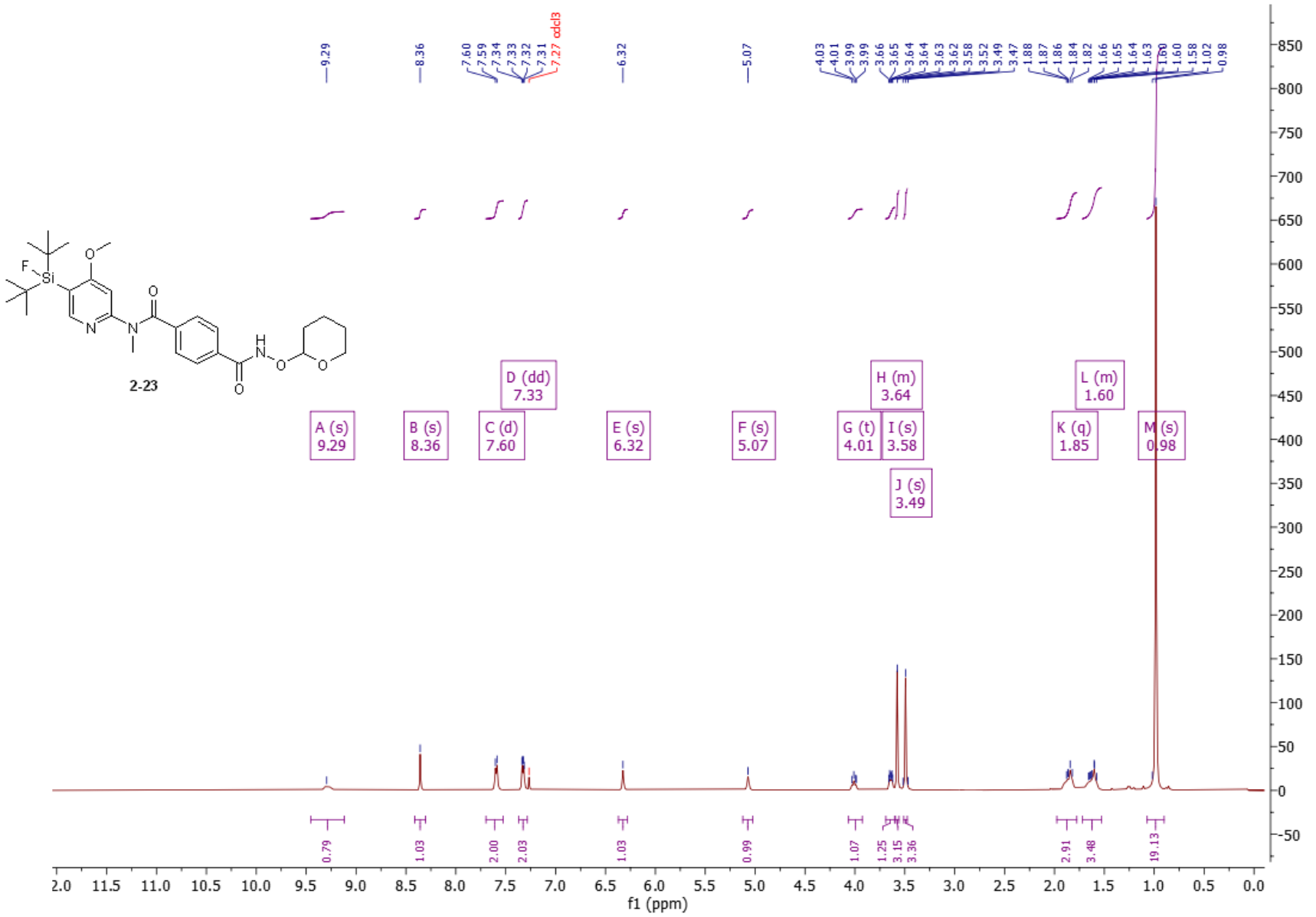
9.29
8.36
7.60
7.59
7.34
7.33
7.32
7.31
7.27 cdcl3
6.32
5.07
4.03
4.01
3.99
3.99
3.66
3.65
3.64
3.64
3.63
3.62
3.58
3.52
3.49
3.47
1.88
1.87
1.86
1.84
1.82
1.66
1.65
1.64
1.63
1.60
1.60
1.58
1.02
0.98
2-23
A (s) 9.29
B (s) 8.36
C (d) 7.60
D (dd) 7.33
E (s) 6.32
F (s) 5.07
G (t) 4.01
H (m) 3.64
I (s) 3.58
J (s) 3.49
K (q) 1.85
L (m) 1.60
M (s) 0.98
0.79
1.03
2.00
2.03
1.03
0.99
1.07
1.25
3.15
3.36
2.91
3.48
19.13
f1 (ppm)

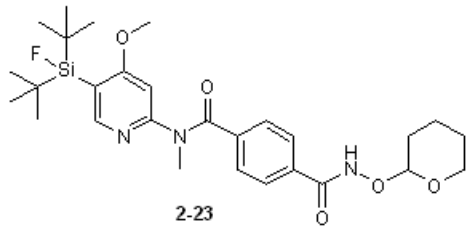
F
Si
O
N
N
O
H
N
O
O
O

2-23

186.55
450
400
350
300
250
200
150
100
50
0
-50
20
10
0
-10
-20
-30
-40
-50
-60
-70
-80
-90
-100
-110
-120
-130
-140
-150
-160
-170
-180
-190
-200
f1 (ppm)

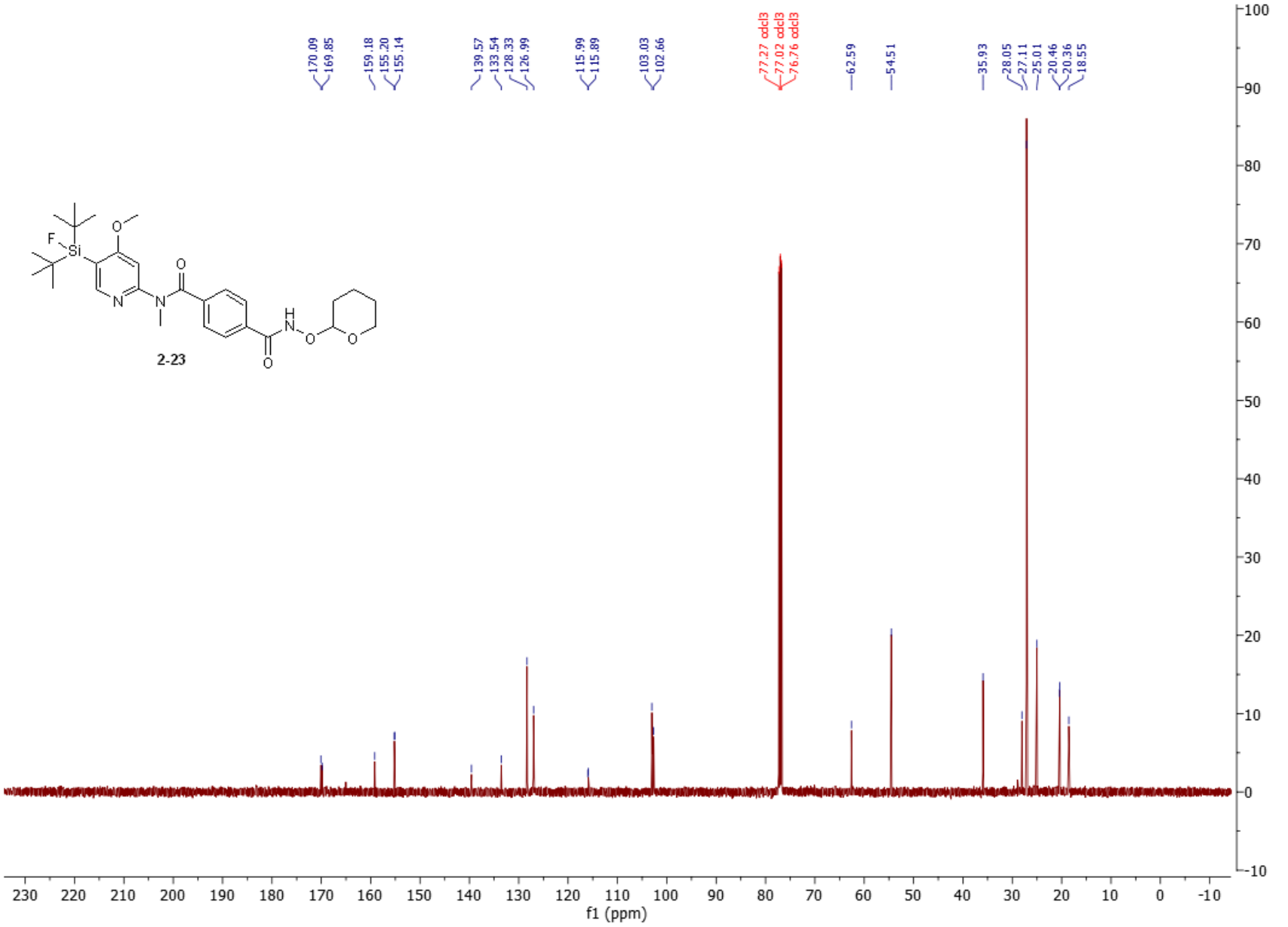
170.09
169.85
159.18
155.20
155.14
139.57
133.54
128.33
126.99
115.99
115.89
103.03
102.66
77.27 cdcl3
77.02 cdcl3
76.76 cdcl3
62.59
54.51
35.93
28.05
27.11
25.01
20.46
20.36
18.55
2-23
f1 (ppm)

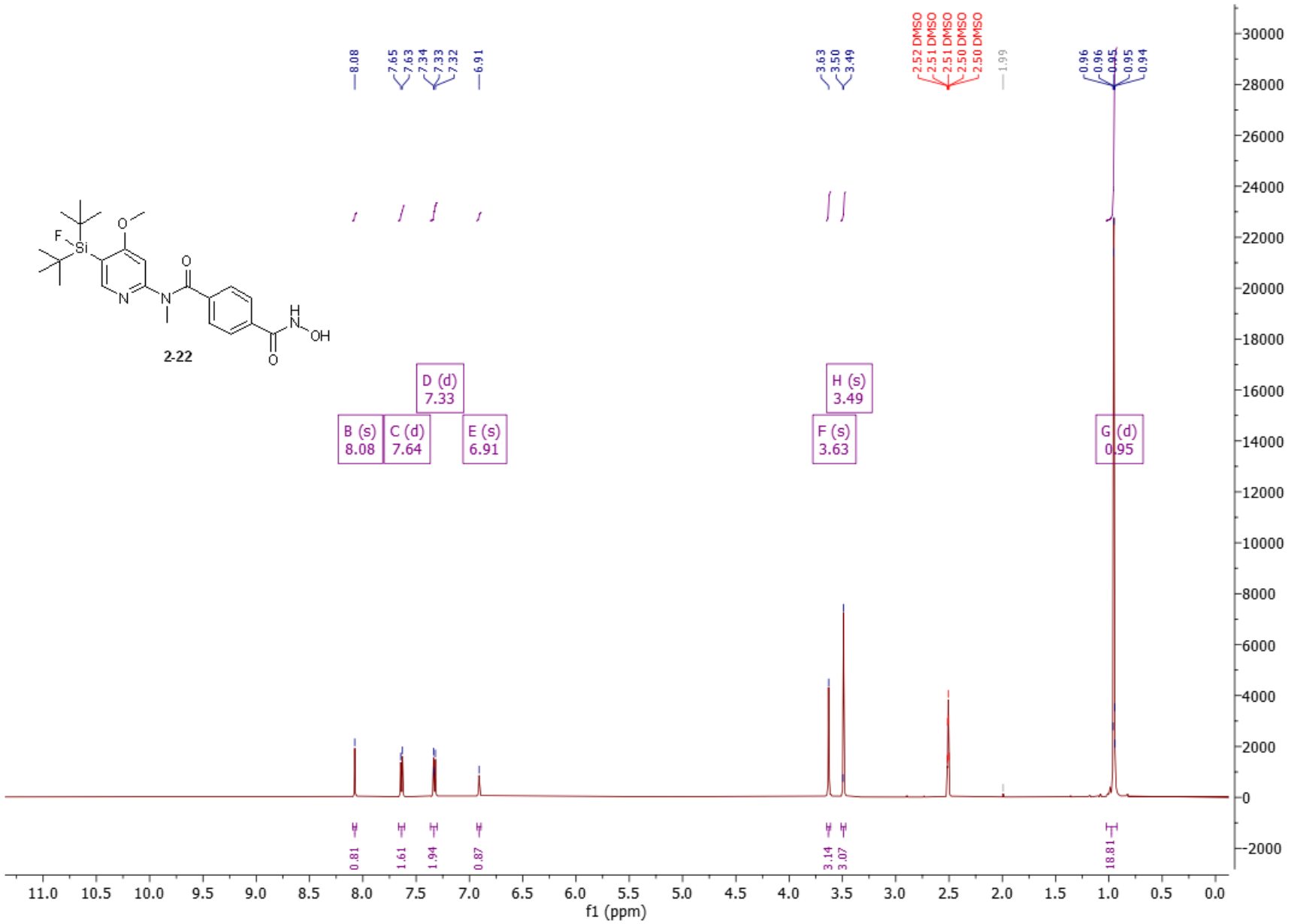
2-22
8.08
7.65
7.63
7.34
7.33
7.32
6.91
3.63
3.50
3.49
2.52 DMSO
2.51 DMSO
2.51 DMSO
2.50 DMSO
2.50 DMSO
1.99
0.96
0.96
0.95
0.95
0.94
B (s) 8.08
C (d) 7.64
D (d) 7.33
E (s) 6.91
F (s) 3.63
H (s) 3.49
G (d) 0.95
0.81
1.61
1.94
0.87
3.14
3.07
18.81
f1 (ppm)

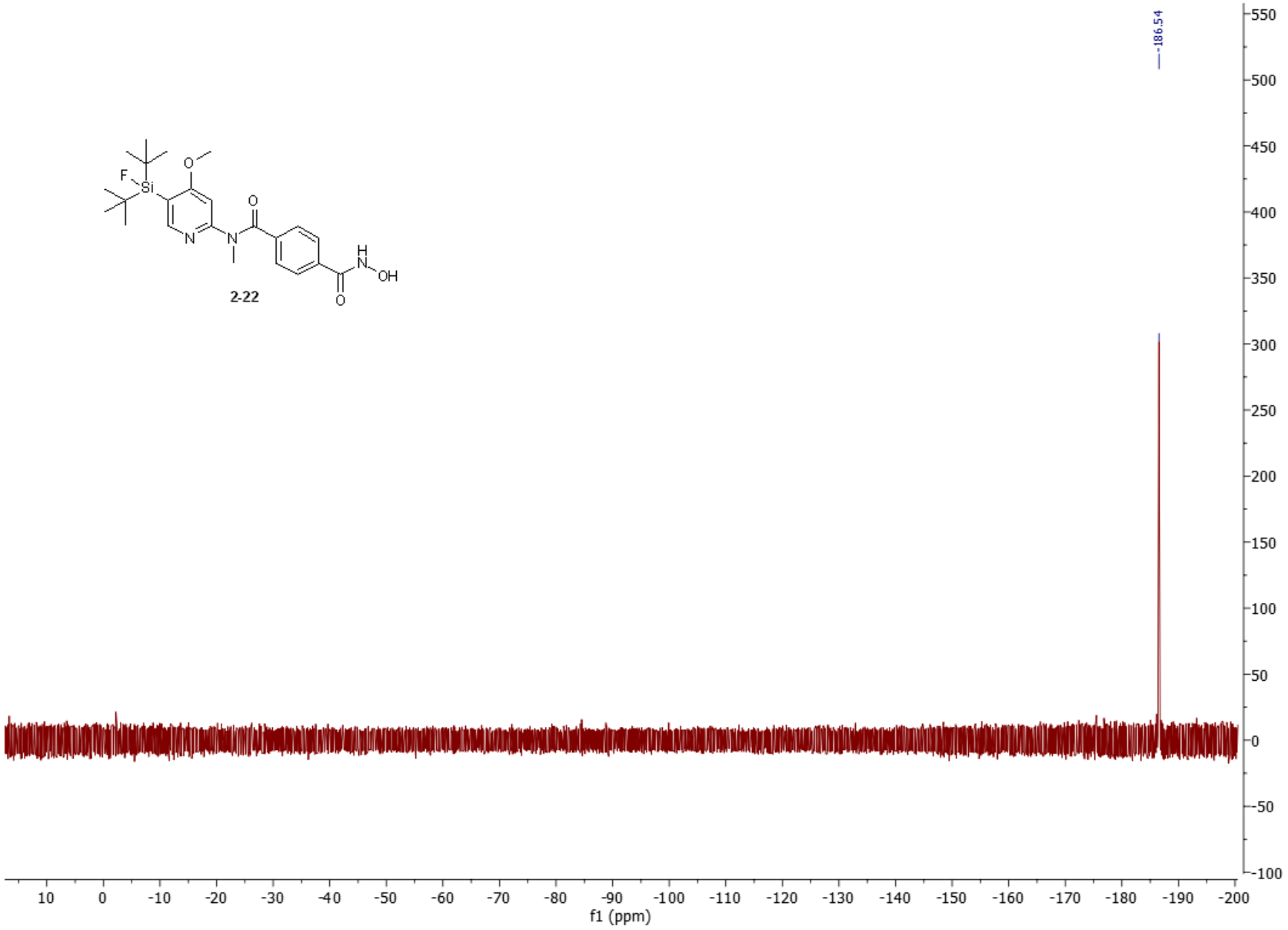
-186.54
550
500
450
400
350
300
250
200
150
100
50
0
-50
-100
F
Si
O
O
N
N
H
N
OH
O
2-22
10
0
-10
-20
-30
-40
-50
-60
-70
-80
-90
-100
-110
-120
-130
-140
-150
-160
-170
-180
-190
-200
f1 (ppm)

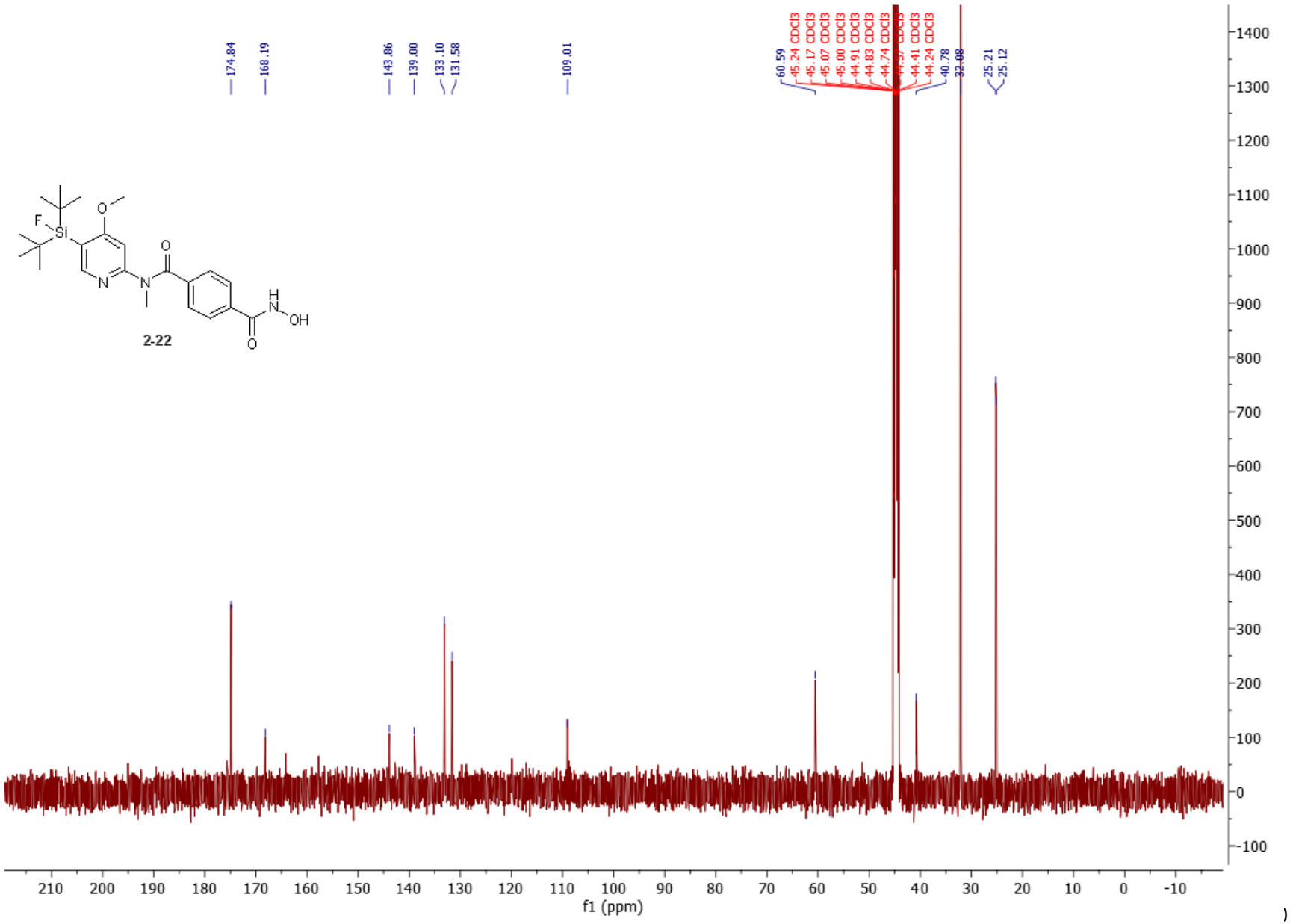
174.84
168.19
143.86
139.00
133.10
131.58
109.01
60.59
45.24 CDCl3
45.17 CDCl3
45.07 CDCl3
45.00 CDCl3
44.91 CDCl3
44.83 CDCl3
44.74 CDCl3
44.41 CDCl3
44.24 CDCl3
40.78
32.08
25.21
25.12
F
Si
O
N
N
O
H
N
OH
O
2-22
f1 (ppm)

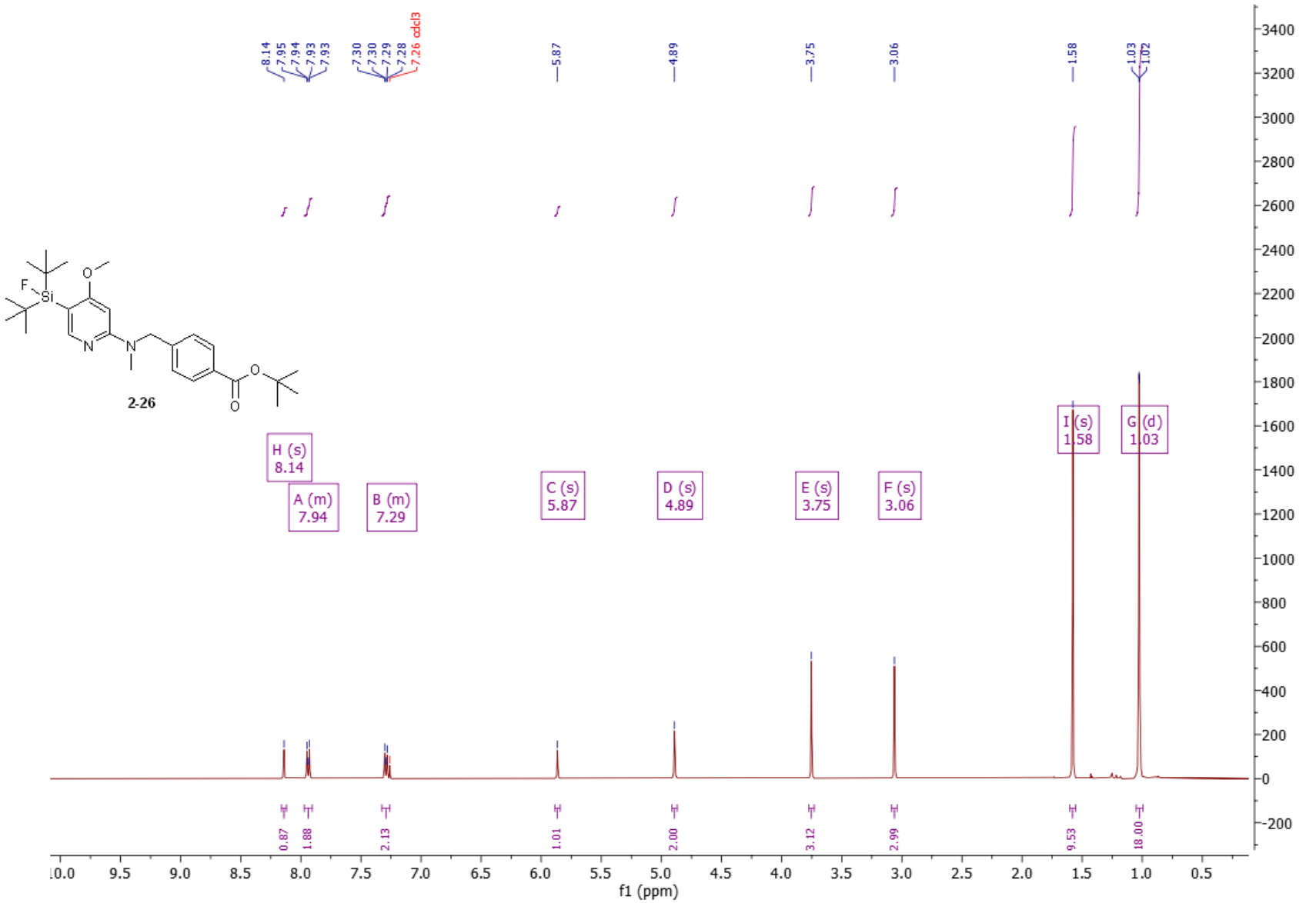
8.14
7.95
7.94
7.93
7.93
7.30
7.30
7.29
7.28
7.26 cdcl3
5.87
4.89
3.75
3.06
1.58
1.03
1.02
F
Si
O
N
N
O
O
2-26
H (s)
8.14
A (m)
7.94
B (m)
7.29
C (s)
5.87
D (s)
4.89
E (s)
3.75
F (s)
3.06
I (s)
1.58
G (d)
1.03
0.87
1.88
2.13
1.01
2.00
3.12
2.99
9.53
18.00
f1 (ppm)

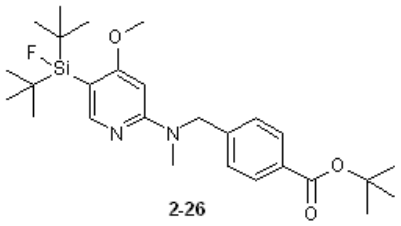
F
Si
O
N
N
O
O

2-26

-187.46
800
750
700
650
600
550
500
450
400
350
300
250
200
150
100
50
0
-50
-100
-150
20
10
0
-10
-20
-30
-40
-50
-60
-70
-80
-90
-100
-110
-120
-130
-140
-150
-160
-170
-180
-190
-200
f1 (ppm)

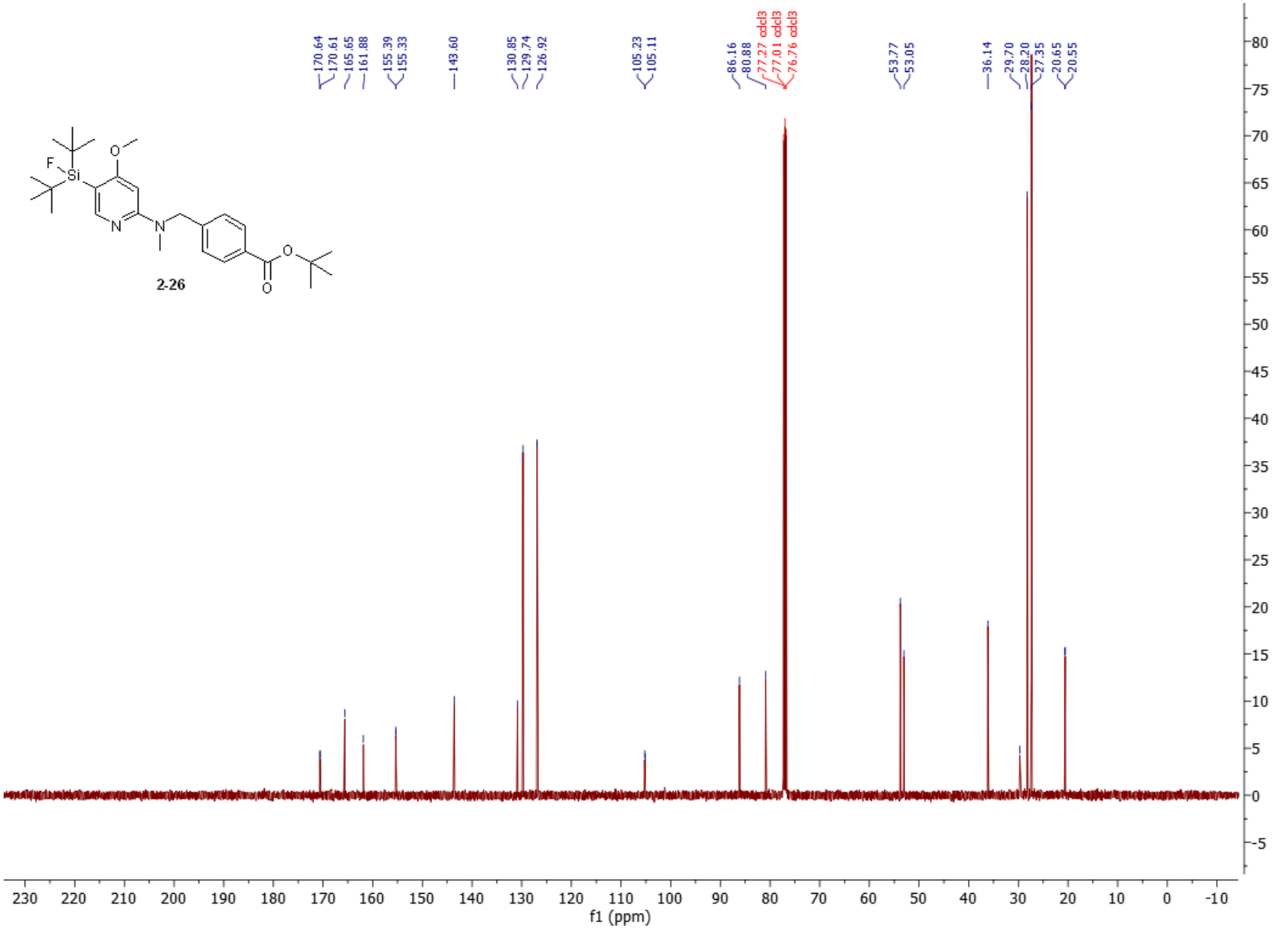
170.64
170.61
165.65
161.88
155.39
155.33
143.60
130.85
129.74
126.92
105.23
105.11
86.16
80.88
77.27 cdcl3
77.01 cdcl3
76.76 cdcl3
53.77
53.05
36.14
29.70
28.20
27.35
20.65
20.55
F
Si
O
N
N
O
O
2-26
f1 (ppm)

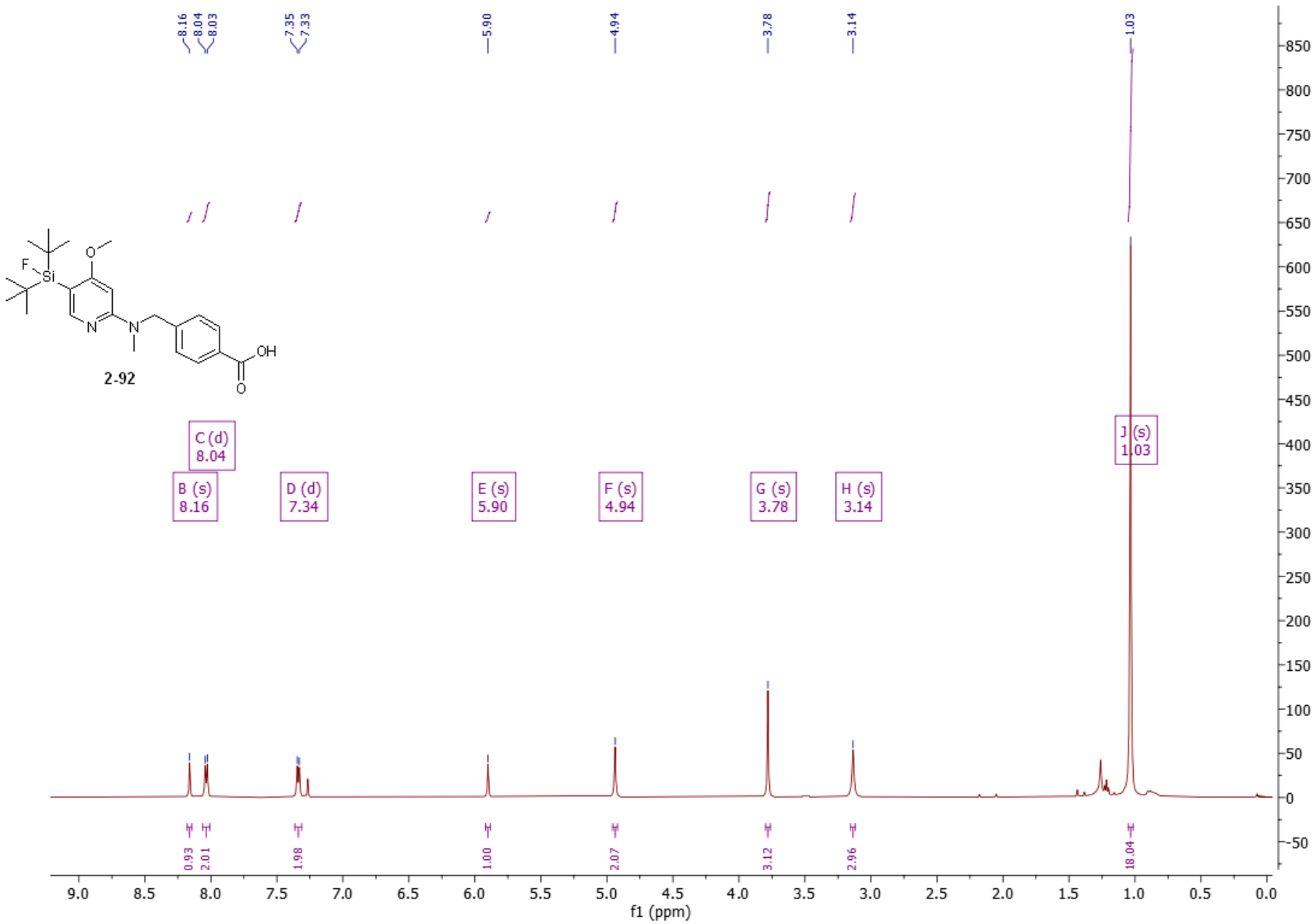
8.16
8.04
8.03
7.35
7.33
5.90
4.94
3.78
3.14
1.03
F
Si
O
N
N
OH
O
2-92
C (d)
8.04
B (s)
8.16
D (d)
7.34
E (s)
5.90
F (s)
4.94
G (s)
3.78
H (s)
3.14
J (s)
1.03
0.93
2.01
1.98
1.00
2.07
3.12
2.96
18.04
f1 (ppm)

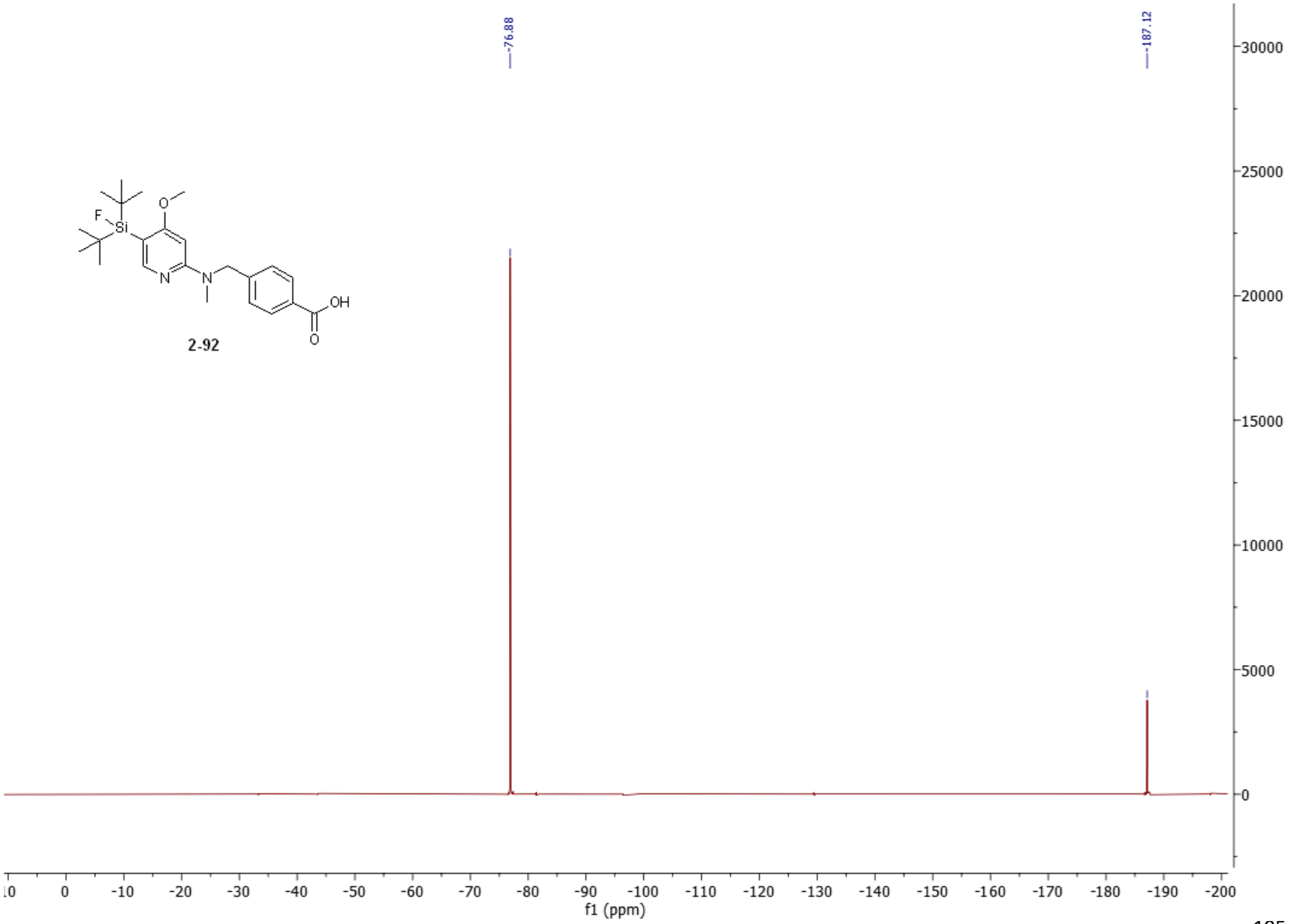
-76.88
-187.12
30000
25000
20000
15000
10000
5000
0
F
Si
O
N
N
OH
O
2-92
.0 0 -10 -20 -30 -40 -50 -60 -70 -80 -90 -100 -110 -120 -130 -140 -150 -160 -170 -180 -190 -200
f1 (ppm)

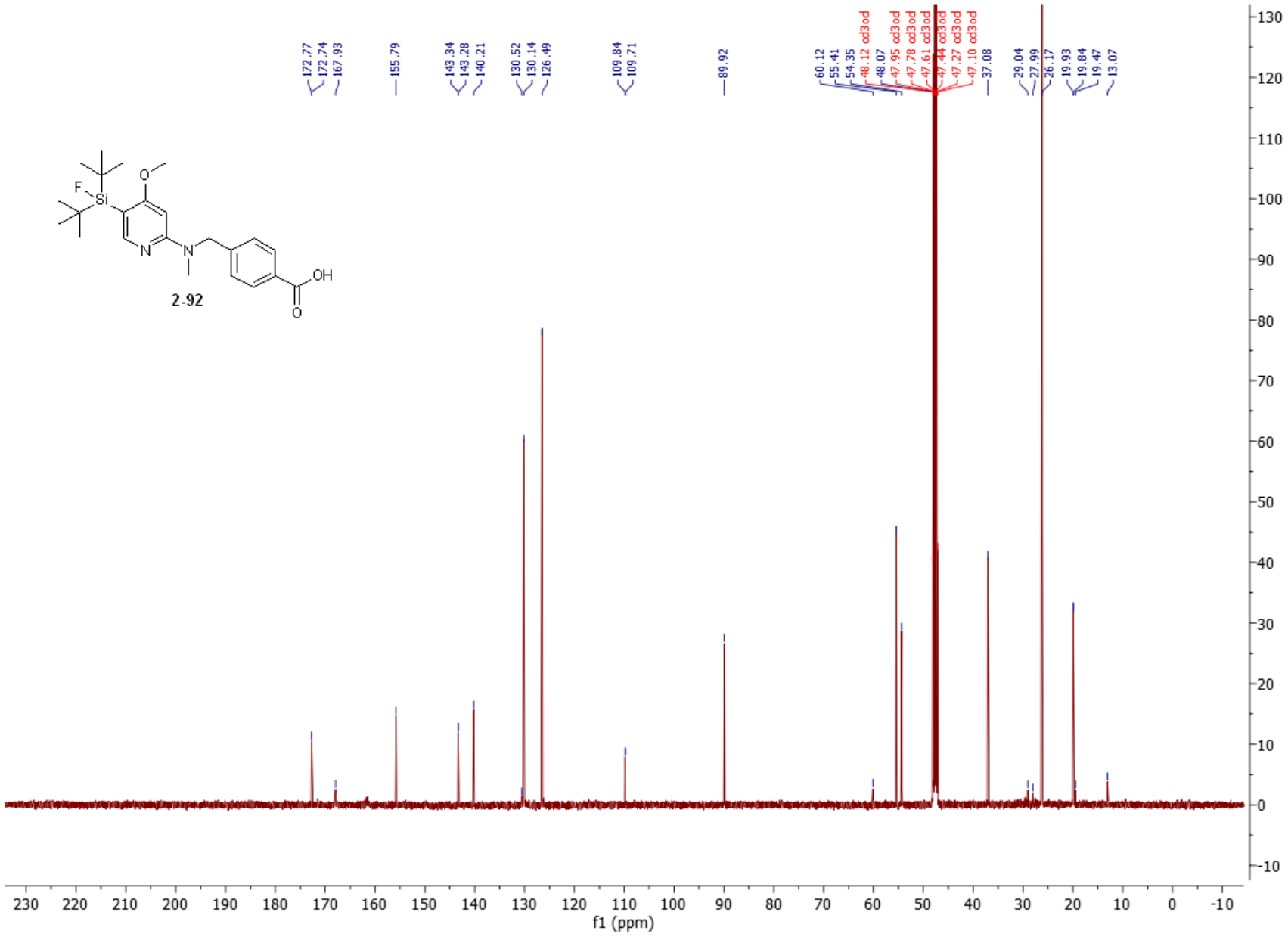
172.77
172.74
167.93
155.79
143.34
143.28
140.21
130.52
130.14
126.49
109.84
109.71
89.92
60.12
55.41
54.35
48.12 cd3od
48.07
47.95 cd3od
47.78 cd3od
47.61 cd3od
47.44 cd3od
47.27 cd3od
47.10 cd3od
37.08
29.04
27.99
26.17
19.93
19.84
19.47
13.07
F
Si
O
N
N
OH
O
2-92
f1 (ppm)

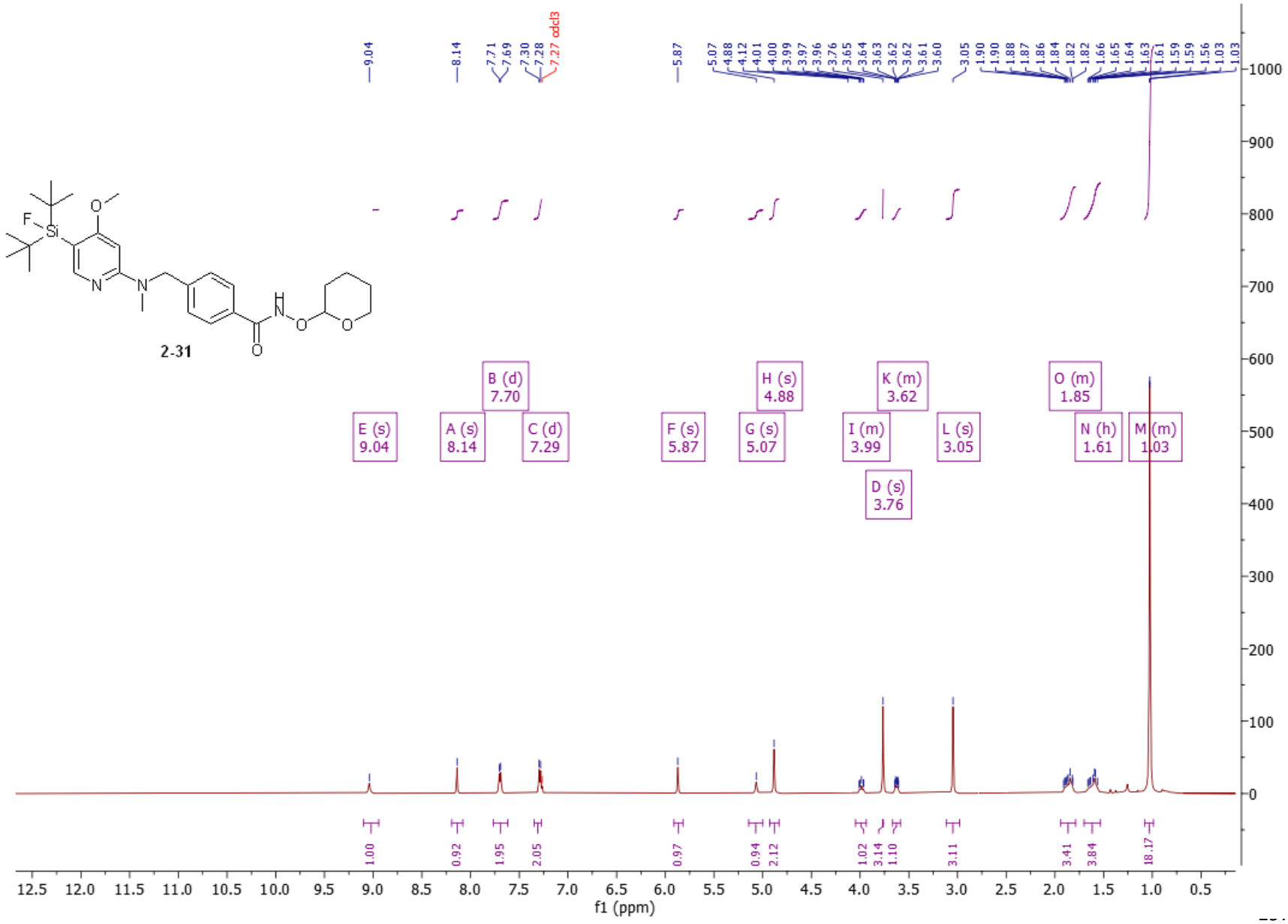
2-31
E (s) 9.04
A (s) 8.14
B (d) 7.70
C (d) 7.29
F (s) 5.87
G (s) 5.07
H (s) 4.88
I (m) 3.99
D (s) 3.76
K (m) 3.62
L (s) 3.05
O (m) 1.85
N (h) 1.61
M (m) 1.03
f1 (ppm)

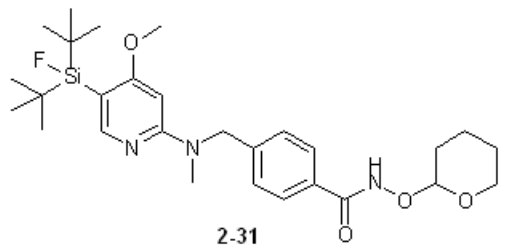
F
Si
O
N
N
H
N
O
O
O

2-31

-187.39
3000
2800
2600
2400
2200
2000
1800
1600
1400
1200
1000
800
600
400
200
0
-200
-400
10
0
-10
-20
-30
-40
-50
-60
-70
-80
-90
-100
-110
-120
-130
-140
-150
-160
-170
-180
-190
-200
f1 (ppm)

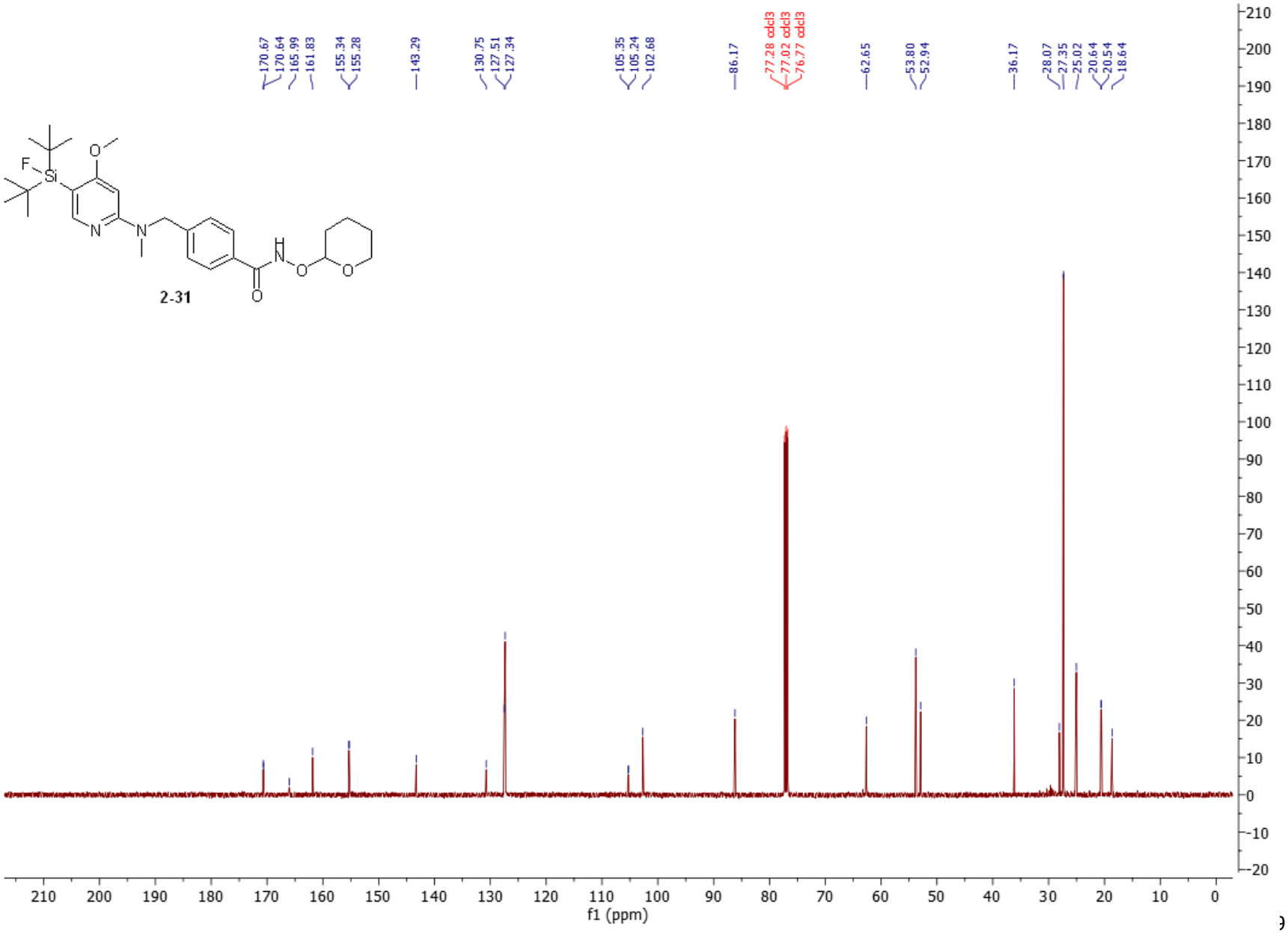
170.67
170.64
165.99
161.83
155.34
155.28
143.29
130.75
127.51
127.34
105.35
105.24
102.68
86.17
77.28 cdcl3
77.02 cdcl3
76.77 cdcl3
62.65
53.80
52.94
36.17
28.07
27.35
25.02
20.64
20.54
18.64
F
Si
O
N
N
H
N
O
O
O
2-31
f1 (ppm)

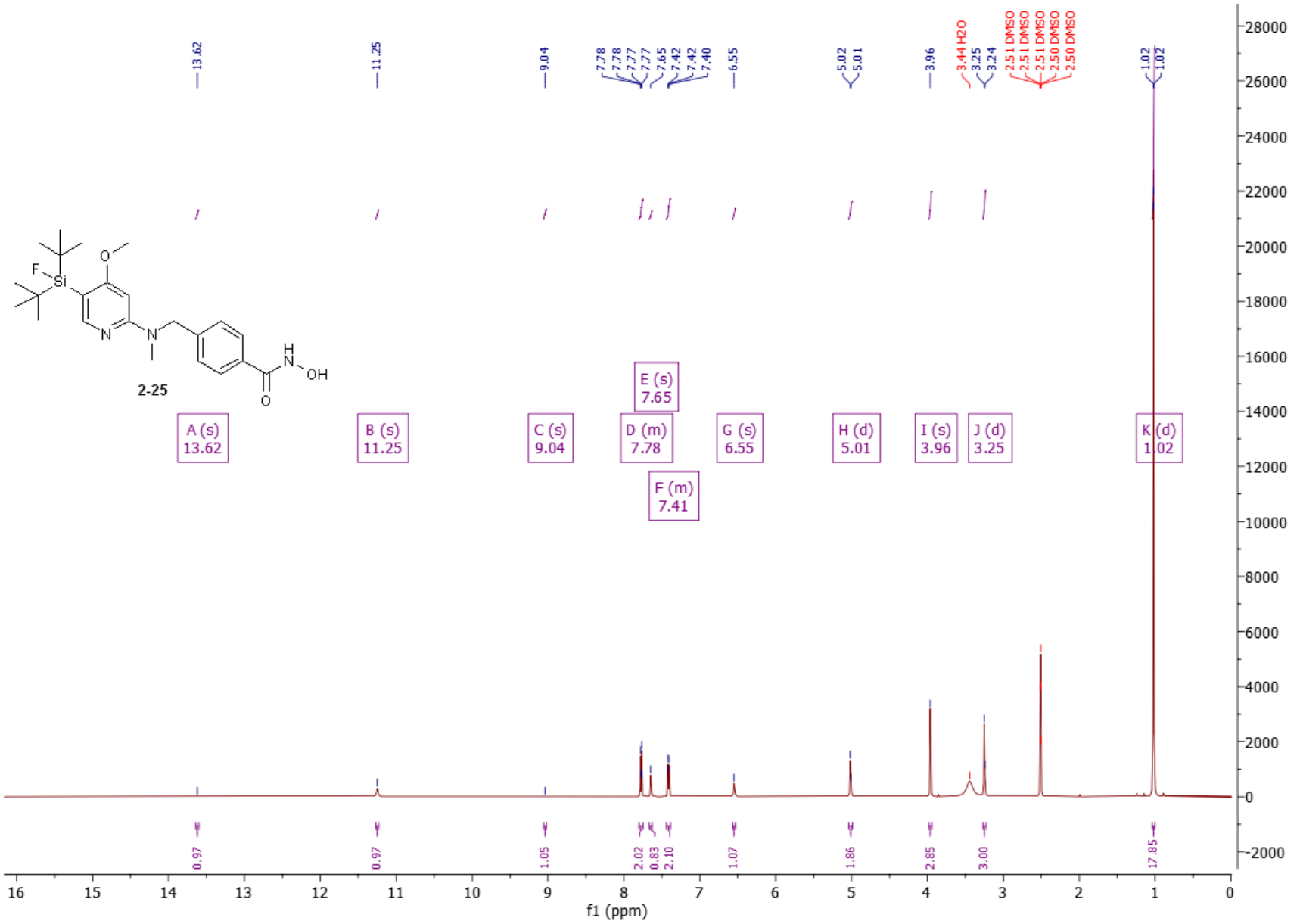
13.62
11.25
9.04
7.78
7.78
7.77
7.77
7.65
7.42
7.42
7.40
6.55
5.02
5.01
3.96
3.44 H2O
3.25
3.24
2.51 DMSO
2.51 DMSO
2.51 DMSO
2.50 DMSO
2.50 DMSO
1.02
1.02
F
Si
O
N
N
H
N
OH
O
2-25
A (s) 13.62
B (s) 11.25
C (s) 9.04
D (m) 7.78
E (s) 7.65
F (m) 7.41
G (s) 6.55
H (d) 5.01
I (s) 3.96
J (d) 3.25
K (d) 1.02
0.97
0.97
1.05
2.02
0.83
2.10
1.07
1.86
2.85
3.00
17.85
f1 (ppm)

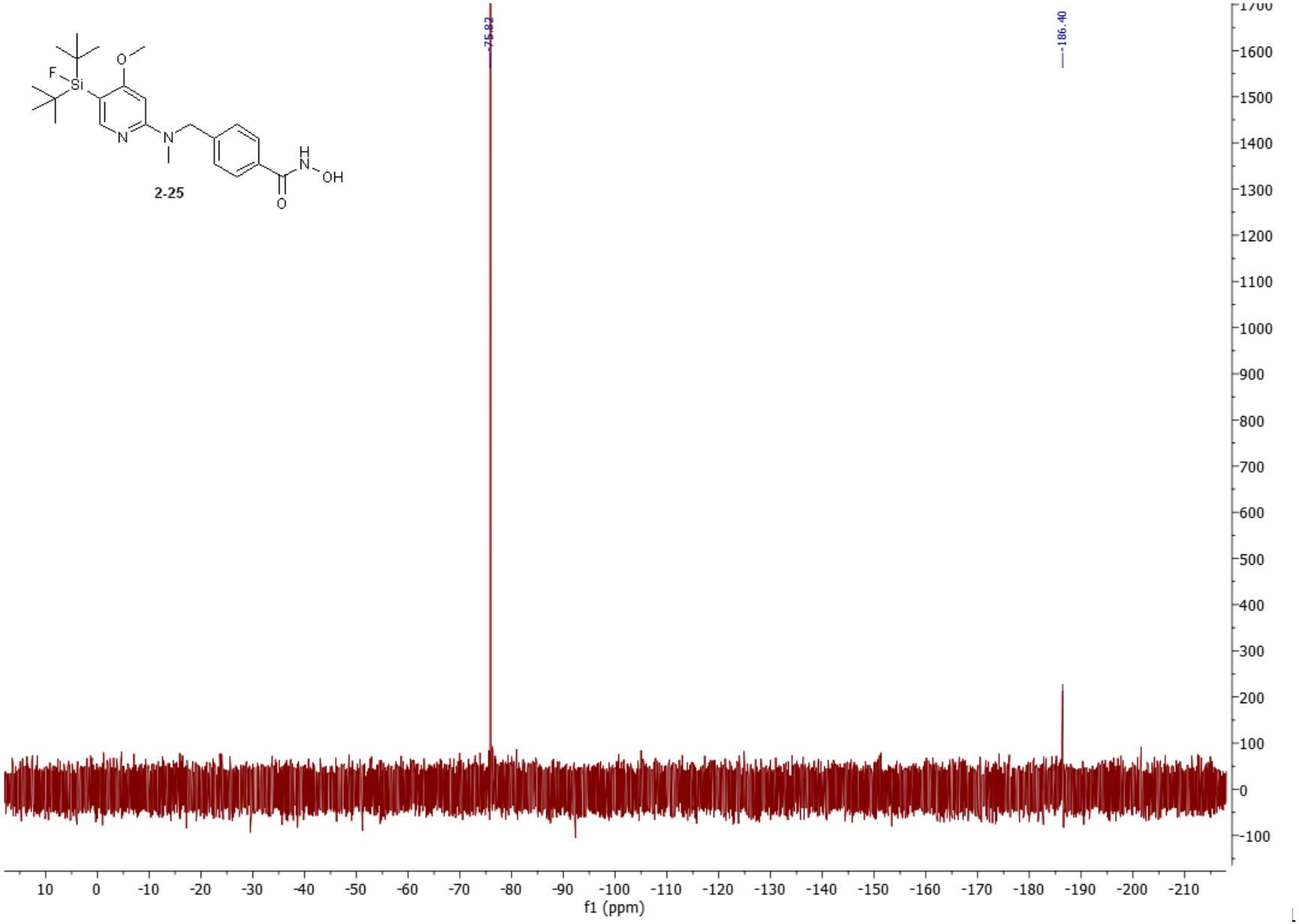
2-25
-75.82
-186.40
f1 (ppm)

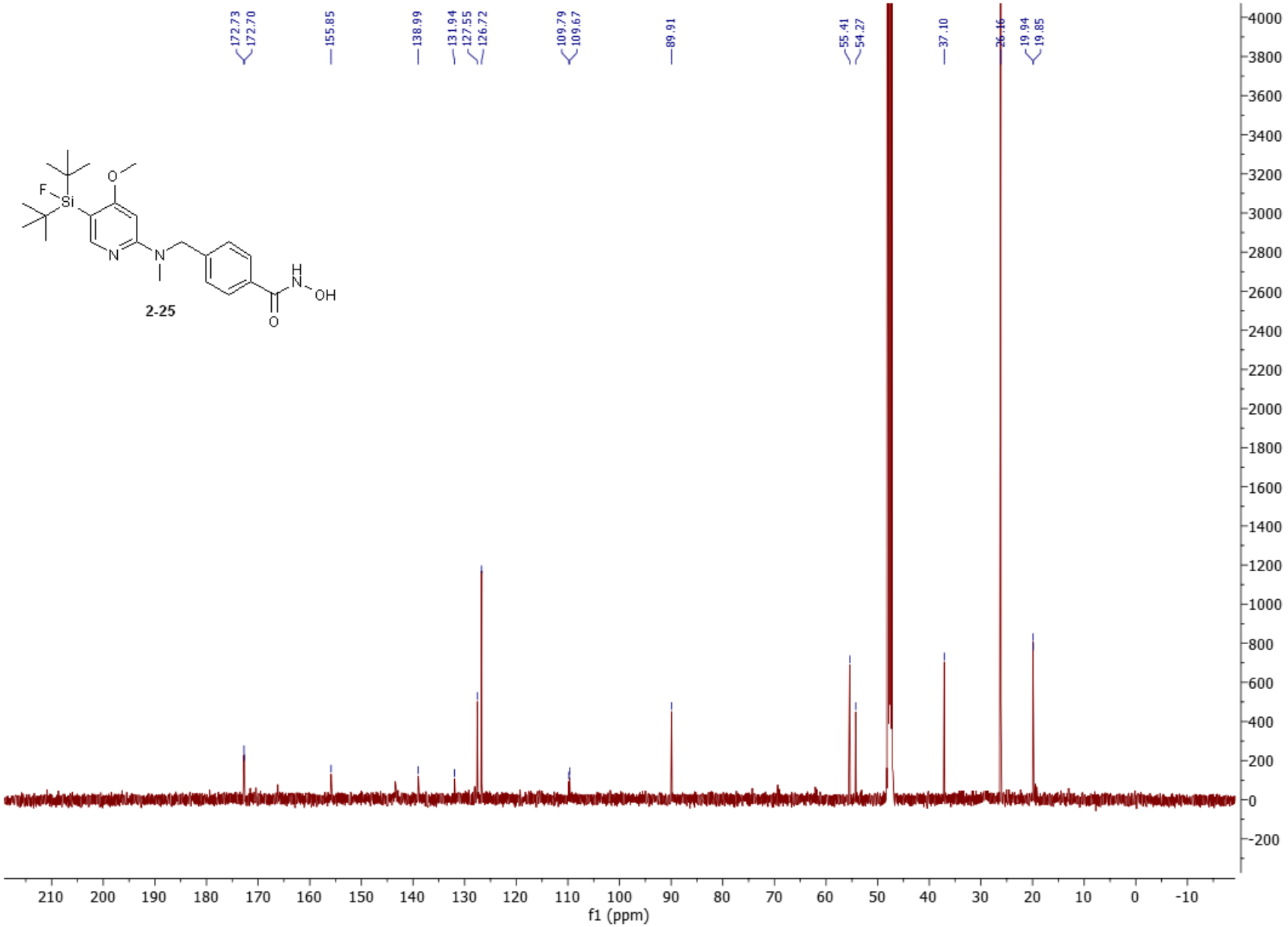
172.73
172.70
155.85
138.99
131.94
127.55
126.72
109.79
109.67
89.91
55.41
54.27
37.10
26.16
19.94
19.85
F
Si
O
N
N
H
N
OH
O
2-25
f1 (ppm)

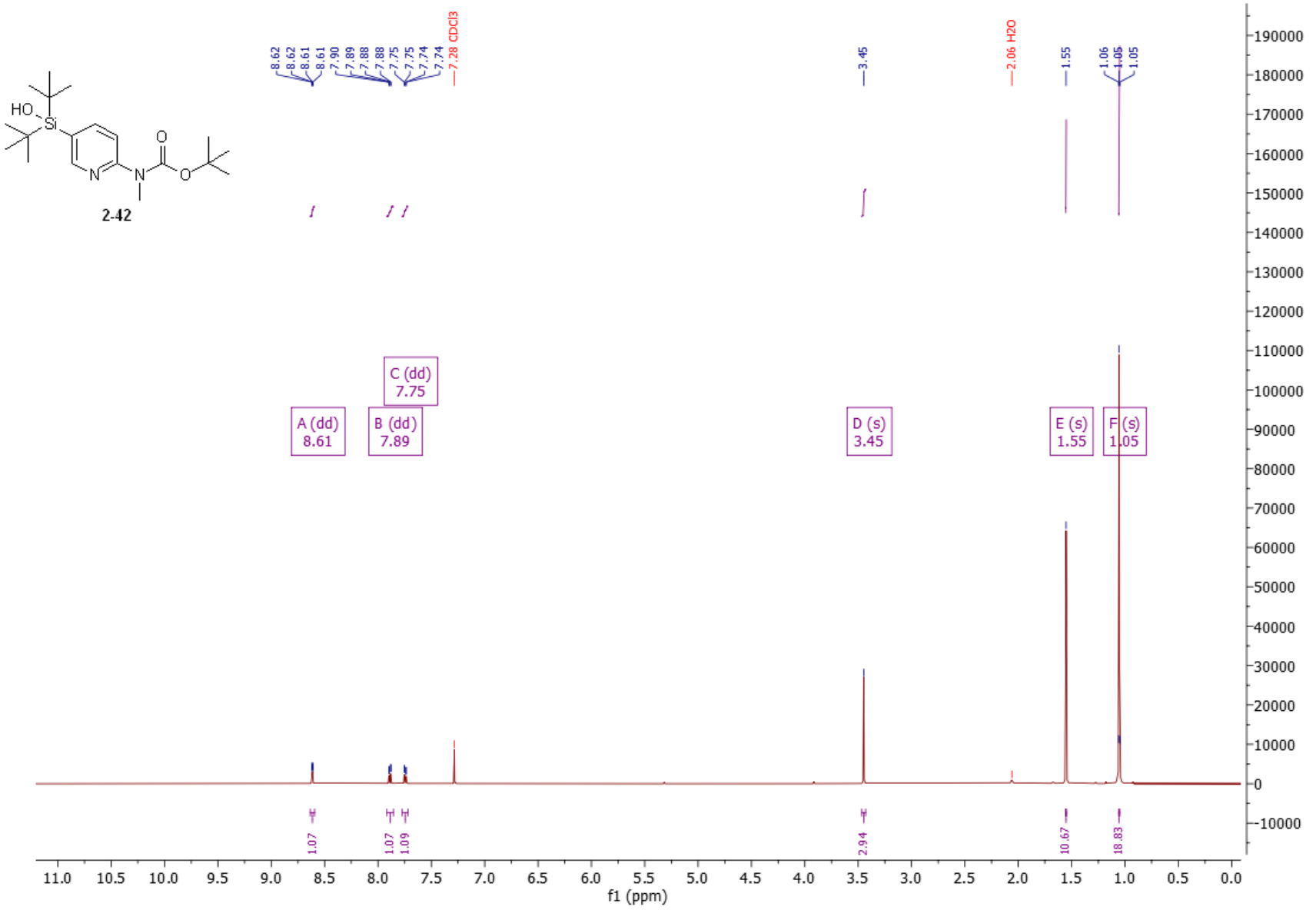
HO
Si
N
N
O
O
2-42
8.62
8.62
8.61
8.61
7.90
7.89
7.88
7.88
7.75
7.75
7.74
7.74
7.28 CDCl3
3.45
2.06 H2O
1.55
1.06
1.05
1.05
A (dd)
8.61
B (dd)
7.89
C (dd)
7.75
D (s)
3.45
E (s)
1.55
F (s)
1.05
1.07
1.07
1.09
2.94
10.67
18.83
f1 (ppm)

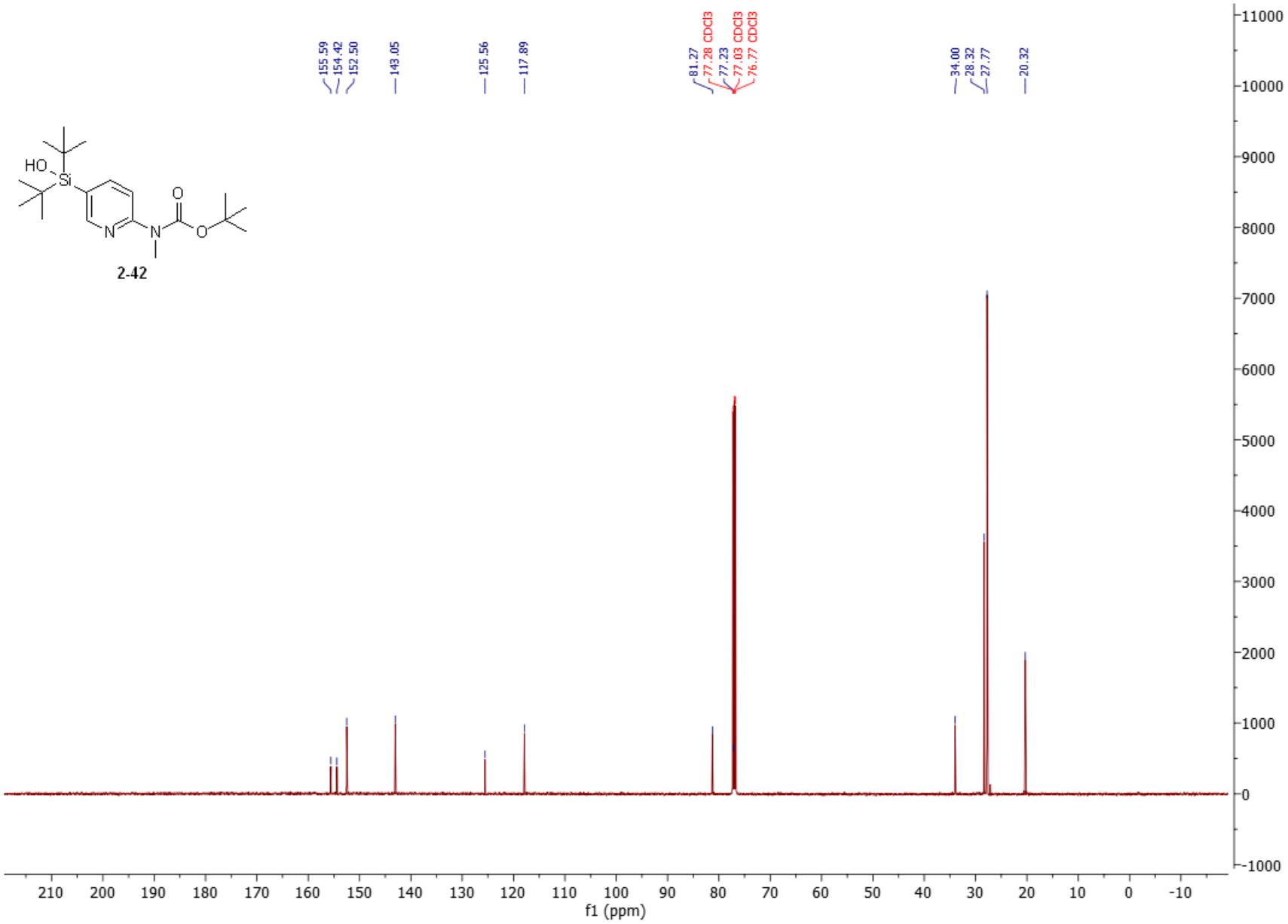
155.59
154.42
152.50
143.05
125.56
117.89
81.27
77.28 CDCl3
77.23
77.03 CDCl3
76.77 CDCl3
34.00
28.32
27.77
20.32
HO
Si
N
N
O
O
2-42
f1 (ppm)

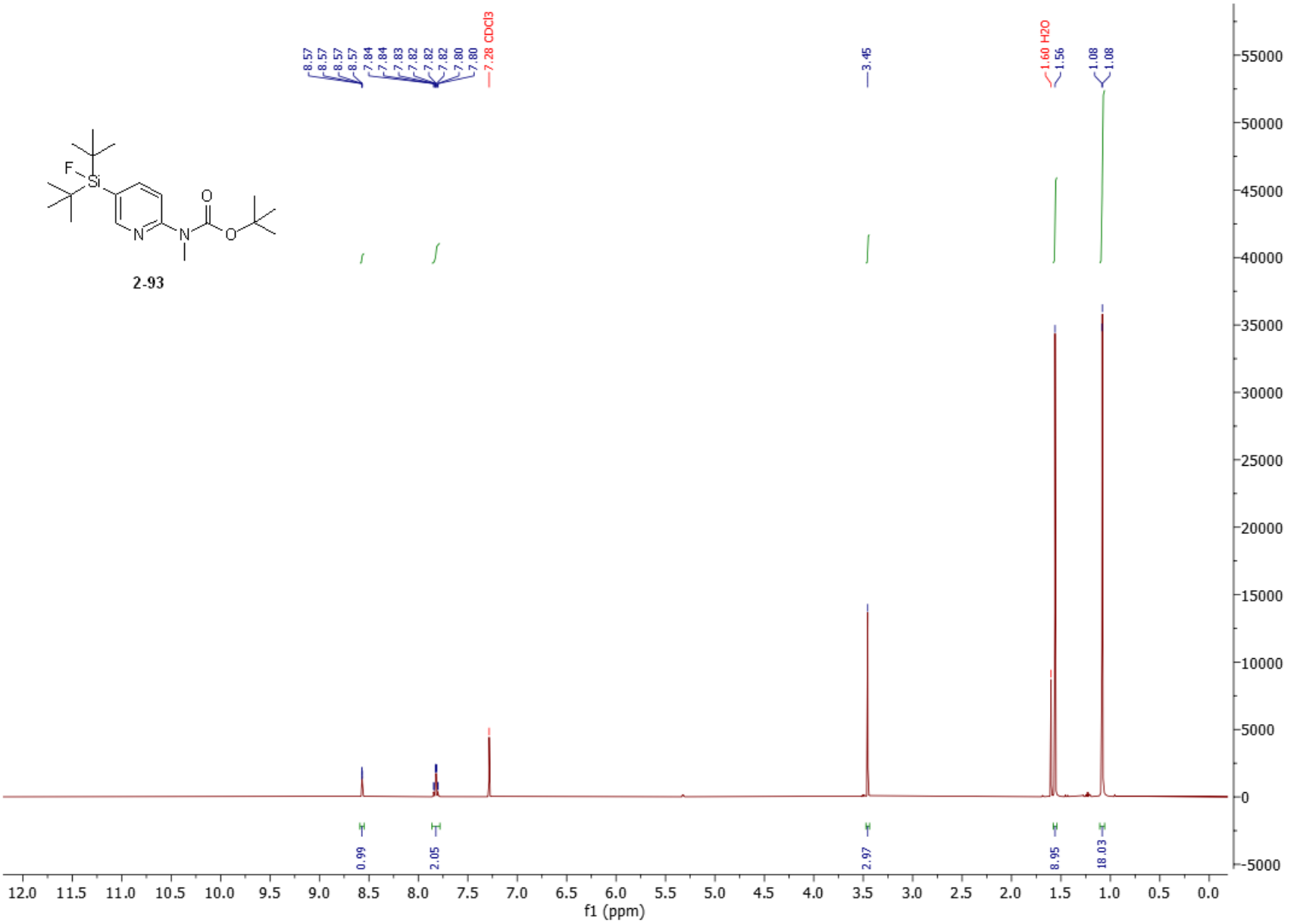
8.57
8.57
8.57
8.57
7.84
7.84
7.83
7.82
7.82
7.82
7.80
7.80
7.28 CDCl3
3.45
1.60 H2O
1.56
1.08
1.08
F
Si
N
N
O
O
2-93
55000
50000
45000
40000
35000
30000
25000
20000
15000
10000
5000
0
-5000
0.99
2.05
2.97
8.95
18.03
12.0
11.5
11.0
10.5
10.0
9.5
9.0
8.5
8.0
7.5
7.0
6.5
6.0
5.5
5.0
4.5
4.0
3.5
3.0
2.5
2.0
1.5
1.0
0.5
0.0
f1 (ppm)

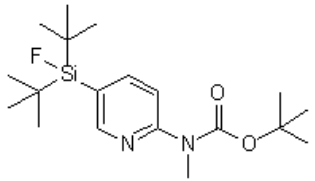
F
Si
N
N
O
O

2-93

-189.22
130
120
110
100
90
80
70
60
50
40
30
20
10
0
-10
-20
-30
10 0 -10 -20 -30 -40 -50 -60 -70 -80 -90 -100 -110 -120 -130 -140 -150 -160 -170 -180 -190 -200 -210
f1 (ppm)

06

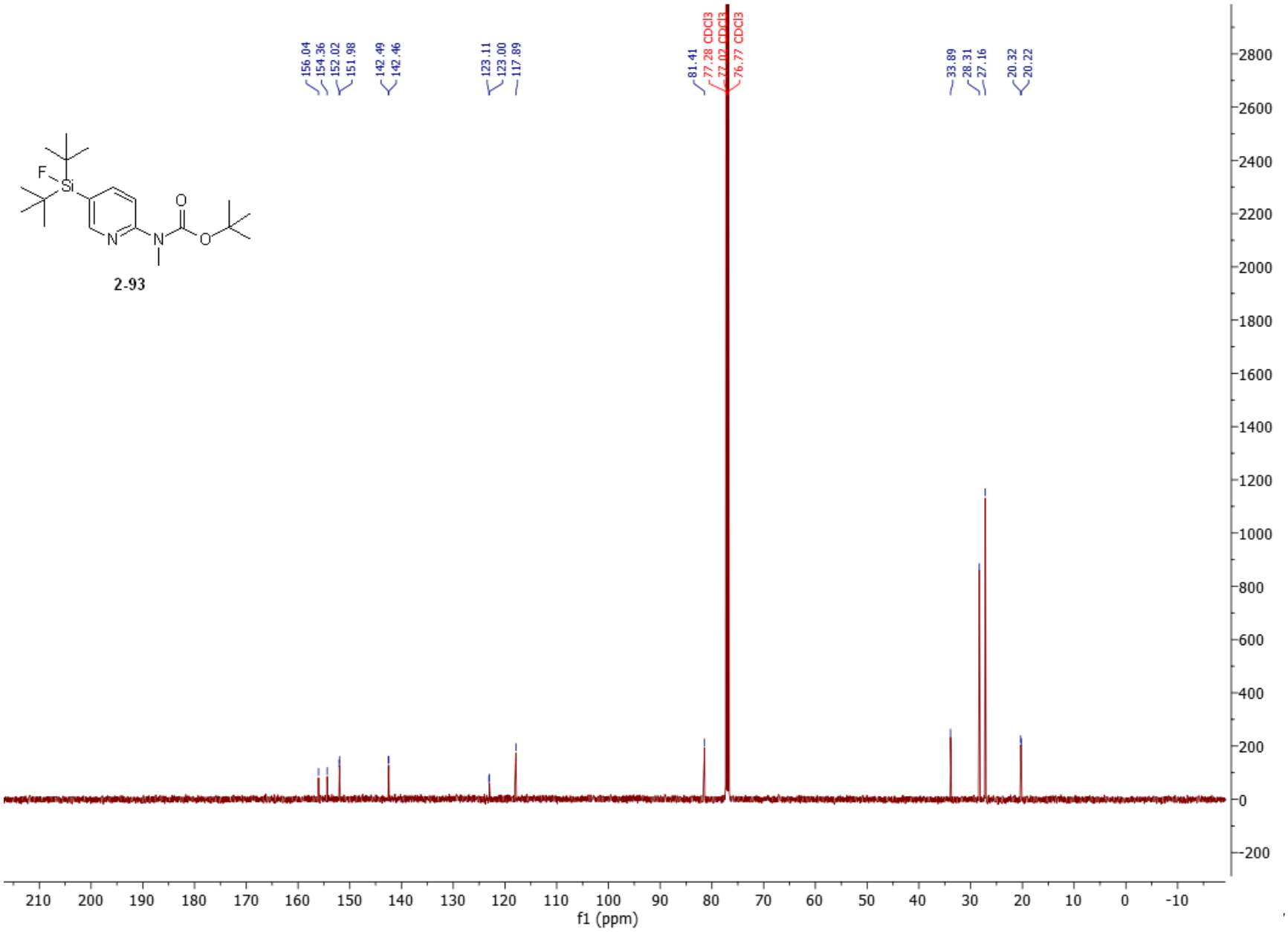
156.04
154.36
152.02
151.98
142.49
142.46
123.11
123.00
117.89
81.41
77.28 CDCl3
77.02 CDCl3
76.77 CDCl3
33.89
28.31
27.16
20.32
20.22
F
Si
N
N
O
O
2-93
f1 (ppm)

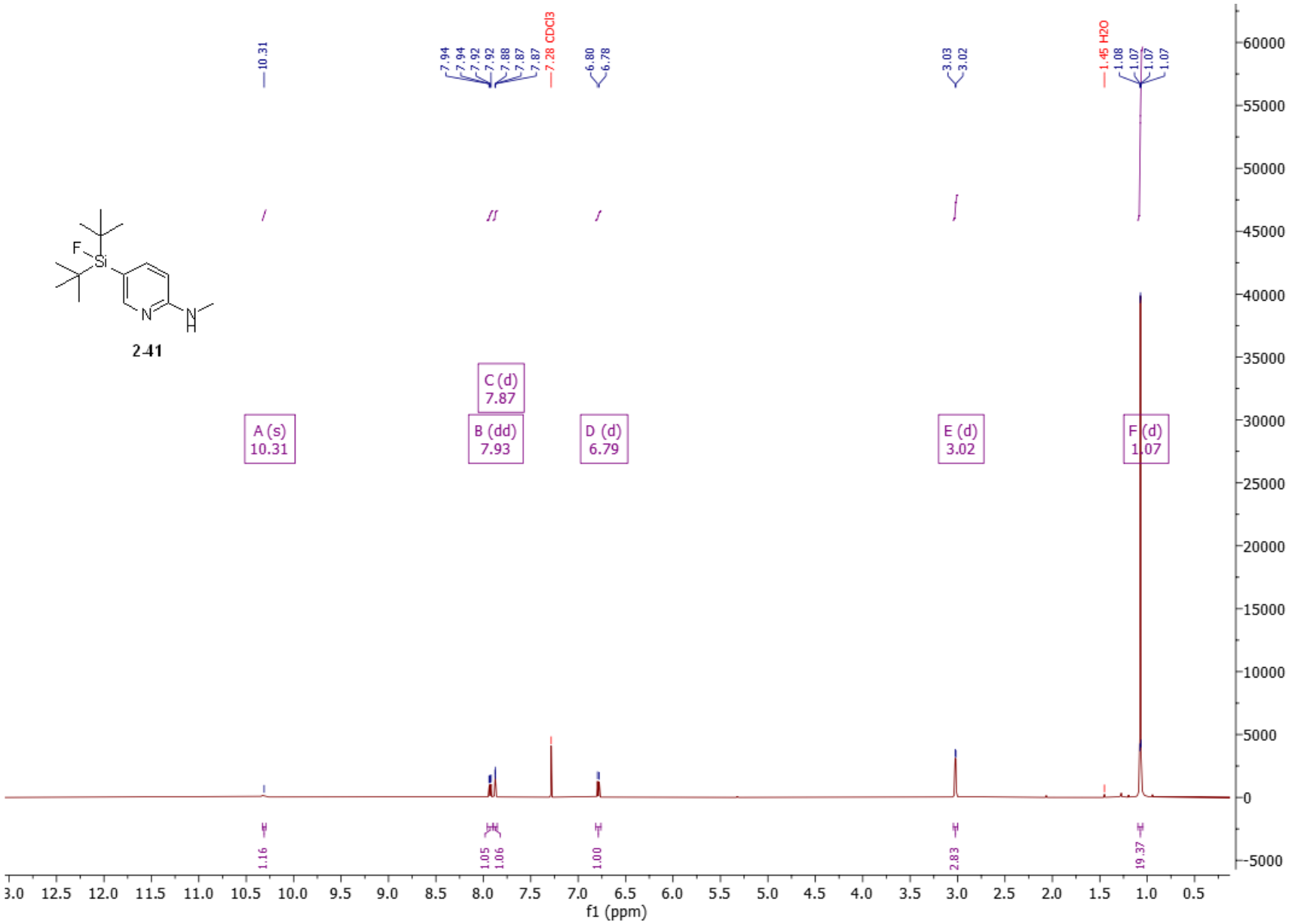
10.31
7.94
7.94
7.92
7.92
7.88
7.87
7.87
7.28 CDCl3
6.80
6.78
3.03
3.02
1.45 H2O
1.08
1.07
1.07
1.07
F
Si
N
N
H
2-41
A (s)
10.31
C (d)
7.87
B (dd)
7.93
D (d)
6.79
E (d)
3.02
F (d)
1.07
1.16
1.05
1.06
1.00
2.83
19.37
f1 (ppm)

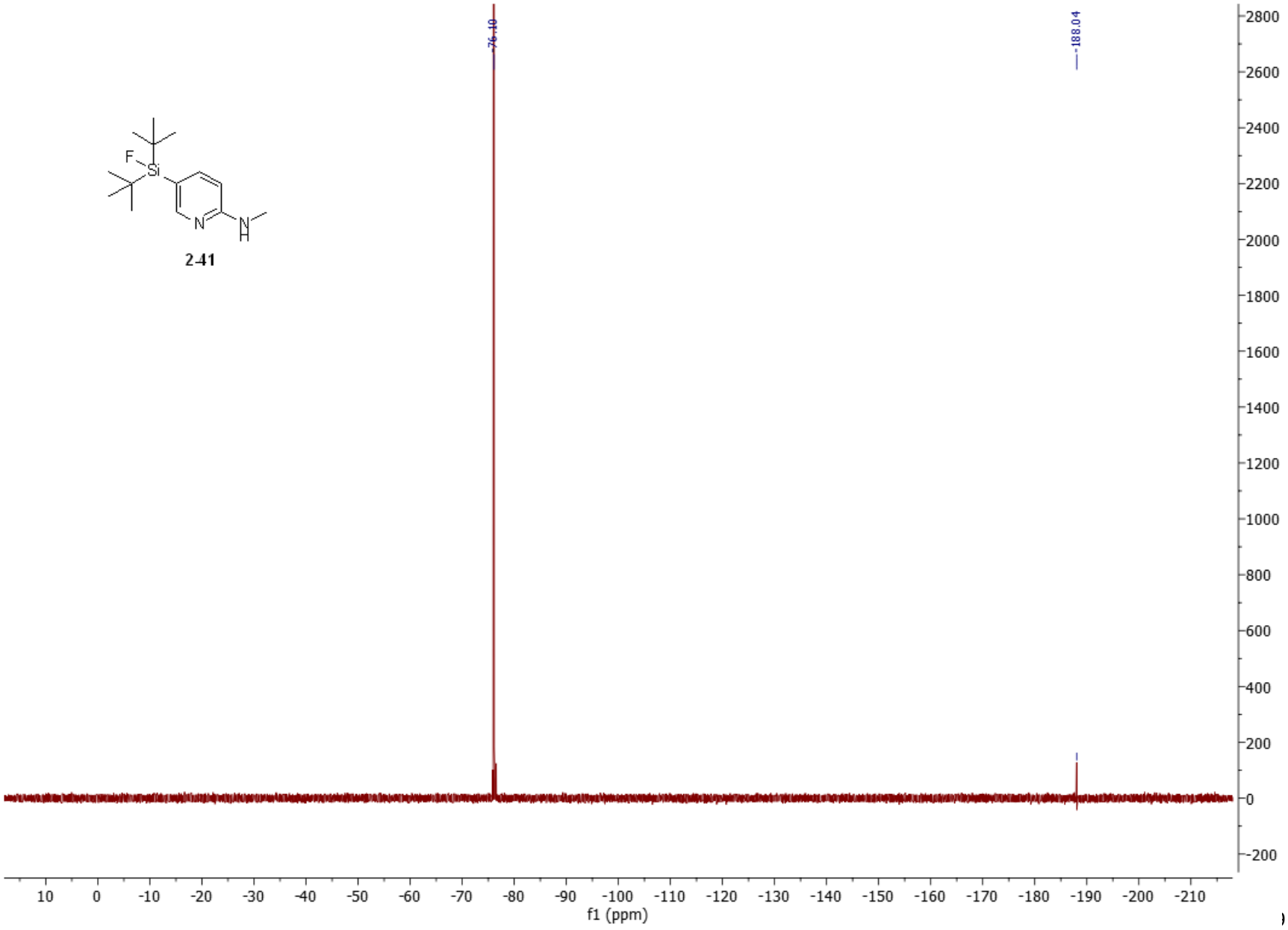
F
Si
N
H
2-41
-76.10
-188.04
2800
2600
2400
2200
2000
1800
1600
1400
1200
1000
800
600
400
200
0
-200
10
0
-10
-20
-30
-40
-50
-60
-70
-80
-90
-100
-110
-120
-130
-140
-150
-160
-170
-180
-190
-200
-210
f1 (ppm)

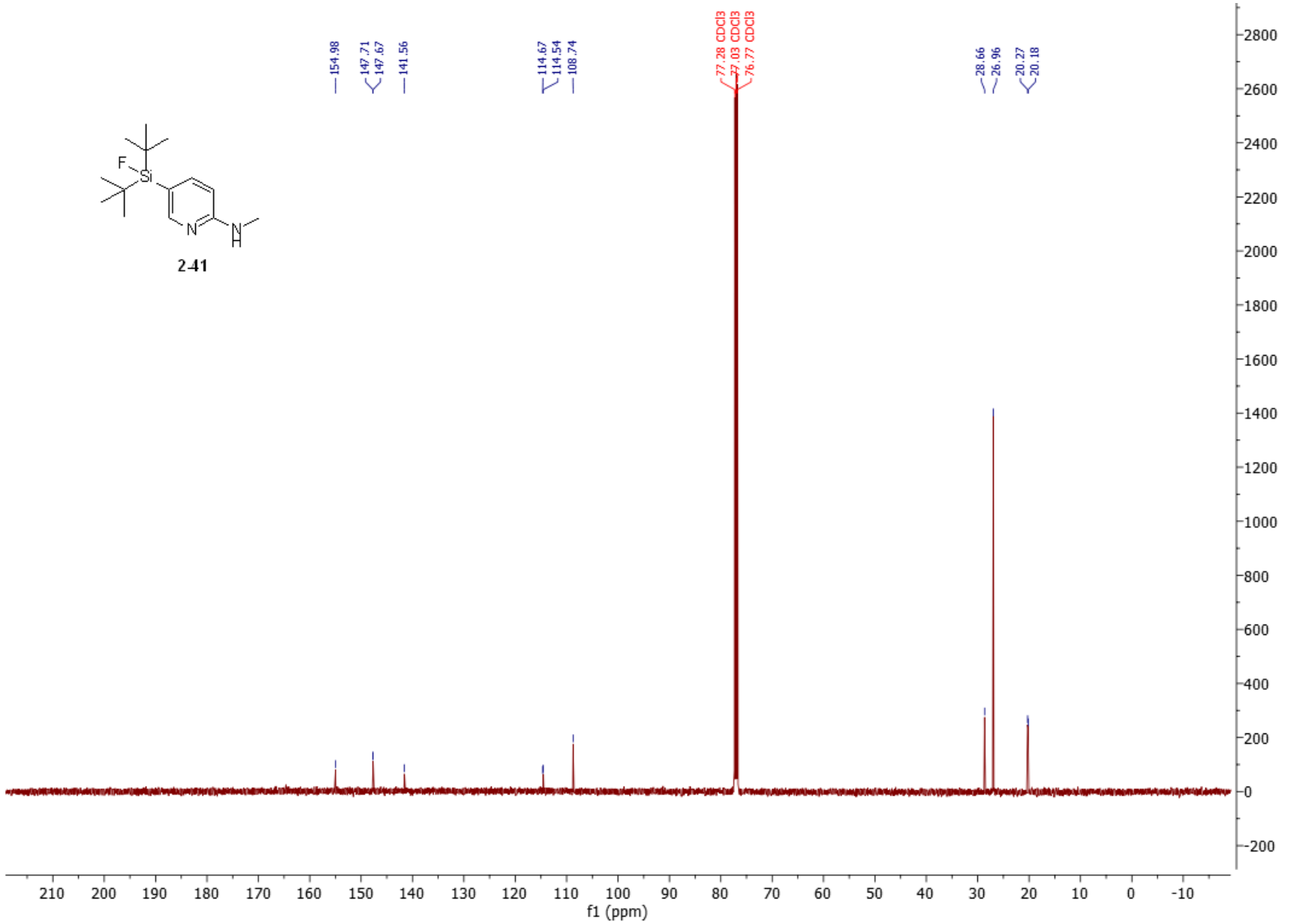
154.98
147.71
147.67
141.56
114.67
114.54
108.74
77.28 CDCl3
77.03 CDCl3
76.77 CDCl3
28.66
26.96
20.27
20.18
F
Si
N
H
2-41
f1 (ppm)

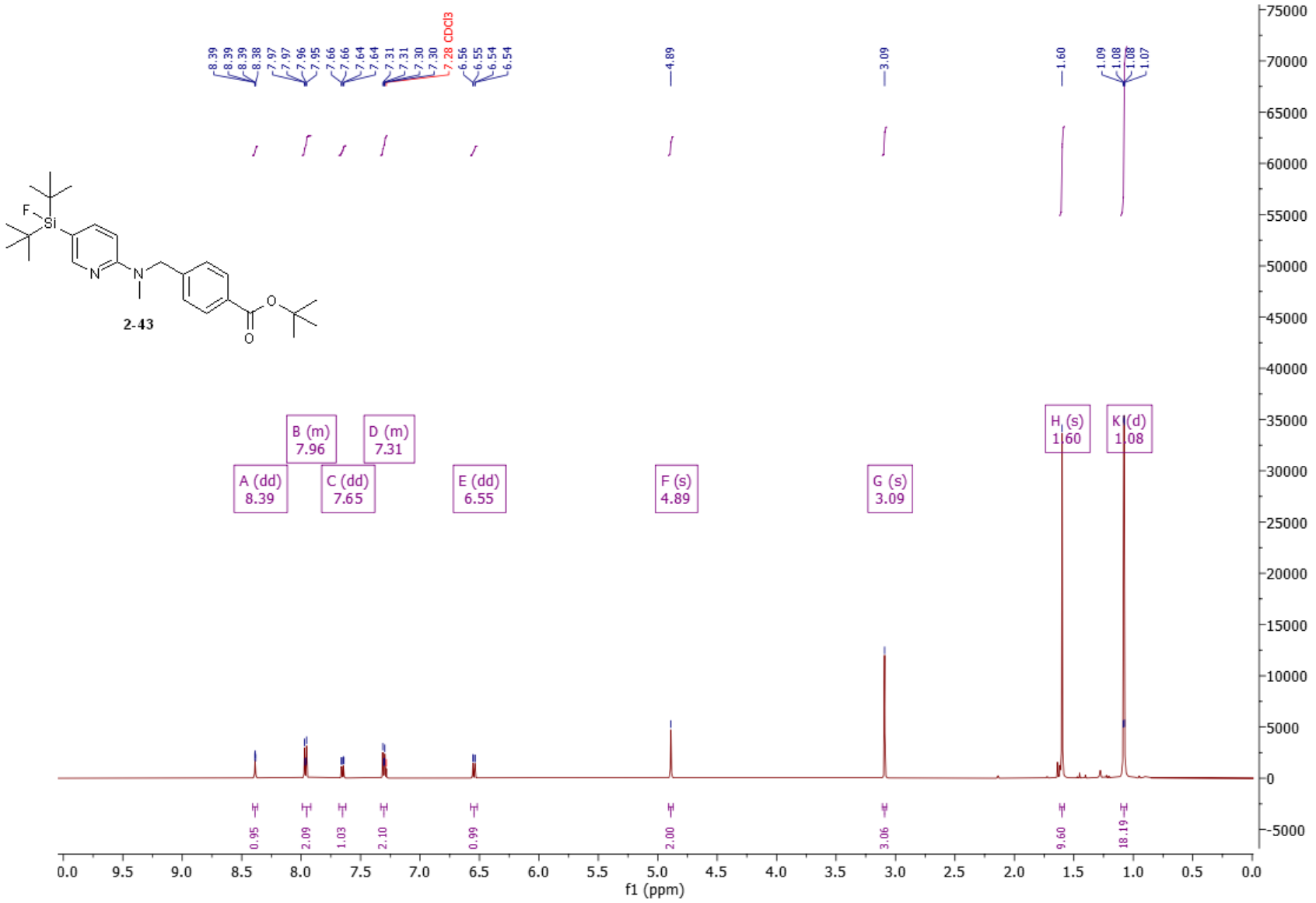
2-43
A (dd) 8.39
B (m) 7.96
C (dd) 7.65
D (m) 7.31
E (dd) 6.55
F (s) 4.89
G (s) 3.09
H (s) 1.60
K (d) 1.08
f1 (ppm)

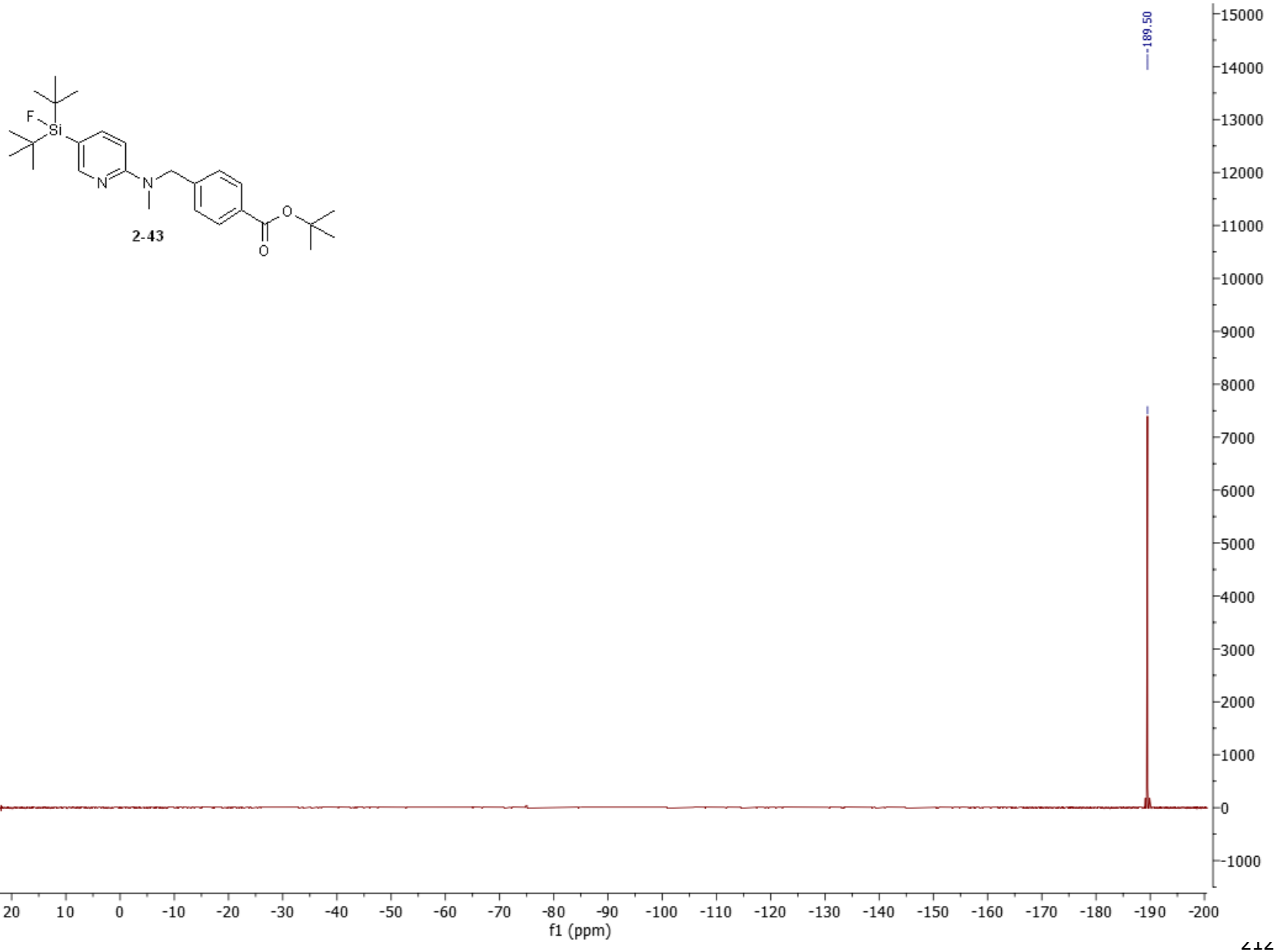
F
Si
N
N
O
O
2-43
-189.50
15000
14000
13000
12000
11000
10000
9000
8000
7000
6000
5000
4000
3000
2000
1000
0
-1000
20
10
0
-10
-20
-30
-40
-50
-60
-70
-80
-90
-100
-110
-120
-130
-140
-150
-160
-170
-180
-190
-200
f1 (ppm)

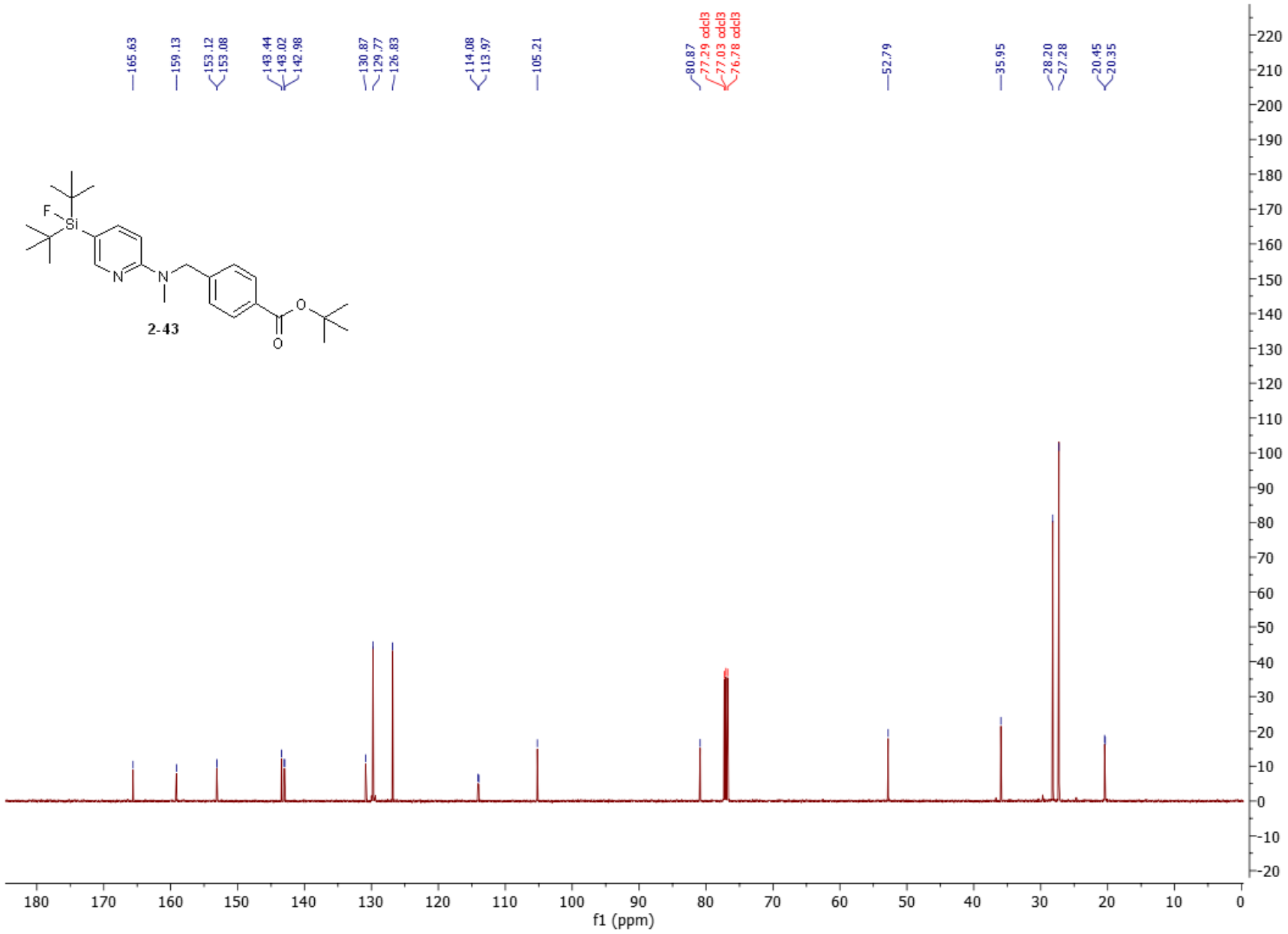
165.63
159.13
153.12
153.08
143.44
143.02
142.98
130.87
129.77
126.83
114.08
113.97
105.21
80.87
77.29 cdcl3
77.03 cdcl3
76.78 cdcl3
52.79
35.95
28.20
27.28
20.45
20.35
F
Si
N
N
O
O
2-43
f1 (ppm)

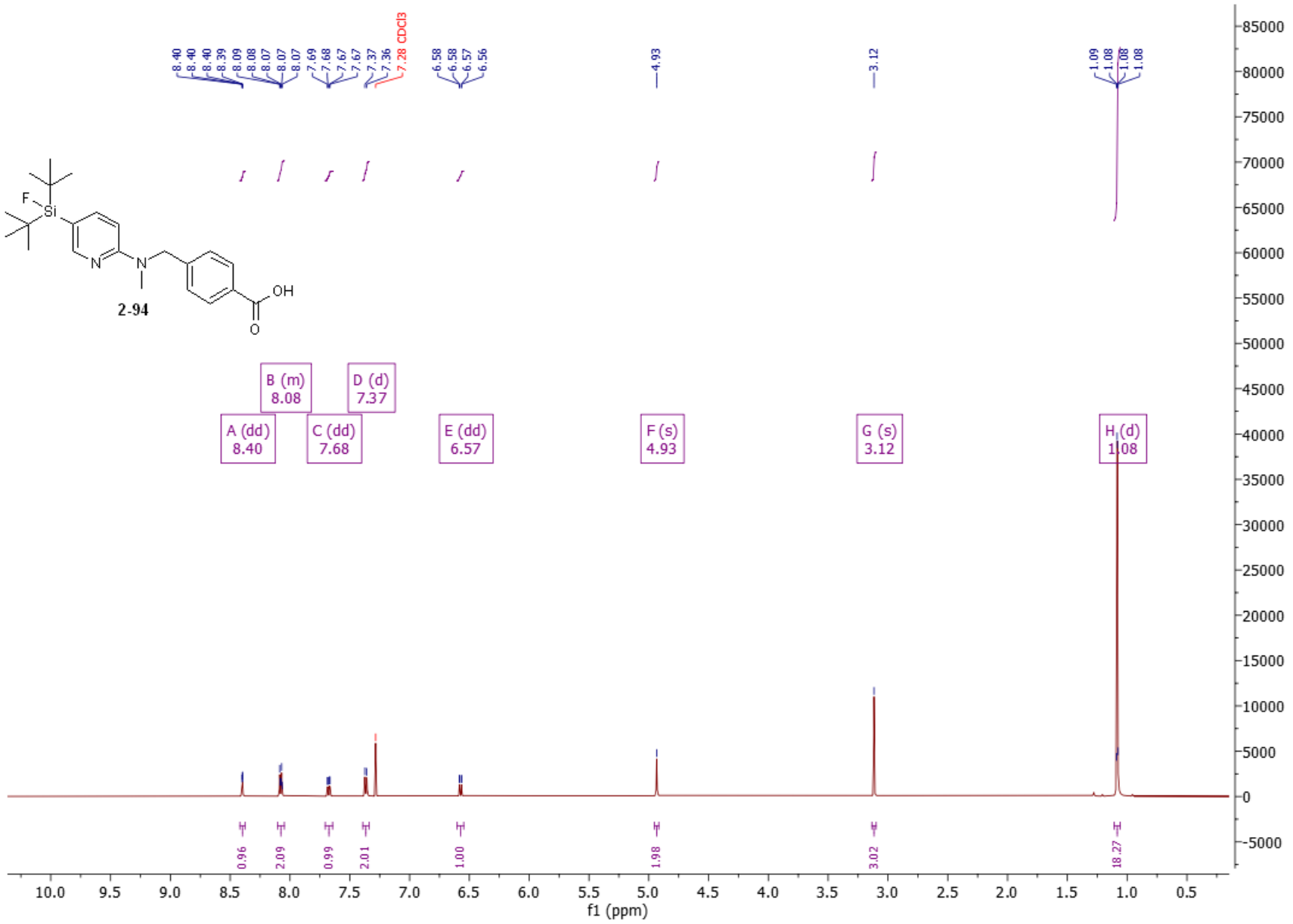
8.40
8.40
8.40
8.39
8.09
8.08
8.07
8.07
8.07
7.69
7.68
7.67
7.67
7.37
7.36
7.28 CDCl3
6.58
6.58
6.57
6.56
4.93
3.12
1.09
1.08
1.08
1.08
F
Si
N
N
OH
O
2-94
B (m)
8.08
D (d)
7.37
A (dd)
8.40
C (dd)
7.68
E (dd)
6.57
F (s)
4.93
G (s)
3.12
H (d)
1.08
0.96
2.09
0.99
2.01
1.00
1.98
3.02
18.27
f1 (ppm)

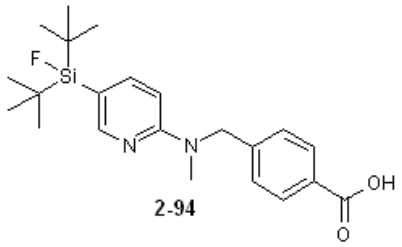
F
Si
N
N
OH
O

2-94

-189.45
240
230
220
210
200
190
180
170
160
150
140
130
120
110
100
90
80
70
60
50
40
30
20
10
0
-10
10 0 -10 -20 -30 -40 -50 -60 -70 -80 -90 -100 -110 -120 -130 -140 -150 -160 -170 -180 -190 -200 -210
f1 (ppm)

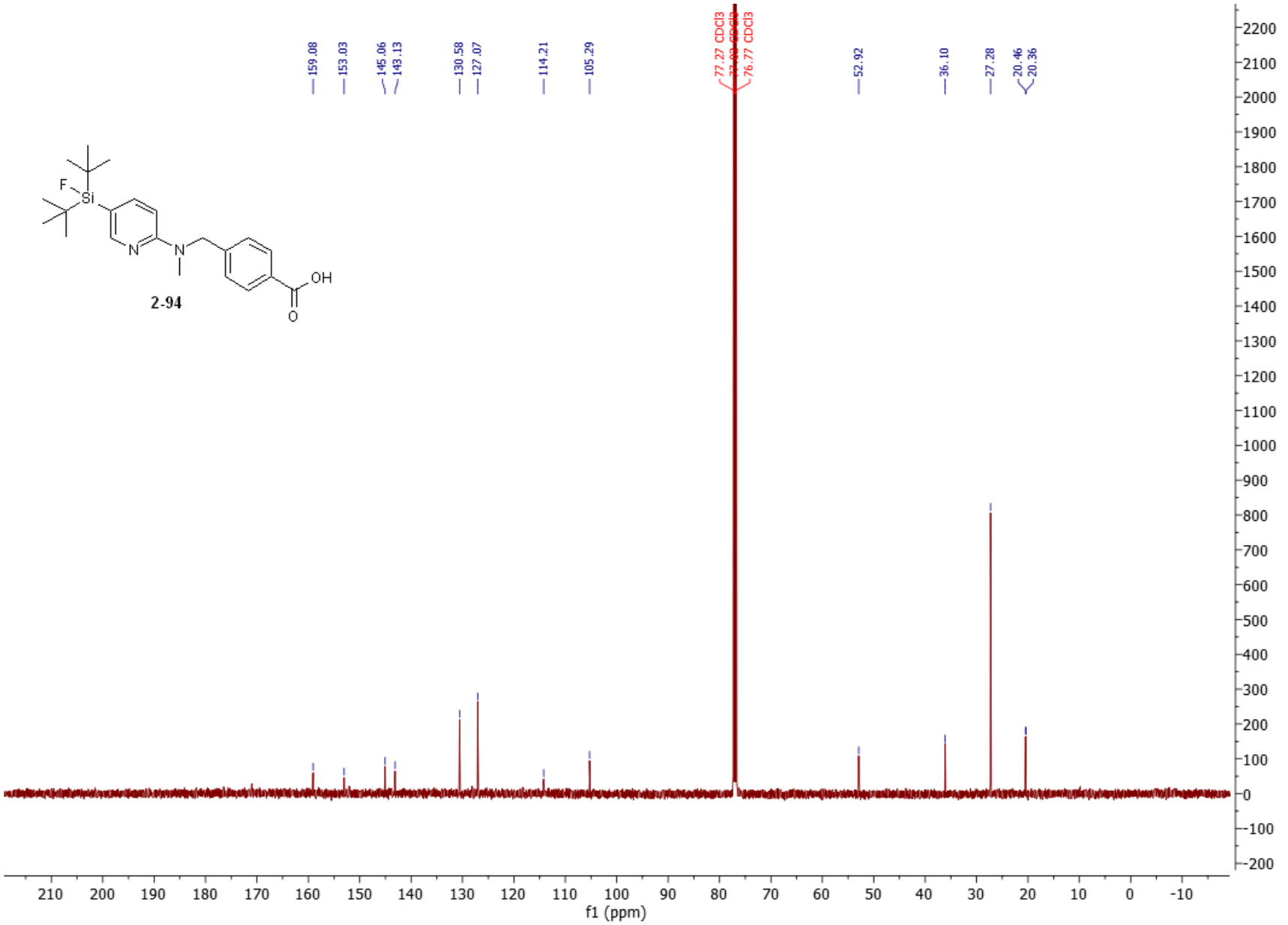
159.08
153.03
145.06
143.13
130.58
127.07
114.21
105.29
77.27 CDCl3
76.77 CDCl3
52.92
36.10
27.28
20.46
20.36
F
Si
N
N
OH
O
2-94
f1 (ppm)

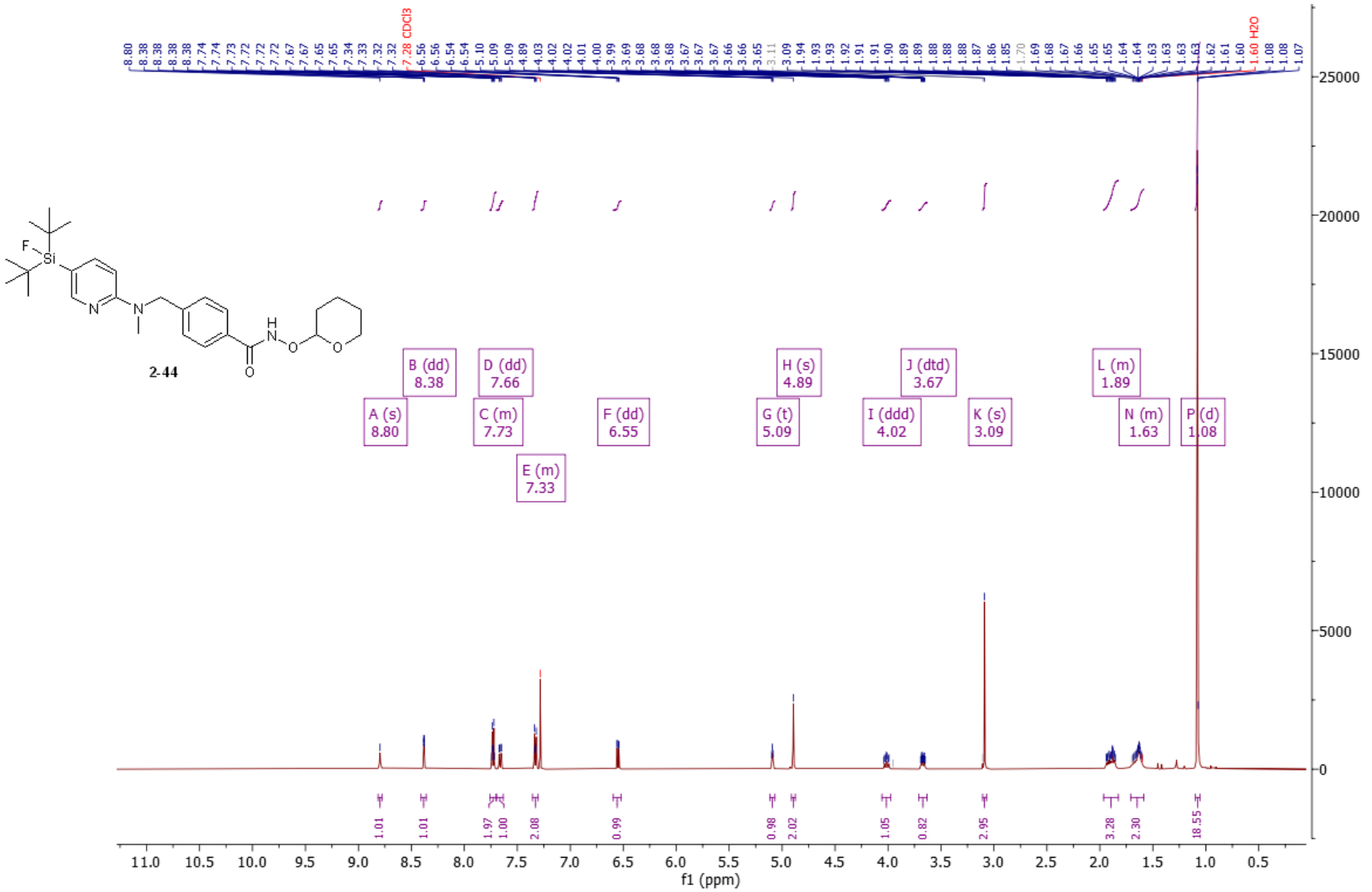
2-44
A (s) 8.80
B (dd) 8.38
C (m) 7.73
D (dd) 7.66
E (m) 7.33
F (dd) 6.55
G (t) 5.09
H (s) 4.89
I (ddd) 4.02
J (dtd) 3.67
K (s) 3.09
L (m) 1.89
N (m) 1.63
P (d) 1.08
f1 (ppm)

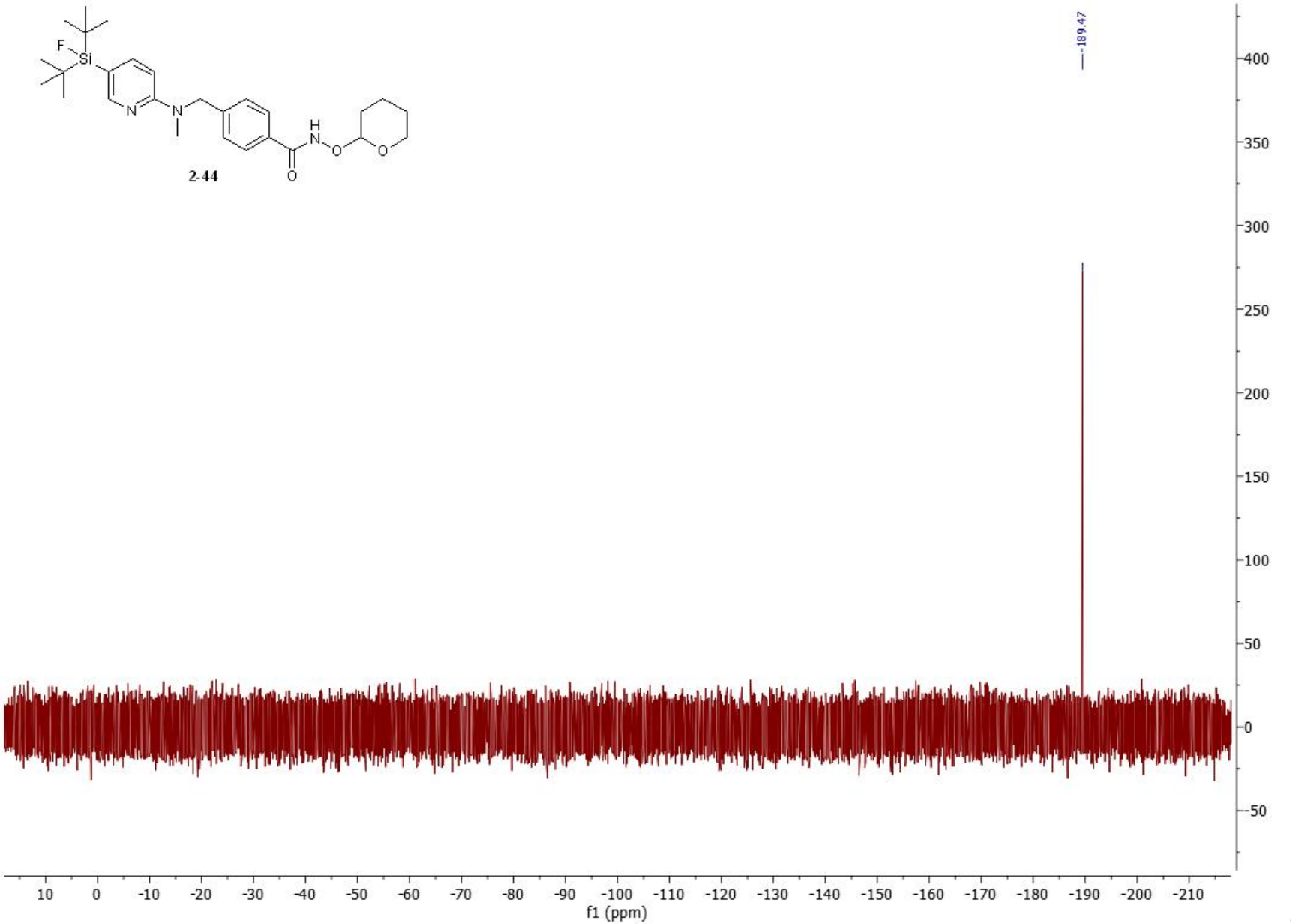
F
Si
N
N
H
N
O
O
O
2-44
-189.47
400
350
300
250
200
150
100
50
0
-50
10
0
-10
-20
-30
-40
-50
-60
-70
-80
-90
-100
-110
-120
-130
-140
-150
-160
-170
-180
-190
-200
-210
f1 (ppm)

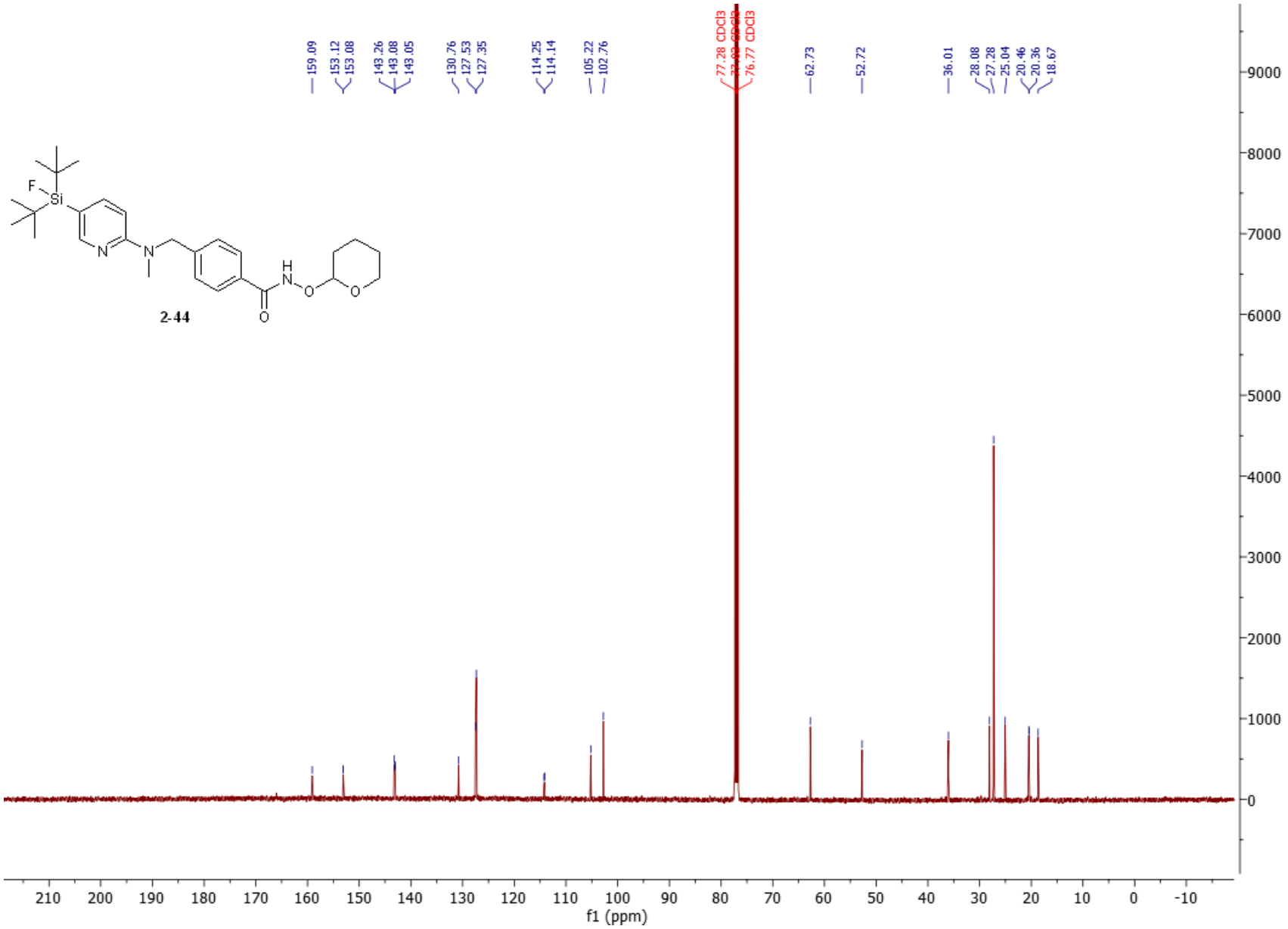
159.09
153.12
153.08
143.26
143.08
143.05
130.76
127.53
127.35
114.25
114.14
105.22
102.76
77.28 CDCl3
76.77 CDCl3
62.73
52.72
36.01
28.08
27.28
25.04
20.46
20.36
18.67
F
Si
N
N
H
N
O
O
O
2-44
9000
8000
7000
6000
5000
4000
3000
2000
1000
0
210
200
190
180
170
160
150
140
130
120
110
100
90
80
70
60
50
40
30
20
10
0
-10
f1 (ppm)

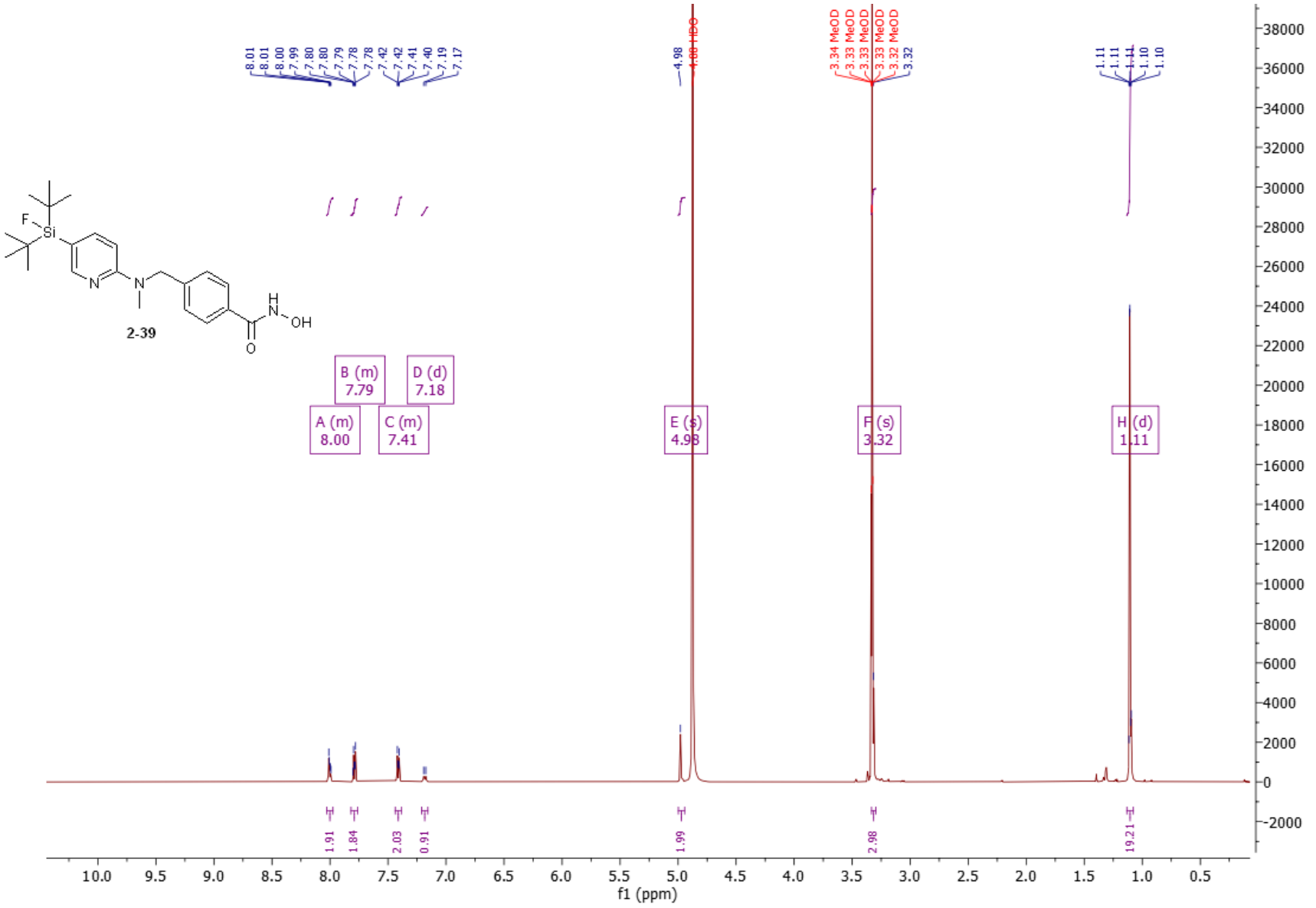
2-39
A (m) 8.00
B (m) 7.79
C (m) 7.41
D (d) 7.18
E (s) 4.98
F (s) 3.32
H (d) 1.11
1.91
1.84
2.03
0.91
1.99
2.98
19.21
f1 (ppm)

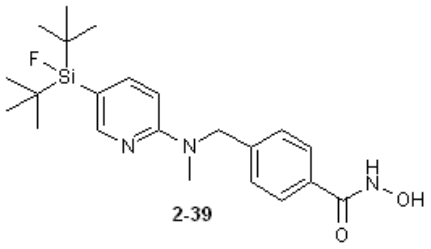
F
Si
N
N
H
N
OH
O

2-39

-190.34
1900
1800
1700
1600
1500
1400
1300
1200
1100
1000
900
800
700
600
500
400
300
200
100
0
10
0
-10
-20
-30
-40
-50
-60
-70
-80
-90
-100
-110
-120
-130
-140
-150
-160
-170
-180
-190
-200
f1 (ppm)

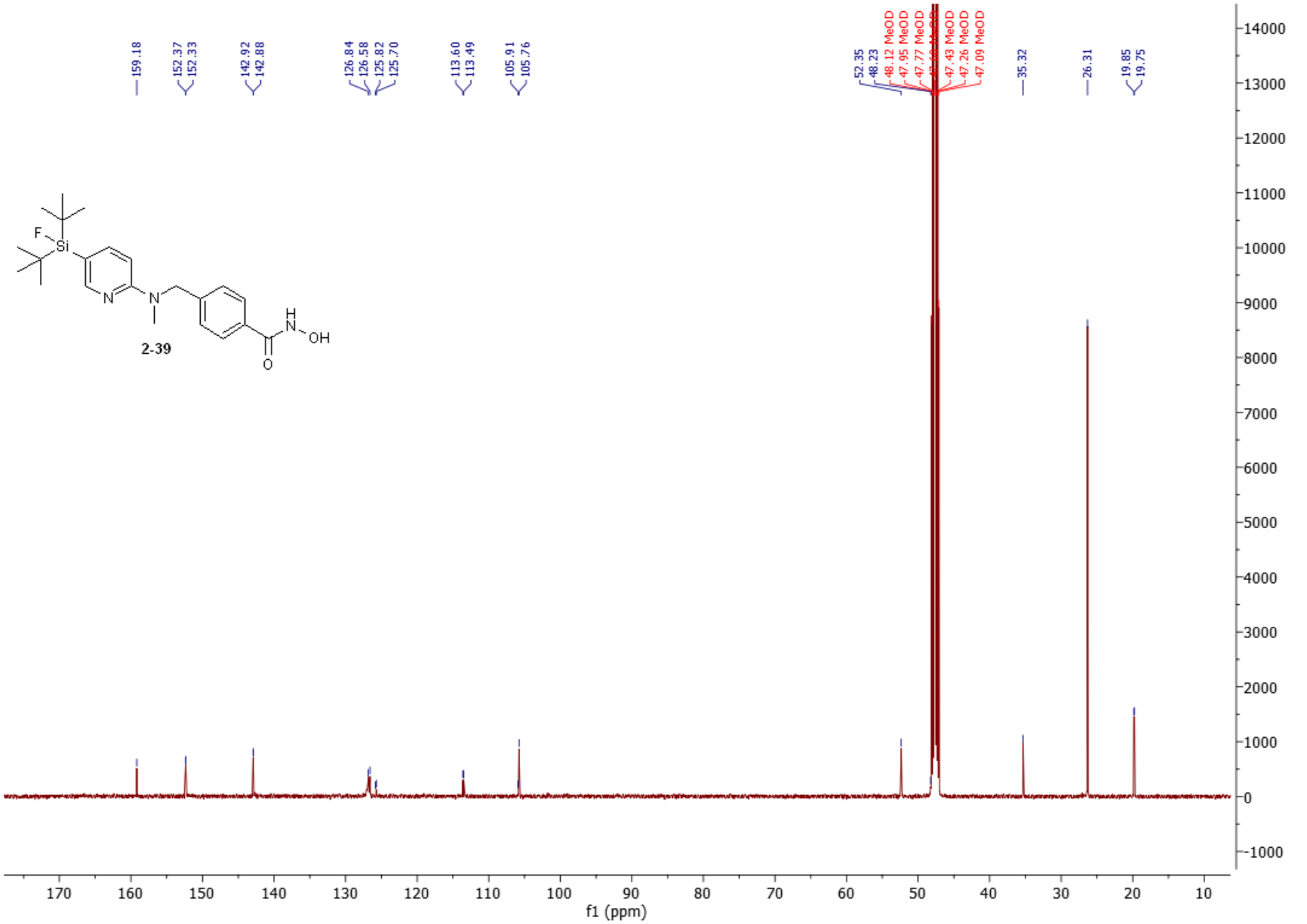
159.18
152.37
152.33
142.92
142.88
126.84
126.58
125.82
125.70
113.60
113.49
105.91
105.76
52.35
48.23
48.12 MeOD
47.95 MeOD
47.77 MeOD
47.43 MeOD
47.26 MeOD
47.09 MeOD
35.32
26.31
19.85
19.75
F
Si
N
N
H
N
OH
O
2-39
14000
13000
12000
11000
10000
9000
8000
7000
6000
5000
4000
3000
2000
1000
0
-1000
170
160
150
140
130
120
110
100
90
80
70
60
50
40
30
20
10
f1 (ppm)

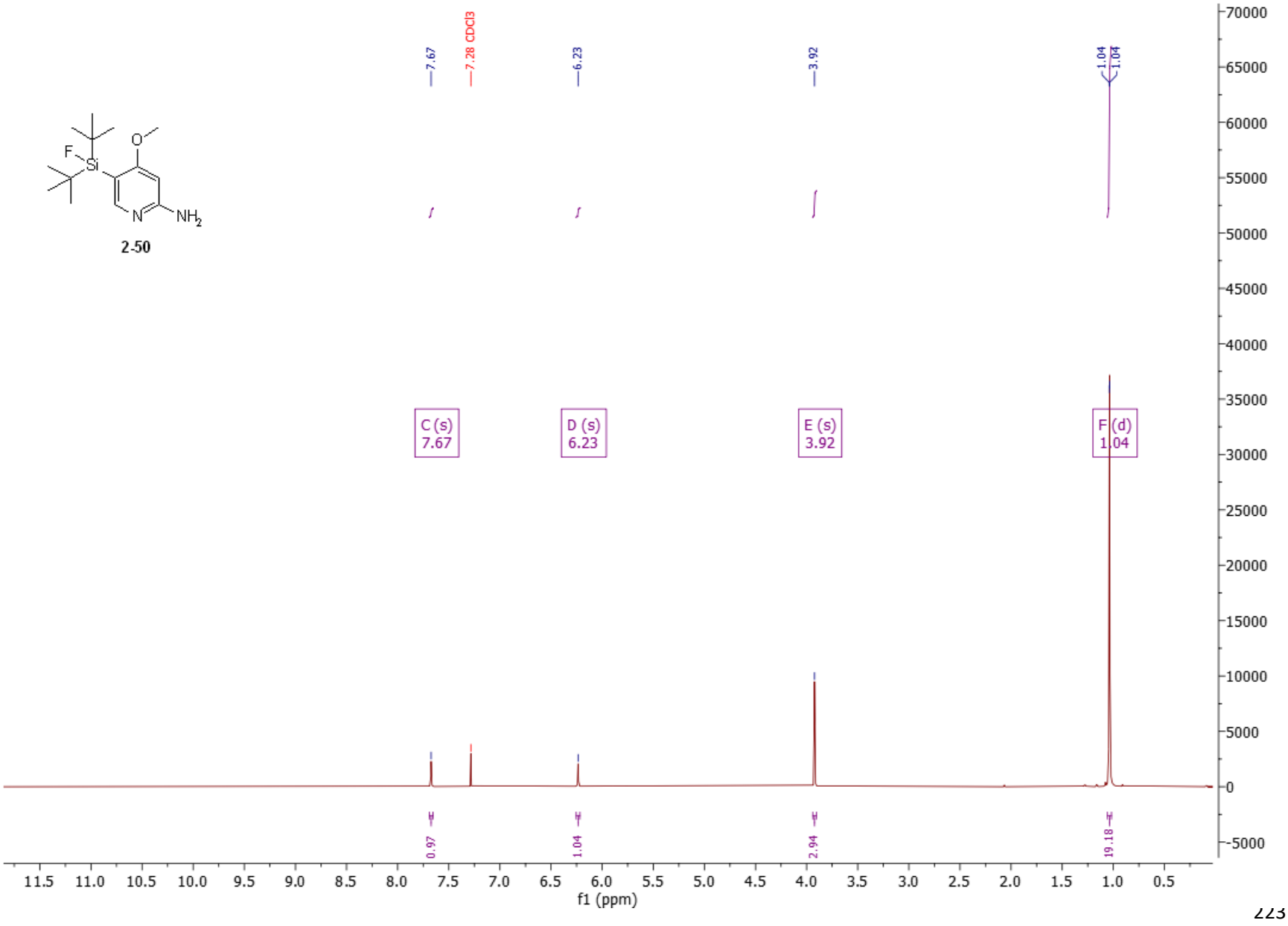
F
Si
O
N
NH2
2-50
7.67
7.28 CDCl3
6.23
3.92
1.04
1.04
C (s)
7.67
D (s)
6.23
E (s)
3.92
F (d)
1.04
0.97
1.04
2.94
19.18
f1 (ppm)

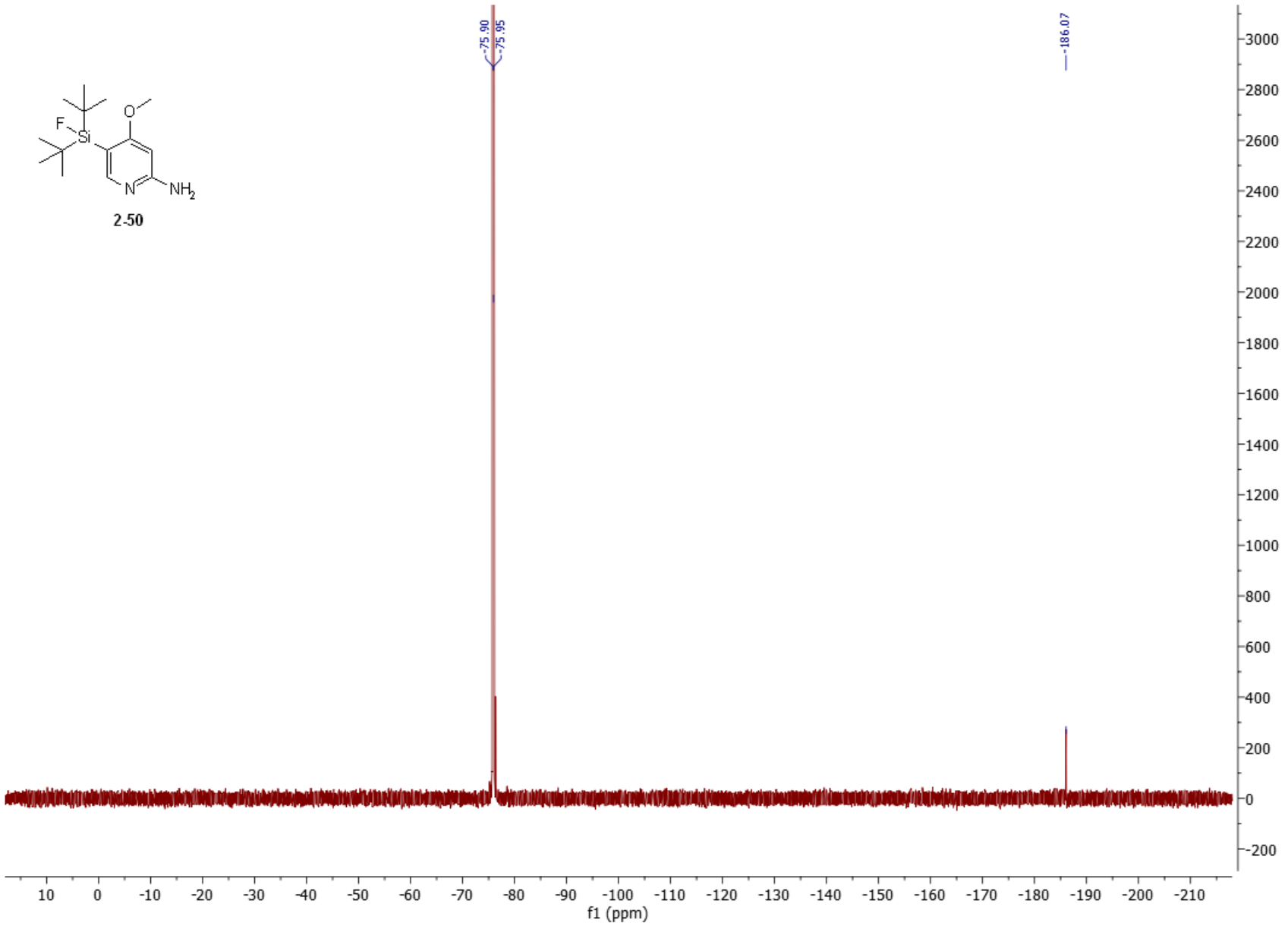
F
Si
O
N
NH2
2-50
-75.90
-75.95
-186.07
3000
2800
2600
2400
2200
2000
1800
1600
1400
1200
1000
800
600
400
200
0
-200
10
0
-10
-20
-30
-40
-50
-60
-70
-80
-90
-100
-110
-120
-130
-140
-150
-160
-170
-180
-190
-200
-210
f1 (ppm)

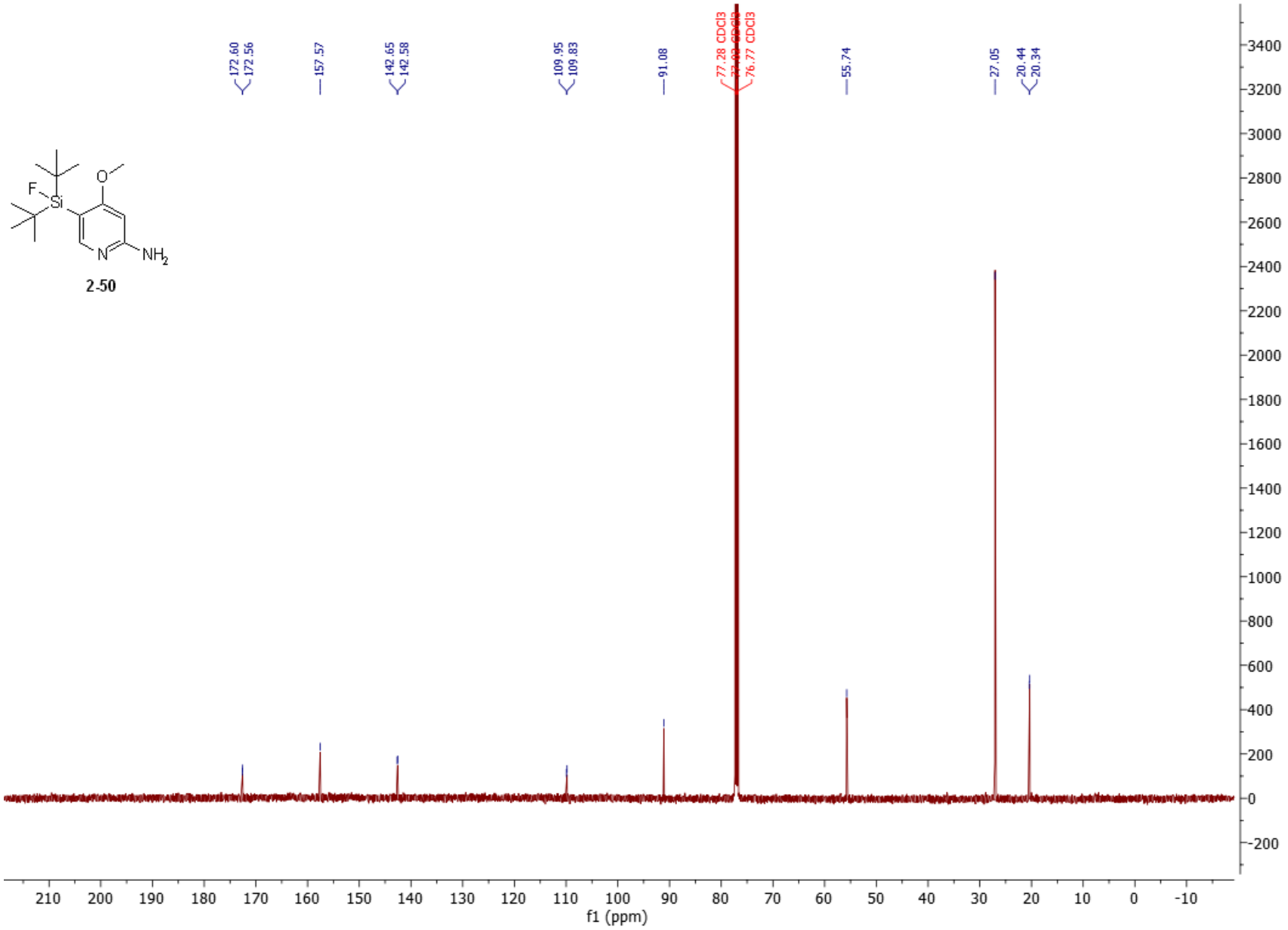
172.60
172.56
157.57
142.65
142.58
109.95
109.83
91.08
77.28 CDCl3
77.03 CDCl3
76.77 CDCl3
55.74
27.05
20.44
20.34
F
Si
O
N
NH2
2-50
f1 (ppm)

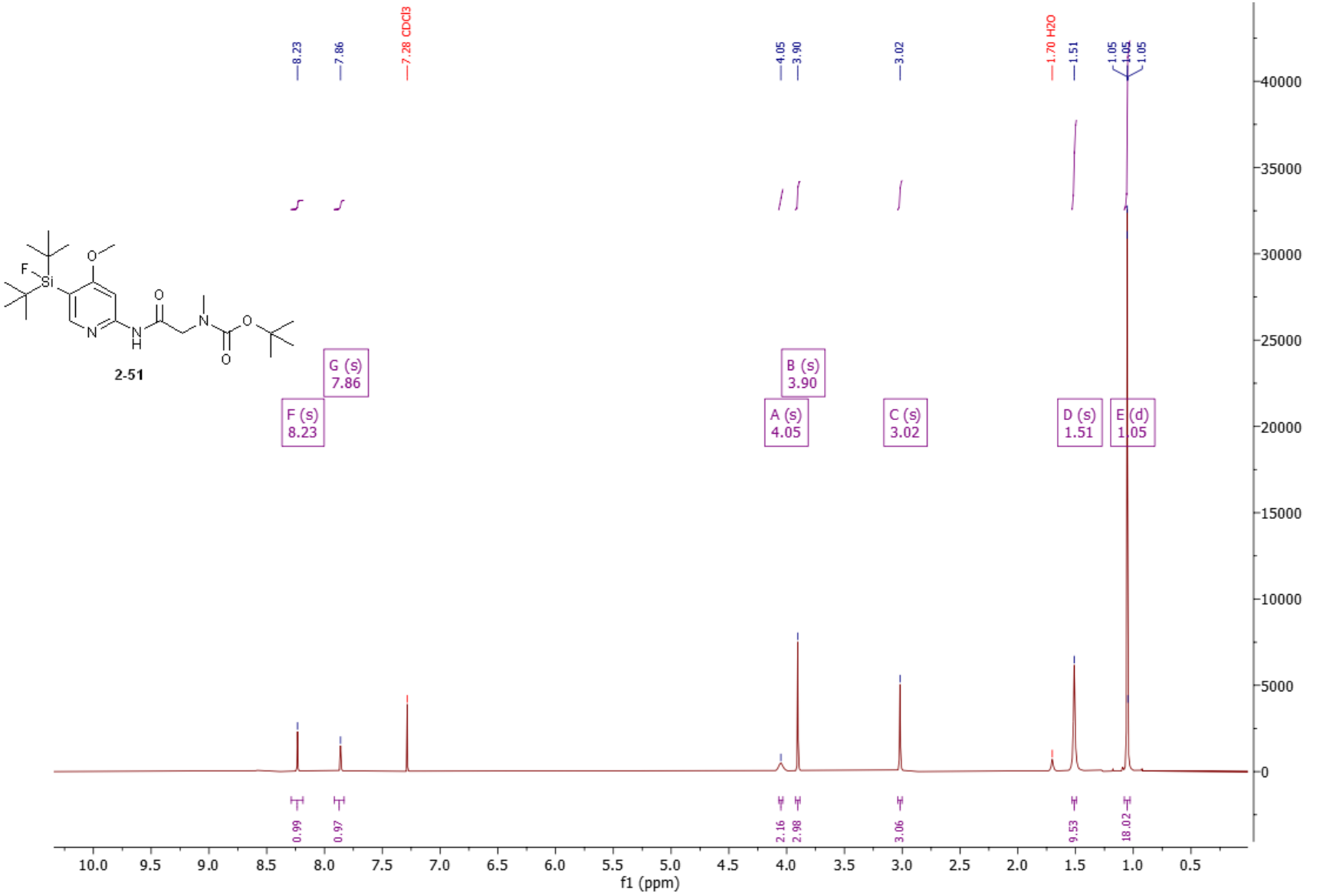
8.23
7.86
7.28 CDCl3
4.05
3.90
3.02
1.70 H2O
1.51
1.05
1.05
1.05
F (s) 8.23
G (s) 7.86
A (s) 4.05
B (s) 3.90
C (s) 3.02
D (s) 1.51
E (d) 1.05
2-51
0.99
0.97
2.16
2.98
3.06
9.53
18.02
f1 (ppm)

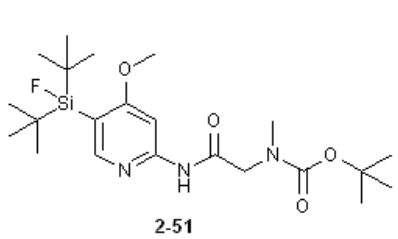
F
Si
O
O
N
N
H
N
O
O

2-51

-187.01
180
170
160
150
140
130
120
110
100
90
80
70
60
50
40
30
20
10
0
-10
-20
-30
-40
-50
-60
-70
-80
10
0
-10
-20
-30
-40
-50
-60
-70
-80
-90
-100
-110
-120
-130
-140
-150
-160
-170
-180
-190
-200
-210
f1 (ppm)

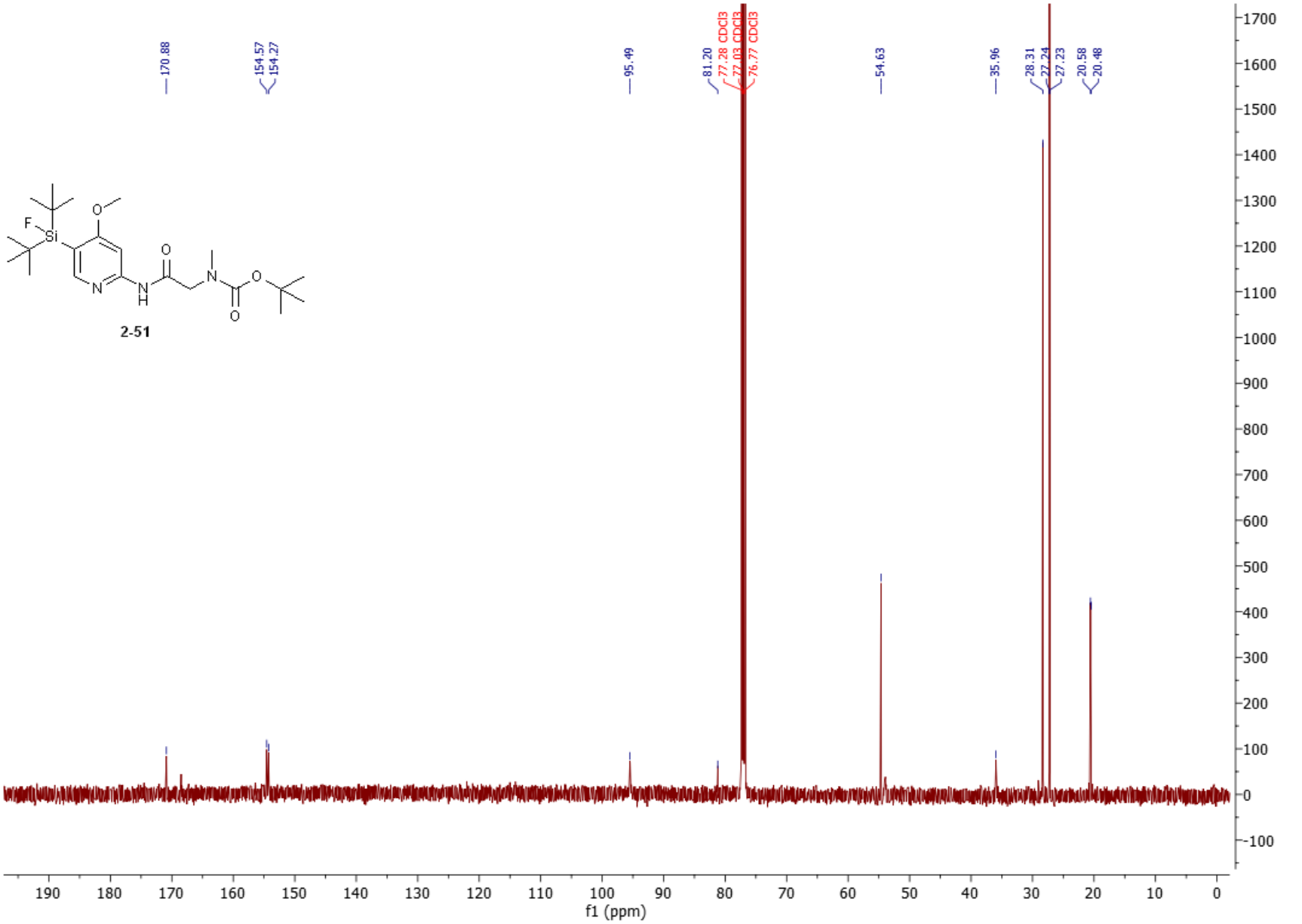
170.88
154.57
154.27
95.49
81.20
77.28 CDCl3
77.03 CDCl3
76.77 CDCl3
54.63
35.96
28.31
27.24
27.23
20.58
20.48
F
Si
O
O
N
H
N
O
O
2-51
f1 (ppm)

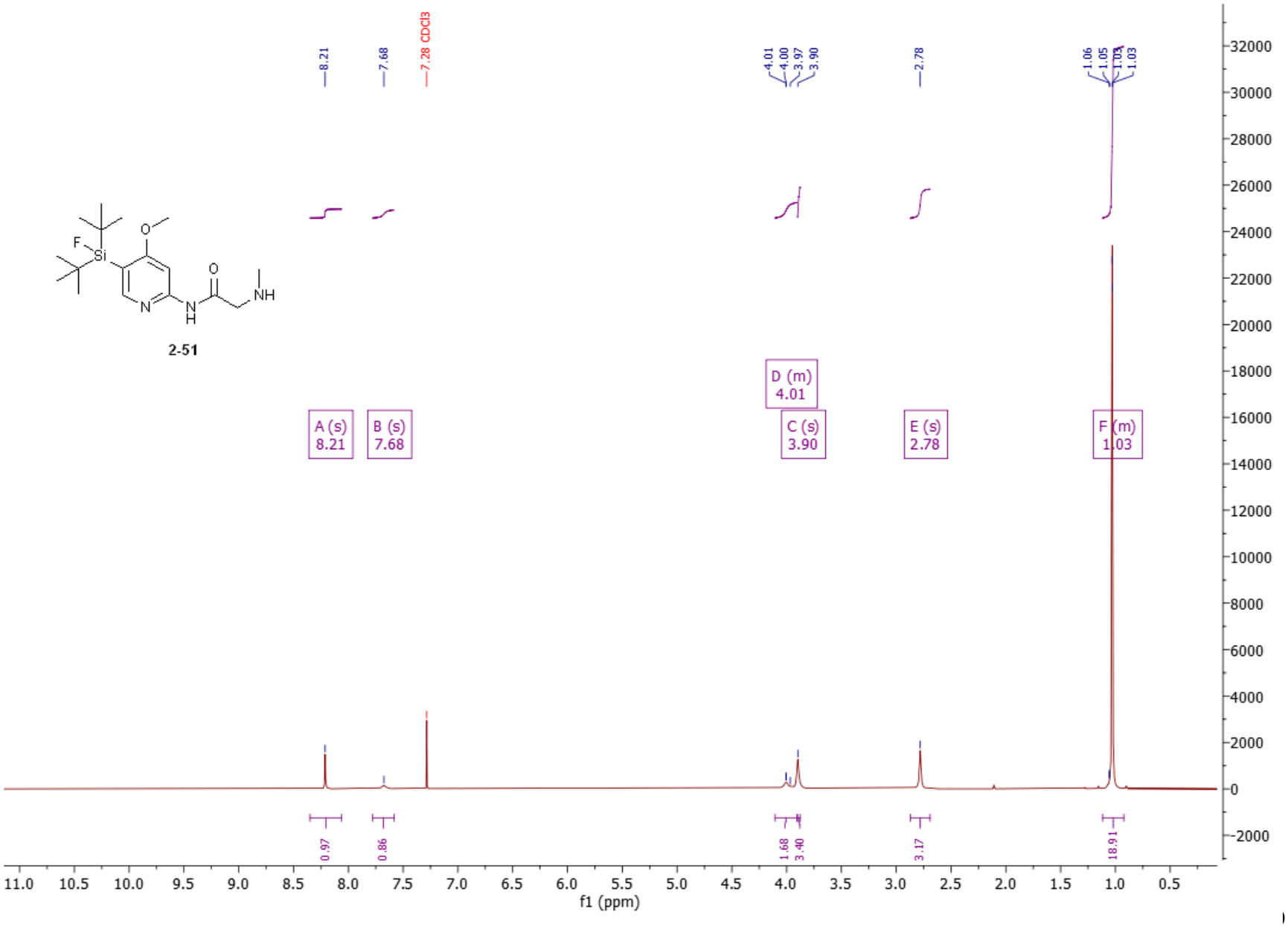
8.21
7.68
7.28 CDCl3
4.01
4.00
3.97
3.90
2.78
1.06
1.05
1.03
1.03
F
Si
O
N
H
N
O
NH
2-51
A (s)
8.21
B (s)
7.68
D (m)
4.01
C (s)
3.90
E (s)
2.78
F (m)
1.03
0.97
0.86
1.68
3.40
3.17
18.91
f1 (ppm)

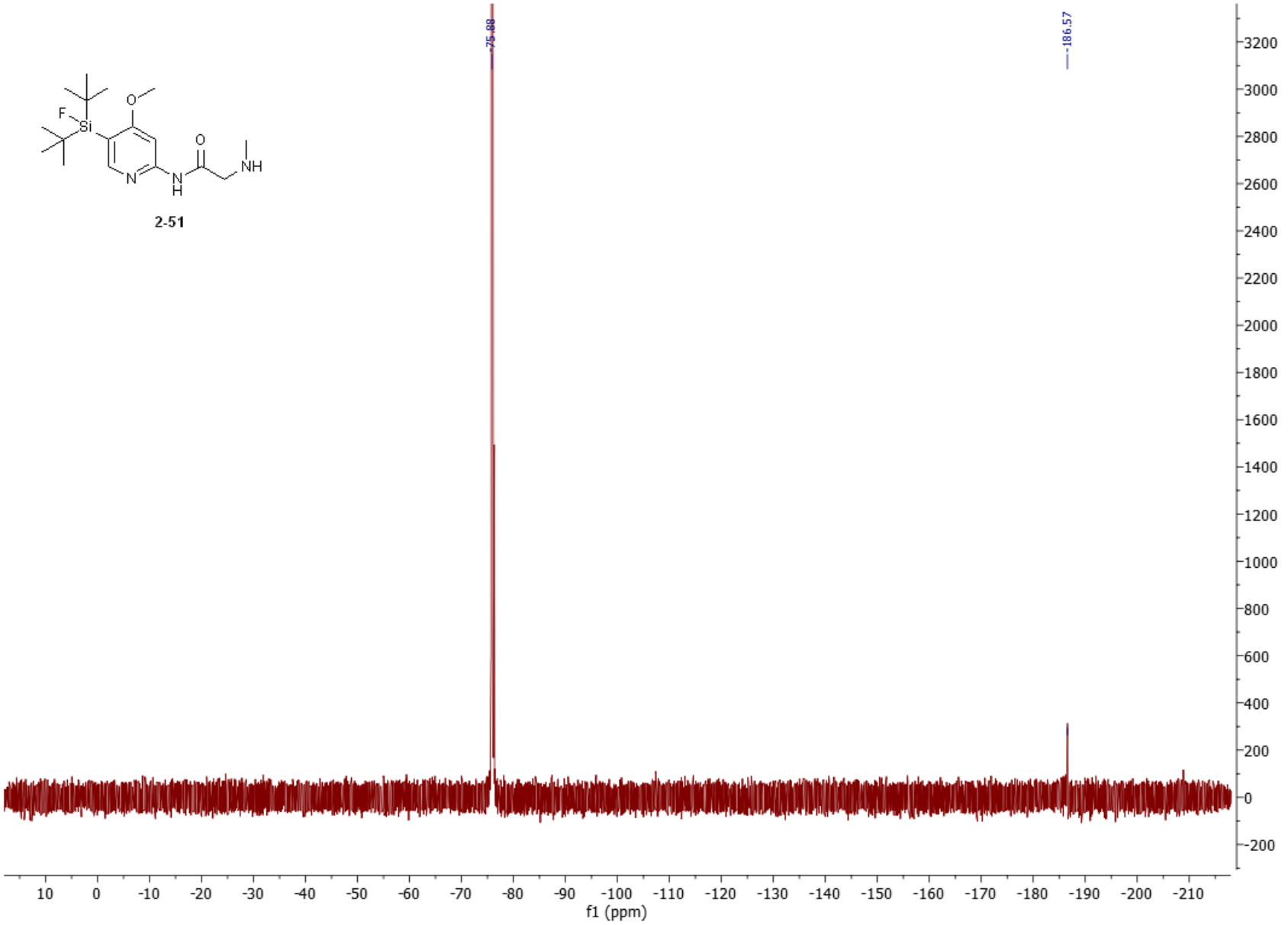
-75.88
-186.57
F
Si
O
O
NH
N
H
N
2-51
3200
3000
2800
2600
2400
2200
2000
1800
1600
1400
1200
1000
800
600
400
200
0
-200
10 0 -10 -20 -30 -40 -50 -60 -70 -80 -90 -100 -110 -120 -130 -140 -150 -160 -170 -180 -190 -200 -210
f1 (ppm)

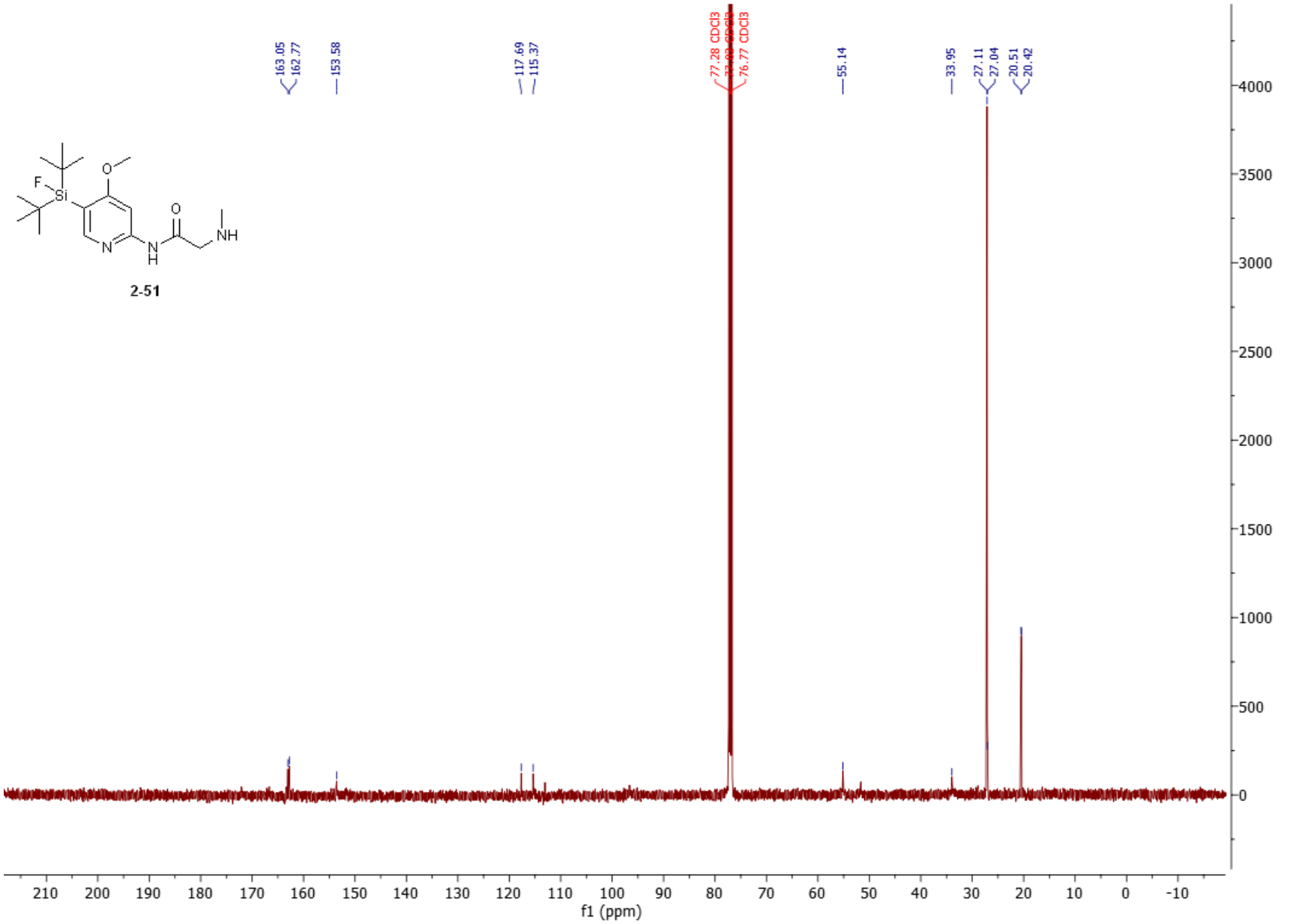
163.05
162.77
153.58
117.69
115.37
77.28 CDCl3
77.03 CDCl3
76.77 CDCl3
55.14
33.95
27.11
27.04
20.51
20.42
F
Si
O
O
N
H
N
NH
2-51
4000
3500
3000
2500
2000
1500
1000
500
0
210 200 190 180 170 160 150 140 130 120 110 100 90 80 70 60 50 40 30 20 10 0 -10
f1 (ppm)

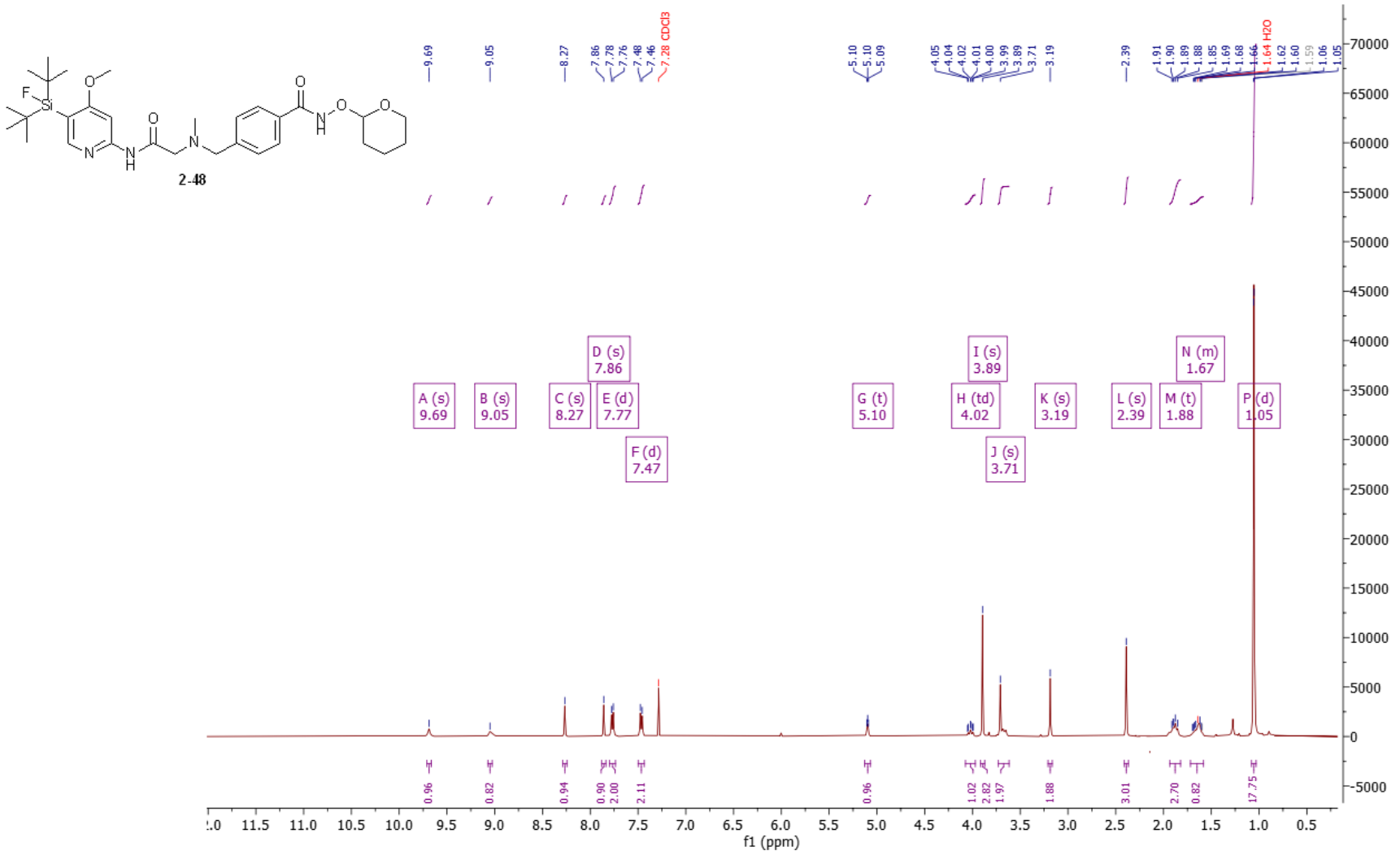
2-48
A (s) 9.69
B (s) 9.05
C (s) 8.27
D (s) 7.86
E (d) 7.77
F (d) 7.47
G (t) 5.10
H (td) 4.02
I (s) 3.89
J (s) 3.71
K (s) 3.19
L (s) 2.39
M (t) 1.88
N (m) 1.67
P (d) 1.05
f1 (ppm)

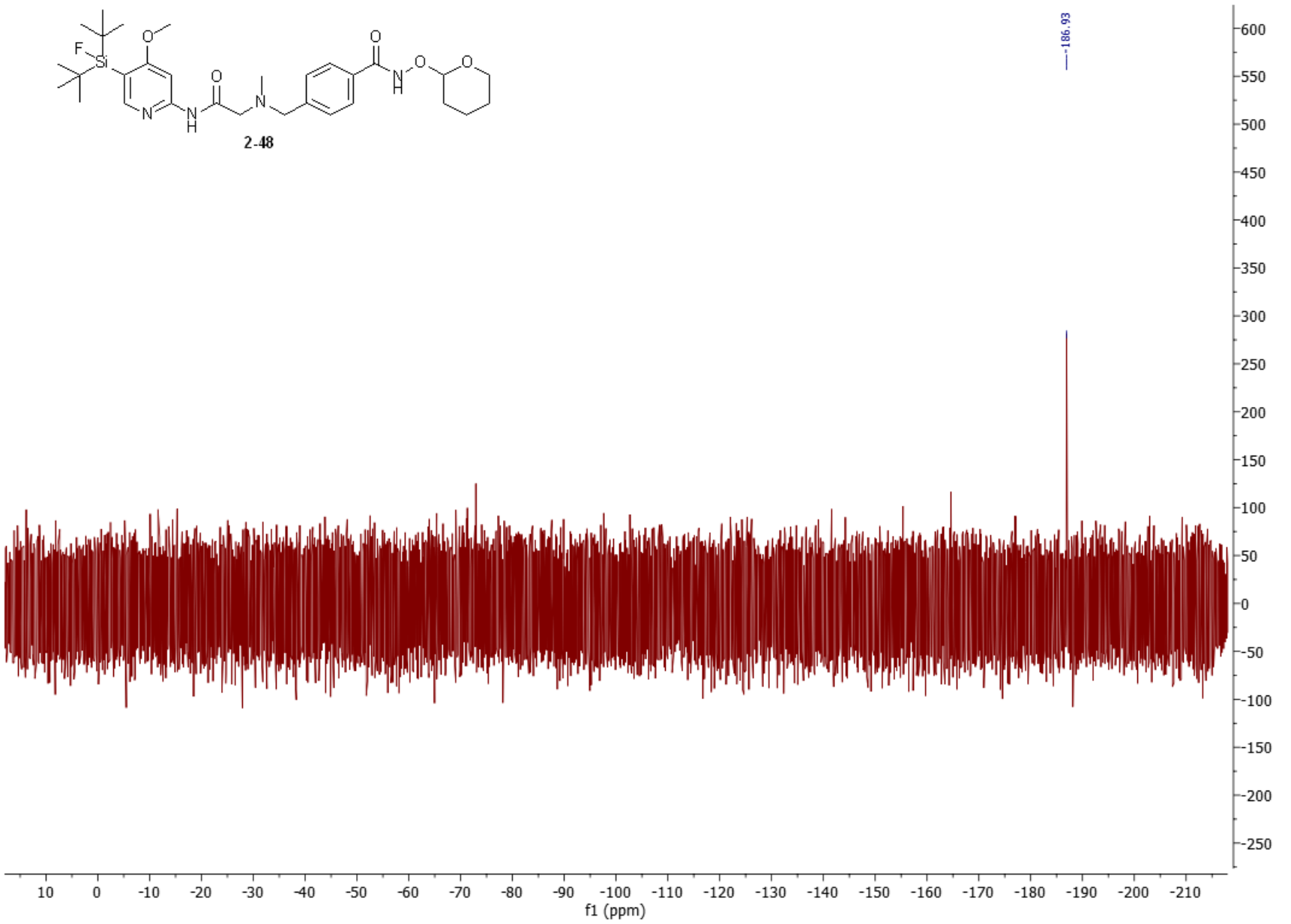
F
Si
O
O
N
H
N
O
N
O
O
2-48
-186.93
600
550
500
450
400
350
300
250
200
150
100
50
0
-50
-100
-150
-200
-250
10
0
-10
-20
-30
-40
-50
-60
-70
-80
-90
-100
-110
-120
-130
-140
-150
-160
-170
-180
-190
-200
-210
f1 (ppm)

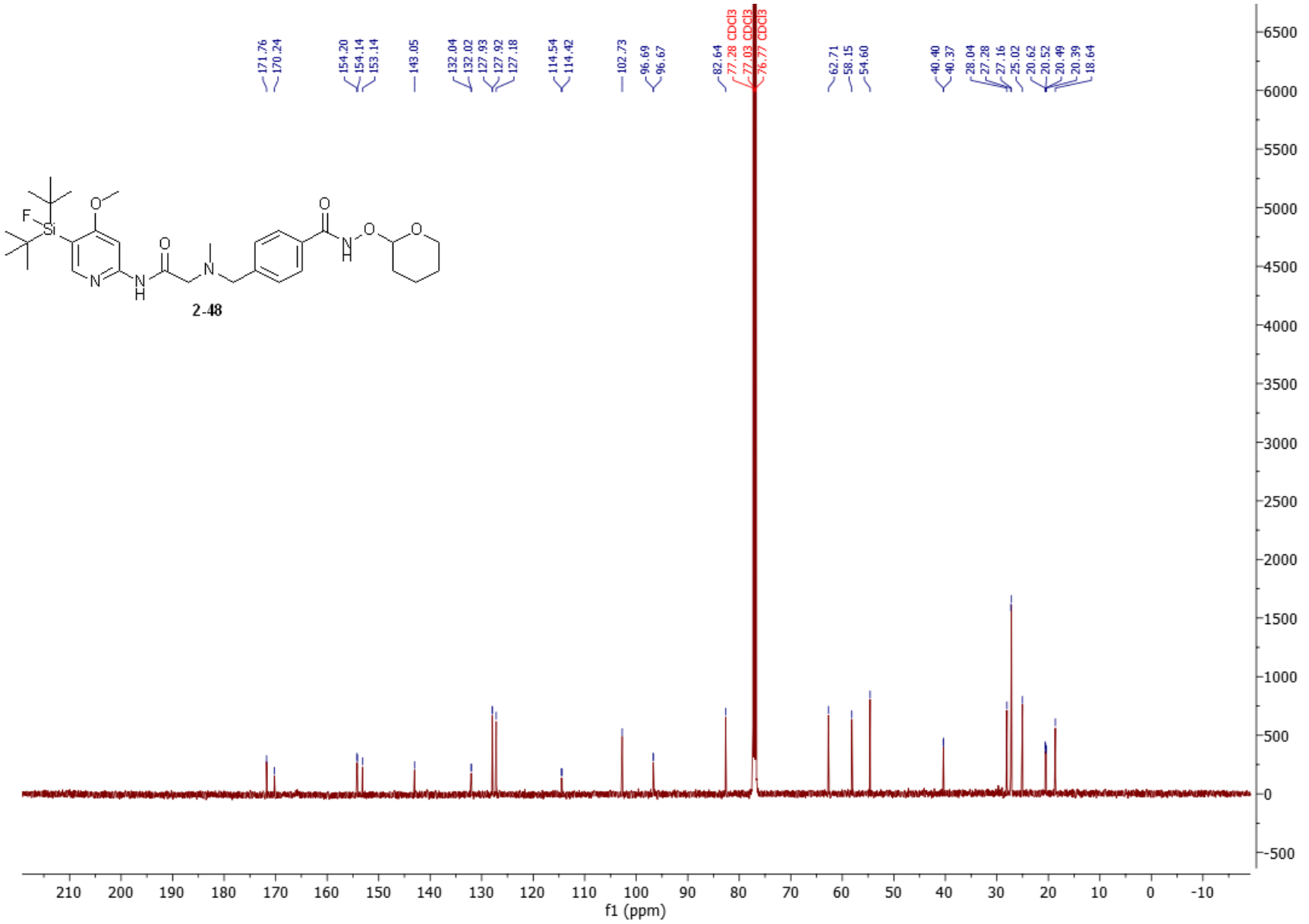
171.76
170.24
154.20
154.14
153.14
143.05
132.04
132.02
127.93
127.92
127.18
114.54
114.42
102.73
96.69
96.67
82.64
77.28 CDCl3
77.03 CDCl3
76.77 CDCl3
62.71
58.15
54.60
40.40
40.37
28.04
27.28
27.16
25.02
20.62
20.52
20.49
20.39
18.64
6500
6000
5500
5000
4500
4000
3500
3000
2500
2000
1500
1000
500
0
-500
210
200
190
180
170
160
150
140
130
120
110
100
90
80
70
60
50
40
30
20
10
0
-10
f1 (ppm)
F
Si
O
N
H
O
N
O
N
H
O
O
2-48

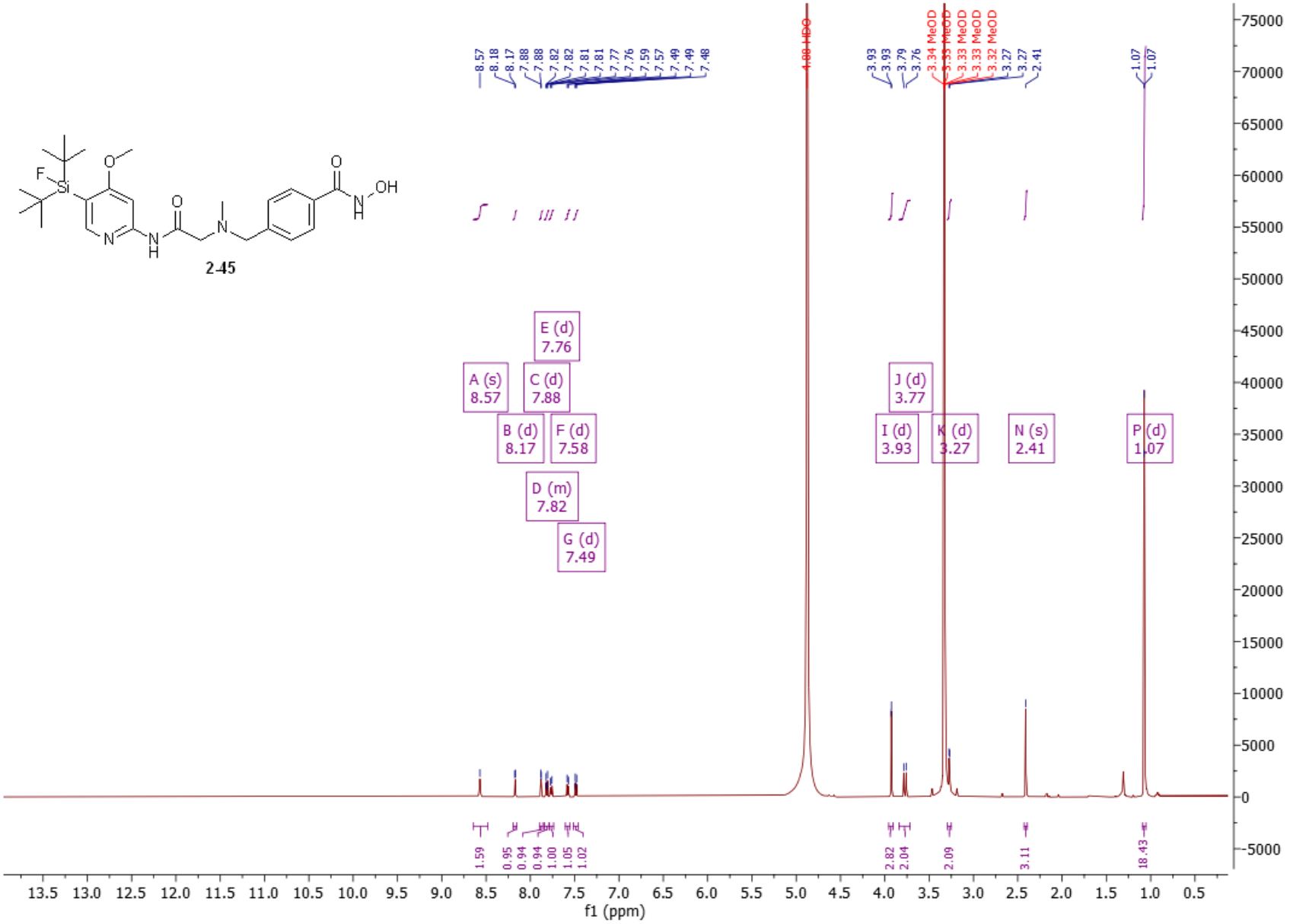
2-45
A (s) 8.57
B (d) 8.17
C (d) 7.88
D (m) 7.82
E (d) 7.76
F (d) 7.58
G (d) 7.49
I (d) 3.93
J (d) 3.77
K (d) 3.27
N (s) 2.41
P (d) 1.07
f1 (ppm)

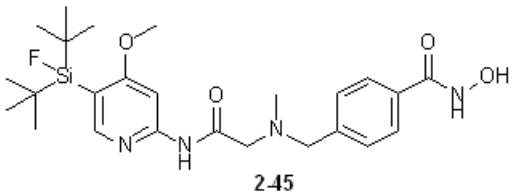
F
Si
O
O
N
H
N
O
N
OH

2-45

-186.51
1400
1300
1200
1100
1000
900
800
700
600
500
400
300
200
100
0
-100
-200
-300
10
0
-10
-20
-30
-40
-50
-60
-70
-80
-90
-100
-110
-120
-130
-140
-150
-160
-170
-180
-190
-200
f1 (ppm)

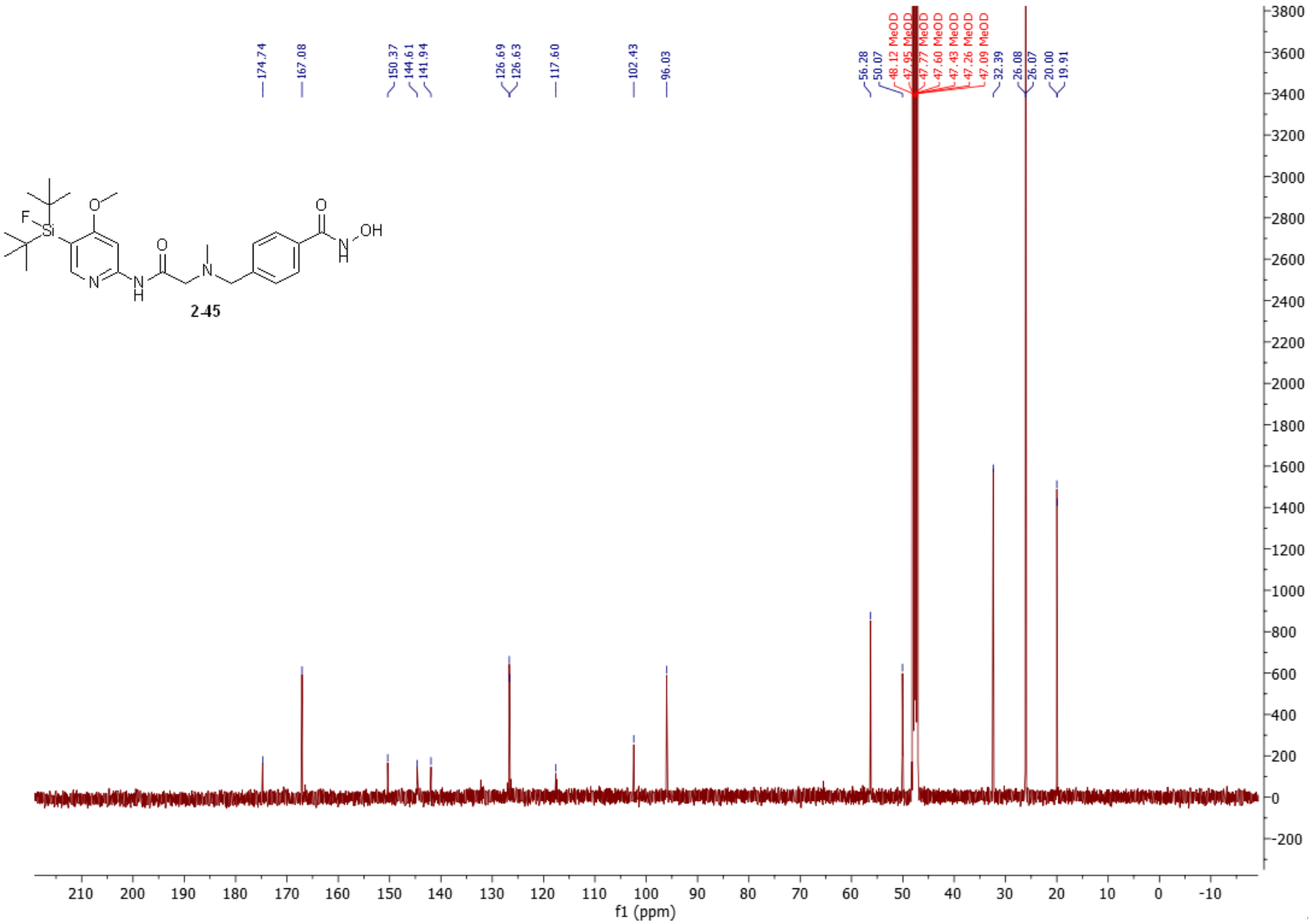
174.74
167.08
150.37
144.61
141.94
126.69
126.63
117.60
102.43
96.03
56.28
50.07
48.12 MeOD
47.95 MeOD
47.77 MeOD
47.60 MeOD
47.43 MeOD
47.26 MeOD
47.09 MeOD
32.39
26.08
26.07
20.00
19.91
F
Si
O
N
H
O
N
H
OH
2-45
f1 (ppm)

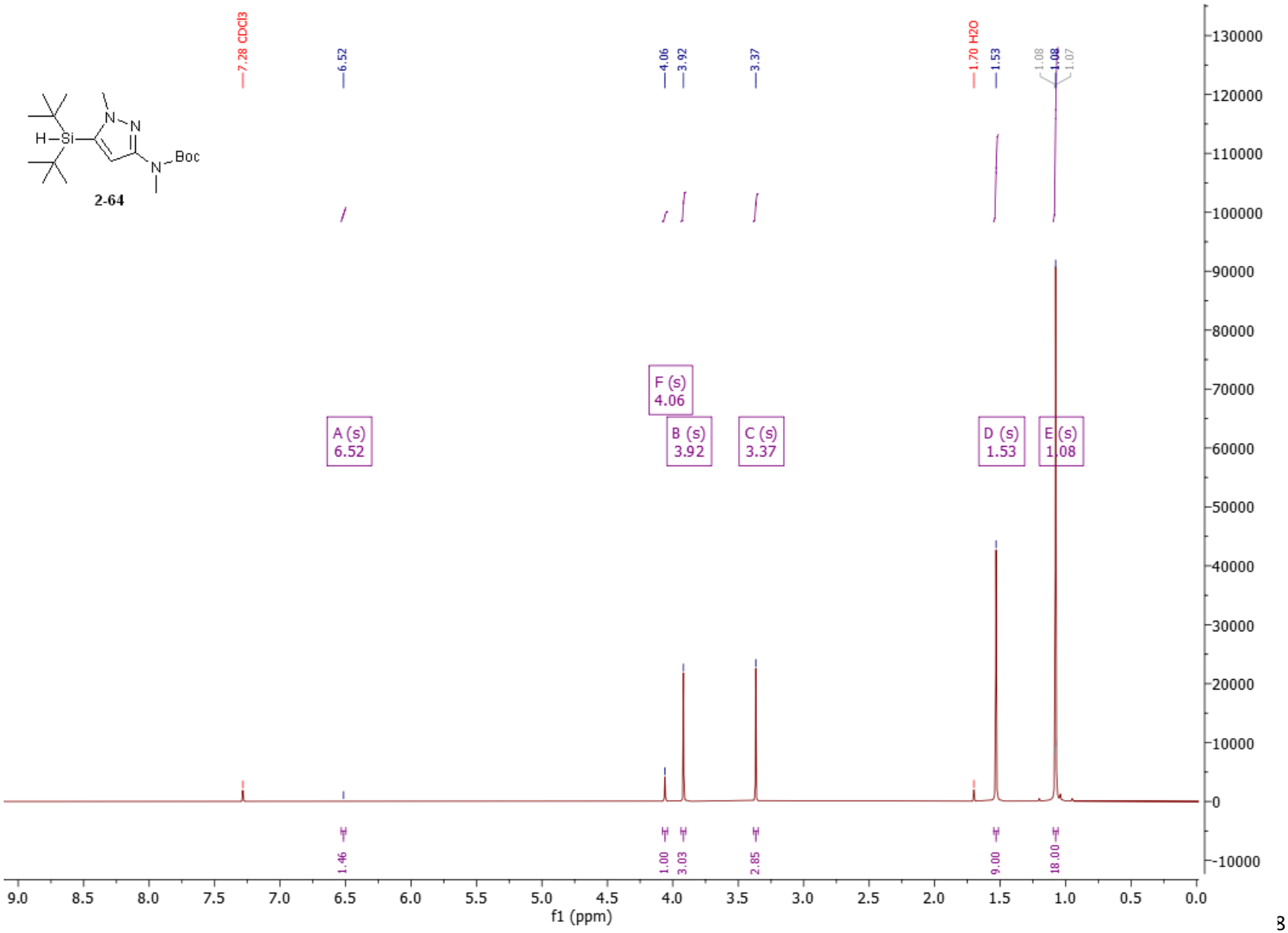
7.28 CDCl3
6.52
4.06
3.92
3.37
1.70 H2O
1.53
1.08
1.07
H–Si
N
Boc
2-64
A (s)
6.52
F (s)
4.06
B (s)
3.92
C (s)
3.37
D (s)
1.53
E (s)
1.08
1.46
1.00
3.03
2.85
9.00
18.00
f1 (ppm)

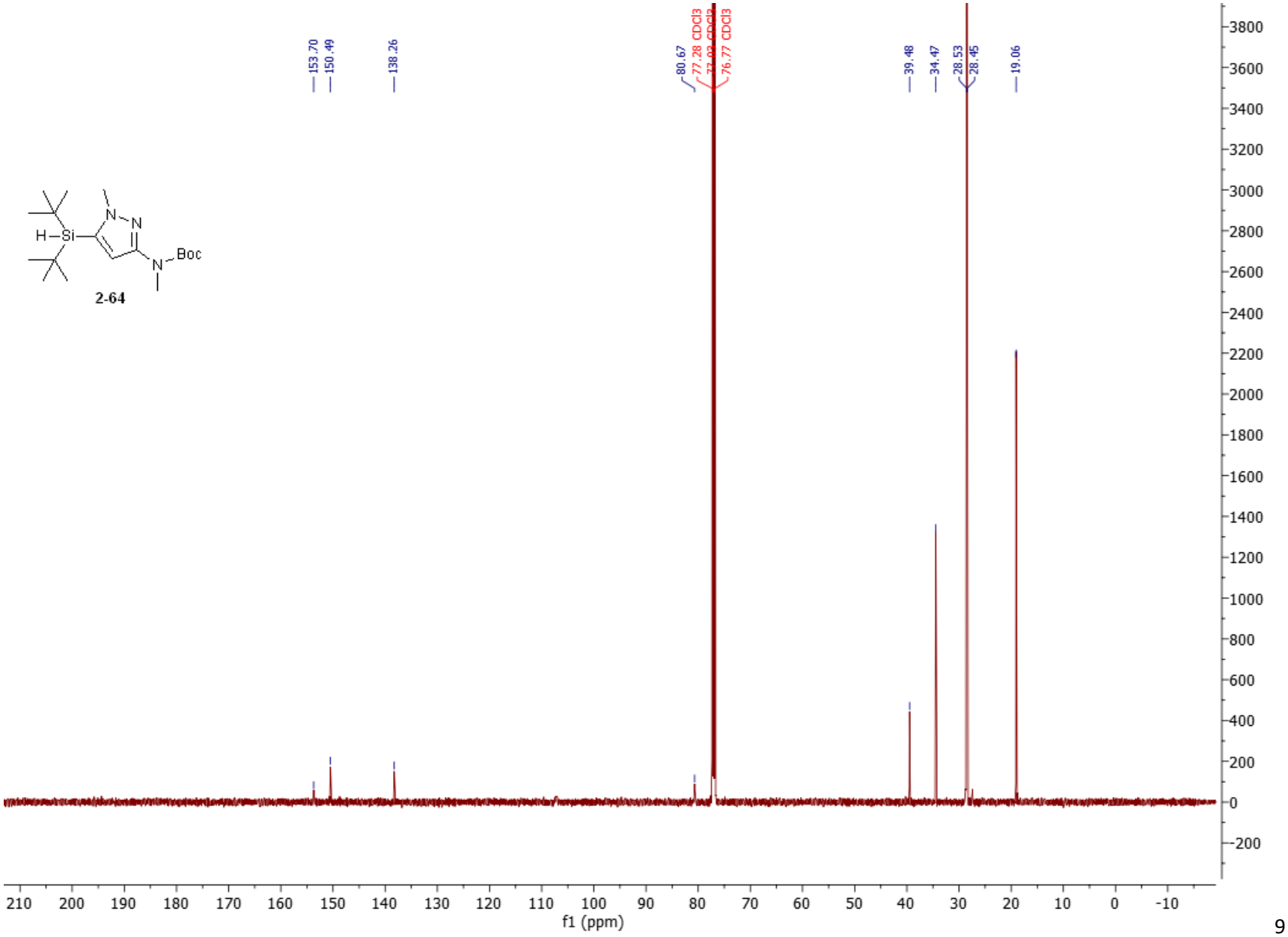
153.70
150.49
138.26
80.67
77.28 CDCl3
77.03 CDCl3
76.77 CDCl3
39.48
34.47
28.53
28.45
19.06
H–Si
N
N
N
Boc
2-64
f1 (ppm)

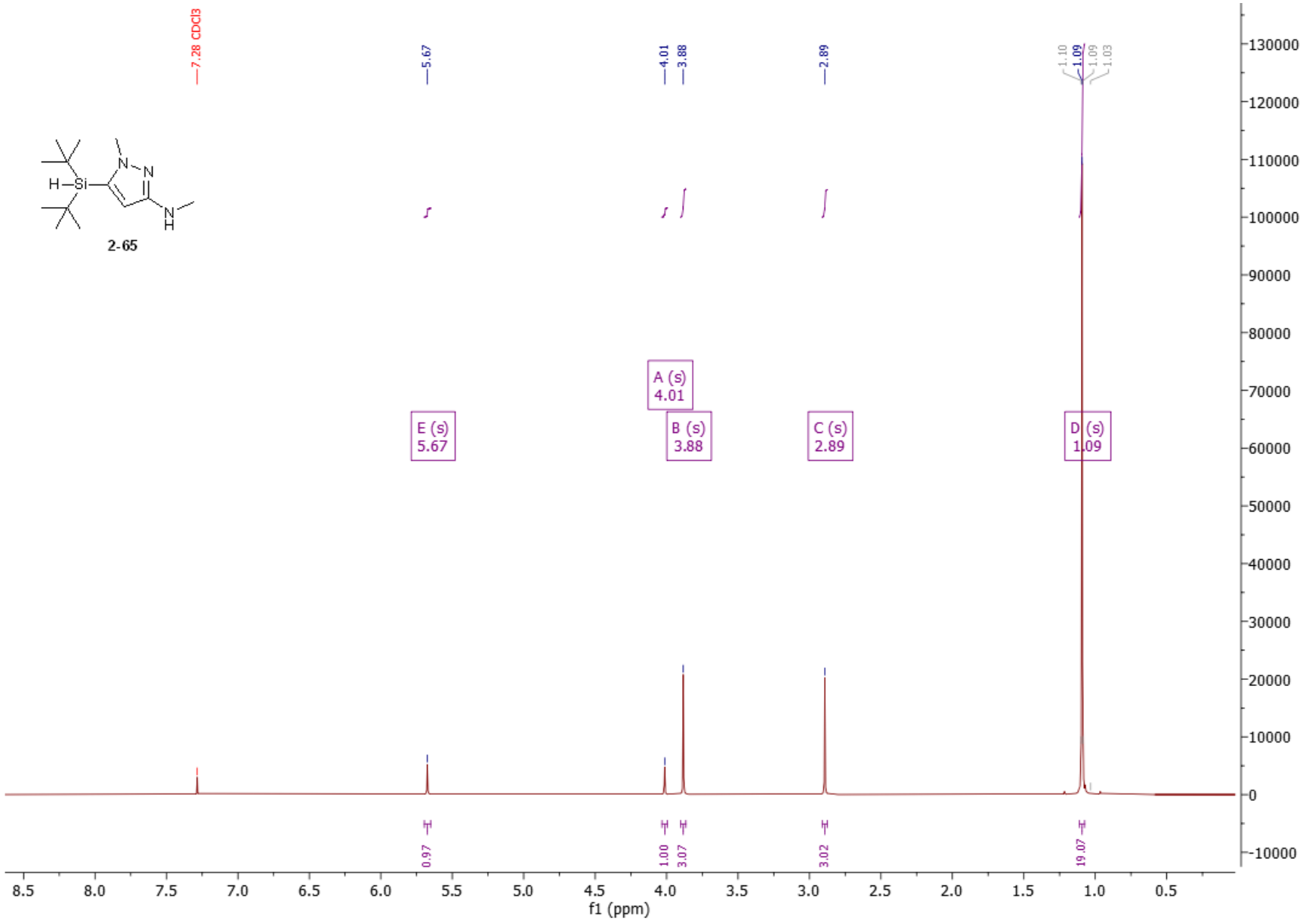
7.28 CDCl3
5.67
4.01
3.88
2.89
1.10
1.09
1.09
1.03
H
Si
N
N
N
H
2-65
A (s)
4.01
E (s)
5.67
B (s)
3.88
C (s)
2.89
D (s)
1.09
0.97
1.00
3.07
3.02
19.07
f1 (ppm)

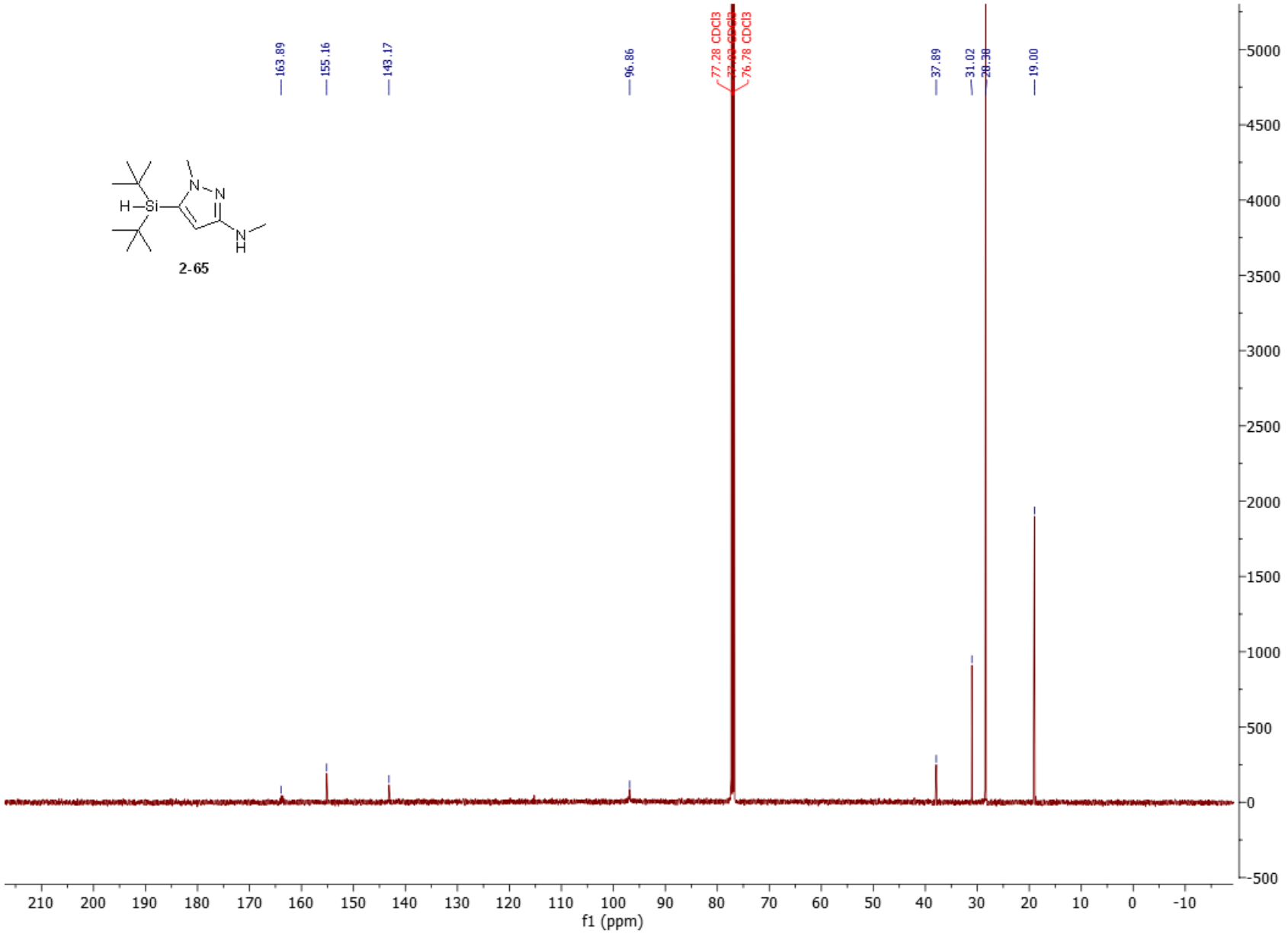
163.89
155.16
143.17
96.86
77.28 CDCl3
76.78 CDCl3
37.89
31.02
28.38
19.00
H—Si
N
N
NH
2-65
f1 (ppm)

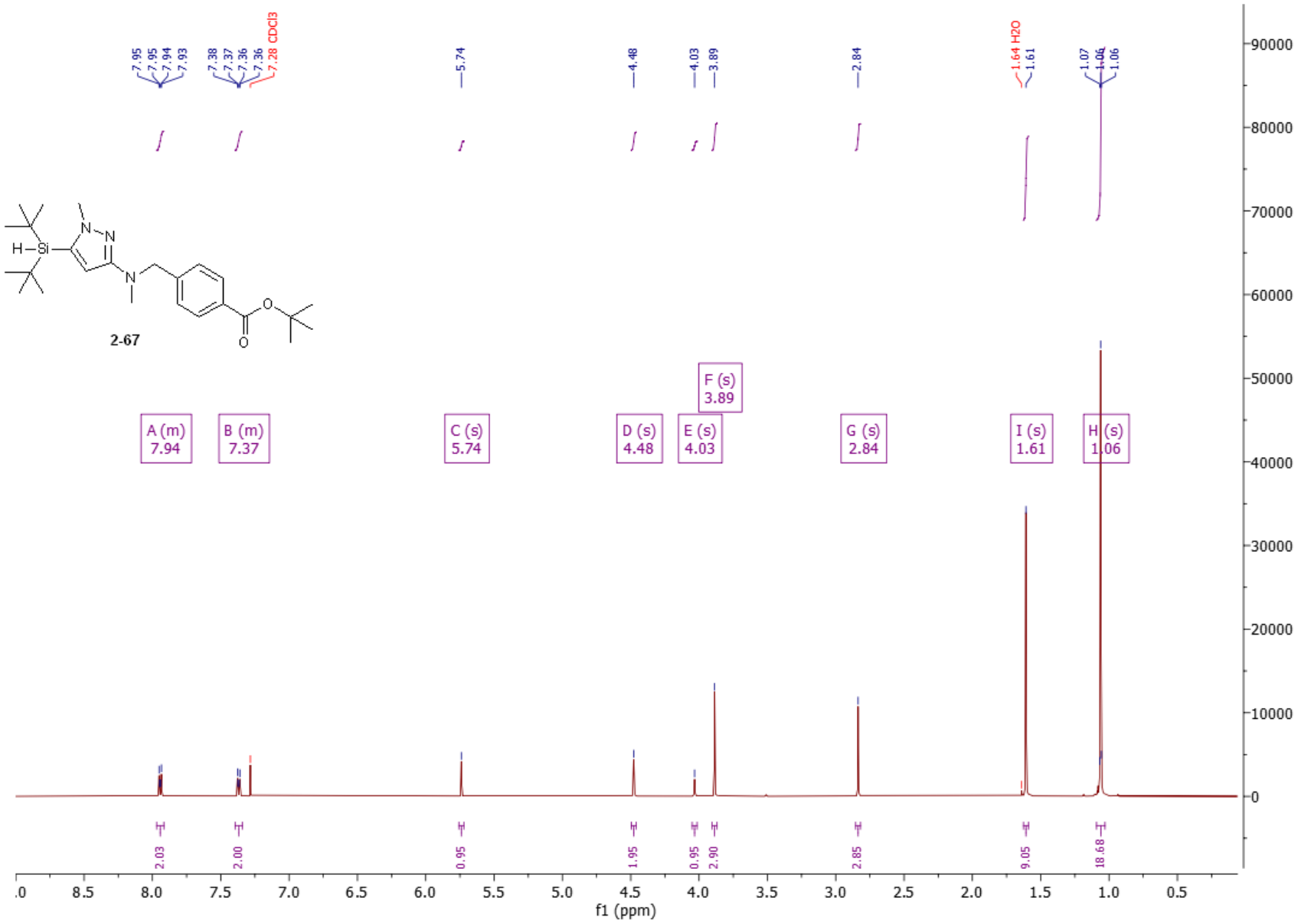
7.95
7.95
7.94
7.93
7.38
7.37
7.36
7.36
7.28 CDCl3
5.74
4.48
4.03
3.89
2.84
1.64 H2O
1.61
1.07
1.06
1.06
2-67
A (m)
7.94
B (m)
7.37
C (s)
5.74
D (s)
4.48
F (s)
3.89
E (s)
4.03
G (s)
2.84
I (s)
1.61
H (s)
1.06
2.03
2.00
0.95
1.95
0.95
2.90
2.85
9.05
18.68
f1 (ppm)

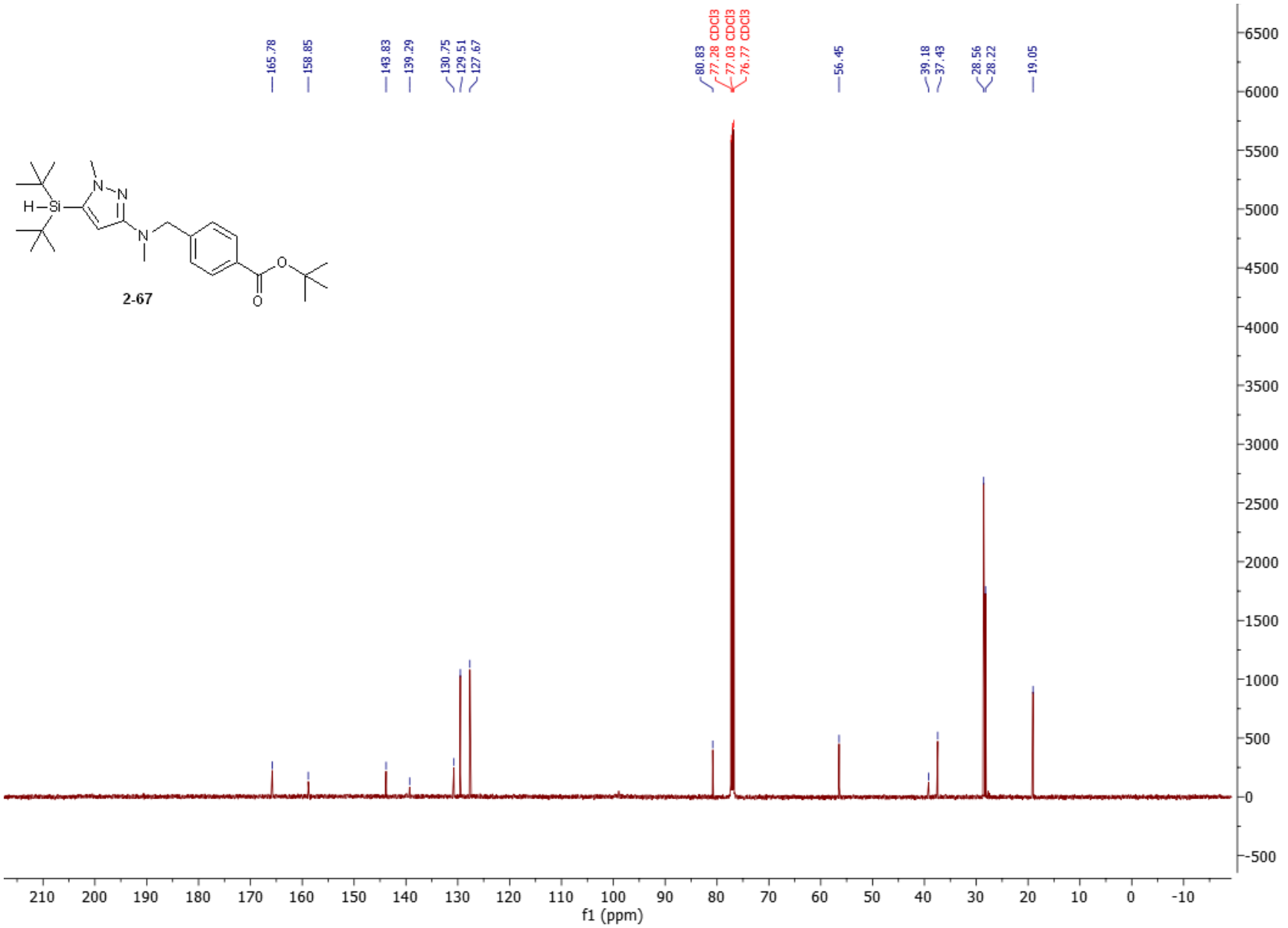
165.78
158.85
143.83
139.29
130.75
129.51
127.67
80.83
77.28 CDCl3
77.03 CDCl3
76.77 CDCl3
56.45
39.18
37.43
28.56
28.22
19.05
H–Si
N
N
N
O
O
2-67
f1 (ppm)

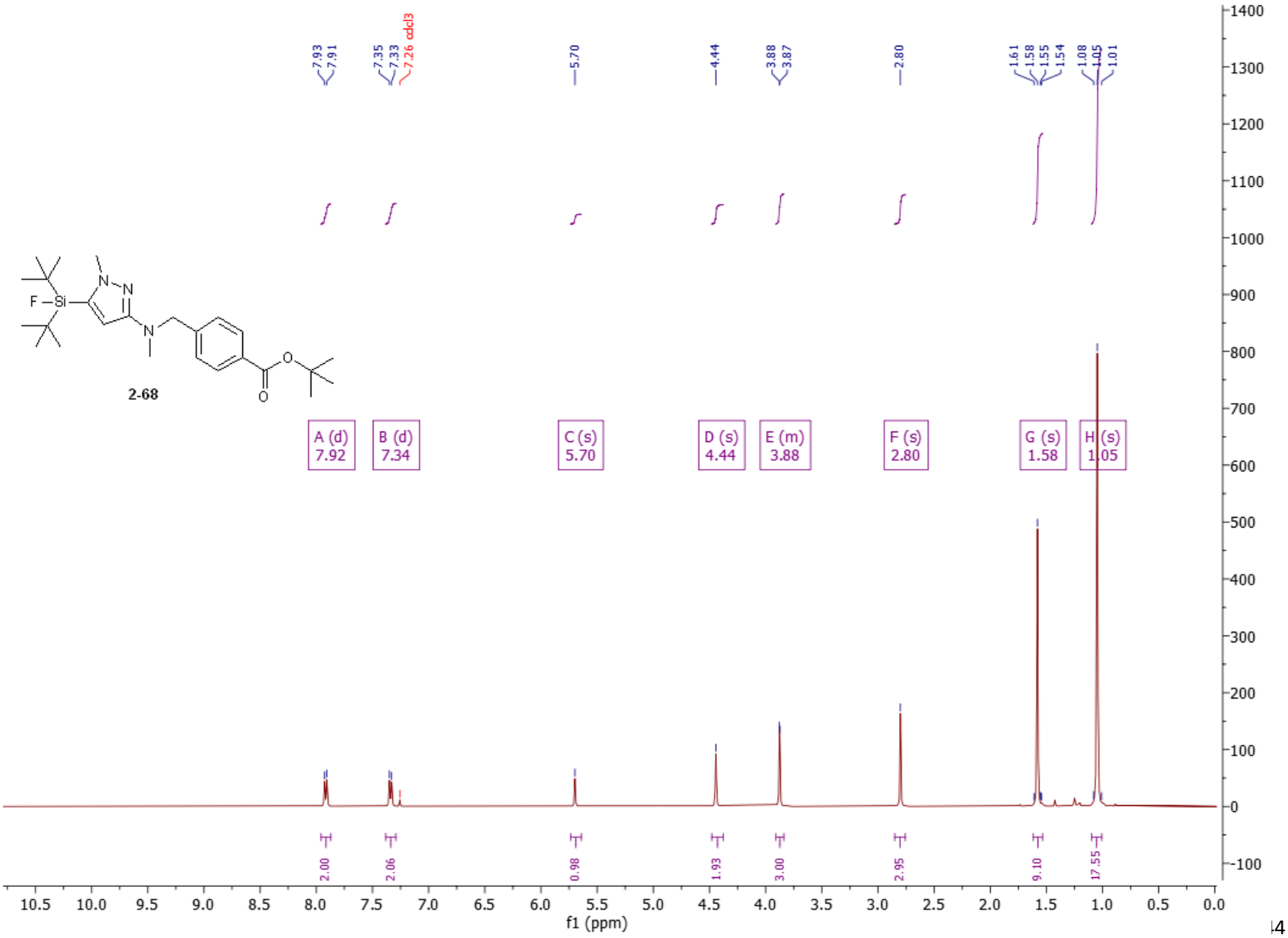
7.93
7.91
7.35
7.33
7.26 cdcl3
5.70
4.44
3.88
3.87
2.80
1.61
1.58
1.55
1.54
1.08
1.05
1.01
F
Si
N
N
N
O
O
2-68
A (d)
7.92
B (d)
7.34
C (s)
5.70
D (s)
4.44
E (m)
3.88
F (s)
2.80
G (s)
1.58
H (s)
1.05
2.00
2.06
0.98
1.93
3.00
2.95
9.10
17.55
f1 (ppm)

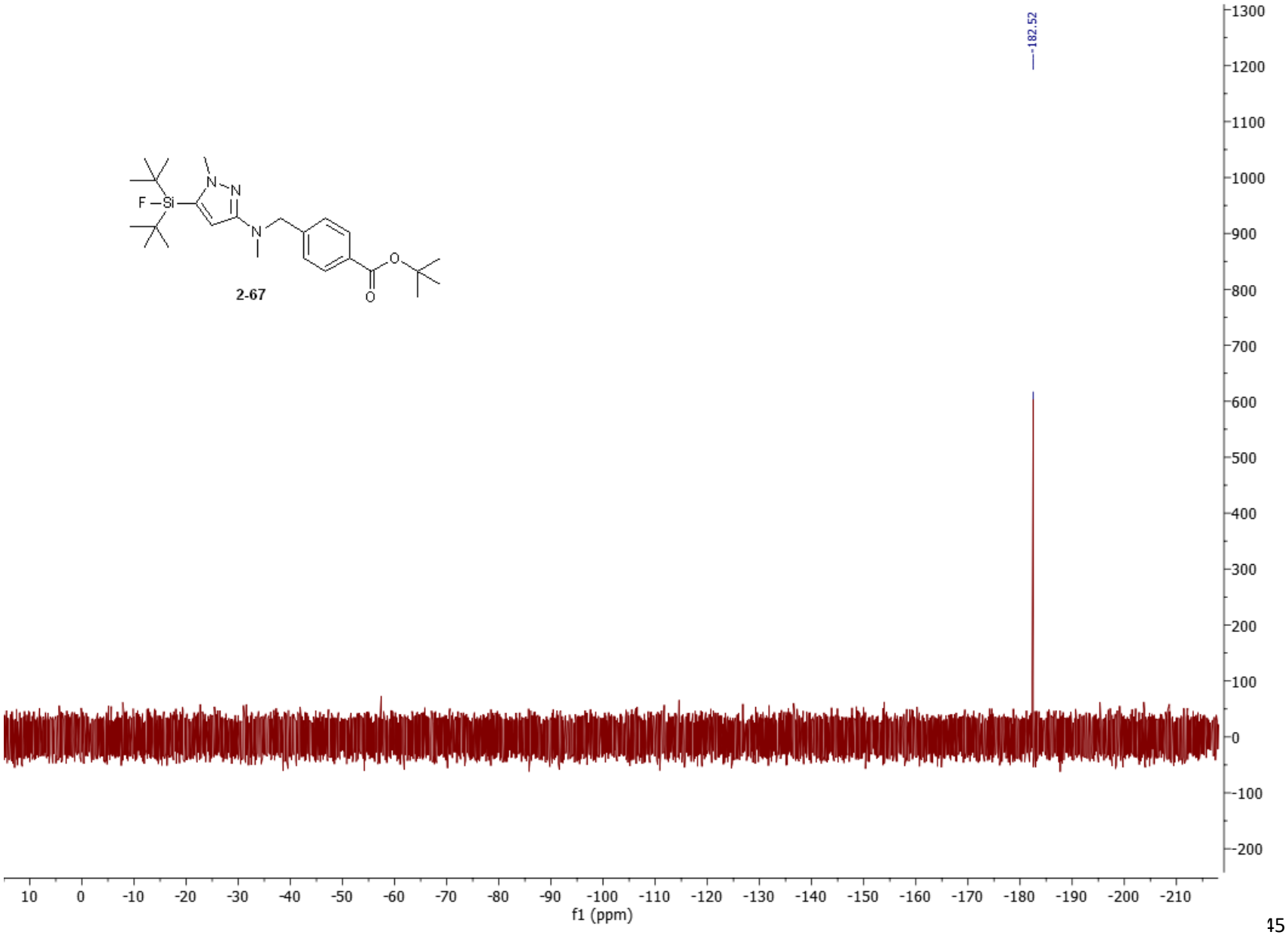
-182.52
1300
1200
1100
1000
900
800
700
600
500
400
300
200
100
0
-100
-200
10 0 -10 -20 -30 -40 -50 -60 -70 -80 -90 -100 -110 -120 -130 -140 -150 -160 -170 -180 -190 -200 -210
f1 (ppm)
F
Si
N
N
N
O
O
2-67

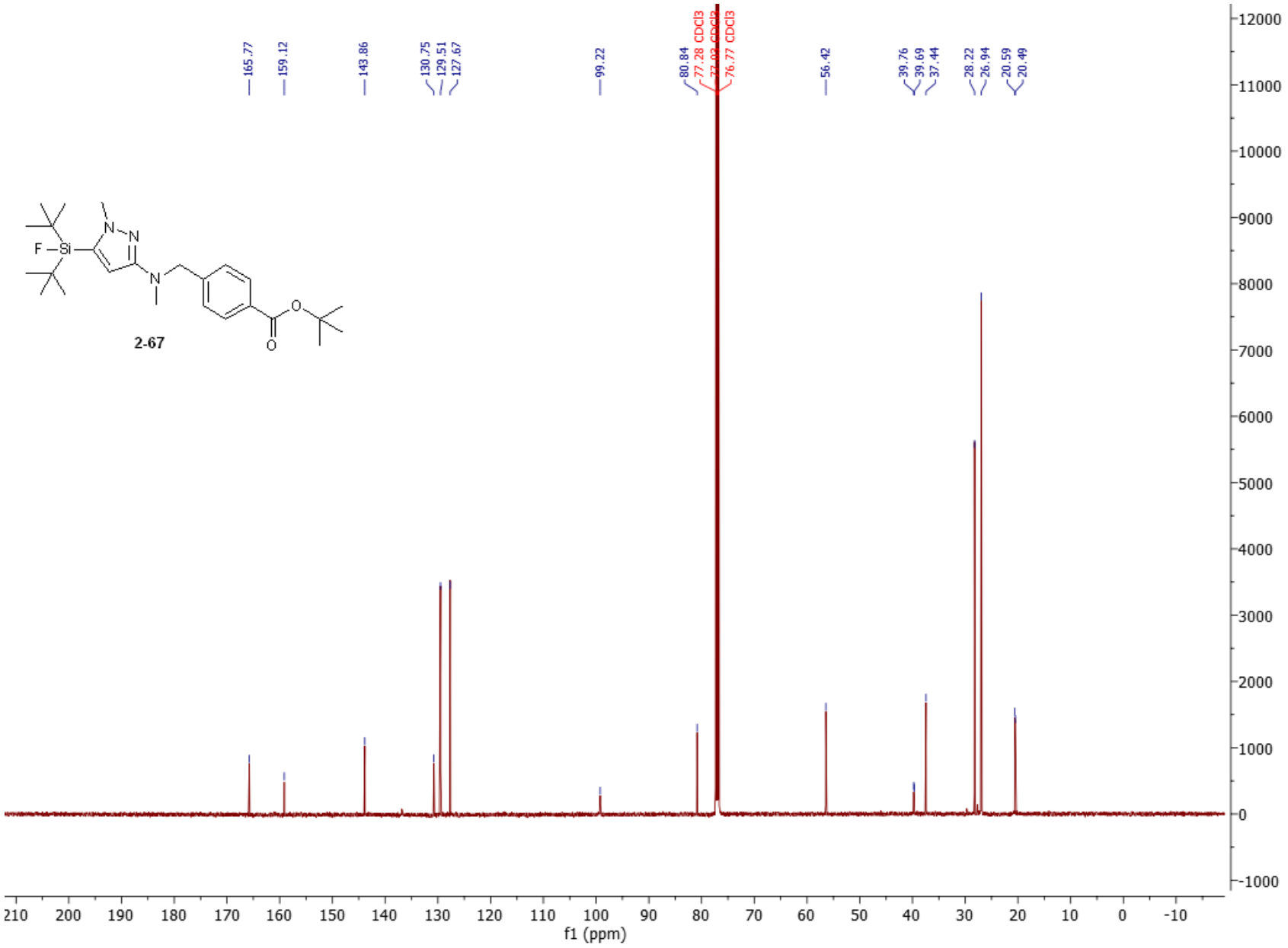
165.77
159.12
143.86
130.75
129.51
127.67
99.22
80.84
77.28 CDCl3
76.77 CDCl3
56.42
39.76
39.69
37.44
28.22
26.94
20.59
20.49
F
Si
N
N
N
O
O
2-67
f1 (ppm)

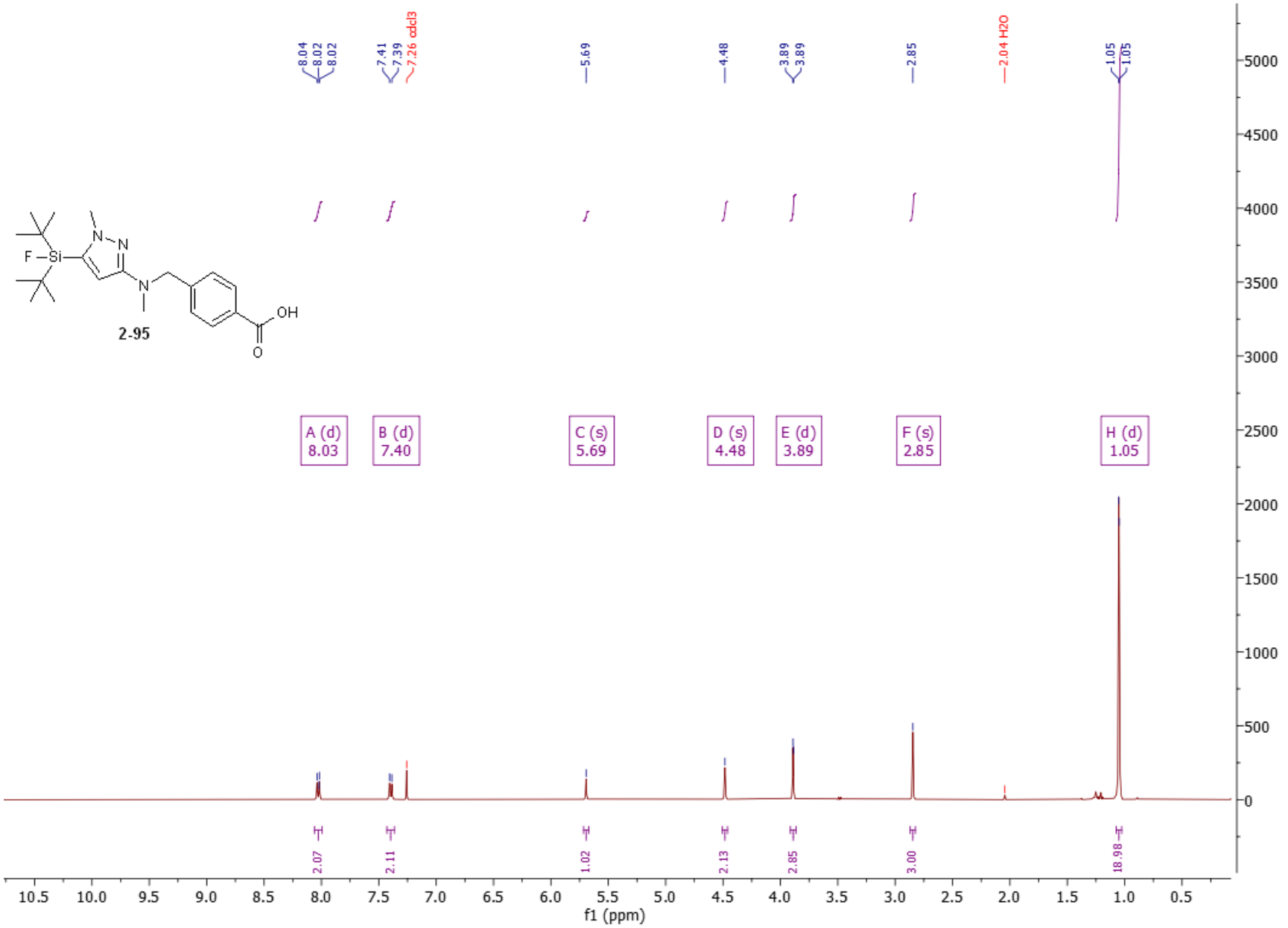
8.04
8.02
8.02
7.41
7.39
7.26 cdcl3
5.69
4.48
3.89
3.89
2.85
2.04 H2O
1.05
1.05
F
Si
N
N
N
OH
O
2-95
A (d)
8.03
B (d)
7.40
C (s)
5.69
D (s)
4.48
E (d)
3.89
F (s)
2.85
H (d)
1.05
2.07
2.11
1.02
2.13
2.85
3.00
18.98
f1 (ppm)

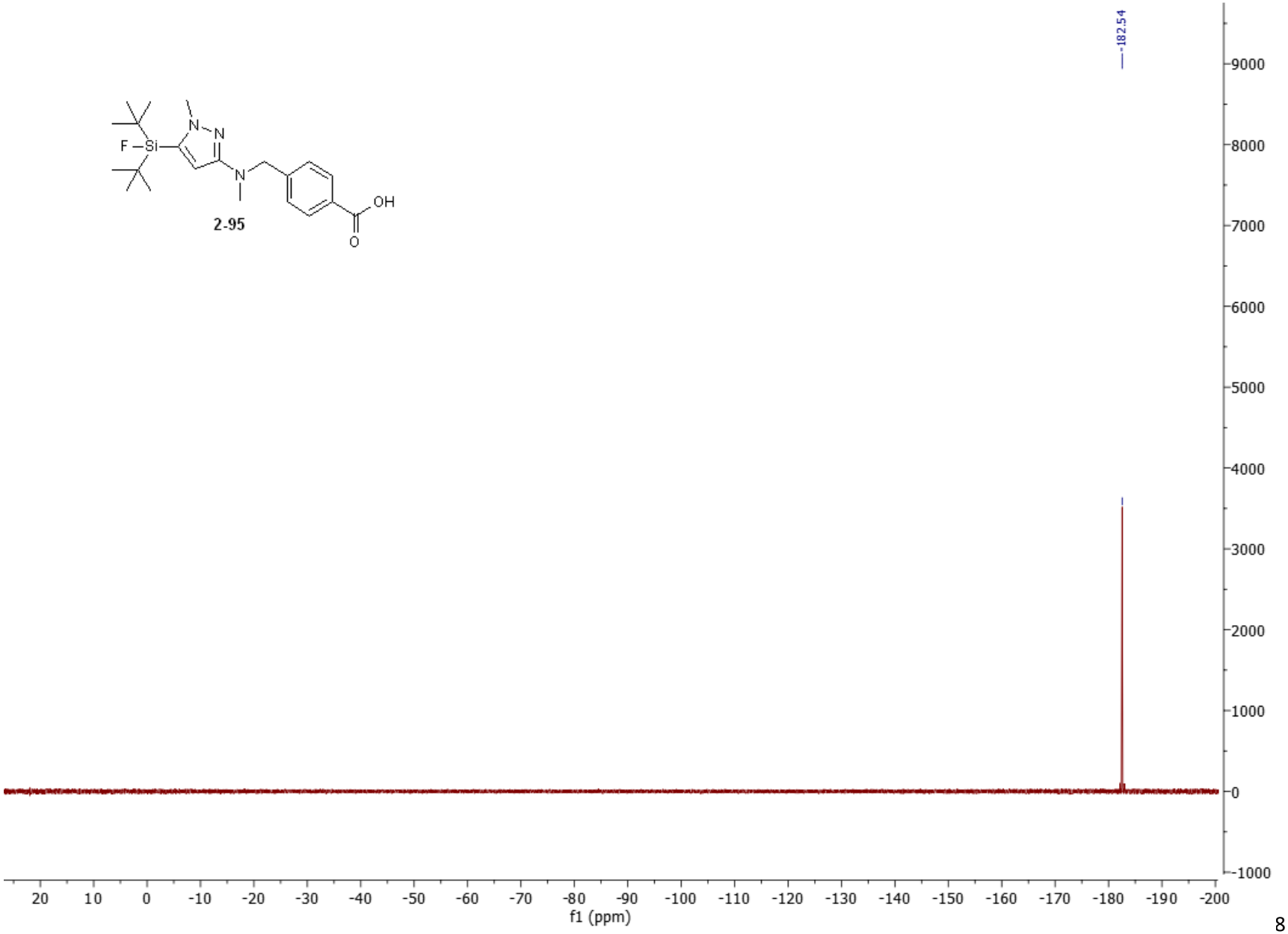
-182.54
9000
8000
7000
6000
5000
4000
3000
2000
1000
0
-1000
20 10 0 -10 -20 -30 -40 -50 -60 -70 -80 -90 -100 -110 -120 -130 -140 -150 -160 -170 -180 -190 -200
f1 (ppm)
F
Si
N
N
N
OH
O
2-95

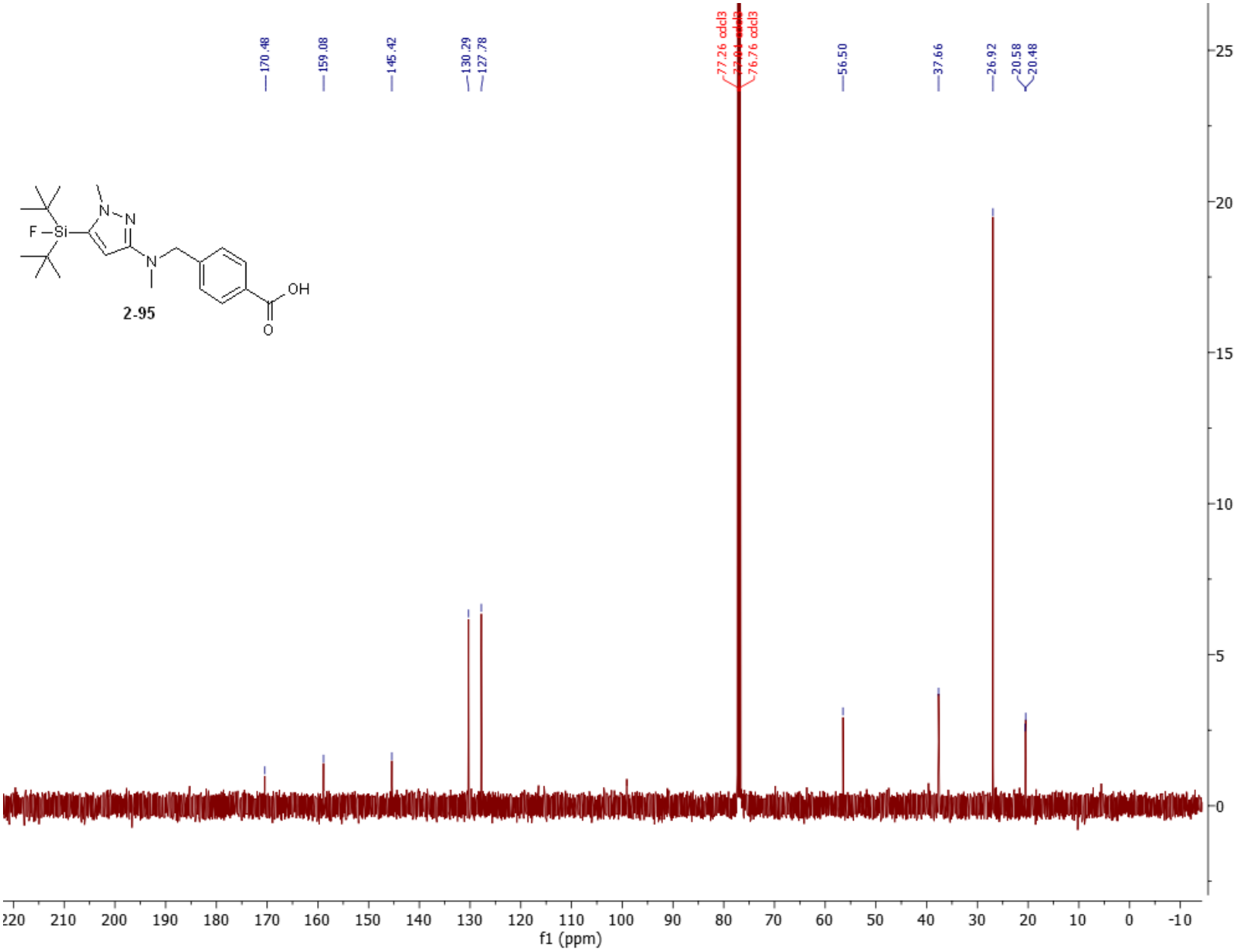
170.48
159.08
145.42
130.29
127.78
77.26 cdcl3
76.76 cdcl3
56.50
37.66
26.92
20.58
20.48
F
Si
N
N
N
OH
O
2-95
25
20
15
10
5
0
220 210 200 190 180 170 160 150 140 130 120 110 100 90 80 70 60 50 40 30 20 10 0 -10
f1 (ppm)

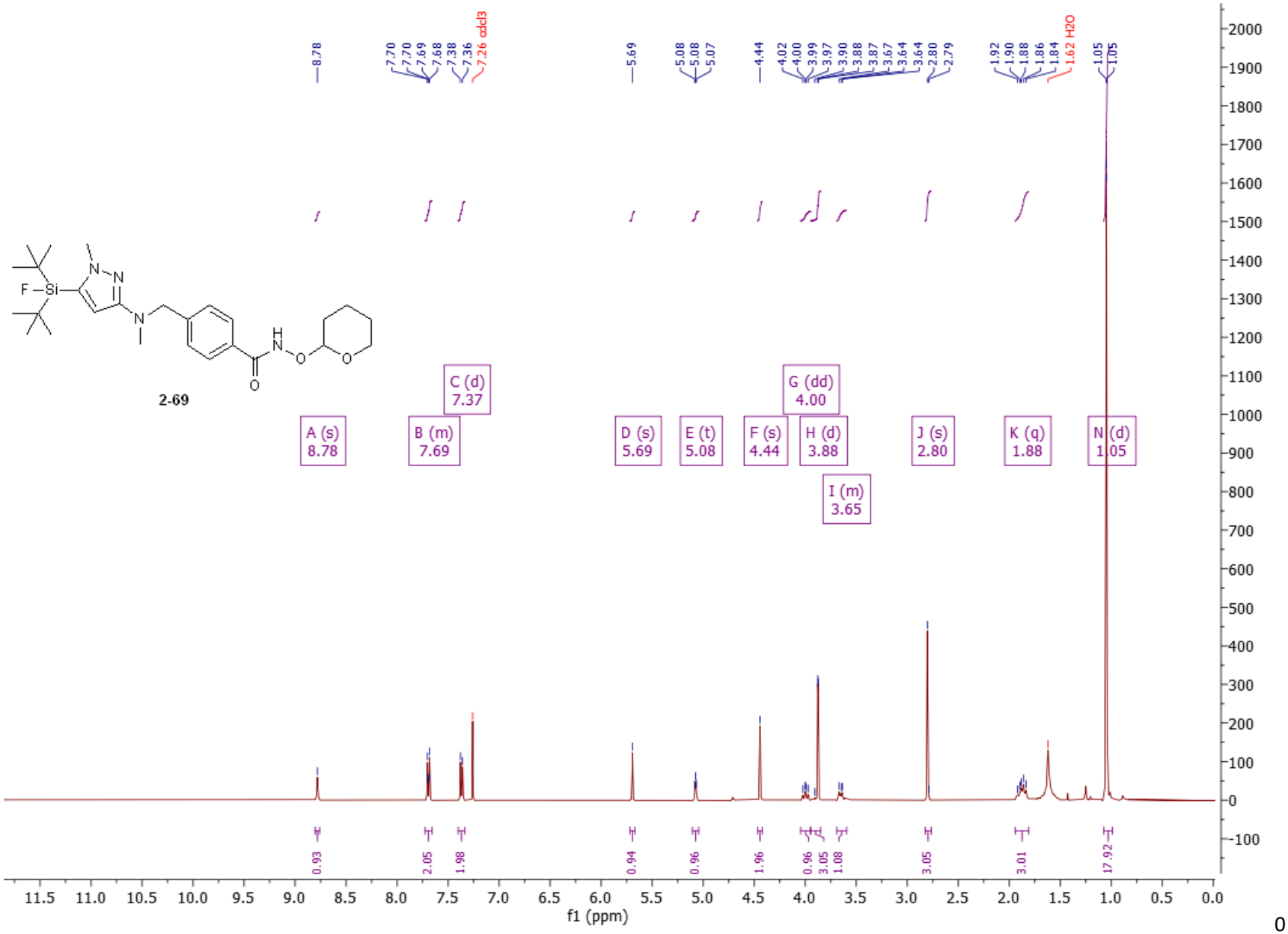
8.78
7.70
7.70
7.69
7.68
7.38
7.36
7.26 cdcl3
5.69
5.08
5.08
5.07
4.44
4.02
4.00
3.99
3.97
3.90
3.88
3.87
3.67
3.64
3.64
2.80
2.79
1.92
1.90
1.88
1.86
1.84
1.62 H2O
1.05
1.05
2-69
A (s) 8.78
B (m) 7.69
C (d) 7.37
D (s) 5.69
E (t) 5.08
F (s) 4.44
G (dd) 4.00
H (d) 3.88
I (m) 3.65
J (s) 2.80
K (q) 1.88
N (d) 1.05
0.93
2.05
1.98
0.94
0.96
1.96
0.96
3.05
1.08
3.05
3.01
17.92
f1 (ppm)

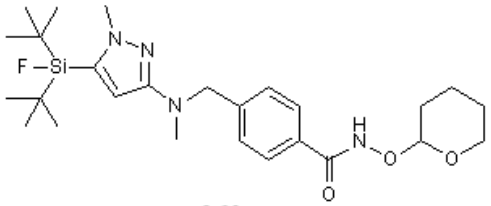

2-69

-182.54
13000
12000
11000
10000
9000
8000
7000
6000
5000
4000
3000
2000
1000
0
-1000
10 0 -10 -20 -30 -40 -50 -60 -70 -80 -90 -100 -110 -120 -130 -140 -150 -160 -170 -180 -190 -200
f1 (ppm)

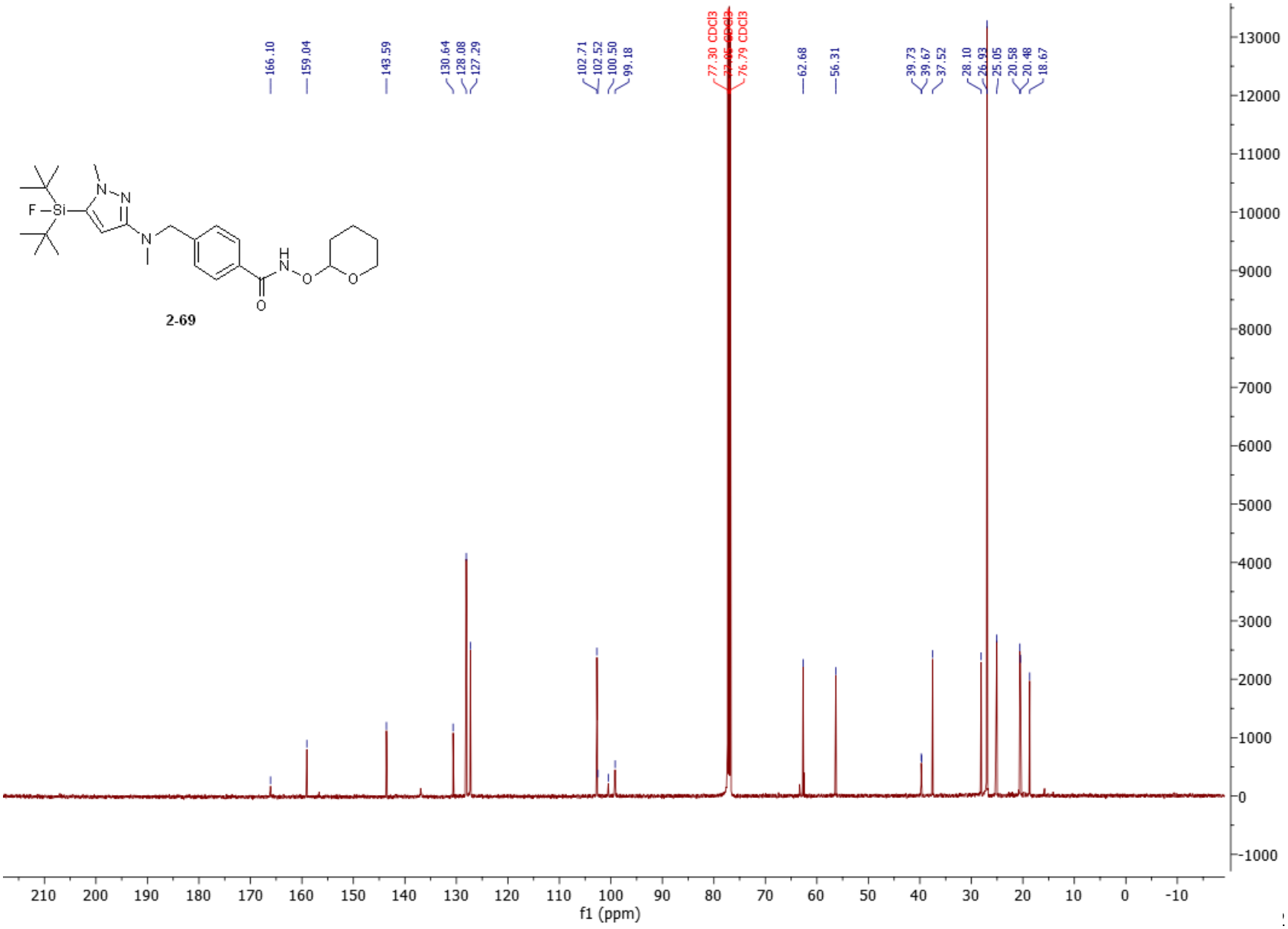
166.10
159.04
143.59
130.64
128.08
127.29
102.71
102.52
100.50
99.18
77.30 CDCl3
76.79 CDCl3
62.68
56.31
39.73
39.67
37.52
28.10
26.93
25.05
20.58
20.48
18.67
F
Si
N
N
N
H
N
O
O
O
2-69
f1 (ppm)

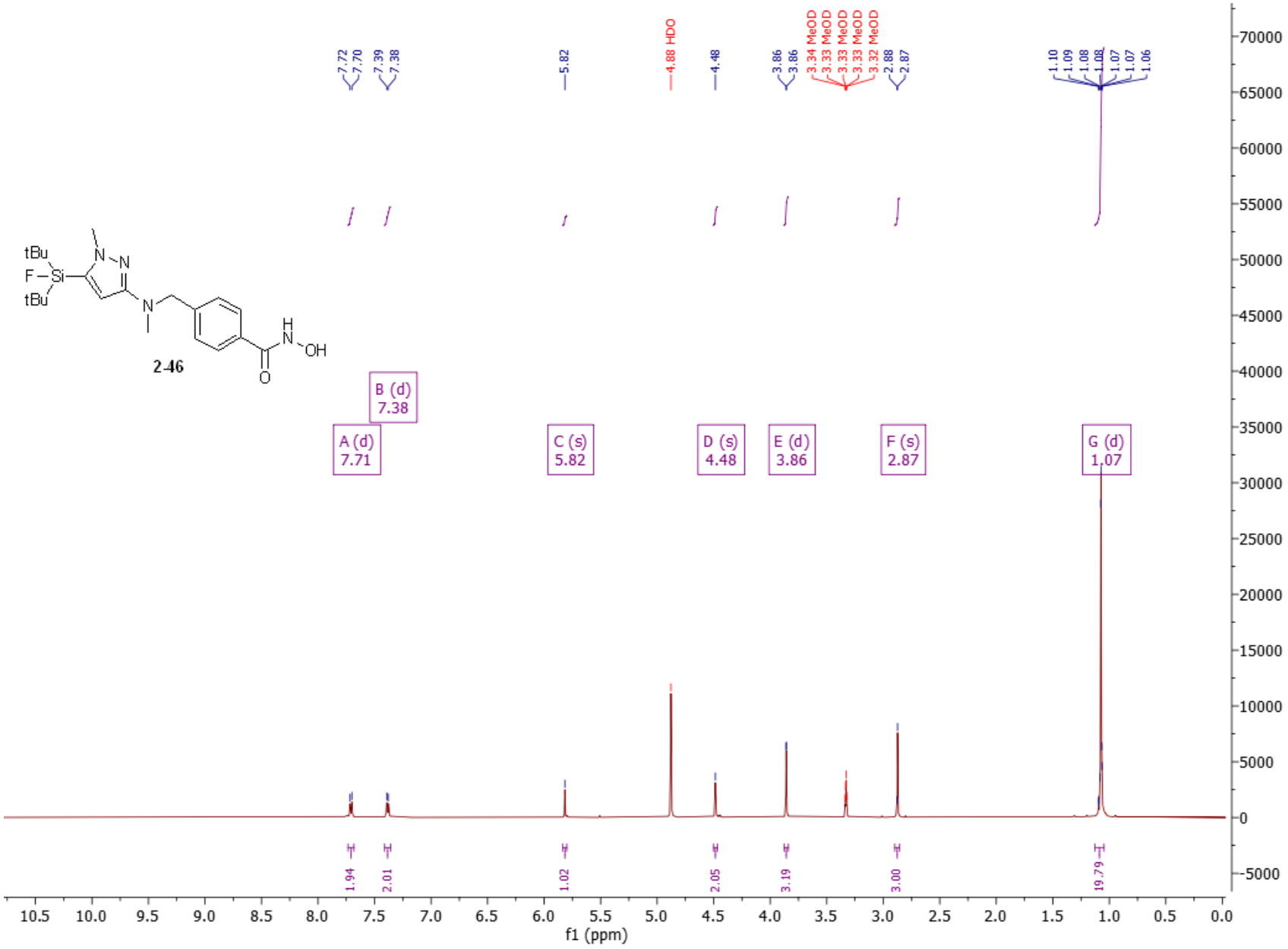
7.72
7.70
7.39
7.38
5.82
4.88 HDO
4.48
3.86
3.86
3.34 MeOD
3.33 MeOD
3.33 MeOD
3.33 MeOD
3.32 MeOD
2.88
2.87
1.10
1.09
1.08
1.08
1.07
1.07
1.06
tBu
F—Si
tBu
N
N
N
H
N
OH
O
2-46
B (d)
7.38
A (d)
7.71
C (s)
5.82
D (s)
4.48
E (d)
3.86
F (s)
2.87
G (d)
1.07
1.94
2.01
1.02
2.05
3.19
3.00
19.79
f1 (ppm)

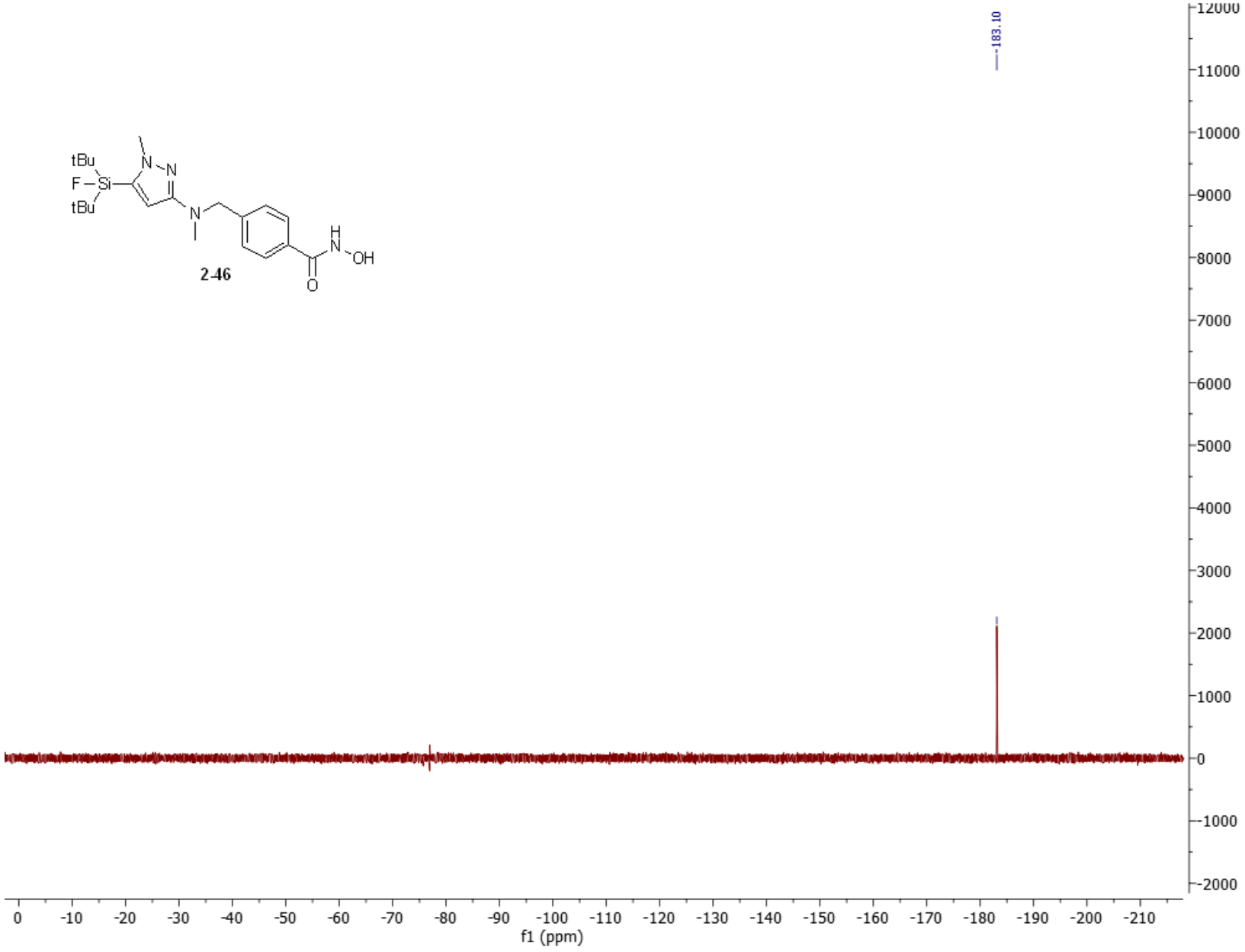
tBu
F–Si
tBu
N
N
N
H
N
OH
O
2-46
-183.10
12000
11000
10000
9000
8000
7000
6000
5000
4000
3000
2000
1000
0
-1000
-2000
0 -10 -20 -30 -40 -50 -60 -70 -80 -90 -100 -110 -120 -130 -140 -150 -160 -170 -180 -190 -200 -210
f1 (ppm)

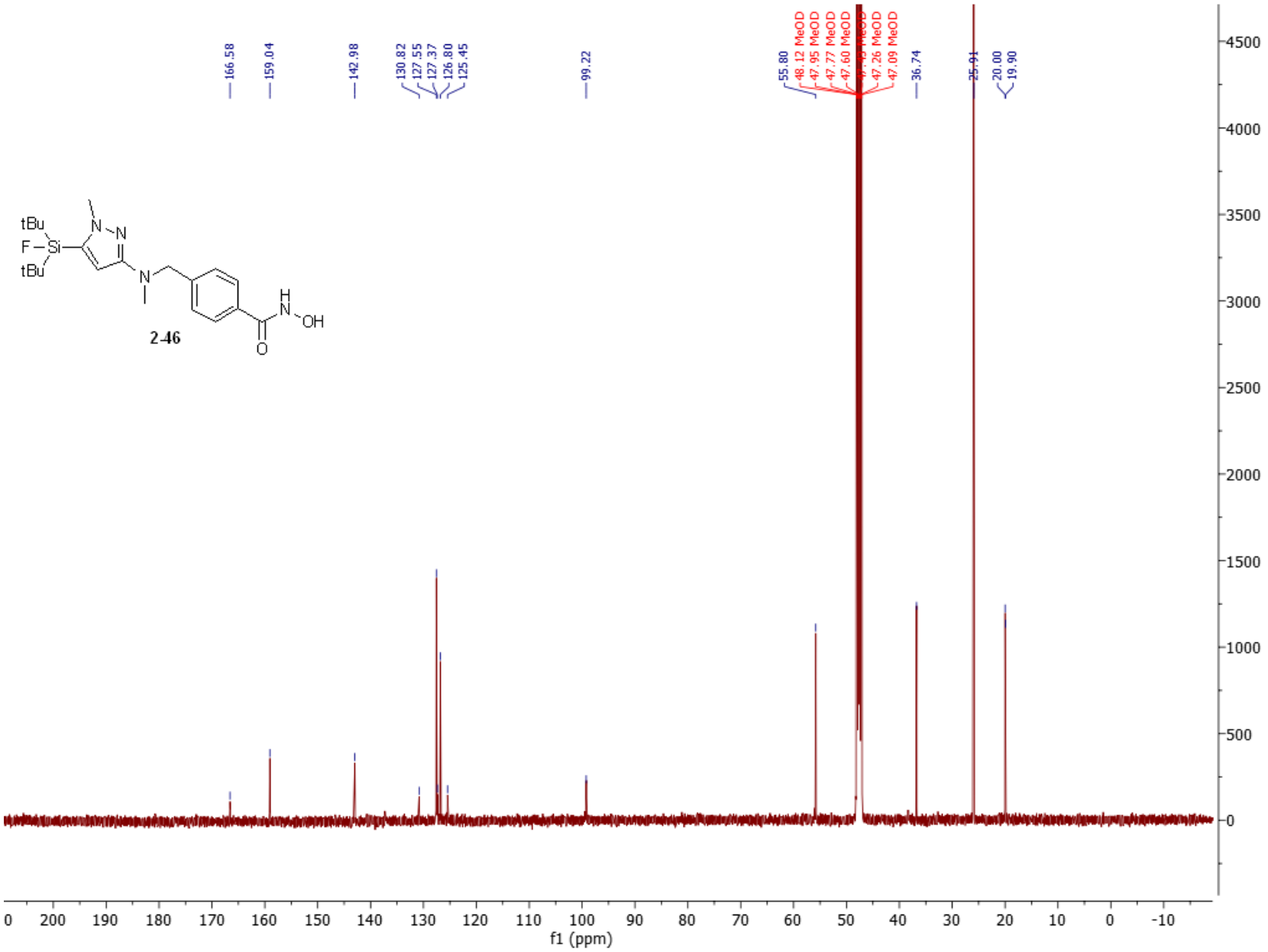
166.58
159.04
142.98
130.82
127.55
127.37
126.80
125.45
99.22
55.80
48.12 MeOD
47.95 MeOD
47.77 MeOD
47.60 MeOD
47.26 MeOD
47.09 MeOD
36.74
25.91
20.00
19.90
tBu
F—Si
tBu
N
N
N
H
N
OH
O
2-46
4500
4000
3500
3000
2500
2000
1500
1000
500
0
0 200 190 180 170 160 150 140 130 120 110 100 90 80 70 60 50 40 30 20 10 0 -10
f1 (ppm)

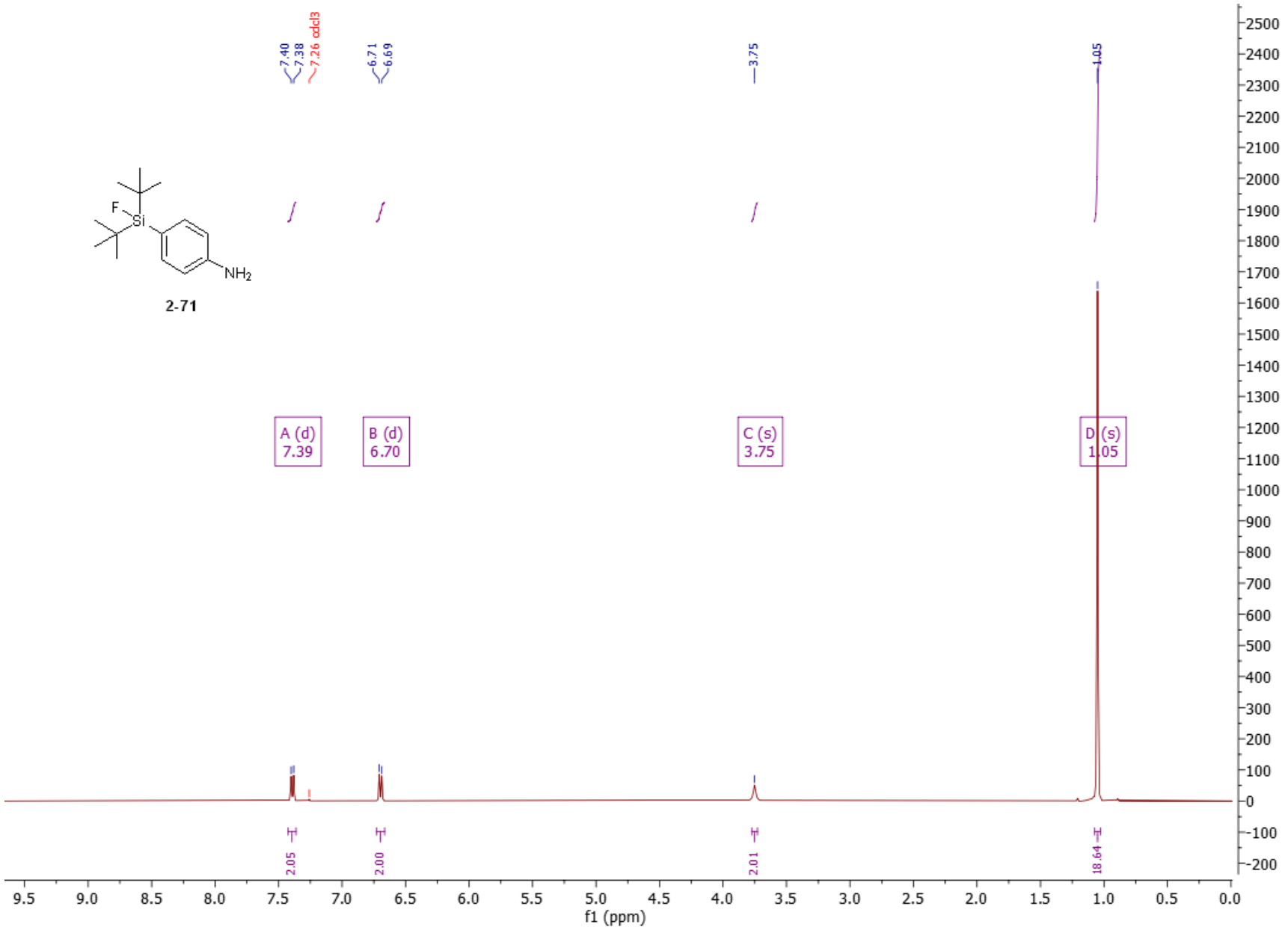
7.40
7.38
7.26 cdcl3
6.71
6.69
3.75
1.05
F
Si
NH2
2-71
A (d)
7.39
B (d)
6.70
C (s)
3.75
D (s)
1.05
2.05
2.00
2.01
18.64
f1 (ppm)

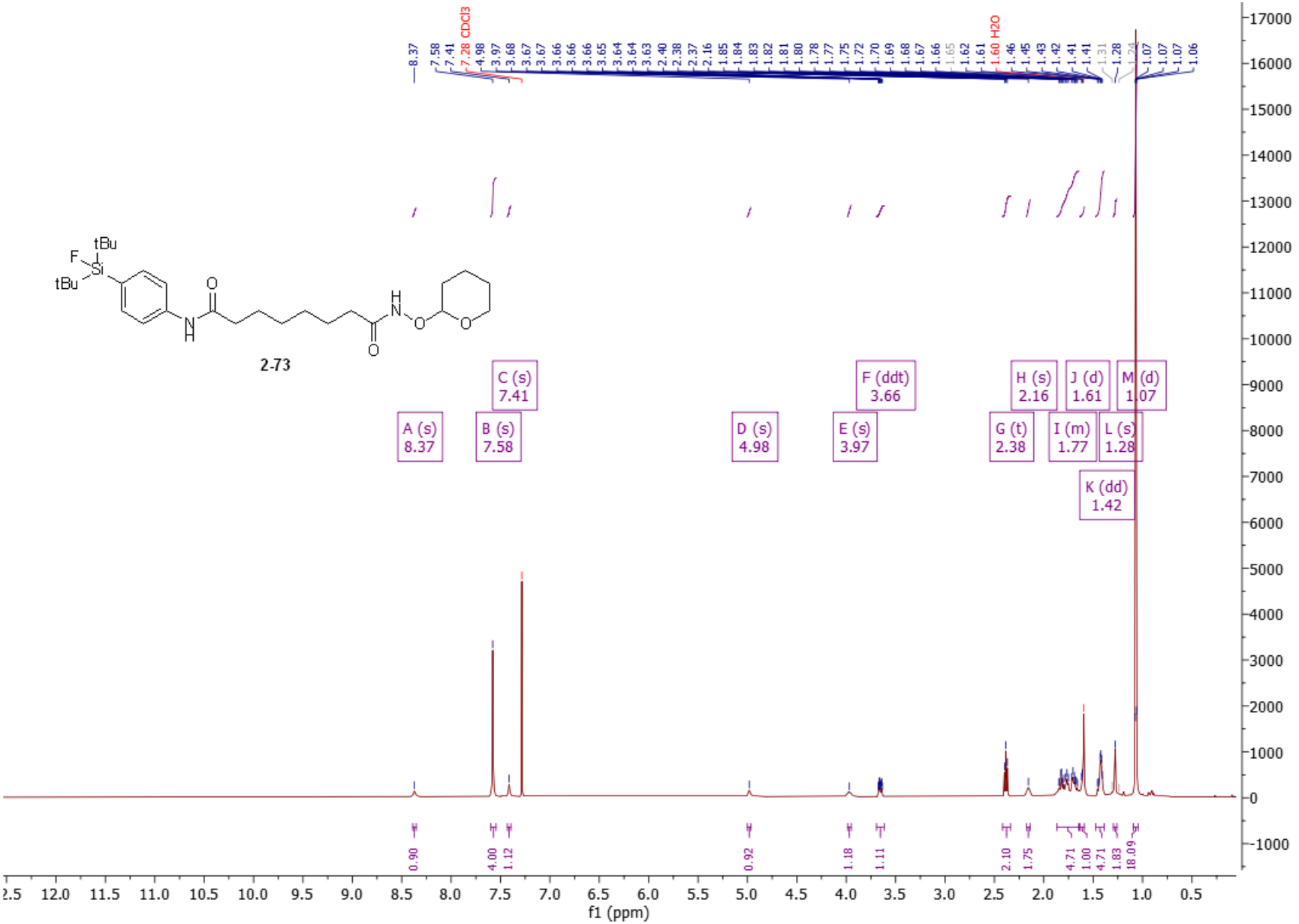
tBu
F
Si
tBu
O
N
H
H
N
O
O
O
2-73
A (s) 8.37
B (s) 7.58
C (s) 7.41
D (s) 4.98
E (s) 3.97
F (ddt) 3.66
G (t) 2.38
H (s) 2.16
I (m) 1.77
J (d) 1.61
K (dd) 1.42
L (s) 1.28
M (d) 1.07
f1 (ppm)

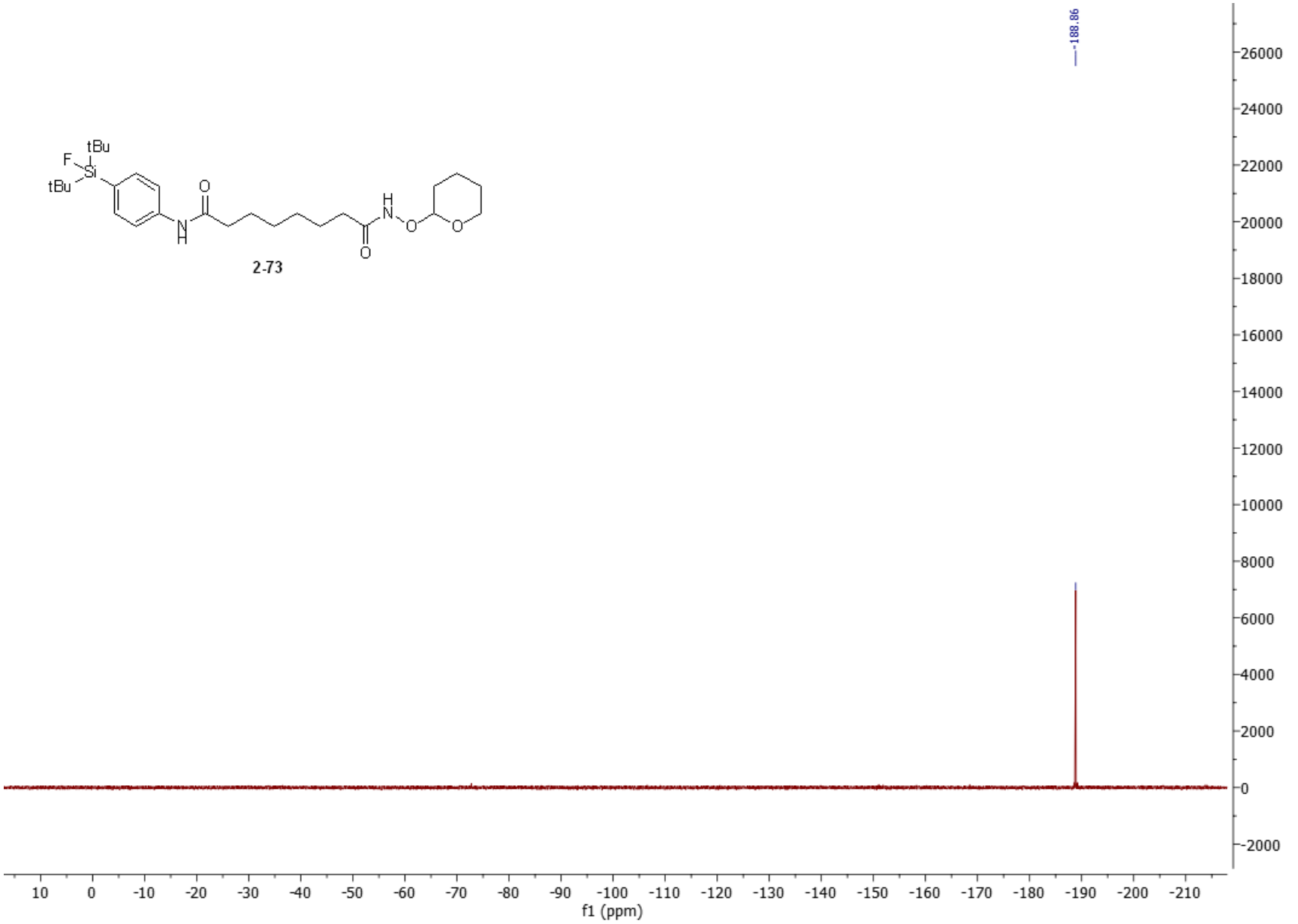
tBu
F
Si
tBu
O
N
H
H
N
O
O
O
2-73
-188.86
26000
24000
22000
20000
18000
16000
14000
12000
10000
8000
6000
4000
2000
0
-2000
10
0
-10
-20
-30
-40
-50
-60
-70
-80
-90
-100
-110
-120
-130
-140
-150
-160
-170
-180
-190
-200
-210
f1 (ppm)

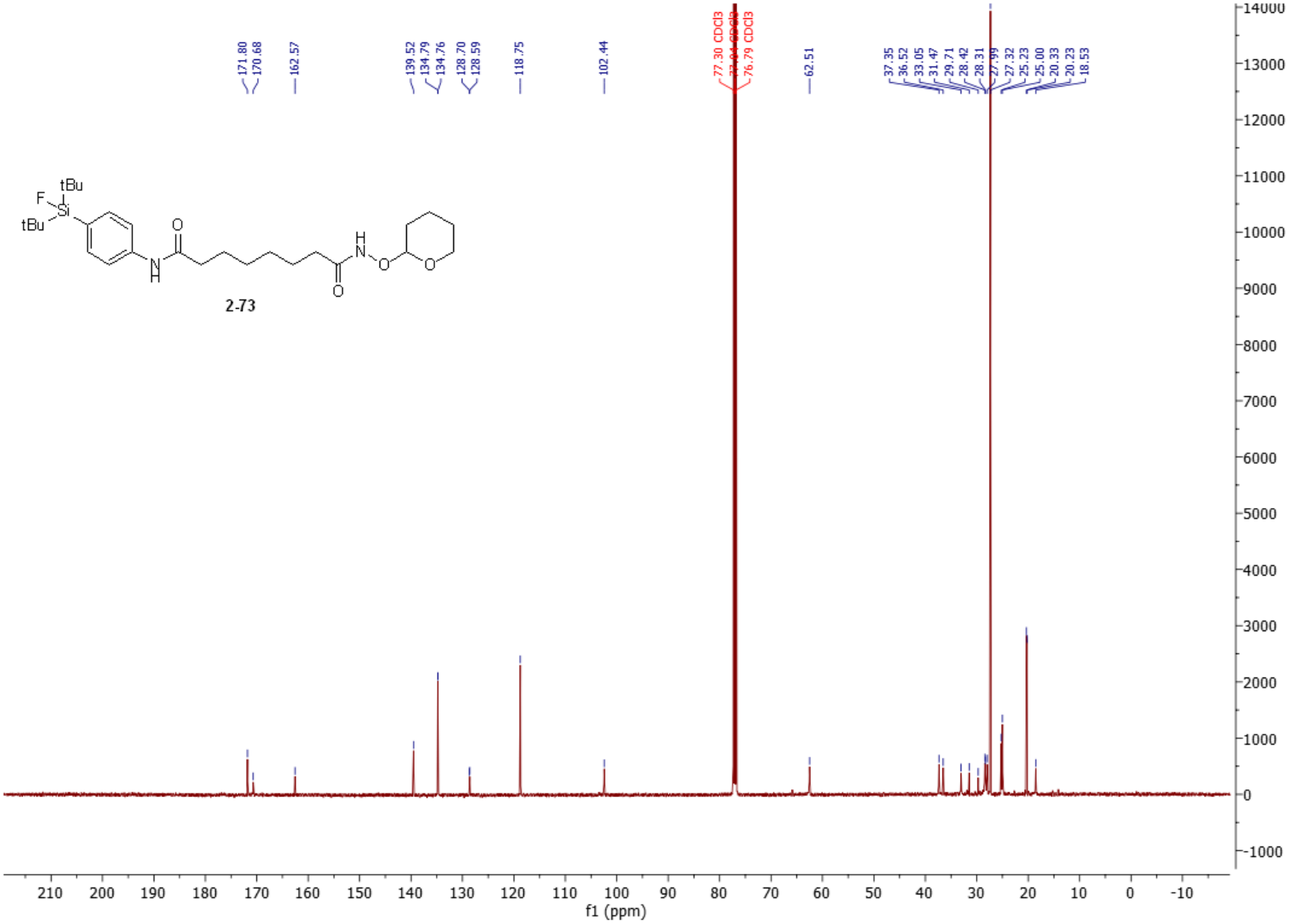
171.80
170.68
162.57
139.52
134.79
134.76
128.70
128.59
118.75
102.44
77.30 CDCl3
76.79 CDCl3
62.51
37.35
36.52
33.05
31.47
29.71
28.42
28.31
27.99
27.32
25.23
25.00
20.33
20.23
18.53
tBu
tBu
F
Si
O
N
H
N
O
O
O
2-73
f1 (ppm)

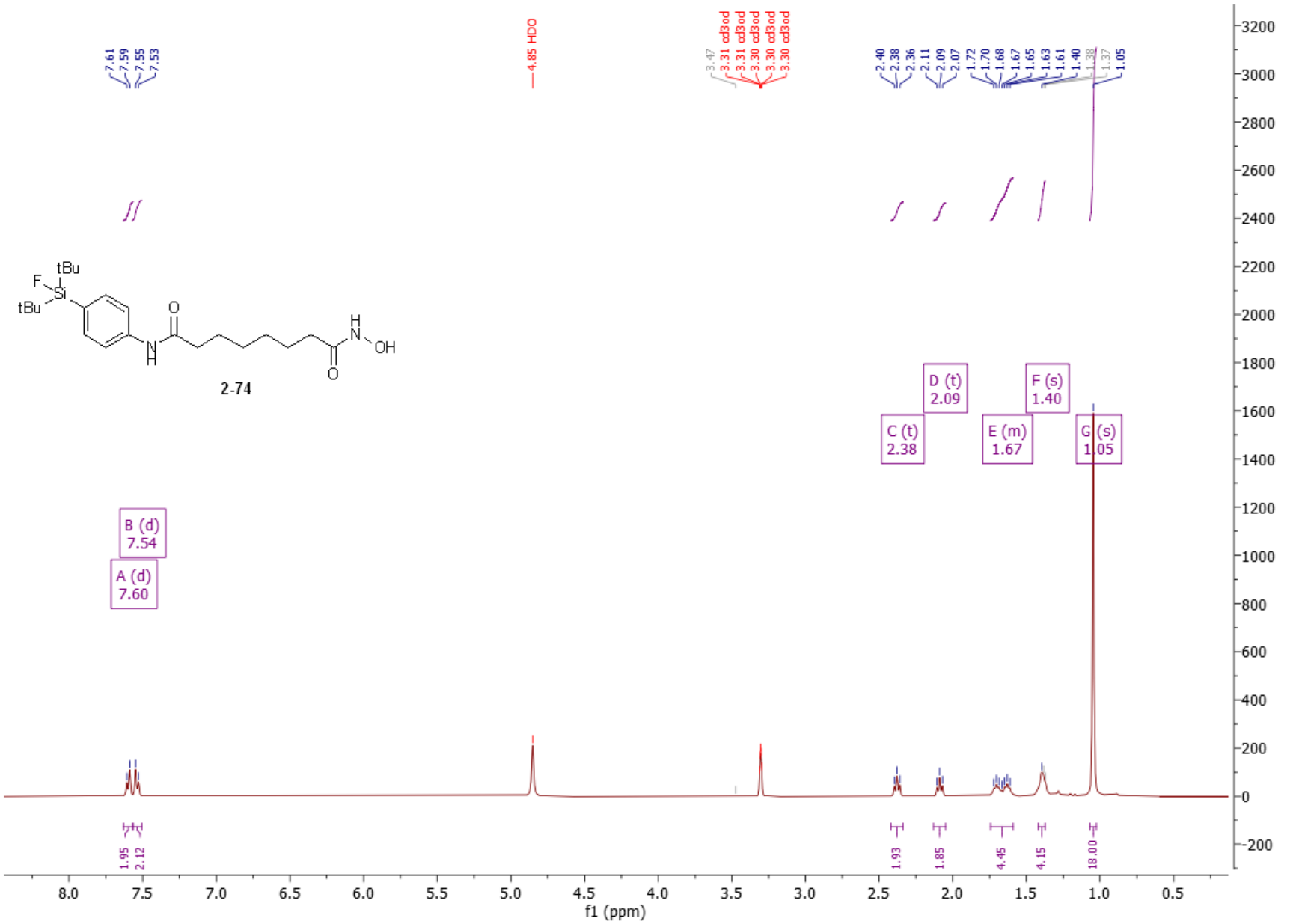
7.61
7.59
7.55
7.53
4.85 HDO
3.47
3.31 cd3od
3.31 cd3od
3.30 cd3od
3.30 cd3od
3.30 cd3od
2.40
2.38
2.36
2.11
2.09
2.07
1.72
1.70
1.68
1.67
1.65
1.63
1.61
1.40
1.38
1.37
1.05
tBu
F
Si
tBu
O
N
H
H
N
OH
O
2-74
B (d)
7.54
A (d)
7.60
C (t)
2.38
D (t)
2.09
E (m)
1.67
F (s)
1.40
G (s)
1.05
1.95
2.12
1.93
1.85
4.45
4.15
18.00
f1 (ppm)

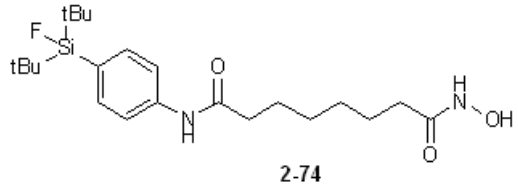
tBu
F
Si
tBu
O
N
H
H
N
OH
O

2-74

-189.82
6000
5500
5000
4500
4000
3500
3000
2500
2000
1500
1000
500
0
-500
10
0
-10
-20
-30
-40
-50
-60
-70
-80
-90
-100
-110
-120
-130
-140
-150
-160
-170
-180
-190
-200
f1 (ppm)

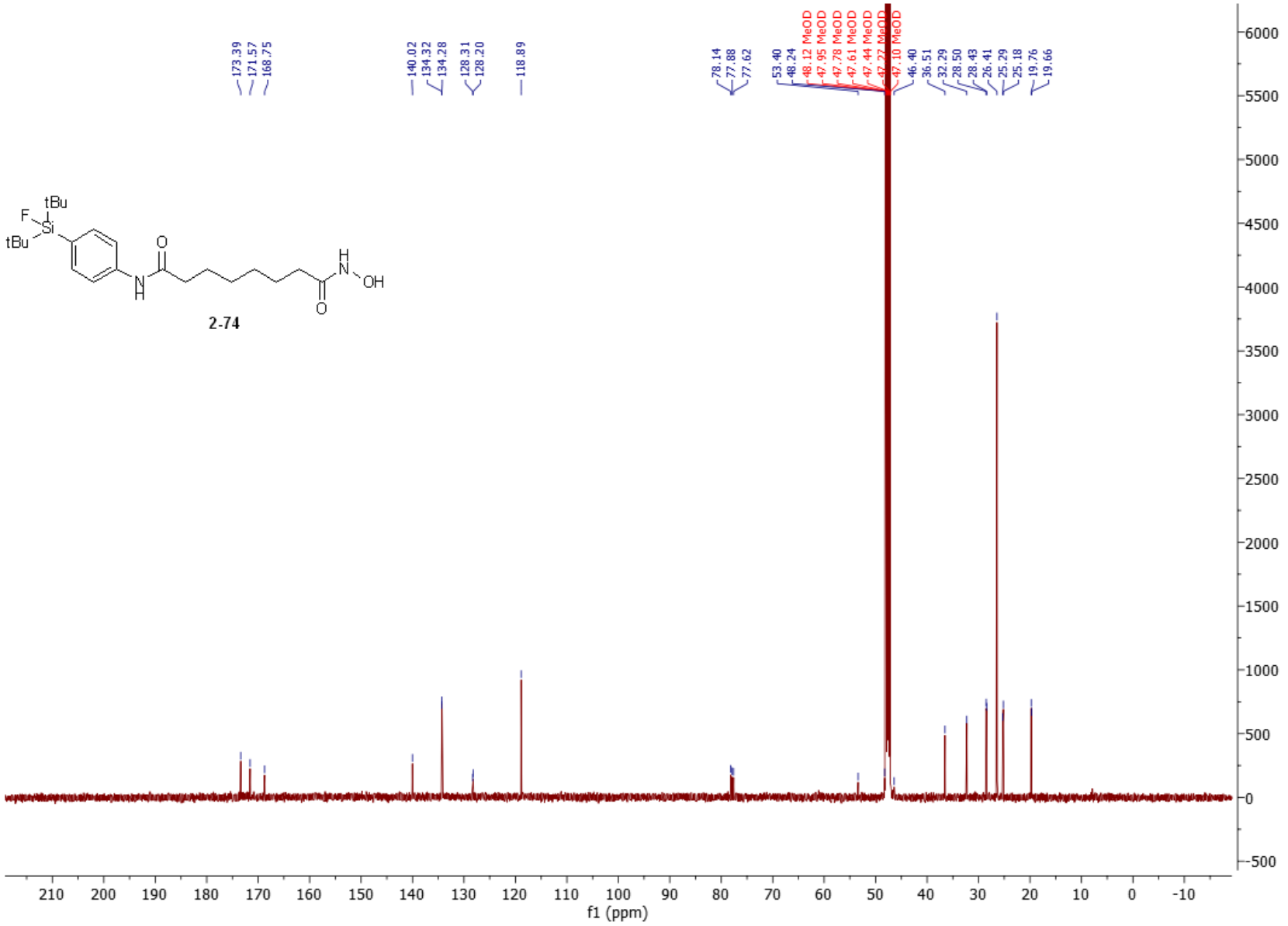
173.39
171.57
168.75
140.02
134.32
134.28
128.31
128.20
118.89
78.14
77.88
77.62
53.40
48.24
48.12 MeOD
47.95 MeOD
47.78 MeOD
47.61 MeOD
47.44 MeOD
47.27 MeOD
47.10 MeOD
46.40
36.51
32.29
28.50
28.43
26.41
25.29
25.18
19.76
19.66
tBu
F
Si
tBu
O
N
H
H
N
OH
O
2-74
f1 (ppm)

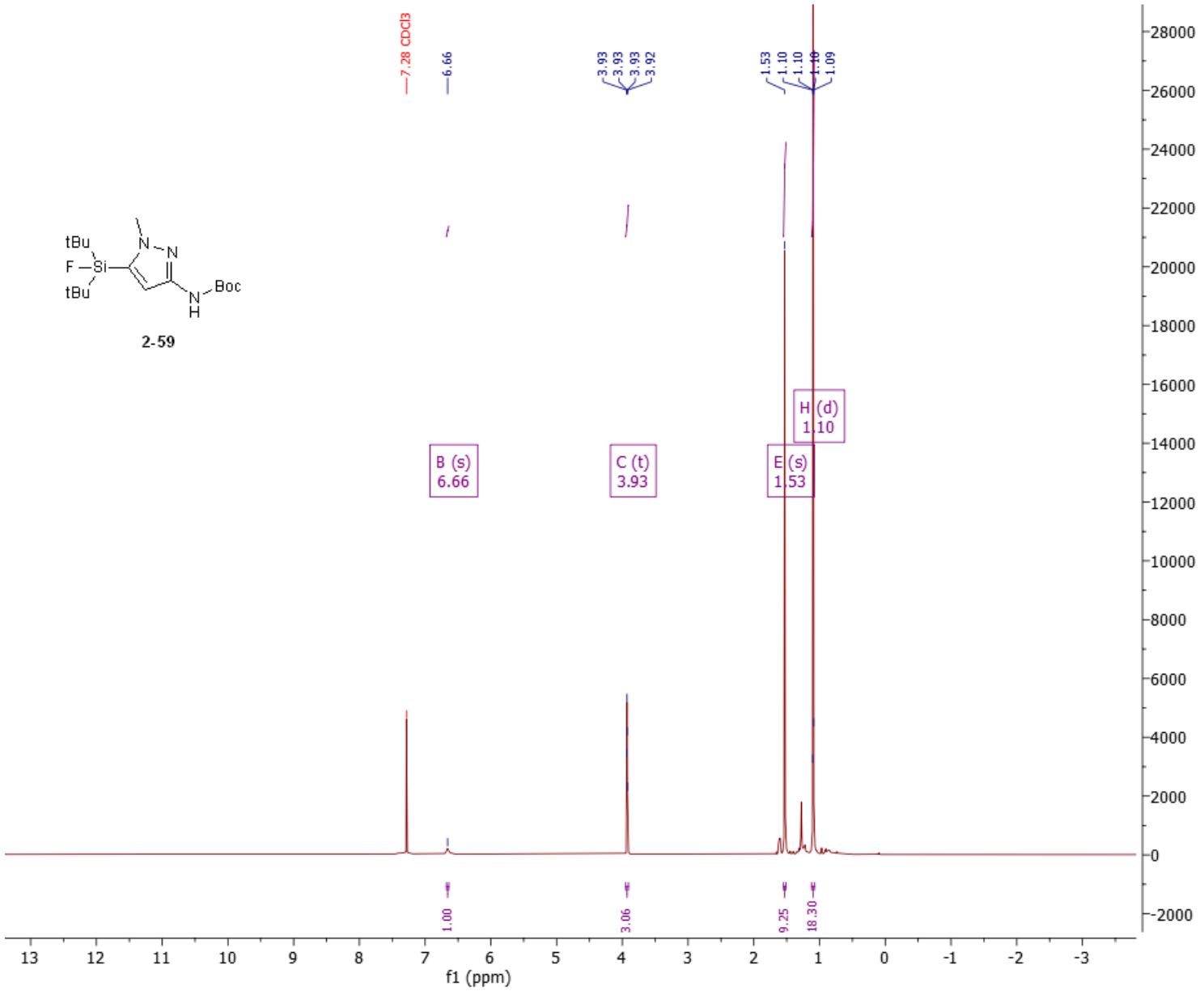
tBu
F
Si
tBu
N
N
N
H
Boc
2-59
7.28 CDCl3
6.66
3.93
3.93
3.93
3.92
1.53
1.10
1.10
1.10
1.09
B (s)
6.66
C (t)
3.93
E (s)
1.53
H (d)
1.10
1.00
3.06
9.25
18.30
f1 (ppm)

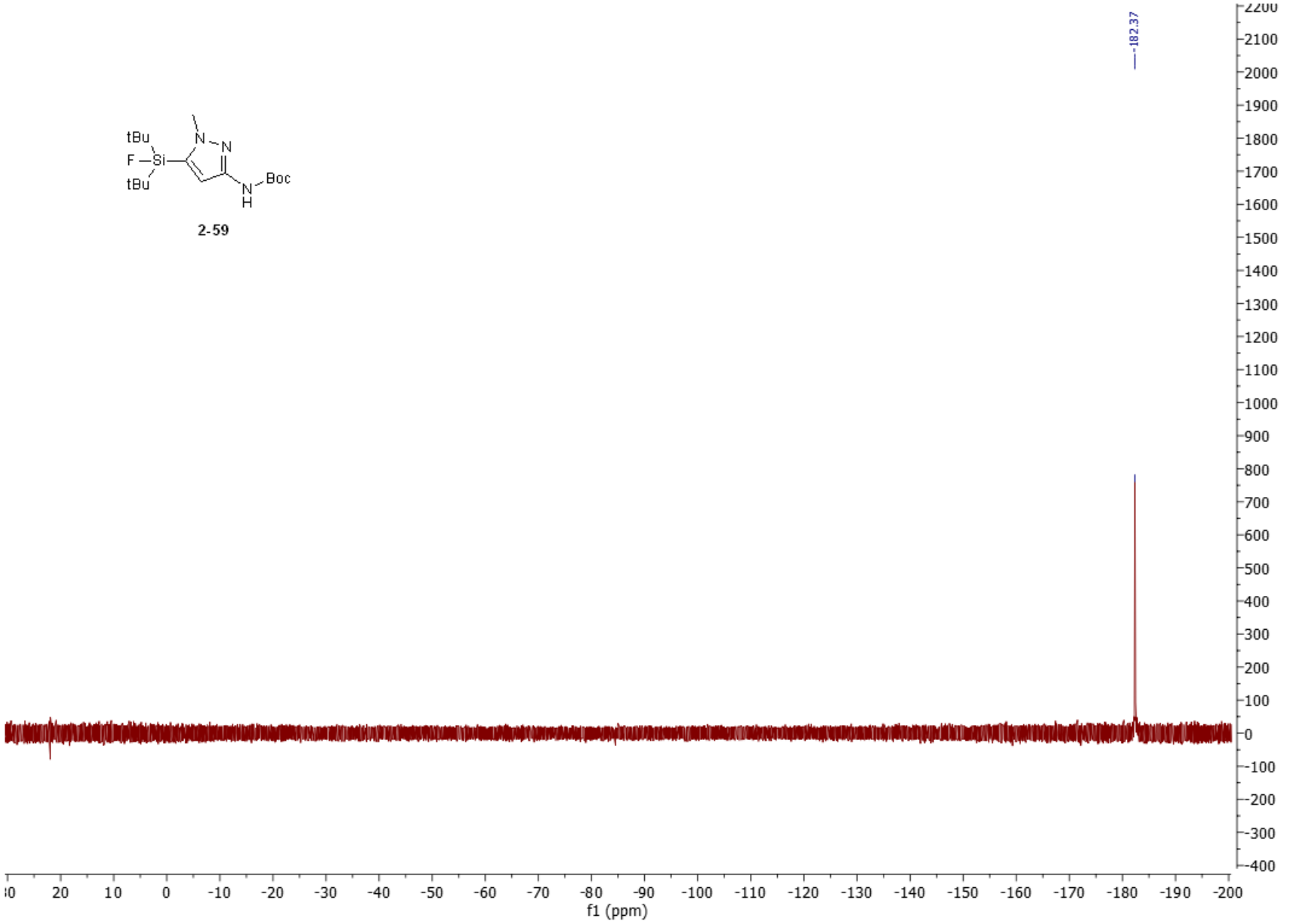
tBu
F
Si
tBu
N
N
N
H
Boc
2-59
-182.37
f1 (ppm)

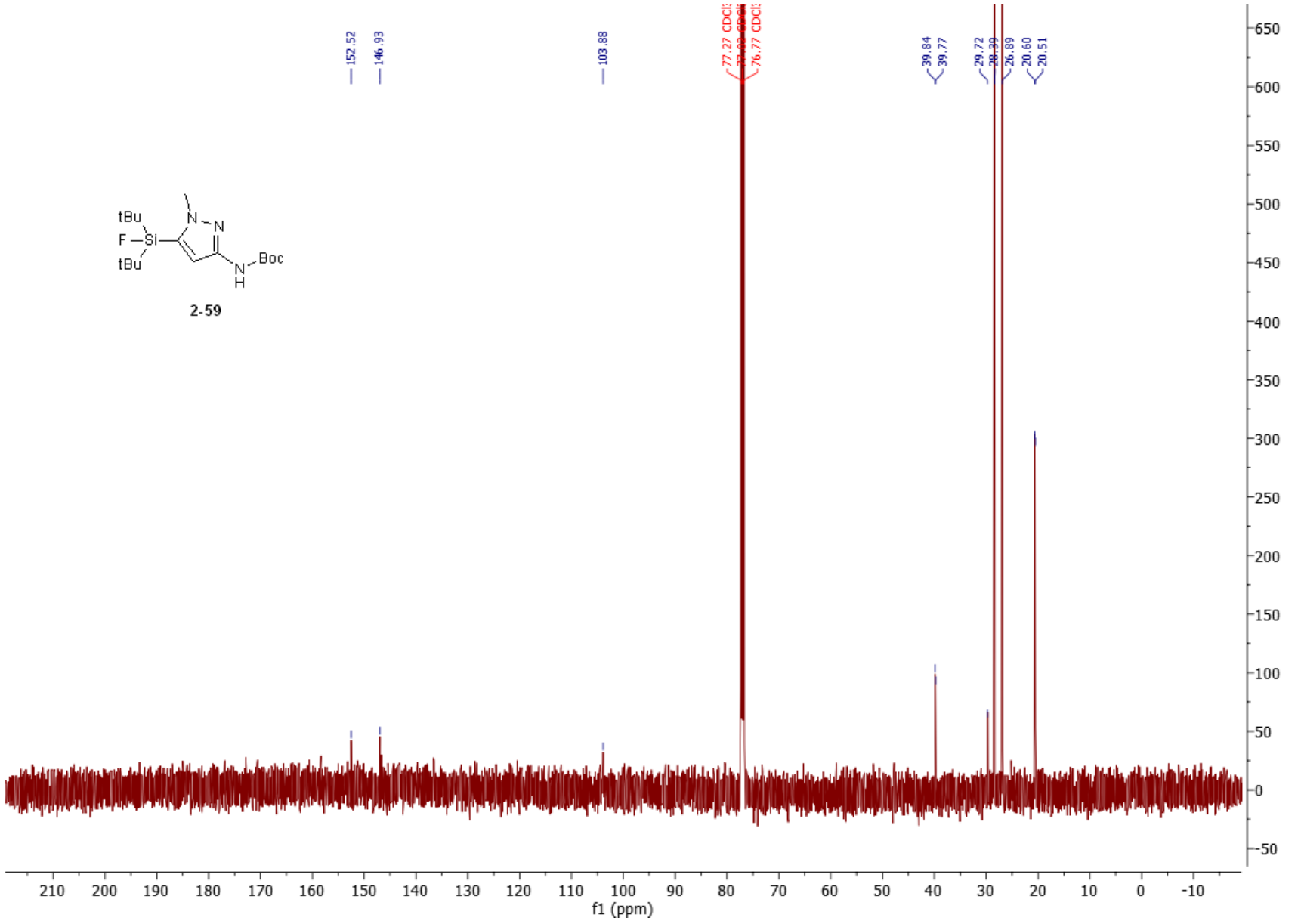
152.52
146.93
103.88
77.27 CDCl3
76.77 CDCl3
39.84
39.77
29.72
26.89
20.60
20.51
tBu
F
Si
tBu
N
N
N
H
Boc
2-59
f1 (ppm)

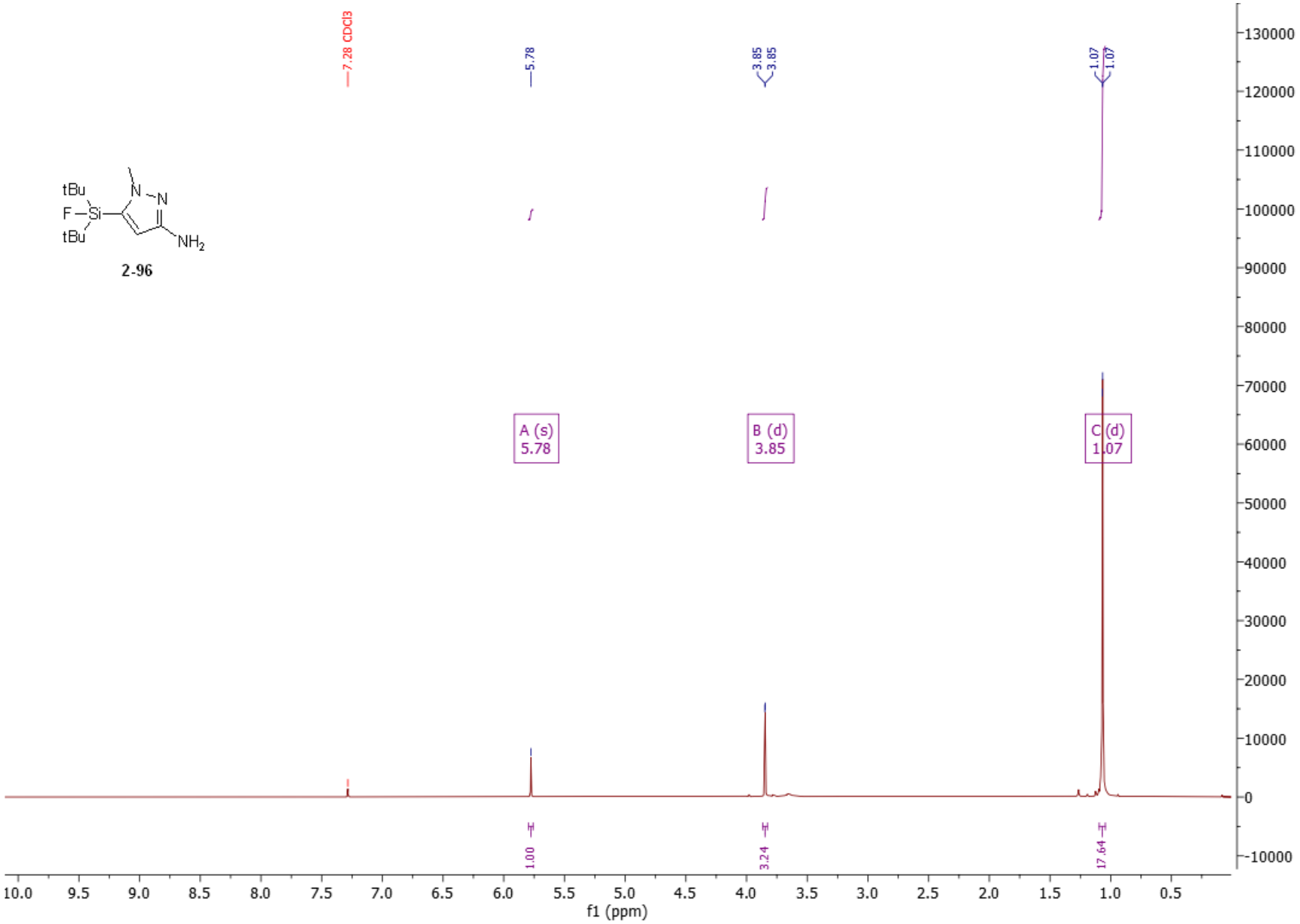
7.28 CDCl3
5.78
3.85
3.85
1.07
1.07
tBu
F
Si
tBu
N
N
NH2
2-96
A (s)
5.78
B (d)
3.85
C (d)
1.07
1.00
3.24
17.64
f1 (ppm)

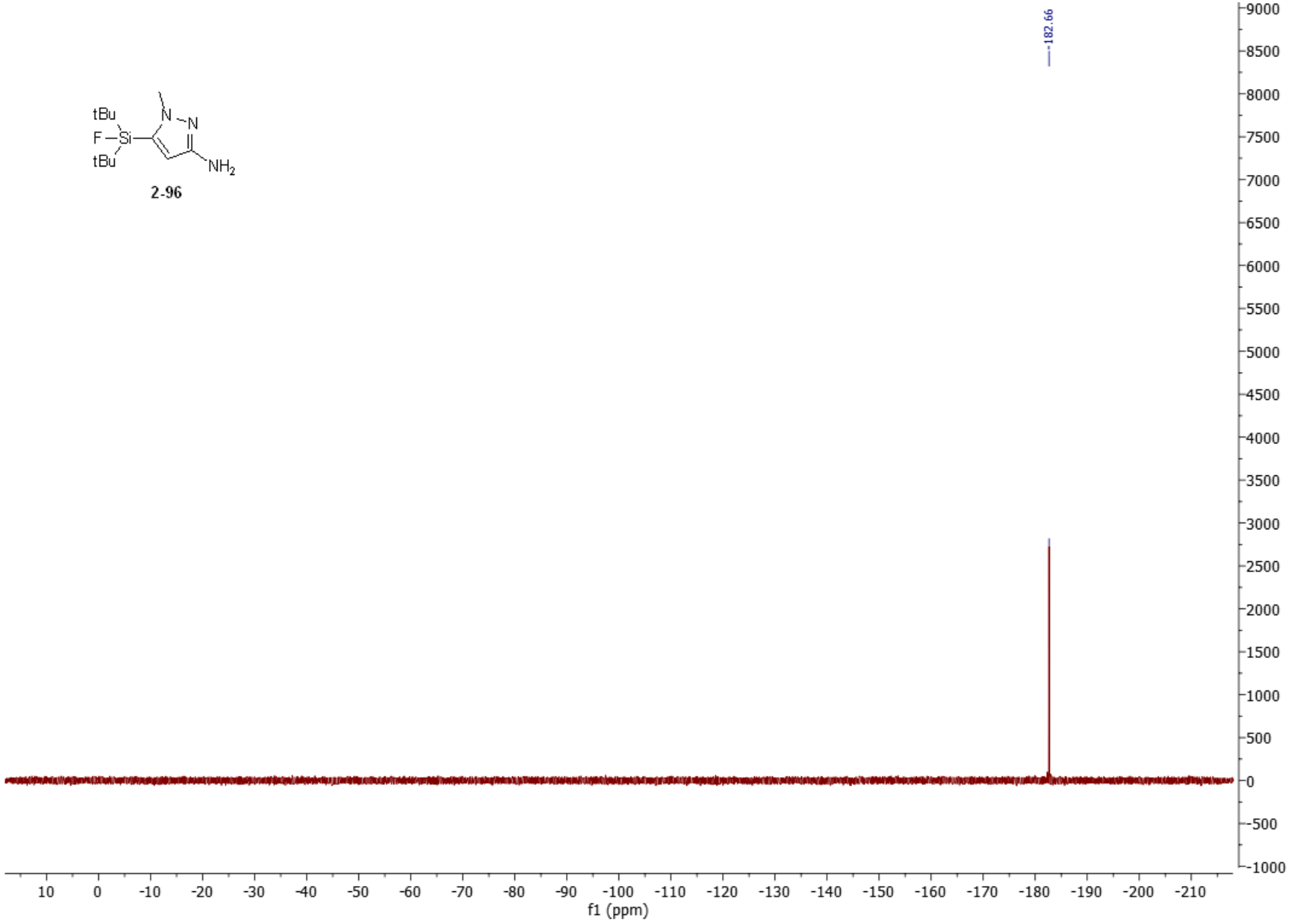
tBu
F
Si
tBu
N
N
NH2
2-96
-182.66
9000
8500
8000
7500
7000
6500
6000
5500
5000
4500
4000
3500
3000
2500
2000
1500
1000
500
0
-500
-1000
10
0
-10
-20
-30
-40
-50
-60
-70
-80
-90
-100
-110
-120
-130
-140
-150
-160
-170
-180
-190
-200
-210
f1 (ppm)

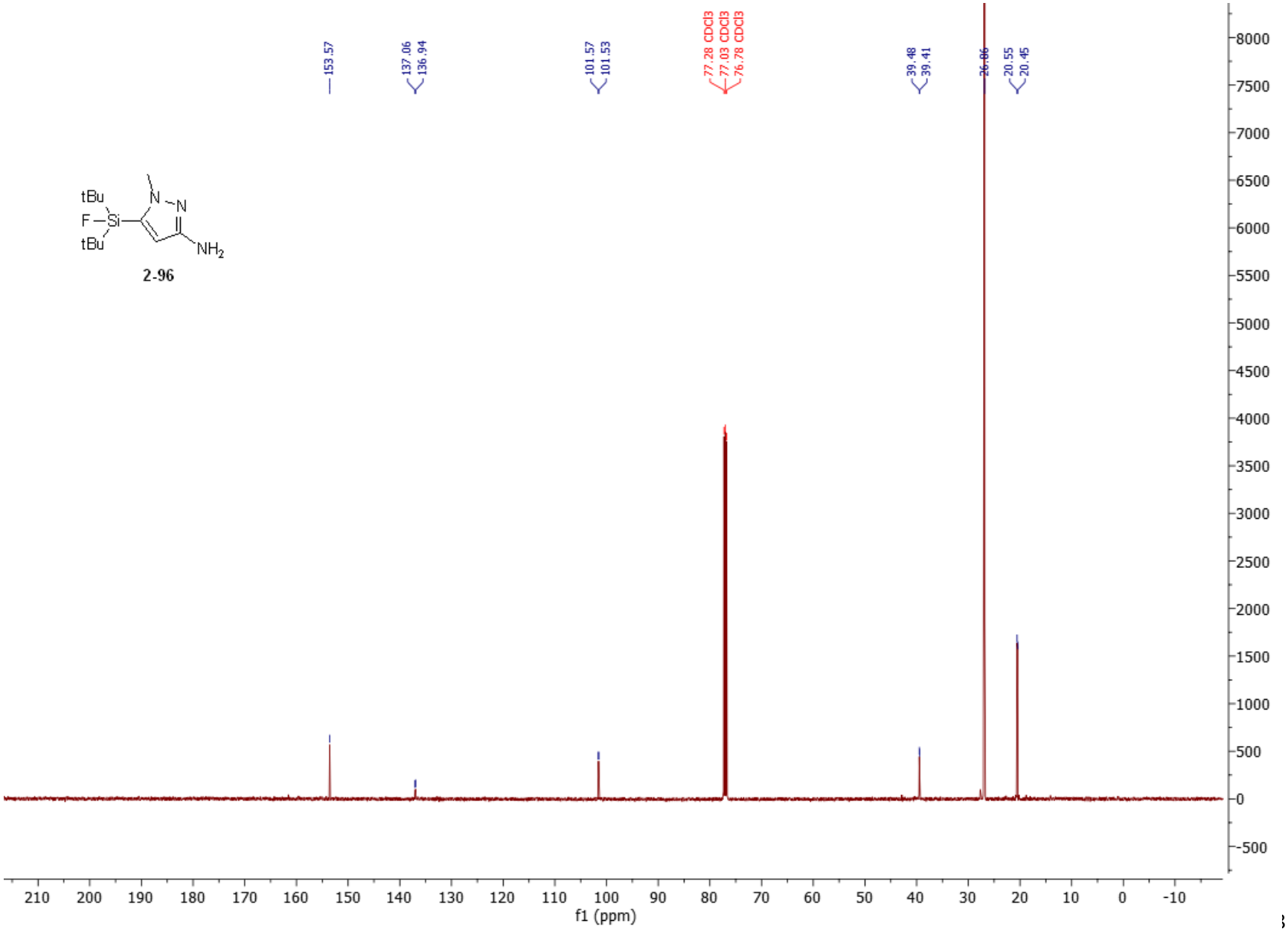
153.57
137.06
136.94
101.57
101.53
77.28 CDCl3
77.03 CDCl3
76.78 CDCl3
39.48
39.41
26.86
20.55
20.45
tBu
F
Si
tBu
N
N
NH2
2-96
f1 (ppm)

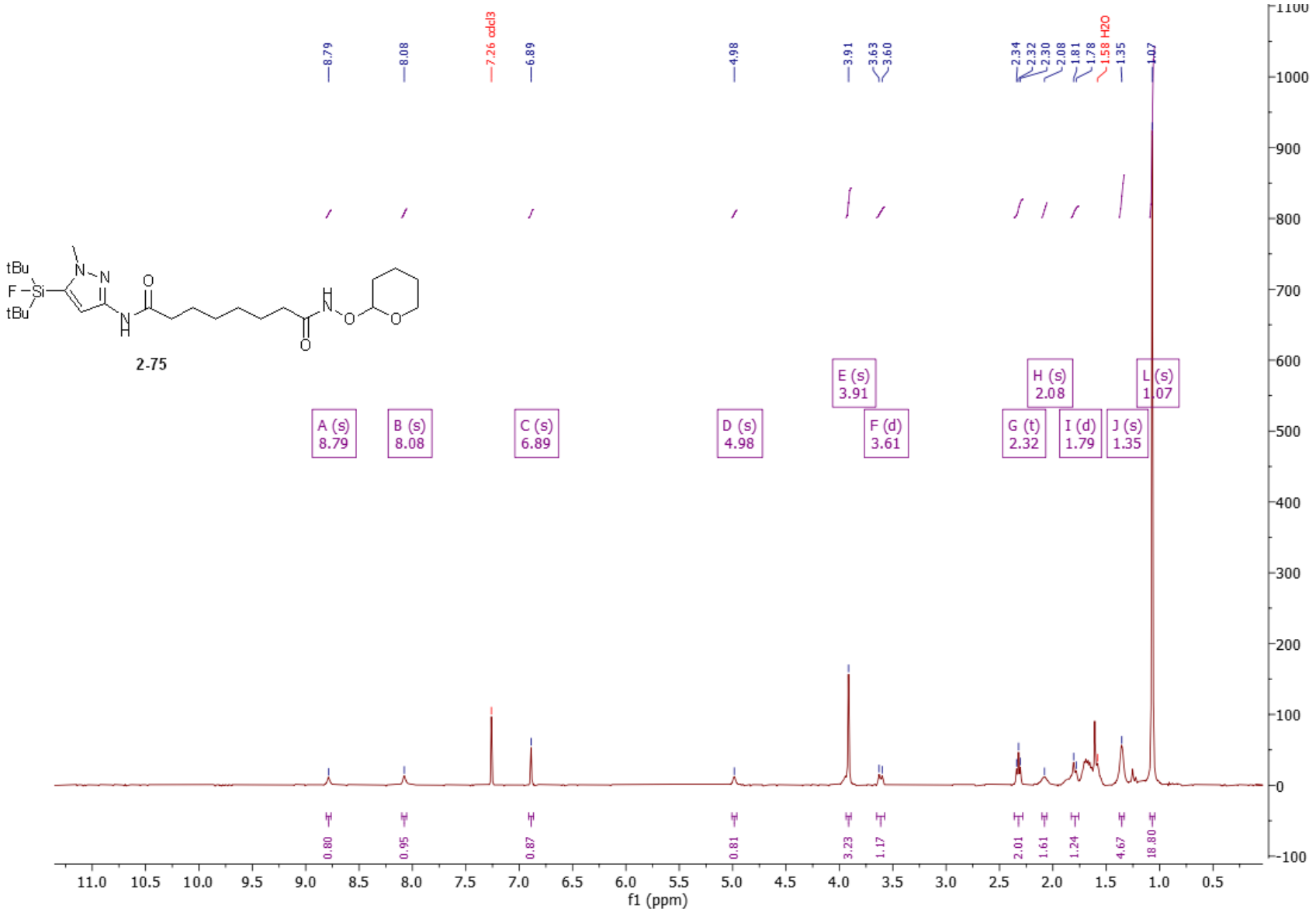
8.79
8.08
7.26 cdcl3
6.89
4.98
3.91
3.63
3.60
2.34
2.32
2.30
2.08
1.81
1.78
1.58 H2O
1.35
1.07
tBu
F
Si
tBu
N
N
O
N
H
O
N
H
O
O
2-75
A (s) 8.79
B (s) 8.08
C (s) 6.89
D (s) 4.98
E (s) 3.91
F (d) 3.61
G (t) 2.32
H (s) 2.08
I (d) 1.79
J (s) 1.35
L (s) 1.07
0.80
0.95
0.87
0.81
3.23
1.17
2.01
1.61
1.24
4.67
18.80
f1 (ppm)

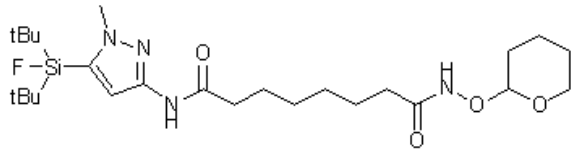
tBu
F
Si
tBu
N
N
O
H
N
O
O
O

2-75

182.40
2100
2000
1900
1800
1700
1600
1500
1400
1300
1200
1100
1000
900
800
700
600
500
400
300
200
100
0
-100
-200
-300
-400
10
0
-10
-20
-30
-40
-50
-60
-70
-80
-90
-100
-110
-120
-130
-140
-150
-160
-170
-180
-190
-200
-210
f1 (ppm)

)

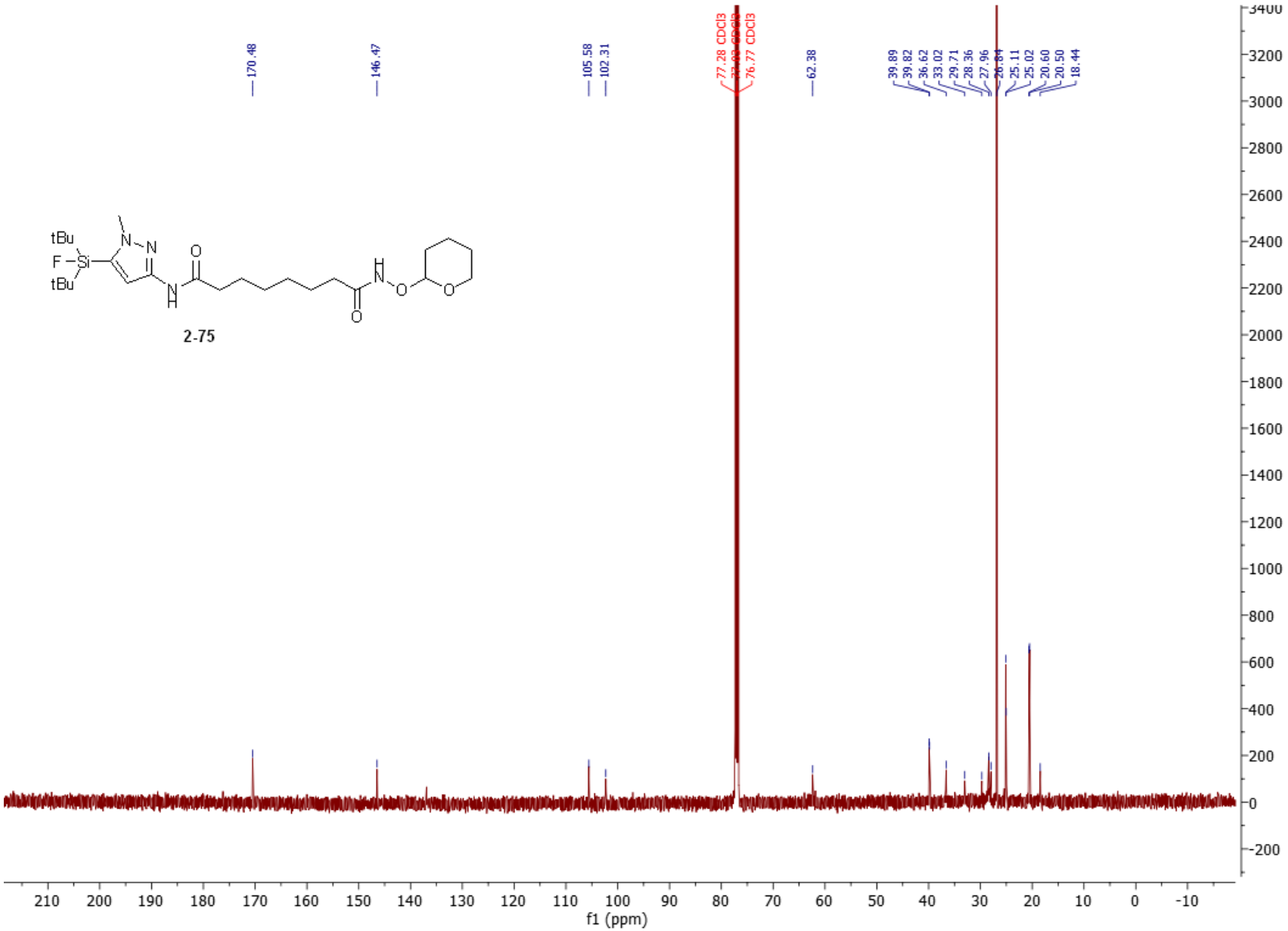
170.48
146.47
105.58
102.31
77.28 CDCl3
76.77 CDCl3
62.38
39.89
39.82
36.62
33.02
29.71
28.36
27.96
26.84
25.11
25.02
20.60
20.50
18.44
tBu
F
Si
tBu
N
N
H
O
O
O
O
2-75
f1 (ppm)

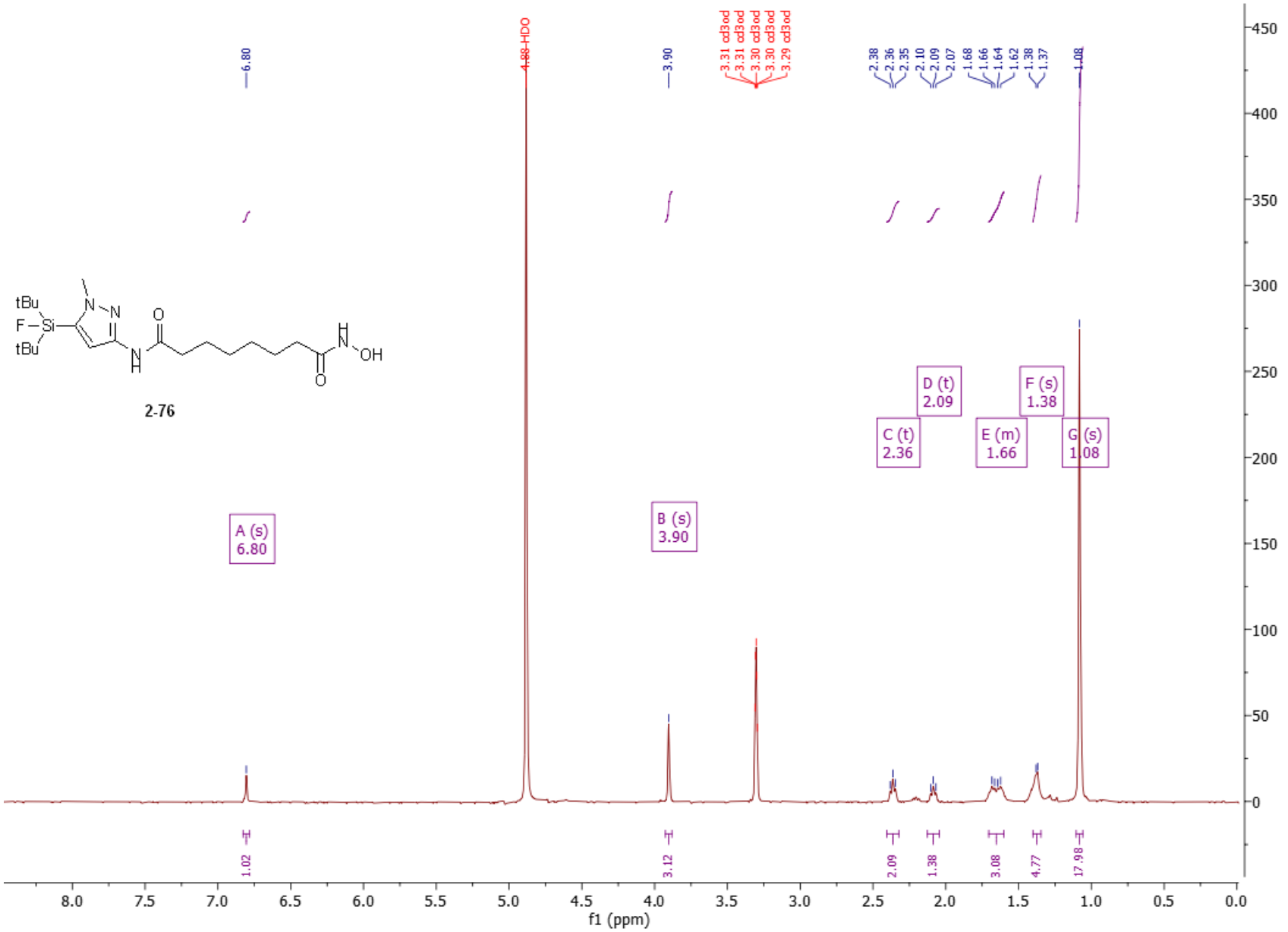
2-76
A (s)
6.80
B (s)
3.90
C (t)
2.36
D (t)
2.09
E (m)
1.66
F (s)
1.38
G (s)
1.08
f1 (ppm)

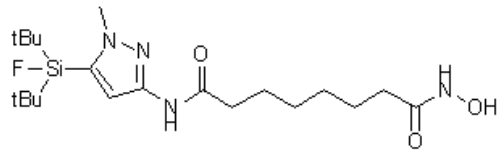
tBu
F
Si
tBu
N
N
O
N
H
H
N
OH
O

2-76

450
400
350
300
250
200
150
100
50
0
10
0
-10
-20
-30
-40
-50
-60
-70
-80
-90
-100
-110
-120
-130
-140
-150
-160
-170
-180
-190
-200
f1 (ppm)

3

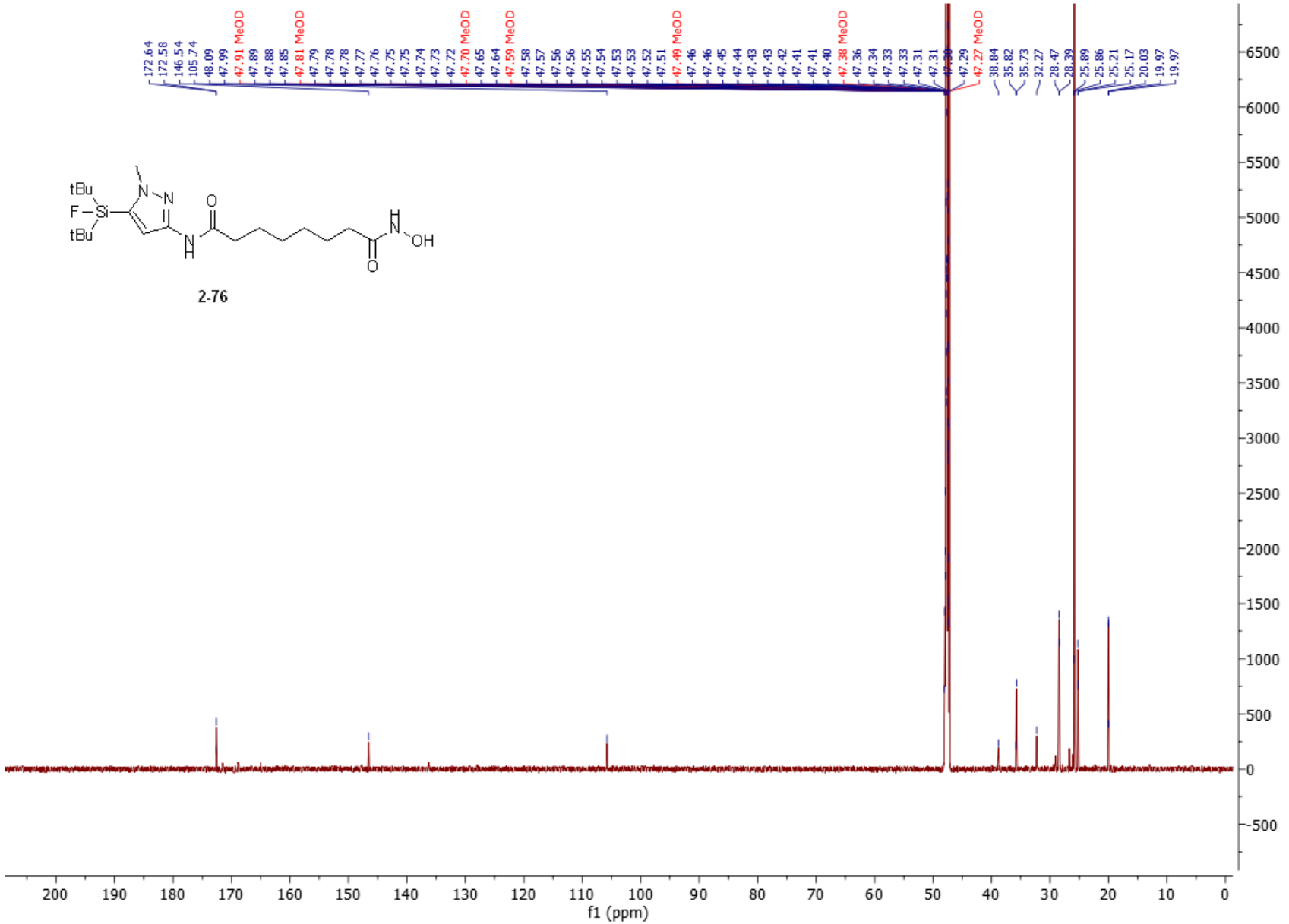
172.64
172.58
146.54
105.74
48.09
47.99
47.91 MeOD
47.89
47.88
47.85
47.81 MeOD
47.79
47.78
47.78
47.77
47.76
47.75
47.75
47.74
47.73
47.72
47.70 MeOD
47.65
47.64
47.59 MeOD
47.58
47.57
47.56
47.56
47.55
47.54
47.53
47.53
47.52
47.51
47.49 MeOD
47.46
47.46
47.45
47.44
47.43
47.43
47.42
47.41
47.41
47.40
47.38 MeOD
47.36
47.34
47.33
47.33
47.31
47.31
47.30
47.29
47.27 MeOD
38.84
35.82
35.73
32.27
28.47
28.39
25.89
25.86
25.21
25.17
20.03
19.97
19.97
tBu
F
Si
tBu
N
N
O
N
H
O
N
OH
6500
6000
5500
5000
4500
4000
3500
3000
2500
2000
1500
1000
500
0
-500
200
190
180
170
160
150
140
130
120
110
100
90
80
70
60
50
40
30
20
10
0
f1 (ppm)

2-76

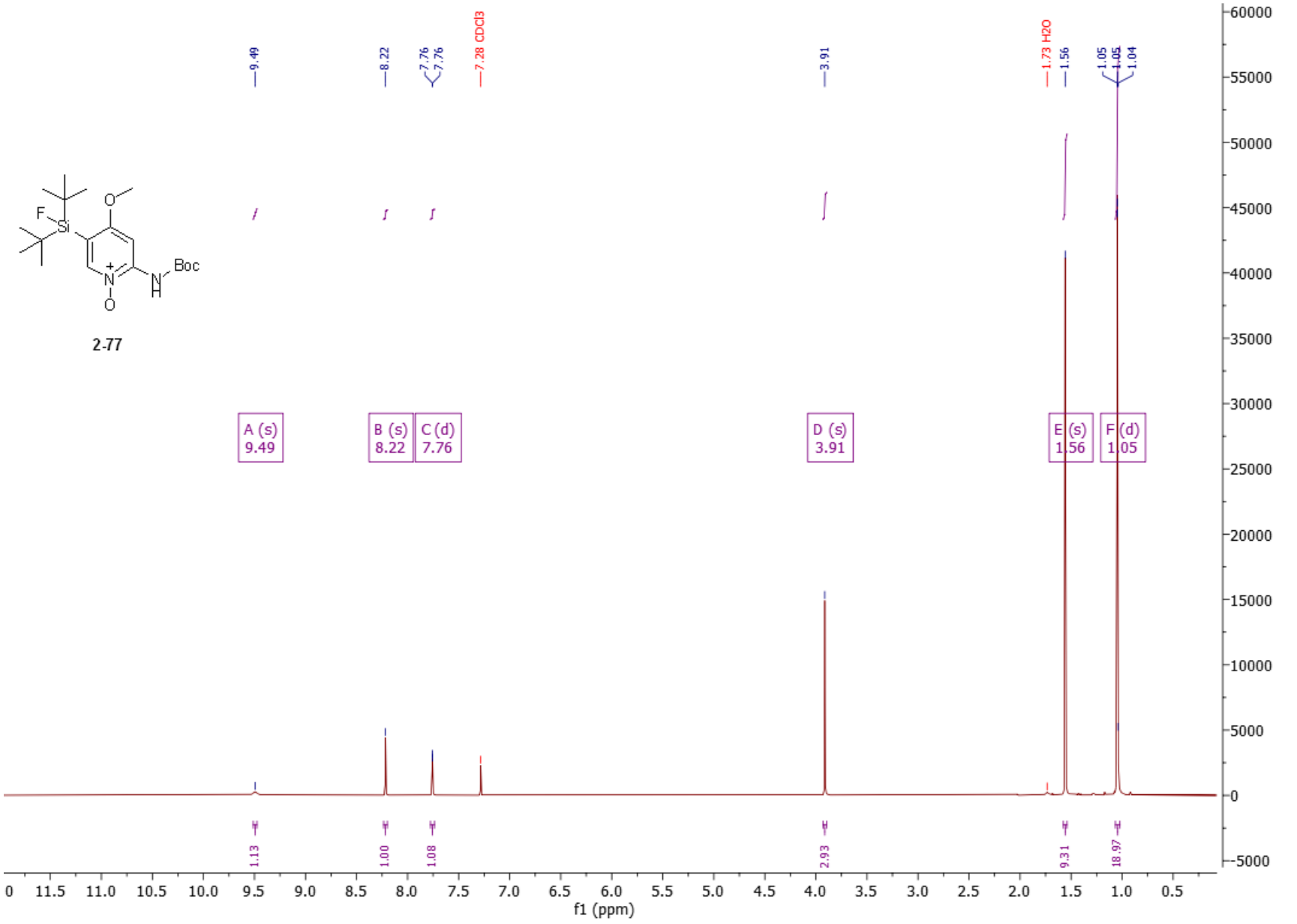
9.49
8.22
7.76
7.76
7.28 CDCl3
3.91
1.73 H2O
1.56
1.05
1.05
1.04
A (s) 9.49
B (s) 8.22
C (d) 7.76
D (s) 3.91
E (s) 1.56
F (d) 1.05
1.13
1.00
1.08
2.93
9.31
18.97
f1 (ppm)
F
Si
O
N
O
Boc
N
H

2-77

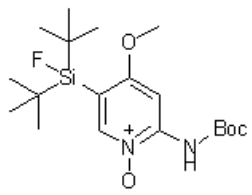
F
Si
O
Boc
N
H
N
O

2-77

185.72
500
450
400
350
300
250
200
150
100
50
0
-50
-100
-150
-200
10
0
-10
-20
-30
-40
-50
-60
-70
-80
-90
-100
-110
-120
-130
-140
-150
-160
-170
-180
-190
-200
-210
f1 (ppm)

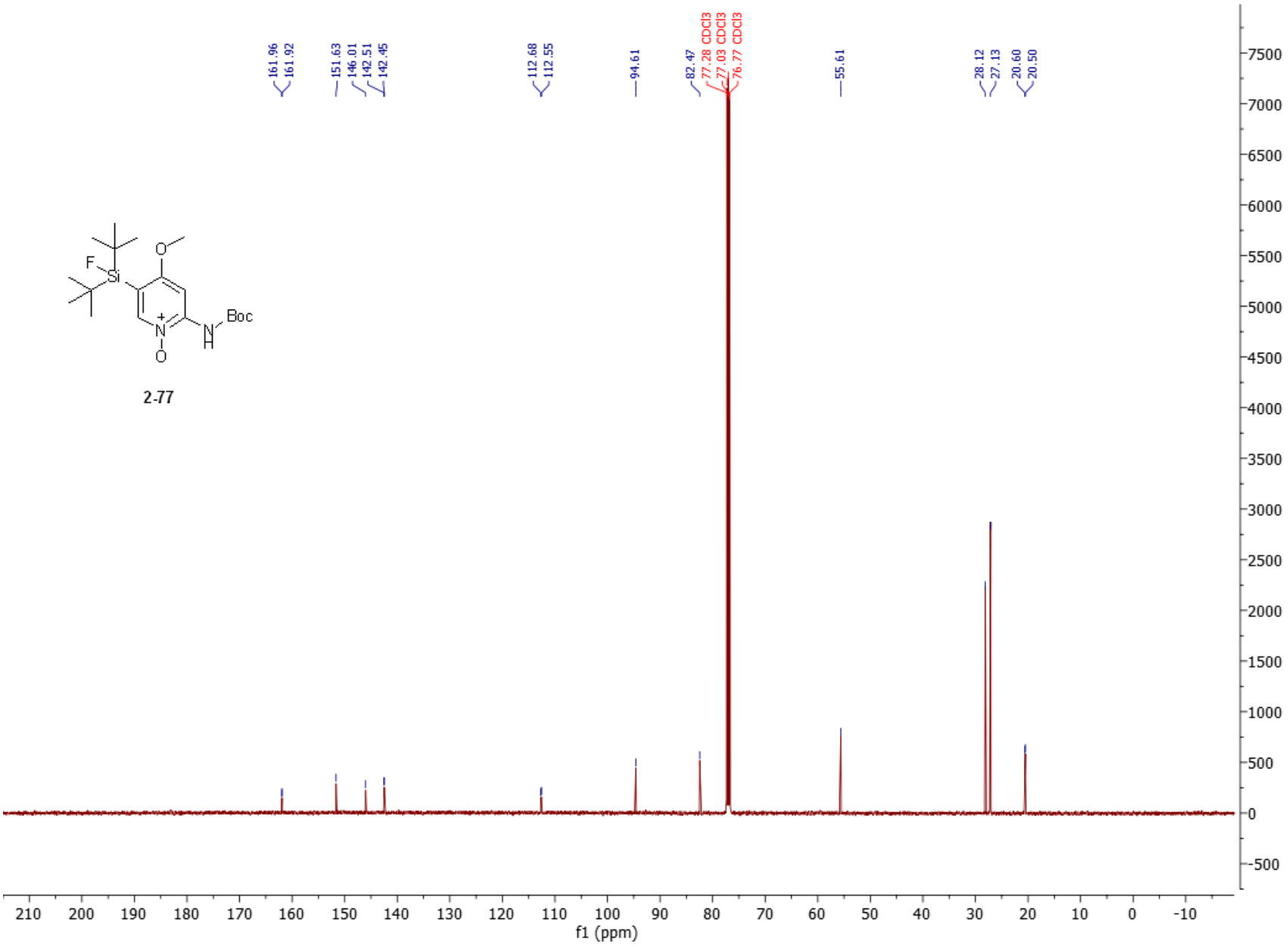
161.96
161.92
151.63
146.01
142.51
142.45
112.68
112.55
94.61
82.47
77.28 CDCl3
77.03 CDCl3
76.77 CDCl3
55.61
28.12
27.13
20.60
20.50
F
Si
O
N
+
O
N
H
Boc
2-77
f1 (ppm)

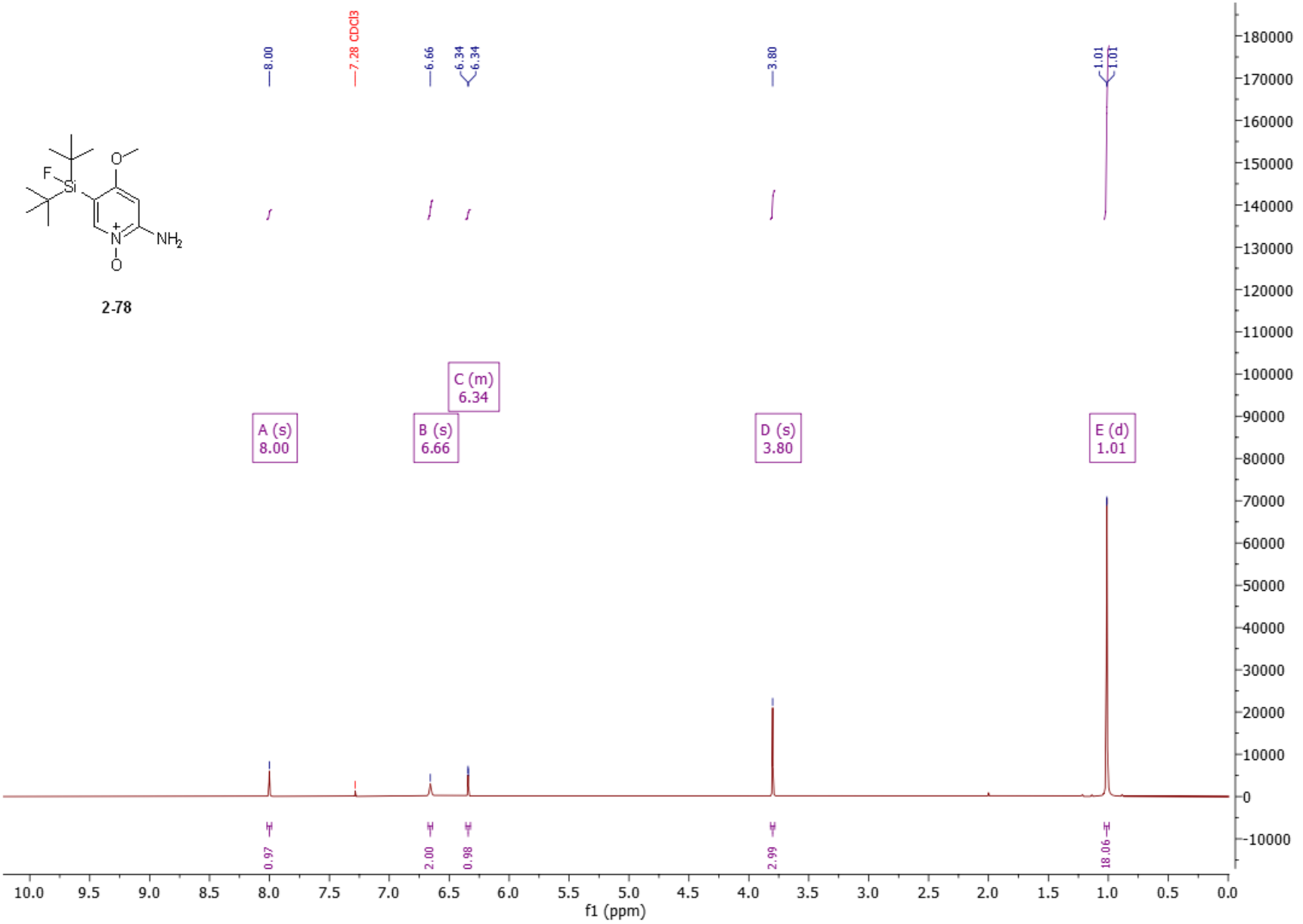
8.00
7.28 CDCl3
6.66
6.34
6.34
3.80
1.01
1.01
F
Si
O
N
+
O
NH2
2-78
A (s)
8.00
B (s)
6.66
C (m)
6.34
D (s)
3.80
E (d)
1.01
0.97
2.00
0.98
2.99
18.06
f1 (ppm)

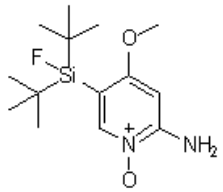
F
Si
O
N
+
O
NH2

2-78

-75.15
-185.85
8000
7500
7000
6500
6000
5500
5000
4500
4000
3500
3000
2500
2000
1500
1000
500
0
-500
10
0
-10
-20
-30
-40
-50
-60
-70
-80
-90
-100
-110
-120
-130
-140
-150
-160
-170
-180
-190
-200
-210
f1 (ppm)

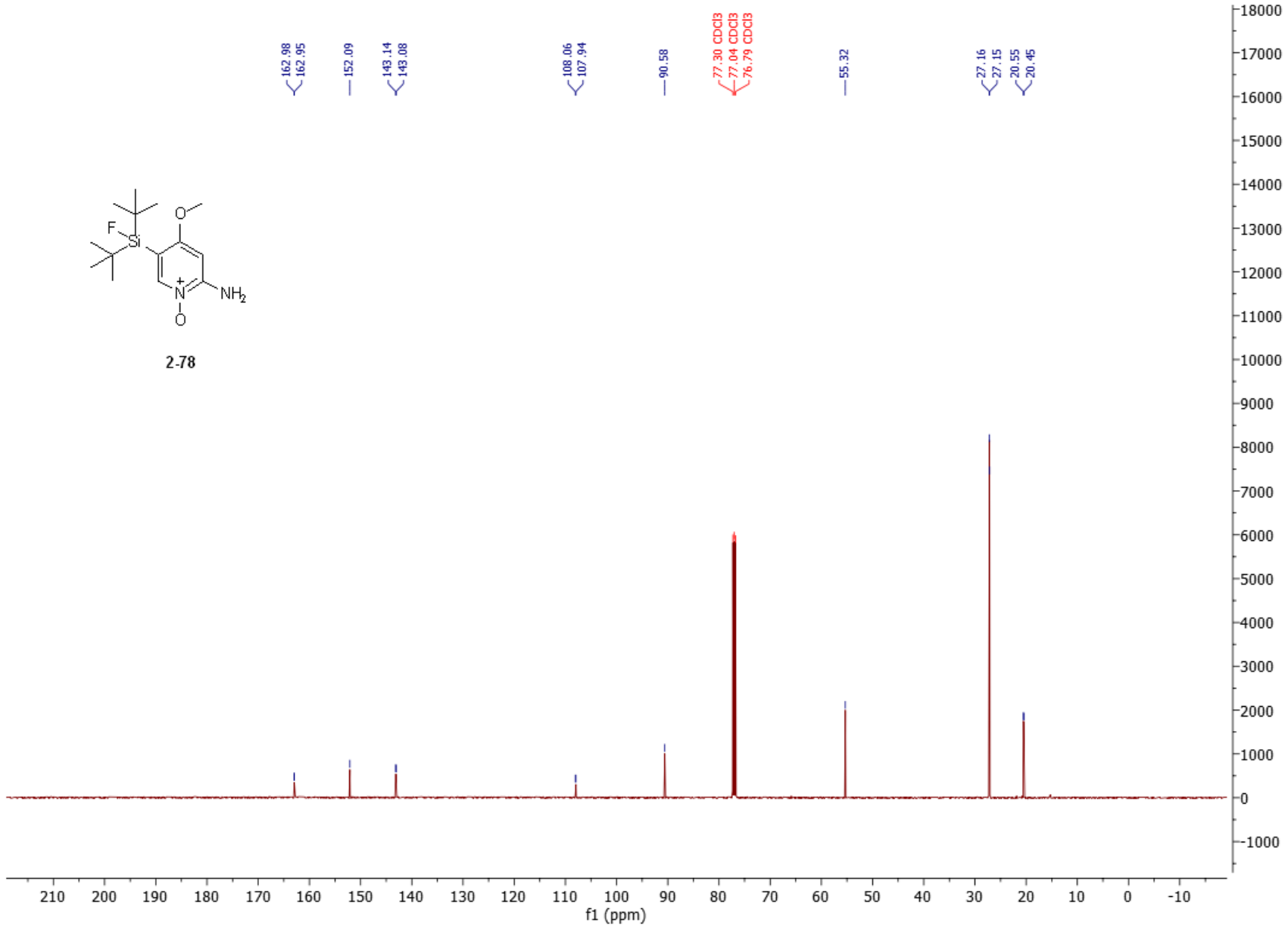
162.98
162.95
152.09
143.14
143.08
108.06
107.94
90.58
77.30 CDCl3
77.04 CDCl3
76.79 CDCl3
55.32
27.16
27.15
20.55
20.45
F
Si
O
N
O
NH2
f1 (ppm)

2-78

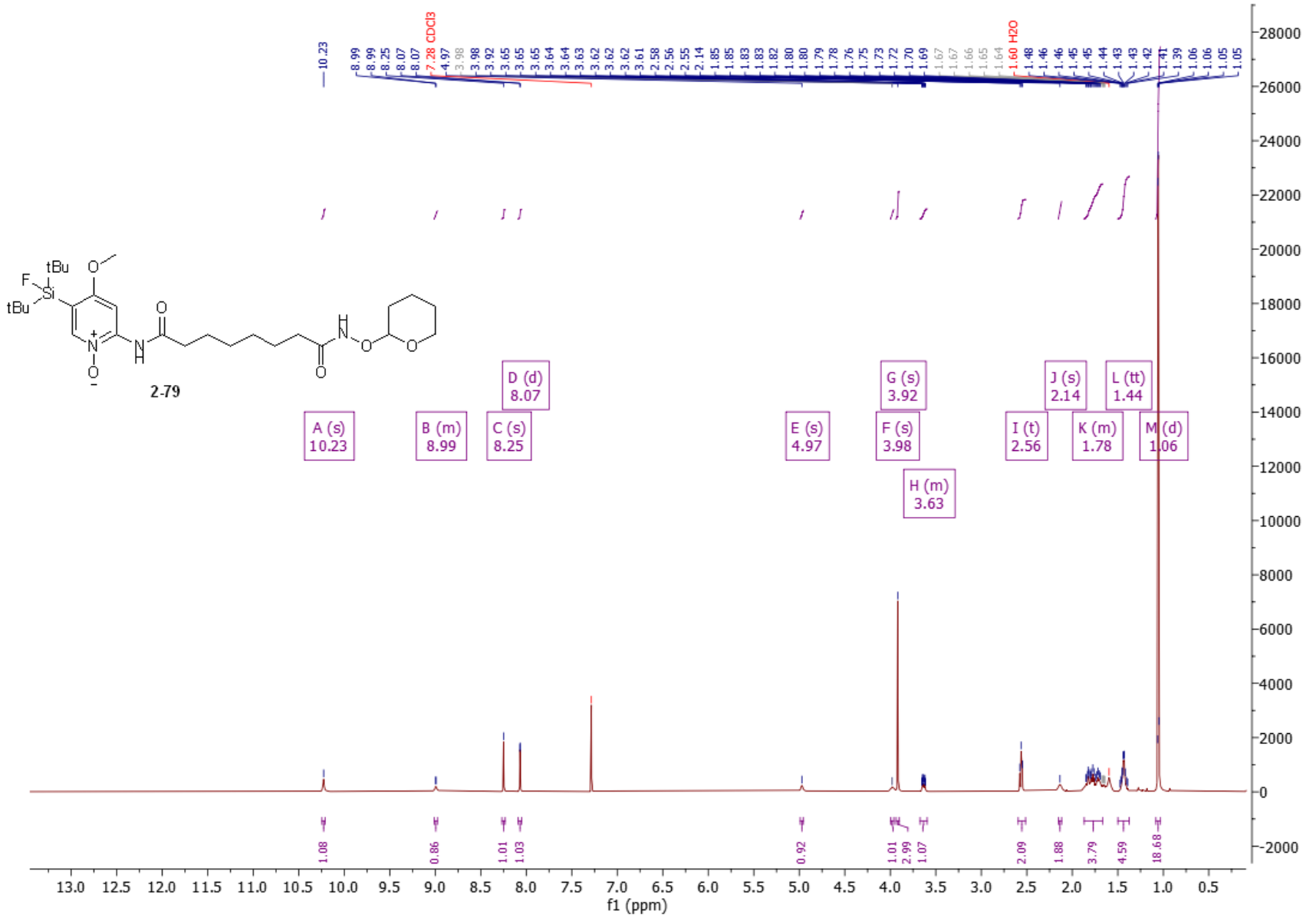
2-79
A (s) 10.23
B (m) 8.99
C (s) 8.25
D (d) 8.07
E (s) 4.97
F (s) 3.98
G (s) 3.92
H (m) 3.63
I (t) 2.56
J (s) 2.14
K (m) 1.78
L (tt) 1.44
M (d) 1.06
CDCl3
H2O
f1 (ppm)

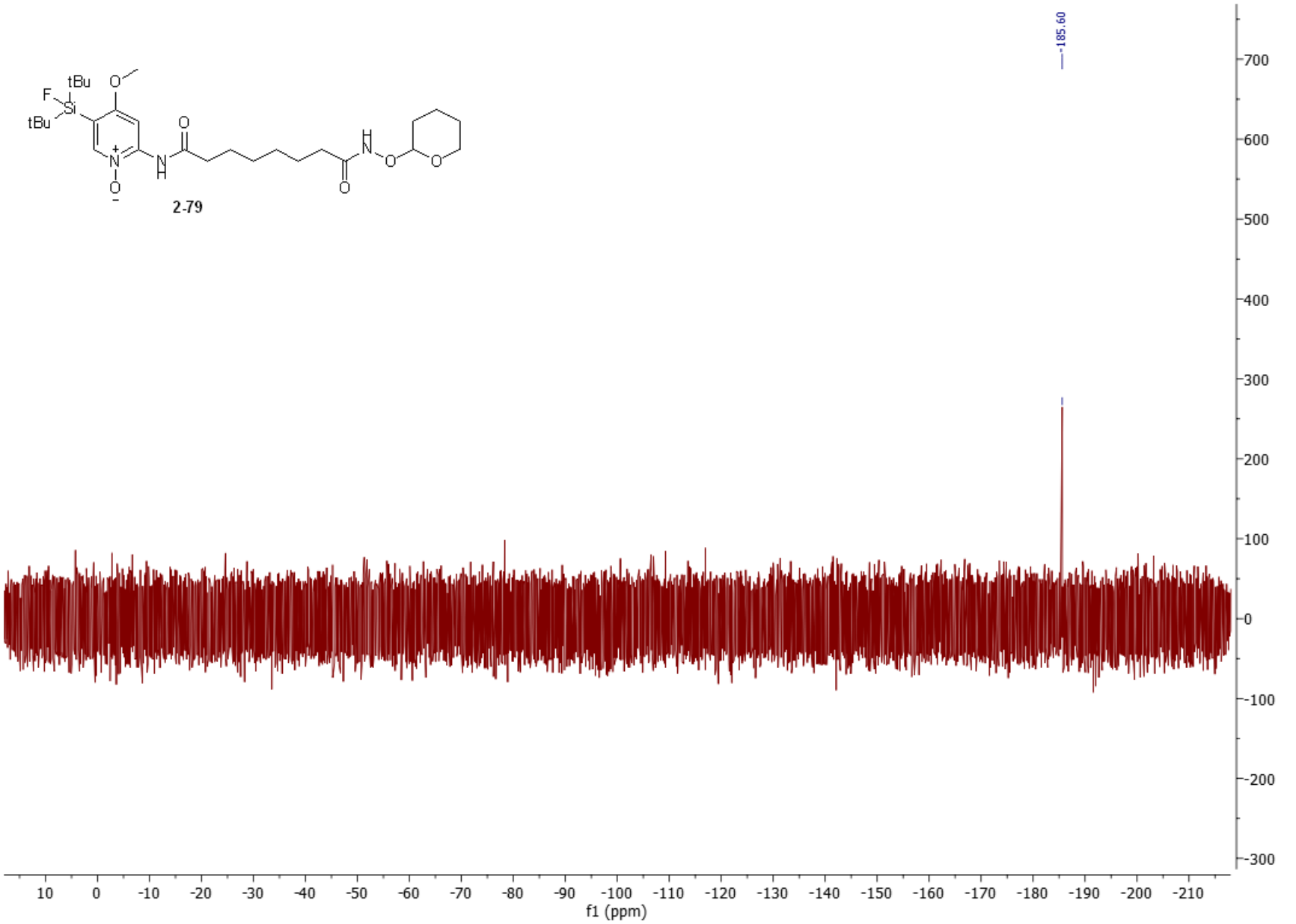
tBu
O
F
Si
tBu
O
N
H
N
O
O
O
O
2-79
-185.60
700
600
500
400
300
200
100
0
-100
-200
-300
10
0
-10
-20
-30
-40
-50
-60
-70
-80
-90
-100
-110
-120
-130
-140
-150
-160
-170
-180
-190
-200
-210
f1 (ppm)

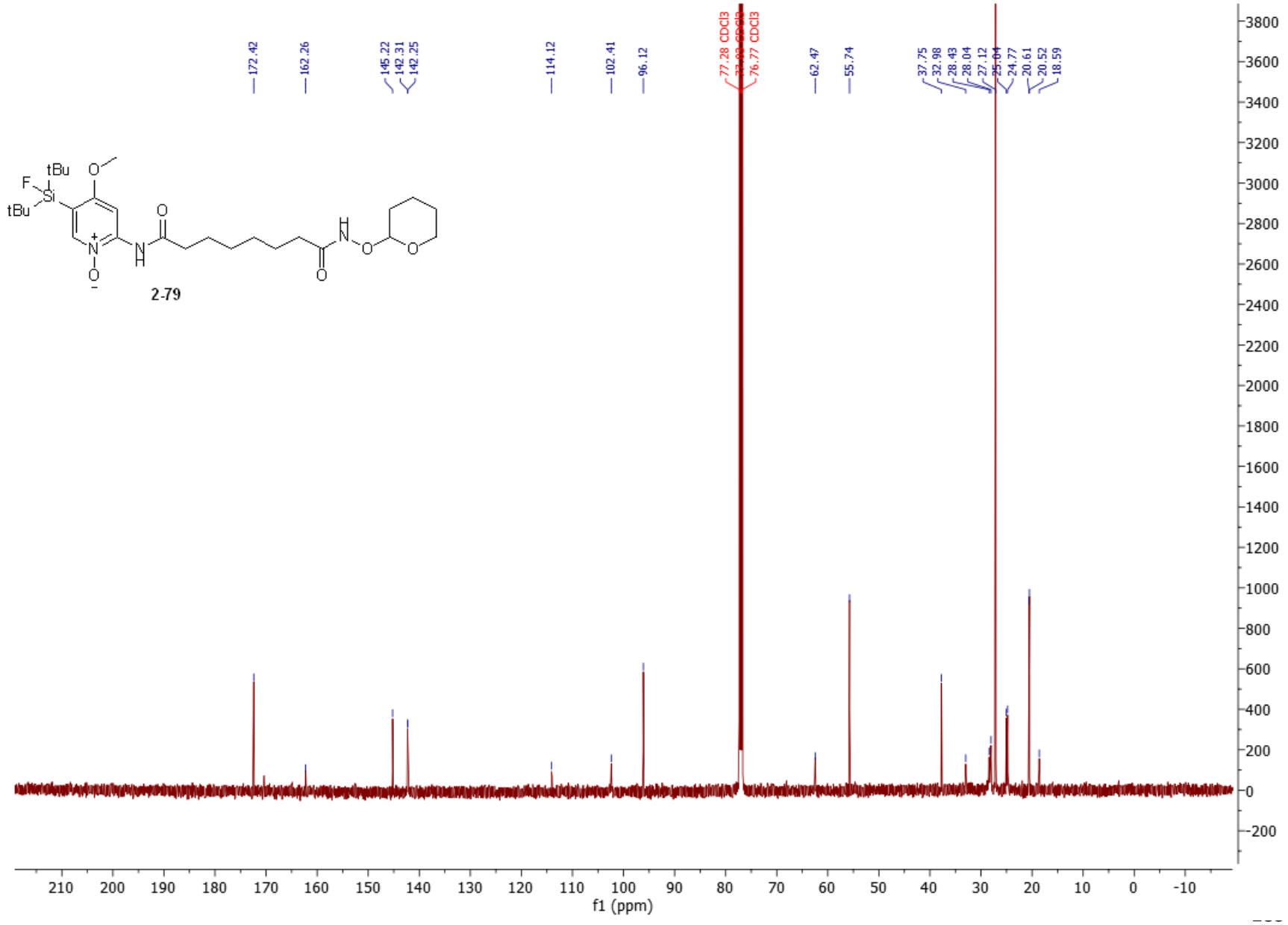
172.42
162.26
145.22
142.31
142.25
114.12
102.41
96.12
77.28 CDCl3
76.77 CDCl3
62.47
55.74
37.75
32.98
28.43
28.04
27.12
25.04
24.77
20.61
20.52
18.59
tBu
tBu
F
Si
O
O
N
H
N
O
O
O
O
2-79
f1 (ppm)

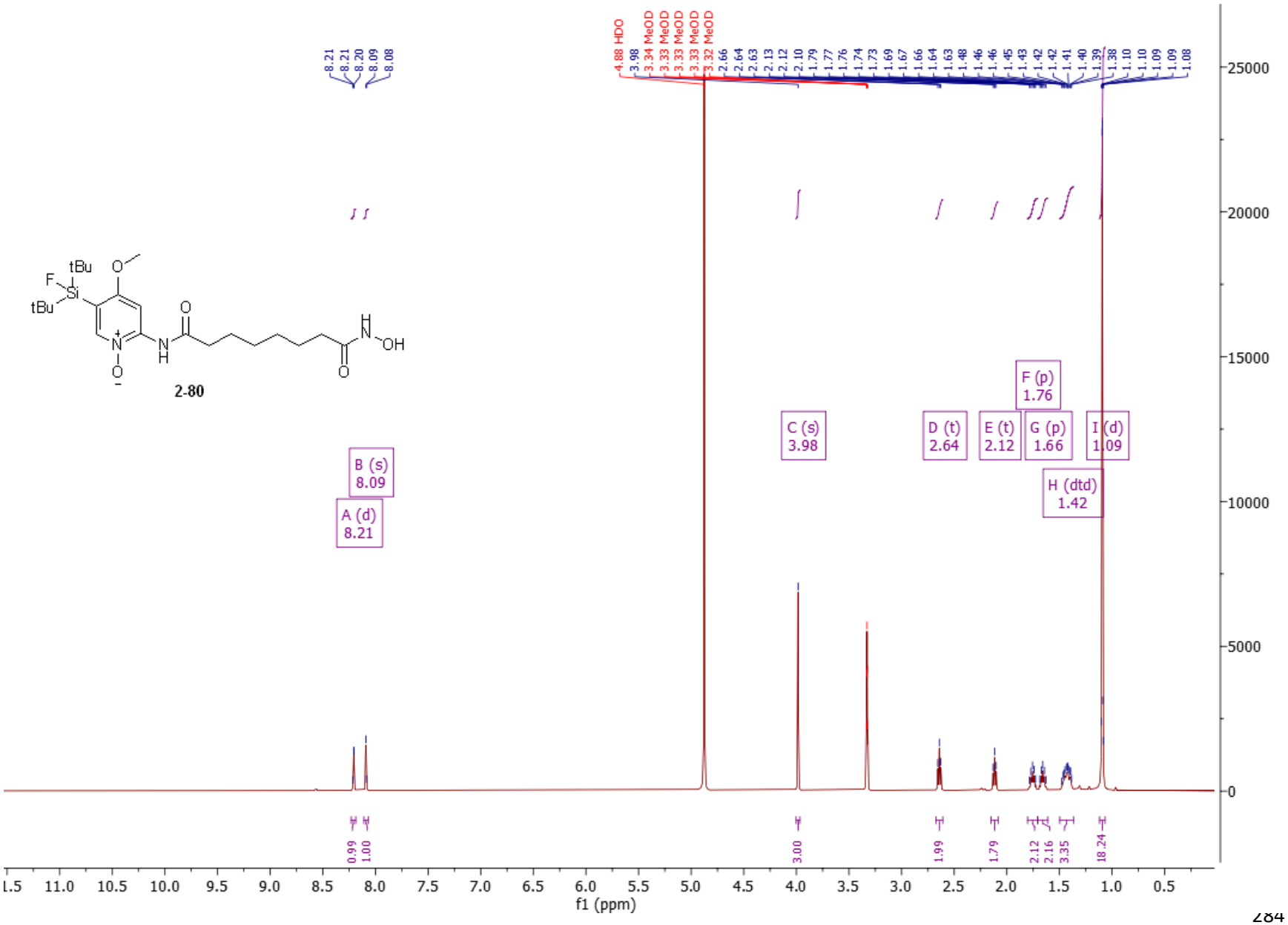
2-80
A (d) 8.21
B (s) 8.09
C (s) 3.98
D (t) 2.64
E (t) 2.12
F (p) 1.76
G (p) 1.66
H (dtd) 1.42
I (d) 1.09
f1 (ppm)

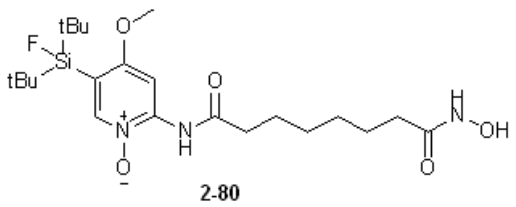
tBu
O
F
Si
tBu
O
N
H
N
OH
O
O

2-80

-186.69
1400
1300
1200
1100
1000
900
800
700
600
500
400
300
200
100
0
-100
-200
-300
10 0 -10 -20 -30 -40 -50 -60 -70 -80 -90 -100 -110 -120 -130 -140 -150 -160 -170 -180 -190 -200 -210
f1 (ppm)

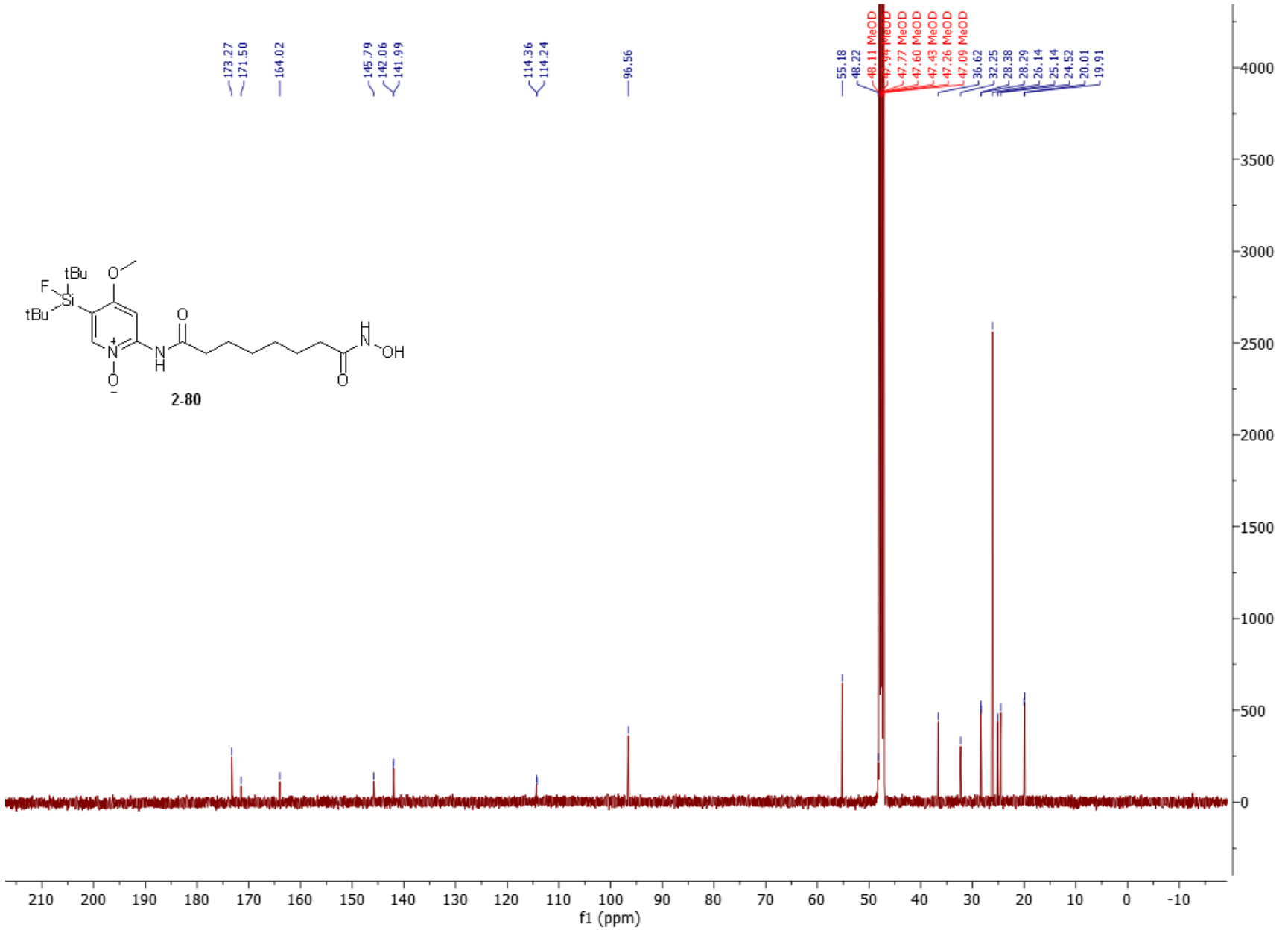
173.27
171.50
164.02
145.79
142.06
141.99
114.36
114.24
96.56
55.18
48.22
48.11 MeOD
47.94 MeOD
47.77 MeOD
47.60 MeOD
47.43 MeOD
47.26 MeOD
47.09 MeOD
36.62
32.25
28.38
28.29
26.14
25.14
24.52
20.01
19.91
4000
3500
3000
2500
2000
1500
1000
500
0
210 200 190 180 170 160 150 140 130 120 110 100 90 80 70 60 50 40 30 20 10 0 -10
f1 (ppm)
tBu
O
F
Si
tBu
O
N
H
N
OH
O
O
2-80

RadioTLC Spectra Relevant to Chapter 2

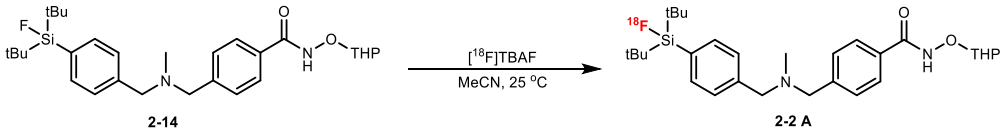

2-14 2-2 A

Labelling time: 5 min

TLC conditions: 10% MeOH in DCM

Integration TLC

Substance	R_f	Area	%Area
		Counts	%
Free fluoride	0.044	257.600	11.56
Labeled Compound	0.171	1970.067	88.44

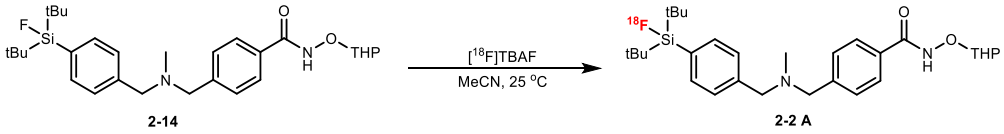

2-14 2-2 A

Labelling time: 10 min

TLC conditions: 10% MeOH in DCM

Integration TLC

Substance	R_f	Area	%Area
		Counts	%
Free fluoride	0.044	183.571	8.76
Labeled Compound	0.171	1912.143	91.24

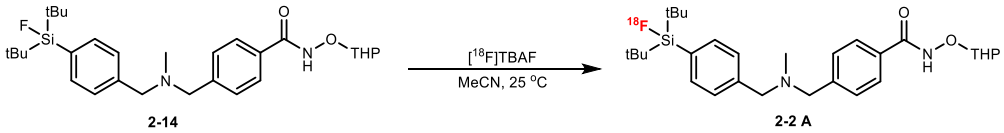

2-14 2-2 A

Labelling time: 5 min

TLC conditions: 10% MeOH in DCM

Integration TLC

Substance	R_f	Area	%Area
		Counts	%
Free fluoride	0.044	173.714	7.55
Labeled Compound	0.171	2126.429	92.45

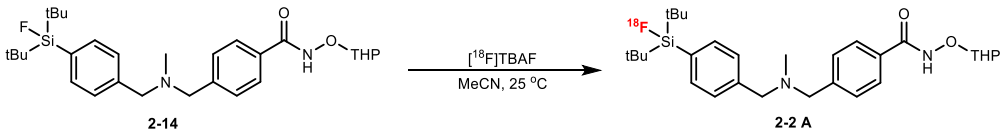

2-14 2-2 A

Labelling time: 5 min

TLC conditions: 10% MeOH in DCM

Integration TLC

Substance	R_f	Area	%Area
		Counts	%
Free fluoride	0.044	96.882	5.96
Labeled Compound	0.171	1528.882	94.04

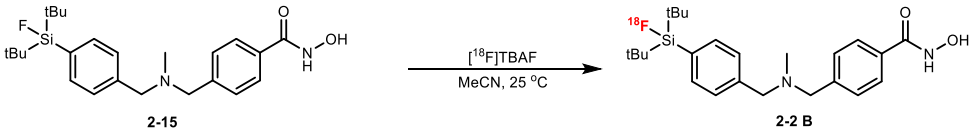

Labelling time: 5 min

TLC conditions: 10% MeOH in DCM

Integration TLC

Substance	R_f	Area Counts	%Area %
Free fluoride	0.044	842.6207	53.30
Labeled Compound	0.171	738.2759	46.70

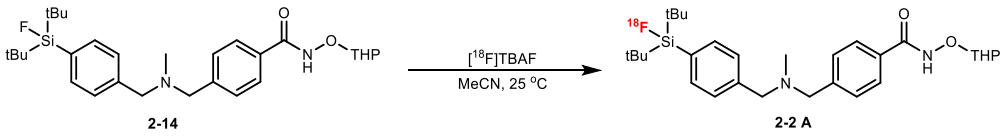

Labelling time: 10 min

TLC conditions: 10% MeOH in DCM

Integration TLC

Substance	R_f	Area Counts	%Area %
Free fluoride	0.044	816.259	44.16
Labeled Compound	0.171	1032.037	55.84

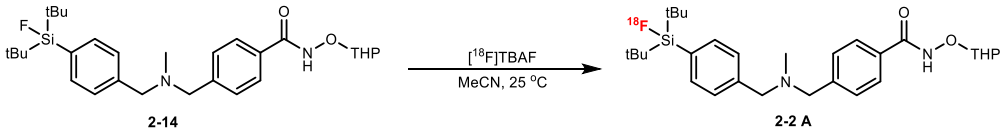

Labelling time: 5 min

TLC conditions: 10% MeOH in DCM

Integration TLC

Substance	R_f	Area	%Area
		Counts	%
Free fluoride	0.044	741.364	33.97
Labeled Compound	0.171	1441.273	66.03

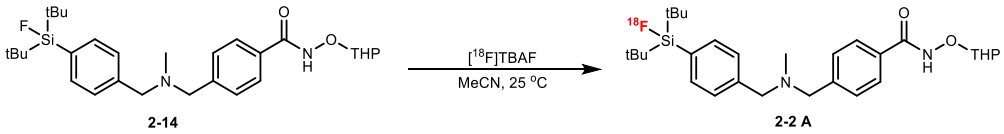

Labelling time: 5 min

TLC conditions: 10% MeOH in DCM

Integration TLC

Substance	R_f	Area	%Area
		Counts	%
Free fluoride	0.044	282.423	21.23
Labeled Compound	0.171	1047.923	78.77

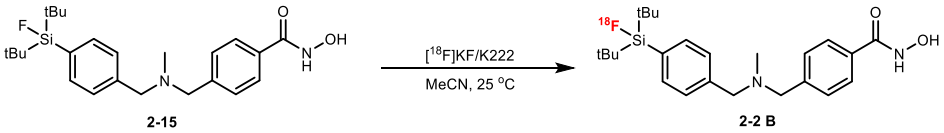

Labelling time: 5 min

TLC conditions: 10% MeOH in DCM

Integration TLC

Substance	R_f	Area	%Area
		Counts	%
Free fluoride	0.044	4264.549	56.72
Labeled Compound	0.171	3253.824	43.28

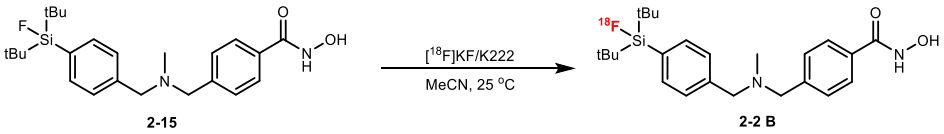

Labelling time: 10 min

TLC conditions: 10% MeOH in DCM

Integration TLC

Substance	R_f	Area	%Area
		Counts	%
Free fluoride	0.044	4094.000	34.40
Labeled Compound	0.171	7806.000	65.60

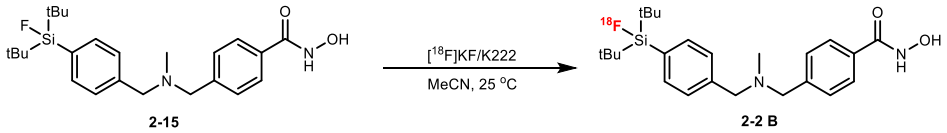

Labelling time: 15 min

TLC conditions: 10% MeOH in DCM

Integration TLC

Substance	R_f	Area	%Area
		Counts	%
Free fluoride	0.044	3616.059	27.96
Labeled Compound	0.171	9315.235	72.04

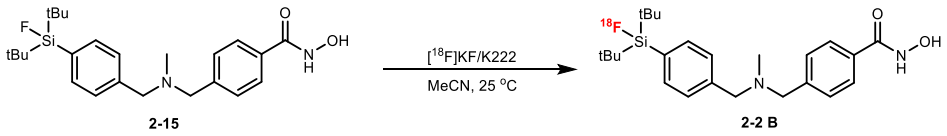

Labelling time: 60 min

TLC conditions: 10% MeOH in DCM

Integration TLC

Substance	R_f	Area	%Area
		Counts	%
Free fluoride	0.044	2049.108	17.54
Labeled Compound	0.171	9633.631	82.46

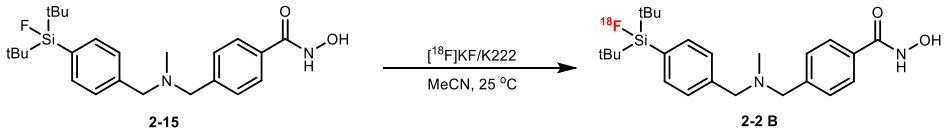

Labelling time: 5 min

TLC conditions: 10% MeOH in DCM

Integration TLC

Substance	R_f	Area	%Area
		Counts	%
Free fluoride	0.044	7056.328	47.39
Labeled Compound	0.171	7832.131	52.61

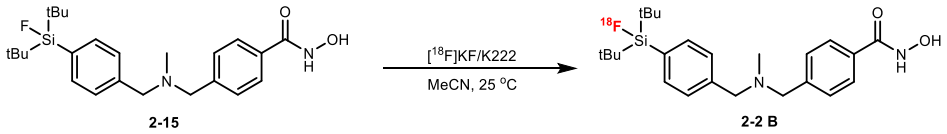

Labelling time: 10 min

TLC conditions: 10% MeOH in DCM

Integration TLC

Substance	R_f	Area	%Area
		Counts	%
Free fluoride	0.044	3960.75	24.97
Labeled Compound	0.171	11899.50	75.03

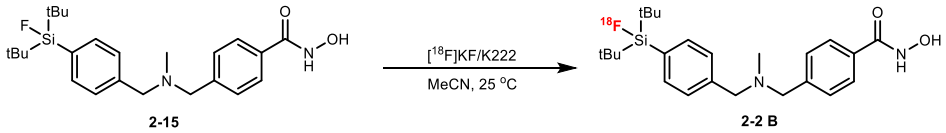

Labelling time: 15 min

TLC conditions: 10% MeOH in DCM

Integration TLC

Substance	R_f	Area	%Area
		Counts	%
Free fluoride	0.044	3032.119	24.34
Labeled Compound	0.171	9424.610	75.66

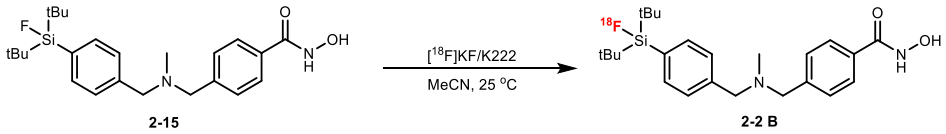

Labelling time: 60 min

TLC conditions: 10% MeOH in DCM

Integration TLC

Substance	R_f	Area	%Area
		Counts	%
Free fluoride	0.044	2293.815	18.74
Labeled Compound	0.171	9948.278	81.26

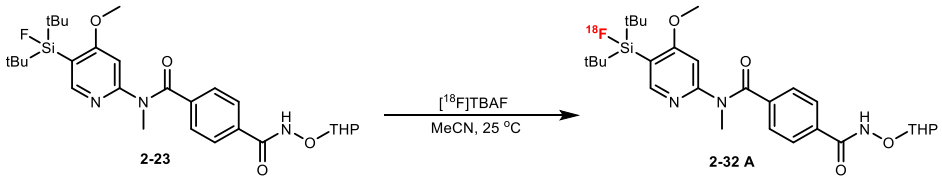

Labelling time: 5 min

TLC conditions: 10% MeOH in DCM

Integration TLC

Substance	R_f	Area Counts	%Area %
Free fluoride	0.044	1369.939	59.38
Labeled Compound	0.171	937.000	40.62

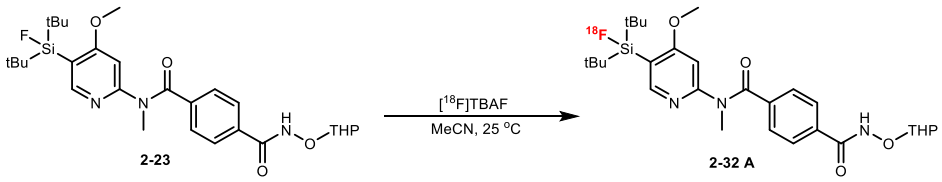

Labelling time: 10 min

TLC conditions: 10% MeOH in DCM

Integration TLC

Substance	R_f	Area Counts	%Area %
Free fluoride	0.044	1630.978	53.52
Labeled Compound	0.171	1416.304	46.48

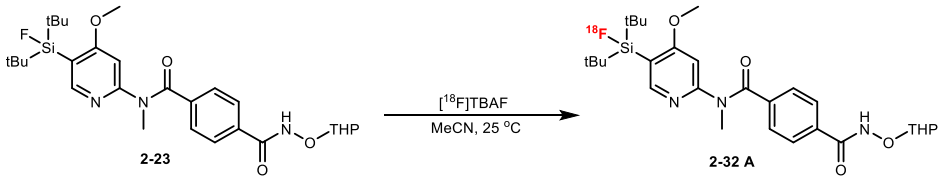

Labelling time: 15 min

TLC conditions: 10% MeOH in DCM

Integration TLC

Substance	R_f	Area Counts	%Area %
Free fluoride	0.044	1393.206	53.68
Labeled Compound	0.171	1201.971	46.32

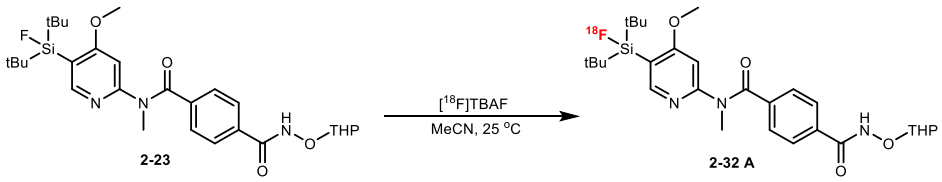

Labelling time: 60 min

TLC conditions: 10% MeOH in DCM

Integration TLC

Substance	R_f	Area Counts	%Area %
Free fluoride	0.044	790.632	38.37
Labeled Compound	0.171	1270.000	61.63

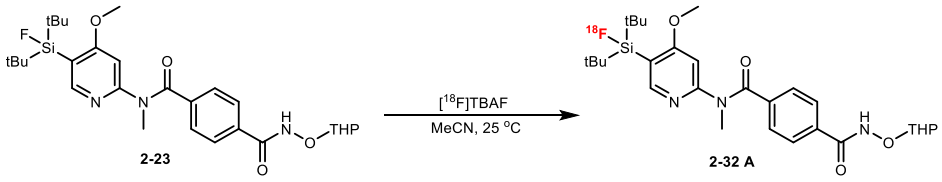

Labelling time: 5 min

TLC conditions: 10% MeOH in DCM

Integration TLC

Substance	R_f	Area Counts	%Area %
Free fluoride	0.044	1537.327	57.31
Labeled Compound	0.171	1144.939	42.69

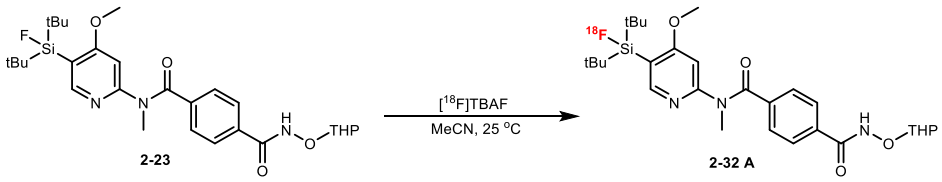

Labelling time: 10 min

TLC conditions: 10% MeOH in DCM

Integration TLC

Substance	R_f	Area Counts	%Area %
Free fluoride	0.044	1735.086	56.02
Labeled Compound	0.171	1362.429	43.98

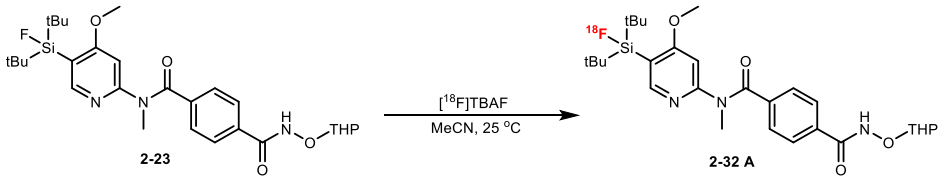

Labelling time: 15 min

TLC conditions: 10% MeOH in DCM

Integration TLC

Substance	R_f	Area Counts	%Area %
Free fluoride	0.044	1530.238	46.32
Labeled Compound	0.171	1773.619	53.68

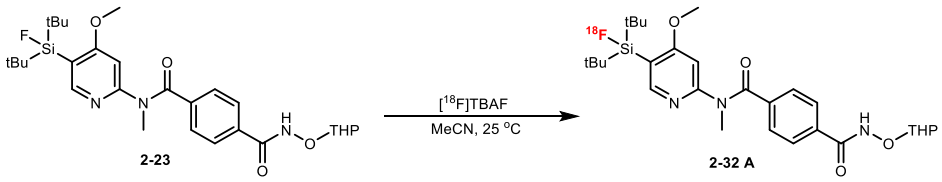

Labelling time: 60 min

TLC conditions: 10% MeOH in DCM

Integration TLC

Substance	R_f	Area Counts	%Area %
Free fluoride	0.044	856.714	35.16
Labeled Compound	0.171	1579.786	64.84

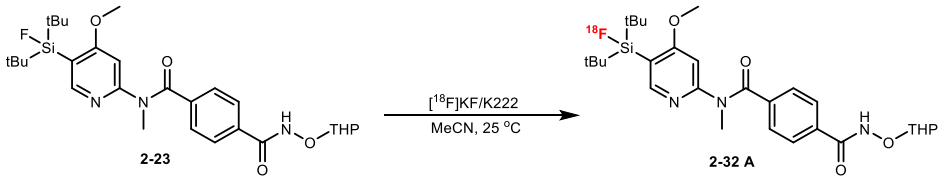

Labelling time: 5 min

TLC conditions: 10% MeOH in DCM

Integration TLC

Substance	R_f	Area	%Area
		Counts	%
Free fluoride	0.044	3299.078	49.76
Labeled Compound	0.171	3330.294	50.24

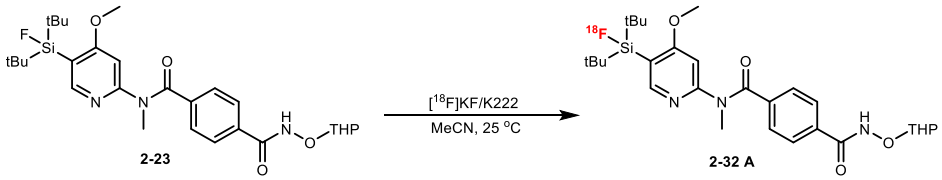

Labelling time: 10 min

TLC conditions: 10% MeOH in DCM

Integration TLC

Substance	R_f	Area	%Area
		Counts	%
Free fluoride	0.044	1945.953	27.25
Labeled Compound	0.171	5193.977	72.75

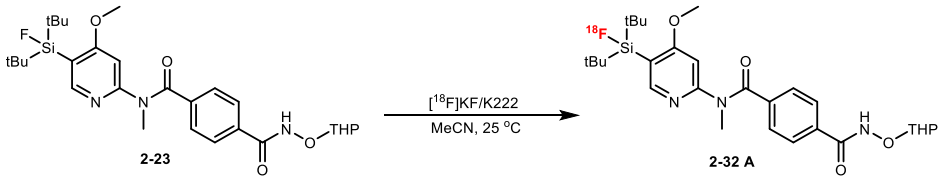

Labelling time: 15 min

TLC conditions: 10% MeOH in DCM

Integration TLC

Substance	R_f	Area	%Area
		Counts	%
Free fluoride	0.044	947.310	18.66
Labeled Compound	0.171	4128.667	81.34

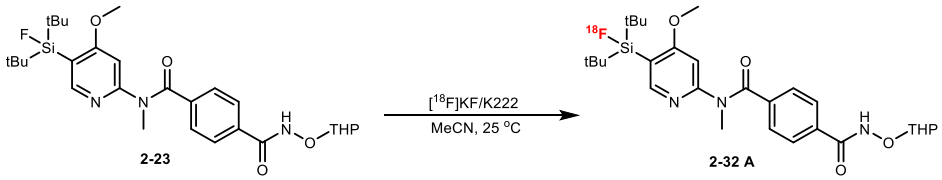

Labelling time: 60 min

TLC conditions: 10% MeOH in DCM

Integration TLC

Substance	R_f	Area	%Area
		Counts	%
Free fluoride	0.044	455.000	7.58
Labeled Compound	0.171	5548.000	92.42

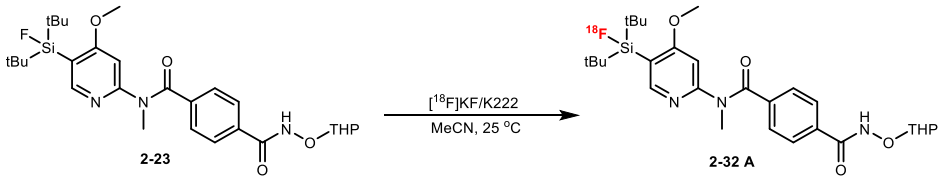

Labelling time: 5 min

TLC conditions: 10% MeOH in DCM

Integration TLC

Substance	R_f	Area	%Area
		Counts	%
Free fluoride	0.044	3934.854	51.37
Labeled Compound	0.171	3724.500	48.63

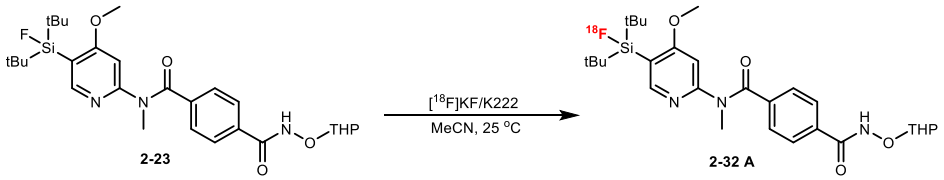

Labelling time: 10 min

TLC conditions: 10% MeOH in DCM

Integration TLC

Substance	R_f	Area	%Area
		Counts	%
Free fluoride	0.044	2259.167	29.30
Labeled Compound	0.171	5451.556	70.70

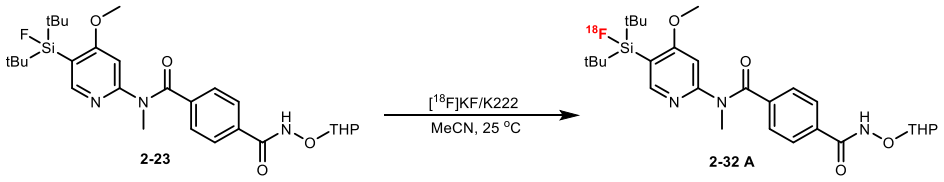

Labelling time: 15 min

TLC conditions: 10% MeOH in DCM

Integration TLC

Substance	R_f	Area	%Area
		Counts	%
Free fluoride	0.044	1093.545	20.20
Labeled Compound	0.171	4320.545	79.80

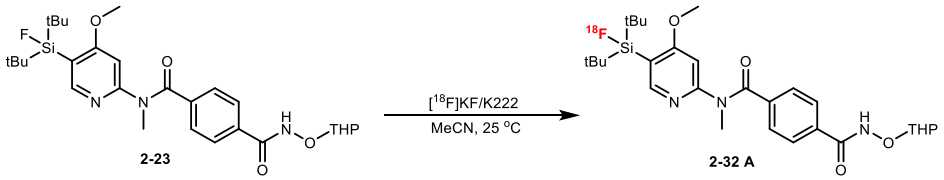

Labelling time: 60 min

TLC conditions: 10% MeOH in DCM

Integration TLC

Substance	R_f	Area	%Area
		Counts	%
Free fluoride	0.044	371.563	6.80
Labeled Compound	0.171	5091.625	93.20

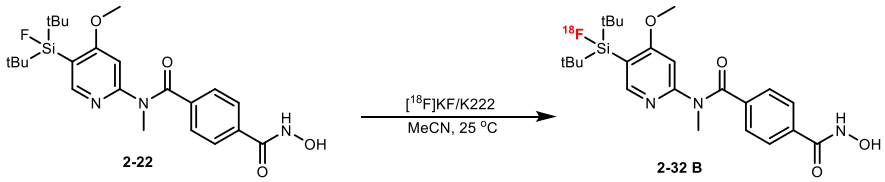

Labelling time: 5 min

TLC conditions: 10% MeOH in DCM

Integration TLC

Substance	R_f	Area	%Area
		Counts	%
Free fluoride	0.044	9394.000	75.64
Labeled Compound	0.171	3025.000	24.36

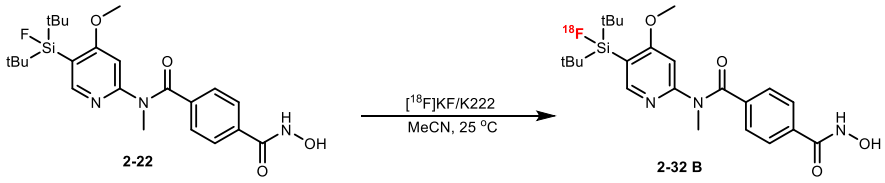

Labelling time: 10 min

TLC conditions: 10% MeOH in DCM

Integration TLC

Substance	R_f	Area	%Area
		Counts	%
Free fluoride	0.044	9232.074	64.30
Labeled Compound	0.171	5126.605	35.70

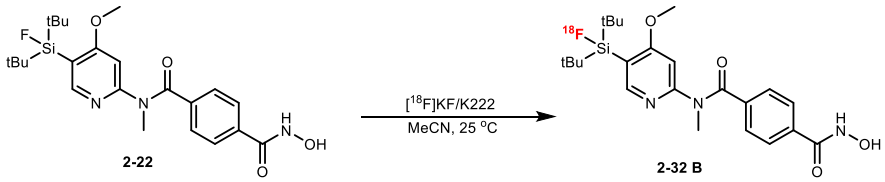

Labelling time: 15 min

TLC conditions: 10% MeOH in DCM

Integration TLC

Substance	R_f	Area	%Area
		Counts	%
Free fluoride	0.044	7708.836	50.71
Labeled Compound	0.171	7494.382	49.29

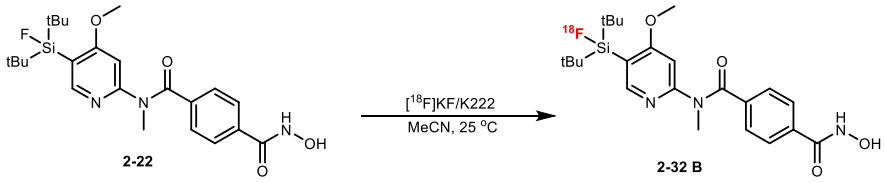

Labelling time: 60 min

TLC conditions: 10% MeOH in DCM

Integration TLC

Substance	R_f	Area	%Area
		Counts	%
Free fluoride	0.044	2577.653	21.25
Labeled Compound	0.171	9552.020	78.75

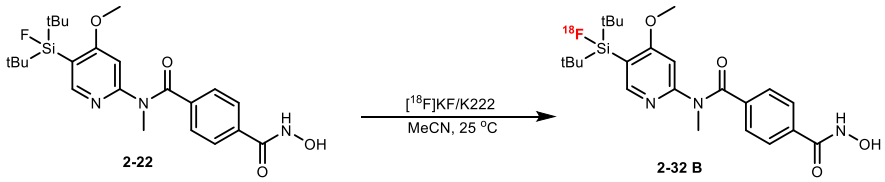

Labelling time: 5 min

TLC conditions: 10% MeOH in DCM

Integration TLC

Substance	R_f	Area	%Area
		Counts	%
Free fluoride	0.044	6698.053	70.32
Labeled Compound	0.171	2826.421	29.68

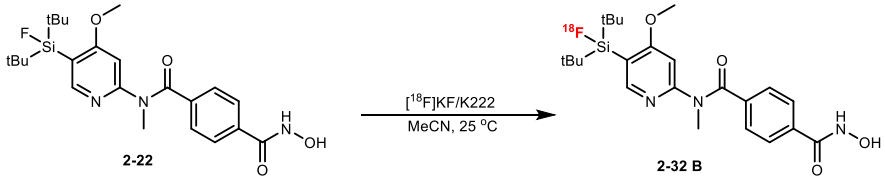

Labelling time: 10 min

TLC conditions: 10% MeOH in DCM

Integration TLC

Substance	R_f	Area	%Area
		Counts	%
Free fluoride	0.044	7604.429	56.43
Labeled Compound	0.171	5871.143	43.57

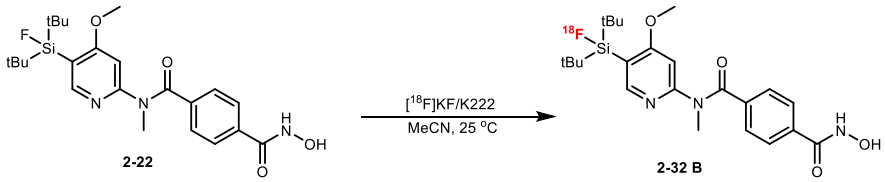

Labelling time: 15 min

TLC conditions: 10% MeOH in DCM

Integration TLC

Substance	R_f	Area	%Area
		Counts	%
Free fluoride	0.044	7042.794	44.99
Labeled Compound	0.171	8610.632	55.01

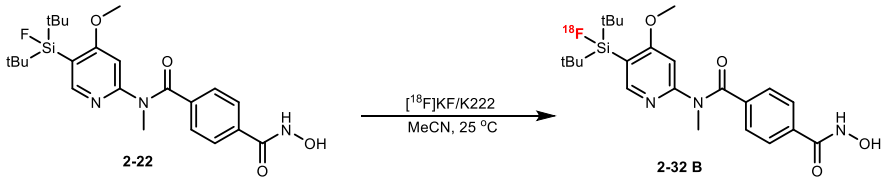

Labelling time: 60 min

TLC conditions: 10% MeOH in DCM

Integration TLC

Substance	R_f	Area	%Area
		Counts	%
Free fluoride	0.044	1282.377	14.16
Labeled Compound	0.171	7773.117	85.84

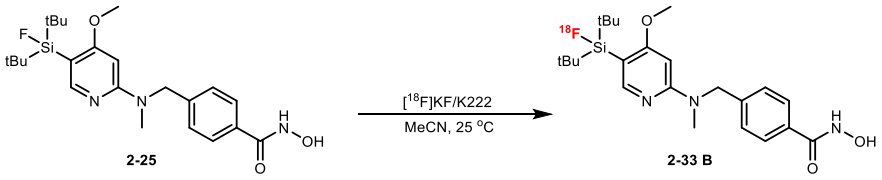

Labelling time: 5 min

TLC conditions: 1:1 MeCN:H2O(1% TFA, 1% NaOAc)

Integration TLC

Substance	R_f	Area Counts	%Area %
Free fluoride	0.044	10303.00	95.89
Labeled Compound	0.171	442.00	4.11

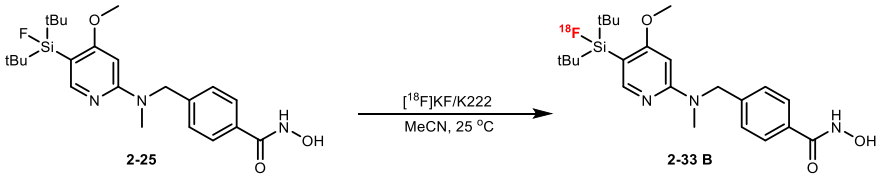

Labelling time: 10 min

TLC conditions: 1:1 MeCN:H2O(1% TFA, 1% NaOAc)

Integration TLC

Substance	R_f	Area Counts	%Area %
Free fluoride	0.044	10713.92	95.49
Labeled Compound	0.171	506.08	4.51

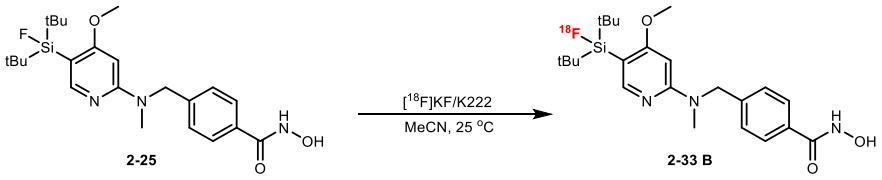

Labelling time: 15 min

TLC conditions: 1:1 MeCN:H2O(1% TFA, 1% NaOAc)

Integration TLC

Substance	R_f	Area	%Area
		Counts	%
Free fluoride	0.044	12976.14	94.51
Labeled Compound	0.171	754.31	5.49

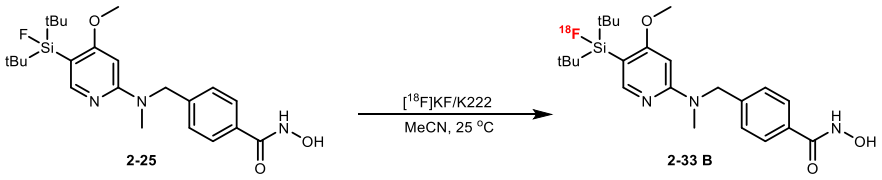

Labelling time: 60 min

TLC conditions: 1:1 MeCN:H2O(1% TFA, 1% NaOAc)

Integration TLC

Substance	R_f	Area	%Area
		Counts	%
Free fluoride	0.044	8000.200	82.98
Labeled Compound	0.171	1640.400	17.02

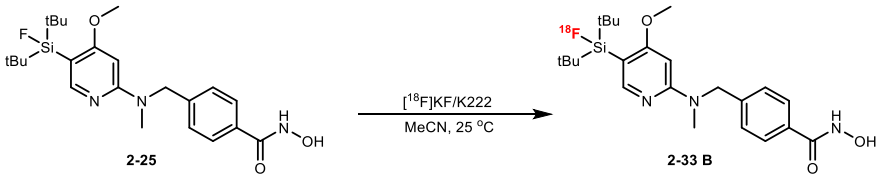

Labelling time: 5 min

TLC conditions: 1:1 MeCN:H2O(1% TFA, 1% NaOAc)

Integration TLC

Substance	R_f	Area	%Area
		Counts	%
Free fluoride	0.044	7157.304	97.02
Labeled Compound	0.171	220.174	2.98

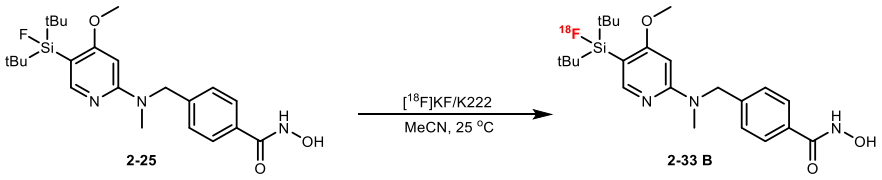

Labelling time: 10 min

TLC conditions: 1:1 MeCN:H2O(1% TFA, 1% NaOAc)

Integration TLC

Substance	R_f	Area	%Area
		Counts	%
Free fluoride	0.044	12672.94	94.75
Labeled Compound	0.171	701.77	5.25

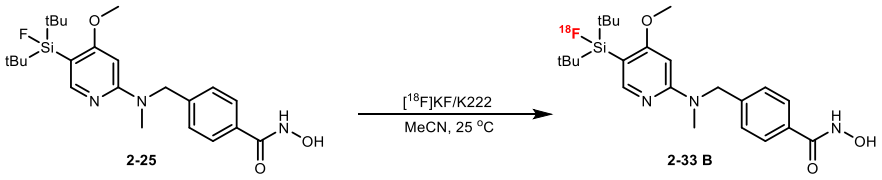

Labelling time: 15 min

TLC conditions: 1:1 MeCN:H2O(1% TFA, 1% NaOAc)

Integration TLC

Substance	R_f	Area	%Area
		Counts	%
Free fluoride	0.044	13337.44	93.00
Labeled Compound	0.171	1003.63	7.00

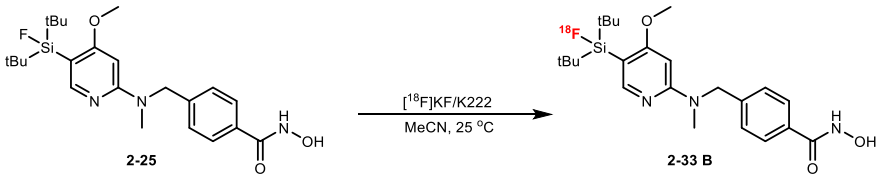

Labelling time: 60 min

TLC conditions: 1:1 MeCN:H2O(1% TFA, 1% NaOAc)

Integration TLC

Substance	R_f	Area	%Area
		Counts	%
Free fluoride	0.044	6926.963	87.31
Labeled Compound	0.171	1006.519	12.69

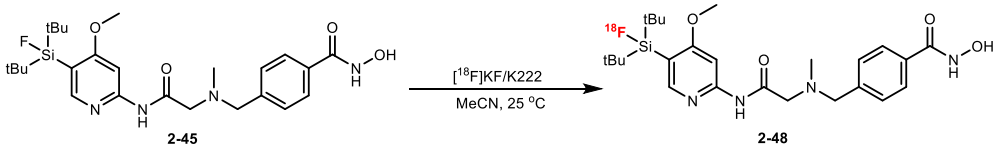

Labelling time: 5 min

TLC conditions: 1:1 MeCN:H2O(1% TFA, 1% NaOAc)

Integration TLC

Substance	R_f	Area	%Area
		Counts	%
Free fluoride	0.044	10649.00	93.87
Labeled Compound	0.171	695.00	6.13

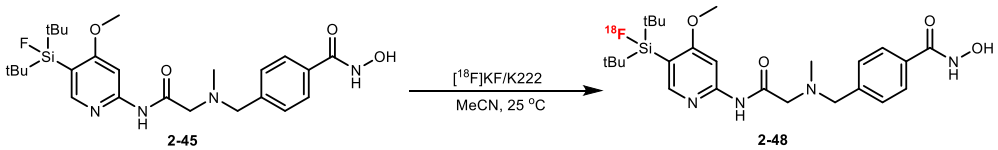

Labelling time: 10 min

TLC conditions: 1:1 MeCN:H2O(1% TFA, 1% NaOAc)

Integration TLC

Substance	R_f	Area	%Area
		Counts	%
Free fluoride	0.044	8895.571	85.36
Labeled Compound	0.171	1525.286	14.64

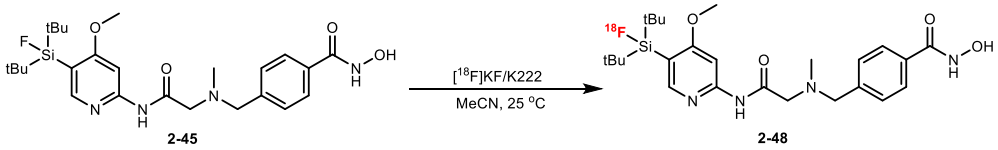

Labelling time: 15 min

TLC conditions: 1:1 MeCN:H2O(1% TFA, 1% NaOAc)

Integration TLC

Substance	R_f	Area	%Area
		Counts	%
Free fluoride	0.044	9500.000	72.72
Labeled Compound	0.171	3564.000	27.28

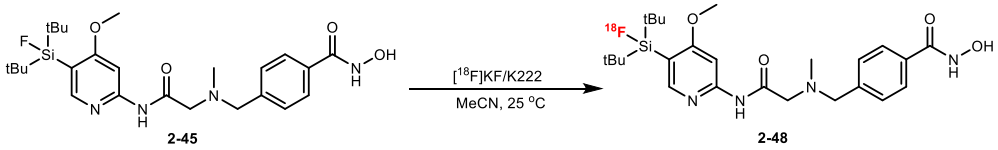

Labelling time: 60 min

TLC conditions: 1:1 MeCN:H2O(1% TFA, 1% NaOAc)

Integration TLC

Substance	R_f	Area	%Area
		Counts	%
Free fluoride	0.044	2105.647	37.08
Labeled Compound	0.171	3573.059	62.92

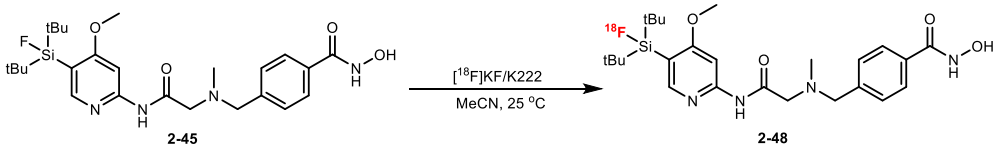

Labelling time: 5 min

TLC conditions: 1:1 MeCN:H2O(1% TFA, 1% NaOAc)

Integration TLC

Substance	R_f	Area	%Area
		Counts	%
Free fluoride	0.044	11431.18	93.85
Labeled Compound	0.171	749.18	6.15

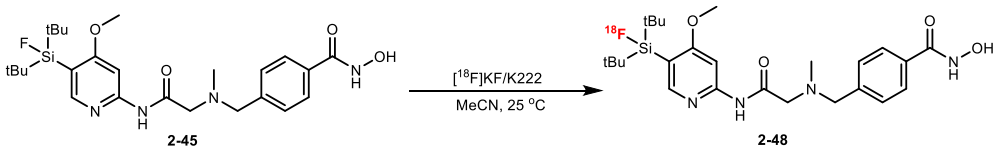

Labelling time: 10 min

TLC conditions: 1:1 MeCN:H2O(1% TFA, 1% NaOAc)

Integration TLC

Substance	R_f	Area	%Area
		Counts	%
Free fluoride	0.044	8103.182	76.66
Labeled Compound	0.171	2466.758	23.34

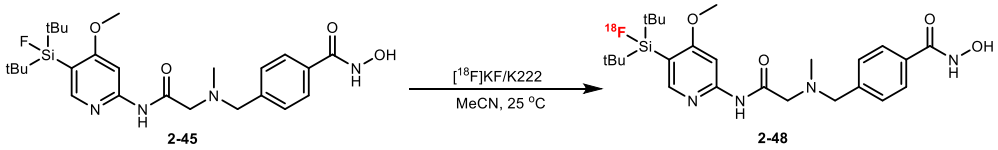

Labelling time: 15 min

TLC conditions: 1:1 MeCN:H2O(1% TFA, 1% NaOAc)

Integration TLC

Substance	R_f	Area	%Area
		Counts	%
Free fluoride	0.044	9335.553	72.00
Labeled Compound	0.171	3629.681	28.00

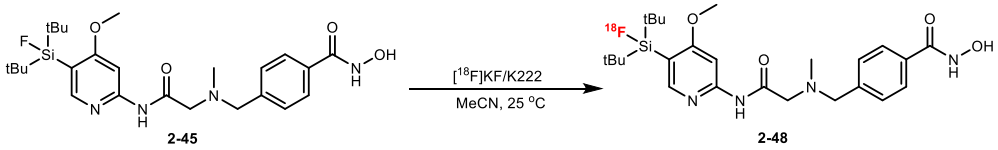

Labelling time: 60 min

TLC conditions: 1:1 MeCN:H2O(1% TFA, 1% NaOAc)

Integration TLC

Substance	R_f	Area	%Area
		Counts	%
Free fluoride	0.044	2123.667	41.20
Labeled Compound	0.171	3030.917	58.80

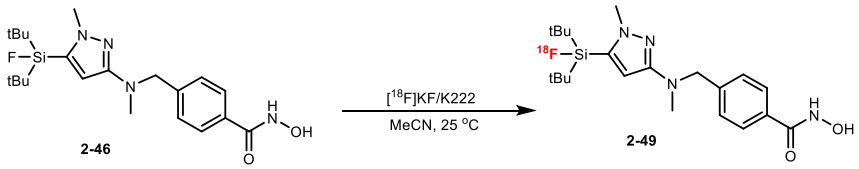

Labelling time: 5 min

TLC conditions: 1:1 MeCN:H2O(1% TFA, 1% NaOAc)

Integration TLC

Substance	R_f	Area	%Area
		Counts	%
Free fluoride	0.044	12811.22	99.06
Labeled Compound	0.171	121.33	0.94

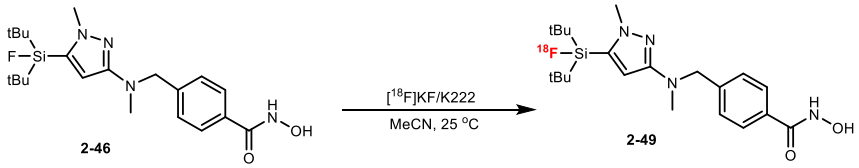

Labelling time: 10 min

TLC conditions: 1:1 MeCN:H2O(1% TFA, 1% NaOAc)

Integration TLC

Substance	R_f	Area	%Area
		Counts	%
Free fluoride	0.044	13026.25	99.78
Labeled Compound	0.171	28.19	0.22

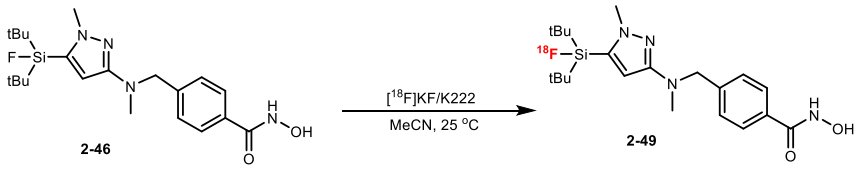

Labelling time: 15 min

TLC conditions: 1:1 MeCN:H2O(1% TFA, 1% NaOAc)

Integration TLC

Substance	R_f	Area	%Area
		Counts	%
Free fluoride	0.044	13957.68	99.20
Labeled Compound	0.171	112.00	0.80

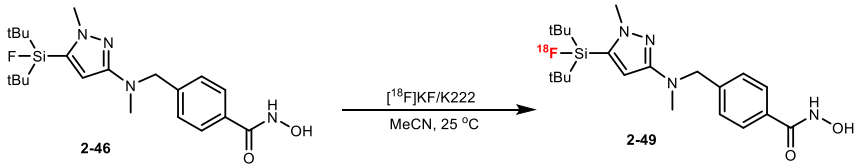

Labelling time: 60 min

TLC conditions: 1:1 MeCN:H2O(1% TFA, 1% NaOAc)

Integration TLC

Substance	R_f	Area	%Area
		Counts	%
Free fluoride	0.044	9453.105	98.85
Labeled Compound	0.171	110.105	1.15

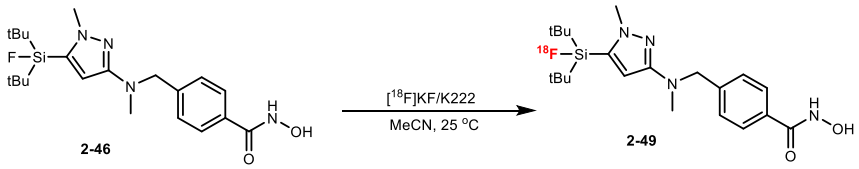

Labelling time: 5 min

TLC conditions: 1:1 MeCN:H2O(1% TFA, 1% NaOAc)

Integration TLC

Substance	R_f	Area	%Area
		Counts	%
Free fluoride	0.044	12487.18	98.87
Labeled Compound	0.171	142.64	1.13

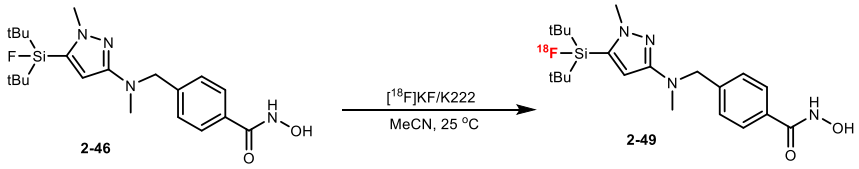

Labelling time: 10 min

TLC conditions: 1:1 MeCN:H2O(1% TFA, 1% NaOAc)

Integration TLC

Substance	R_f	Area	%Area
		Counts	%
Free fluoride	0.044	12673.88	99.41
Labeled Compound	0.171	75.06	0.59

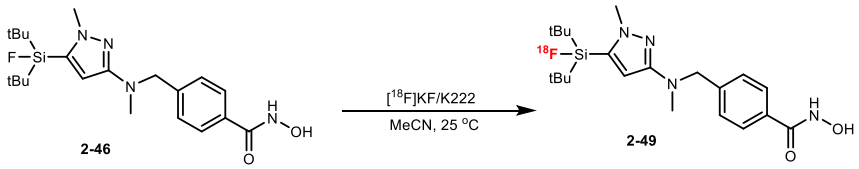

Labelling time: 15 min

TLC conditions: 1:1 MeCN:H2O(1% TFA, 1% NaOAc)

Integration TLC

Substance	R_f	Area	%Area
		Counts	%
Free fluoride	0.044	10648.00	99.98
Labeled Compound	0.171	2.41	0.02

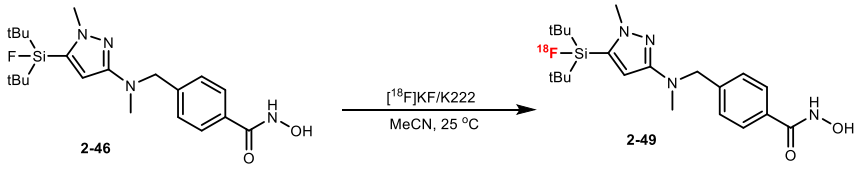

Labelling time: 60 min

TLC conditions: 1:1 MeCN:H2O(1% TFA, 1% NaOAc)

Integration TLC

Substance	R_f	Area	%Area
		Counts	%
Free fluoride	0.044	12023.56	94.14
Labeled Compound	0.171	748.21	5.86

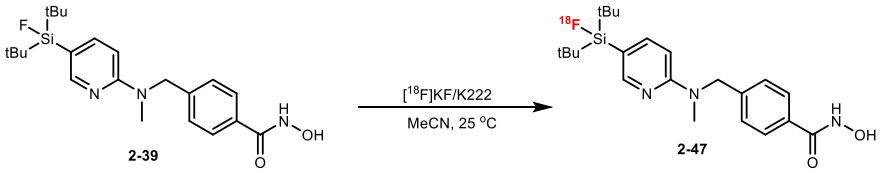

Labelling time: 5 min

TLC conditions: 1:1 MeCN:H2O(1% TFA, 1% NaOAc)

Integration TLC

Substance	R_f	Area	%Area
		Counts	%
Free fluoride	0.044	1172.500	24.19
Labeled Compound	0.171	3675.038	75.81

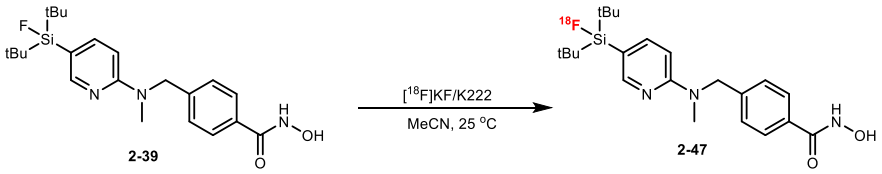

Labelling time: 10 min

TLC conditions: 1:1 MeCN:H2O(1% TFA, 1% NaOAc)

Integration TLC

Substance	R_f	Area	%Area
		Counts	%
Free fluoride	0.044	1058.182	20.59
Labeled Compound	0.171	4081.636	79.41

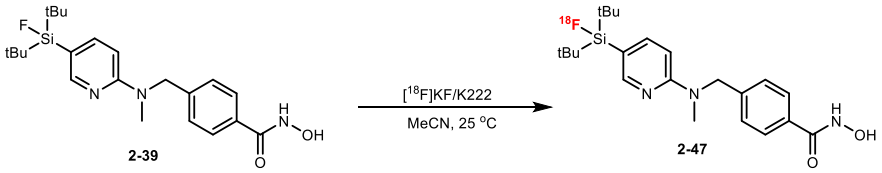

Labelling time: 15 min

TLC conditions: 1:1 MeCN:H2O(1% TFA, 1% NaOAc)

Integration TLC

Substance	R_f	Area	%Area
		Counts	%
Free fluoride	0.044	1097.091	16.16
Labeled Compound	0.171	5690.182	83.84

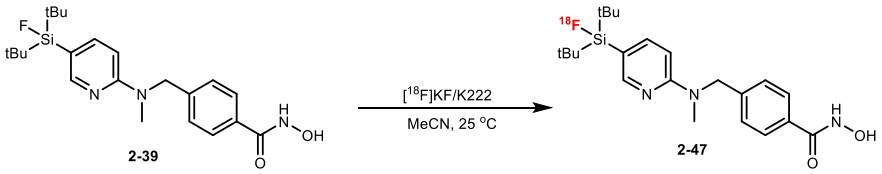

Labelling time: 60 min

TLC conditions: 1:1 MeCN:H2O(1% TFA, 1% NaOAc)

Integration TLC

Substance	R_f	Area	%Area
		Counts	%
Free fluoride	0.044	438.905	12.85
Labeled Compound	0.171	2977.952	87.15

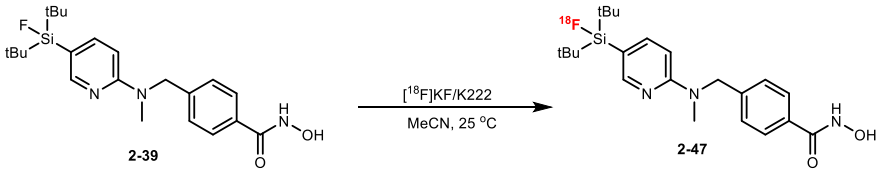

Labelling time: 5 min

TLC conditions: 1:1 MeCN:H2O(1% TFA, 1% NaOAc)

Integration TLC

Substance	R_f	Area	%Area
		Counts	%
Free fluoride	0.044	1545.115	28.02
Labeled Compound	0.171	3968.846	71.98

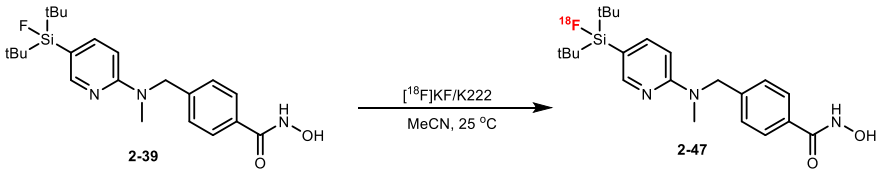

Labelling time: 10 min

TLC conditions: 1:1 MeCN:H2O(1% TFA, 1% NaOAc)

Integration TLC

Substance	R_f	Area	%Area
		Counts	%
Free fluoride	0.044	1382.250	20.98
Labeled Compound	0.171	5206.208	79.02

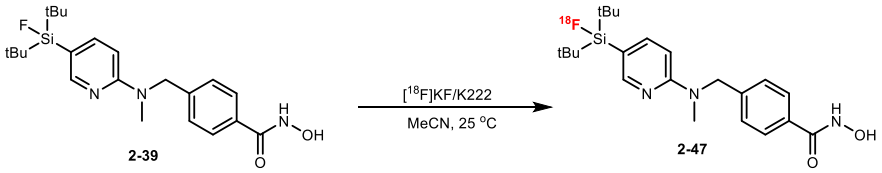

Labelling time: 15 min

TLC conditions: 1:1 MeCN:H2O(1% TFA, 1% NaOAc)

Integration TLC

Substance	R_f	Area	%Area
		Counts	%
Free fluoride	0.044	934.000	17.50
Labeled Compound	0.171	4402.000	82.50

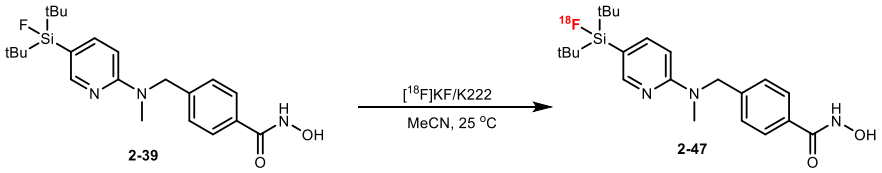

Labelling time: 60 min

TLC conditions: 1:1 MeCN:H2O(1% TFA, 1% NaOAc)

Integration TLC

Substance	R_f	Area	%Area
		Counts	%
Free fluoride	0.044	376.200	12.77
Labeled Compound	0.171	2570.400	87.23

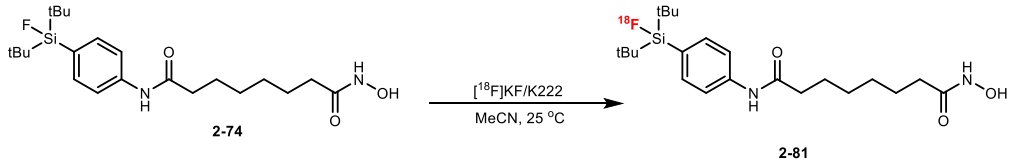

Labelling time: 5 min

TLC conditions: 10% MeOH in DCM

Integration TLC

Substance	R_f	Area	%Area
		Counts	%
Free fluoride	0.044	6054.839	39.59
Labeled Compound	0.171	9237.323	60.41

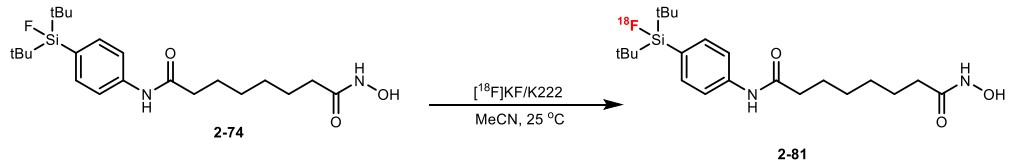

Labelling time: 10 min

TLC conditions: 10% MeOH in DCM

Integration TLC

Substance	R_f	Area	%Area
		Counts	%
Free fluoride	0.044	4182.49	29.32
Labeled Compound	0.171	10081.80	70.68

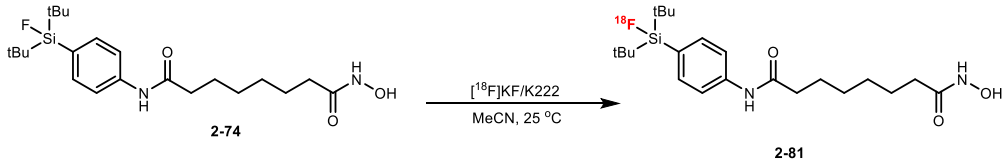

Labelling time: 15 min

TLC conditions: 10% MeOH in DCM

Integration TLC

Substance	R_f	Area	%Area
		Counts	%
Free fluoride	0.044	2378.06	18.20
Labeled Compound	0.171	10691.73	81.80

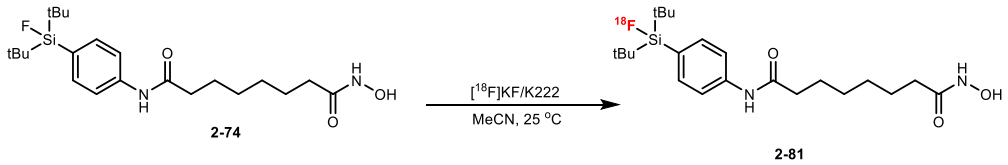

Labelling time: 60 min

TLC conditions: 10% MeOH in DCM

Integration TLC

Substance	R_f	Area	%Area
		Counts	%
Free fluoride	0.044	1066.000	11.21
Labeled Compound	0.171	8442.484	88.79

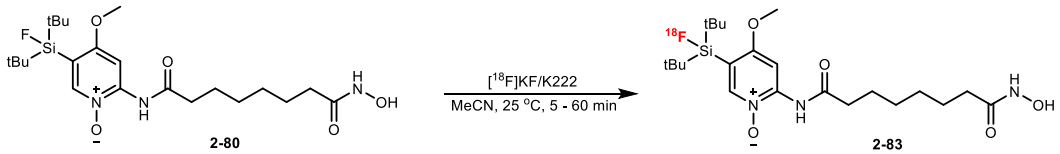

Labelling time: 5 min

TLC conditions: 1:1 MeCN:H2O(1% TFA, 1% NaOAc)

Integration TLC

Substance	R_f	Area	%Area
		Counts	%
Free fluoride	0.044	1386.690	35.71
Labeled Compound	0.171	2496.069	64.29

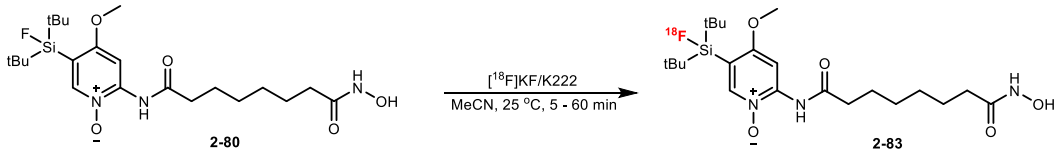

Labelling time: 10 min

TLC conditions: 1:1 MeCN:H2O(1% TFA, 1% NaOAc)

Integration TLC

Substance	R_f	Area	%Area
		Counts	%
Free fluoride	0.044	1643.000	25.76
Labeled Compound	0.171	4736.000	74.24

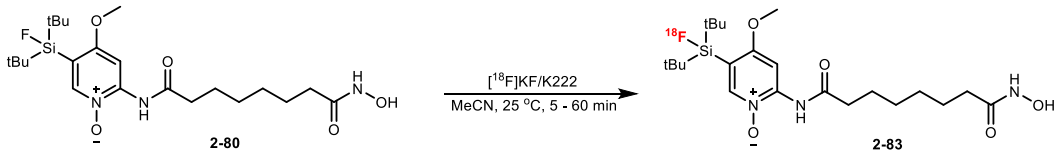

Labelling time: 15 min

TLC conditions: 1:1 MeCN:H2O(1% TFA, 1% NaOAc)

Integration TLC

Substance	R_f	Area	%Area
		Counts	%
Free fluoride	0.044	1735.333	19.28
Labeled Compound	0.171	7264.000	80.72

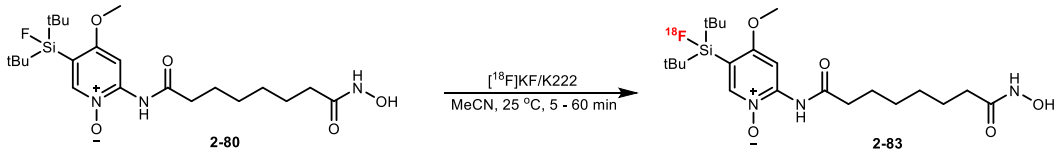

Labelling time: 60 min

TLC conditions: 1:1 MeCN:H2O(1% TFA, 1% NaOAc

Integration TLC

Substance	R_f	Area	%Area
		Counts	%
Free fluoride	0.044	1134.000	20.02
Labeled Compound	0.171	4531.000	79.98

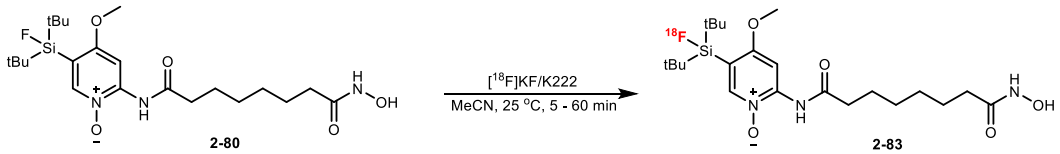

Labelling time: 5 min

TLC conditions: 1:1 MeCN:H2O(1% TFA, 1% NaOAc)

Integration TLC

Substance	R_f	Area	%Area
		Counts	%
Free fluoride	0.044	7088.875	58.90
Labeled Compound	0.171	4946.500	41.10

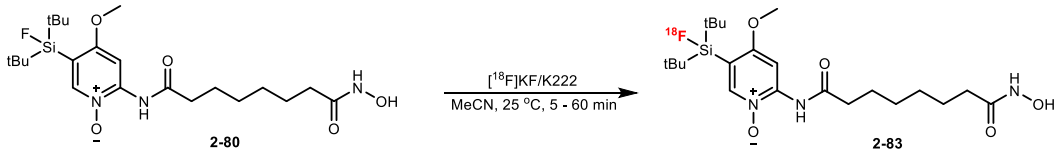

Labelling time: 10 min

TLC conditions: 1:1 MeCN:H2O(1% TFA, 1% NaOAc)

Integration TLC

Substance	R_f	Area	%Area
		Counts	%
Free fluoride	0.044	6441.000	52.60
Labeled Compound	0.171	5804.308	47.40

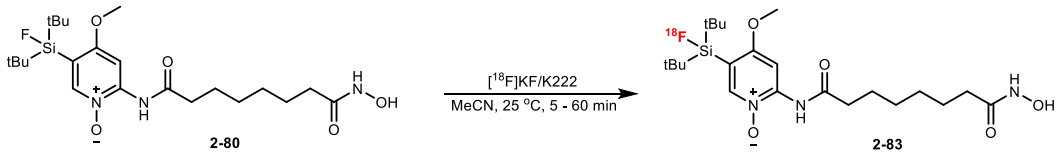

Labelling time: 15 min

TLC conditions: 1:1 MeCN:H2O(1% TFA, 1% NaOAc)

Integration TLC

Substance	R_f	Area	%Area
		Counts	%
Free fluoride	0.044	6441.000	52.60
Labeled Compound	0.171	5804.308	47.40

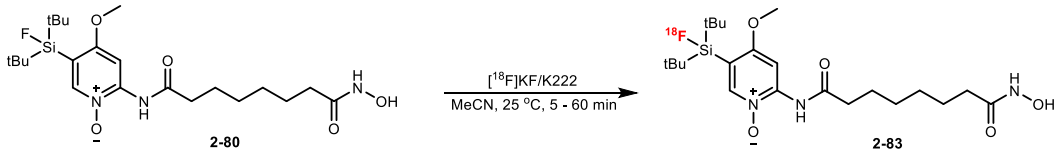

Labelling time: 60 min

TLC conditions: 1:1 MeCN:H2O(1% TFA, 1% NaOAc)

Integration TLC

Substance	R_f	Area	%Area
		Counts	%
Free fluoride	0.044	5265.769	40.84
Labeled Compound	0.171	7628.077	59.16

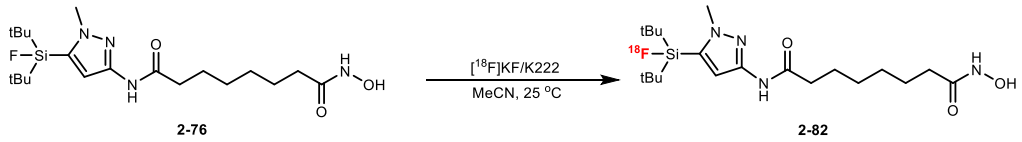

2-76 2-82

Labelling time: 5 min

TLC conditions: 1:1 MeCN:H2O(1% TFA, 1% NaOAc)

Integration TLC

Substance	R_f	Area	%Area
		Counts	%
Free fluoride	0.044	10084.19	69.19
Labeled Compound	0.171	4490.89	30.81

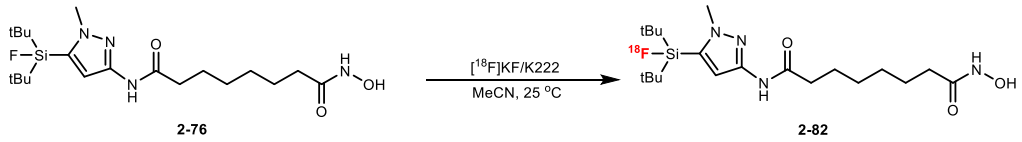

2-76 2-82

Labelling time: 10 min

TLC conditions: 1:1 MeCN:H2O(1% TFA, 1% NaOAc)

Integration TLC

Substance	R_f	Area	%Area
		Counts	%
Free fluoride	0.044	9268.793	72.90
Labeled Compound	0.171	3445.793	27.10

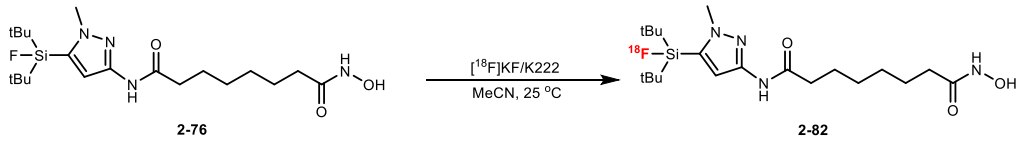

Labelling time: 15 min

TLC conditions: 1:1 MeCN:H2O(1% TFA, 1% NaOAc)

Integration TLC

Substance	R_f	Area	%Area
		Counts	%
Free fluoride	0.044	9545.000	68.90
Labeled Compound	0.171	4309.000	31.10

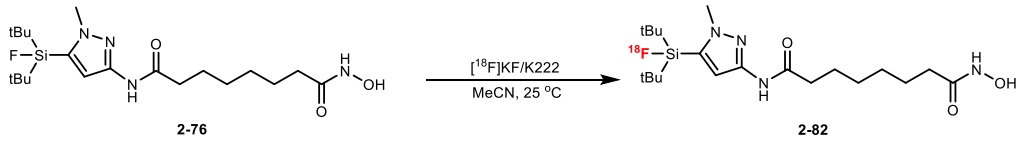

Labelling time: 60 min

TLC conditions: 1:1 MeCN:H2O(1% TFA, 1% NaOAc)

Integration TLC

Substance	R_f	Area	%Area
		Counts	%
Free fluoride	0.044	7160.500	66.39
Labeled Compound	0.171	3625.500	33.61

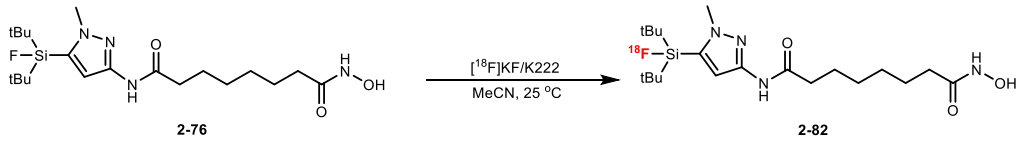

2-76 2-82

Labelling time: 5 min

TLC conditions: 1:1 MeCN:H2O(1% TFA, 1% NaOAc)

Integration TLC

Substance	R_f	Area	%Area
		Counts	%
Free fluoride	0.044	9113.625	66.74
Labeled Compound	0.171	4541.063	33.26

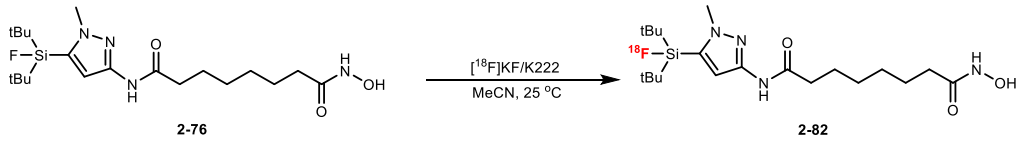

2-76 2-82

Labelling time: 10 min

TLC conditions: 1:1 MeCN:H2O(1% TFA, 1% NaOAc)

Integration TLC

Substance	R_f	Area	%Area
		Counts	%
Free fluoride	0.044	8666.500	62.27
Labeled Compound	0.171	5251.167	37.73

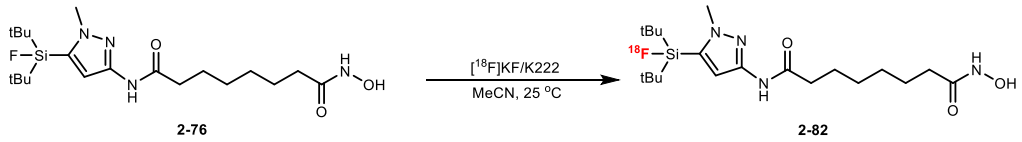

2-76 2-82

Labelling time: 15 min

TLC conditions: 1:1 MeCN:H2O(1% TFA, 1% NaOAc)

Integration TLC

Substance	R_f	Area	%Area
		Counts	%
Free fluoride	0.044	9193.000	57.94
Labeled Compound	0.171	6672.179	42.06

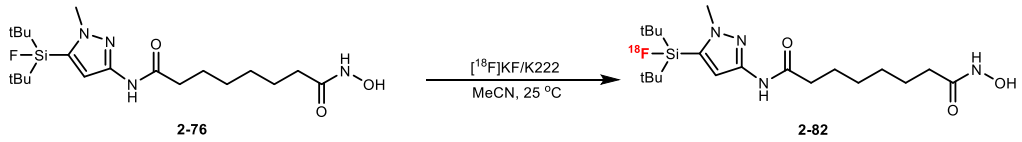

2-76 2-82

Labelling time: 60 min

TLC conditions: 1:1 MeCN:H2O(1% TFA, 1% NaOAc)

Integration TLC

Substance	R_f	Area	%Area
		Counts	%
Free fluoride	0.044	6590.000	52.67
Labeled Compound	0.171	5923.000	47.33

HDAC6 binding assay results

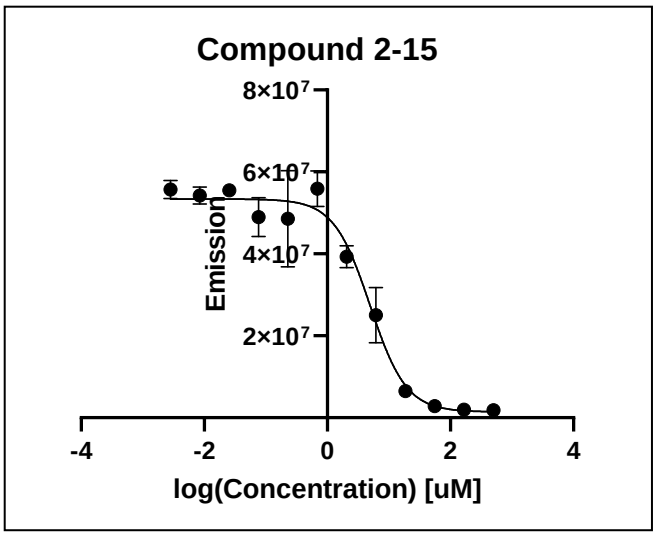

Structure

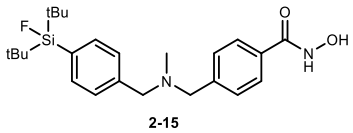

2-15

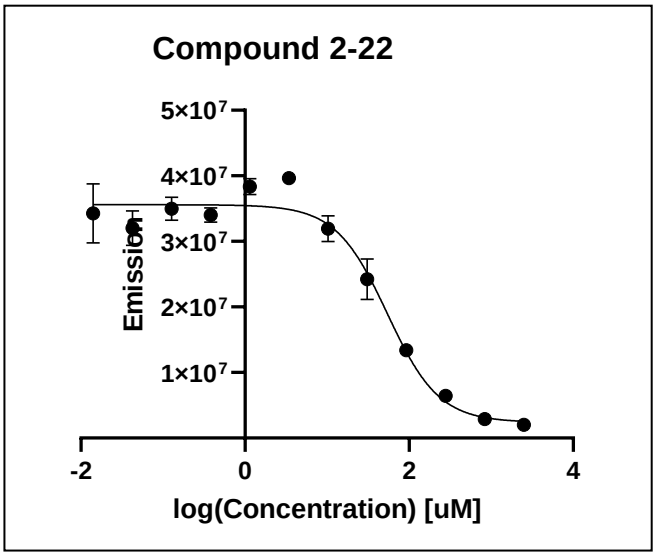

Structure

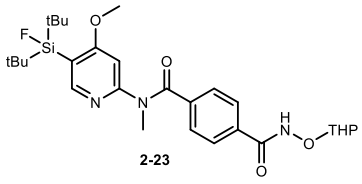

2-23

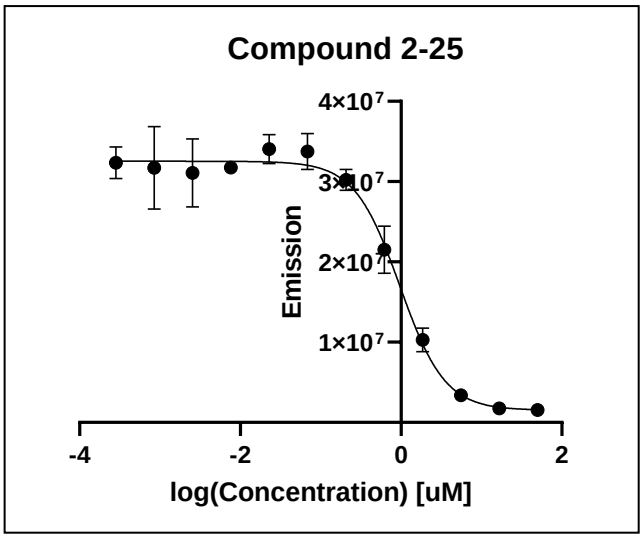

Structure

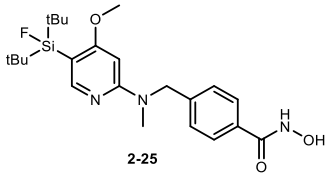

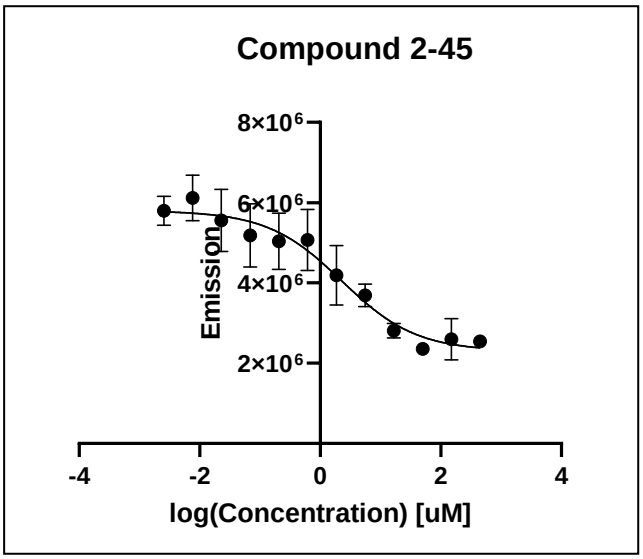

Structure

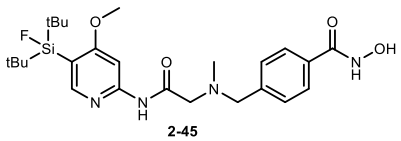

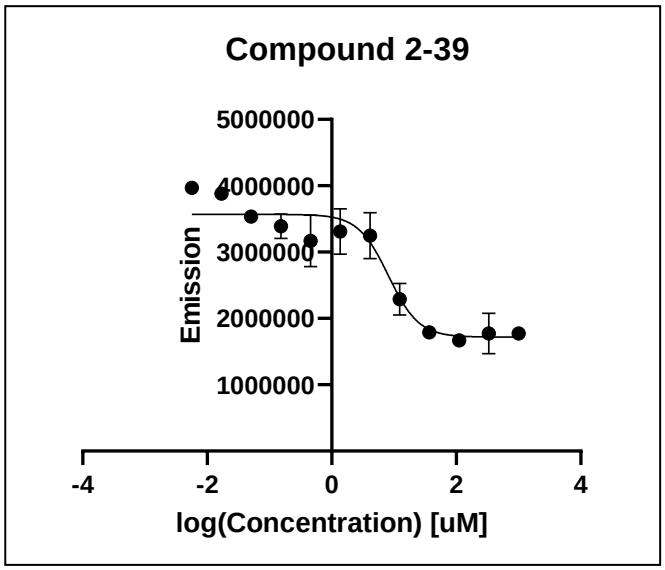

Structure:

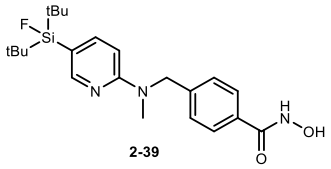

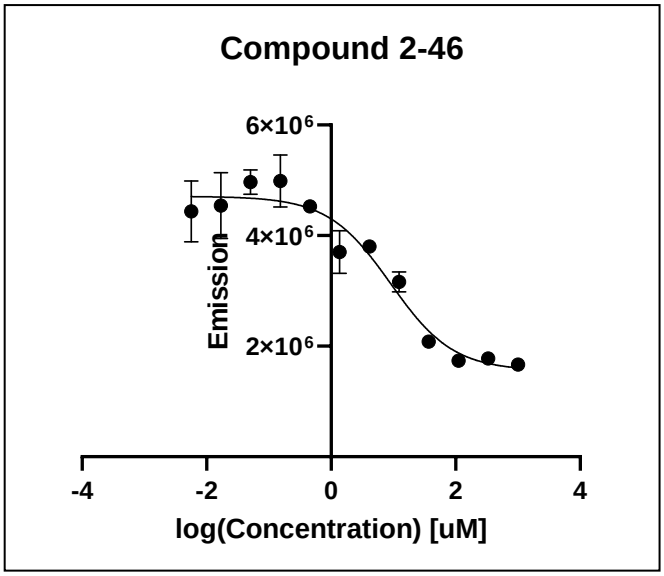

Structure

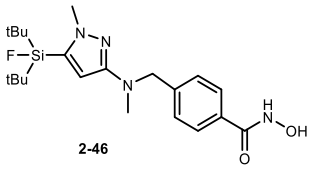

2-46

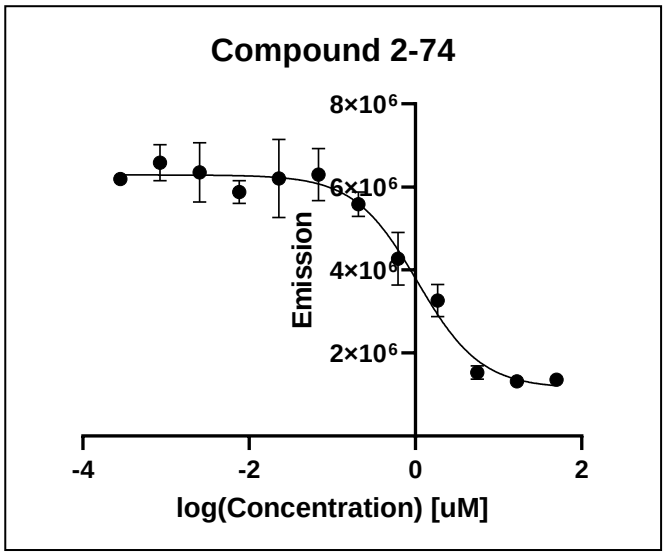

Structure:

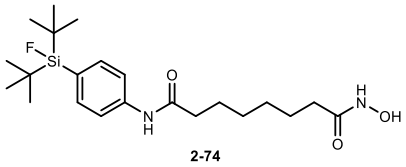

2-74

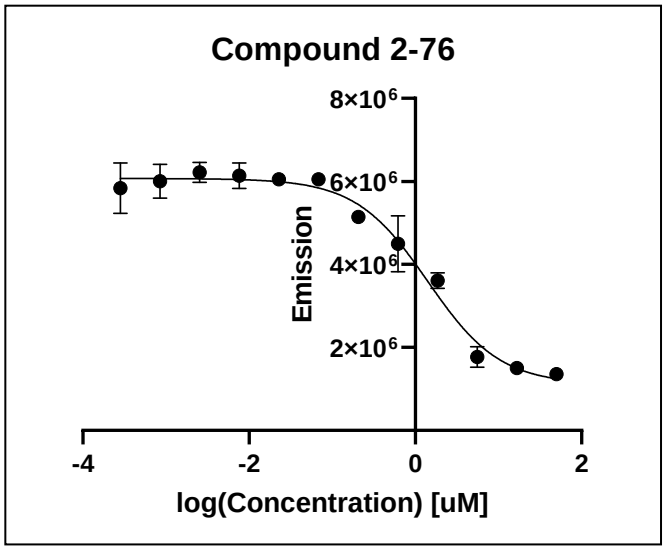

Structure:

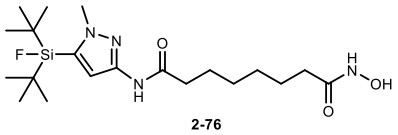

2-76

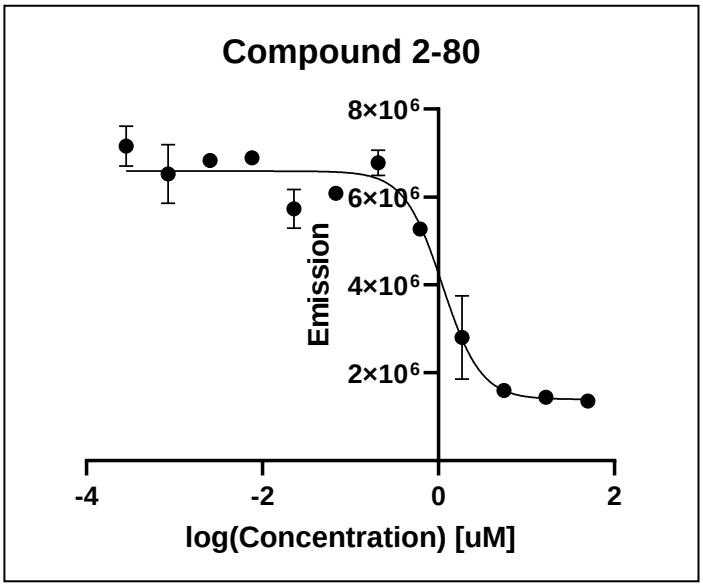

Structure:

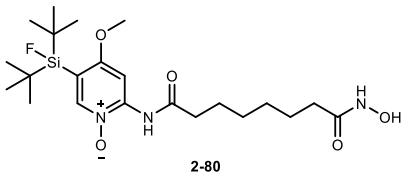

2-80